hangya.balazs_256_24

MTA Doktori Értekezés

(Rövid értekezés)

HANGYA BALÁZS

A BAZÁLIS ELŐAGY SZEREPE A TANULÁSI- ÉS MEMÓRIAFOLYAMATOK SZABÁLYOZÁSÁBAN

HUN-REN Kísérleti Orvostudományi Kutatóintézet

Budapest, 2024

Tartalomjegyzék

Rövidítések jegyzéke

CA: cornu ammonis

GABA: gamma-amino vajsav

HCN: hiperpolarizáció által aktivált, ciklikus nukleotidok által szabályozott nem-szelektív kation csatorna

HDB: a Broca-féle diagonális köteg horizontális szára

MS: mediális szeptum

NB: nucleus basalis

PV: parvalbumin

RPE: jutalom előrejelzési hiba

UPE: előjel nélküli előrejelzési hiba

tSC: théta-oszcillációba ágyazott spektrális komponens

Bevezetés

A tanulás és memória egymással összefüggő folyamatok, melyek tágan értelmezve agyunk változási képességét írják le: ezen változások hatására agyunk azonos körülmények között jelentkező megegyező ingerek hatására különböző módon viselkedhet. Ezek az agyi változások, összefoglaló néven agyi plaszticitás, jellegüket és mechanizmusukat tekintve is rendkívül sokfélék. Ennek megfelelően a memóriafolyamatoknak többféle felosztása is létezik, melyek közül a hosszútávú memória Larry Squire nevével fémjelzett funkcionális felosztásának kontextusába helyezem saját kutatásainkat[1,2].

A hosszútávú memóriát deklaratív és non-deklaratív memóriára oszthatjuk. Az előbbi részei az epizodikus és szemantikus memória: azon képességünk, hogy emlékszünk életünk bizonyos korábbi eseményeire, valamint képesek vagyunk a konkrét eseményektől független tények agyi tárolására[1,3]. A non-deklaratív memória magában foglalja többek között a motoros feladatok és szokások, „beidegződések" elsajátítását (procedurális tanulás), érzékszervi ingerek hatékony feldolgozásának tudattalan tanulását (perceptuális tanulás és „priming"), valamint az asszociatív tanulást (klasszikus [pavlovi] és operáns kondicionálás).

Ezek a memóriafolyamatok sokféle, részben átfedő agyi mechanizmusokat foglalnak magukban. A deklaratív memória folyamataiban a hippokampális formáció (hippokapmusz, gyrus dentatus vagy fogas tekervény, entorhinális kéreg, parahippokampális kéreg, subiculum), míg a non-deklaratív memória létrehozásában az amygdala vagy mandulamag, a neocortex és a striatum szerepét hangsúlyozták[4–7]. Celluláris szinten az agysejtek közötti kapcsolatok, szinapszisok erősségének plasztikus változásai a legtöbb memória típus létrehozásában igazoltan fontos szerepet játszanak[8–10].

Ezek a gyakran jellemzően agykérgi folyamatok jelentős kéreg alatti szabályozás alatt állnak, mely tekintetben a neuromodulátoros rendszereknek kiemelt szerepük van[11,12]. Ezek közül kutatásaink elsősorban az acetilkolin neurotranszmittert ürítő kolinerg rendszert magában foglaló bazális előagyra összpontosítottak[13–17].

Az acetilkolin több időskálán képes a szinapszisok erősségének változásait szabályozni, befolyásolva a változások amplitúdóját, a változásokat létrehozó folyamatokat megengedő időablakok hosszát, de akár magát a változás szabályait, belső logikáját is[12,18–20]. Ezek alapján a kolinerg rendszert a tanulás- és memóriafolyamatok fontos szabályozójának tekintik[9,11,21–24].

Az agyi folyamatok megfelelő időzítése kulcsfontosságú a plaszticitás, ezáltal a tanulás és memória megfelelő működésében: a szinapszis két oldalán (pre- és posztszinaptikus oldal) fellépő elektromos potenciálváltozások megfelelő időbeli szekvenciája és időintervalluma szükséges a szinapszisok erősségének kontrollált változásaihoz[6,19,25]. Ebben az agy ritmikus aktivitása játszik

fontos szerepet[6]: lassabb és gyorsabb ritmusok bonyolult egymásra hatása hangolja össze a tanulásban és memóriában részt vevő agyi hálózatokat[26–30]. Ez az összehangolódás (szinkronizáció) dinamikusan változik (gyakran szintén ritmikus módon) az adott pillanatban fellépő külső és belső szükségleteknek megfelelően[31–33]. Az agy ritmikus tevékenységét agyi oszcillációk, más szóval agyhullámok formában regisztrálhatjuk. Ezek közül a lassabb théta- és gyorsabb gamma-hullámoknak kiemelt jelentőségük van a tanulás és memória szempontjából[6,30,34].

A bazális előagy a kolinerg sejteken kívül egyéb sejttípusokat: GABAerg gátló és glutamáterg serkentő sejteket is tartalmaz[35,36]. Ezek közül a GABAerg sejtek szerepét felismerték a tanulással és memóriával kapcsolatos agyhullámok szabályozásában[37–41]. Emiatt kutatásainkban a bazális előagy kolinerg sejtjei mellett a GABAerg sejtek aktivitását is behatóan vizsgáltuk.

A bazális előagy elülső (rostralis, anterior) részét a mediális szeptum nevű középvonali (medián) struktúra foglalja el, mely elsősorban a hippokampális formációba küldi rostjait, ezáltal a deklaratív memória szabályozásában tulajdonítanak neki fontos szerepet[15,42,43]. A bazális előagy hátsó (caudalis, posterior) részét a Broca-féle diagonális köteg, a substantia innominata és a nucleus basalis (NB, szerzői nevén Meynert-mag) képezi, mely elsősorban a nagyagykéreg (neocortex) és az amygdala kolinerg beidegzését adja, ezáltal vélhetően fontos szerepet játszik az asszociatív tanulásban[15,24].

Kutatásaink két funkcionálisan összefüggő részre oszthatók. A rostralis bazális előagy szerepét a hippokampális memóriafolyamatok szabályozásában vizsgáljuk, különös tekintettel a memóriával kapcsolatos agyhullámokra, melyekről a hippokampusz kontextusában számos ismeret áll rendelkezésünkre[6]. A caudalis bazalis előagy szerepét elsősorban az asszociatív tanulással kapcsolatosan vizsgáljuk, különböző klasszikus és operáns tanulási paradigmákat alkalmazva. Ezen kutatásainkat egereken végezzük.

A bazális előagyi kolinerg és GABAerg neuronok szerepe a tanulási- és memóriafolyamatok szabályozásában

A bazális előagy memória funkciókban betöltött fontos szerepének ténye régóta ismert[13,44]. Bazális előagyi szelektív kolinerg léziók kísérleti állatokban tanulási és memória zavarokhoz vezettek[43,44]. A bazális előagy elektromos stimulációja szenzoros ingerekkel párosítva kérgi plaszticitási folyamatokat indított el, mely folyamatok kolinerg blokkolókra érzékenyek voltak[9,21]. További farmakológiai kísérletek is megerősítették a kolinerg sejtek tanulásban betöltött szerepét[45,46]. A humán agy egy vaszkuláris fejlődési rendellenessége az arteria communicans arterioron kialakuló aneurysma, melynek ruptúrája olyan, a féltekék közé hatoló vérzést okozhat, ami viszonylag szelektív bazális előagyi léziót okoz, mely amnéziához vezet[47]. Régóta ismert az is, hogy Alzheimer-kór során kolinerg funkcióvesztés, majd sejtpusztulás alakul ki, melynek mértéke

korrelál a demencia fokával; erre a megfigyelésre épül az Alzheimer-kór kolinészteráz-blokkolókon alapuló farmakoterápiája[48–50].

Újabban felismerték, hogy a bazális előagy kolinerg sejtjei mellett a GABAerg sejteknek, azon belül is a parvalbumin kalcium-kötő fehérjét kifejező „parvalbuminos" sejteknek is fontos szerepe lehet a tanulási- és memóriafolyamatokban. Erre utal, hogy a teljes bazális előagyi léziók tipikusan súlyosabb memóriazavarokat okoztak, mint a szelektív kolinerg léziók[51–54]. Nemrégiben lehetővé vált szelektív GABAerg léziók létrehozása, mely szintén tanulási és memória problémákat okozott[55]. Elektrofiziológiai kísérletek során azt figyelték meg, hogy a bazális előagy nem-kolinerg sejtjei is reagáltak a tanulás szempontjából fontos viselkedési eseményekre[56,57]. Végül a közelmúltban felismerték, hogy az öregedés és Alzheimer-kór patológiájában nemcsak a bazális előagyi kolinerg, hanem a GABAerg sejtek is részt vesznek[58–61]. A parvalbuminos sejtek kiemelt szerepére utal, hogy kiterjedt agykérgi vetítésekkel rendelkeznek[62], melyek szabályozzák a plaszticitási folyamatok szempontjából fontos gamma-oszcillációkat[41,63], és stimulációjuk javítja a memória funkciókat Alzheimer-kór egér modelljében[58].

A hippokampális théta-oszcilláció szerepe a tanulási- és memóriafolyamatokban

A hippokampális formáció területéről regisztrálható egy 4–12 Hz-es ritmikus populációs aktivitás, az úgynevezett théta-oszcilláció, vagy théta-ritmus[6,64]. Már a 60-as években felfedezték, hogy a théta-ritmus megjelenése felfedező (explorációs) magatartásokhoz köthető[65]. Míg szenzoros ingerek fokozott feldolgozása is növeli a hippokampális théta-aktivitást, legstabilabban mozgás, futás során észlelhető[6]. A théta-ritmus az egyedi neuronok szintjén is detektálható: a legtöbb hippokampális idegsejt théta-ritmikus aktivitást és/vagy a théta-ritmus fázisával összefüggő, ún. fáziskapcsolt aktivitást mutat, valamint a hippokampális idegsejtek intracellulárisan mérhető membránpotenciálját is a théta-ritmusnak megfelelő ritmikus ingadozás jellemzi[66–68].

A jelenleg elfogadott elmélet szerint a théta-oszcilláció olyan ritmikus időzítési folyamatokat tükröz, melyek az epizodikus emléknyomok elraktározását és memóriából való előhívást segítik[69]. A hippokampális piramis sejtek képesek egy-egy théta-ciklus alatt meghatározott időbeli szekvencia szerint aktiválódni[70]. Ezek a théta-szekvenciák tükrözhetik korábbi esemény-láncolatok előhívását, mely talán legkönnyebben sorrendben meglátogatott fizikai helyek reprezentációján keresztül vizsgálható[6,71,72]. Ez alapján feltételezhetően komplexebb eseménysorozatok is hasonló aktivitás szekvenciákat hoznak létre a hippokampuszban[73].

A théta-hullámok különböző fázistartományait összefüggésbe hozták a tanulási- és memóriafolyamatok különböző aspektusaival: feltételezhetően a théta-csúcsok körül jellemzően tanulás, míg a „théta-völgyek" körül memória előhívás történik[46]. Ennek eddig legközvetlenebb bizonyítékát olyan kísérletek szolgáltatták, ahol a hippokampusz aktivitásába a théta-fázis által meghatározott módon (ún. „closed loop") avatkoztak be, és ezzel specifikusan a tárolás vagy az

előhívás zavarát érték el[74]. Az elméletből következik, hogy a memória elraktározása és előhívása ritmikusan, másodpercenként 4–12-szer alternál, melyet nem érzékelünk tudatosan: a kétféle folyamatot egyidejűnek éljük meg. Kutatásaink egyik kérdése közvetlenül azt célozza, hogy hogyan koordinálja az agy a kétféle memória folyamatot az agyi hálózatok szintjén. Ez azért nem nyilvánvaló, mert mind az epizodikus memóriatárolás, mind az előhívás kiterjedt, részben átfedő, de részben eltérő agyi rendszereket érint, így egymástól távol eső agyterületeknek is „tudniuk kell", hogy mikor történik tanulás, és mikor előhívás.

A mediális szeptum szerepe a hippokampális théta-oszcilláció létrehozásában

A hippokampális théta-oszcilláció létrehozásában fontos szerepet tölt be a bazális előagy rostralis magja, a mediális szeptum (MS). A MS ritmusgeneráló szerepét alátámasztja, hogy (1) a MS és a hippokampusz között rostgazdag kétirányú kapcsolat áll fenn[37,75], (2) a MS neuronjai erősen théta-ritmikus, a hippokampuszból mért théta-oszcillációhoz fáziskapcsolt aktivitást mutatnak[39,40], (3) a MS sértése a théta-oszcilláció megszűnését okozza[76], (4) a MS ritmikus aktivitásában beálló kis változásokat a hippokampuszban mért théta-hullám korrelált változásai követik[38], és (5) a mediális szeptális GABAerg neuronok stimulációja théta-oszcillációt hoz létre a hippokampuszban[77,78].

A MS, a bazális előagy többi magjához hasonlóan, három alapvető sejttípust tartalmaz. A GABAerg sejtek fontos szerepet töltenek be a ritmus genezisben, közülük is a parvalbumint (PV), valamint hiperpolarizáció által aktivált nem-szelektív kation csatornát (HCN) kifejező sejtek szerepét találták döntő jelentőségűnek[39,79,80]. A PV-t kifejező sejtek a hippokampusz GABAerg sejtjeit idegezik be, ezért feltételezték, hogy ritmusgeneráló hatásukat a piramis sejteken közvetve kifejtett gátlásoldás (diszinhibíció) révén hozzák létre[37]. A GABAerg sejtek fő serkentő bemeneteit a helyi glutamáterg sejtek adják[81]. Emellett a glutamáterg sejtek egy kis része hippokampális vetítéssel is rendelkezik[82]. Ezen sejtek théta-ritmussal kapcsolatos *in vivo* aktivitása azonban korábban nem volt ismert. A MS fontos, szintén a hippokampuszba vetítő sejtcsoportja a kolinerg neuronok[83,84]. Míg ezen sejtek fontosságát számtalan tanulási és memória folyamatban azonosították[85–87], az epizodikus memóriában fontos théta-ritmus genezisében szerepük a GABAerg sejtek mellett másodlagosnak tűnik. Szelektív léziójuk a théta-hullámok amplitúdó csökkenéséhez vezet, de az oszcilláció nem szűnik meg[76]. A kolinerg sejtek aktivitása legfeljebb mérsékelt théta-ritmicitást mutat a GABAerg sejtekkel összehasonlítva[88,89].

A MS tanulás és memória folyamatban betöltött jelentőségét az is erősíti, hogy emberekben ritkán létrejövő traumás sérülése teljes Korszakov-triászt (anterográd és retrográd amnézia, confabulatio) okoz. A MS viszonylagosan izolált sérülését leggyakrabban az arteria communicans anterioron előforduló aneurysma ruptúrája okozza, mely anterior irányban a féltekék közé hatoló erős artériás vérzést (ún. „jet bleading") hozhat létre[47,90].

A hippokampális gamma-oszcilláció szerepe az emléknyomok létrehozásában és előhívásában

A hippokampális théta-ritmus mellett a gyorsabb (30-80 Hz-es) gamma-ritmus memóriafolyamatokban betöltött szerepét is felismerték[30]. A gamma-ritmus gyakran egymástól távol eső agyterületek összehangolásában játszik szerepet, az ún. „binding hipotézis" szerint biztosítva a két régió közti hatékony információ átadást[29]. A ciklushossza ideális az akciós potenciál időzítéstől függő szinaptikus plaszticitás optimális szabályozásához[26].

A hippokampális tanulási- és memóriafolyamatokkal összefüggésben azt fedezték fel, hogy a hippokampális CA1 (CA: cornu ammonis, az elnevezés a hippokampuszra utal) alrégióban többféle, egymástól eltérő gyorsaságú gamma-ritmus regisztrálható, melyek az egyidejűleg jelen levő théta-oszcilláció eltérő fázisaiban jelennek meg, és vélhetően az epizodikus memória különböző folyamataihoz köthetők[91,92]. A 30-50 Hz-es ún. „lassú gamma-ritmus" a théta-ciklusok völgyeiben jelenik meg, a CA1 és egy másik hippokampális alrégió, a CA3 közti kommunikációt jelzi, és az emléknyomok előhívásában van szerepe. Az 50-100 Hz-es ún. „középső gamma-ritmus" ezzel szemben a théta-hullámok csúcsain jelenik meg, a CA1 és az entorhinális kéreg közti kommunikációt tükrözi, és az epizodikus emléknyomok elraktározásában fontos. Jelen van még a CA1-ben egy ún. „gyors gamma-ritmus" is (100-140 Hz), mely szintén a théta-ciklusok csúcsához kötődik, és feltételezhetően helyi szabályozási folyamatokkal áll összefüggésben[30,93].

A bazális előagyi kolinerg és parvalbuminos neuronok szerepe a figyelmi-, tanulási- és memóriafolyamatok szabályozásában

A tématerülethez tartozó mellékelt publikációk

Hangya B, Ranade SP, Lorenc M, Kepecs A (2015) Central cholinergic neurons are rapidly recruited by reinforcement feedback. *Cell*, 162:1155–1168.

Laszlovszky T, Schlingloff D, Hegedüs P, Freund TF, Gulyás A, Kepecs A, **Hangya B** (2020) Distinct synchronization, cortical coupling and behavioral function of two basal forebrain cholinergic neuron types. *Nat Neurosci*, 23:992-1003.

Hegedüs P, Velencei A, Belval CH, Heckenast J, **Hangya B** (2021) Training protocol for probabilistic Pavlovian conditioning in mice using an open-source head-fixed setup. *STAR Protoc,* 2:100795.

Hegedüs P, Sviatkó K, Király B, Martínez-Bellver S, **Hangya B** (2022) Cholinergic activity reflects reward expectations and predicts behavioral responses. *iScience*, 26:105814.

Hegedüs P, Király B, Schlingloff D, Lyakhova V, Velencei A, Szabó I, Mayer MI, Zelenak Z, Nyiri G, Hangya B (2024) Parvalbumin-expressing basal forebrain neurons mediate learning from negative experience. *Nat Commun*, 15:4768.

Bevezetés

Az acetilkolint mint perifériás idegrendszeri neurotranszmittert viszonylag korán, az 1910-1920-as években fedezte fel Sir Henry Dale és Otto Loewi, és rögtön feltételezték, hogy a központi idegrendszerben is hasonló szerepet tölthet be. Ennek ellenére az agyi kémiai neurotranszmisszió gondolata csak az 1960-as években vált elfogadottá. A központi kolinerg vetítő rendszer feltérképezése a acetilkolin-észteráz enzim szövettani vizualizációjával kezdődött, azonban a kezdeti cikkek összevonták a kolinerg és dopaminerg vetítő rendszereket, mert a dopamin sejtek is jelentős mennyiségű acetilkolin-észterázt fejeznek ki[94]. Újabb áttörést a kolin-acetiltranszferáz ellen termeltetett antitestek hoztak[95], melyek az 1980-as években lehetővé tették a centrális kolinerg rendszer pontos anatómiai feltérképezését[16,96,97].

A kolinerg rendszer funkciójáról alkotott képet alapvetően meghatározta a korai felismerés, hogy ezek a sejtek Alzheimer-kóros betegek post mortem mintáiban erős pusztulást mutattak, ráadásul a demencia klinikai súlyossága pozitív korrelációt mutatott a kolinerg sejtpusztulással[48–50,98]. A kolinerg rendszer kognitív funkciókban betöltött szerepét farmakológiai vizsgálatok is alátámasztották[99–102], bár ezek értelmezését nehezítették a potenciális „off target" hatások és a negatív visszacsatolást közvetítő preszinaptikus muszkarinos m2 receptorok széleskörű jelenléte[103]. A bazális előagy elektromos serkentésével kérgi plaszticitást lehetett kiváltani, mely hatás kolinerg farmakonokra érzékeny volt[9,21]. Mindazonáltal ezek az eredmények sem zárták ki az aspecifikus farmakológiai hatásokat, és az elektromos serkentés sokszor a teljes capsula

internát érinthette számos felszálló pályát egyidejűleg serkentve. A kolinerg sejtek által kifejezett nerve growth factor receptor ellen termelt antitesthez konjugált riboszóma inaktiváló protein (saporin) segítségével szelektív kolinerg léziót lehetett létrehozni, mely szintén megerősítette a kolinerg sejtek szerepét a tanulási és figyelmi folyamatokban[52,76,104,105], de a technikát nehéz volt úgy alkalmazni, hogy a lézió egyszerre teljes, de sejttípus szelektív legyen[44,106]. Emellett lehetőség volt az extraszinaptikus acetilkolin koncentráció becslésére először kérgi likvor mintavételezéssel[107], később mikrodialízis[108] és voltammetriás[109] technikákkal, azonban ezek időfelbontása többnyire a másodperces-perces-órás tartományban maradt. Számos sejttípus esetében a neuronok elektrofiziológiai mérése szolgáltatott kulcsfontosságú információt, például a dopaminerg neuronokat trifázikus akciós potenciál alakjuk alapján azonosítani lehetett majmokban végzett extracelluláris elektrofiziológiai mérések során, mely mérések a nagyhatású „jutalom előrejelzési hiba" hipotézis alapját adták[110]. Ilyen lehetőség azonban a kolinerg rendszer esetében nem adódott, ráadásul a „vak" mintavételezés lehetőségeit korlátozta, hogy a kolinerg sejtek a lokális neuron populációnak régiófüggően mindössze 5-20%-át teszik ki[35,111].

Ebben a helyzetben jelentett technológiai áttörést az optogenetika[112,113], később a GRIN lencséken keresztül végezhető 2-foton mikroszkópia, a száloptikás fotometria és a fluoreszcens acetilkolin szenzorok[114] kifejlesztése. Ezáltal lehetővé vált a kolinerg neuronok in vivo aktivitásának megismerése különböző viselkedéseket végző egerekben, akár szubmilliszekundumos időbeli felbontással és egyedi akciós potenciálok regisztrációjával.

A kolinerg sejtek optogenetikai azonosítása viselkedő egerekben

Ezért elsőként azt a kérdést tettük fel, hogy milyen eseményeket és viselkedési változókat tükröz a bazális előagyi kolinerg neuronok tüzelési mintázata kognitív feladatok során[115]. A kolinerg sejteket optogenetikai sejttípus meghatározás („tagging")[116,117] segítségével azonosítottuk extracelluláris elektrofiziológiai (tetród) elvezetésekben, miközben az egerek egy olyan feladatot végeztek, mely fenntartott figyelmi és tanulási komponenst is tartalmazott, időben elválasztott módon. A fejükön elhelyezett fém rúd segítségével rögzített (röviden „fej-rögzített") egereknek rendszertelenül érkező, halk hangokat kellett gyorsan jeleznie, mely fenntartott figyelmet igényelt[118]. A go/no-go paradigmában egy hang jutalmat jelentett, tehát amennyiben az egerek válaszoltak rá a folyadék jutalmat közvetítő cső megnyalásával, vízcsepp jutalmat kaptak. Egy másik, frekvenciájában jelentősen eltérő hang büntetést jelzett, tehát ha az egér válaszolt rá, az apparátus levegőt fújt az arcára, melyet az egerek bizonyítottan averzívnek tartanak. A jutalom illetve büntetés (azaz az állat szempontjából kimenetel vagy megerősítés) után, a fenntartott figyelemtől időben elválasztva megerősítés alapján történő tanulásra volt szükség a feladat elsajátításához.

Ilyen típusú jól kontrollált, részben automatizált, nagy áteresztőképességű kognitív feladatokat csak nemrégiben kezdtek alkalmazni rágcsálókban. Az úgynevezett „rágcsáló kogníció" tudomány terület születése Carlos Brody (jelenleg Princton Egyetem), Karel Svoboda (jelenleg HHMI Janelia Farm), Zachary Mainen (jelenleg Champalimaud Intézet), Adam Kepecs (jelenleg Missouri

Egyetem) és Naoshige Uchida (jelenleg Harvard Egyetem) nevéhez köthető[119,120], akik abban az időben a Cold Spring Harbor Laboratory idegtudományi programjában dolgoztak. Ezeket a kísérleteket én is itt végeztem, Kepecs Ádám laboratóriumában.

A kolinerg sejtek büntetés hatására aktiválódnak

A kolinerg sejtek tüzelési mintázatait elsőként megfigyelve azt a meglepő megállapítást tettük, hogy a kolinerg neuronok rövid késéssel (átlagosan 18 ms), nagy precizitással (szórás: 3.2 ms) válaszoltak a levegőbefújásos büntetésekre. Ez különösen váratlan volt egy olyan neuromodulátoros rendszer esetében, ahol a gyorsnak nevezett válaszokat is több száz milliszekundumos latenciájúaknak gondolták[109,121]. Az eredmény azt is demonstrálja, hogy a vizsgáló módszereink felbontóképessége milyen erősen tudja korlátozni a megismerést és értelmezést[122].

Azt is megállapítottuk, hogy a kolinerg sejtek aktivitása inkább volt köthető a büntetéssel összefüggő szenzoros élményhez, mint sem az egerek motoros válaszához, és hogy ez a büntetésválasz tanulás nélkül is jelen volt, tehát vélhetően a kolinerg sejtek „veleszületett" tulajdonsága. Az averzív ingerekre adott válasz más érzékszervi modalitásban is jelen volt: amikor büntetésként levegő helyett enyhe elektromos áramot alkalmaztunk, a kolinerg sejtek egy része még gyorsabban (átlagosan 9.5 ms) reagált. A bazális előagy nem azonosított sejtjei között hasonló válaszok nagyon ritkán fordultak elő; ezek számuk alapján akár az azonosítást elkerülő (pl. virális vektorok által nem fertőzött) kolinerg sejtek is lehettek.

A kolinerg sejtek jutalomra adott válasza függ az előzetes elvárásoktól

A kolinerg sejtek jutalom hatására is aktiválódtak. Ez az aktiválódás azonban sokkal változatosabb volt, gyorsasága és pontossága időnként elérte a büntetésre adott kolinerg válaszokét, míg máskor lassabb, nagyobb szórású, átlagosan kisebb amplitúdójú válaszokat figyeltünk meg. Ennek a varianciának a megértése érdekében vizsgáltuk, hogy miként függött a kolinerg jutalomválasz a jutalmat megelőző, azt előre jelző hang hangerejétől (precízebben decibelben mért hangnyomás szintjétől).

Azt állapítottuk meg, hogy minél hangosabb volt a detektálandó hang, annál kisebb kolinerg választ váltott ki utána a jutalom érkezése. Ez azt jelentheti, hogy ha az egér magabiztosabban várja, biztosabb a jutalom érkezésében, akkor az kisebb acetilkolin felszabadulást vált ki, mint a kevésbé várt, meglepőbb jutalom. Emellett a jutalomválaszok amplitúdója anatómiai grádienst is mutatott a nucleus basalis magnocellularis dorsoventralis tengelye mentén: a dorsalisabban elhelyezkedő kolinerg sejtek nagyobb jutalomválaszt mutattak, amit nem lehetett pusztán a tanulás előrehaladásával magyarázni.

A megerősítés meglepetésének matematikai modellje

A szisztematikusan változó jutalomválaszok a megelőző hang hangosságának függvényében arra utaltak, hogy a megerősítés meglepő volta nagyobb kolinerg válaszhoz vezethet. Ennek azonban

ellentmondani látszott az a megfigyelés, hogy a büntetésválaszok nagyon kis varianciával, szinte mindig szinte egyformán jelentek meg.

Ennek az ellentmondásnak a jobb megértése érdekében létrehoztunk egy matematikai modellt. Ez a modell egyrészt tükrözte a feladat egerek számára rejtett változóit: elhangzott-e előre jelző hang, és ha igen, melyik. Ezt egy rejtett Markov modellel reprezentáltuk[123], melyben a fenti állapotok közötti átmeneti valószínűségek megfeleltek a kísérletben alkalmazottaknak. A modellezett egerek a rejtett állapotokat csak az állapotokban tett megfigyelések (megfelel a hang meghallásának, a hangerő függvényében változó valószínűséggel) által, bayesi inferencia segítségével becsülhették. A modellben ezek az állapotbecslések lehetővé tették, hogy a megerősítés meglepő voltát számszerűsítsük. Az állapotbecslések a valódi kísérletben természetesen nem mérhetőek, így csak a fenti modell által váltak megbecsülhetővé.

Érdekes módon azt láttuk, hogy míg a jutalom meglepetésereje szisztematikusan nőtt az előre jelző hangok hangosságának csökkenésével, a büntetések mindig egyformán, maximálisan meglepőek voltak, azaz a kolinerg válaszok pontosan tükrözték a megerősítés meglepőségét nemcsak jutalom, hanem büntetés esetén is. Erre valószínűleg az az intuitív magyarázat, hogy operáns feladatban, ahol a kimenetel alapvetően függ az állat válaszaitól, a büntetés mindig meglepő, mert csak olyan esetben következik be, amikor az állat jutalomra számít – hiszen egyébként nem reagálna az előre jelző hangra egy olyan feladatban, ahol a tanulás már befejeződött, és a kontingenciák (azaz a stimulus-kimenetel összefüggések) változása korábbi élmények alapján nem várható.

Egy nem kolinerg bazális előagyi neuron populáció mutatott szoros összefüggést a fenntartott figyelemmel

Az előre jelző hangot megelőzően az egereknek fenntartott figyelemre volt szükségük a feladat elvégzéséhez[124,125]. Megvizsgáltuk, hogy a kolinerg tüzelés a hang előtti, ún. prestimulus időablakban korrelált-e a fenntartott figyelemmel.

A fenntartott figyelmet úgy manipuláltuk, hogy a hang előtti időtartam hosszának eloszlására exponenciális, vagy bimodális eloszlást alkalmaztunk. A szubjektív hazard elmélet alapján az exponenciális eloszlás egyenletes várakozáshoz vezet, míg a bimodális eloszlás esetén az egerek két kitüntetett időpontban jobban számítanak a stimulus megjelenésére[126]. Az egerek reakcióidejének változása a prestimulus időtartam eloszlásának függvényében jól tükrözte ezt az elméleti predikciót. A kolinerg sejtek aktivitása azonban nem mutatott a prestimulus időtartam eloszlásnak megfeleltethető modulációt.

A fenntartott figyelem valamilyen módon mindig javítja a viselkedési teljesítményt: vagy a reakcióidő, vagy a teljesítmény javul. Megvizsgáltuk, hogy a prestimulus időablakban mutatott tüzelési frekvencia előre jelezte-e a gyorsabb válaszokat vagy a jobb viselkedési teljesítményt. Míg a kolinerg neuronok esetén nem találtunk ilyen összefüggést, a nem azonosított bazális előagyi neuronok mintegy 5%-a szignifikáns negatív korrelációt mutatott a reakcióidővel (azaz nagyobb

tüzelés gyorsabb választ jelzett előre), egy másik 5%-a pedig szignifikáns pozitív korrelációt mutatott a teljesítménnyel.

Bár egyedi szinten nem találtunk összefüggést a prestimulus kolinerg aktivitás és a viselkedési teljesítmény között, populációs szinten gyenge negatív korreláció volt megfigyelhető. Jóllehet matematikai értelemben a negatív és a pozitív előrejelzés ugyanolyan erővel bír, a megfigyelt negatív összefüggés biológiai értelemben nehezen összeegyeztethető azzal az elképzeléssel, hogy a fenntartott figyelem nagyobb kérgi acetilkolin felszabadulással jár. Ezt az elképzést tehát a kísérleteink nem támasztották alá, ugyanakkor az acetilkolin továbbra is fontos lehet a figyelem más formáiban (pl. szenzoros inger által kiváltott figyelem, amint azt legújabb kísérleteink alátámasztják).

Többféle in vivo kolinerg tüzelési mintázat

A kolinerg sejtek optogenetikai azonosítása lehetőséget adott annak a kérdésnek a megválaszolására is, hogy vajon a kolinerg sejtek aktivitás szempontjából homogén csoportot képeznek-e, vagy többféle aktivitás mintázat is előfordul. Erre a kérdésre már saját laboromban, a Kísérleti Orvostudományi Kutatóintézetben kerestünk választ, meglevő és új elektrofiziológiai felvételek alapján[127].

In vivo elektrofiziológiai felvételek alapján megállapítottuk, hogy az azonosított kolinerg neuronok többféle tüzelési mintázatot mutattak. Egyes sejtek akciós potenciál csomagokat, ún. burstöket tüzeltek, míg más sejtek ilyen aktivitást sosem mutattak, helyette reguláris ritmikus aktivitás jellemezte őket. Egy harmadik tüzelési típust az akciós potenciálok közötti ún. interspike intervallumok egyenletes eloszlása jellemzett, alkalmankénti burst tüzeléssel. Ezt a típust a Poisson pontfolyamatokkal mutatott hasonlósága alapján „Poisson-szerű”-nek neveztük.

In vitro kísérletek alapján kétféle kolinerg neuron van jelen a bazális előagyban

Az in vivo kísérletek nem adtak egyértelmű választ arra, hogy a változatos tüzelési mintázatok különböző kolinerg sejttípusokhoz tartoztak, vagy inkább csak különböző állapotokat tükröztek egy egyébként homogén sejttípus populációjában. Ezért in vitro elektrofiziológiai elvezetéseket végeztünk akut szelet preparátumokból prof. Gulyás Attila laboratóriumával (HUN-REN KOKI) együttműködésben, melyek során mind a sejtek belső állapota, mind a külső bemenetei jobban kontrollálhatók.

Ezek során azt állapítottuk meg, hogy a burst tüzelés és a Poisson-szerű tüzelés ugyanannak a kolinerg sejttípusnak két különböző állapotát tükrözte: depolarizáltabb membrán potenciál, valamint erősebb aktiváció hatására Poisson-szerű tüzelés, míg hiperpolarizáltabb membránpotenciál és gyengébb aktiváció hatására burst tüzelés alakult ki. Ugyanakkor a reguláris, ritmikus kolinerg sejtek élesen elkülönültek a burstök tüzelésére képes kolinerg sejtektől, és a fiziológiás membránpotenciál és aktivációs tartományban sosem mutattak burst tüzelést.

Mindkét kolinerg sejttípus képes gyors válaszra viselkedési megerősítés hatására

Egy korábbi elmélet szerint a kolinerg rendszer gyors, ún. „fázisos” hatásait, illetve lassabb, „tónusos” hatásait egy gyorsan reagáló és egy lassan reagáló kolinerg sejttípus hozhatja létre[121,128]. Fenti megfigyeléseinkből logikusan adódott a feltételezés, mi szerint a burst tüzelésű kolinerg sejtek hozzák létre a fázisos, míg a reguláris ritmikus tüzelésű kolinerg sejtek hozzák létre a tónusos kolinerg hatásokat.

Ezzel szemben azt állapítottuk meg, hogy mindkét kolinerg sejttípus azonosan képes volt gyors válaszra büntetés és jutalom után, bár a burst válaszok az egyetlen jól időzített akciós potenciálból álló reguláris kolinerg sejtválaszoknál kvantitatívan erősebbek voltak, valamint a burstök szelektívebben a gyors válaszok során jelentek meg. A kétféle típus átlagos tüzelési frekvenciájában sem találtunk olyan különbséget, mely alátámasztotta volna a reguláris ritmikus kolinerg sejtek kiemelt szerepét a lassan változó kolinerg tónus szabályozásában. Ezek alapján valószínűbb, hogy mindkét sejttípus részt vesz a fázisos és tónusos acetilkolin felszabadulás létrehozásában, és a célterületeken a kétféle bemenet aránya, valamint a célsejtek kolinerg receptor repertoárja lehet meghatározó a kiváltott hatás tekintetében.

A burst tüzelésű kolinerg sejtek szinkron aktivitást mutatnak

Időnként sikerült egyszerre két, vagy néha három kolinerg sejtet is azonosítanunk, a sejtek erős térbeli csoportosulása következtében[129], ezért meg tudtuk vizsgálni, hogy megfigyelhető-e egyidejű, szinkron tüzelés kolinerg sejttípusokon belül és sejttípusok között, mely többnyire közös anatómiai bemenet jelenlétére utal, és jelentős következménnyel bír a célterületen létrejövő hatás erősségére vonatkozóan[130].

Érdekes módon a burst tüzelésű sejtek erős szinkronitást mutattak, nemcsak a burstöket, hanem az egyedi akciós potenciáljaikat tekintve is. A reguláris ritmikus kolinerg sejtek között, valamint vegyes párok esetén jóval kisebb fokú szinkron tüzelést figyeltünk meg, bár még ez is jelentősen magasabb volt, mint két véletlenszerűen választott bazális előagyi sejt közötti egyidejű tüzelés. Ez alapján a burst tüzelésű sejtek potens kérgi aktivációt valósíthatnak meg, mely a kolinerg rendszer régóta ismert tulajdonsága[113,131].

A kolinerg burstök összefüggése az agykérgi aktivitással

Hogy a fenti következtetést közvetlenebbül is teszteljük, a kolinerg sejtek aktivitását a hallókéregből mért helyi mezőpotenciállal vetettük össze. A hallókéreg azért volt logikus választás, mert a felvételeket auditoros tanulási feladat alatt készítettük, és a kolinerg sejteket a nucleus basalis caudalis, hallókéregbe vetítő részéből vezettük el[15].

A kolinerg sejtek optogenetikai aktiválása valóban hallókérgi aktivációhoz, deszinkronizációhoz vezetett, megerősítve korábbi tanulmányokat[113]. Emellett a kolinerg burstök erős összefüggést mutattak a kérgi théta-hullámokkal. A burstök ideje alatt mértnél még erősebb kérgi hatásokat

figyeltünk meg, amikor egyidejűleg mért kolinerg sejtek szinkron tüzelést mutattak, megerősítve, hogy a szinkronizált kolinerg aktiváció, főleg a szinkron burst tüzelés jelentős kérgi hatással bír.

A kolinerg tüzelés és a kérgi aktivitás összefüggése megjósolja a viselkedési válasz kimenetelét

A következő lépésben azt vizsgálatuk, hogy a kolinerg tüzelés és a kérgi aktivitás fenti összefüggései befolyásolhatták-e az egerek viselkedési teljesítményét. Azt figyeltük meg, hogy ha a burst tüzelésű sejtek erős összefüggést mutattak a kérgi aktivitással a hang inger alatt, az előre jelezte, hogy az egér várhatóan nyelvcsapással válaszol a stimulusra. Viszont nem volt különbség abban, hogy az egér épp a go stimulusra adott helyes választ, vagy a no-go stimulusra adott rossz választ. A burst tüzelésű kolinerg sejtek tehát a válaszadás tényét, időzítését jelezték előre.

Ezzel szemben a reguláris ritmikus sejtek szelektíven olyankor mutattak erős összefüggést a kérgi aktivitással a hang inger alatt, amikor az egerek go stimulust követő helyes válaszadásra készültek. A reguláris ritmikus sejtek és az agykéreg összefüggéséből tehát előre lehetett jelezni, hogy az egér helyes választ ad-e a go stimulusra, vagyis az egér teljesítménye is becsülhető volt.

A Broca-féle diagonális köteg horizontális szára kevesebb reguláris ritmikus kolinerg sejtet tartalmaz

Végül azt vizsgáltuk, hogy a reguláris ritmikus és burst tüzelésű kolinerg sejtek egyformán vannak-e jelen a bazális előagy különböző agyterületein. Azt állapítottuk meg, hogy a bazális előagy elülső részéhez tartozó Broca-féle diagonális köteg horizontális szárában (angol rövidítése szerint HDB) nagyobb arányban fordultak elő a burst tüzelésű sejtek, míg a bazális előagy hátsó, caudalis részét alkotó nucleus basalis területén jelentős számban fordultak elő reguláris ritmikus kolinerg sejtek. Ezt az anatómiai különbséget az in vivo és in vitro mérések egyaránt alátámasztották. Ez a bazális előagy topografikus anatómiai vetítései miatt[15,132] alátámasztja azt a korábbi feltételezésünket, hogy a különböző agykérgi és kéreg alatti célterületek eltérő arányban kaphatnak burstös és reguláris ritmikus kolinerg bemenetet.

Szabad felhasználású sztochasztikus pavlovi kondicionálási protokoll egerek tanítására

Korábbi kísérleteinkben a kolinerg aktivitást a megerősítés meglepőségével hoztuk összefüggésbe[115]. Ez jelentős hasonlóságot mutat a dopamin rendszer vizsgálata során leírt jutalom előrejelzési hiba (reward prediction error, RPE) kódolással[110,133], azzal a fontos különbséggel, hogy jutalom előrejelzési hiba kódoláskor a büntetés jellemzően gátlódást vált ki, míg a kolinerg sejtek büntetésre is aktiválódtak. Ez alapján elképzelhetőnek tartottuk, hogy a kolinerg neuronok egy előjel nélküli predikciós hibát, matematikailag az RPE abszolút értékét (unsigned prediction error, UPE) reprezentálják. Ezt időnként „inger fontosságnak” („stimulus salience”) is nevezik, mert általában a viselkedés szempontjából fontos ingerek hatására történő aktivációval jár; mindazonáltal erősen függ az ingerrel kapcsolatos várakozásoktól is.

Ahhoz, hogy ezt az elképzelést közvetlenül tesztelhessük, a kísérletezőnek kontrollálnia kell az egér jutalommal és büntetéssel kapcsolatos elvárásait, vagyis olyan előre jelző ingereket kell alkalmaznia, melyek meghatározott valószínűséggel jeleznek előre jutalmat vagy büntetést. Ez operáns kondicionálási feladatban nem lehetséges, hiszen annak során az állatok viselkedésétől függ a pozitív vagy negatív kimenetel. Ezért a RPE típusú változókat hagyományosan pavlovi kondicionálás során tesztelik, ahol az állatok, Pavlov kutyájához hasonlóan, viselkedésüktől független módon kapnak appetitív vagy averzív ingereket (operáns terminológiában jutalmat vagy büntetést): Pavlov kutyája attól függetlenül kapott vacsorát, hogy fokozódott-e a nyálelválasztása a kondicionált stimulus hatására[134].

Ezért kidolgoztunk egy sztochasztikus pavlovi kondicionálási tanítási protokollt egerek tanítására[135], mely során fej-rögzített egerek kétféle hangot hallanak, melyek különböző valószínűséggel jeleznek előre jutalmat, büntetést vagy semmit (kihagyás). A valószínű jutalmat jelző hang 80%-ban jutalmat, 10%-ban levegőbefújásos büntetést és 10%-ban kihagyást jelez előre. A valószínű büntetést jelző hang 65%-ban büntetést, 25%-ban jutalmat és 10%-ban kihagyást jelez előre. A valószínűségeket azért nem szimmetrikusan állítottuk be, mert a túl sok elkerülhetetlen büntetés megszüntette az egerek motivációját. A teszt így alkalmas meglepő és várt jutalom, valamint meglepő és várt büntetés által kiváltott agyi folyamatok tanulmányozására.

Az egerek a kondicionált stimulus hatására várakozó nyelvcsapásokat („anticipatory licking”, AL) végeztek annak arányában, hogy mennyire vártak jutalmat[133]. A különböző koncionált stimulusok között mérhető AL különbség tehát jelezte, hogy az egerek milyen mértékben tanulták meg az ingerekhez kapcsolódó valószínűségeket (ún. kontingenciákat). A kondicionált stimulus kezdetétől az első nyelvcsapásig eltelt időt alapul véve az egerek reakcióideje is különbséget mutatott, amennyiben a valószínű jutalmat jelző hang után az egerek gyorsabban reagáltak. Az egerek 4-7 nap alatt tanulták meg a feladatot, és két hét alatt professzionális szintre jutottak napi fél-egy órás tanítási ülések hatására. A teljesítmény 2-3 hónapig fenntartható volt, ezen az időtartamon túl kevés tapasztalattal rendelkezünk.

A kolinerg neuron populáció a feltételes és feltétlen ingerekre is válaszol pavlovi kondicionálás során

Kolinerg neuronok aktivitását mértük a fent bemutatott sztochasztikus pavlovi kondicionálási feladat során, hogy megállapítsuk, tüzelési aktivitásuk valóban leírható-e az UPE kódolásával[136]. Először a kolinerg populációt több sejt átlagának szintjén reprezentáló száloptikás fotometria eljárással mértük a kolinerg aktivitást a HDB területén, miután kalcium koncentráció-függő fluoreszcens festéket fejeztettünk ki a kolinerg sejtekben virális gén transzfer segítségével. A módszer segítségével a kolinerg populáció intracellularis kalcium koncentrációjának változást mértük, mely ismerten összefügg a sejtek aktivitási szintjével[137].

Megállapítottuk, hogy a kolinerg sejtek fokozták aktivitásukat mind büntetés, mind jutalom után, akárcsak operáns tanulás során[115]. Emellett a sejtek a jutalmat előre jelző hangokra is reagáltak. A nagy valószínűséggel jutalmat (és kis valószínűséggel büntetést) előre jelző hangok nagyobb

kolinerg választ váltottak ki, mint a kis valószínűséggel jutalmat (és nagy valószínűséggel büntetést) előre jelző hangok. A meglepő jutalom szignifikánsan nagyobb kolinerg aktivációt eredményezett, mint a várható jutalom. Ezek az eredmények kvalitatívan megfeleltek annak, amit az UPE kódolási modell alapján vártunk.

Az optogenetikailag azonosított kolinerg neuronok a jutalmat előre jelző ingerekre, a meglepő jutalomra és a büntetésre aktiválódtak

A száloptikás módszer nem tárta fel, hogy az egyes kolinerg sejtek milyen esetleges egyedi varianciát mutatnak pavlovi kondicionálás során, valamint időbeli felbontása nem alkalmas gyorsabb és lassabb kolinerg válaszok elkülönítésére. Ezért optogenetikai sejttípus azonosítást is végeztünk, melynek során egyedi kolinerg sejtek tüzelési mintázatait elemeztük.

Az egyedi sejtek szintjén is azt állapítottuk meg, hogy a kolinerg aktiválódás jelentősebb volt a valószínű jutalmat, mint a valószínű büntetést előre jelző kondicionált stimulus után. A kondicionált stimulusra adott válaszok lassabbak voltak a büntetést és jutalmat követő gyors, precíz kolinerg tüzelésnél, viszont több akciós potenciált tartalmaznak, ami a célterületen jelentősen eltérő hatásokat okozhat. A meglepő jutalom nagyobb aktivációt okozott az egyedi kolinerg sejtekben, mint a várt jutalom. Mindazonáltal a büntetésválasz mértéke nem függött annak várt vagy meglepő voltától, várakozásaink ellenére. Ezt az magyarázhatja, ha az egerek a jutalommal kapcsolatos várakozásaikat fontosabbnak tartották a büntetés előre jelzésénél. Ezt alátámasztja egy újabb cikk Marshall Shuler laborjából, melyben megmutatták, hogy jelentősebb averziót kiváltó elektromos sokk büntetés esetén kialakult a várakozás függvényében modulált büntetésválasz, jelezve, hogy erősebb büntetés előrejelzése valószínűleg fontosabb az állatok számára[138].

A kolinerg sejt válaszokat kvantitatívan magyarázza egy stimulus által kiváltott, érték-súlyozott UPE modell

Az adataink alkalmasak voltak arra, hogy kvantitatívan is teszteljük, hogy a kolinerg sejtek tüzelése pontosan leírható-e az UPE megerősítéses tanulási („reinforcement learning”) modelljével. A jutalom és a büntetés előrejelzési hibáját két várakozási paraméterrel súlyoztuk, hogy tükrözzük a kétféle kimenetel előrejelzésének eltérő szubjektív fontosságát.

A kolinerg sejtek aktivitását mind egyedi, mind populációs szinten jól leírta a modell, valamint alátámasztotta azt is, hogy a büntetésválasz modulációja valószínűleg a levegőbefújás előrejelzésének alacsonyabb fontossága miatt nem volt detektálható a mintánkban. A megerősítéses tanulási modellre egy tüzelő neuron modellt is építettünk, mely reprodukálta a kolinerg sejtek tüzelési tulajdonságait. Az illesztett modell becslést adott a különböző kimenetelekkel kapcsolatos elvárásra az említett várakozási paramétereken keresztül, mely paraméterek erős pozitív korrelációt mutattak az egerek viselkedési jellemzőivel, konkrétan a kétféle hang után mutatott AL különbségével, mely az eltérő várakozások mértékét mutatja. Ezek

a paraméterek inkább az állatokra és inkább a viselkedési ülésekre voltak jellemzőek, sem mint az egyedi sejtekre, tehát valóban elsősorban a viselkedés varianciájával függtek össze.

Mivel a kolinerg sejtek kihagyás esetén nem mutattak jelentős választ ebben a kísérletben (l. még Robert et al.[139]), csak a stimulus válaszokat modelleztük. A bevezetett várakozási paraméterek miatt a modellt így összességében stimulus által kiváltott, érték-súlyozott UPE modellnek nevezhetjük, mely jól leírta a kolinerg rendszer működését pavlovi kondicionálás során.

A kolinerg sejtek tüzelése előre jelzi a reakcióidőt

Kíváncsiak voltunk, hogy a kondicionált ingereket követő kolinerg aktiváció alkalmas lehet-e az egerek viselkedésének befolyásolására. Először is megállapítottuk, hogy a neuronok válasza megelőzte az egerek első nyelvcsapásait, ami alapján lehetséges, hogy a kolinerg aktiváció hozzájárult az egerek viselkedési reakciójához. Ezt az is altámasztotta, hogy az egerek reakcióideje pozitív korrelációt mutatott a kolinerg sejtek válaszerősségével. Jutalomhoz nem vezető, korai nyelvcsapásokat is megelőzött kolinerg aktiváció, ami szintén arra utal, hogy a kolinerg sejtek aktivitása hozzájárulhat a motoros válasz kiváltásához. Ezt azóta a kolinerg sejtek optogenetikai gátlásának segítségével is megerősítettük: ha a kondicionált stimulus alatt gátoltuk a kolinerg aktivitást, az állatok nem, vagy nehezebben sajátították el a pavlovi tanulási feladatot.

A bazális előagy HDB magjának parvalbuminos GABAerg sejtjei elsősorban a büntetésre válaszolnak

A bazális előagy három jellemző sejttípusa közül a kolinerg sejtek álltak a kutatások gyújtópontjában, korai felfedezésük, egyedi neurotranszmitterük és Alzheimer-kórban korán felismert jelentőségük miatt. Azonban a bazális előagy parvalbumint kifejező GABAerg sejtjei is figyelemre méltóak, mert aktivitásuk lokális kapcsolatokon keresztül összefügg a kolinerg rendszerrel[35,140], szabályozzak a kognitív folyamatokban fontos kérgi gamma-oszcillációkat[41], és szintén szerepük van az Alzheimer-kór és öregedés során fellépő kognitív hanyatlásban[58–61].

Ezért a parvalbuminos HDB sejteket is vizsgáltuk a már bemutatott sztochasztikus pavlovi kondicionálási feladatban[135]. A kolinerg sejtekkel szemben az optogenetikailag azonosított parvalbuminos neuronok elsősorban a büntetések után mutattak jelentős mértékű aktivációt (gyorsaságuk és precizitásuk elmaradt a kolinerg sejtekétől), míg jutalom és koncionált stimulusok után csak kisebb fokú és lassabb, elnyújtott tüzelési frekvenciaemelkedéssel válaszoltak. Ez a büntetésválasz a viselkedési ülések alatt mutatott bizonyos fokú adaptációt (amplitúdó csökkenést), de a megmaradt a viselkedési ülések végén is. A parvalbuminos sejt válaszok, a kolinergekkel szemben, nem voltak érzékenyek a kimenetelek valószínűségére, azaz nem utaltak kimenetel előrejelzési hiba kódolásra.

A HDB parvalbuminos neuronjai averzív ingerekre válaszolnak több érzékszervi modalitásban

Feltételeztük, hogy a bazális előagyi parvalbuminos idegsejtek a tanulási folyamattól és az érzékszervi modalitástól független általános averzív jelzést közvetítenek.

Ezt a feltételezést alátámasztották azok a kísérleteink, ahol naiv, nem tanított egereket vetettünk alá levegőbefújásnak, enyhe elektromos áramnak, vagy róka predátor vizeletének egy erősen averzív szag komponensének. Ezekben a kísérletekben száloptikás fotometriával mértük a parvalbuminos aktivitást, miután a HDB PV-kifejező sejtjeiben virális géntranszfer segítségével GCaMP6s fluoreszcens kalcium szenzort fejeztettünk ki.

A HDB parvalbuminos sejtjeinek optogenetikai gátlása az asszociatív tanulás zavarához vezet

Logikusnak tűnt a feltételezés, hogy a HDB parvalbuminos sejtjei egy olyan általános averziós jelzést közvetítenek a magasabb rendű agyterületek felé, mely elkerülő magatartást vált ki. Ezt a hipotézist kondicionált hely elkerülési tesztben vizsgáltuk, ahol az egerek két, egymástól egy átjárható nyílással elválasztott környezet (doboz) közül választhattak, melyek közül az egyikben a parvalbuminos sejteket optogenetikai úton serkentettük. Azt vártuk, hogy az egerek elkerülik azt a környezetet, ahol a parvalbuminos sejteket aktiváltuk, azonban nem mutattak elkerülést, se másmilyen szignifikáns viselkedési különbséget az apparátus két kompartmentuma között.

Bár az averzív jeleket közvetítő sejtek optogenetikai serkentése gyakran (bár nem mindig, lásd Yawata et al.[141]) elkerülő magatartást vált ki egerekben (ezek egyébként általában glutamáterg neuronok[142–145]), az averzív jelek agyi feldolgozásának többrétű jelentősége van. Az azonnali elkerülésén kívül fontos az averzív ingerekkel kapcsolatos asszociatív tanulás[145], mely segít az állatoknak elkerülni a jövőben a hasonló negatív élményeket. Emellett az averzív stimulusok növelik az éberséget és szelektív figyelmet is kiváltanak[41,62,140]. Ezen agyi folyamatokat szükségszerűen részben eltérő agyi hálózatok szabályozzák.

Ezért teszteltük, hogy a HDB parvalbuminos sejtjei szükségesek-e az averzív ingerek asszociatív tanulásához. Miközben az egereket a sztochasztikus pavlovi kondicionálási feladatra tanítottuk, optogenetikai úton gátoltuk a HDB parvalbuminos sejteket, specifikusan a büntetések alatt és közvetlenül a büntetések után. Ezek az egerek, az optogenetikai aktuátort nem tartalmazó kontrolljaikhoz képest nem tudták azonos idő alatt elsajátítani a feladatot, azaz nem alakult ki náluk AL különbség a kétféle hangot követően. Közelebbről megvizsgálva ez a különbség abból adódott, hogy a kontroll állatokhoz képest nem csökkentették AL tevékenységüket a valószínű büntetést előre jelző hang után. A két hang után bekövetkező első nyelvcsapások idejét összevetve azt tapasztaltuk, hogy a kontroll egerekre jellemző, fent említett reakcióidő különbség sem alakult ki a két kondíció között. Összességében tehát a HDB parvalbuminos sejtjeinek büntetés által kiváltott aktivációja szükséges az averzív asszociatív tanuláshoz, vagyis ahhoz, hogy az állatok képesek legyenek tanulni negatív élményeikből.

A HDB parvalbuminos sejtek több területről kaphatnak averzív információt továbbító jeleket

Kíváncsiak voltunk, mely területekről érkezhet a HDB parvalbuminos sejtjeire az averzív információ. Ezért olyan rabies vírusokkal végzett pályajelölést alkalmaztunk dr. Nyiri Gábor laboratóriumával (HUN-REN KOKI) együttműködésben, mely alkalmas transzgenikus egerekben adott sejttípus monoszinaptikus bemeneteinek azonosítására.

A HDB parvalbuminos sejtek legszámosabb bemeneti populációját a laterális hypothalamus sejtjei adták. Ezt követte a laterális és mediális szeptum, a hypothalamikus preoptikus terület, a Broca-féle diagonális köteg vertikális szára, medián raphe mag és a ventrális pallidum. Ezek közül a magok közül több is ismerten hordoz averzív információt, például a laterális hypohtalamus[146–148], a mediális szeptum[149,150], a ventrális pallidum[144,151] és a raphe magok[142,152,153]. A raphe bemenetnek fontos jelentősége lehet a HDB parvalbuminos sejtjeinek averzív válaszainak kialakításában, mert ezek gyors, potens felszálló glutamáterg pályákon keresztül közvetítik hatásukat[142]. Ezzel összhangban állt az a megfigyelésünk, hogy a HDB parvalbuminos sejtek főleg a medián raphe vezikuláris glutamát transzporter 2 vagy 3 fehérjéket kifejező glutamáterg serkentő sejtjeitől kaptak inputot. Ugyanakkor az is elképzelhető, hogy a HDB több input területről integrál averzív információt. A jövőben a bemeneti populációk sejttípus specifikus azonosítása, és specifikusan a vetítő populációk aktivitásának vizsgálata és manipulálása adhat erre pontosabb választ.

A HDB parvalbuminos sejtjei limbikus területekre vetítenek

Anterográd pályajelölésekkel vizsgáltuk, hogy milyen célterületekre küldenek vetítéseket a HDB parvalbuminos sejtek. Ezek között szerepeltek közeli bazális előagyi területek: a Broca-féle diagonális köteg vertikális szára és a mediális szeptum, neo- és archicorticalis területek, mint a retrosplenialis kéreg és a hippokampusz, emellett mammillaris és supramammillaris magok, anterior thalamus, laterális szeptum és prefrontális kérgi területek. Ezen területek jelentős része a limbikus rendszerhez tartozik, azaz a HDB parvalbuminos sejtek széles körben beidegzik a limbikus rendszert.

Elektronmikroszkópos módszerekkel a megjelölt parvalbuminos axonok különböző célsejtjeit tudtuk azonosítani: a mediális szeptumban kolinerg és mediális szeptális parvalbuminos sejteket, a hippokampusz CA1 területén parvalbuminos és calretinint kifejező GABAerg sejteket, a retrosplenialis kéreg területén pedig szintén parvalbuminos interneuronokat. Ez alapján a HDB parvalbuminos sejtek vélhetően főleg egyéb gátló sejteket idegeznek be, ezáltal a serkentő sejtek aktivációjához, ún. gátlásoldáshoz (diszinhibícióhoz) vezetve.

A HDB parvalbuminos sejtjei homogén averzív információt „sugároznak” célterületeik felé, de az információ feldolgozása célterületenként jelentősen eltérhet

Megvizsgáltuk, hogy a HDB parvalbuminos sejtek hasonló információt közvetítenek-e a legsűrűbben beidegzett célterületeik (mediális szeptum, retrospleniális kéreg, hippokampusz CA1) felé. Ennek érdekében a parvalbuminos sejtek rostjaira jellemző aktivitást mértük a célterületeken végzett száloptikás fotometriával, miközben a HDB parvalbuminos sejtekben GCaMP6s fluoreszcens kalcium szenzort fejeztettünk ki. Egyidejűleg szomatikus aktivitást is regisztráltunk a HDB-ben, mely megerősítette korábbi méréseinket, és erős büntetés által kiváltott aktivációt tárt fel.

A három vizsgált célterület mindegyikén a szomatikus aktivációs mintához hasonló büntetésválaszokat regisztráltunk. Míg dinamikájukban hasonlóak voltak a parvalbuminos válaszok, a legrobusztusabb aktiváció a CA1 területén volt megfigyelhető.

Ezután in vitro akut szelet kísérletekben vizsgáltuk, hogy milyen módon hat a parvalbuminos axonok optogenetikai aktiválása a célsejtekre (ún. optogenetika által asszisztált hálózat térképezés módszere) a három kiválasztott célterületen. Ezek a kísérletek megerősítették a célsejtek típusának fent bemutatott elektron mikroszkópos azonosítását. Ezen felül azt is feltárták, hogy a CA1 sejtjei nagyobb amplitúdójú, gyorsabb áramokkal válaszoltak a retrospleniális kéreg sejtjeinél, míg a mediális szeptum sejtjei átmeneti paramétereket mutattak. Páros stimulálást („paired pulse”) alkalmazva megállapítottuk, hogy a HDB parvalbuminos sejtek a CA1-ben depresszáló, míg a retrospleniális kéregben facilitáló szinapszisokat hoztak létre. A mediális szeptum itt is átmenetet képezett, enyhe rövid távú facilitációt mutatva.

A száloptikás fotometria során mért robosztus büntetésválaszok, valamint a hatékony posztszinaptikus aktiváció a CA1 esetén arra utal, hogy ez a célterület különösen fontos lehet a HDB parvalbuminos sejtek hatásainak kialakításában. Ez összhangban van a hippokampusz asszociatív tanulásban betöltött ismert szerepével[4].

A bazális előagyi kolinerg és parvalbuminos neuronok vizsgálatának jelentősége

A bazális előagy fontos szerepet tölt be a kognitív folyamatok szabályozásában[42,154,155], emiatt a kognitív folyamatok patológiájában (elsősorban a demenciák kialakulásában) is jelentősen érintett[50,58,156]. Ezzel kapcsolatban jelentős mennyiségű, értékes információ gyűlt össze léziós, farmakológiai, elektromos stimulációs, elektrofiziológiai és acetilkolin koncentráció becslésére irányuló mikrodialízis és voltammetria kísérletek révén[13,21,44,121]. Mindeközben azonban a bazális előagyi kolinerg és GABAerg sejtek kognitív viselkedéssel összefüggő aktivitás mintázata ismeretlen maradt, elsősorban technikai korlátok következtében. Az ilyen ismeretek más sejttípusoknál jelentősen hozzájárultak a neuronális hálózatok működésének megértéséhez[110,117,157–160], ezért feltételeztük, hogy hasonló információ a bazális előagy működésének jobb megértéséhez is hozzájárulhat[161].

Ezért elsőként végeztük el a bazális előagyi kolinerg és parvalbuminos GABAerg sejtek optogenetikai azonosítását tanulási feladatokat végző egerekben. Ezek a kísérletek meglepő eredményekhez vezettek. A kolinerg sejtek aktivitása nem mutatott változásokat közepes időskálán a fenntartott figyelemmel összefüggésben, ahogy mások és mi is feltételeztük[109,124], viszont nagyon gyors és precíz aktivációt mutatott viselkedési megerősítés, azaz jutalom és büntetés után[115,127,136]. Ilyen gyors és pontos válaszok leginkább egyes szenzoros rendszerekre jellemzőek, és nem feltételezték jelenlétüket[121,162] a lassabbnak tartott neuromodulátoros rendszerek esetében. A gyors válaszok mindazonáltal értelmet adtak azoknak az in vitro megfigyeléseknek, melyek szerint a kolinerg rostok aktivitásának időzítése akár milliszekundumos skálán is nagy jelentőséggel bírhat a hippokampális és nagyagykérgi plaszticitási folyamatok szabályozásában[12,19,20,163].

A másik meglepetést az jelentette, hogy a kolinerg aktivitás sokban hasonlított a dopamin sejtek által már felfedezett[110,133] jutalom előrejelzési hiba kódoláshoz[115,136]. Ezt a fajta aktivitást többnyire a dopaminerg rendszer sajátjának tekintették, és a kolinerg rendszer kódolási tulajdonságait általában ehhez képest ortogonálisan határozták meg (pl. tanulási ráta, fenntartott figyelem)[11,123,164]. Ha ehhez hozzávesszük a neuromodulátoros rendszerek egyéb funkcionális hasonlóságait, pl. a szenzoros feldolgozás erősítése a kérgi befolyás rovására[123,165], újra felmerül a régi kérdés, hogy miért van ennyi neuromodulátoros rendszerünk, azaz mi a funkcionális munkamegosztás közöttük a kognitív folyamatok szabályozása terén? Laborunk jelenleg aktívan vizsgálja ezt a kérdést a fő neuromodulátoros rendszerek (kolinerg, dopaminerg, szerotonerg és noradrenerg) közvetlen összehasonlítása útján. Cikkeink új kutatási irányt jelöltek ki: első cikkünk óta számos munkacsoport és tanulmány megerősítette és kibővítette eredményeinket[139,166–168].

A kolinerg neuronokkal szemben a parvalbuminos sejtek nem mutattak előrejelzési hiba típusú aktivitást, azaz nem befolyásolta tüzelésüket a pozitív vagy negatív kimenetellel kapcsolatos várakozás, annak ellenére, hogy lokális beneti sejtjeik között kolinerg sejtek is szerepelhetnek[35,140]. Ezzel szemben elsősorban büntetés hatására aktiválódtak, ami tudomásunk szerint feltételezés szintjén sem jelent meg eddig az irodalomban. Optogenetikai gátló kísérletek segítségével igazoltuk, hogy ez a fajta aktivációjuk a negatív élmények hatására fellépő asszociatív tanuláshoz szükséges[169]. Mivel ismert, hogy a bazális előagyi parvalbuminos sejtek akár gyors időskálán is képesek szabályozni az éberséget és a figyelmet[35,41], valószínűleg az agykéreg gátlásoldás révén megvalósuló helyi aktivációján keresztül a tanuláshoz szükséges figyelem („attention for learning”[170,171]) létrehozásában is fontosak.

A kolinerg és parvalbuminos sejtek esetében megfigyelt, viselkedési visszajelzést követő neuronális események egyfajta „tanító szignál”-okat jelenthetnek[172,173], melyek a visszajelzést követő kérgi plaszticitási, tanulási folyamatokat irányítják. Ezáltal a bazális előagy vetítő rendszerei fontos szerepet tölthetnek be az asszociatív tanulásban. Ezek a folyamatok szükségesek ahhoz, hogy neutrális ingerekhez értéket tudjunk rendelni, például megtanuljuk, hogy miért érdemes

dolgozni, tanulni, vagy milyen értékekért érdemes kiállni, és hogyan fektessünk saját és mások hosszútávú jövőjébe.

A bazális előagyi vetítő rendszerek mélyebb ismerete szintén hozzájárulhat az ezeket a sejteket érintő betegségek, főleg az Alzheimer-kór hatékonyabb terápiájához. Elképzelhető például, hogy az általunk feltárt kétféle kolinerg sejt eltérően vesz részt a betegség kialakulásában, mely szelektívebb farmakoterápiás vagy génterápiás lehetőségek alapja lehet. Ez az irány is aktív kutatási téma laborunkban.

A tanulási- és memóriafolyamatokban fontos hippokampális oszcillációk létrehozása és szabályozása

A tématerülethez tartozó mellékelt publikációk

Kocsis B, Martínez-Bellver S, Fiáth R, Domonkos A, Sviatkó K, Schlingloff D, Barthó P, Freund TF, Ulbert I, Káli S, Varga V, **Hangya B** (2022) Huygens synchronization of medial septal pacemaker neurons generates hippocampal theta oscillation. *Cell Rep*, 40:111149.

Király B, Domonkos A, Jelitai M, Lopes-dos-Santos V, Martínez-Bellver S, Kocsis B, Schlingloff D, Joshi A, Salib M, Faith R, Barthó P, Ulbert I, Freund TF, Viney TJ, Dupret D, Varga V, **Hangya B** (2023) The medial septum controls supra-theta oscillations. *Nat Commun*, 14:6159.

Bevezetés

Nagyobb felületű (és ezáltal jellemzően kisebb impedanciájú) elektródák segítségével az agyból olyan feszültségválaszok mérhetők, melyek nem egy-egy idegsejt, hanem az elektróda környezetében található nagyobb sejtpopuláció elektromos aktivitását jellemzik. Az ilyen módon mért agyi populációs aktivitás jellemzően kvázi-ritmusos: nem szabályosan szinusz hullám-szerű, de frekvencia spektrumában sokszor jól elkülönülő csúcsok figyelhetők meg, melyek a nyers adatot megfigyelve is ritmikus tevékenységnek imponálnak[6].

Ezek a ritmikus agyi tevékenységek a 20. század első fele óta folyamatosan foglalkoztatják az agykutatókat, mióta Hans Berger az elektroenkefalográf 1924-es megalkotása után felfedezte az agykérgi alfa hullámokat[174]. A jelenleg uralkodó elmélet szerint a távoli agyterületek ritmikus szinkronizációja segíti az információ átadást azáltal, hogy a fogadó sejtek időzített módon megfelelő serkenthető fázisba kerülnek[91,175]. Az agyi oszcillációk egy területen belül segíthetik a többféle folyamat ritmikus alternáló ütemezését, például emléknyomok eltárolását és előhívását[69]. A legtöbb agyi funkció területén tetten érhető a ritmikusság, beleértve látszólag folytonosnak megélt szenzorimotoros és kognitív funkciókat is, mint például a figyelem[29,176], vagy az érzékelés[177,178].

A tanulási- és memóriafolyamatok terén kiemelten fontos két hippokampuszban mérhető agyi ritmus, a 4–12 Hz-es théta-oszcilláció[38,40] és a 30–140 Hz-es gamma-oszcilláció[30]. Azt vizsgáltunk, hogy hogyan, milyen hálózati szintű mechanizmusokkal hozza létre az agy ezeket a ritmikus aktivitásokat, annak érdekében, hogy jobban megértsük a tanulás és memória agyi folyamatait.

A mediális szeptum és a hippokampusz együttes vizsgálata egerekben és patkányokban

Ismert, hogy a hippokampális théta-ritmus létrehozásában fontos szerepet játszik a bazális előagy elülső középvonali magja, a mediális szeptum[80,179]. A mediális szeptum léziója a hippokampális théta-ritmus eltűnését okozza[76], míg stimulációja aktiválja a hippokampuszt és théta-ritmust vált ki[180–182]. A mediális szeptum GABAerg sejtjei hippokampális GABAerg interneuronokat idegeznek

be[37], és a hippokampális thétához erősen fáziskapcsolt aktivitást mutatnak[39,80,183]. A mediális szeptum GABAerg vetítő sejtjein belül kiemelt szerepe van a parvalbumint[39] és hiperpolarizáció által aktivált kation-csatornát (HCN) kifejező sejteknek[80], melyek aktivitás változásai megelőzik a hippokampusz korrelált változásait[38].

A mediális szeptum sejtjeinek egy populációja állandó théta-ritmikus aktivitást mutatnak, függetlenül attól, hogy a hippokampuszban mérhető-e théta-oszcilláció. Ezeket a sejteket a hippokampális théta-ritmusképző, „pacemaker" sejtjeinek tartják[38]. Azonban nem volt ismert, hogy az egyes pacemaker sejtek milyen mechanizmussal hozzák létre a théta-ritmust a hippokampuszban. Ennek kiderítése érdekében egyidejűleg számos egyedi mediális szeptális neuron aktivitását regisztráltuk modern szilikon elektróda vektorok segítségével. Ezalatt hippokampális helyi mező potenciált is mértünk, mely a hippokampális populációs aktivitásról adott képet. Az utóbbi szignál segítségével spektrális elemzéseket alkalmazva detektáltuk, hogy mikor volt jelen a théta-ritmus a hippokampuszban. Ezeket a méréseket altatott patkányokban, altatott egerekben és éber, szabadon mozgó egerekben is elvégeztük[184]. A kísérletekben dr. Varga Viktor (HUN-REN KOKI) és prof. Ulbert István (HUN-REN TTK) laboratóriumai is közreműködtek.

A feltételezett pacemaker sejtek állandó théta-ritmikus aktivitást mutatnak

A mediális szeptális sejtek théta-, illetve annál lassabb, delta-frekvencia (0.5–4 Hz) sávba eső ritmikus aktivitását auto-korrelációjuk (azaz önmagukkal való időfüggő lineáris korrelációjuk) statisztikai elemzésével határoztuk meg. Mindhárom felvételtípusban azonosítottuk a mediális szeptum feltételezett ritmusgeneráló sejtjeit. Ezek a neuronok mind hippokampális théta jelenlétében, mind annak hiányában théta-ritmikus aktivitást mutattak.

Ezeket a sejtek hippokampális théta-oszcilláció jelenlétében gyorsabb tüzelés, valamint a hippokampális helyi mezőpotenciálból szűrt théta-oszcilláció ciklusaihoz viszonyított fáziskapcsoltság jellemezte. A sejtek cirkuláris statisztikai módszerrel megállapított átlagos fázisa két egymással ellentétes fázisérték köré csoportosult, ahogy azt korábbi tanulmányok már megállapították[38,185]. A ritmusképző sejtek théta-ritmikus akciós potenciál csomagokat: burstöket tüzeltek, ez alapján théta-burst tüzelésű sejteknek is nevezik őket.

A feltételezett „követő", théta-kihagyó és tónusosan aktív mediális szeptális neuronok

A mediális szeptum többi sejtje különböző kategóriákba volt sorolható tüzelési mintázatuk alapján. Az ún. „követő" sejtek követték a hippokampális helyi mező potenciálváltozásait abban az értelemben, hogy hippokampális théta jelenlétében théta-ritmikus aktivitást mutattak, viszont ez a fajta ritmikusság nem volt jelen, amikor a hippokampuszból is hiányzott a théta; helyette lassabb delta-ritmikus aktivitás (patkányokban gyakoribb), vagy nem ritmikus aktivitás (egerekben gyakoribb) jelent meg. Megjegyzem, hogy a „követés" nem feltétlenül jelentett időbeli késést a hippokampuszhoz képest, ezért ennek a félreértésnek az elkerülése érdekében a „követő" helyett már a talán nehézkesebb, de pontosabb „théta-asszociált théta-ritmikus" elnevezést használjuk.

A théta-kihagyó sejtek[186] a hippokampális thétához fáziskapcsolt aktivitást mutattak, de nem tüzeltek minden théta-ciklusban, ezért ők maguk théta-ritmikusságot nem mutattak. Ezen sejtek egy része többé-kevésbé szabályosan minden második théta-ciklusban tüzelt, ezáltal hippokampális théta jelenlétében is lassabb, delta-ritmicitást mutatott. Érdekes módon egerekben nagyon kevés théta-kihagyó sejtet találtunk, valószínűsítve, hogy egyes korábbi feltevésekkel szemben a mediális szeptális théta-kihagyó sejtek nem szükségesek a nevezetes entorhinális grid sejtek[187] kialakulásához[188].

Mind egerekben, mind patkányokban megfigyeltünk tónusosan aktív sejteket, melyek mások által leírt tüzelési mintázatuk[179,189,190] és saját korábbi megfigyeléseink[127] alapján kolinerg neuronok lehettek. Ezt alátámasztotta az is, hogy bár mutattak théta-frekvencia sávba eső ritmikusságot, nem voltak fáziskapcsoltak a hippokampális thétához. Korábbi publikációk alapján ezen sejtek théta-ritmikussága, mely a hippokampális thétánál többnyire gyorsabb, nagyagykérgi eredetű[191,192].

A mediális szeptális ritmusképző sejtek szinkronizálják ritmikus burst tüzelésüket

A mediális szeptális neuronok fenti karakterizálását követően rátértünk fő kérdésünkre: miként hozzák létre a mediális szeptális ritmusgeneráló sejtek a tanulási- és memóriafolyamatokhoz elengedhetetlen hippokampális théta-oszcillációt.

Ehhez egyidőben regisztrált ritmusképző sejtek egymással való szinkronizációját vizsgáltuk, feltételezve, hogy az egyedi pacemaker sejtek együttes aktivitásának megváltozása okozza a hippokampusz mediális szeptális bemenetének olyan változását, mely a hippokampuszban théta-ritmikus aktivitáshoz vezet. Amikor a ritmusos sejtek frekvenciáját összehasonlítottuk, azt figyeltük meg, hogy ezek a frekvenciák jelentősen különbözőbbek voltak hippokampális théta-ritmus hiányában, mint jelenlétében (az egyedi sejtek frekvenciájában mutatkozó különbségekkel való körültekintő normalizálás után). Ezt a frekvencia-szinkronizációs folyamatot abban is tetten értük, hogy a mediális szeptális pacemaker párok közötti koherencia egy szűk thétán belüli frekvencia sávban megerősödött hippokampális théta-ritmus jelenlétében.

A mediális szeptum hálózati modellje Huygens-szinkronizációra utal

A fenti eredmények alapján feltételeztük, hogy a mediális szeptum ritmusgeneráló sejtjei nagyobb tónusos serkentést kapva, és ennek következtében többet tüzelve több információt adnak át egymásnak gátló szinapszisaikon keresztül, melynek hatására frekvenciájuk összehangolódik (egymáshoz hasonlóbbá válik). Ennek következtében átlagos együttes aktivitásuk, mely a mediális szeptum hippokampális kimenetét meghatározza, jelentősen erősebb théta-ritmikusságot mutat, és az így közvetített ritmikus gátlásoldás théta-frekvencián szinkronizálja a hippokampális hálózatot is. Ez azt is jelenti, hogy egy homogén GABAerg neuron populáció – kitüntetett alcsoportok jelenléte nélkül – képes lehet a hippokampális théta-ritmus létrehozása, a korábbi modellekkel szemben[193,194].

Ennek tesztelésére egy egyszerű konduktancia-alapú egy-kompartmentumos ritmikus gátló sejtekből álló neuronmodellt építettünk dr. Káli Szabolccsal (HUN-REN KOKI) együttműködésben. A modell sejtek serkentő bemeneteik erősségének függvényében képesek voltak nem-ritmikus, delta-ritmikus és théta-ritmikus aktivitásra, melyet a késleltetett egyenirányító kálium csatornájuk és a HCN csatornájuk határozott meg. A modell neuronokból gátló szinapszisok modellezésével épített hálózati modell az összes kísérletes adatot reprodukálta, és képes volt nagyobb tónusos külső serkentés alatt théta-szinkronizációra, majd csökkenő serkentés esetén újból deszinkronizációra. A modell pacemaker neuronokra is teljesült, hogy ritmikussági frekvencia különbségük hippokampális théta alatt kisebb volt, aminek következtében egy nagyobb amplitúdójú théta-ritmusos kimenetet hozott létre a hálózat. Ezt a fajta frekvencia-szinkronizációs mechanizmust Huygens-szinkronizációnak nevezik Christiaan Huygens azon 17. századi megfigyelése alapján[195], hogy a közös alapon nyugvó ingaórák szinkronizálják frekvenciájukat az alapon keresztül terjedő gyenge mechanikus kölcsönhatások révén[196–198].

A parvalbuminos mediális szeptális sejtek nagy része théta-ritmikus, míg a glutamáterg sejtek “tónusos théta ON” sejtek

Elvégeztük a mediális szeptum GABAerg, parvalbuminos GABAerg és glutamáterg sejtjeinek optogenetikai azonosítását altatott egerekben. Ezekből a kísérletekből kiderült, hogy a korábbi eredményeknek megfelelően a parvalbuminos GABAerg sejtek nagy része théta-ritmikus aktivitást mutatott[39,80], míg a teljes GABAerg populáció vizsgálata alapján a nem parvalbuminos GABAerg sejtek között a théta-ritmikus aktivitás valószínűleg ritka.

A mediális szeptális glutamáterg sejtek között csak kevés théta-ritmusos sejtet találtunk, és nagy részük olyan tónusos tüzelést mutatott, mely a hippokampális théta-ritmus jelenlétében gyorsabbá vált. Az ilyen aktivitást korábban Bland és munkatársai „tónusos théta ON” aktivitásnak nevezték[199]. A glutamáterg mediális szeptális sejtek in vivo aktivitása korábban nem volt ismert. A felfedezésnek az a jelentősége, hogy a mediális szeptális glutamáterg sejteken keresztül érkezhet az a tónusos serkentő bemenet a parvalbuminos pacemaker sejtekre, mely a pacemaker sejtek erősebb aktivációján keresztül végül frekvencia-szinkronizációhoz vezet. Ezt támasztja alá az a korábbi felfedezés, hogy a mediális szeptum GABAerg sejtjein a serkentő szinapszisok nagy része helyi glutamáterg sejtektől származik[81].

A fenti lehetőség tesztelése végett optogenetikai úton aktiváltuk a mediális szeptum glutamáterg sejtjeit a théta-frekvenciasávon kívül eső frekvenciával (20 Hz). Ez az ingerlés a hippokampuszban théta-oszcillációt váltott ki, alátámasztva a feltevést, hogy a parvalbuminos sejtek a rájuk érkező, lokális glutamáterg sejtekből származó tónusos serkentést ritmikus gátlássá „alakítják”.

Thétánál gyorsabb („supra-théta”) komponensek jelenléte a mediális szeptumban

A mediális szeptum sejtaktivitásában a thétánál gyorsabb, ún. „supra-théta” komponensek is jelen vannak. Ezek a spektrális komponensek a béta- (12–30 Hz) és a gamma-sávokba (30–140 Hz) esnek. Ezen spektrális komponensek jelenlétét bizonyítottuk olyan elektrofiziológiai méréseken

keresztül a HUN-REN KOKI Kéreg Alatti Moduláció Kutatócsoportjával együttműködésben, melyek során éber egerek mediális szeptumából többszörös egysejt-elvezetést, ezzel párhuzamosan a hippokampusz CA1 területéről pedig réteg-függő helyi mező potenciál elvezetéseket végeztünk. A supra-théta spektrális komponensek mind a szeptális, mind a hippokampális elvezetések frekvencia spektrumában megtalálhatóak voltak.

Egy új statisztikai eszköz, az ún. Empirikus Mód Dekompozíció[200,201] segítségével torzítatlan módon, rögzített frekvencia sávok meghatározása nélkül 5 supra-théta komponenst azonosítottunk a CA1-ben, megerősítve egy korábbi tanulmány eredményeit[200]. Ezek a béta- (20 Hz), lassú gamma- (32 Hz), alsó közepes gamma- (50 Hz), felső közepes gamma- (74 Hz) és gyors gamma-sávoknak (179 Hz) voltak megfeleltethetőek. A gyorsabb frekvencia sávok amplitúdóját a théta-oszcilláció fázisa korábban leírt módon modulálta[200,202], azaz a béta/gamma-ciklusok preferenciálisan adott théta-fázisokon jelentek meg[200,203].

A supra-théta spektrális komponenseket ez alapján, egy korábbi tanulmányhoz hasonlóan tSC-nek, azaz „theta-nested spectral component”-nek neveztük. A théta-ciklusok tulajdonságai összefüggéseket mutattak a bennük dominánsan fellelhető tSC-kkel: a domináns tSC-t nem tartalmazó théta-ciklusok lassabbak voltak, míg a tSC4-es közepes gamma-ciklusokat tartalmazó théta-ciklusok voltak a leggyorsabbak. A rövid és átmeneti théta-szakaszokat a tSC1-es béta-ritmus dominálta. Az egerek gyors futási szakaszaira megint a tSC4-es közepes gamma-oszcilláció jelenléte volt jellemző.

A mediális szeptum neuronjainak tüzelése összefüggött a hippokampális tSC-kkel

Megvizsgáltuk, hogy a mediális szeptum sejtjeinek aktivitása tükrözi-e valamilyen formában a hippokampuszban egyidejűleg mérhető tSC-ket. Azt találtuk, hogy mind a sejtek tüzelési frekvenciája, mind a hippokampális théta-oszcillációhoz viszonyított tüzelési fázisa függött a tSC-k jelenlététől.

A leggyorsabb tüzelést a tSC4 közepes gamma jelenlétében mutatták a szeptális neuronok. Ugyancsak ezekben a théta-ciklusokban mutatták a legerősebb fáziskapcsoltságot a hippokampális thétához, a tSC1 által dominált théta-ciklusokhoz képest egy némileg későbbi théta-fázist preferálva. Ezek a különbségek különösen szembetűnőek voltak a feltételezett théta-ritmusképző sejtek és a théta-asszociált théta-ritmikus (korábbi nevükön „követő”) szeptális sejtek esetében. Ezzel szemben a sejtek burst tüzelési tulajdonságai nem mutattak jelentős varianciát a tSC-k jelenlétének függvényében.

A legtöbb mediális szeptális neuron fáziskapcsoltságot mutat a hippokampális beta/gamma tSC-khez

A mediális szeptum sejtjeinek tüzelése a théta-ciklusoknál rövidebb időskálán is korrelált a hippokampális beta/gamma-hullámokkal: a legtöbb MS neuron szignifikáns fáziskapcsoltságot mutatott ezekkel a gyorsabb ritmusokkal is. Ezt nem magyarázta önmagában a tSC-k fázis

kapcsoltsága a théta-ciklusokhoz. Egyes szeptális sejtek burstökün belüli akciós potenciál időzítése is közvetlen összefüggést mutatott a hippokampális tSC-kkel.

Számos MS neuron több tSC-hez is tudott kapcsolódni, és a lassabb tSC-khez történő fáziskapcsoltság gyakoribb volt. A théta-ritmikus MS sejtek gyakrabban mutattak tSC-kapcsoltságot, és a tSC-kapcsolt neuronok erősebb théta-kapcsoltságot és hosszabb burstöket mutattak a tSC-khez nem kapcsolt szeptális sejteknél. A feltételezett pacemaker sejtek és a théta-asszociált théta-ritmikus sejtek esetében különösen általános volt a tSC-kkel mutatott fáziskapcsoltság (78% és 59%).

A mediális szeptális sejtek aktivitás változásai megelőzik a hippokampális tSC-k korrelált változásait

Hogy megállapítsuk, vélhetően a mediális szeptum sejtjei szabályozzák a hippokampális tSC-ket vagy fordítva, kiszámoltuk a két szignál közötti fáziskapcsoltság erősségét a jelek között bevezetett időbeli eltolás függvényében. Ha például a hippokampális tSC-k a mediális szeptális tüzelés egy korábbi időpontjával korrelálnak a legjobban, az arra utal, hogy a mediális szeptális aktivitás változások megelőzik a hippokampusz korrelált változásait, azt valószínűsítve, hogy a mediális szeptum szerepet játszik a tSC-k szabályozásában.

A legerősebb fáziskapcsoltságot többnyire negatív eltolás-értékeknél mértük, és az optimális időeltolások átlaga is negatív volt, arra utalva, hogy a MS aktivitását a hippokampusz néhány milliszekundumos késéssel követi. Ez az összefüggés különösen erős volt a feltételezett pacemaker sejteknél, és a théta-asszociált théta-ritmikus sejteknél. Ez az elemzés tehát a mediális szeptum vezető szerepét valószínűsítette.

Anatómiailag azonosított mediális szeptális sejtek fáziskapcsoltsága hippokampális tSC-kkel

A mediális szeptum több anatómiailag elkülönülő sejtcsoportot tartalmaz, melyek különböznek génexpressziójukban, beidegzési mintázatukban és aktivitásukban. Feltételeztük, hogy ezek a sejttípusok a hippokampális tSC-k szabályozásában is eltérően vesznek részt. Ennek tesztelése érdekében olyan mediális szeptális juxtacelluláris technikával készült regisztrátumokat elemeztünk az Oxfordi Egyetemmel (dr. Tim Viney, prof. David Dupret) együttműködésben, ahol az elvezetett mediális szeptális sejtek anatómiai besorolása ismert volt[185,204,205].

A GABAerg MS Teevra sejtek rövid théta-ritmikus burstökben tüzelnek, főleg a hippokampális CA3 területére vetítenek, ahol parvalbuminos axo-axonikus, valamint kolecisztokinit kifejező sejteket céloznak; maguk is termelnek parvalbumin fehérjét[185]. Ezek a sejtek a lassabb tSC1-hez (béta) és tSC2-höz (lassú gamma) kapcsolódtak. A szintén GABAerg MS „Orchidea” sejtek hosszabb burstöket tüzelnek, az entorhinális kéregbe, a subiculum területére és a retrospleniális kéregbe vetítenek, ahol parvalbumint és neuronális nitrogén-monoxid szintázt termelő sejteket idegeznek be, és maguk is termelnek parvalbumint[205]. Ezek a sejtek mind a lassú gamma-, mind a közepes

gamma-sávba eső tSC-khez kapcsolódtak, és jellemzően megelőzték a hippokampális aktivitás változásokat. A „low rhythmic" (LRN) sejtek[204] kevéssé ritmikusak, hippokampális éles hullámok alatt csökkentik a tüzelésüket, nem termelnek parvalbumint, és főleg a CA3 és a gyrus dentatus területére vetítenek. Ezek a sejtek főleg a tSC1-hez (béta), és kisebb mértékben a tSC2-höz (lassú gamma) kapcsolódtak.

Ezek alapján a mediális szeptális neuronok valószínűleg részben közvetve fejtik ki hatásukat a CA1-ben mérhető tSC-kre: a lassú gammákat részben a Teevra sejtek szabályozzák a CA3 területen keresztül, míg a közepes gammák kialakításában fontos szerepe lehet az „Orchidea" sejteknek az entorhinális kérgen keresztül. Ez összhangban van azzal a korábbi felfedezéssel, hogy a lassú gamma-komponensek gyakran CA1-CA3 kommunikációt, míg a közepes gamma-komponensek CA1-entorhinális kéreg kommunikációt tükrözhetnek[34,91,203,206].

A mediális szeptum parvalbuminos sejtjeinek optogenetikai serkentése tSC-szerű aktivitás mintákat okoz a hippokampális CA1-ben

Az a két felfedezés, hogy egyrészt a feltételezett ritmusgeneráló sejtek mutatták a legerősebb időbeli különbséget a hippokampuszhoz képest (melyek többnyire parvalbuminosak, l. fent), másrészt a parvalbuminos „Orchidea" és Teevra sejtek kiemelten fontosnak tűntek a tSC-k létrehozásában, újra a mediális szeptum parvalbuminos GABAerg populációjára irányította a figyelmünket. Közvetlenül vizsgáltuk, hogy ez a populáció képes-e tSC-szerű spektrális komponensek létrehozására a CA1-ben.

Dr. Varga Viktor kutatócsoportjával (HUN-REN KOKI) együttműködésben éber egerekben aktiváltuk a parvalbuminos MS neuronokat optogenetikai módszerrel a tSC-knek megfelelő frekvenciával. Mind a hippokampális mező potenciálban, mind egyedi hippokampális interneuronok tüzelési mintázatában létrejöttek a fiziológiás tSC-khez hasonló aktivitás mintázatok, mutatva, hogy a mediális szeptum valóban képes lehet hippokampális tSC-k generálására.

Vizsgáltuk a hippokampo-szeptális GABAerg (szomatosztatin fehérjét kifejező) visszacsatoló neuronok[75] szerepét is. Ha ezeket a sejteket optogenetikai úton gátoltuk, akkor megnőtt a hippokampális tSC-k jelenléte, valószínűsítve, hogy ezek a sejtek negatív visszacsatolási kört hoznak létre.

Végül kimutattuk, hogy a tSC komponensek, bár kisebb mértékben, de altatott egerek és patkányok hippokampuszában is jelen vannak, valamint a ventrális hippokampuszból is mérhetők tSC-k, tehát valószínűleg hasonló oszcillációs mechanizmusok működnek azon a területen is. Érdekes módon a tSC5-ös gyors gamma-komponens a legtöbb vizsgálatban nem mutatott összefüggést a mediális szeptummal, ami alátámasztja azt a korábbi elképzelést, hogy ezek a ritmusok lokálisan jönnek létre a hippokampuszban[34,92].

A mediális szeptum hippokampális ritmusképzésben betöltött szerepének jelentősége

A hippokampusz théta- és gamma-ritmusai az epizodikus memória hálózati szintű folyamatait, azon belül a memória eltárolásának és előhívásának feltételezett gyors váltakozását tükrözik[69,74]. Az eltárolás alatt közepes gamma-oszcillációk jelennek meg a hippokampális théta-csúcsain, melyek az entorhinális kéreg – CA1 információ átadást tükrözik. Előhívás során lassú gamma-oszcillációk jelennek meg a théta-völgyekben, melyek CA3 – CA1 információ átadásra utalnak[30,91,93].

Ezeket a ritmusokat feltételezhetően koordinálni kell: „honnan tudja” a CA3 és entorhiális kéreg, „mikor jött el az ő idejük”? A mediális szeptum ideális pozícióban van egy ilyen feladathoz, hiszen rostokat küld az összes érintett területre. Bár a théta létrehozásában betöltött szerepe régóta ismert, a gyorsabb oszcillációk koordinálásban eddig mégsem feltételezték a szerepét[30,206]. Számos kísérlet és összetett elemzés segítségével megmutattuk[63], hogy a mediális szeptum valószínűleg fontos szerepet tölt be ebben a koordinációs folyamatban.

A mediális szeptum théta-genezisben betöltött szerepe ugyan régóta ismert[37,40], azonban az, hogy a szeptumon belül milyen mechanizmus vezet théta-szinkronizációhoz, sokáig nyitott kérdés maradt. Szeptális neuronok egyidejű vizsgálatán keresztül azt a felfedezést tettük[184], hogy a mechanizmus nagyon hasonló a fizikában ismert Huygens-szinkronizációhoz[195–197,207]. Az utóbbi általános matematikai-fizikai törvényszerűségekben gyökerezik, ezért korábban is felvetődött, hogy az agyi hálózatok szinkronizációjában is lehet szerepe, ez azonban korábban az aggyal kapcsolatban nem nyert bizonyítást.

Összefoglalás

A bazális előagy középső és caudalis részét (Broca-féle diagonáláis köteg, substantia innominata, nucleus basalis) figyelmi és tanulási folyamatokkal hozták összefüggésbe[9,13,208,209]. Megvizsgáltuk, hogy ennek a területnek a két jelentős vetítő sejt populációja, a kolinerg és parvalbuminos GABAerg neuronok[15] hogyan vesznek részt a fenti kognitív folyamatokban.

A kolinerg neuronok egy tanító szignált közvetítettek: az előjel nélküli jutalom előrejelzési hiba (stimulus fontosság, salience) reprezentációján keresztül olyan információt továbbítottak a célterületeik felé, mely mind a figyelem, mind az asszociatív tanulás fokozására alkalmas lehet[12,19,21,210]. További kutatásaink arra utaltak, hogy a kolinerg sejtek a fenntarott figyelemben kevésbé, míg az asszociatív tanulás szabályozásában kifejezetten fontosak lehetnek[115,136]. Ez nem zárja ki, hogy egyéb figyelmi folyamatokban, például az ingerek által kiváltott szelektív figyelemben lényegesek a kolinerg sejtek.

A parvalbuminos GABAerg sejtek nem mutattak összefüggést a kimenetel előrejelzésével, hanem elsősorban az averzív, negatív visszajelzések aktiválták őket. Megmutattuk, hogy ez az aktivitásuk szükséges a negatív élmények alapján történő asszociatív tanuláshoz[169].

A bazális előagy elülső, rostrális részét (mediális szeptum) elsősorban a hippokampális ritmusképzés kontextusában vizsgálták[211]. Ezzel kapcsolatban megállapítottuk[184], hogy a terület parvalbuminos ritmusképző sejtjei az ingaórák esetében Huygens által a 17. században leírt[195] szinkronizációs folyamathoz hasonló módon[207] hangolódnak össze, így létrehozva a tanulási- és memóriafolyamatokban fontos[69] hippokampális théta-ritmust.

A mediális szeptum parvalbuminos sejtjei nem csak a théta, de a thétánál gyorsabb, théta-ciklusokba ágyazott béta/gamma-ritmusok[200] genezisében is szerepet játszik tanulmányunk szerint[63]. Azaz a mediális szeptum komplex módon koordinálja a hippokampális oszcillációkat, melyet egy karmester munkájához hasonlíthatunk.

Mivel a bazális előagy elülső és középső-hátsó része valójában egy folytonos anatómiai struktúrát képez meghatározott topografikus projekciós logikával[15,132,212], felmerül annak a lehetősége, hogy valójában a bazális előagy minden része részt vesz mind ritmus-genezisben[35,41], mind a plaszticitási folyamatok közvetlen szabályozásában[19,20]. Jelenlegi kutatásainkban ezért azt vizsgáljuk, vajon hogyan tudja a bazális előagy kolinerg és parvalbuminos GABAerg populációja integrálni ezt a két látszólag eltérő aktivitás mintázatot igénylő funkciót.

Köszönetnyilvánítás

Köszönet illeti korábbi tanáraimat és mentoraimat, akik elindítottak és egyengették utamat ezen a pályán: dr. Müllner Erzsébet biológia tanárnő; prof. Falus András, dr. László Valéria és prof. Csermely Péter (Semmelweis Egyetem); dr. Borhegyi Zsolt, dr. Varga Viktor és prof. Freund Tamás (KOKI); prof. Adam Kepecs (Cold Spring Harbor Laboratory); korábbi kollaborátoraimat: dr. Czurkó András (Richter Gedeon Nyrt.), prof. Robert Muller (SUNY Downstate University), dr. Stefanics Gábor és prof. Ulbert István (Kognitív Idegtudományi és Pszichológiai Intézet), dr. Slézia Andrea és prof. Acsády László (KOKI); munkatársaimat posztoktor periódusomból: dr. Hyun-Jae Pi, dr. Duda Kvitsiani, dr. Sachin Ranade, dr. Joshua Sanders, dr. Junya Hirokawa és Maja Lorenc.

Köszönöm azon munkatársak odaadó kitartását, akik a doktori mű alapjául szolgáló publikációkban részt vettek, a laboromból: dr. Laszlovszky Tamás, dr. Király Bálint, dr. Hegedüs-Jámbor Panna, Kocsis Barnabás, dr. Schlingloff Dániel, Lengyel Katalin, Victoria Lyakhova, Velencei Anna, dr. Sergio Martínez-Bellver, Sviatkó Katalin, Claire-Helene de Belval, Julia Heckenast és Zsofia Zelenak; kollaborátorként: dr. Domonkos Andor, dr. Jelitai Márta, dr. Varga Viktor, Mayer Márton, dr. Nyiri Gábor, dr. Káli Szabolcs, dr. Barthó Péter, prof. Gulyás Attila, prof. Freund Tamás (KOKI); dr. Fiáth Richárd és prof. Ulbert István (Kognitív Idegtudományi és Pszichológiai Intézet); prof. David Dupret, dr. Tim Viney, dr. Minas Salib, dr. Abhilasha Johsi (University of Oxford). Köszönöm a HUN-REN Kísérleti Orvostudományi Intézet összes kutatást segítő munkatársának, hogy lehetővé teszik az intézetben a színvonalas kutatómunka folytatását.

Köszönöm szüleimnek: Hangya Lászlónak és Hangyáné Szalkai Mártának, testvéreimnek: Hangya Dánielnek és Miklósnak, nagybátyámnak: Szalkai Istvánnak, páromnak: dr. Szilágyi Emőke Ritának és kislányomnak: Hangya Johannának kitartó támogatásukat és szeretetüket.

Hivatkozások

1. Squire, L. R. Memory systems of the brain: A brief history and current perspective. *Neurobiol. Learn. Mem.* **82**, 171–177 (2004).
2. Kihlstrom, J. F., Dorfman, J. & Park, L. Conscious and Unconscious Memory. in *The Blackwell Companion to Consciousness* 562–575 (Wiley, 2017). doi:10.1002/9781119132363.ch40.
3. Squire, L. R. & Wixted, J. T. Remembering. *Daedalus* **144**, 53–66 (2015).
4. Fanselow, M. S. & Poulos, A. M. The Neuroscience of Mammalian Associative Learning. *Annu. Rev. Psychol.* **56**, 207–234 (2005).
5. Buzsáki, G. & Moser, E. I. Memory, navigation and theta rhythm in the hippocampal-entorhinal system. *Nat. Neurosci.* **16**, 130–8 (2013).
6. Buzsáki, G. *Rhythms of the Brain*. (Oxford University Press, 2006). doi:10.1093/acprof:oso/9780195301069.001.0001.
7. LeDoux, J. E. Emotion circuits in the brain. *Annu. Rev. Neurosci.* **23**, 155–84 (2000).
8. Hayashi-Takagi, A. *et al.* Labelling and optical erasure of synaptic memory traces in the motor cortex. *Nature* **525**, 333–338 (2015).
9. Froemke, R. C., Merzenich, M. M. & Schreiner, C. E. A synaptic memory trace for cortical receptive field plasticity. *Nature* **450**, 425–429 (2007).
10. Harvey, C. D. & Svoboda, K. Locally dynamic synaptic learning rules in pyramidal neuron dendrites. *Nature* **450**, 1195–1200 (2007).
11. Dayan, P. Twenty-five lessons from computational neuromodulation. *Neuron* **76**, 240–56 (2012).
12. Seol, G. H. *et al.* Neuromodulators control the polarity of spike-timing-dependent synaptic plasticity. *Neuron* **55**, 919–929 (2007).
13. Hasselmo, M. E. & Sarter, M. Modes and models of forebrain cholinergic neuromodulation of cognition. *Neuropsychopharmacology* **36**, 52–73 (2011).
14. Zaborszky, L., Pang, K., Somogyi, J., Nadasdy, Z. & Kallo, I. The basal forebrain corticopetal system revisited. *Ann. N. Y. Acad. Sci.* **877**, 339–367 (1999).
15. Zaborszky, L., van den Pol, A. & Gyengesi, E. The Basal Forebrain Cholinergic Projection System in Mice. in *The Mouse Nervous System* (eds. Watson, C., Paxinos, G. & Puelles, L.) 684–718 (Elsevier, 2012). doi:10.1016/B978-0-12-369497-3.10028-7.
16. Saper, C. B. Organization of cerebral cortical afferent systems in the rat. II. Magnocellular basal nucleus. *J. Comp. Neurol.* **222**, 313–42 (1984).
17. Aguilar, D. D. & McNally, J. M. Subcortical control of the default mode network: Role of the basal forebrain and implications for neuropsychiatric disorders. *Brain Res. Bull.* **185**, 129–139 (2022).
18. Kirkwood, a, Rozas, C., Kirkwood, J., Perez, F. & Bear, M. F. Modulation of long-term synaptic depression in visual cortex by acetylcholine and norepinephrine. *J. Neurosci.* **19**, 1599–609 (1999).

19. Gu, Z. & Yakel, J. L. Timing-dependent septal cholinergic induction of dynamic hippocampal synaptic plasticity. *Neuron* **71**, 155–65 (2011).

20. Berg, D. K. Timing is everything, even for cholinergic control. *Neuron* **71**, 6–8 (2011).

21. Kilgard, M. P. & Merzenich, M. M. Cortical Map Reorganization Enabled by Nucleus Basalis Activity. *Science (80-.).* **279**, 1714–1718 (1998).

22. Chubykin, A. A., Roach, E. B., Bear, M. F. & Shuler, M. G. H. A cholinergic mechanism for reward timing within primary visual cortex. *Neuron* **77**, 723–35 (2013).

23. Shuler, M. G. & Bear, M. F. Reward timing in the primary visual cortex. *Science* **311**, 1606–1609 (2006).

24. Lin, S. S.-C., Brown, R. E., Hussain Shuler, M. G., Petersen, C. C. H. & Kepecs, A. Optogenetic Dissection of the Basal Forebrain Neuromodulatory Control of Cortical Activation, Plasticity, and Cognition. *J. Neurosci.* **35**, 13896–903 (2015).

25. Markram, H., Lübke, J., Frotscher, M. & Sakmann, B. Regulation of Synaptic Efficacy by Coincidence of Postsynaptic APs and EPSPs. *Science (80-.).* **275**, 213–215 (1997).

26. Harris, K. D., Csicsvari, J., Hirase, H., Dragoi, G. & Buzsáki, G. Organization of cell assemblies in the hippocampus. *Nature* **424**, 552–556 (2003).

27. Shirvalkar, P. R., Rapp, P. R. & Shapiro, M. L. Bidirectional changes to hippocampal theta-gamma comodulation predict memory for recent spatial episodes. *Proc. Natl. Acad. Sci.* **107**, 7054–7059 (2010).

28. Wulff, P. *et al.* Hippocampal theta rhythm and its coupling with gamma oscillations require fast inhibition onto parvalbumin-positive interneurons. *Proc. Natl. Acad. Sci.* **106**, 3561–3566 (2009).

29. Fries, P. *et al.* Rhythms for Cognition: Communication through Coherence. *Neuron* **88**, 220–35 (2015).

30. Colgin, L. L. & Moser, E. I. Gamma Oscillations in the Hippocampus. *Physiology* **25**, 319–329 (2010).

31. Ranade, S., Hangya, B. & Kepecs, A. Multiple modes of phase locking between sniffing and whisking during active exploration. *J. Neurosci.* **33**, 8250–6 (2013).

32. Moore, J. D. *et al.* Hierarchy of orofacial rhythms revealed through whisking and breathing. *Nature* **497**, 205–210 (2013).

33. Lakatos, P., Karmos, G., Mehta, A. D., Ulbert, I. & Schroeder, C. E. Entrainment of Neuronal Oscillations as a Mechanism of Attentional Selection. *Science (80-.).* **320**, 110–113 (2008).

34. Colgin, L. L. Rhythms of the hippocampal network. *Nat. Rev. Neurosci.* **17**, 239–249 (2016).

35. Yang, C., Thankachan, S., McCarley, R. W. & Brown, R. E. The menagerie of the basal forebrain: how many (neural) species are there, what do they look like, how do they behave and who talks to whom? *Curr. Opin. Neurobiol.* **44**, 159–166 (2017).

36. Manseau, F., Danik, M. & Williams, S. A functional glutamatergic neurone network in the medial septum and diagonal band area. *J. Physiol.* **566**, 865–884 (2005).

37. Freund, T. F. & Antal, M. GABA-containing neurons in the septum control inhibitory interneurons in the hippocampus. *Nature* **336**, 403–405 (1988).

38. Hangya, B., Borhegyi, Z., Szilagyi, N., Freund, T. F. & Varga, V. GABAergic Neurons of the Medial Septum Lead the Hippocampal Network during Theta Activity. *J. Neurosci.* **29**, 8094–8102 (2009).

39. Borhegyi, Z. *et al.* Phase segregation of medial septal GABAergic neurons during hippocampal theta activity. *J. Neurosci.* **24**, 8470–8479 (2004).

40. Petsche, H., Stumpf, C. & Gogolak, G. The significance of the rabbit's septum as a relay station between the midbrain and the hippocampus I. The control of hippocampus arousal activity by the septum cells. *Electroencephalogr. Clin. Neurophysiol.* **14**, 202–211 (1962).

41. Kim, T. *et al.* Cortically projecting basal forebrain parvalbumin neurons regulate cortical gamma band oscillations. *Proc. Natl. Acad. Sci.* **112**, 3535–3540 (2015).

42. Solari, N. & Hangya, B. Cholinergic modulation of spatial learning, memory and navigation. *Eur. J. Neurosci.* **48**, 2199–2230 (2018).

43. Everitt, B. J. & Robbins, T. W. Central cholinergic systems and cognition. *Annu. Rev. Psychol.* **48**, 649–84 (1997).

44. Wrenn, C. C. & Wiley, R. G. The behavioral functions of the cholinergic basalforebrain : lessons from 192 IgG-SAPORIN. *Int. J. Dev. Neurosci.* **16**, 595–602 (1998).

45. Ragozzino, M. E. & Kesner, R. P. The effects of muscarinic cholinergic receptor blockade in the rat anterior cingulate and Prelimbic/Infralimbic cortices on spatial working memory. *Neurobiol. Learn. Mem.* **69**, 241–257 (1998).

46. Hasselmo, M. E., Wyble, B. P. & Wallenstein, G. V. Encoding and retrieval of episodic memories: role of cholinergic and GABAergic modulation in the hippocampus. *Hippocampus* **6**, 693–708 (1996).

47. Damasio, A. R., Graff-Radford, N. R., Eslinger, P. J., Damasio, H. & Kassell, N. Amnesia Following Basal Forebrain Lesions. *Arch. Neurol.* **42**, 263–271 (1985).

48. Whitehouse, P. J. *et al.* Alzheimer's disease and senile dementia: loss of neurons in the basal forebrain. *Science* **215**, 1237–9 (1982).

49. Arendt, T. & Bigl, V. Alzheimer plaques and cortical cholinergic innervation. *Neuroscience* **17**, 277–9 (1986).

50. Schliebs, R. & Arendt, T. The cholinergic system in aging and neuronal degeneration. *Behav. Brain Res.* **221**, 555–563 (2011).

51. Burk, J. . & Sarter, M. Dissociation between the attentional functions mediated via basal forebrain cholinergic and GABAergic neurons. *Neuroscience* **105**, 899–909 (2001).

52. McGaughy, J., Dalley, J. W., Morrison, C. H., Everitt, B. J. & Robbins, T. W. Selective Behavioral and Neurochemical Effects of Cholinergic Lesions Produced by Intrabasalis Infusions of 192 IgG-Saporin on Attentional Performance in a Five-Choice Serial Reaction Time Task. *J. Neurosci.* **22**, 1905–1913 (2002).

53. Roßner, S. Cholinergic immunolesions by 192IgG-saporin—a useful tool to simulate pathogenic

aspects of alzheimer's disease. *Int. J. Dev. Neurosci.* **15**, 835–850 (1997).

54. Muir, J. L., Page, K. J., Sirinathsinghji, D. J. S., Robbins, T. W. & Everitt, B. J. Excitotoxic lesions of basal forebrain cholinergic neurons: Effects on learning, memory and attention. *Behav. Brain Res.* **57**, 123–131 (1993).

55. Roland, J. J., Janke, K. L., Servatius, R. J. & Pang, K. C. H. GABAergic neurons in the medial septum-diagonal band of Broca (MSDB) are important for acquisition of the classically conditioned eyeblink response. *Brain Struct. Funct.* **219**, 1231–7 (2014).

56. Lin, S.-C. & Nicolelis, M. a L. Neuronal ensemble bursting in the basal forebrain encodes salience irrespective of valence. *Neuron* **59**, 138–49 (2008).

57. Avila, I. & Lin, S.-C. Motivational Salience Signal in the Basal Forebrain Is Coupled with Faster and More Precise Decision Speed. *PLoS Biol.* **12**, e1001811 (2014).

58. Etter, G. *et al.* Optogenetic gamma stimulation rescues memory impairments in an Alzheimer's disease mouse model. *Nat. Commun.* **10**, 1–11 (2019).

59. Stanley, E. M., Fadel, J. R. & Mott, D. D. Interneuron loss reduces dendritic inhibition and GABA release in hippocampus of aged rats. *Neurobiol. Aging* **33**, 431.e1-431.e13 (2012).

60. Bañuelos, C. *et al.* Cognitive Aging and the Primate Basal Forebrain Revisited: Disproportionate GABAergic Vulnerability Revealed. *J. Neurosci.* **43**, 8425–8441 (2023).

61. Chaves-Coira, I., García-Magro, N., Zegarra-Valdivia, J., Torres-Alemán, I. & Núñez, Á. Cognitive Deficits in Aging Related to Changes in Basal Forebrain Neuronal Activity. *Cells* **12**, 1477 (2023).

62. McKenna, J. T. *et al.* Basal Forebrain Parvalbumin Neurons Mediate Arousals from Sleep Induced by Hypercarbia or Auditory Stimuli. *Curr. Biol.* **30**, 2379-2385.e4 (2020).

63. Király, B. *et al.* The medial septum controls hippocampal supra-theta oscillations. *Nat. Commun.* **14**, 6159 (2023).

64. Buzsáki, G. Theta oscillations in the hippocampus. *Neuron* **33**, 325–40 (2002).

65. Grastyán, E., Karmos, G., Vereczkey, L. & Kellényi, L. The hippocampal electrical correlates of the homeostatic regulation of motivation. *Electroencephalogr. Clin. Neurophysiol.* **21**, 34–53 (1966).

66. Harvey, C. D., Collman, F., Dombeck, D. A. & Tank, D. W. Intracellular dynamics of hippocampal place cells during virtual navigation. *Nature* **461**, 941–946 (2009).

67. Csicsvari, J., Hirase, H., Czurkó, A., Mamiya, A. & Buzsáki, G. Oscillatory Coupling of Hippocampal Pyramidal Cells and Interneurons in the Behaving Rat. *J. Neurosci.* **19**, 274–287 (1999).

68. Klausberger, T. & Somogyi, P. Neuronal diversity and temporal dynamics: the unity of hippocampal circuit operations. *Science* **321**, 53–7 (2008).

69. Hasselmo, M. E. & Stern, C. E. Theta rhythm and the encoding and retrieval of space and time. *Neuroimage* **85**, 656–666 (2014).

70. Wikenheiser, A. M. & Redish, D. A. The balance of forward and backward hippocampal sequences shifts across behavioral states. *Hippocampus* **23**, 22–29 (2013).

71. Geisler, C., Robbe, D., Zugaro, M., Sirota, A. & Buzsáki, G. Hippocampal place cell assemblies are

speed-controlled oscillators. *Proc. Natl. Acad. Sci. U. S. A.* **104**, 8149–8154 (2007).

72. Geisler, C. *et al.* Temporal delays among place cells determine the frequency of population theta oscillations in the hippocampus. *Proc. Natl. Acad. Sci.* **107**, 7957–7962 (2010).

73. Pastalkova, E., Itskov, V., Amarasingham, A. & Buzsáki, G. Internally generated cell assembly sequences in the rat hippocampus. *Science* **321**, 1322–7 (2008).

74. Siegle, J. H. & Wilson, M. A. Enhancement of encoding and retrieval functions through theta phase-specific manipulation of hippocampus. *Elife* **3**, e03061 (2014).

75. Toth, K., Borhegyi, Z. & Freund, T. F. Postsynaptic targets of GABAergic hippocampal neurons in the medial septum-diagonal band of Broca complex. *J. Neurosci.* **13**, 3712–3724 (1993).

76. Yoder, R. M. & Pang, K. C. H. Involvement of GABAergic and cholinergic medial septal neurons in hippocampal theta rhythm. *Hippocampus* **15**, 381–392 (2005).

77. Zutshi, I. *et al.* Hippocampal Neural Circuits Respond to Optogenetic Pacing of Theta Frequencies by Generating Accelerated Oscillation Frequencies. *Curr. Biol.* **28**, 1179-1188.e3 (2018).

78. Dannenberg, H. *et al.* Synergy of direct and indirect cholinergic septo-hippocampal pathways coordinates firing in hippocampal networks. *J. Neurosci.* **35**, 8394–8410 (2015).

79. Freund, T. F. GABAergic septohippocampal neurons contain parvalbumin. *Brain Res.* **478**, 375–381 (1989).

80. Varga, V. *et al.* The presence of pacemaker HCN channels identifies theta rhythmic GABAergic neurons in the medial septum. *J. Physiol.* **586**, 3893–915 (2008).

81. Hajszan, T., Alreja, M. & Leranth, C. Intrinsic vesicular glutamate transporter 2-immunoreactive input to septohippocampal parvalbumin-containing neurons: Novel glutamatergic local circuit cells. *Hippocampus* **14**, 499–509 (2004).

82. Huh, C. Y. L., Goutagny, R. & Williams, S. Glutamatergic neurons of the mouse medial septum and diagonal band of broca synaptically drive hippocampal pyramidal cells: Relevance for hippocampal theta rhythm. *J. Neurosci.* **30**, 15951–15961 (2010).

83. Vandecasteele, M. *et al.* Optogenetic activation of septal cholinergic neurons suppresses sharp wave ripples and enhances theta oscillations in the hippocampus. *Proc. Natl. Acad. Sci. U. S. A.* **111**, 13535–13540 (2014).

84. Kimura, H., McGeer, P. L., Peng, F. & McGeer, E. G. Choline acetyltransferase-containing neurons in rodent brain demonstrated by immunohistochemistry. *Science* **208**, 1057–9 (1980).

85. Khakpai, F., Nasehi, M., Haeri-Rohani, A., Eidi, A. & Zarrindast, M. R. Septo-hippocampo-septal loop and memory formation. *Basic Clin. Neurosci.* **4**, 5–23 (2013).

86. Damborsky, J. C. & Yakel, J. L. Regulation of hippocamposeptal input within the medial septum/diagonal band of Broca. *Neuropharmacology* **191**, 108589 (2021).

87. Hasselmo, M. E. & Giocomo, L. M. Cholinergic modulation of cortical function. *J. Mol. Neurosci.* **30**, 133–5 (2006).

88. Hassani, O. K., Lee, M. G., Henny, P. & Jones, B. E. Discharge profiles of identified GABAergic in comparison to cholinergic and putative glutamatergic basal forebrain neurons across the sleep-

wake cycle. *J. Neurosci.* **29**, 11828–40 (2009).

89. Simon, A. P., Poindessous-Jazat, F., Dutar, P., Epelbaum, J. & Bassant, M. H. Firing properties of anatomically identified neurons in the medial septum of anesthetized and unanesthetized restrained rats. *J. Neurosci.* **26**, 9038–9046 (2006).

90. Irle, E., Wowra, B., Kunert, H. J., Hampl, J. & Kunze, S. Memory disturbances following anterior communicating artery rupture. *Ann. Neurol.* **31**, 473–80 (1992).

91. Colgin, L. L. *et al.* Frequency of gamma oscillations routes flow of information in the hippocampus. *Nature* **462**, 353–357 (2009).

92. Lasztóczi, B. & Klausberger, T. Distinct gamma oscillations in the distal dendritic fields of the dentate gyrus and the CA1 area of mouse hippocampus. *Brain Struct. Funct.* **222**, 3355–3365 (2017).

93. Schomburg, E. W. *et al.* Theta Phase Segregation of Input-Specific Gamma Patterns in Entorhinal-Hippocampal Networks. *Neuron* **84**, 470–485 (2014).

94. Shute, C. C. D. & Lewis, P. R. Cholinesterase-Containing Systems of the Brain of the Rat. *Nature* **199**, 1160–1164 (1963).

95. McGeer, P. L., McGeer, E. G., Singh, V. K. & Chase, W. H. Choline acetyltransferase localization in the central nervous system by immunohistochemistry. *Brain Res.* **81**, 373–9 (1974).

96. Lehmann, J., Nagy, J. I., Atmadia, S. & Fibiger, H. C. The nucleus basalis magnocellularis: the origin of a cholinergic projection to the neocortex of the rat. *Neuroscience* **5**, 1161–74 (1980).

97. Mesulam, M.-M., Mufson, E. J., Levey, A. I. & Wainer, B. H. Cholinergic innervation of cortex by the basal forebrain: Cytochemistry and cortical connections of the septal area, diagonal band nuclei, nucleus basalis (Substantia innominata), and hypothalamus in the rhesus monkey. *J. Comp. Neurol.* **214**, 170–197 (1983).

98. Bartus, R. T., Dean, R. L., Beer, B. & Lippa, A. S. The cholinergic hypothesis of geriatric memory dysfunction. *Science* **217**, 408–14 (1982).

99. Herrero, J. L. *et al.* Acetylcholine contributes through muscarinic receptors to attentional modulation in V1. *Nature* **454**, 1110–4 (2008).

100. Rokem, A. & Silver, M. a. Cholinergic enhancement augments magnitude and specificity of visual perceptual learning in healthy humans. *Curr. Biol.* **20**, 1723–8 (2010).

101. Mirza, N. R. & Stolerman, I. P. The role of nicotinic and muscarinic acetylcholine receptors in attention. *Psychopharmacology (Berl).* **148**, 243–250 (2000).

102. Levin, E. D. & Simon, B. B. Nicotinic acetylcholine involvement in cognitive function in animals. *Psychopharmacology (Berl).* **138**, 217–230 (1998).

103. Phillis, J. W. Acetylcholine Release from the Central Nervous System: A 50-Year Retrospective. *Crit. Rev. Neurobiol.* **17**, 161–217 (2005).

104. Baxter, M. G., Bucci, D. J., Gorman, L. K., Wiley, R. G. & Gallagher, M. Selective immunotoxic lesions of basal forebrain cholinergic cells: effects on learning and memory in rats. *Behav. Neurosci.* **109**, 714–22 (1995).

105. McGaughy, J. & Sarter, M. Sustained attention performance in rats with intracortical infusions of 192 IgG-saporin-induced cortical cholinergic deafferentation: effects of physostigmine and FG 7142. *Behav. Neurosci.* **112**, 1519–25 (1998).

106. Berger-Sweeney, J. *et al.* Differential effects on spatial navigation of immunotoxin-induced cholinergic lesions of the medial septal area and nucleus basalis magnocellularis. *J. Neurosci.* **14**, 4507–4519 (1994).

107. Erickson, C. K., Graham, D. T. & U'Prichard, T. Cortical cups for collecting free acetylcholine in awake rats. *Pharmacol. Biochem. Behav.* **1**, 743–746 (1973).

108. Fournier, G. ., Semba, K. & Rasmusson, D. . Modality- and region-specific acetylcholine release in the rat neocortex. *Neuroscience* **126**, 257–262 (2004).

109. Parikh, V., Kozak, R., Martinez, V. & Sarter, M. Prefrontal acetylcholine release controls cue detection on multiple timescales. *Neuron* **56**, 141–54 (2007).

110. Schultz, W., Dayan, P. & Montague, P. R. A neural substrate of prediction and reward. *Science* **275**, 1593–1599 (1997).

111. Gritti, I. *et al.* Stereological estimates of the basal forebrain cell population in the rat, including neurons containing choline acetyltransferase, glutamic acid decarboxylase or phosphate-activated glutaminase and colocalizing vesicular glutamate transporters. *Neuroscience* **143**, 1051–64 (2006).

112. Fenno, L., Yizhar, O. & Deisseroth, K. The development and application of optogenetics. *Annu. Rev. Neurosci.* **34**, 389–412 (2011).

113. Pinto, L. *et al.* Fast modulation of visual perception by basal forebrain cholinergic neurons. *Nat. Neurosci.* **16**, 1857–63 (2013).

114. Jing, M. *et al.* An optimized acetylcholine sensor for monitoring in vivo cholinergic activity. *Nat. Methods* **17**, 1139–1146 (2020).

115. Hangya, B., Ranade, S. P., Lorenc, M. & Kepecs, A. Central Cholinergic Neurons Are Rapidly Recruited by Reinforcement Feedback. *Cell* **162**, 1155–1168 (2015).

116. Lima, S. Q., Hromádka, T., Znamenskiy, P. & Zador, A. M. PINP: a new method of tagging neuronal populations for identification during in vivo electrophysiological recording. *PLoS One* **4**, e6099 (2009).

117. Kvitsiani, D. *et al.* Distinct behavioural and network correlates of two interneuron types in prefrontal cortex. *Nature* **498**, 363–6 (2013).

118. Paolone, G., Lee, T. M. & Sarter, M. Time to pay attention: attentional performance time-stamped prefrontal cholinergic activation, diurnality, and performance. *J. Neurosci.* **32**, 12115–28 (2012).

119. Kepecs, A., Uchida, N., Zariwala, H. A. & Mainen, Z. F. Neural correlates, computation and behavioural impact of decision confidence. *Nature* **455**, 227–231 (2008).

120. Kepecs, A. & Mainen, Z. F. A computational framework for the study of confidence in humans and animals. *Philos. Trans. R. Soc. B Biol. Sci.* **367**, 1322–1337 (2012).

121. Sarter, M. *et al.* What do phasic cholinergic signals do? *Neurobiol. Learn. Mem.* **130**, 135–141 (2016).

122. Solari, N., Sviatkó, K., Laszlovszky, T., Hegedüs, P. & Hangya, B. Open Source Tools for Temporally Controlled Rodent Behavior Suitable for Electrophysiology and Optogenetic Manipulations. *Front. Syst. Neurosci.* **12**, 18 (2018).

123. Yu, A. J. & Dayan, P. Acetylcholine in cortical inference. *Neural Networks* **15**, 719–730 (2002).

124. Paolone, G., Angelakos, C. C., Meyer, P. J., Robinson, T. E. & Sarter, M. Cholinergic control over attention in rats prone to attribute incentive salience to reward cues. *J. Neurosci.* **33**, 8321–35 (2013).

125. Sarter, M., Lustig, C., Howe, W. M., Gritton, H. & Berry, A. S. Deterministic functions of cortical acetylcholine. *Eur. J. Neurosci.* **39**, 1912–1920 (2014).

126. Janssen, P. & Shadlen, M. N. A representation of the hazard rate of elapsed time in macaque area LIP. *Nat. Neurosci.* **8**, 234–41 (2005).

127. Laszlovszky, T. *et al.* Distinct synchronization, cortical coupling and behavioral function of two basal forebrain cholinergic neuron types. *Nat. Neurosci.* **23**, 992–1003 (2020).

128. Unal, C. T., Golowasch, J. P. & Zaborszky, L. Adult mouse basal forebrain harbors two distinct cholinergic populations defined by their electrophysiology. *Front. Behav. Neurosci.* **6**, 21 (2012).

129. Kiss, J., Patel, A. J., Baimbridge, K. G. & Freund, T. F. Topographical localization of neurons containing parvalbumin and choline acetyltransferase in the medial septum-diagonal band region of the rat. *Neuroscience* **36**, 61–72 (1990).

130. Kepecs, A. & Lisman, J. Information encoding and computation with spikes and bursts. *Netw. Comput. Neural Syst.* **14**, 103–118 (2003).

131. Buzsaki, G. *et al.* Nucleus basalis and thalamic control of neocortical activity in the freely moving rat. *J. Neurosci.* **8**, 4007–4026 (1988).

132. Gielow, M. R. & Zaborszky, L. The Input-Output Relationship of the Cholinergic Basal Forebrain. *Cell Rep.* **18**, 1817–1830 (2017).

133. Cohen, J. Y., Haesler, S., Vong, L., Lowell, B. B. & Uchida, N. Neuron-type-specific signals for reward and punishment in the ventral tegmental area. *Nature* **482**, 85–8 (2012).

134. Pavlov, I. P. *Lectures on conditioned reflexes: Twenty-five years of objective study of the higher nervous activity (behaviour) of animals.* (Liverwright Publishing Corporation, 1928). doi:10.1037/11081-000.

135. Hegedüs, P., Velencei, A., Belval, C.-H. de, Heckenast, J. & Hangya, B. Training protocol for probabilistic Pavlovian conditioning in mice using an open-source head-fixed setup. *STAR Protoc.* **2**, 100795 (2021).

136. Hegedüs, P., Sviatkó, K., Király, B., Martínez-Bellver, S. & Hangya, B. Cholinergic activity reflects reward expectations and predicts behavioral responses. *iScience* **26**, 105814 (2023).

137. Zariwala, H. A. *et al.* A Cre-dependent GCaMP3 reporter mouse for neuronal imaging in vivo. *J Neurosci* **32**, 3131–3141 (2012).

138. Allard, S. & Hussain Shuler, M. G. Cholinergic Reinforcement Signaling Is Impaired by Amyloidosis Prior to Its Synaptic Loss. *J. Neurosci.* **43**, 6988–7005 (2023).

139. Robert, B. *et al.* A functional topography within the cholinergic basal forebrain for encoding sensory cues and behavioral reinforcement outcomes. *Elife* **10**, 1–28 (2021).

140. Xu, M. *et al.* Basal forebrain circuit for sleep-wake control. *Nat. Neurosci.* **18**, 1641–1647 (2015).

141. Yawata, Y. *et al.* Mesolimbic dopamine release precedes actively sought aversive stimuli in mice. *Nat. Commun.* **14**, 2433 (2023).

142. Szőnyi, A. *et al.* Median raphe controls acquisition of negative experience in the mouse. *Science* **366**, eaay8746 (2019).

143. Faget, L. *et al.* Opponent control of behavioral reinforcement by inhibitory and excitatory projections from the ventral pallidum. *Nat. Commun.* **9**, 849 (2018).

144. Stephenson-Jones, M. *et al.* Opposing Contributions of GABAergic and Glutamatergic Ventral Pallidal Neurons to Motivational Behaviors. *Neuron* **105**, 921-933.e5 (2020).

145. Manning, E. E., Bradfield, L. A. & Iordanova, M. D. Adaptive behaviour under conflict: Deconstructing extinction, reversal, and active avoidance learning. *Neurosci. Biobehav. Rev.* **120**, 526–536 (2021).

146. Kai, Y., Oomura, Y. & Shimizu, N. Responses of rat lateral hypothalamic neurons to periaqueductal gray stimulation and nociceptive stimuli. *Brain Res.* **461**, 107–117 (1988).

147. Berthoud, H.-R. & Münzberg, H. The lateral hypothalamus as integrator of metabolic and environmental needs: From electrical self-stimulation to opto-genetics. *Physiol. Behav.* **104**, 29–39 (2011).

148. Burstein, R., Cliffer, K. & Giesler, G. Direct somatosensory projections from the spinal cord to the hypothalamus and telencephalon. *J. Neurosci.* **7**, 4159–4164 (1987).

149. Zhang, G.-W. *et al.* A Non-canonical Reticular-Limbic Central Auditory Pathway via Medial Septum Contributes to Fear Conditioning. *Neuron* **97**, 406-417.e4 (2018).

150. Ang, S. T. *et al.* GABAergic neurons of the medial septum play a nodal role in facilitation of nociception-induced affect. *Sci. Rep.* **5**, 15419 (2015).

151. Hegedüs, P., Heckenast, J. & Hangya, B. Differential recruitment of ventral pallidal e-types by behaviorally salient stimuli during Pavlovian conditioning. *iScience* **24**, 102377 (2021).

152. Cohen, J. Y., Amoroso, M. W. & Uchida, N. Serotonergic neurons signal reward and punishment on multiple timescales. *Elife* **4**, 06346 (2015).

153. Ranade, S. P. & Mainen, Z. F. Transient firing of dorsal raphe neurons encodes diverse and specific sensory, motor, and reward events. *J. Neurophysiol.* **102**, 3026–37 (2009).

154. Woolf, N. J. & Butcher, L. L. Cholinergic systems mediate action from movement to higher consciousness. *Behav. Brain Res.* **221**, 488–98 (2011).

155. Baxter, M. G. & Chiba, a a. Cognitive functions of the basal forebrain. *Curr. Opin. Neurobiol.* **9**, 178–83 (1999).

156. Gallagher, M. & Colombo, P. J. Ageing: the cholinergic hypothesis of cognitive decline. *Curr. Opin. Neurobiol.* **5**, 161–8 (1995).

157. Adamantidis, A. R., Zhang, F., Aravanis, A. M., Deisseroth, K. & de Lecea, L. Neural substrates of awakening probed with optogenetic control of hypocretin neurons. *Nature* **450**, 420–424 (2007).

158. DeLong, M. R. *et al.* Functional organization of the basal ganglia: contributions of single-cell recording studies. *Ciba Found. Symp.* **107**, 64–82 (1984).

159. Pi, H.-J. *et al.* Cortical interneurons that specialize in disinhibitory control. *Nature* **503**, 521–524 (2013).

160. Hangya, B., Pi, H.-J., Kvitsiani, D., Ranade, S. P. & Kepecs, A. From circuit motifs to computations: Mapping the behavioral repertoire of cortical interneurons. *Curr. Opin. Neurobiol.* **26**, (2014).

161. Sviatkó, K. & Hangya, B. Monitoring the Right Collection: The Central Cholinergic Neurons as an Instructive Example. *Front. Neural Circuits* **11**, 31 (2017).

162. Sarter, M., Parikh, V. & Howe, W. M. Phasic acetylcholine release and the volume transmission hypothesis: time to move on. *Nat. Rev. Neurosci.* **10**, 383–90 (2009).

163. Gu, Z., Lamb, P. W. & Yakel, J. L. Cholinergic Coordination of Presynaptic and Postsynaptic Activity Induces Timing-Dependent Hippocampal Synaptic Plasticity. *J. Neurosci.* **32**, 12337–12348 (2012).

164. Yu, A. J. & Dayan, P. Uncertainty, neuromodulation, and attention. *Neuron* **46**, 681–92 (2005).

165. Lottem, E., Lorincz, M. L. & Mainen, Z. F. Optogenetic Activation of Dorsal Raphe Serotonin Neurons Rapidly Inhibits Spontaneous But Not Odor-Evoked Activity in Olfactory Cortex. **36**, 7–18 (2016).

166. Crouse, R. B. *et al.* Acetylcholine is released in the basolateral amygdala in response to predictors of reward and enhances the learning of cue-reward contingency. *Elife* **9**, 1–31 (2020).

167. Guo, W., Robert, B. & Polley, D. B. The Cholinergic Basal Forebrain Links Auditory Stimuli with Delayed Reinforcement to Support Learning. *Neuron* **103**, 1164-1177.e6 (2019).

168. Harrison, T. C., Pinto, L., Brock, J. R. & Dan, Y. Calcium Imaging of Basal Forebrain Activity during Innate and Learned Behaviors. *Front. Neural Circuits* **10**, 1–12 (2016).

169. Hegedüs, P. *et al.* Parvalbumin-expressing basal forebrain neurons mediate learning from negative experience. *Nat. Commun.* **15**, 4768 (2024).

170. Maness, E. B. *et al.* Role of the locus coeruleus and basal forebrain in arousal and attention. *Brain Res. Bull.* **188**, 47–58 (2022).

171. Lewthwaite, R. & Wulf, G. Optimizing motivation and attention for motor performance and learning. *Curr. Opin. Psychol.* **16**, 38–42 (2017).

172. Hollerman, J. R. & Schultz, W. Dopamine neurons report an error in the temporal prediction of reward during learning. *Nat. Neurosci.* **1**, 304–9 (1998).

173. Coddington, L. T. & Dudman, J. T. The timing of action determines reward prediction signals in identified midbrain dopamine neurons. *Nat. Neurosci.* **21**, 1563–1573 (2018).

174. Millett, D. Hans Berger: From Psychic Energy to the EEG. *Perspect. Biol. Med.* **44**, 522–542 (2001).

175. Engel, A. K., Fries, P. & Singer, W. Dynamic predictions: oscillations and synchrony in top-down processing. *Nat. Rev. Neurosci.* **2**, 704–16 (2001).

176. Landau, A. N. & Fries, P. Attention Samples Stimuli Rhythmically. *Curr. Biol.* **22**, 1000–1004 (2012).

177. Mathewson, K. E., Gratton, G., Fabiani, M., Beck, D. M. & Ro, T. To See or Not to See: Prestimulus Phase Predicts Visual Awareness. *J. Neurosci.* **29**, 2725–2732 (2009).

178. Stefanics, G. *et al.* Phase Entrainment of Human Delta Oscillations Can Mediate the Effects of Expectation on Reaction Speed. *J. Neurosci.* **30**, 13578–13585 (2010).

179. Tsanov, M. Septo-hippocampal signal processing: Breaking the code. *Prog. Brain Res.* **219**, 103–120 (2015).

180. Mattis, J. *et al.* Frequency-Dependent, Cell Type-Divergent Signaling in the Hippocamposeptal Projection. *J. Neurosci.* **34**, 11769–11780 (2014).

181. Robinson, J. *et al.* Optogenetic activation of septal glutamatergic neurons drive hippocampal theta rhythms. *J. Neurosci.* **36**, 3016–3023 (2016).

182. Fuhrmann, F. *et al.* Locomotion, Theta Oscillations, and the Speed-Correlated Firing of Hippocampal Neurons Are Controlled by a Medial Septal Glutamatergic Circuit. *Neuron* **86**, 1253–1264 (2015).

183. Bland, B. H. & Oddie, S. D. Theta band oscillation and synchrony in the hippocampal formation and associated structures: the case for its role in sensorimotor integration. *Behav. Brain Res.* **127**, 119–136 (2001).

184. Kocsis, B. *et al.* Huygens synchronization of medial septal pacemaker neurons generates hippocampal theta oscillation. *Cell Rep.* **40**, 111149 (2022).

185. Joshi, A., Salib, M., Viney, T. J., Dupret, D. & Somogyi, P. Behavior-Dependent Activity and Synaptic Organization of Septo-hippocampal GABAergic Neurons Selectively Targeting the Hippocampal CA3 Area. *Neuron* **96**, 1342-1357.e5 (2017).

186. Brandon, M. P., Bogaard, A. R., Schultheiss, N. W. & Hasselmo, M. E. Segregation of cortical head direction cell assemblies on alternating theta cycles. *Nat. Neurosci.* **16**, 739–748 (2013).

187. Poucet, B. *et al.* Independence of landmark and self-motion-guided navigation: a different role for grid cells. *Philos. Trans. R. Soc. Lond. B. Biol. Sci.* **369**, 20130370 (2014).

188. Hasselmo, M. E. Neuronal rebound spiking, resonance frequency and theta cycle skipping may contribute to grid cell firing in medial entorhinal cortex. *Philos. Trans. R. Soc. B Biol. Sci.* **369**, 20120523 (2014).

189. Brazhnik, E. S. & Fox, S. E. Intracellular recordings from medial septal neurons during hippocampal theta rhythm. *Exp. Brain Res.* **114**, 442–453 (1997).

190. Mamad, O., McNamara, H. M., Reilly, R. B. & Tsanov, M. Medial septum regulates the hippocampal spatial representation. *Front. Behav. Neurosci.* **9**, 1–16 (2015).

191. Lee, M. G., Hassani, O. K., Alonso, A. & Jones, B. E. Cholinergic basal forebrain neurons burst with theta during waking and paradoxical sleep. *J. Neurosci.* **25**, 4365–9 (2005).

192. Destrade, C. & Ott, T. Is a retrosplenial (cingulate) pathway involved in the mediation of high frequency hippocampal rhythmical slow activity (theta)? *Brain Res.* **252**, 29–37 (1982).

193. Ujfalussy, B. & Kiss, T. How do glutamatergic and GABAergic cells contribute to synchronization in the medial septum? *J. Comput. Neurosci.* **21**, 343–357 (2006).

194. Wang, X.-J. Pacemaker Neurons for the Theta Rhythm and Their Synchronization in the Septohippocampal Reciprocal Loop. *J. Neurophysiol.* **87**, 889–900 (2002).

195. Huygens, C. *Horologium Oscillatorium: sive de motu pendulorum ad horologia aptato demonstrationes geometricae*. (F. Muguet, 1673).

196. Willms, A. R., Kitanov, P. M. & Langford, W. F. Huygens' clocks revisited. *R. Soc. open Sci.* **4**, 170777 (2017).

197. Ramirez, J. P., Fey, R. H. B., Aihara, K. & Nijmeijer, H. An improved model for the classical Huygens ' experiment on synchronization of pendulum clocks. *J. Sound Vib.* **333**, 7248–7266 (2014).

198. Oliveira, H. M. & Melo, L. V. Huygens synchronization of two clocks. *Sci. Rep.* **5**, 1–12 (2015).

199. Ford, R. D., Colom, L. V. & Bland, B. H. The classification of medial septum-diagonal band cells as σ-on or σ-off in relation to hippocampal EEG states. *Brain Res.* **493**, 269–282 (1989).

200. Lopes-dos-Santos, V. *et al.* Parsing Hippocampal Theta Oscillations by Nested Spectral Components during Spatial Exploration and Memory-Guided Behavior. *Neuron* **100**, 940-952.e7 (2018).

201. Wu, Z. & Huang, N. E. Ensemble Empirical Mode Decomposition: a Noise-Assisted Data Analysis Method. *Adv. Adapt. Data Anal.* **01**, 1–41 (2009).

202. Lisman, J. E. & Jensen, O. The Theta-Gamma Neural Code. *Neuron* **77**, 1002–1016 (2013).

203. Jensen, O. & Colgin, L. L. Cross-frequency coupling between neuronal oscillations. *Trends Cogn. Sci.* **11**, 267–269 (2007).

204. Salib, M. *et al.* GABAergic Medial Septal Neurons with Low-Rhythmic Firing Innervating the Dentate Gyrus and Hippocampal Area CA3. *J. Neurosci.* **39**, 4527–4549 (2019).

205. Viney, T. J. *et al.* Shared rhythmic subcortical GABAergic input to the entorhinal cortex and presubiculum. *Elife* **7**, 1–35 (2018).

206. Lasztóczi, B. & Klausberger, T. Layer-Specific GABAergic Control of Distinct Gamma Oscillations in the CA1 Hippocampus. *Neuron* **81**, 1126–1139 (2014).

207. Ramirez, J. P., Olvera, L. A., Nijmeijer, H. & Alvarez, J. The sympathy of two pendulum clocks: Beyond Huygens' observations. *Sci. Rep.* **6**, 1–16 (2016).

208. Thiele, A., Herrero, J. L., Distler, C. & Hoffmann, K.-P. Contribution of cholinergic and GABAergic mechanisms to direction tuning, discriminability, response reliability, and neuronal rate correlations in macaque middle temporal area. *J. Neurosci.* **32**, 16602–15 (2012).

209. Disney, A. A., Aoki, C. & Hawken, M. J. Gain modulation by nicotine in macaque v1. *Neuron* **56**, 701–13 (2007).

210. Buzsáki, G., Gage, F. H., Czopf, J. & Björklund, A. Restoration of rhythmic slow activity (θ) in the subcortically denervated hippocampus by fetal CNS transplants. *Brain Res.* **400**, 334–347 (1987).

211. Hangya, B. & Varga, V. Editorial: The medial septum as a smart clock: New aspects of its function beyond pacemaking. *Front. Neural Circuits* **16**, (2023).

212. Zaborszky, L. *et al.* Neurons in the Basal Forebrain Project to the Cortex in a Complex Topographic Organization that Reflects Corticocortical Connectivity Patterns: An Experimental Study Based on Retrograde Tracing and 3D Reconstruction. *Cereb. Cortex* **25**, 118–137 (2015).

Eredeti publikációk

Article

Cell

Central Cholinergic Neurons Are Rapidly Recruited by Reinforcement Feedback

Graphical Abstract

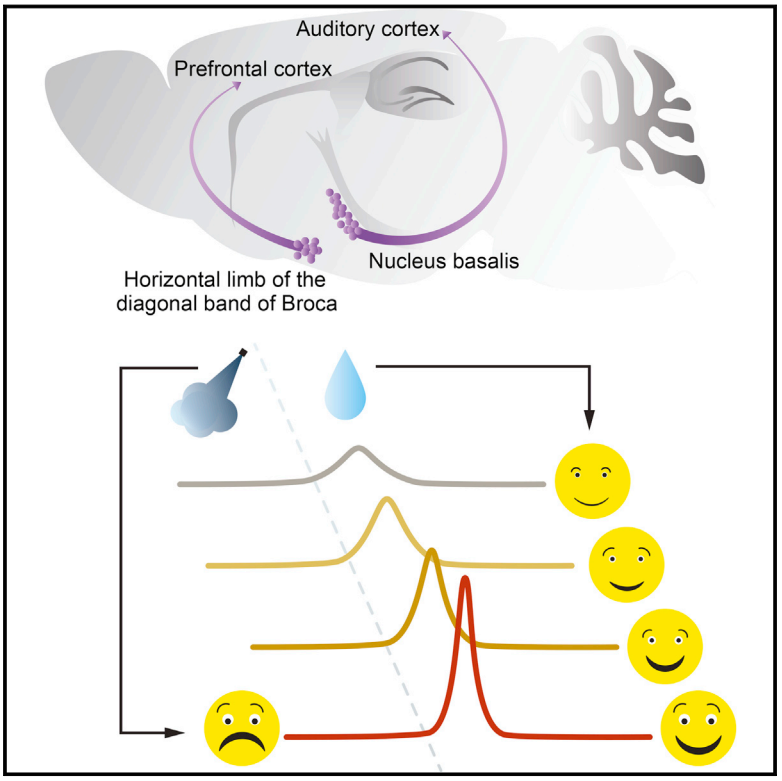

Highlights

- Basal forebrain cholinergic neurons respond to reward and punishment
- Cholinergic responses are scaled by reinforcement surprise
- Neural correlates of attention are found in a non-cholinergic population

Authors

Balázs Hangya, Sachin P. Ranade, Maja Lorenc, Adam Kepecs

Correspondence

hangya.balazs@koki.mta.hu (B.H.), kepecs@cshl.edu (A.K.)

In Brief

Recordings in basal forebrain cholinergic neurons during behavior show unexpectedly fast and precisely timed responses to reward and punishment that are modulated by outcome expectations, suggesting that the central cholinergic system may also convey cognitive information.

Hangya et al., 2015, Cell *162*, 1155–1168
August 27, 2015
http://dx.doi.org/10.1016/j.cell.2015.07.057

CellPress

Central Cholinergic Neurons Are Rapidly Recruited by Reinforcement Feedback

Balázs Hangya,[1,2,*] Sachin P. Ranade,[1] Maja Lorenc,[1] and Adam Kepecs[1,*]
[1]Cold Spring Harbor Laboratory, Cold Spring Harbor, NY 11724, USA
[2]Institute of Experimental Medicine, Hungarian Academy of Sciences, Budapest 1083, Hungary
*Correspondence: hangya.balazs@koki.mta.hu (B.H.), kepecs@cshl.edu (A.K.)
http://dx.doi.org/10.1016/j.cell.2015.07.057

SUMMARY

Basal forebrain cholinergic neurons constitute a major neuromodulatory system implicated in normal cognition and neurodegenerative dementias. Cholinergic projections densely innervate neocortex, releasing acetylcholine to regulate arousal, attention, and learning. However, their precise behavioral function is poorly understood because identified cholinergic neurons have never been recorded during behavior. To determine which aspects of cognition their activity might support, we recorded cholinergic neurons using optogenetic identification in mice performing an auditory detection task requiring sustained attention. We found that a non-cholinergic basal forebrain population—but not cholinergic neurons—were correlated with trial-to-trial measures of attention. Surprisingly, cholinergic neurons responded to reward and punishment with unusual speed and precision (18 ± 3 ms). Cholinergic responses were scaled by the unexpectedness of reinforcement and were highly similar across neurons and two nuclei innervating distinct cortical areas. These results reveal that the cholinergic system broadcasts a rapid and precisely timed reinforcement signal, supporting fast cortical activation and plasticity.

INTRODUCTION

Neuromodulators are central to brain function and have the ability to dramatically reconfigure circuits and change their dynamics (Bargmann and Marder, 2013). As the only classic neuromodulatory system with cell bodies located in the forebrain, as opposed to the evolutionarily more ancient midbrain, the cholinergic system has been implicated in a range of cognitive functions from arousal and vigilance to attention and learning, and even consciousness (Everitt and Robbins, 1997; Hasselmo and Sarter, 2011). Cholinergic cell loss is a major feature of multiple diseases of cognition: the severity of cognitive impairment in Alzheimer's disease and Parkinson's dementia is correlated with the extent of deterioration of basal forebrain cholinergic neurons (Whitehouse et al., 1982). Notably, deep brain stimulation of the basal forebrain is being tested as a therapeutic option for dementia and can improve the cognitive symptoms of some Alzheimer's and Parkinson's-dementia patients (Freund et al., 2009; Kuhn et al., 2015). Thus, progressive degeneration of central cholinergic neurons is thought to play a key role in neurodegenerative dementias and age-related cognitive decline, lending acute pathophysiological significance to basal forebrain research.

It may not be surprising then that perturbations of the central cholinergic system affect a wide range of behaviors. Rodents with selective lesions of cholinergic neurons, pharmacological blockade of acetylcholine receptors, or optogenetic suppression of cholinergic activity show performance deficits in detecting and discriminating sensory stimuli (Everitt and Robbins, 1997; McGaughy et al., 2000, 2002; Parikh et al., 2007; Pinto et al., 2013; Wrenn and Wiley, 1998), pointing to a causal role of the cholinergic system in these behaviors. However, how behavioral efficiency is modulated by higher level cognitive processes through the recruitment of the cholinergic system is largely unknown, and there is a plethora of candidate behavioral functions that have been suggested to tap into cholinergic mechanisms.

One hypothesis is that cholinergic neurons are involved in the control of arousal (Buzsaki et al., 1988; Richardson and DeLong, 1991; Zhang et al., 2011), vigilance (Hassani et al., 2009; Lee et al., 2005), and attention (Everitt and Robbins, 1997; Sarter et al., 2009). Attention-demanding tasks are accompanied by elevated cortical choline levels (Parikh et al., 2007; Sarter et al., 2009) and impaired by cholinergic blockers and lesions (Everitt and Robbins, 1997; McGaughy et al., 2002), suggesting that the cholinergic system may play a role in allocating attention at short temporal scales (Disney et al., 2007; Herrero et al., 2008). At the network level, cholinergic activation leads to rapid cortical activation and desynchronization in sensory cortices (Buzsaki et al., 1988; Eggermann et al., 2014; Kalmbach et al., 2012; Metherate et al., 1992; Pinto et al., 2013). These cholinergic effects are thought to be signatures of altered cortical operations that underlie the increased capacity for sensory detection and discrimination.

Another line of investigation has focused on the role of the cholinergic system in cortical plasticity and learning. Cholinergic lesions or pharmacological manipulations impair learning in spatial memory, working memory, and other mnemonic tasks (Everitt and Robbins, 1997; McGaughy et al., 2000), pointing to a causal role for cholinergic neurons. Cholinergic activation is capable of changing the strength, sign, and underlying molecular mechanisms of synaptic plasticity (Gu and Yakel, 2011; Gu et al.,

2012; Seol et al., 2007), effects that likely underlie the widely observed cholinergic enhancement of receptive field plasticity in sensory cortices (Chubykin et al., 2013; Disney et al., 2007; Froemke et al., 2013; Kilgard and Merzenich, 1998). Through these mechanisms, the sensory cortex projecting cholinergic neurons may boost learning and thereby contribute to improvements in behavioral performance.

Nonetheless, it remains unclear why behavioral performance decreases after loss of cholinergic tone, and the possible underlying mechanisms range from arousal to attention to learning processes. To gain insight into these processes, it is critical to first understand at which timescales the firing of cholinergic neurons vary with behavioral performance. For instance, fast modulation of cortical arousal might occur within a behavioral trial, leading to a trial-by-trial co-variation of cholinergic activity and behavioral performance. On the other hand, a slow, but steady, decrease in vigilance throughout a behavioral session, due to a concomitant diminution of cholinergic firing, could lead to deterioration of behavioral performance. Importantly, these possibilities would be expected to lead to similar changes in overall behavioral accuracy that are difficult to disentangle.

Therefore, we reasoned that determining the conditions under which cholinergic neurons are normally active is essential for revealing their behavioral functions across multiple timescales. Although there have been some recordings of unidentified neurons from the basal forebrain (Lin and Nicolelis, 2008; Richardson and DeLong, 1991; Wilson and Rolls, 1990; Zhang et al., 2011), there are no recordings of verified cholinergic neurons in behaving animals. The reasons for this are 2-fold. First, cholinergic neurons lie deep in the forebrain intermingled with other cell types, including two cortically projecting populations: GABAergic and glutamatergic cells (Freund and Gulyás, 1991; Gritti et al., 1997, 2006). In addition, they lack distinguishing spike shape features or firing characteristics that could aid in identification. Second, the cholinergic basal forebrain is comprised of a number of topographically projecting nuclei representing a high degree of anatomical complexity (Saper, 1984; Zaborszky et al., 2013), including the prefrontally projecting horizontal limb of the diagonal band (HDB) and the auditory/parietal cortex projecting caudal nucleus basalis (NB). Auditory projecting cholinergic neurons of the caudal nucleus basalis are present in a thin sheet on the lateral border of the internal capsule, making these experiments technically challenging even in the era of optogenetics (Lehmann et al., 1980; Saper, 1984; Zaborszky et al., 2013). Here, we recorded identified cholinergic neurons from both the NB and the HDB during behavior for the first time. We report surprising dynamics of cholinergic firing, including exceptionally fast and precise responses to innate reward (water) and punishment (air puff)—collectively referred to as primary reinforcers. The responses of cholinergic neurons were indistinguishable between the two nuclei despite their different projection targets, suggesting they constitute a unified broadcast system to cortex. Finally, we constructed a computational model to understand the variations in cholinergic responses and found they could be explained as responding to reinforcement surprise, showing stronger activation after unexpected reinforcement.

RESULTS

Optogenetic Identification of Central Cholinergic Neurons

We sought to record identified basal forebrain cholinergic neurons to determine when and how they are recruited during behavior. We targeted two distinct nuclei of the cholinergic basal forebrain. First, we identified the auditory projecting portion of the nucleus basalis (NB) revealed by retrograde tracing (Figure 1A, bottom). Second, we performed recordings from the prefrontally projecting horizontal limb of the diagonal band (HDB). These two nuclei are not only far apart (1.5 mm) but send non-overlapping cortical projections that are thought to underlie distinct functions (Nelson et al., 2005; Parikh et al., 2007). Virtually all cholinergic cells are projection neurons (Zaborszky et al., 2012, 2013), obviating the need for retrograde or antidromic identification of a projection subpopulation. However, both NB and HDB contain a diversity of cell types, including GABAergic and glutamatergic projection neurons (Freund and Gulyás, 1991; Gritti et al., 1997), that lack distinct electrophysiological signatures or pharmacological properties that could enable identification in extracellular recordings. Therefore, we used optogenetic tagging to identify cholinergic neurons in extracellular recordings. We rendered cholinergic neurons light-sensitive using either viral transfection to deliver channelrhodopsin-2 in ChAT-Cre mice (Figure 1B), or a ChAT-ChR2 mouse line (Figures S1A–S1F; we observed no differences between the two lines; see the Experimental Procedures). We recorded well-isolated single units and delivered brief (1 ms) blue light pulses to elicit short-latency action potentials. Cholinergic neurons were identified by their significant short latency light responses ($n = 34$ out of 1,580 units; $p < 0.01$; SALT test for optogenetic identification; Figures 1C–1E and S1G–S1K). Note that only around 6% of the basal forebrain neurons are cholinergic (Gritti et al., 2006), and since our methods are designed to minimize false positives, they might have missed some cholinergic cells because of insufficient viral infection or light access (see the Experimental Procedures).

Slow fluctuations of cortical acetylcholine levels have been long hypothesized to mediate gradual changes of vigilance or arousal (Buzsaki et al., 1988). Therefore, we first examined whether the baseline firing of cholinergic neurons was correlated with behavioral and brain states in freely moving mice. Video-tracking data were used to differentiate segments of sleep (no motion, accompanied by delta band, 1–4 Hz oscillations in cortical local field potentials) and quiet wakefulness (characterized by head movements without locomotion) from freely moving epochs (Figure 1F; see the Experimental Procedures). Cholinergic neurons showed the highest activity in freely moving mice (5.0 ± 1.4 Hz, median ± SE; $n = 5$; Figure 1G), which decreased during quiet wakefulness (4.0 ± 1.7 Hz) and further in sleep (2.0 ± 1.1 Hz), in agreement with previous observations (Hassani et al., 2009; Lee et al., 2005).

Punishment Promptly Activates Cholinergic Neurons

Cholinergic lesions of the basal forebrain have been shown to impair sensory detection under attention-demanding circumstances (Everitt and Robbins, 1997; McGaughy et al., 2002;

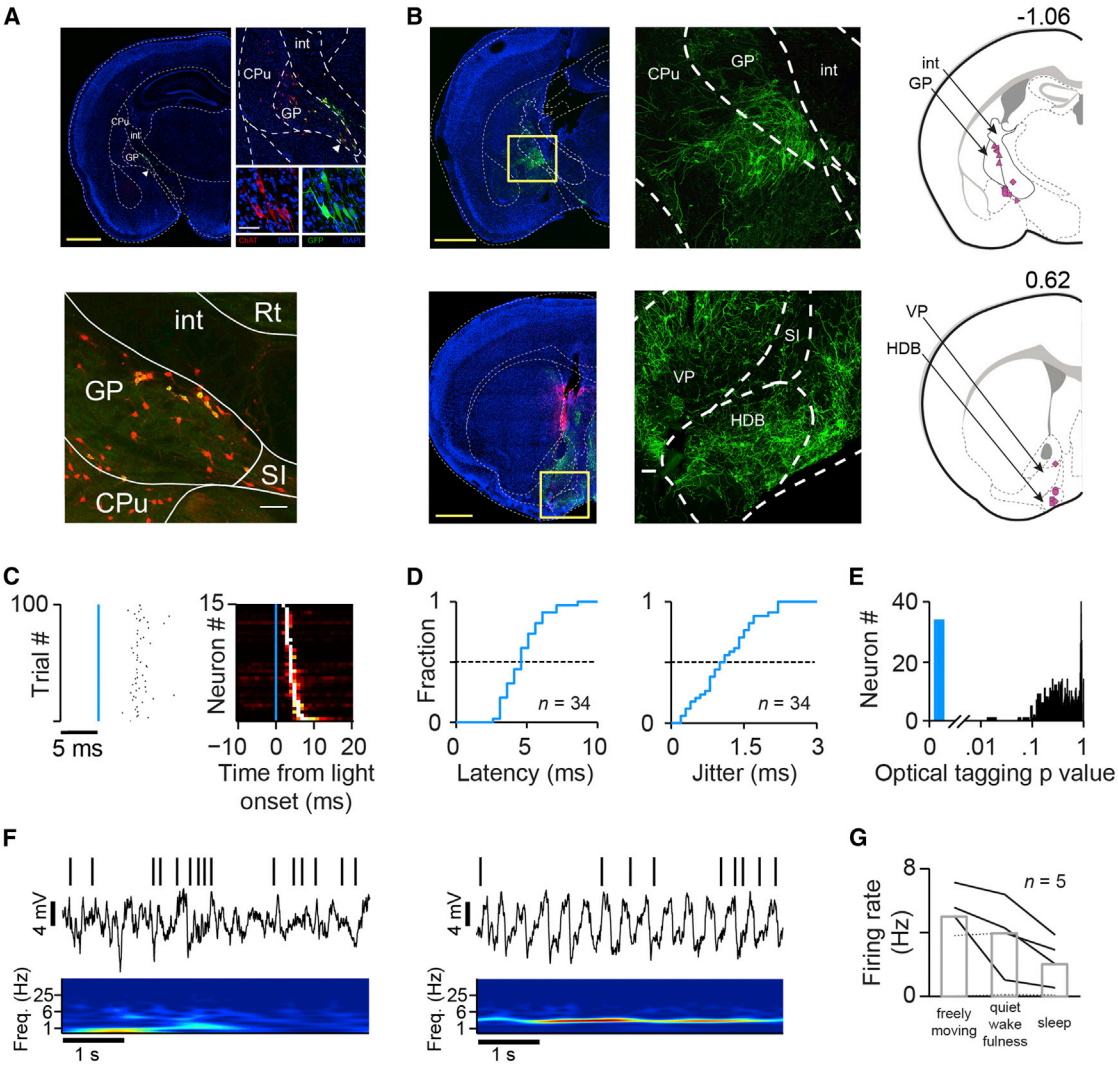

Figure 1. Optogenetic Tagging of Central Cholinergic Neurons

(A) Auditory projecting cholinergic neurons are in the caudal nucleus basalis (NB; Figure S1), including the ventromedial globus pallidus (GP) and the caudal substantia innominata (SI). Top: coronal section with increased magnification. ChAT-Cre mouse: green, neurons infected with AAV-flex-GFP; red, ChAT staining; white arrowhead, location of neurons enlarged on the right. Scale bars: left, 1 mm; right, 50 μm. Bottom: retrograde labeling from the auditory cortex. Red, cholinergic neurons; green, retrograde Lumafluor beads; yellow, double-labeled neurons. Scale bar, 150 μm. CPu, caudate putamen; int, internal capsule; Rt, reticular thalamic nucleus.

(B) Left: coronal sections showing expression of virally transfected ChR2-eYFP in the caudal NB (top) and horizontal limb of the diagonal band (HDB; bottom). Scale bar, 1 mm. Middle: enlarged images of the marked areas. Right: reconstructed location of identified cholinergic neurons projected onto two coronal planes (top, NB; bottom, HDB; numbers, antero-posterior distance from bregma). The different symbols indicate individual mice. VP, ventral pallidum.

(C) Left: spike raster of an identified cholinergic neuron aligned to light stimulation (blue line). Right: peri-stimulus time histograms aligned to photostimulation onset (blue line) for all identified cholinergic neurons (normalized by peak value, sorted by peak latency; all pulses of the most efficient stimulation frequency were used; colors from black to white reflect increasing firing rates).

(D) Cumulative histograms of light-evoked spike latency (left) and jitter (right) for all identified cholinergic neurons.

(E) SALT (stimulus-associated spike latency test) for optical tagging showed strongly bimodal p value distribution (blue, $p < 0.01$).

(F) Left: an example recording of a cholinergic neuron in an awake freely moving mouse. Top: spike times; middle: auditory cortical local field potential (LFP); bottom: wavelet spectrogram of the LFP. Right: example recording of the same cell during sleep. Note the lower firing rate and delta oscillations in the cortical LFP.

(G) Median firing rates of cholinergic neurons were highest in awake freely moving epochs, lower in quiet wakefulness, and lowest during sleep. Black lines, individual cells; solid lines, significantly different firing rate ($p < 0.01$; Mann-Whitney test).

See also Figure S1.

Sarter et al., 2009). To investigate how the cholinergic system controls such cortical functions, we recorded cholinergic neurons in an auditory detection task that requires sustained attention (Figures 2 and S2). Head-fixed mice (n = 22) were trained to detect two pure tones, well separated at distinct frequencies, and respond to the "go" tone with a lick, while ignoring the

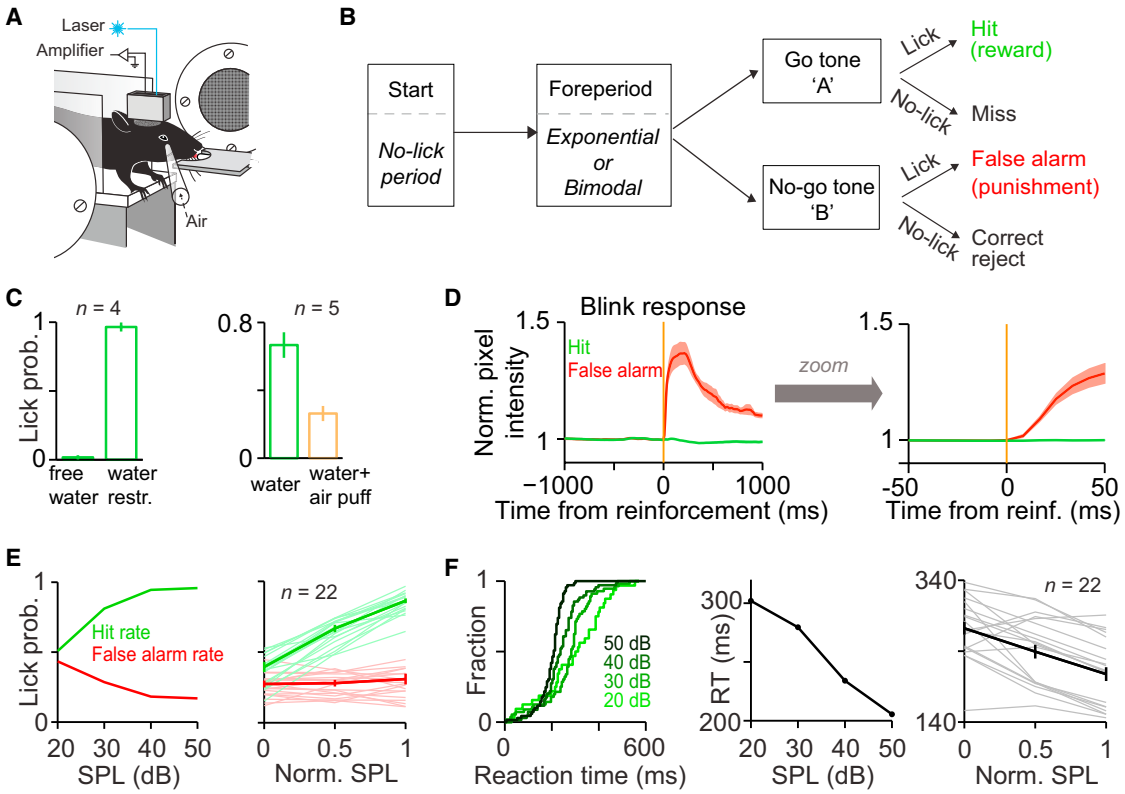

Figure 2. Auditory Detection Task

(A) A schematic of the head-fixed auditory detection task setup.

(B) Structure of a trial and possible outcomes. The trial start was signaled by turning off an LED. After a variable delay, pure tones of well-separated pitch but varying intensity signaled water reward or air-puff punishment upon licking.

(C) Left, thirsty (water restricted) mice learned to lick for water, showing a median lick probability close to 1 after training. The same mice did not lick for water when water was available ad libitum in their home cage (free water condition; n = 4; $p < 0.0001$ in all animals; chi-square test). Right, mice licked significantly more for water than the same amount of water combined with air puff (n = 5; $p < 0.0001$ on the population level; $p < 0.05$ in 4/5 individual mice; chi-square test).

(D) Left: average eye blink response after air puff (red) and water (green) delivery, quantified by normalized pixel density based on video analysis (34 sessions from 7 mice). Right: zoomed in to the first 50 ms after reinforcement delivery.

(E) Left: performance in a single session: lick probability in "go" (green) and "no-go" (red) trials (labeled "hit rate" and "false alarm rate," respectively) as a function of stimulus difficulty (psychometric function; SPL, sound pressure level of the cue). Right: average performance for individual mice (light; mice contributing at least three sessions are shown) and grand average (dark). Norm. SPL, intermediate SPLs were pooled to allow averaging across sessions.

(F) Left: cumulative reaction time (RT) histograms and median RT as a function of stimulus difficulty in the same session as (E). Right: average for individual mice (light) and grand average (dark). Error bars, SEM.

See also Figure S2.

"no-go" tone. Responses to the "go" tone were considered hits and resulted in the delivery of a drop of water reward, while responses to the "no-go" tone constituted false alarms triggering a mild puff of air directed to the face as punishment (Figures 2A and 2B). Thirsty mice learned to lick for water (Figure 2C, left) and avoid air puffs (Figure 2C, right; Figure S2), thus demonstrating that water and air puff have positive and negative motivational value, respectively (Cohen et al., 2015). Mice consistently responded to air puffs by blinking, likely reflecting the aversive quality of the punishment (Figure 2D). To make the task attention demanding, the stimulus was presented at unexpected moments following the trial start signal and tones of varying loudness were interleaved across trials in a white-noise background to create graded difficulty levels. Mice performed the task well and their accuracy and reaction time (RT) varied systematically as a function of signal-to-noise ratio (Figures 2E, 2F, and S2A).

Next, we examined whether there are specific behavioral events that phasically recruit cholinergic neurons. Our major observation is that almost all cholinergic neurons showed short latency activation after the delivery of punishment, a brief, mild air puff (n = 30/34; $p < 0.05$, Mann-Whitney test; Figures 3A–3C). This was characteristic of both NB (n = 19/22) and HDB (n = 11/12) cholinergic neurons despite their anatomical separation and distinct projection targets.

Encouraged by the phasic nature of cholinergic activation after punishment, we further examined its temporal properties. The phasic activation of NB cholinergic neurons showed remarkably short latency (17.5 ± 0.6 ms, median ± SE; range, 15–31 ms; Figure 3D) and extremely high temporal precision (jitter, 3.2 ± 0.7 ms),

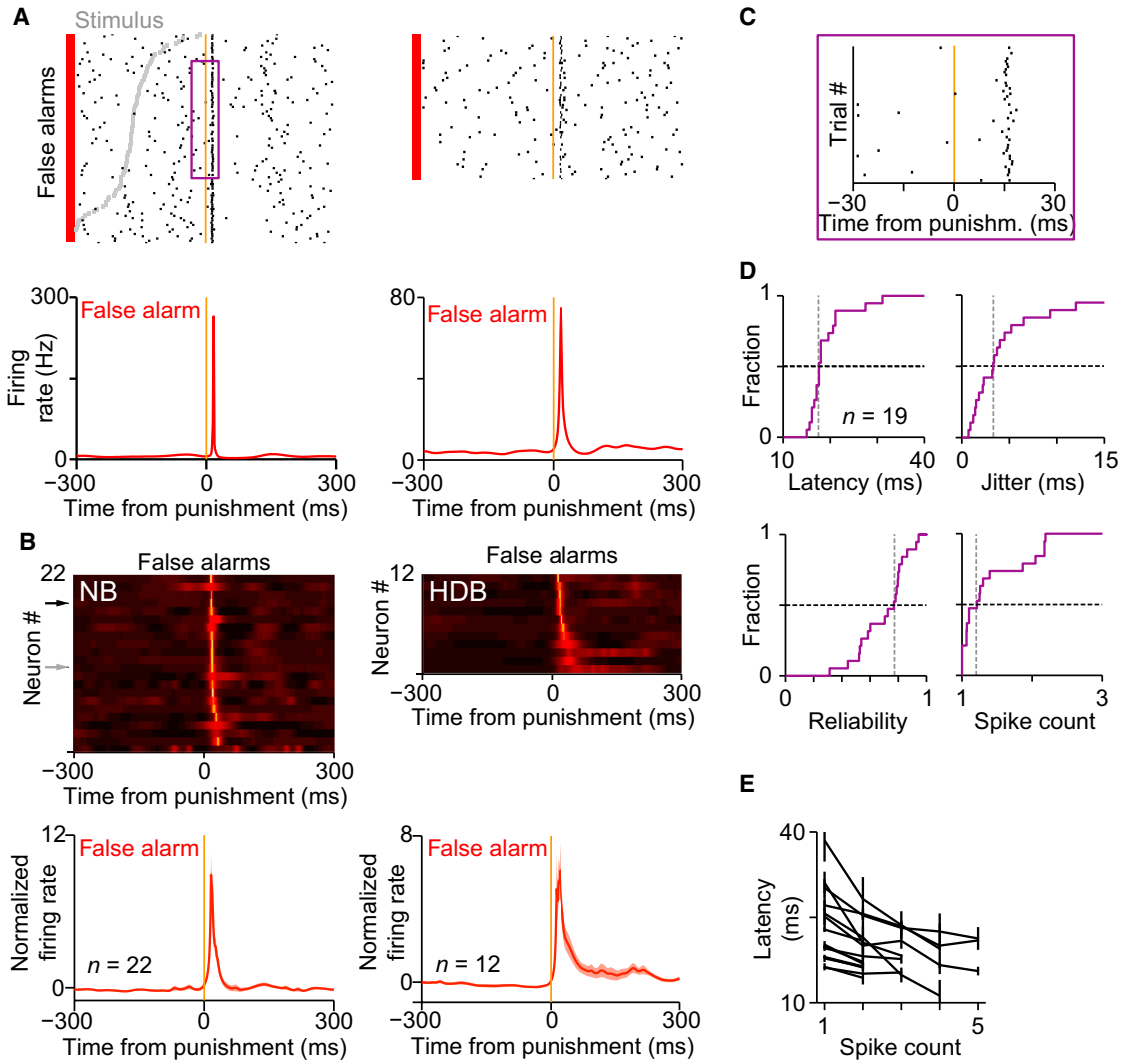

Figure 3. Punishment Uniformly Activates Cholinergic Neurons

(A) Spike rasters (top) and peri-event time histograms (PETHs, bottom) of two identified cholinergic neurons aligned to air-puff punishment (orange line). Trials were sorted by RT (gray ticks, stimulus onset). Cholinergic neurons showed precisely timed short latency response to air puff.

(B) Top: individual PETHs (color coded from black to white) of all identified cholinergic neurons revealed homogeneous phasic responses to punishment (left, NB; right, HDB). Cells are sorted by response latency. Arrows indicate the example neurons in (A) (black, left neuron). Bottom: average PETH.

(C) The area in the purple rectangle in (A) is magnified to reveal the low latency and jitter of the response.

(D) Cumulative histogram of punishment response peak latency, first spike jitter, reliability, and number of spikes in response to punishment (spike count).

(E) Spike latency showed negative correlation with spike count. Error bars, SEM.

See also Figure S3.

unexpected for a neuromodulatory system. Cholinergic neurons either fired a single spike or a brief burst of action potentials in response to punishment, with high reliability (76.9% ± 6.2%; Figures 3D and S3A). Within the narrow range of spike latencies, shorter response times were associated with higher spike counts (Figure 3E; $p < 0.01$ for 8 out of 11 neurons firing at least three bursts; remaining 3/11 p values, $p = 0.011$, $p = 0.06$, $p = 0.14$), consistent with stronger excitatory drive. Similar to NB, identified cholinergic neurons recorded from the HDB also exhibited fast response kinetics (median latency, 18.7 ± 2.3 ms; jitter, 3.8 ± 2.9 ms excluding two neurons showing atypical 220–230 ms activation with 15 ms onset; reliability, 75.5% ± 8.4%). Such rapid punishment-elicited responses may be either related to cues associated with punishment (termination of the stimulus, touch of air on the face or click of the air valve) or the execution of a stereotypic motor program (mouth opening or licking). To dissociate these possibilities, we introduced a variable delay (200–400 ms Gaussian, SD = 30 ms) between the animal's motor response and the feedback (punishment or reward) delivery (n = 16 cholinergic neurons). We found that the phasic activation of cholinergic neurons was aligned to the timing of feedback, and not the animals' motor response (Figures 4A, 4B, S3A, and S3B). This

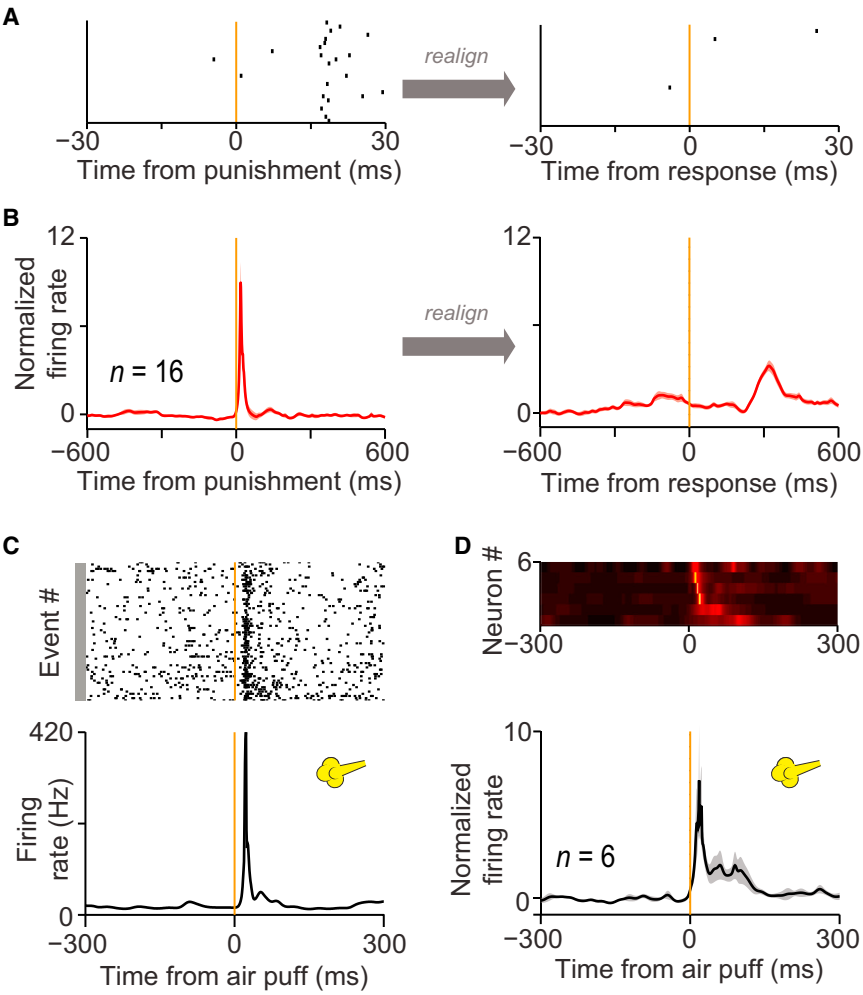

Figure 4. Cholinergic Neurons Respond to Primary Reinforcers

(A) Raster plot aligned to air puff (left) and realigned to the animal's response (right; same cell as in Figure 3A, right).

(B) Average PETH aligned to punishment (left) and realigned to the animals' motor response (right). Shading, SEM.

(C) Spike raster and PETH aligned to air puff of a cholinergic neuron outside the detection task.

(D) Top: individual PETHs of cholinergic neurons recorded outside the task (sorted by response latency) revealed homogeneous phasic responses to air puffs. Bottom: average PETH.

See also Figure S4.

demonstrates that the rapid activation of cholinergic neurons was triggered by sensory cues associated with the behavioral feedback, and not motor events.

Because air-puff punishment acts as an innate, primary reinforcer, we hypothesized that rapid, unconditional neural responses to reinforcers should also occur outside of task performance. To test this, we delivered air puffs at random, unsignaled moments to head-fixed mice. All cholinergic neurons (n = 6 neurons from five mice; two from NB and four from HDB) showed fast, reliable activation after air-puff delivery ($p < 0.05$, Mann-Whitney test; median latency, 19.8 ± 5.5 ms; jitter, 3.7 ± 2.7 ms; reliability, 70.6% ± 14.5%; Figures 4C and 4D). In addition, one NB cholinergic neuron also responded to mild foot shocks (latency, 9.5 ms; jitter, 5.4 ms; reliability, 89%; Figures S3C and S3D). Thus, primary punishment elicits rapid reliable cholinergic firing in naive mice.

We wondered whether this phasic response to negative reinforcers is unique to cholinergic neurons. Therefore, we selected all NB neurons significantly responding after punishment with either increased or suppressed firing (n = 717/1,360; $p < 0.01$, Mann-Whitney test) and performed hierarchical clustering on several response features (Figure S4A; Experimental Procedures). Identified cholinergic neurons clustered together with 22 unidentified cells that we labeled as putative cholinergic neurons (pChAT, probable false negatives; see the Experimental Procedures). pChAT neurons were similar to identified cholinergic neurons in their responses to punishment (Figure S4), while the rest of the population showed distinct response properties (Figures S5A–S5C). Thus, fast responses to punishment defined a separate, unique subpopulation of NB neurons.

Cholinergic Responses Are Scaled by Reward Expectations

Cholinergic neurons were also activated after positive behavioral feedback, the water reward, albeit with greater heterogeneity. Some cholinergic neurons exhibited precise reward-associated responses similar to their responses to punishment (n = 8/22; $p < 0.05$, Mann-Whitney test; Figures 5A and 5B). Other cholinergic neurons exhibited more delayed and less precise responses (n = 10/22), while a few neurons were entirely unresponsive to reward delivery (n = 4/22; Figures 5A and 5B). NB neurons characterized as putative cholinergic (pChAT, see above) based on their punishment responses exhibited reward responses similar to identified cholinergic neurons (Figures S4 and S5), while no other NB cells were found to exhibit such rapid activation by reward delivery. Identified cholinergic neurons recorded from the HDB were also similar in their reward responses (Figure 5B). This diversity of response properties could arise from session-wise differences in behavior or variations in anatomical location. The long dorsoventral axis of the NB (3.2 to 5 mm) allowed us to dissociate these hypotheses by correlating the ratio of reward to punishment responses with anatomical position and variables parameterizing behavior and training history (number of previous sessions, trials performed, performance). The ratio of reward to punishment responses showed the strongest correlation with recording depth ($R = -0.75$, $p < 0.0001$; $|R| > 0.63$ in partial correlations controlling for training history; see the Experimental Procedures),

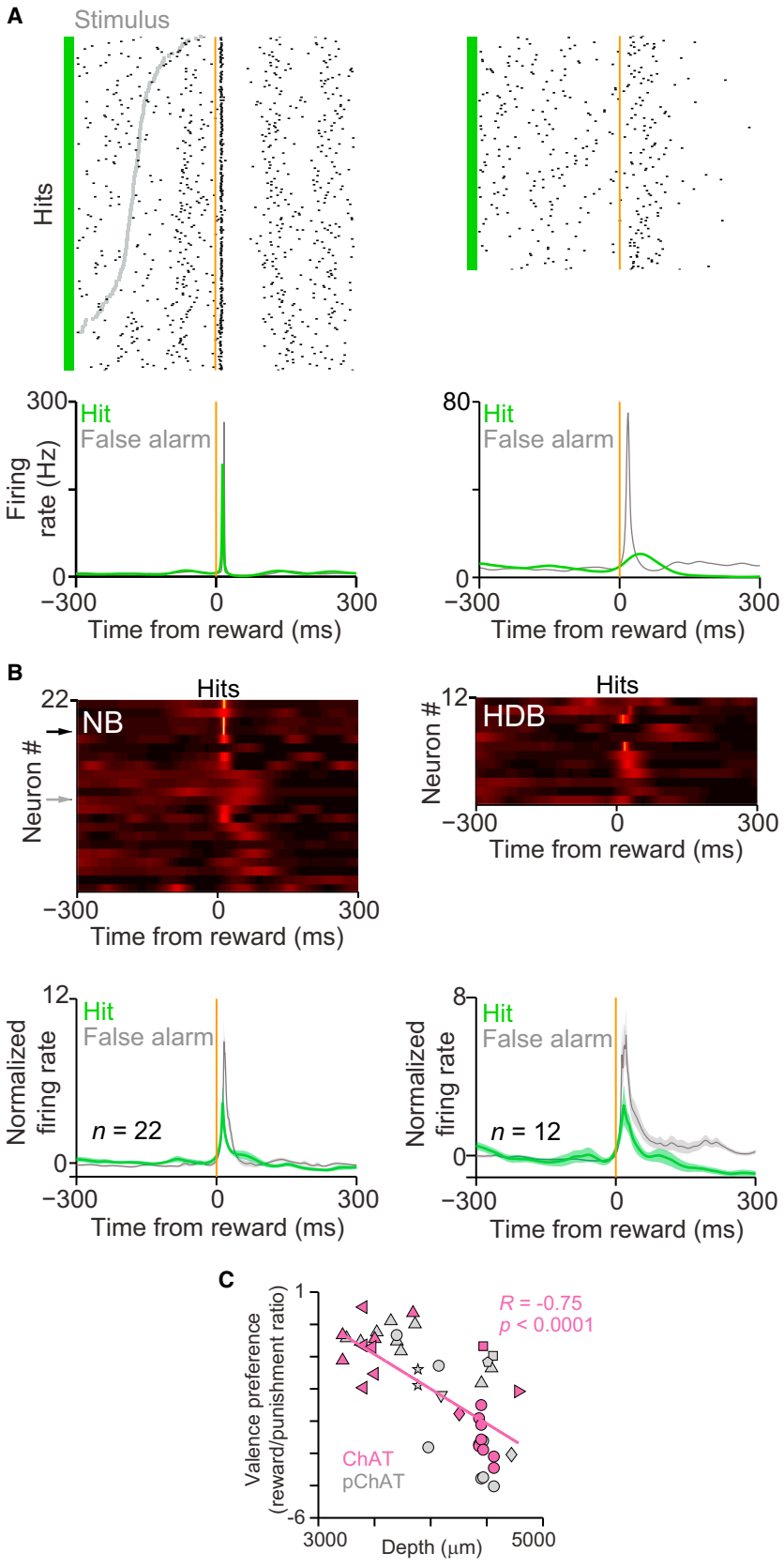

Figure 5. Cholinergic Neurons Are Activated by Water Reward

(A) Spike rasters (top) and PETHs (bottom) of two identified cholinergic neurons (same as in Figure 3A) aligned to water reward (orange line). Trials were sorted by RT (gray ticks, stimulus onset). The cholinergic neuron on left showed precisely timed short latency response to water, while the neuron on right exhibited a weaker and less precise reward response.

(B) Top: individual PETHs of all identified cholinergic neurons revealed heterogeneous responses to water reward (left, NB; right, HDB). Arrows indicate the example neurons in (A) (black, left neuron). The order of neurons corresponds to that of Figure 3B. Bottom: average PETHs.

(C) Identified cholinergic neurons (purple) showed a valence preference toward negative reinforcement with increasing depth (Figure S5). Putative cholinergic neurons are overlaid in gray (regression statistics were calculated from identified neurons). The different symbols indicate individual mice.

See also Figure S5.

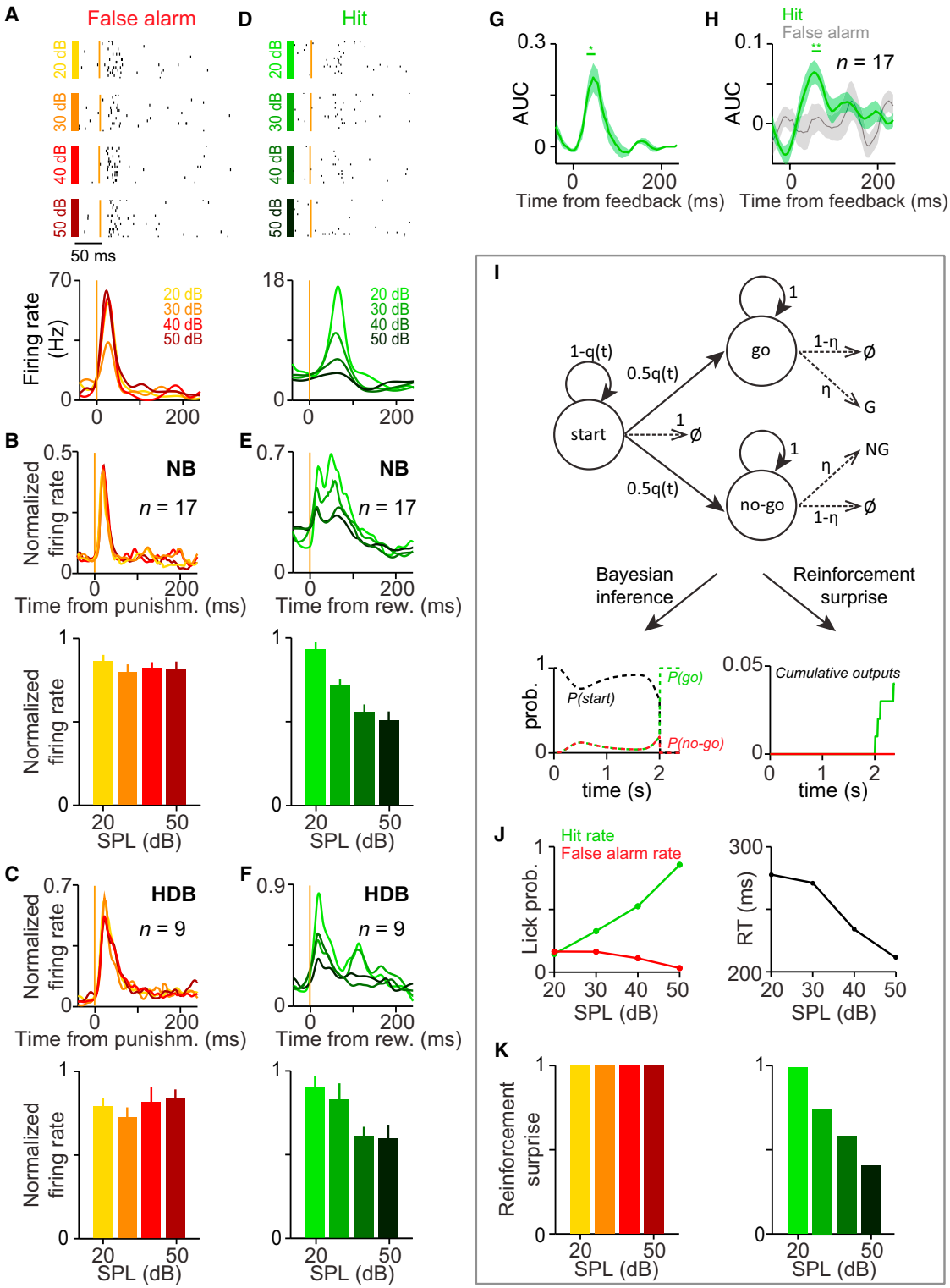

Figure 6. Cholinergic Responses Are Scaled by Reinforcement Surprise

(A) Spike rasters and PETHs aligned to punishment separated according to the stimulus signal-to-noise ratio of an identified NB cholinergic neuron.

(B) Top: average PETH across identified NB cholinergic neurons (n = 17; neurons for which the application of four different stimulus intensities allowed this analysis were included). Bottom: bar graph showing no modulation of punishment-evoked cholinergic activation by the strength of the preceding stimulus. Punishm., punishment.

(legend continued on next page)

suggesting that the differences in response magnitude are related to anatomical location (Figures 5C and S5D). These data point to a potential anatomical gradient of valence preference within the cholinergic NB.

Next, we wondered whether these high fidelity responses are solely triggered by primary reinforcers or also modulated by behavioral expectancies. We compared trials with different levels of uncertainty, in which lower or higher signal-to-noise levels in the stimulus differentially predicted outcome probability. Punishment invariably elicited strong responses independent of stimulus strength (NB, $p = 0.90$; HDB, $p = 0.76$; repeated-measures ANOVA; Figures 6A–6C). In contrast, we found that responses to water reward were differentially modulated based on the preceding signal-to-noise ratio of the stimulus with strongest activation by the least expected reward (NB, $p < 0.0001$; HDB, $p = 0.0015$; repeated-measures ANOVA; Figures 6D–6F). While the earliest responses were typically not influenced by expectancy (Figures 6G and 6H), differential activation started as early as 20-30 ms after reward delivery for some cholinergic neurons ($p < 0.01$, receiver operator characteristic, ROC, analysis for quantifying the discriminability of the two distributions of firing rates) and was statistically significant from 50 to 70 ms post-reward on average ($p < 0.01$; $n = 17$; Wilcoxon signed-rank test).

A Computational Model for Reinforcement Surprise

The graded cholinergic responses we observed led us to wonder whether these might represent reinforcement surprise, the deviation from outcome expectation. To test this hypothesis, we formally defined "reinforcement surprise" through a hidden Markov model (Dayan and Yu, 2006) for the auditory detection task (Figures 6I and S6). This model accounted for psychometric detection performance (Figure 6J) and also generated a measure of surprise for each reinforcement event. Since mice were well trained by the time of the recordings, we assumed that the animals knew the task contingencies; i.e., they learned a statistically veridical model of the task. In this model hidden states of the task are not directly observable to the decision maker, but generate probabilistic outputs ("observations") that allow Bayesian inference to produce an internal belief about the presence of tone stimuli (Figure 6I).

Next, we considered how reinforcement surprise can be computed within this framework. Observations of the stimulus resolve the ambiguity about the hidden states and therefore make trial outcomes more expected and correspondingly less surprising. Thus, the cumulative number of observations provides a natural measure of reinforcement expectations, allowing us to test whether cholinergic responses to reinforcers match formally defined reinforcement surprise. We found that a theoretical reward surprise was graded by the stimulus signal-to-noise ratio, whereas punishment surprise was uniformly high (Figure 6K). The lack of modulation of punishment surprise reflects that false detections arise independent of the stimulus, and thus punishment is always behaviorally unexpected in detection tasks. In summary, we found that reinforcement surprise in the model closely matched the amplitudes of cholinergic responses to reinforcers (Figures 6A–6F and 6K). These results point to the possibility that the graded responses of cholinergic neurons represent differential reinforcement surprise.

A Non-cholinergic Subpopulation of Basal Forebrain Neurons Shows Trial-by-Trial Correlations with Attention

Finally, we set out to test the long-standing hypothesis that the cholinergic system is involved in attentional functions (Everitt and Robbins, 1997; Sarter et al., 2009). The cholinergic system could theoretically control attention in two fundamentally different ways: either through slow modulation of vigilance (Figures 1F and 1G) or by rapid control of the momentary state of attention. To dissociate between these possibilities, we next asked whether the activity of cholinergic neurons varies with and is predictive of behavior on a rapid trial-to-trial basis. Mice in our task had to sustain attentional effort during the foreperiod from the start of the trial to stimulus delivery in order to respond to faint "go" tones. In humans it is well established that the temporal focus of attention can be manipulated by varying the expected moments of stimulus presentation (temporal expectancy), which is reflected in a faster reaction time for expected stimuli (Barnes and Jones, 2000; Coull and Nobre, 1998). To assess this in mice, we used a bimodal foreperiod distribution (Janssen and Shadlen, 2005) to manipulate temporal focus. We observed that RT was inversely correlated with temporal expectancy as characterized by the subjective hazard rate, the relative probability of the stimulus to be delivered at a given moment of time (Figures 7A and 7B). Importantly, this variation was only observed for difficult to detect stimuli, revealing that temporal expectations aid signal detection in our task, a hallmark of sustained temporal attention.

Sustained attention can wander from moment to moment, and reaction time and performance are expected to correlate with the

(C) Average PETH and bar graph for HDB cholinergic neurons (two neurons that did not show any response to water reward were excluded).
(D) Spike rasters and PETHs aligned to water reward corresponding to the same neuron as in (A).
(E) Average PETH across identified NB cholinergic neurons. Bottom: bar graph showing significant modulation of reward-evoked cholinergic activation by the strength of the preceding stimulus ($p < 0.0001$). Rew., reward.
(F) Average PETH and bar graph of mean firing rates for HDB cholinergic neurons show significant modulation of reward responses ($p = 0.0015$).
(G) ROC analysis quantifying the firing rate difference after faint (20–30 dB) or loud (40–50 dB) tones for an example cholinergic neuron. Firing rates were significantly different after water reward during the period marked by the green bar ($p < 0.05$). AUC, area under the ROC curve; a measure of discrimination between two distributions.
(H) Average AUC for identified NB cholinergic neurons. AUC was significantly positive after water reward during the period marked by the green bar ($p < 0.01$).
(I) A HMM of the auditory detection task (see the Results and Experimental Procedures).
(J) The HMM successfully reproduced psychometric functions (left) and RT (right) of the animals (compare with Figure 2).
(K) The HMM provided a measure of reinforcement surprise that closely matched the firing responses of cholinergic neurons (Figure S6).
See also Figure S6.

momentary level of attention at the time of the stimulus. Therefore, we operationalized attentional modulation as neural activity before stimulus onset that predicts either RT (i.e., shows significant negative correlation) or accuracy (i.e., shows positive correlations). Surprisingly, only two out of 34 cholinergic neurons (one in NB and one in HDB) showed activity that was predictive of RT and none predicted accuracy. In fact taken as a population the pre-stimulus firing of cholinergic neurons was slightly negatively correlated with behavioral performance ($p = 0.043$ in difficult trials, Wilcoxon signed-rank test). On the other hand, a subpopulation of non-cholinergic neurons exhibited attention-related firing based on our operational definition. Figures 7C and 7D show an example neuron with an increased firing rate up to 1 s before stimulus onset that is strongly correlated with short reaction times ($R = -0.36$, $p < 0.00001$). We found that a subset of NB neurons (96/1360 neurons, 7%, $p < 0.01$; only 2/220, 1% of HDB neurons) showed similar RT-predicting activity in the late foreperiod (Figures 7E and S7A–S7C). We also found a population of NB neurons (68/1,360 neurons, 5%; 8/220, 4% of HDB neurons) whose pre-stimulus firing predicted the animals' accuracy (Figures 7F–7H and S7D–S7F). Thus, the behavioral task enabled us to identify attention-like responses that were predictive of future performance. These responses were present in a small non-cholinergic population but did not appear as significant features of cholinergic neurons, suggesting that cholinergic neurons might contribute to attentional functions mostly through their slower modulation of brain states (Figures 1F and 1G).

DISCUSSION

Here, we recorded identified basal forebrain cholinergic neurons during behavior for the first time. We found that in addition to the behavioral state-dependent modulation of their tonic firing, cholinergic neurons were phasically activated with millisecond precision during behavior. Our experiments revealed that cholinergic neurons exhibit fast, precise, and reliable responses to natural, primary reinforcers: water reward and air-puff punishment. The response properties of cholinergic neurons were similar across two distinct nuclei, the prefrontally projecting HDB in the rostral forebrain and the auditory projecting NB located at the caudal end of the basal forebrain complex, despite the fact that these nuclei are often implicated in different functions. Cholinergic responses were graded by outcome expectancy, and we could account for this with a quantitative model of reinforcement surprise.

A Cholinergic Broadcast Signal to Cortex

Cholinergic neurons responded most strongly and uniformly to punishment. This response was reliably elicited by reinforcement feedback (Figure 3), unrelated to the signal-to-noise ratio of preceding stimuli (Figure 6) and locked not to the motor event eliciting reinforcement feedback but to cues immediately preceding them (Figures 4A and 4B). Primary negative reinforcers elicited similar responses outside the behavioral task (Figure 4C). Therefore, we suspect that the sensory cues triggering these responses must be related to the delivery of the reinforcers, such as clicks of the valves controlling water or air flow, the touch of water, air on the face, or the sound of air.

Neuromodulators are thought to broadcast signals widely to impact ongoing processing across brain regions. However, whether cholinergic neurons across different basal forebrain nuclei respond in a sufficiently uniform manner to consider them a functionally single system has been unclear. We found that cholinergic responses were nearly identical in two distinct central cholinergic nuclei with non-overlapping projections thought to support different functions: the prefrontally projecting HDB mediating top-down attention, while the NB is implicated in bottom-up attention (Nelson et al., 2005). These results indicate that the cholinergic system is capable of reliably broadcasting a unified signal to large areas of the brain.

Cholinergic Neurons May Signal Reinforcement Surprise

Reward-elicited responses showed greater diversity across cholinergic neurons (Figure 5). We found that reward responses were scaled by the signal-to-noise ratio of auditory stimuli that usually occurred hundreds of milliseconds before reward delivery, suggesting that cholinergic activation was modulated by outcome expectations (Figures 6A–6H). These data indicate that the central cholinergic system does not simply relay primary reinforcements but can also convey cognitive information. To better understand the potential computational significance of this graded signal, we constructed a hidden Markov model (Dayan and Yu, 2006) of the detection task that could reproduce behavioral performance (Figures 6I and 6J). This model enabled us to show that a formally defined reinforcement surprise (unsigned inverse outcome expectation) could account for both the uniform response to punishment and the graded response to reward (Figure 6K).

Mice interpret water reward and a puff of air to the face with opposing motivational valence: they express strong approach behavior to water, while they avoid air puffs (Figures 2C and S2D). This raises the interesting possibility that basal forebrain cholinergic firing is related to the motivational value of the outcomes. Alternatively, our model suggests that differences between reward and punishment responses can be to a large degree attributed to reinforcement surprise. Our definition of reinforcement surprise bears resemblance to reward prediction errors (RPE) represented by midbrain dopaminergic neurons (Schultz et al., 1997). Indeed, the response of cholinergic neurons is consistent with a representation of unsigned RPE, sometimes called ''salience.'' Note, however, that reinforcement surprise and RPE are defined in two different behavioral contexts (sensory detection task versus cued outcome task) and require distinct computations (trial-to-trial belief state inference versus experience-dependent reinforcement learning). Therefore, further experiments will be required to understand whether and how the signals represented by the dopaminergic and cholinergic systems are related.

The overall magnitude of the difference between punishment and reward responses was not fully captured by the model. Indeed, a correlation analysis revealed that there is an anatomical correlate of this difference, the scaling of reward responses along the unusually long dorso-ventral axis of the NB (Figure 5C). This could be explained by a systematic difference in the excitability of NB cholinergic neurons or a systematic variation

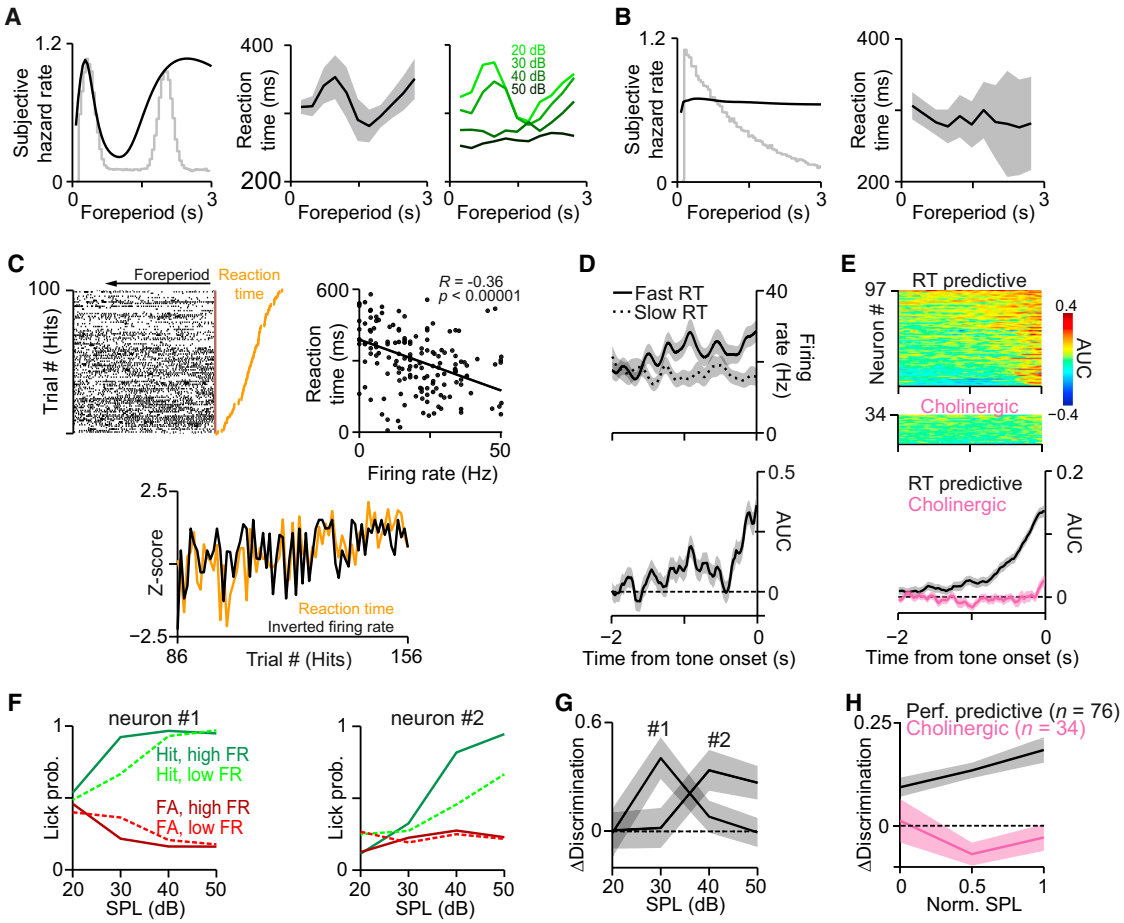

Figure 7. Attentional Correlates Are Characteristic of a Population of Non-cholinergic Neurons

(A) Left: subjective hazard rate corresponding to the bimodal foreperiod distribution (overlaid in gray). Middle: median RT as a function of the foreperiod from a single mouse, smoothed with a moving average of order 3 (only 20 and 30 dB trials included). Right: RT as a function of the foreperiod separated by the signal-to-noise ratio of stimuli. RT for difficult stimuli was modulated by the foreperiod. Shading, SE.

(B) As a control, reaction times (right) were constant for constant subjective hazard rates (left) corresponding to exponential foreperiod distributions (overlaid in gray).

(C) Top left: raster plot of an unidentified NB neuron during the foreperiod. Trials are aligned to stimulus onset (brown line) and sorted by RT (orange ticks). High firing rate in the foreperiod predicted fast RT. Top right: RT and pre-stimulus firing rate showed negative trial-to-trial correlation. Bottom: RT (orange) tracked firing rate changes (black) at multiple timescales.

(D) Top: PETH for the same neuron separated by slow and fast RT (median split). Bottom: ROC analysis quantifying the difference between firing rates for slow and fast RT trials. Shading, SEM. AUC, area under the curve, quantifying predictive value.

(E) Top: the ROC analysis for all unidentified basal forebrain neurons (NB and HDB combined) that showed significant RT predictive firing. Middle: the ROC analysis for identified cholinergic neurons. Bottom: the average ROC for the two populations.

(F) Performance was plotted separately for trials with high (solid lines) and low firing rate (dashed lines) in the foreperiod (median-split) for two NB neurons. Pre-stimulus firing rate predicted performance accuracy.

(G) Difference in discrimination performance between high and low firing rate trials (quantifying predictive value) as a function of stimulus intensity for the neurons in (F). Shading, bootstap SEM.

(H) Average discrimination difference for all performance predictive unidentified basal forebrain cells (black; NB and HDB combined) and all cholinergic neurons (purple). Shading, SEM. FR, firing rate.

See also Figure S7.

in the strength of bottom-up excitatory connectivity, which may constitute a gradient of surprise representation. Thus, our findings resonate with previous theoretical accounts, which suggest that acetylcholine signals different forms of uncertainty, thereby boosting learning and attention (Dayan et al., 2000; Doya, 2002; Yu and Dayan, 2005).

Cholinergic Control of Plasticity and Learning

Lesions of cholinergic neurons and pharmacological studies have established a causal role of the cholinergic system in learning (Everitt and Robbins, 1997; McGaughy et al., 2000). For instance, stimulating auditory projecting NB neurons have been shown to reorganize receptive field maps in the auditory

cortex (Froemke et al., 2013; Kilgard and Merzenich, 1998). However, there is a gap between the long-term impact of irreversible lesions or slow pharmacological manipulations and the cellular mechanisms of neuronal plasticity thought to underlie learning (Chubykin et al., 2013; Seol et al., 2007). Recent results revealed that at the synaptic level precisely timed acetylcholine can control the strength, sign, and molecular rules of hippocampal plasticity with millisecond precision (Gu and Yakel, 2011; Gu et al., 2012). Our results demonstrate that the cholinergic system is indeed capable of such millisecond precision in behaving mice (Figures 3, 4, and 5). This may provide the missing link between the cellular mechanisms of cholinergic control over cortical plasticity and behavioral learning. Indeed, behavioral reward can be replaced by optogenetic activation of basal forebrain input to visual cortex and thus be sufficient to entrain reward timing activity in cortex (Liu et al., 2015). Taking our observations together with previous in vitro and theoretical studies on plasticity (Jimenez Rezende and Gerstner, 2014), we speculate that fast central cholinergic responses to reinforcers provide supervisory control over local unsupervised cortical plasticity and thereby support learning.

Another possibility is that cholinergic neurons drive learning by activating disinhibitory circuits in cortex and thereby gate plasticity. This is in agreement with a recent finding that some auditory cortical interneurons receive cholinergic input elicited by punishment during fear conditioning (Letzkus et al., 2011). Indeed, cortical inhibitory interneurons express both ionotropic and metabotropic cholinergic receptors (Alitto and Dan, 2012; Demars and Morishita, 2014; Disney et al., 2007). Thus, cholinergic neurons could also drive reinforcement responses observed in cortical VIP^+ (Pi et al., 2013) and hippocampal SOM^+ interneurons (Kaifosh et al., 2013)

Role of Cholinergic and Non-cholinergic Basal Forebrain Neurons in Arousal and Attention

A long-standing hypothesis is that cholinergic neurons are involved in the control of arousal and forms of attention (Everitt and Robbins, 1997; Hasselmo and Sarter, 2011). In agreement with previous observations we found that the tonic firing rates of cholinergic cells vary as a function of the sleep-wake cycle and arousal (Figures 1F and 1G) (Duque et al., 2000; Hassani et al., 2009; Lee et al., 2005). These slower changes may underlie attention-like effects associated with the cholinergic system (Disney et al., 2007; Everitt and Robbins, 1997; Herrero et al., 2008), including recent results that optogenetic manipulations of cholinergic neurons can lead to performance changes in a visual discrimination task (Pinto et al., 2013).

On the other hand, whether the cholinergic system modulates attention at rapid timescales has not been previously tested. We probed two central cholinergic nuclei that are considered good candidates for such attentional effects: the NB projecting to primary auditory, as well as other sensory cortices, capable of influencing sensory detection and input processing functions (Froemke et al., 2013), and the HDB, sending prefrontal projections thought to underlie top-down attentional modulation (Hasselmo and Sarter, 2011; Nelson et al., 2005; Parikh et al., 2007). Surprisingly, not the cholinergic but a subpopulation of unidentified neurons' activity predicted behavioral variables classically associated with attention, such as reaction time and performance accuracy (Figure 7). This supports the idea that the basal forebrain also has attentional functions, albeit served by non-cholinergic neurons. This is also consistent with previous recordings of unidentified basal forebrain neurons showing a diversity of responses that were likely sampled from the more numerous and fast firing non-cholinergic populations (Lin and Nicolelis, 2008; Richardson and DeLong, 1991; Wilson and Rolls, 1990), some correlated with reaction time (Avila and Lin, 2014).

Conclusions

Our results support previous computational theories proposing that acetylcholine conveys a global reinforcement signal that enables the brain to associate prior events with behavioral outcomes (Doya, 2002; Hasselmo and Sarter, 2011; Jimenez Rezende and Gerstner, 2014; Yu and Dayan, 2005). Cholinergic responses were remarkably fast, 30–50 ms faster than midbrain dopamine neurons (Cohen et al., 2012), raising important questions about how acetylcholine might impact processing. First, cholinergic cells may recruit disinhibitory circuitry via nicotinic receptors (Letzkus et al., 2011; Pi et al., 2013), leading to rapid dynamic modulation of cortical arousal (Buzsaki et al., 1988; Richardson and DeLong, 1991; Zhang et al., 2011). Second, the fast and precisely timed cholinergic responses can provide a powerful computational mechanism for global modulation of timing-dependent synaptic plasticity across cortex (Frémaux et al., 2010; Gu and Yakel, 2011). Thus, we propose that the rapid phasic responses of basal forebrain cholinergic neurons represent reinforcement surprise and their broadcast serves as an alert signal capable of triggering rapid reconfiguration of cortical state and plasticity.

EXPERIMENTAL PROCEDURES

Adult (over 2 months old) ChAT-Cre (n = 15), ChAT-ChR2 (n = 5), and PV-Cre (n = 4) mice were used for behavioral recording experiments, and nine additional mice were used for behavior-only experiments under a protocol approved by the Cold Spring Harbor Laboratory Institutional Animal Care and Use Committee in accordance with NIH standards. See the Supplemental Experimental Procedures for details.

Microdrive Construction, Injection, and Microdrive Implantation

Custom-built light-weight (2.2 g) microdrives (Figure S1G) were constructed for deep brain recording and optogenetic stimulation. A moveable shuttle held an optic fiber and 7–8 tetrodes for unit recordings. Two stereotrodes were also connected for cortical local field potential recordings. Standard surgical techniques were employed for virus injection and microdrive implantation.

Behavior, Recording, and Optogenetics

Mice were trained on an auditory detection attention task in a head-fixed go/no-go detection paradigm using a custom-built apparatus. Extracellular recordings were performed using a DigitalLynx data acquisition system (Neuralynx). A blue laser (473 nm; 100 mW; Lasermate Group) was triggered through a data acquisition board (National Instruments) controlled by custom-built MATLAB programs (MathWorks) for optogenetic stimulation.

Histology and Track Reconstruction

To identify the recording sites, electrolytic lesions were made under deep anesthesia. After perfusion, brains were post-fixed and sections were imaged

by fluorescence (Olympus MVX10) and confocal microscopes (Zeiss 710LSM); then images were aligned to an atlas to accurately reconstruct the recording locations.

Data Analysis

Data analyses were carried out using built-in and custom-built software in Matlab (MathWorks). Action potentials were sorted into clusters (MClust software, A. D. Redish). Significant light-activation was assessed by the stimulus-associated spike latency test (SALT; http://kepecslab.cshl.edu/salt.m). Peri-event firing rates were estimated using an adaptive spike density function (SDF) approach. We implemented a hidden Markov model (HMM) of the auditory go/no-go detection task to test whether cholinergic neurons signal reinforcement surprise.

SUPPLEMENTAL INFORMATION

Supplemental Information includes Supplemental Experimental Procedures and seven figures and can be found with this article online at http://dx.doi.org/10.1016/j.cell.2015.07.057.

AUTHOR CONTRIBUTIONS

B.H. and A.K. designed the experiments, data analyses, and the model; B.H. performed the experiments, analyzed the data, performed model simulations, and prepared the figures; M.L. performed additional experiments during the revision; S.P.R. and B.H. established the behavior; S.P.R. performed retrograde tracing and video analysis; and B.H. and A.K. wrote the paper.

ACKNOWLEDGMENTS

This work was supported by grants from the John Merck and McKnight Foundations and the National Institute of Neurological Disorders and Stroke (R01NS075531) (to A.K.). B.H. received support from the Swartz Foundation and Marie Curie International Outgoing Fellowship within the EU Seventh Framework Programme for Research and Technological Development. The authors are grateful to Barry Burbach and Rob Eifert for invaluable technical assistance; Goncalo Lopez for help with Bonsai; Sanchari Ghosh for assisting in recording cholinergic neurons outside the behavioral task; and Hyun-Jae Pi, Duda Kvitsiani, Joshua I. Sanders, Michael Long, Stephen Shea, and Jessica Tollkuhn for helpful comments and discussions.

Received: April 1, 2015
Revised: May 27, 2015
Accepted: July 27, 2015
Published: August 27, 2015

REFERENCES

Alitto, H.J., and Dan, Y. (2012). Cell-type-specific modulation of neocortical activity by basal forebrain input. Front. Syst. Neurosci. *6*, 79.

Avila, I., and Lin, S.-C. (2014). Motivational salience signal in the basal forebrain is coupled with faster and more precise decision speed. PLoS Biol. *12*, e1001811.

Bargmann, C.I., and Marder, E. (2013). From the connectome to brain function. Nat. Methods *10*, 483–490.

Barnes, R., and Jones, M.R. (2000). Expectancy, attention, and time. Cognit. Psychol. *41*, 254–311.

Buzsaki, G., Bickford, R.G., Ponomareff, G., Thal, L.J., Mandel, R., and Gage, F.H. (1988). Nucleus basalis and thalamic control of neocortical activity in the freely moving rat. J. Neurosci. *8*, 4007–4026.

Chubykin, A.A., Roach, E.B., Bear, M.F., and Shuler, M.G.H. (2013). A cholinergic mechanism for reward timing within primary visual cortex. Neuron *77*, 723–735.

Cohen, J.Y., Haesler, S., Vong, L., Lowell, B.B., and Uchida, N. (2012). Neuron-type-specific signals for reward and punishment in the ventral tegmental area. Nature *482*, 85–88.

Cohen, J.Y., Amoroso, M.W., and Uchida, N. (2015). Serotonergic neurons signal reward and punishment on multiple timescales. Elife *4*. http://dx.doi.org/10.7554/eLife.06346.

Coull, J.T., and Nobre, A.C. (1998). Where and when to pay attention: the neural systems for directing attention to spatial locations and to time intervals as revealed by both PET and fMRI. J. Neurosci. *18*, 7426–7435.

Dayan, P., and Yu, A.J. (2006). Phasic norepinephrine: a neural interrupt signal for unexpected events. Network *17*, 335–350.

Dayan, P., Kakade, S., and Montague, P.R. (2000). Learning and selective attention. Nat. Neurosci. *3* (*Suppl*), 1218–1223.

Demars, M.P., and Morishita, H. (2014). Cortical parvalbumin and somatostatin GABA neurons express distinct endogenous modulators of nicotinic acetylcholine receptors. Mol. Brain *7*, 75.

Disney, A.A., Aoki, C., and Hawken, M.J. (2007). Gain modulation by nicotine in macaque v1. Neuron *56*, 701–713.

Doya, K. (2002). Metalearning and neuromodulation. Neural Netw. *15*, 495–506.

Duque, A., Balatoni, B., Detari, L., and Zaborszky, L. (2000). EEG correlation of the discharge properties of identified neurons in the basal forebrain. J. Neurophysiol. *84*, 1627–1635.

Eggermann, E., Kremer, Y., Crochet, S., and Petersen, C.C.H. (2014). Cholinergic signals in mouse barrel cortex during active whisker sensing. Cell Rep. *9*, 1654–1660.

Everitt, B.J., and Robbins, T.W. (1997). Central cholinergic systems and cognition. Annu. Rev. Psychol. *48*, 649–684.

Frémaux, N., Sprekeler, H., and Gerstner, W. (2010). Functional requirements for reward-modulated spike-timing-dependent plasticity. J. Neurosci. *30*, 13326–13337.

Freund, T.F., and Gulyás, A.I. (1991). GABAergic interneurons containing calbindin D28K or somatostatin are major targets of GABAergic basal forebrain afferents in the rat neocortex. J. Comp. Neurol. *314*, 187–199.

Freund, H.-J., Kuhn, J., Lenartz, D., Mai, J.K., Schnell, T., Klosterkoetter, J., and Sturm, V. (2009). Cognitive functions in a patient with Parkinson-dementia syndrome undergoing deep brain stimulation. Arch. Neurol. *66*, 781–785.

Froemke, R.C., Carcea, I., Barker, A.J., Yuan, K., Seybold, B.A., Martins, A.R., Zaika, N., Bernstein, H., Wachs, M., Levis, P.A., et al. (2013). Long-term modification of cortical synapses improves sensory perception. Nat. Neurosci. *16*, 79–88.

Gritti, I., Mainville, L., Mancia, M., and Jones, B.E. (1997). GABAergic and other noncholinergic basal forebrain neurons, together with cholinergic neurons, project to the mesocortex and isocortex in the rat. J. Comp. Neurol. *383*, 163–177.

Gritti, I., Henny, P., Galloni, F., Mainville, L., Mariotti, M., and Jones, B.E. (2006). Stereological estimates of the basal forebrain cell population in the rat, including neurons containing choline acetyltransferase, glutamic acid decarboxylase or phosphate-activated glutaminase and colocalizing vesicular glutamate transporters. Neuroscience *143*, 1051–1064.

Gu, Z., and Yakel, J.L. (2011). Timing-dependent septal cholinergic induction of dynamic hippocampal synaptic plasticity. Neuron *71*, 155–165.

Gu, Z., Lamb, P.W., and Yakel, J.L. (2012). Cholinergic coordination of presynaptic and postsynaptic activity induces timing-dependent hippocampal synaptic plasticity. J. Neurosci. *32*, 12337–12348.

Hassani, O.K., Lee, M.G., Henny, P., and Jones, B.E. (2009). Discharge profiles of identified GABAergic in comparison to cholinergic and putative glutamatergic basal forebrain neurons across the sleep-wake cycle. J. Neurosci. *29*, 11828–11840.

Hasselmo, M.E., and Sarter, M. (2011). Modes and models of forebrain cholinergic neuromodulation of cognition. Neuropsychopharmacology *36*, 52–73.

Herrero, J.L., Roberts, M.J., Delicato, L.S., Gieselmann, M.A., Dayan, P., and Thiele, A. (2008). Acetylcholine contributes through muscarinic receptors to attentional modulation in V1. Nature *454*, 1110–1114.

Janssen, P., and Shadlen, M.N. (2005). A representation of the hazard rate of elapsed time in macaque area LIP. Nat. Neurosci. *8*, 234–241.

Jimenez Rezende, D., and Gerstner, W. (2014). Stochastic variational learning in recurrent spiking networks. Front. Comput. Neurosci. *8*, 38.

Kaifosh, P., Lovett-Barron, M., Turi, G.F., Reardon, T.R., and Losonczy, A. (2013). Septo-hippocampal GABAergic signaling across multiple modalities in awake mice. Nat. Neurosci. *16*, 1182–1184.

Kalmbach, A., Hedrick, T., and Waters, J. (2012). Selective optogenetic stimulation of cholinergic axons in neocortex. J. Neurophysiol. *107*, 2008–2019.

Kilgard, M.P., and Merzenich, M.M. (1998). Cortical map reorganization enabled by nucleus basalis activity. Science *279*, 1714–1718.

Kuhn, J., Hardenacke, K., Lenartz, D., Gruendler, T., Ullsperger, M., Bartsch, C., Mai, J.K., Zilles, K., Bauer, A., Matusch, A., et al. (2015). Deep brain stimulation of the nucleus basalis of Meynert in Alzheimer's dementia. Mol. Psychiatry *20*, 353–360.

Lee, M.G., Hassani, O.K., Alonso, A., and Jones, B.E. (2005). Cholinergic basal forebrain neurons burst with theta during waking and paradoxical sleep. J. Neurosci. *25*, 4365–4369.

Lehmann, J., Nagy, J.I., Atmadia, S., and Fibiger, H.C. (1980). The nucleus basalis magnocellularis: the origin of a cholinergic projection to the neocortex of the rat. Neuroscience *5*, 1161–1174.

Letzkus, J.J., Wolff, S.B.E., Meyer, E.M.M., Tovote, P., Courtin, J., Herry, C., and Lüthi, A. (2011). A disinhibitory microcircuit for associative fear learning in the auditory cortex. Nature *480*, 331–335.

Lin, S.-C., and Nicolelis, M.A. (2008). Neuronal ensemble bursting in the basal forebrain encodes salience irrespective of valence. Neuron *59*, 138–149.

Liu, C.-H., Coleman, J.E., Davoudi, H., Zhang, K., and Hussain Shuler, M.G. (2015). Selective activation of a putative reinforcement signal conditions cued interval timing in primary visual cortex. Curr. Biol. *25*, 1551–1561.

McGaughy, J., Everitt, B.J., Robbins, T.W., and Sarter, M. (2000). The role of cortical cholinergic afferent projections in cognition: impact of new selective immunotoxins. Behav. Brain Res. *115*, 251–263.

McGaughy, J., Dalley, J.W., Morrison, C.H., Everitt, B.J., and Robbins, T.W. (2002). Selective behavioral and neurochemical effects of cholinergic lesions produced by intrabasalis infusions of 192 IgG-saporin on attentional performance in a five-choice serial reaction time task. J. Neurosci. *22*, 1905–1913.

Metherate, R., Cox, C.L., and Ashe, J.H. (1992). Cellular bases of neocortical activation: modulation of neural oscillations by the nucleus basalis and endogenous acetylcholine. J. Neurosci. *12*, 4701–4711.

Nelson, C.L., Sarter, M., and Bruno, J.P. (2005). Prefrontal cortical modulation of acetylcholine release in posterior parietal cortex. Neuroscience *132*, 347–359.

Parikh, V., Kozak, R., Martinez, V., and Sarter, M. (2007). Prefrontal acetylcholine release controls cue detection on multiple timescales. Neuron *56*, 141–154.

Pi, H.-J., Hangya, B., Kvitsiani, D., Sanders, J.I., Huang, Z.J., and Kepecs, A. (2013). Cortical interneurons that specialize in disinhibitory control. Nature *503*, 521–524.

Pinto, L., Goard, M.J., Estandian, D., Xu, M., Kwan, A.C., Lee, S.-H., Harrison, T.C., Feng, G., and Dan, Y. (2013). Fast modulation of visual perception by basal forebrain cholinergic neurons. Nat. Neurosci. *16*, 1857–1863.

Richardson, R.T., and DeLong, M.R. (1991). Electrophysiological studies of the functions of the nucleus basalis in primates. Adv. Exp. Med. Biol. *295*, 233–252.

Saper, C.B. (1984). Organization of cerebral cortical afferent systems in the rat. II. Magnocellular basal nucleus. J. Comp. Neurol. *222*, 313–342.

Sarter, M., Parikh, V., and Howe, W.M. (2009). Phasic acetylcholine release and the volume transmission hypothesis: time to move on. Nat. Rev. Neurosci. *10*, 383–390.

Schultz, W., Dayan, P., and Montague, P.R. (1997). A neural substrate of prediction and reward. Science *275*, 1593–1599.

Seol, G.H., Ziburkus, J., Huang, S., Song, L., Kim, I.T., Takamiya, K., Huganir, R.L., Lee, H.K., and Kirkwood, A. (2007). Neuromodulators control the polarity of spike-timing-dependent synaptic plasticity. Neuron *55*, 919–929.

Whitehouse, P.J., Price, D.L., Struble, R.G., Clark, A.W., Coyle, J.T., and Delon, M.R. (1982). Alzheimer's disease and senile dementia: loss of neurons in the basal forebrain. Science *215*, 1237–1239.

Wilson, F.A., and Rolls, E.T. (1990). Learning and memory is reflected in the responses of reinforcement-related neurons in the primate basal forebrain. J. Neurosci. *10*, 1254–1267.

Wrenn, C.C., and Wiley, R.G. (1998). The behavioral functions of the cholinergic basal forebrain: lessons from 192 IgG-saporin. Int. J. Dev. Neurosci. *16*, 595–602.

Yu, A.J., and Dayan, P. (2005). Uncertainty, neuromodulation, and attention. Neuron *46*, 681–692.

Zaborszky, L., Van Den Pol, A., and Gyengesi, E. (2012). The basal forebrain cholinergic projection system in mice. In The Mouse Nervous System, C. Watson, G. Paxinos, and L. Puelles, eds. (Amsterdam: Elsevier), pp. 684–718.

Zaborszky, L., Csordas, A., Mosca, K., Kim, J., Gielow, M.R., Vadasz, C., and Nadasdy, Z. (2013). Neurons in the basal forebrain project to the cortex in a complex topographic organization that reflects corticocortical connectivity patterns: an experimental study based on retrograde tracing and 3D reconstruction. Cereb. Cortex. *25*, 118–137.

Zhang, H., Lin, S.-C., and Nicolelis, M.A.L. (2011). A distinctive subpopulation of medial septal slow-firing neurons promote hippocampal activation and theta oscillations. J. Neurophysiol. *106*, 2749–2763.

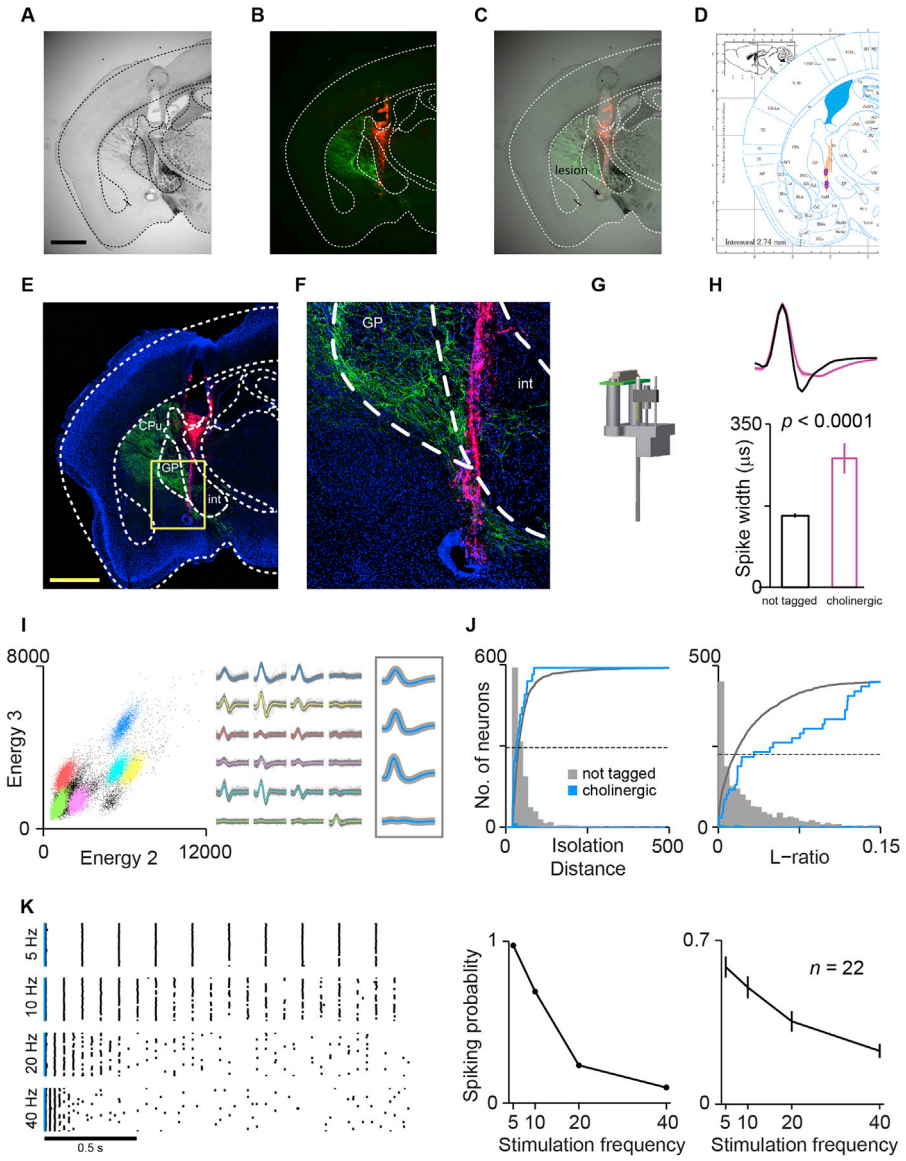

Figure S1. Optogenetic Tagging of Central Cholinergic Neurons, Related to Figure 1

(A) Bright field image of a coronal section containing the tetrode tracks and the electrolytic lesion. Scale bar, 1 mm.

(B) Fluorescent image of the same section. Green, ChAT-ChR2-eYFP; red, DiI.

(C) Overlay image.

(D) The corresponding atlas image was morphed on the section and the reconstructed tetrode tracks (red) were projected on the atlas, allowing registering recording positions of cholinergic neurons (purple) to atlas coordinates.

(E) Confocal image of the same section. Blue, nuclear staining (DAPI). Scale bar, 1 mm.

(F) Magnified image of the marked area.

(G) Schematic of the microdrive.

(H) Top, average spike shape of cholinergic (purple) and unidentified (black) neurons. Shading, s.e. Bottom, comparison of median spike width (peak to valley) between unidentified and cholinergic neurons. Error bars, s.e. Cholinergic neurons had broader spikes on average.

(I) Example of clustering from a single session. Left, spike waveform projections in feature space. Individual neurons are indicated in different colors. The dark blue neuron was cholinergic. Middle, spike shape of the neurons (gray, individual spikes; colored, average) on each tetrode lead. Right, Average light-evoked spikes (blue) and average spontaneous spikes (gray) of the cholinergic neuron were identical.

(J) Histogram and cumulative histogram of cluster quality measures Isolation Distance (left) and L-ratio (right). Blue, cholinergic neurons; gray, unidentified neurons.

(K) Left, spike response of a cholinergic neuron to increasing stimulation frequencies. Blue, onset of the first light pulse. Middle, response reliability of the same neuron as a function of stimulation frequency. Right, average response reliability. Error bars, s.e.

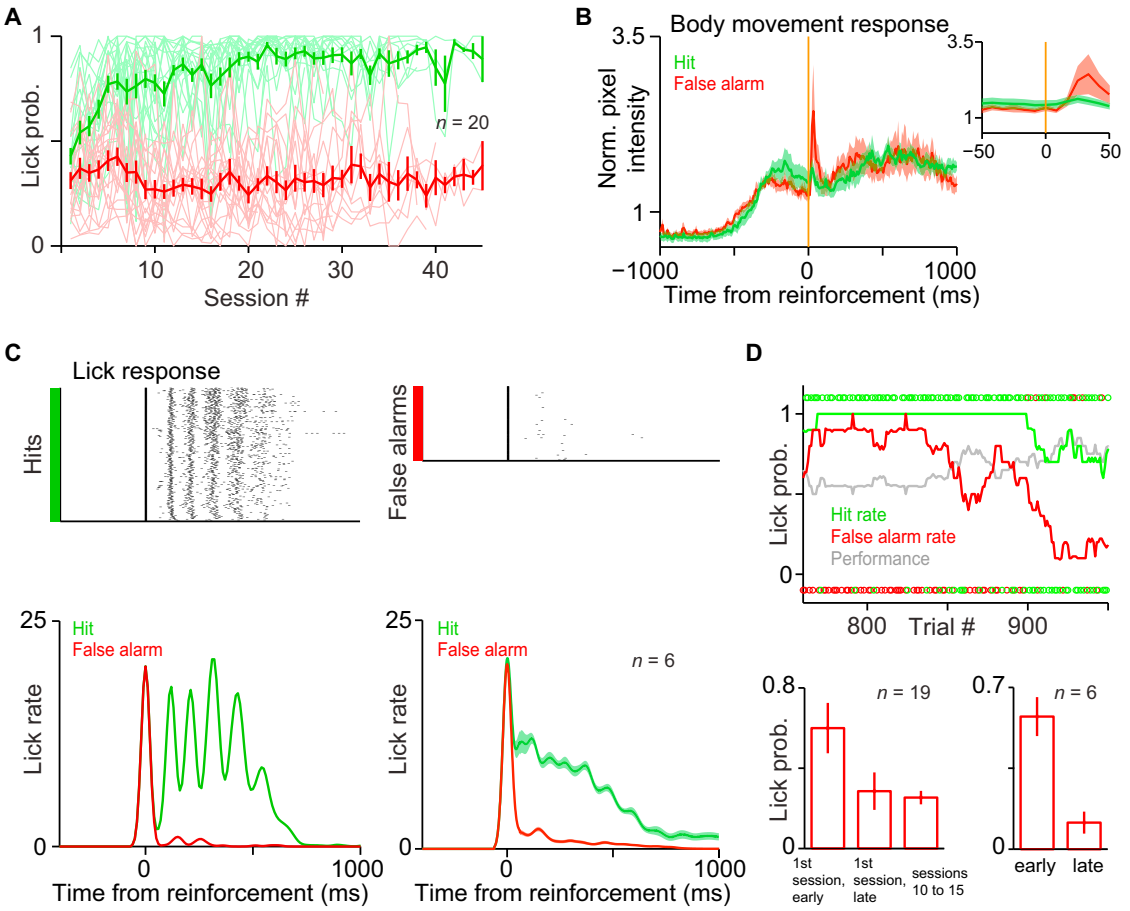

Figure S2. Auditory Detection Task, Related to Figure 2

(A) Learning curve. Green, response rate to go tones; red, response rate to no-go tones. Light lines, individual mice; dark lines, average; the easiest condition was used; n = 20 (2 mice were excluded because of missing data or extensive stimulation that could potentially influence learning); error bars, s.e.

(B) Average body movement response after air puff (red) and water delivery (green) at two different timescales (32 sessions from 7 mice).

(C) Top, lick responses aligned to water (left) or air-puff delivery (right) in an example session. Bottom left, PETH of lick responses from the same session. Bottom right: average lick response aligned to reward and punishment (n = 6 mice trained with no delay between the animal's response and reinforcement; the last 10 sessions of each mice were used).

(D) Top, example of avoidance learning. Green, hit rate; red, false alarm rate; gray, performance. Below and above the graphs, individual outcomes of go and no-go trials, respectively; green, hit/correct rejection; red, miss/false alarm. Note the performance increase around trial no. 850 caused by a sudden drop in false alarm rate. Bottom left, false alarm rates in the beginning and end of the first session and in sessions 10-15 (n = 19). False alarm rates significantly dropped in the first session ($p = 0.0015$; Wilcoxon signed rank test). Bottom right, false alarm rate in the first session ('early') and after training ('late'), with comparable task difficulty (n = 6; $p = 0.03$, Wilcoxon signed rank test).

Cell

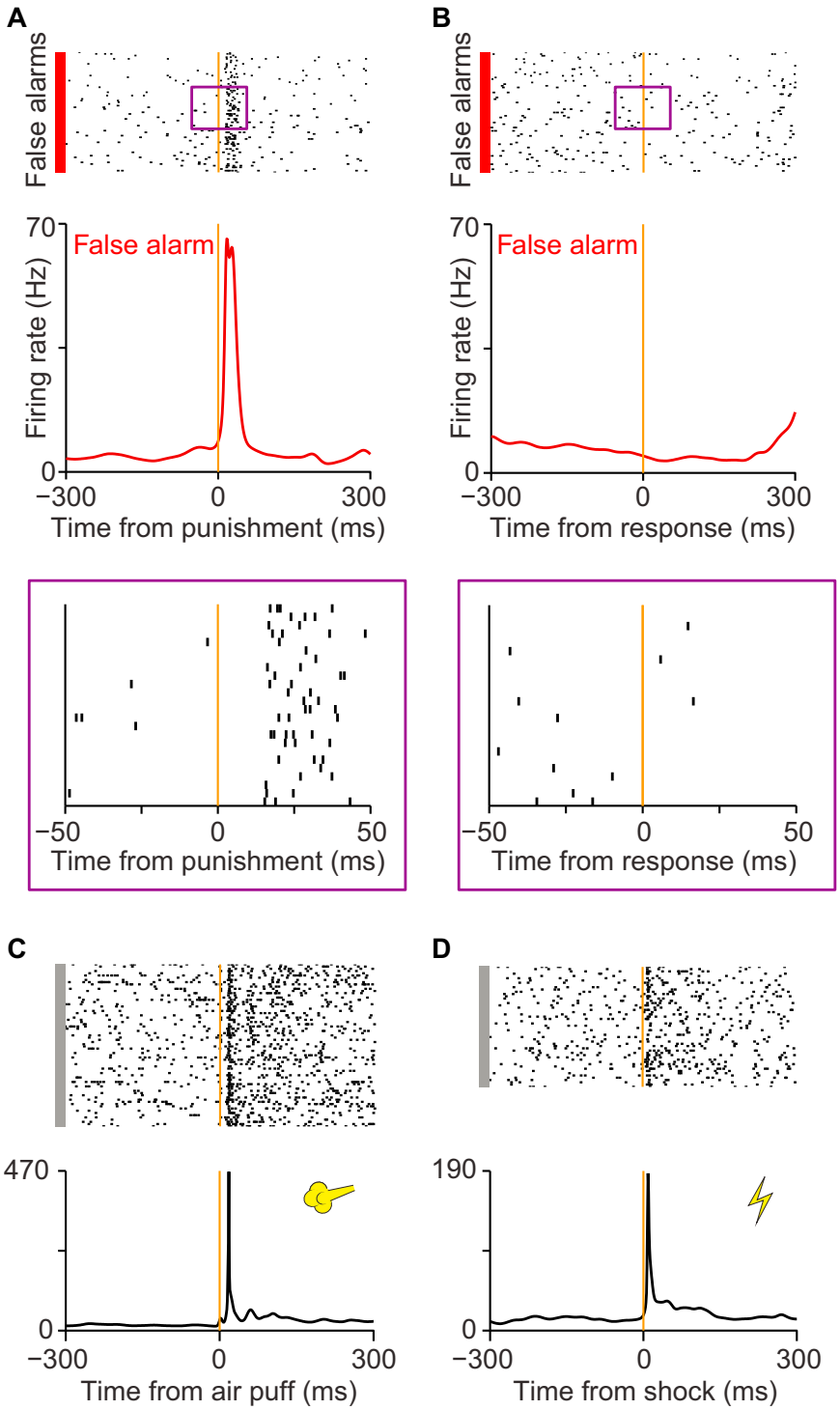

Figure S3. Punishment Uniformly Activates Cholinergic Neurons, Related to Figure 3

(A) Example cholinergic neuron firing a burst of action potentials in response to air puff punishment. From top to bottom: raster plot of false alarm trials, aligned to air puffs, sorted by RT; PETH; the area in the purple rectangle in the top panel was enlarged to show that this neuron was firing short bursts in response to air puffs.

(B) The trials were realigned to the animal's motor response (lick detection). Layout follows that of (A). The spikes align to the reinforcement and not the motor response.

(C) Spike raster and PETH of a cholinergic NB neuron aligned to air puffs outside the detection task.

(D) Spike raster and PETH of the same neuron aligned to mild foot shocks.

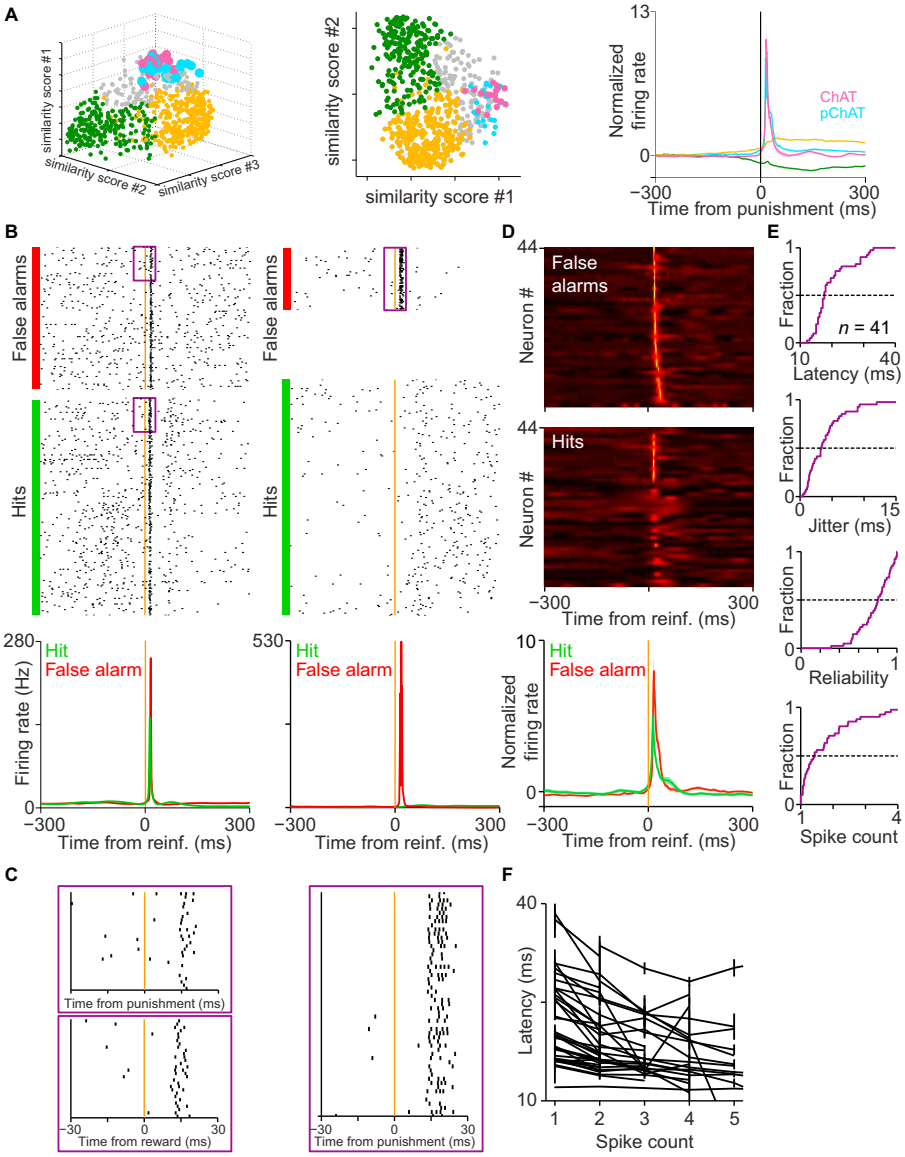

Figure S4. Cholinergic Neurons Respond to Primary Reinforcers, Related to Figure 4

(A) Hierarchical clustering was used to identify putative cholinergic neurons (cyan), which clustered together with identified NB cholinergic neurons (purple) based on punishment response properties. Left and middle, 3-D and 2-D projections of the 4-D clusters. Similarity scores were derived from average PETH of neurons activated/inhibited after punishment or from identified cholinergic neurons (see the Experimental Procedures). Right, average PETH of cholinergic (purple), putative cholinergic (cyan), sustained activated (orange cluster) and inhibited (green cluster) NB neurons. Note the almost complete overlap of punishment response in cholinergic and putative cholinergic neurons. Shading, s.e.

(B) Spike rasters (top) and PETHs (bottom) of two putative cholinergic neurons aligned to reinforcement delivery (orange line), air puff for false alarms and water for hits. Trials were sorted by RT. The putative cholinergic neuron on the left showed precisely timed short latency response to both air puff and water, while the neuron on the right exhibited a similar punishment response and a weaker and less precise reward response.

(C) The areas in the purple rectangles in (B) were magnified.

(D) Top, individual PETHs (color coded from black to white) of all cholinergic neurons (identified and putative) showed homogeneous phasic responses to punishment. Middle, the reward response of cholinergic neurons showed more variability. Cells were sorted by punishment response latency. Bottom, average PETHs.

(E) Cumulative histogram of punishment response peak latency, first spike jitter, reliability and number of spikes in response to punishment (spike count) for all responsive cholinergic (identified and putative) neurons.

(F) Spike latency showed negative correlation with spike count. Error bars, s.e. Note the overall similarity of responses in identified (Figures 3, 4, and 5) and putative cholinergic neurons.

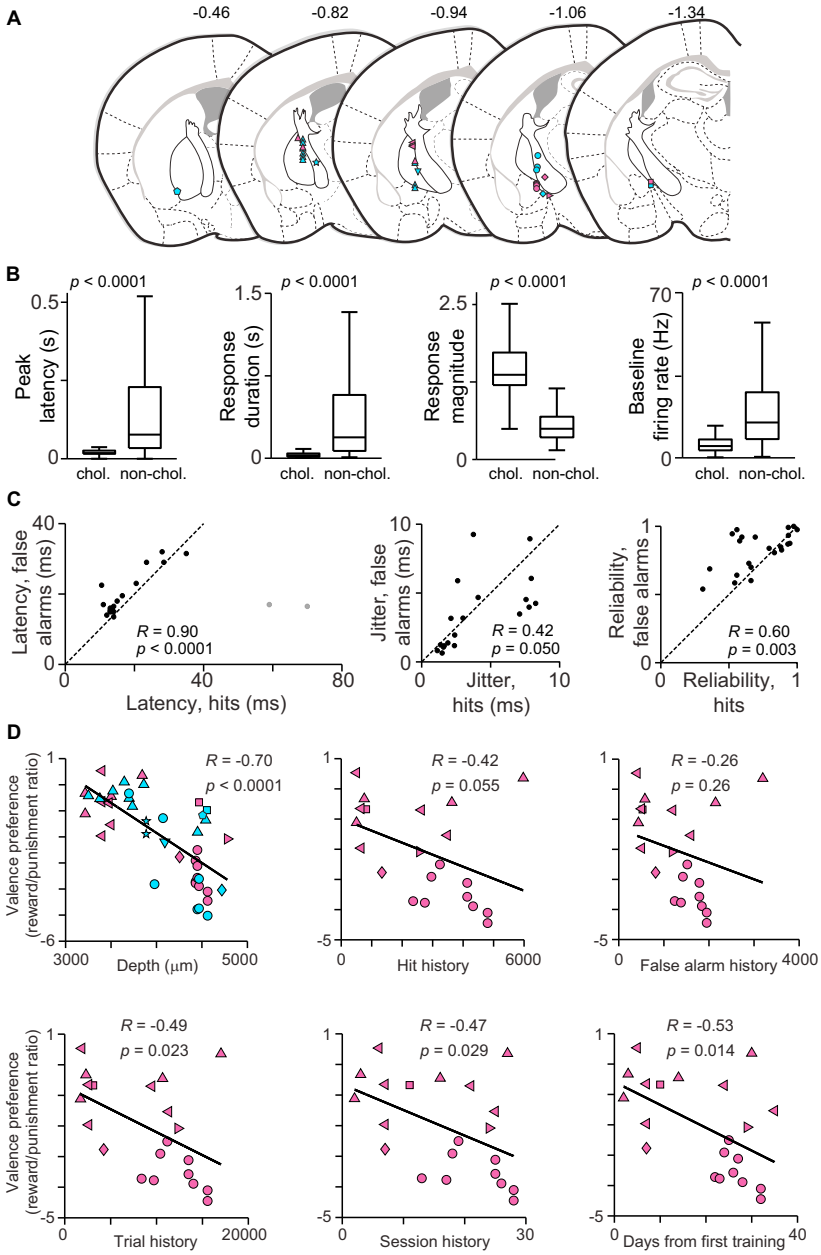

Figure S5. Cholinergic Neurons Are Activated by Water Reward, Related to Figure 5

(A) Reconstruction of recording positions of identified (purple) and putative cholinergic (cyan) neurons. Numbers, antero-posterior distance from Bregma. Different symbols represent individual mice.

(B) Box plots comparing properties of punishment response of cholinergic (identified and putative) and responsive putative non-cholinergic neurons. The plots indicate median, interquartile interval and non-outlier range. Cholinergic neurons showed short response latency and duration, large response magnitude and low baseline firing rate compared to non-cholinergic neurons.

(C) Scatter plots comparing properties of response to punishment versus reward in reward-responding ($p < 0.01$, Mann-Whitney test) cholinergic neurons (identified and putative). Latency, jitter and reliability of firing in response to punishment and reward were significantly positively correlated (for latency, the 2 outliers in gray were excluded).

(D) Correlation of valence preference with training history. Top left, correlation of valence preference and recording depth including both identified and putative NB cholinergic neurons. See Figure 5C for the same correlation with identified cholinergic neurons only. Middle and right, scatter plot of valence preference and cumulative number of hits or false alarms in previous sessions. Bottom left to right, scatter plot of valence preference and number of previous trials, sessions or days from first session. Different symbols represent individual mice. Reward response variability was best explained by recording depth (compare to Figure 5C; see the Experimental Procedures for partial correlations).

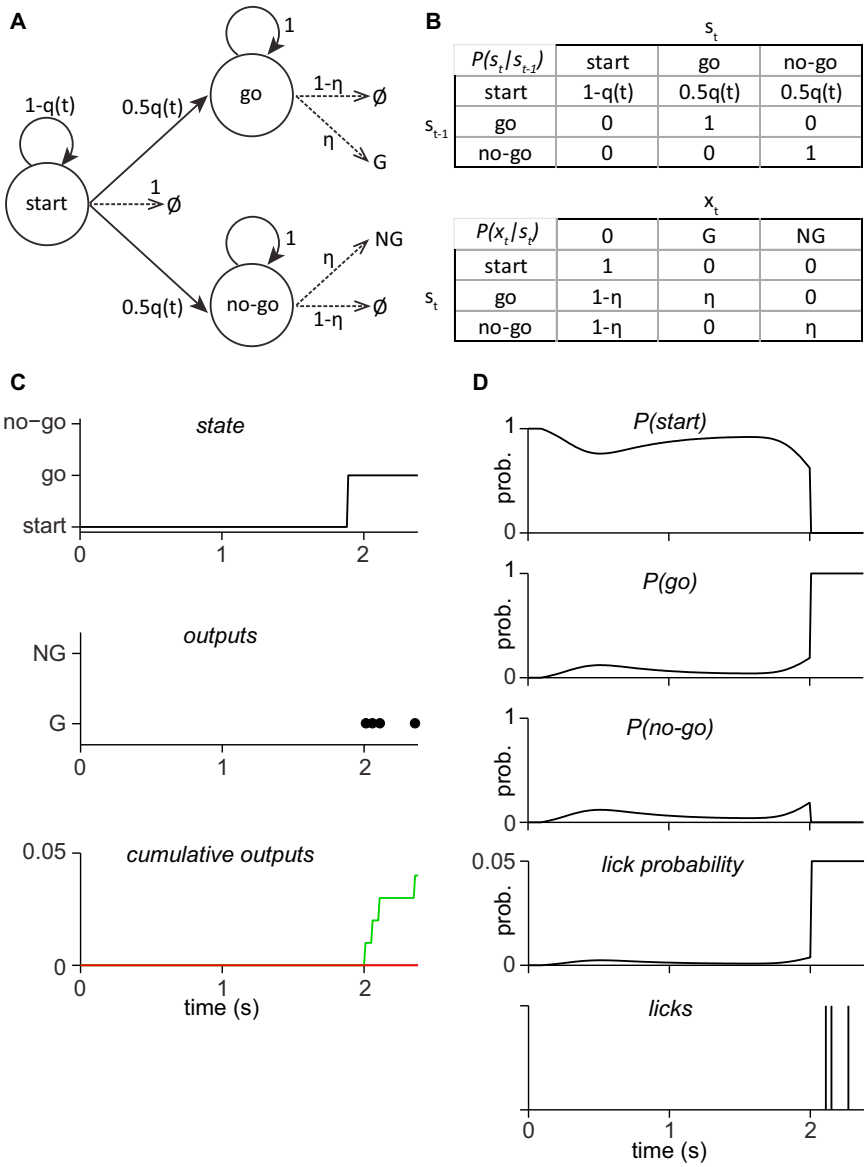

Figure S6. Cholinergic Responses Are Scaled by Reinforcement Surprise, Related to Figure 6

(A) Model schematic.

(B) State transition and output probabilities.

(C) States, outputs and cumulative outputs in a single run ('trial') of the model.

(D) Inferred state probabilities, lick probability and simulated licks corresponding to (C).

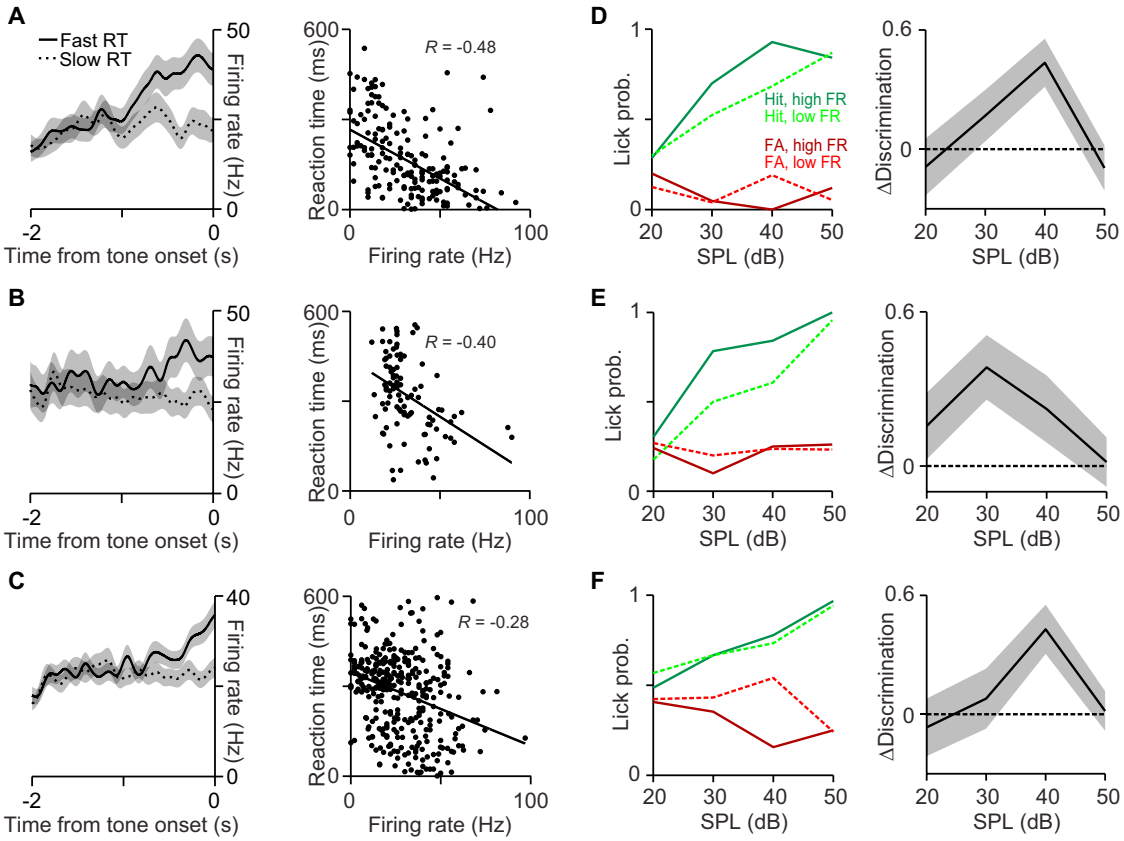

Figure S7. Attentional Correlates Are Characteristic of a Population of Non-cholinergic Neurons, Related to Figure 7

(A–C) Three not tagged example neurons that showed pre-stimulus firing rate predictive of reaction time. Left, peri-event time histogram (PETH) separated to slow (dashed line) and fast (solid line) RT trials (median split). Right, RT and pre-stimulus firing rate showed negative trial-to-trial correlation.

(D–F) Three not tagged example neurons that showed pre-stimulus firing rate predictive of performance accuracy. Left, performance was plotted separately for trials with high (solid lines) and low firing rate (dashed lines) in the foreperiod (median-split). Right, difference in discrimination performance between high and low firing rate trials as a function of stimulus intensity. Shading, bootstap s.e. SPL, sound pressure level.

Cell

Supplemental Information

Central Cholinergic Neurons Are Rapidly Recruited by Reinforcement Feedback

Balázs Hangya, Sachin P. Ranade, Maja Lorenc, and Adam Kepecs

Supplemental Experimental Procedures

Animals

Adult (over 2 months old) ChAT-Cre (n = 15, 14/15 male, Higley et al., 2011), ChAT-ChR2 (n = 3, 3/3 male, Zhao et al., 2011) and PV-Cre (n = 4, 4/4 male) mice were used for behavioral recording experiments, two additional mice (ChAT-ChR2) were used for recordings and nine additional mice (n = 6 ChAT-Cre and n = 3 wild type) were used for behavioral experiments under the protocol approved by Cold Spring Harbor Laboratory Institutional Animal Care and Use Committee in accordance with National Institutes of Health regulations.

Microdrive construction

Custom-built light-weight (2.2g) microdrives (Fig. S1G) were constructed for deep brain recording and optogenetic stimulation. The parts were mounted on a plastic frame designed in AutoCAD Inventor (Autodesk) and 3D printed (Vista Technologies). A moveable shuttle held a polyimide coated multimode optic fiber (50 μm core diameter, NA = 0.2, Polymicro Technologies) and 7 or 8 tetrodes twisted from polyimide-insulated nichrome wires (diameter, 12.7 μm; California Fine Wire). The shuttle was mounted on a miniature screw (0.6mm outer diameter, 12mm length) with a pitch of 160 μm. An optic ferrule (LC ferrule 80 μm, Precision Fiber Products) was attached to the optic fiber. The ferrule end of the fiber was polished using standard optical methods for efficient light coupling and the other end was precisely cleaved for insertion into the brain. The tetrode wires were connected to an electrode interface board (EIB-36-Narrow, Neuralynx) that held a connector (Omnetics) using gold electrode contact pins (Neuralynx). Ground and reference wires were soldered to the EIB. Two stereotrodes twisted from platinum-iridium wires (diameter, 17.8 μm; California Fine Wire) were also connected to the EIB for local field potential recordings (n = 16/22 mice). The optic fiber and the tetrodes were tunneled into a polyimide tube (29 Ga) fixed to the shuttle. As the shuttle was lowered by turning the screw, the polyimide tube moved inside a stainless steel cannula (25 Ga, 0.002'' wall) attached to the plastic frame thereby lowering the tetrodes and fiber. The outer diameter of the cannula was kept minimal (0.02'') to reduce brain damage. A stopper was placed on the cannula to prevent the drive from penetrating too deep into brain tissue. Before implantation, tetrodes were cut to final length (300-600 μm between optic fiber and tetrode tips), dipped in DiI (Life Technologies) to aid later track reconstruction and then gold-plated; impedances measured at 1 kHz were kept between 200-500 kΩ. The tetrodes and the optic fiber were retracted in the cannula and were protected with a drop of mineral oil.

Injection and microdrive implantation

Mice were anaesthetized with a mixture of ketamine (100 mg kg^{-1}) and xylazine (10 mg kg^{-1}) administered intraperitoneally after a brief induction with isoflurane. Surgical anaesthesia was maintained with supplementary doses of ketamine/xylazine as necessary. The skin and connective tissues of the scalp were injected with lidocaine subcutaneously; eyes were protected with ophthalmic lubricant (Puralube Vet Ointment, Dechra Pharmaceuticals Plc.). Mice were placed in a stereotax (David Kopf Instrunments) and the skull was leveled along both the lateral and antero-posterior axis to allow precise targeting. A cranial window was opened above the caudal NB (antero-posterior -0.9 mm, lateral 2.2 mm(Franklin and Paxinos, 2007)) or HDB (antero-posterior 0.75 mm, lateral 0.6 mm) and three additional small craniotomies were drilled for ground, reference and auditory cortical electrodes. Adeno-associated virus (AAV) serotype 2/9 carrying the construct EF1α.DIO.ChETA.EYFP (UNC Vector Core Facility; titer, 8×10^{12} virus particles per ml) was injected into the caudal NB or HDB using stereotactic targeting (3- 4 dorso-ventral levels between 3.3 and 5 mm (NB) or 2-4 levels between 4.5 and 5.5 mm (HDB); up to 1 µl full volume; Fig. 1B) via a glass pipette pulled (P-97 Flaming/Brown Micropipette Puller, Sutter Instruments Co.) from borosilicate capillaries (5 µl; tip diameter, 15-18µm). Mice already expressing channelrhodopsin2 (ChR2) under the control of the choline-acetyltransferase (ChAT) promoter (ChAT-ChR2, n = 3; Fig. S1A-F) did not undergo virus injection. Next, a stainless steel guiding tube (22Ga, 0.0035'' wall) was placed above the cranial window using stereotactic positioning to maintain vertical orientation of the drive. Two ~15 mm pieces of 30 AWG insulated copper wires, stripped at both ends, were implanted to serve as ground (parietal cortex or occipital cortex) and reference (parietal cortex). The craniotomies were covered by low viscosity silicone elastomer sealant (Kwik-Cast, World Precision Instruments) and adhesive cement (C&B MetaBond, Parkell Inc.) was applied on the skull surface. After the adhesive cured, the drive was gently lowered into the brain through the guide tube. The cannula penetrated the primary somatosensory cortex and the lateral ventricle (NB, n = 16) or M2/AGm (HDB, n = 1) to a depth of 2-2.6 mm (2.75 mm and 3.25 mm in 1-1 NB mice) precisely controlled with the stopper (see above). Five mice were implanted without brain penetration of the cannula, fixed by a custom designed holder instead of a guiding tube. Once in place, the drive was secured to the skull by multiple layers of dental acrylic (Lang Dental). Two stereotrodes were implanted in the ipsilateral auditory cortex (antero-posterior -2.5, lateral 4 mm) for local field potential recordings. A titanium head-bar was attached to the frontal plate for head-fixation. Finally, the ground and reference electrodes were connected and the tetrodes were lowered 480 µm below the cannula tip. Mice received a subcutaneous injection of analgesic (Ketofen, 2 mg kg^{-1}) and local application of antibiotics (Neo-Predef). Additional doses of analgesics

were injected throughout the three days postoperative monitoring period. Mice were allowed two weeks to recover.

Behavioral setup, sustained attention task, training

The behavioral setup consisted of a custom-built apparatus allowing head-restraining mice in a plastic half-tube. Licks were detected instantaneously when the tongue of the mouse broke an infrared beam of a custom designed lickometer (Island Motion Co.). Precisely controlled amounts of water (3 µl, 3.5 µl or 4 µl per reward; the amount was chosen in the initial training period to optimize behavior and kept fixed afterwards) were delivered through a plastic lick tube and brief puffs of air were delivered via a separate tubing system. Water- and air flow was controlled by precisely timed opening and closing of solenoid valves. Auditory stimuli were played using two speakers with sound intensities calibrated separately for pure tones and white noise at the position of the mouse's head. Mice were monitored by a USB camera. For n = 7 mice, high speed video (120 Hz) was acquired with a Point Grey Flea3 USB camera (FL3-U3-13S2M-CS) under IR illumination. Video timestamps were synchronized with behavior with a TTL signal at stimulus onset for each trial. High-speed video was collected for 7 identified cholinergic neurons recorded from 4 mice. The entire apparatus was placed in a sound attenuated chamber (Industrial Acoustics Co.). All hardware peripheries were controlled by a real-time Linux computer through a data acquisition board (National Instruments PCI-MIO-16E-1) and a breakout box via digital input/output lines, allowing sub-millisecond precision. The custom-written user interface for behavior control (BControl, C. Brody) was run on a separate computer sending a finite state machine to the real-time Linux computer before every trial. Sleep sessions were recorded in the home cage placed in the same sound-attenuated chamber. Mice were tracked by an overhead camera using a red and a green LED mounted on the headstage (Neuralynx). Sleep segments were selected based on the tracking data, aided by the auditory LFP recordings (no head motion and presence of delta activity in the LFP). Freely moving segments (non-zero speed) were differentiated from 'quiet wakefulness' (only head movements).

Mice were trained on an auditory sustained attention task according to a head-fixed go/no-go detection paradigm. Mice were water-scheduled to achieve 85-90% of normal body weight. After a very brief period of operant conditioning (10-20 trials), the mice proceeded to a direct delivery phase in which they received water if they licked any time within 90 s after a go tone (50 or 60 dB, 20 kHz pure tone played for 0.5 s or first lick, whichever happened earlier). At the end of each trial an LED was turned on and it remained on until the mouse refrained from licking for at least 1.5 s. The LED turning off signaled the start of a new trial. Each stimulus was preceded by a random foreperiod. If the mouse licked during the foreperiod, the LED was turned on and the trial was restarted (except for two mice, where no restart was

implemented). After forming tone-reward association (~35-70 hits within the final response window), the response window was abruptly shortened to the final 600 ms from tone onset. This initial training phase typically lasted 3-5 days from first time in setup (median, 4 training days; range, 1-7 training days). Once the animals learned to lick for water (typically immediately after a very short delivery of free water in the first session), they quickly habituated to head-restraining and showed no sign of discomfort by the end of the initial training period. Next, mice were introduced to the full task in which they had to lick after go tones (50 or 60 dB, 20 kHz, 0.5 s) within 600 ms from tone onset to obtain water reward and withhold licking after no-go tones (50 or 60 dB, 4 kHz, 0.5s) for 600 ms to avoid punishment (a mild facial air-puff for 100 or 200 ms; Fig. 2). To make the task attention-demanding, the stimulus presentation was preceded by a random foreperiod and mice were required to respond only in a brief response window of 600 ms. Each trial was concluded with one of the four following possible outcomes: two types of correct trials, hit (response to go tone) or correct rejection (no response to no-go tone) and two types of incorrect trials, miss (no response to go tone) or false alarm (response to no-go tone). Mice showed periods of good performance already on the first (n = 16/22; sometimes second, n = 5/22 or third, n = 1/22) day of full task (Fig. S2). Attentional load was increased by introducing fainter tones (20, 30, 40 and 50 dB) and gradually increasing background white noise to 20-60 dB (median, 45 dB). Trials with different signal-to-noise ratios were interleaved pseudo-randomly. Attentional demand was high because of (i) the random foreperiod that introduced temporal uncertainty about the stimulus, (ii) the short response window (600 ms from tone onset) which mandated quick detection and (iii) the low signal-to-noise ratio for difficult trials (20 dB signal over 45 dB noise). Stable psychometric performance was reached after a median of 12 training days from first time in setup (range, 8-22 training days). For visualizing average data as a function of signal to noise ratio, intermediate stimulus intensities were pooled (referred to as ‘normalized SPL’ in the figures).

To manipulate temporal attention, the foreperiods were drawn either from an exponential (mean, 1.4 s; cutoffs at 0.1 and 5 s; Fig. 7B) or a bimodal distribution (mixture of two Gaussians and a uniform distribution with mixing probabilities 0.35, 0.35 and 0.3; means, 0.3 and 2 s; s.d., 0.15 s; cutoffs at 0.1 and 3 s; Fig. 7A). The two distributions had the same effective mean of approximately 1.28 s. Exponential foreperiod distributions result in a constant hazard rate (Janssen and Shadlen, 2005), with equal probability of stimulus occurrence throughout the foreperiod on any given trial (Fig. 7A). Bimodal foreperiod distributions result in temporal expectations with the stimulus more likely to be delivered at two time points according to the modes, determined by the subjective hazard model (Janssen and Shadlen, 2005) (Fig. 7B).

Six cholinergic neurons (4 located in the HDB and 2 in the NB from 5 mice) were tested for responses to primary negative reinforcement (air puff) outside the detection task. One of these neurons (in NB) also responded to mild foot shocks (foot shock protocol as described in (Pi et al., 2013)).

Behavioral experiments demonstrating motivated behavior

We performed the following behavioral experiments to demonstrate negative motivational value of air puffs and positive motivational value of water.

1. Hit rate to 50 dB tones in a late session of well-trained mice was compared to hit rate in the same mice after keeping them on free water (Fig. 2C; $n = 4$; $p < 0.0001$ in all animals; chi-square test).

2. False alarm rates were compared in the beginning and end of the first session (Fig. S2D; $n = 19$; first session beginning vs. end, $p = 0.0015$; first session beginning vs sessions 10-15, $p = 0.0025$; first session end vs sessions 10-15, $p = 0.44$; Wilcoxon signed rank test; Fig. S2D). To ensure that differences were not due to fatigue or a general decrease in motivation to lick, we restricted the analysis to a period of task engagement defined by the trials between the first and last crossing of 0.7 hit rate, calculated in a sliding window of 20 trials. Only sessions with at least 50 trials of task engagement were considered.

3. We adjusted task difficulty (background noise level) before each session based on previous performance to keep false alarm rates constant (see Behavioral setup, sustained attention task, training subsection); this ensured testing neural responses to punishment. However, to test false alarm rates under comparable conditions, we trained mice on the detection task ($n = 6$) and then tested them using initial conditions (50 dB cue tones, no background noise; in one mouse, 5 dB background noise). Mice performed significantly less false alarms when compared to the first session, demonstrating learned avoidance behavior ($p = 0.03$, Wilcoxon signed rank test; Fig. S2D). The same engagement criteria were used as above.

4. Mice ($n = 5$) were trained on a variation of the task in which the go tone still predicted water but the no-go tone predicted a combination of the same amount of water with an air puff. It should be noted that withholding licks to the no-go tones had an additional time cost in this version, because the animal had to wait until the next stimulus to obtain water. However, mice still preferred to lick for water over the combination of water and air puff, thus even the combination of water and time gain did not fully compensate for the negative motivational value of air puffs ($p < 0.0001$ on the population level; $p < 0.05$ in 4/5 individual mice; chi-square test). An engagement threshold of 0.5 hit rate was used.

Recording and optogenetic stimulation

Extracellular recordings were conducted using a DigitalLynx data acquisition system (Neuralynx) and Cheetah data acquisition software (Neuralynx). A pre-amplifier (Neuralynx Headstage HS-36) was connected to the electrode interface board. A fine wire tether (TETH-HS-36-FWT, Neuralynx) connected the pre-amplifier to DigitalLynx. Voltage data was collected from each tetrode referenced to the reference electrode (parietal cortex) or a silent tetrode channel. Continuous broad-band (0.1-9000 Hz) data was acquired from one lead of each tetrode (NB or HDB) and stereotrode (auditory cortex) to record local field potentials. A band-pass filter (600-6000 Hz) was applied to record action potentials from all tetrode leads in trigger mode. Signals were sampled at 32.552 kHz. Digital input was recorded from the behavior control system at the time of stimulus presentations to synchronize neural and behavioral data.

Laser light emitted by a blue laser (473 nm; 100 mW; Lasermate Group Inc.) was collimated into a fiber patch cable (126 μm diameter, NA = 0.27, CablesPlus USA) through a fibre port (Thorlabs). The patch cord was connected to the optic ferrule on the microdrive via a modified LC–LC type connector. For optogenetic identification, bursts of brief laser pulses (1 ms @5-40 Hz; burst length, 2s; inter-burst-interval, 3 s; 0.16-16 mW output range at the optic fiber tip) were delivered in the brain. The laser was triggered through a data acquisition board (National Instruments PCI-MIO-16E-1) controlled by custom-built MATLAB programs (MathWorks). The trigger TTL pulses were also recorded by the data acquisition system for synchronization. The tetrodes and the optic fiber were advanced 20-100 μm after each data acquisition session based on single unit activity and the presence or absence of light-evoked potentials.

Histology and track reconstruction

After the last recording session, mice were deeply anaesthetized with ketamine/xylazine. Electrolytic lesions were made through individual leads of each tetrode on which a cholinergic neuron was recorded (5-30 μA for 5 s; stimulus isolator, World Precision Instruments or A-M Systems; Fig. S1A-F). Mice were perfused transcardially with 4% para-formaldehyde (PFA). The brain was removed from the skull and post-fixed in PFA overnight. After post-fixation it was washed in phosphate-buffer, a block containing the full extent of the NB was excised and 50-70 μm sections were cut with vibratome (Leica VT1000S). The sections were washed in phosphate-buffer and those containing the electrode tracks were mounted on microscope slides covered in mounting medium (Vectashield, Vector Labs). They were imaged by fluorescence (Olympus MVX10) and confocal microscopes (Zeiss 710LSM; Fig. 1B; Fig. S1A-F).

The images were processed to accurately reconstruct the recording locations. Although the estimated electrode positions based on the entry coordinates and the extent of cumulative descent were registered for each recording session, individual variability in brain shape and slight deviations from a vertical descent mandated post hoc adjustment of the estimated recording coordinates. Mouse brain atlas images (Franklin and Paxinos, 2007) were morphed onto bright field images in order to register the recording sites to standard coordinates. The atlas images were carried over to fluorescent images that showed the DiI traces of the electrode tracks. The lesion site was correlated with the final protruding length of the tetrodes and the coordinates for each recording session were interpolated from the depth estimates based on electrode descent. A brain area was assigned to each recording site based on the atlas. Because the NB is a diffuse nucleus not delineated in the atlas, based on established literature (Lehmann et al., 1980; Saper, 1984; Zaborszky et al., 2013) and our retrograde tracings the following areas were included as NB: substantia innominata, globus pallidus, internal capsule, extended amygdala. Recordings were along the border of the globus pallidus and the internal capsule, which is the location of the auditory projecting NB cholinergic neurons (Fig. 1A,B; Fig. S1A-F). The recovered position of identified (Fig. 1B and Fig. S5A in more detail) and putative (Fig. S5A) cholinergic neurons agreed well with their expected positions based on our retrograde labeling experiments (Fig. 1A) and previous literature (Saper, 1984; Zaborszky et al., 2013). In some of the mice, clear visual responses were recorded after the tetrodes were ventral to the NB; the recovered position of these recordings showed very good correlation with the optic tract. Regarding the 12 identified cholinergic HDB neurons, the recording position of 11 cells were mapped to the HDB while one cell was located more dorsally at the ventral pallidum/substantia innominata border.

Data analysis

Spike sorting

Data analyses were carried out using built-in and custom-built software in Matlab (Mathworks). Action potentials were manually sorted into clusters (presumptive neurons) off-line based on amplitude (peak-to-valley) and waveform energy features using MClust software (A. D. Redish). Cluster quality was quantified by isolation distance and L-ratio (Schmitzer-Torbert et al., 2005). Putative neurons with isolation distance > 20 or L-ratio < 0.15 were excluded (L-ratio median ± standard error of median; 0.016 ± 0.0008 for all neurons and 0.033 ± 0.021 for cholinergic neurons; Fig. S1I-J). Auto-correlation functions were inspected and in case of absolute refractory period violations, an additional effort was made to improve cluster separation. If refractory violations persisted, the cluster was excluded. We also included two cholinergic neurons, for which isolation distance and L-ratio did not reach the above thresholds, but the light-evoked spikes formed a clear cluster and thus it was possible to isolate the neuron

based on the waveform information carried by light-evoked action potentials (Pi et al., 2013). Cluster drift precluded direct comparison of reward and punishment responses (as in Fig. 5C) of one neuron.

Optogenetic identification of cholinergic neurons

Cholinergic neurons were identified using optogenetic tagging (Kvitsiani et al., 2013; Lima et al., 2009; Pi et al., 2013). Significant light-activation was assessed by the Stimulus-Associated spike Latency Test (SALT). The test evaluates whether the spike latency distribution after light stimuli is different from a stimulus free baseline using an information theory measure (modified Jensen-Shannon divergence) to provide distance measure between distributions. The approach was described in detail previously (Kvitsiani et al., 2013) and Matlab code is available at http://kepecslab.cshl.edu/salt.m. Neurons significantly activated at $p < 0.01$ were included as cholinergic neurons (Fig. 1E; the figure includes all NB cells that were recorded from mice that yielded cholinergic neurons).

Light-evoked spikes were defined based on the peak of peri-stimulus time histogram (PSTH) aligned to light stimuli (spikes within full width at half height windows). These spikes were marked on the feature space projections used for spike sorting (see above). For 4 neurons, the light-evoked spikes showed only partial overlap with spontaneous action potentials, indicating probable contaminations from other neurons; these cells were excluded from the cholinergic population, resulting in n = 34 identified cholinergic neurons. (Cholinergic neurons recorded in multiple sessions were counted only once.) All cholinergic neurons showed short latency and low jitter of light-evoked spikes (Fig. 1D) and strong correlation of the light-evoked and spontaneous spike waveforms (median correlation coefficient, 0.99; s.e., 0.004; range, 0.93 to 1.0; Fig. S1I). The median reliability of light-evoked responses was 0.46 (s.e., 0.05; range, 0.17 to 0.99) for low-frequency stimulation (5 Hz for n = 23 neurons; 10 Hz for n = 10 neurons; 4 Hz for one neuron). Out of the 34 identified cholinergic neurons, 10 were recorded from ChAT-ChR2 mice (NB: 9, 1 from 2 mice) and 24 from ChAT-Cre mice (NB: 1, 4, 5, 2; HDB: 7, 3, 2 from 7 mice). Note that we did not observe any differences in hit rate, false alarm rate and reaction time between these two mouse lines ($p = 0.65$, 0.48 and 0.95, respectively; two-way ANOVA with stimulus signal-to-noise ratio and genotype as factors; p-values refer to main effect in genotype). In addition, there were no statistical differences between punishment response latency, jitter or reliability between the two mouse lines ($p = 0.43$, 0.37 and 0.31, respectively, tested for the NB). To compare reward responses, it was necessary to control for the effect of recording depth demonstrated in Figure 5C. An analysis of covariance (ANCOVA) taking depth as the dependent variable and genotype as the factor also did not reveal differences between mouse lines in terms of reward response latency, jitter and reliability ($p = 0.65$, 0.12 and 0.64, respectively).

NB neurons predicting reaction time or accuracy

We added data (n = 216 single units) from 4 non-ChAT (PV-Cre) mice to augment our data set of unidentified NB neurons (n = 1360 altogether). We were looking for NB neurons of which pre-stimulus firing rates significantly predicted reaction time (RT) on a trial-by-trial basis. RTs in hit trials were regressed against firing rates in a half second window of the foreperiod preceding stimulus delivery. The window was restricted to the foreperiod for foreperiods shorter than half second to avoid potential confounds from other task events. The lower and upper 10 percentile of the RT distribution were excluded to discount impulsive and accidental hits. Neurons with significant negative regression ($p < 0.01$) were selected. For each of these 'predictive' neurons, trials were split into slow (10-50 percentile) and fast (50-90 percentile) RT groups. Adaptive peri-event time histograms (PETH; see below) were calculated for slow and fast RT trials to visualize pre-stimulus firing rate differences. Receiver operator characteristic (ROC) analysis was performed to compare slow and fast RT trials (50 ms causal sliding windows with 20 ms overlap; smoothed by a moving average of order 5 for visualization).

We also tested whether pre-stimulus firing rates of some NB neurons predicted the animal's performance. Trials were split at median pre-stimulus firing rate to low and high firing trials and performance curves were calculated according to these groups. We tested whether the difference in hit and false alarm rates (ΔDiscrimination, a measure of the animal's ability to discriminate between go and no-go tones) were different for low and high firing trials (permutation test, $p< 0.01$; 1000 permutations). Neurons with significantly positive differences at any stimulus intensities were labeled as 'predictive'.

Adaptive peri-event time histograms

We estimated peri-stimulus (stimulus-aligned) and peri-event firing rates by using an adaptive spike density function (SDF) approach (termed peri-stimulus and peri-event time histogram, PSTH and PETH respectively). Spike rasters were convolved with a variable kernel Gaussian window to provide a SDF estimate. The kernel width of the Gaussian as well as the window size was adapted to the local estimate of spiking probability to implement stronger smoothing when information was sparse. Variance was mapped onto spiking probability between 0 (53 ms moving average window, corresponding to probability of 0) and infinity (9 ms Dirac-delta window, corresponding to probability of 1).

Cluster analysis

We performed hierarchical clustering to investigate whether identified NB cholinergic neurons form a separate cluster based on their distinctive response to punishment. All units responding to punishment were selected for this analysis ($p < 0.01$, one-sided Mann-Whitney test; firing rate change was tested in 0.5 s windows before and after punishment delivery). Simple response (PETH) features were used as clustering variables: (1) response magnitude (logarithm of maximal evoked per baseline firing rate,) (2)

similarity to the response profile of cholinergic neurons (maximal cross-correlation within a ±8 ms window with the average cholinergic PETH) and (3-4) similarity scores to templates derived from all unidentified neurons and unidentified neurons showing firing rate suppression after punishment. We performed hierarchical clustering on Z-scored variables in this 4-dimensional space. The analysis uncovered three separate clusters (2D and 3D projections shown in Fig. S4A): a small cluster containing most identified NB cholinergic neurons activated by punishment as well as 22 unidentified cells showing similar response profiles (labeled as 'putative cholinergic', pChAT), and two large clusters containing no cholinergic neurons but NB neurons showing sustained activation (n = 330) or inhibition (n = 224) after punishment (Fig. S4A, right). A part of the neurons did not fall in any of these clusters but was more distributed between the clusters ('noise cluster', n = 129).

We calculated linear correlation between valence preference (ratio of reward and punishment response magnitude, calculated as logarithm of baseline-subtracted maximal evoked firing rates) and dorso-ventral position (depth), which resulted in a significant negative correlation of R = -0.75 (Fig. 5C). This correlation was stronger than any significant correlations between reward response magnitude and training history (Fig. S5D). To test whether the correlation between response magnitude and depth could partially be explained by training history, we calculated partial correlations. Controlling for training variables resulted in no or only a slight decrease of the correlation between reward response strength and depth: R = -0.73 controlling for false alarm history, R = -0.68 controlling for hit history, R = -0.65controlling for trial history, R = -0.66 controlling for number of previous sessions, R = -0.63 controlling for days from first training. On the other hand, the correlation between reward response magnitude and number of days from the first training largely vanished when controlling for depth (R = -0.14).

Video analysis

Offline video analysis was conducted using the Bonsai framework (Lopes et al., 2014). Rectangular regions of interest (ROI) were manually drawn surrounding the eye and body. Total pixel intensity within the eye ROI was extracted for analysis of blink response. Absolute difference of the total pixel intensity in the body ROI was used to analyze body movement response.

Hidden Markov model of the auditory detection task

Basal forebrain neurons showed graded responses to water reward with stronger response if reward followed more difficult stimuli. Theoretical accounts of the cholinergic system have emphasized its role in learning and perception under uncertainty and proposed that it signals prediction uncertainty or the validity of expectations based on sensory cues (Dayan et al., 2000; Moran et al., 2013; Yu and Dayan,

2005). In our task, the strength of evidence can lead to differential outcome expectations. Therefore we wondered whether the graded cholinergic responses we observed could represent reinforcement surprise, the deviation from this outcome expectation. To explore this possibility we formally defined 'reinforcement surprise' through a computational model for the auditory detection task (Fig. 6I, Fig. S6). We designed a hidden Markov model (HMM) (Dayan and Yu, 2006) that accounted for psychometric detection performance and also computed a measure of surprise for each reinforcement event.

As mice were well trained on the task by the time of the recordings, we assumed that the animals learned a statistically veridical model of the task. This task model consisted of three states: 'start', 'go' and 'no-go' (Fig. S6). The transition probability from 'start' to other states, denoted by *q(t)*, was determined by the hazard function of stimulus onset. More precisely, leaving the 'start' state (that is, the presentation of a tone stimulus) was governed by the conditional probability of a stimulus to occur in the present time bin provided no stimulus had been presented before, based on the bimodal foreperiod distribution (see above). The 'go' and 'no-go' states were assigned equal probabilities, mimicking the go/no-go task learned by the mice (Fig. S6B, top).

The 'start' state generated no outputs (observations). The 'go' state generated a G observation with η probability and no observation with $1-\eta$ probability, reflecting the stochastic detection of the tone stimuli. Symmetrically, the 'no-go' state generated an NG output with η probability and no output with $1-\eta$ probability (Fig. S6B, bottom). The detection probability, η, depended on the stimulus difficulty (cumulative probability set to 0.01, 0.33, 0.66 and 0.99 for four levels of difficulty). The time step was set to 0.01 s. An example run of the model for a single trial is shown in Fig. S6C. After the transition to 'go' state, some G observations were generated. Mice only had access to the cumulative outputs (Fig. S6C, bottom) without direct access to the hidden states. Therefore, they had to make decisions about the stimuli based on the ambiguous observations by performing Bayesian inference (Dayan and Yu, 2006):

$$P(s_t|x_1,\dots,x_t) \propto P(x_t|s_t)\sum_{s_{t-1}} P(s_t|s_{t-1})P(s_{t-1}|x_1,\dots,x_{t-1})$$

Separately for the three states (Fig. S6D),

$$P('start'|x_1,\dots,x_t) \propto P(x_t|'start')\big[\big(1-q(t)\big)P('start'|x_1,\dots,x_{t-1})\big]$$

$$P('go'|x_1,\dots,x_t) \propto P(x_t|'go')[0.5q(t)P('start'|x_1,\dots,x_{t-1}) + P('go'|x_1,\dots,x_{t-1})]$$

$$P('no-go'|x_1,\dots,x_t) \propto P(x_t|'no-go')[0.5q(t)P('start'|x_1,\dots,x_{t-1}) + P('no-go'|x_1,\dots,x_{t-1})]$$

Since trials of varying difficulty were randomly interleaved in the task without providing mice with explicit information about difficulty, an average level of detection probability was used for the inference.

Response (lick) probability at each time stamp was defined by

$$\alpha P('go'|x_1, \dots, x_t) - \beta P('no-go'|x_1, \dots, x_t)$$

where α and β were constant parameters set to 0.05 and 0.03, respectively (Fig. S6D). If a lick occurred within 0.5 s of stimulus onset (tone duration in the detection task), a response was assigned to the trial. Responses in 'go' state resulted in hits and responses in 'no-go' state were counted as false alarms. Lack of responses in these states produced misses and correct rejections, respectively. Reaction time was determined by the time from tone onset to the animal's response. Psychometric functions and reaction times produced by the HMM closely reproduced those from the auditory detection task (Fig. 6J).

To account for graded responses to go tones by cholinergic neurons, we defined 'reinforcement surprise' in the HMM based on the cumulative number of G (hit trials) or NG (false alarm trials) observations before the animal's response. A reciprocal function: *1/(1+x)* was used to transform this number to an index ranging from 0 to 1, where 0 corresponded to no surprise and 1 corresponded to maximal surprise. The rationale behind this definition was that in hit trials, more G observation resulted in higher reward expectation and therefore less surprise. Conversely, on false alarm trials, more NG observations resulted in stronger expectation of a punishment, and thus less surprise. Next, we averaged reinforcement surprise for hit and false alarm trials per different tone intensities.

Supplemental references

Dayan, P., and Yu, A.J. (2006). Phasic norepinephrine: a neural interrupt signal for unexpected events. Network *17*, 335–350.

Dayan, P., Kakade, S., and Montague, P.R. (2000). Learning and selective attention. Nat. Neurosci. *3 Suppl*, 1218–1223.

Franklin, K.B., and Paxinos, G. (2007). The Mouse Brain in Stereotaxic Coordinates, Third Edition (Academic Press).

Higley, M.J., Gittis, A.H., Oldenburg, I. a, Balthasar, N., Seal, R.P., Edwards, R.H., Lowell, B.B., Kreitzer, A.C., and Sabatini, B.L. (2011). Cholinergic interneurons mediate fast VGluT3-dependent glutamatergic transmission in the striatum. PLoS One *6*, e19155.

Janssen, P., and Shadlen, M.N. (2005). A representation of the hazard rate of elapsed time in macaque area LIP. Nat. Neurosci. *8*, 234–241.

Kvitsiani, D., Ranade, S., Hangya, B., Taniguchi, H., Huang, J.Z., and Kepecs, A. (2013). Distinct behavioural and network correlates of two interneuron types in prefrontal cortex. Nature *498*, 363–366.

Lehmann, J., Nagy, J.I., Atmadia, S., and Fibiger, H.C. (1980). The nucleus basalis magnocellularis: the origin of a cholinergic projection to the neocortex of the rat. Neuroscience *5*, 1161–1174.

Lima, S.Q., Hromádka, T., Znamenskiy, P., and Zador, A.M. (2009). PINP: a new method of tagging neuronal populations for identification during in vivo electrophysiological recording. PLoS One *4*, e6099.

Lopes, G., Bonacchi, N., Frazão, J., and Neto, J. (2014). Bonsai: An event-based framework for processing and controlling data streams. bioRxiv.

Moran, R.J., Campo, P., Symmonds, M., Stephan, K.E., Dolan, R.J., and Friston, K.J. (2013). Free energy, precision and learning: the role of cholinergic neuromodulation. J. Neurosci. *33*, 8227–8236.

Pi, H.-J., Hangya, B., Kvitsiani, D., Sanders, J.I., Huang, Z.J., and Kepecs, A. (2013). Cortical interneurons that specialize in disinhibitory control. Nature *503*, 521–524.

Saper, C.B. (1984). Organization of cerebral cortical afferent systems in the rat. II. Magnocellular basal nucleus. J. Comp. Neurol. *222*, 313–342.

Schmitzer-Torbert, N., Jackson, J., Henze, D., Harris, K., and Redish, a D. (2005). Quantitative measures of cluster quality for use in extracellular recordings. Neuroscience *131*, 1–11.

Yu, A.J., and Dayan, P. (2005). Uncertainty, neuromodulation, and attention. Neuron *46*, 681–692.

Zaborszky, L., Csordas, A., Mosca, K., Kim, J., Gielow, M.R., Vadasz, C., and Nadasdy, Z. (2013). Neurons in the Basal Forebrain Project to the Cortex in a Complex Topographic Organization that Reflects Corticocortical Connectivity Patterns: An Experimental Study Based on Retrograde Tracing and 3D Reconstruction. Cereb. Cortex.

Zhao, S., Ting, J.T., Atallah, H.E., Qiu, L., Tan, J., Gloss, B., Augustine, G.J., Deisseroth, K., Luo, M., Graybiel, A.M., et al. (2011). Cell type–specific channelrhodopsin-2 transgenic mice for optogenetic dissection of neural circuitry function. Nat. Methods *8*, 745–752.

ARTICLES
https://doi.org/10.1038/s41593-020-0648-0

nature neuroscience

Distinct synchronization, cortical coupling and behavioral function of two basal forebrain cholinergic neuron types

Tamás Laszlovszky[1,2], Dániel Schlingloff[2,3], Panna Hegedüs[1,2], Tamás F. Freund[3], Attila Gulyás[3], Adam Kepecs[4,5] and Balázs Hangya[1]✉

Basal forebrain cholinergic neurons (BFCNs) modulate synaptic plasticity, cortical processing, brain states and oscillations. However, whether distinct types of BFCNs support different functions remains unclear. Therefore, we recorded BFCNs in vivo, to examine their behavioral functions, and in vitro, to study their intrinsic properties. We identified two distinct types of BFCNs that differ in their firing modes, synchronization properties and behavioral correlates. Bursting cholinergic neurons (Burst-BFCNs) fired synchronously, phase-locked to cortical theta activity and fired precisely timed bursts after reward and punishment. Regular-firing cholinergic neurons (Reg-BFCNs) were found predominantly in the posterior basal forebrain, displayed strong theta rhythmicity and responded with precise single spikes after behavioral outcomes. In an auditory detection task, synchronization of Burst-BFCNs to the auditory cortex predicted the timing of behavioral responses, whereas tone-evoked cortical coupling of Reg-BFCNs predicted correct detections. We propose that differential recruitment of two basal forebrain cholinergic neuron types generates behavior-specific cortical activation.

Basal forebrain cholinergic neurons have been associated with learning, memory, plasticity, attention, arousal, regulation of food intake, the sleep–wake cycle and even consciousness[1–7]. These processes are modulated at different timescales; indeed, the cholinergic system has been hypothesized to exhibit both slow tonic and fast phasic effects[8,9], similar to the dopaminergic or noradrenergic systems[10]. In vitro studies associated heterogeneous firing patterns with varying temporal scales, suggesting that subtypes of cholinergic neurons may underlie this temporal and functional heterogeneity, that is, early-firing cholinergic neurons are dedicated to phasic activation, and late-firing neurons fire slowly to set ambient acetylcholine levels[11–14]. However, in vivo studies[15–17] have not examined the functional heterogeneity of cholinergic neurons. Therefore, we tested whether there are distinct types of BFCNs in vivo and in vitro and, if so, whether these types show differences in responding to behaviorally salient events, synchronizing within and across types, as well as with cortical activities.

Inter-area synchrony has been proposed as a hallmark of neural communication and efficient information transfer. Distant brain areas can engage in synchronous oscillations, and this oscillatory activity is thought to orchestrate neuronal processing[18,19]. This clock-like organization results in the phase locking of neuronal spiking to ongoing oscillations at the cellular level, different patterns of synchrony within and across cell types at the network level, and rhythmic fluctuation of sensory detection, attention and reaction time at the behavioral level[20,21]. Therefore, synchronous versus asynchronous activation of subcortical inputs may have a substantially different impact on cortical functions, including plasticity, attention, learning and other aspects of cognition. However, recording of pairs of cholinergic neurons simultaneously has not been carried out and thus synchrony between individual cholinergic units has not yet been tested. In addition, assessment of synchrony between cholinergic firing and cortical oscillations has been sparse and seemingly contradictory[22–24].

We found two distinct cholinergic cell types in the basal forebrain (BF) by recording BFCNs both in vivo and in vitro. Burst-BFCNs exhibited early-firing in response to current injections in vitro, strongly bursting or irregular 'Poisson-like' firing in vivo, within-cell-type synchrony, and strong correlation to cortical theta oscillation. Characteristically, these neurons fired rapid, brief bursts of action potentials (APs) after reward and punishment in an auditory detection task. Synchrony between Burst-BFCNs and auditory local field potentials (LFPs) predicted response timing, but did not differentiate correct and incorrect responses. In addition, we uncovered a unique, regular rhythmic cholinergic neuron type (Reg-BFCNs) in the posterior basal forebrain. This type showed late firing in response to current injections in vitro which could not be transformed into burst mode. Reg-BFCNs showed largely asynchronous firing with other BFCNs. In contrast to the bursting neurons, synchronization of Reg-BFCNs with auditory cortical LFPs specifically predicted response accuracy of mice. Therefore, differences in the firing mode, synchrony and anatomical distribution of distinct cholinergic neuron types might produce differential regulation of cortical activation and behavior.

Results

Distinct firing patterns of cholinergic neurons in vivo. We performed extracellular tetrode recordings from the BF of awake mice (Fig. 1a; see also Methods and Nature Research Reporting Summary)[25]. Cholinergic neurons were identified using an

[1]Lendület Laboratory of Systems Neuroscience, Institute of Experimental Medicine, Budapest, Hungary. [2]János Szentágothai Doctoral School of Neurosciences, Semmelweis University, Budapest, Hungary. [3]Laboratory of Cerebral Cortex Research, Institute of Experimental Medicine, Budapest, Hungary. [4]Cold Spring Harbor Laboratory, Cold Spring Harbor, NY, USA. [5]Departments of Neuroscience and Psychiatry, Washington University in St Louis, St Louis, MO, USA. ✉e-mail: hangya.balazs@koki.mta.hu

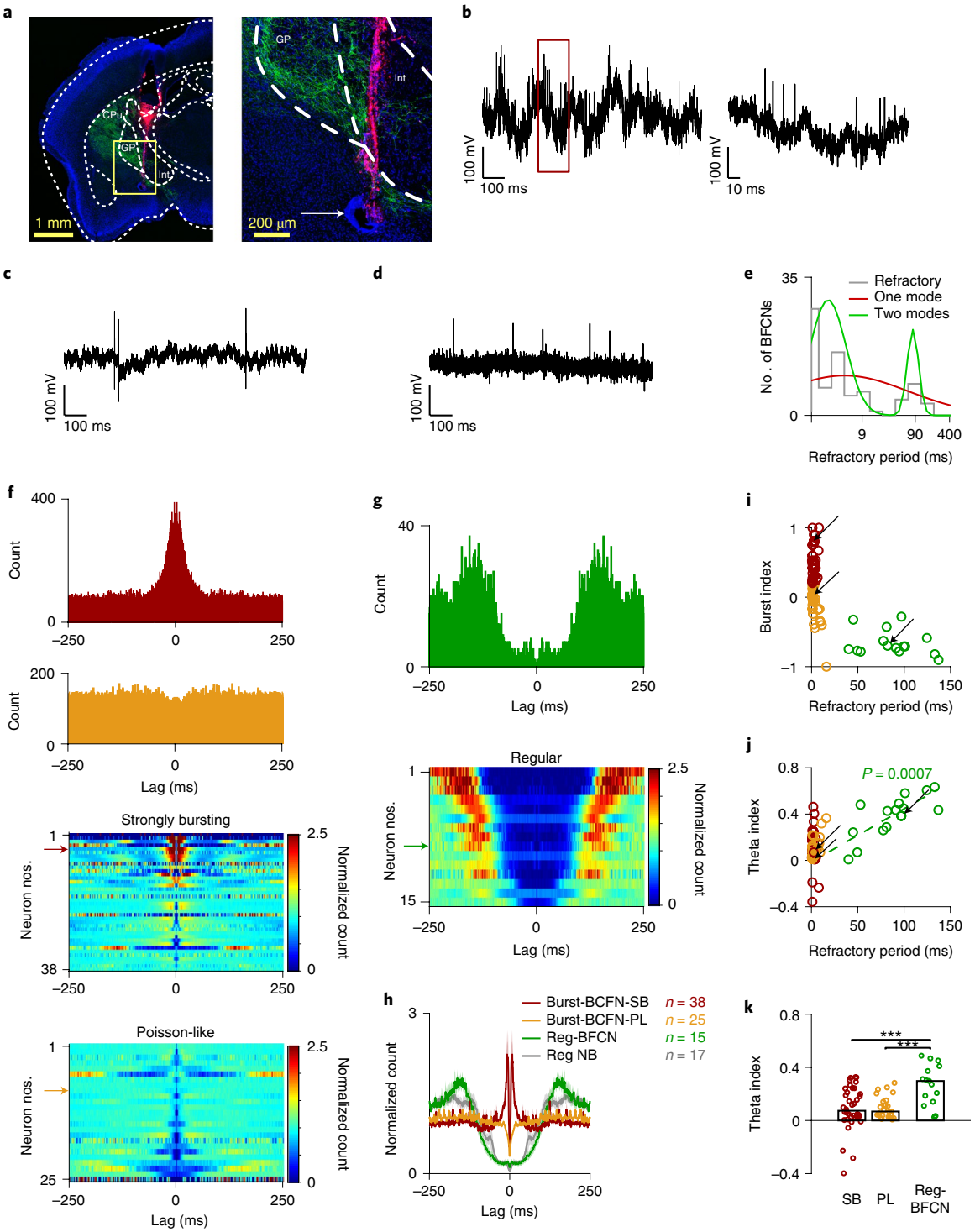

Fig. 1 | In vivo recordings revealed two types of central cholinergic neurons, Burst-BFCNs and Reg-BFCNs. a, Coronal section with the tetrode tracks (red, DiI) and the electrolytic lesion (arrow) (green, ChAT-ChR2-eYFP; blue, nuclear staining (DAPI)). **b**, Left: example of a raw trace of a Burst-BFCN; right: burst enlarged. **c**, Example short ISI of a Burst-BFCN-PL. **d**, Example raw trace of a Reg-BFCN. **e**, Distribution of relative refractory periods ($n = 78$ BFCNs). The log(refractory) values (gray bars) were fitted with one (red) or two (green) modes. **f**, Top: example ACGs of a Burst-BFCN-SB (red) and a Burst-BFCN-PL (orange); bottom: all neurons as individual rows. **g**, Top: example ACG of a Reg-BFCN (green); bottom: all neurons as individual rows. **h**, Average ACGs. Unidentified regular firing neurons (Reg NB, gray) are few and resemble Reg-BFCN (green) based on their auto-correlograms (solid lines, mean; shading, s.e.m.). **i**, Scatter plot showing the burst index and relative refractory period. **j**, Pearson's correlation between relative refractory period and theta index ($P = 0.0007$ for $n = 15$ Reg-BFCNs, one-sided F-test, $F(1,13) = 19.67$). **k**, Median theta index. ***$P < 0.001$; Burst-BFCN-SBs versus Reg-BFCNs, $P = 1.91 \times 10^{-5}$; Burst-BFCN-PLs versus Reg-BFCNs, $P = 5.1 \times 10^{-5}$; Burst-BFCN-SBs versus Burst-BFCN-PLs, $P = 0.63$; two-sided Mann–Whitney U-test; $n = 38$ Burst-BFCN-SBs (red), $n = 25$ Burst-BFCN-PLs (orange), $n = 15$ Reg-BFCNs (green). Arrows in **f**–**j** indicate example cells shown in **f** and **g**.

optogenetic tagging approach. Neurons responding with statistically significant short latency firing (stimulus-associated spike latency test (SALT): $P<0.01$) to blue laser light in transgenic mice expressing the photosensitive channelrhodopsin (ChAT-Cre infected by AAV-DIO-EF1a-ChETA, $n=15$ or by AAV-DIO-EF1a-hChR2(H134R), $n=3$; or ChAT-ChR2, $n=3$ mice) were considered to be optogenetically identified cholinergic neurons ($n=56$). In addition, neurons that fell in the same cluster by hierarchical clustering of response properties were considered to be putative cholinergic neurons ($n=22$; the algorithm was detailed in ref. [17]). We detected no systematic differences between optogenetically identified and putative cholinergic neurons (Extended Data Figs. 1 and 2, and also Fig. S4 in ref. [17]), therefore these neurons were pooled and resulted in a dataset of 78 BFCNs.

Previous in vitro studies suggested that cholinergic neurons may exhibit heterogeneous firing patterns[11,13,22]; however, this has not been tested in vivo and the potential diversity of BFCNs is unexplored in awake animals. We noticed that some cholinergic neurons were capable of firing bursts of action potentials in vivo with short, <10 ms interspike intervals (ISIs), whereas others exhibited a markedly different pattern of regular rhythmic firing dominated by long ISIs (Fig. 1b–d). To quantify this, we defined relative refractory periods of basal forebrain cholinergic neurons based on their auto-correlograms, characterized by low probability of firing (inspired by Royer et al.[26]; see Methods). The distribution of the relative refractory period duration covered a broad range (1–137 ms) and showed a bimodal distribution with two distinct, approximately log-normal modes[27] (Fig. 1e–h). This was confirmed by a model selection approach based on Akaike and Bayesian information criteria (Extended Data Fig. 2c). This demonstrated the existence of a separate, short-refractory, burst-firing and long-refractory, regular-firing group of cholinergic neurons. Therefore, we called these cholinergic neurons Burst-BFCNs and Reg-BFCNs, respectively.

We further analyzed the burst-firing properties of Burst-BFCNs and found considerable heterogeneity based on their spike auto-correlations (ACGs). Many short-refractory neurons exhibited strongly bursting patterns with classic 'burst shoulders'[26] in their auto-correlograms (Burst-BFCN-SBs, strongly bursting), whereas others showed irregular patterns of ISIs, resembling a Poisson process (Burst-BFCN-PLs, 'Poisson like'; Fig. 1f). Of note, the lack of a central peak in the autocorrelation did not preclude the occasional presence of bursts (Fig. 1c). These firing patterns were, on average, distinct (Fig. 1h); however, this separation was less evident than the bimodal relative refractory distribution, and a few neurons could have been categorized in either group (Fig. 1i).

We note that the long-refractory neurons exhibited strong rhythmicity in the theta frequency band (5–10 Hz; Fig. 1j,k). The strength of rhythmic firing, quantified based on autocorrelation peaks in the theta band (theta index, see Methods), correlated with the length of the relative refractory period (Pearson's correlation, $P=0.0007$, one-tailed F-test).

Next, we analyzed the firing patterns of a large dataset of untagged BF neurons. Burst firing has been shown for GABAergic BF neurons before[24,28]; in agreement with this, we found that many noncholinergic cells were capable of burst firing (Extended Data Fig. 3a,b). Surprisingly, however, only a small proportion of untagged BF neurons showed regular rhythmic firing with a long refractory period ($n=17$; Extended Data Fig. 3c–g). These neurons were similar to those that we had characterized as cholinergic ($n=12$; Fig. 1h). This suggests that at least about 40% of regular rhythmic BF neurons are cholinergic, and may provide the means to identify this subgroup of putative cholinergic neurons based on firing rate and regular rhythmic activity pattern, when their response to air-puffs is not available (Extended Data Fig. 3h).

In vitro recordings confirmed two types of cholinergic neurons. We wondered whether the different cholinergic firing patterns observed in our in vivo recordings reflect intrinsic properties produced by distinct cell types. Alternatively, distinct firing patterns may be determined by the current state of the network or variations in the input strength of individual cells. To answer this, we turned to in vitro preparations, where the membrane potential of the neuron and the strength of activation are precisely controlled and monitored.

We performed whole-cell patch clamp recordings from $n=60$ cholinergic neurons from the BF in acute slices. Cholinergic neurons were identified by their red epifluorescence in $n=12$ mice injected with AAV2/5-EF1a-DIO-hChR2(H134R)-mCherry-WPRE-HGHpA (Fig. 2a). We applied a somatic current injection protocol (Fig. 2b) containing a 3-s-long, incremental 'prepolarization' step followed by a positive square pulse (1 s), to elicit spiking starting from different membrane potentials. We found two distinct behaviors on current injection (Fig. 2b–i) using similar testing conditions

Fig. 2 | In vitro recordings confirmed two types of central cholinergic neurons. a, Representative confocal image of recorded and biocytin-filled cholinergic cells expressing ChR2 in the nucleus basalis of the BF. **b**, Top: firing pattern of an early-firing cell, showing short spike delay and high-frequency spike clusters on positive current injections. Bottom: firing pattern of a representative late-firing cholinergic cell, showing low maximal firing rate and prominent spike delay when driven from hyperpolarized membrane states. **c**, The same cells show similar responses on photostimulation (0.5 s). **d**, ISI histograms of the same cells show bimodal (early-firing) or unimodal (late-firing) distributions. **e**, Average AP shape from an example early-firing (red) and late-firing (green) cholinergic cell (100 APs per cell in gray, average in color). **f**, Spike delay depended on the membrane potential ($n=31$ for late-firing and $n=29$ for early-firing cholinergic cells). **g**, Normalized spike delay showed stereotypical behavior in late-firing cholinergic neurons ($n=31$). **h**, Maximal burst frequency as a function of the membrane potential ($n=31$ late-firing and $n=29$ early-firing cholinergic cells). **i**, Maximal burst frequency plotted against maximal spike delay in all recorded cells ($n=31$ late-firing and $n=29$ early-firing cholinergic cells). $^{***}P<0.001$; maximal spike delay, $P=2.08\times10^{-11}$; maximal burst frequency, $P=1.54\times10^{-11}$; two-sided Mann–Whitney U-test. Box-and-whisker plots show median, interquartile range, nonoutlier range and outliers. **j**, Spike auto-correlograms during somatic current injection protocols for all cells (top: $n=29$ early-firing cholinergic cells; bottom: $n=31$ late-firing cholinergic cells). **k**, Average auto-correlograms of early-firing (red, $n=29$) and late-firing (green, $n=31$) cholinergic cells (solid lines, mean; shading, s.e.m.). **l**, Firing pattern of an early-firing cell in response to three current injection protocols, with different current magnitude applied before the depolarization step. The protocol was designed to model the internal state (membrane potential) dependence of the spiking pattern in response to a uniform input. Raster plot represents 20 trials with each protocol (deeper red, more hyperpolarized states). Bottom: corresponding auto-correlograms and burst indices. **m**, Firing pattern of the same cell in response to current injection protocols with different depolarization step magnitudes. The protocol was designed to mimic input strength dependence of the spiking pattern. Raster plot shows 20 trials for each protocol, with a deeper red corresponding to smaller injected currents. **n**, Average ACGs and corresponding burst indices of early-firing cells ($n=29$) driven from depolarized (top) and hyperpolarized (bottom) states. Three groups were formed from all early-firing cells based on the 3-s-long prepolarization magnitude (right inset). **o**, Burst index plotted against maximal spike delay ($n=31$ late-firing and $n=29$ early-firing cholinergic cells). Dots overlaid on the y axis correspond to the burst indices presented in **n**. Burst indices: $^{***}P<0.001$, $P=2.11\times10^{-12}$; two-sided Mann–Whitney U-test. Box-and-whisker plots show median, interquartile range, nonoutlier range and outliers.

(Extended Data Fig. 4a). Cholinergic cells from the first group (red, $n=29$) displayed a short spike delay (8.05 ± 0.74 ms, median ± s.e. of median) and bimodal ISI distribution (Fig. 2d, top) with short ISIs corresponding to high-frequency 'burst' firing (maximum, 122.69 ± 18.99 Hz; Fig. 2h,i). The second group (green, $n=31$) displayed low maximal firing rate (13.81 ± 2.32 Hz, $P=1.54\times10^{-11}$, two-sided Mann–Whitney U-test), unimodal ISI distribution (Fig. 2d, bottom) and a prominent spike delay (maximum spike

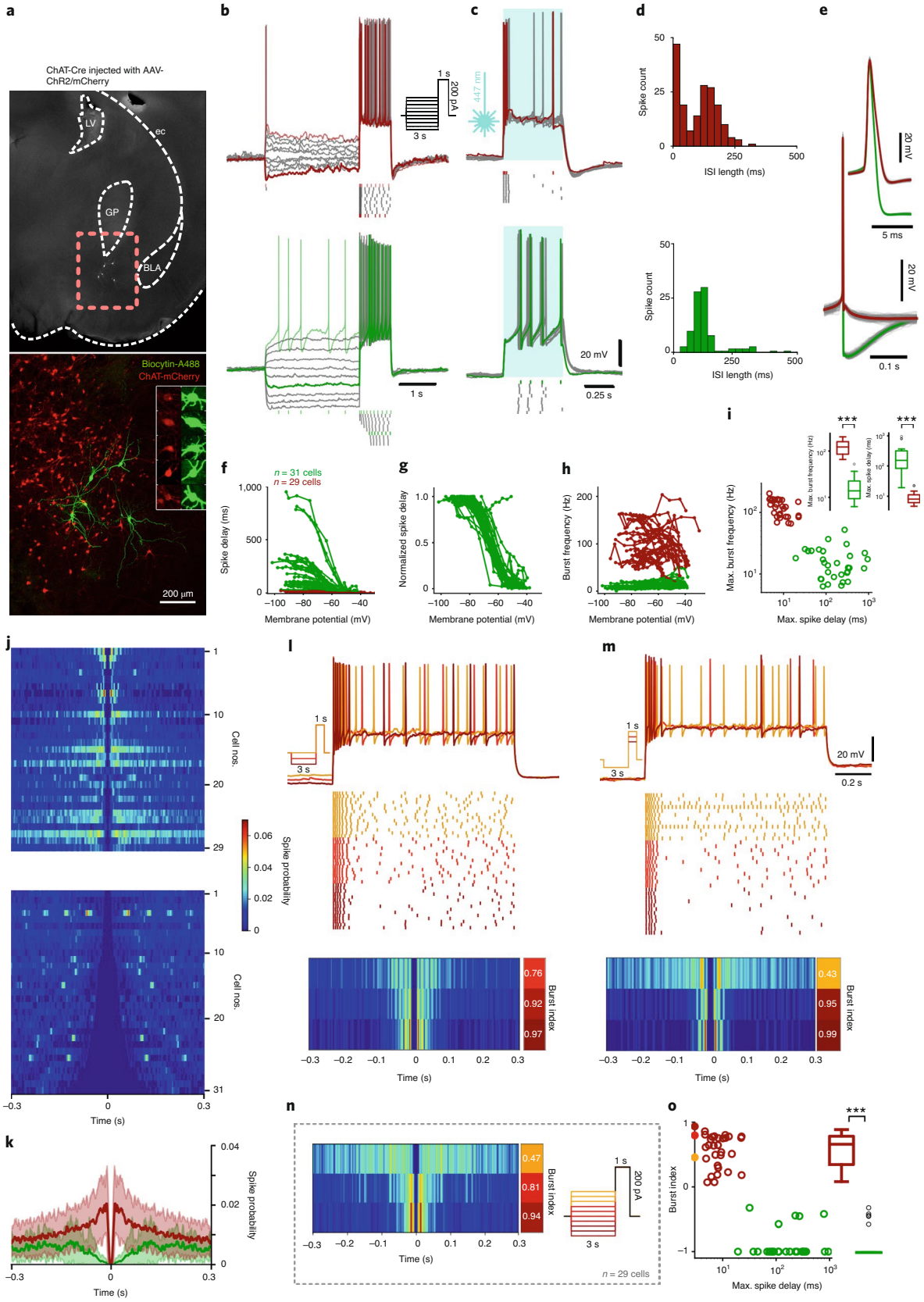

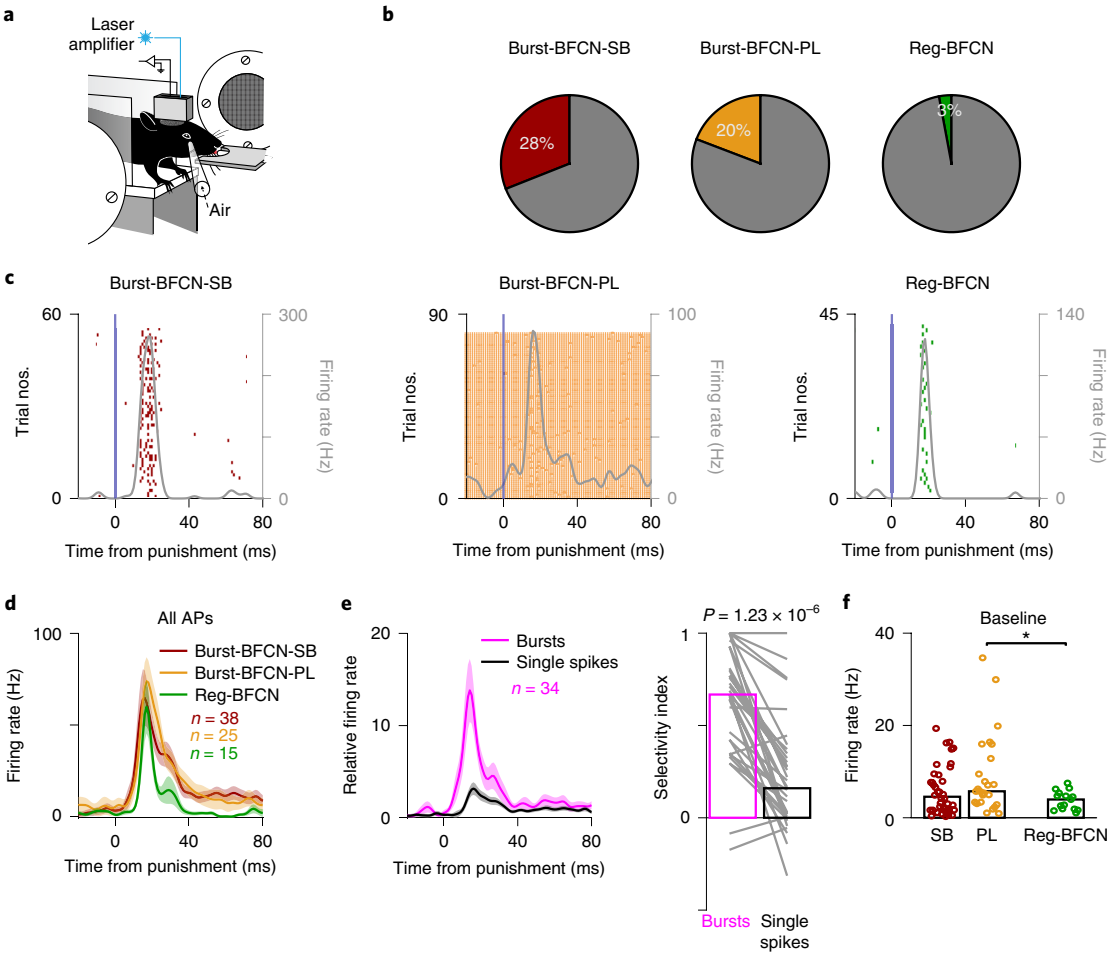

Fig. 3 | Cholinergic bursts transmit phasic information about reinforcers. a, Mice were trained to lick for cue stimuli of pure tones. Hits were rewarded with a drop of water, whereas false alarms were punished by an air-puff (modified from ref. [17]). **b**, Percentage of intraburst APs ($n = 38$ Burst-BFCN-SBs, red; $n = 25$ Burst-BFCN-PLs, orange; $n = 15$ Reg-BFCNs, green). **c**, Example raster plots of phasic responses to punishment by Burst-BFCN-SB (left), Burst-BFCN-PL (middle) and Reg-BFCN (right). PETHs smoothed by moving average are overlaid in gray. **d**, Average response of cholinergic neurons to punishment ($n = 38$ Burst-BFCN-SBs, red; $n = 25$ Burst-BFCN-PLs, orange; $n = 15$ Reg-BFCNs, green) (solid lines, mean; shading, s.e.m.). **e**, Left: occurrence of bursts and single spikes in Burst-BFCN-SBs normalized to the baseline (solid lines, mean; shading, s.e.m.). Right: median selectivity index calculated as spike number in 20–50 ms relative to 100–250 ms post-event windows. Bursts of Burst-BFCN-SBs ($n = 34$) are more concentrated after punishment compared with single spikes ($P = 1.23 \times 10^{-6}$, two-sided Wilcoxon's signed-rank test). **f**, Median baseline firing rate (red, $n = 38$ Burst-BFCN-SBs; orange, $n = 25$ Burst-BFCN-PLs; green, $n = 15$ Reg-BFCNs). $^*P < 0.05$, $P = 0.0236$, two-sided Mann–Whitney U-test.

delay, 153.05 ± 55.59 ms, 2.08×10^{-11} compared with the first group; two-sided Mann–Whitney U-test) which depended on the membrane potential before spiking (Fig. 2f,g). Importantly, depolarized late-firing cells responded to suprathreshold current injections with a short spike delay as opposed to the hyperpolarized state where late firing was prominent (Extended Data Fig. 4b). These distinct early responding/burst-firing or late responding/nonbursting modes were also reliably elicited by optogenetic depolarization (Fig. 2c). Spontaneous action potentials revealed shorter spikes and large-amplitude, slowly decaying afterhyperpolarization in late-firing compared with early-firing (bursting) cells (Fig. 2e). To compare in vivo and in vitro firing patterns, we calculated ACGs and burst indices (early-firing, 0.64 ± 0.08; late-firing, -1.0 ± 0, 2.11×10^{-12}, two-sided Mann–Whitney U-test) from spike trains during the current injection protocol (Fig. 2j,k). Early and late-firing neurons in vitro matched Burst-BFCNs and Reg-BFCNs in vivo, suggesting that these groups are the same.

Next, we tested whether the different in vivo firing modes of bursting cholinergic neurons (Burst-BFCN-SBs versus Burst-BFCN-PLs) could be explained by variations in the membrane potential and input strength. To investigate this possibility, we applied somatic current injection protocols designed to test input and state dependency of the degree of bursting. Indeed, we found that the same Burst-BFCNs were capable of producing both strongly bursting and Poisson-like firing patterns. This property depended on both the membrane potential of the neuron (Fig. 2l–o) and the strength of the activation (Fig. 2m), with Poisson-like firing occurring more frequently in more depolarized states and in response to stronger depolarizing inputs. In summary, we identified two types of BFCNs. Reg-BFCNs showed regular theta-rhythmic firing in vivo and late, regular responses to current injections in vitro; Burst-BFCNs exhibited burst firing both in vivo and in vitro, where the strength of bursting was determined by the level of excitation.

Cholinergic bursts transmit phasic information about reinforcers. Cholinergic neurons act at different timescales regulating different aspects of cognition, from slow sleep–wake and arousal processes to fast subsecond or even millisecond timescales of reinforcement learning and plasticity[9,17,29]. Based on in vitro studies it was hypothesized that bursting specifically represents fast

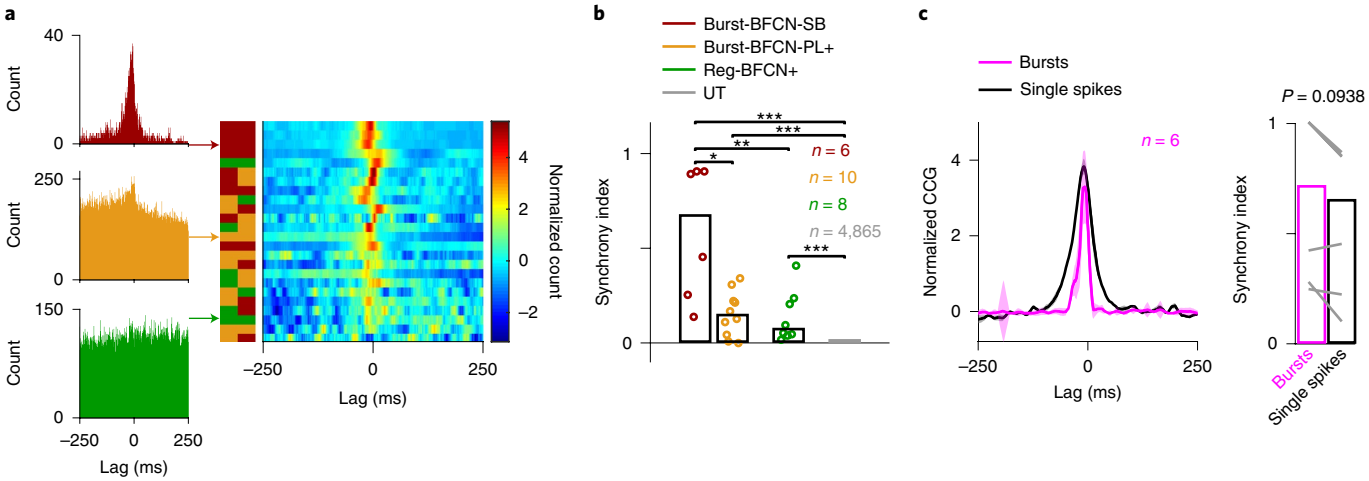

Fig. 4 | Bursting cholinergic neurons show synchronous activity. a, Cross-correlations of pairs of cholinergic neurons. Left: examples (red, Burst-BFCN-SB; orange Burst-BFCN-PL; green, Reg-BFCN). Right: all pairs; left: color bar indicates the firing mode of the two neurons that form the pair. Please note, that, in some cases, the *Z*-score normalization necessary to show all CCG pairs can magnify central peaks that are otherwise small relative to baseline; therefore, all individual CCG pairs are shown in Extended Data Fig. 5 without normalization. **b**, Pairs of Burst-BFCN-SBs show stronger synchrony than pairs that contain Burst-BFCN-PLs or Reg-BFCNs. The synchrony index calculated as average cross-correlation in −30 to +30ms windows normalized to 100–250 ms baseline period (bars, median) ($n=6$ Burst-BFCN-SB pairs (red); $n=10$ Burst-BFCN pairs containing PL, denoted by PL+ (orange); $n=8$ pairs continaing Reg-BFCN, denoted by Reg-BFCN+ (green); $n=4{,}865$ untagged (UT, gray) cholinergic cell pairs). $^{*}P<0.05$; $^{**}P<0.01$; $^{***}P<0.001$. Burst-BFCN-SB versus Burst-BFCN-PL+, $P=0.011$; Burst-BFCN-SB versus Reg-BFCN+, $P=0.008$; Burst-BFCN-SB versus UT, $P=2.7\times10^{-5}$; Burst-BFCN-PL+ versus UT, $P=3.02\times10^{-4}$; Reg-BFCN+ versus UT neurons, $P=9.81\times10^{-5}$; two-sided Mann–Whitney *U*-test. **c**, Both bursts and single spikes of Burst-BFCN-SBs ($n=6$) showed zero-lag synchrony. Left: solid lines, mean; shading s.e.m. Right: bars show median. $P=0.0938$, two-sided Wilcoxon's signed-rank test.

'phasic' information transfer[11]; however, this has not been tested. Therefore, we analyzed the activity of basal forebrain cholinergic neurons after reward and punishment in mice performing auditory conditioning[17] (Fig. 3a).

We defined a burst as a series of action potentials starting with an ISI <10 ms and subsequent ISI durations of <15 ms to allow for typical ISI accommodation patterns[26]. As expected, Burst-BFCNs, categorized based on auto-correlograms, showed a high percentage of burst firing: 28% for Burst-BFCN-SBs and 20% for Burst-BFCN-PLs, whereas little burst activity was detected in Reg-BFCNs (3%; Fig. 3b).

We have shown previously that the strongest response of cholinergic neurons occurred after air-puff punishments[17]: BFCNs responded phasically with short latency (18 ± 1.9 ms, median ± s.e. of median), low jitter (5.7 ± 0.1 ms) and high reliability (81.7 ± 2.6%). In the present study, we compared bursting and regular rhythmic cholinergic neurons, and found that both types showed strong response to air-puff punishment (Fig. 3c,d). Contrary to previous hypotheses, Reg-BFCNs were also capable of surprisingly fast and precise phasic firing, emitting a precisely timed single action potential, typically followed by a pause and then a reset of their intrinsic theta oscillation (Fig. 3c,d, and Extended Data Fig. 5a). This clearly distinguished them from tonically active striatal interneurons, which did not show such responses (Extended Data Fig. 5b–d).

Burst-BFCNs are capable of emitting both bursts of action potentials and single spikes. Therefore, we wondered whether bursts and single spikes represent salient events such as air-puffs differently, in which case this should be reflected in a difference in peri-event time histograms (PETHs) of bursts versus single APs aligned to punishment events. We found that bursts of Burst-BFCNs significantly concentrated after punishment compared with single spikes in most neurons ($P=1.23\times10^{-6}$, two-sided Wilcoxon's signed-rank test; Fig. 3e and Extended Data Fig. 5e). We observed similar concentration of bursts after reward, but not cue stimuli or trial start signals (Extended Data Fig. 5f,g), suggesting that bursts represent external events differently compared with single spikes.

In vitro studies also predicted that tonically active neurons would be more important in controlling slow tonic changes in acetylcholine levels, which could potentially be reflected in higher baseline firing rates of Reg-BFCNs. However, we found that baseline firing rates were largely similar across cholinergic cell types and firing patters (median ± s.e.: Burst-BFCN-SBs, 4.55 ± 1.26; Burst-BFCN-PLs, 5.74 ± 1.39; Reg-BFCNs, 3.96 ± 1.0), with slightly faster firing in Burst-BFCN-PLs, consistent with the more depolarized membrane potentials and stronger excitatory inputs suggested by our in vitro recordings in Fig. 2l–o (Burst-BFCN-SBs versus Burst-BFCN-PLs, $P=0.11$; Burst-BFCN-SBs versus Reg-BFCNs, $P=0.41$; Burst-BFCN-PLs versus Reg-BFCNs; $P=0.0236$; two-sided Mann–Whitney *U*-test; Fig. 3f).

Bursting cholinergic neurons show synchronous activity. Bursts of cholinergic neurons were found to precisely align to reinforcement (Fig. 3c–e), generating a strong synchronous activation of the cholinergic system after reward and punishment. Is synchronous firing specific to these unique behaviorally relevant events or do they occur at other times as well? Synchronous versus asynchronous activation of subcortical inputs has a fundamentally different impact on cortical computations. However, although there is a lot known about synchrony in cortical circuits both within and across cell types, there is little information on synchronous firing in subcortical nuclei. Specifically, no recordings of multiple identified cholinergic neurons have been performed.

In some cases, we recorded 2 ($n=15$) or 3 ($n=3$) cholinergic neurons simultaneously, resulting in 24 pairs of concurrent cholinergic recordings. By calculating pairwise cross-correlations, we found that Burst-BFCNs, especially Burst-BFCN-SBs, showed strong zero-phase synchrony with each other (6/6 pairs of two Burst-BFCN-SBs and 5/11 pairs containing Burst-BFCN-SBs and -PLs showed significant co-activation, $P<0.05$). Reg-BFCNs showed little synchrony with other BFCNs (2/7 pairs that contained at least one Reg-BFCN were significantly co-activated, $P<0.05$, bootstrap test; Fig. 4a,b and Extended Data Fig. 6). Co-activation of

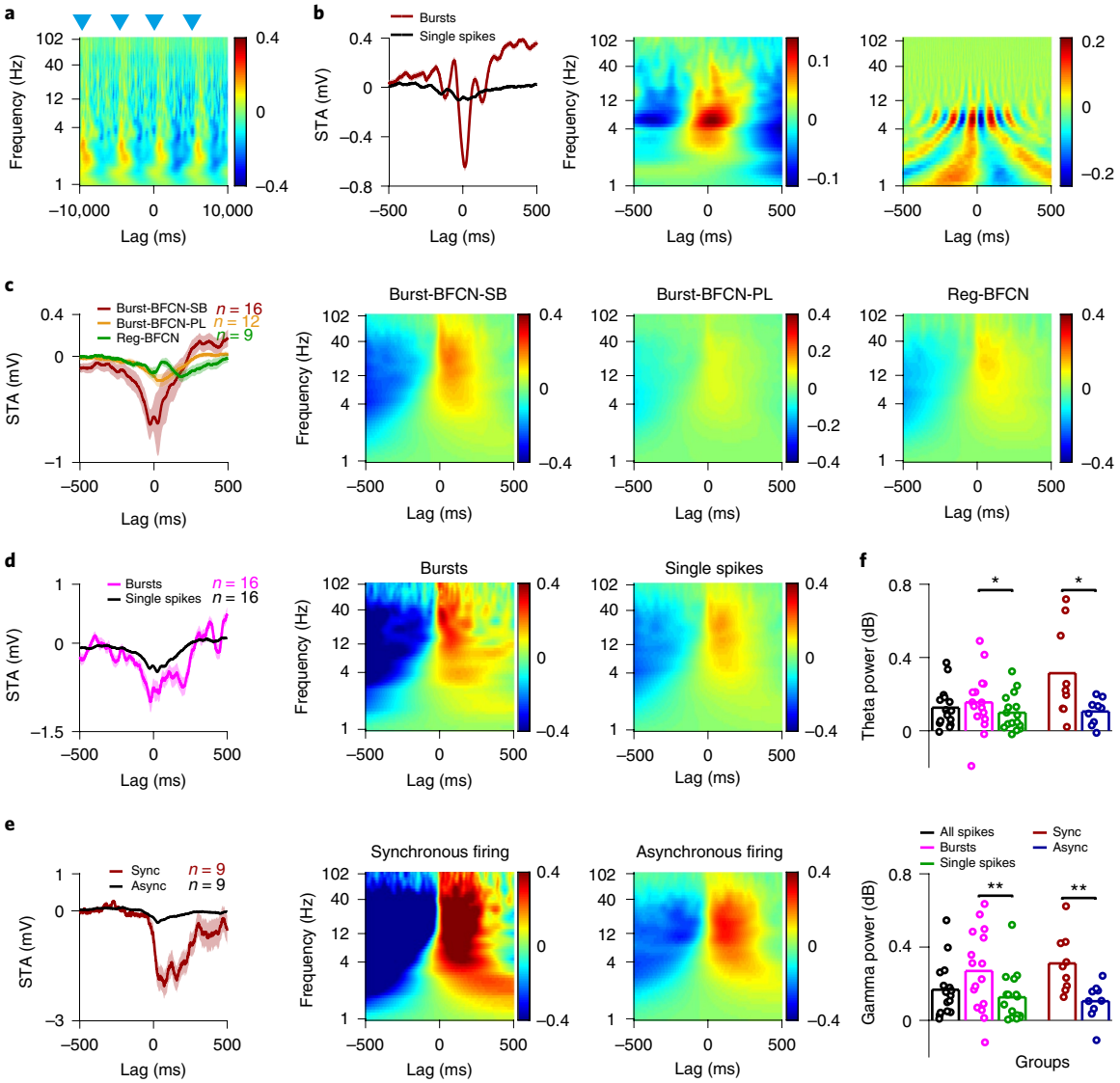

Fig. 5 | Cholinergic bursts are coupled to cortical activity. a, Photostimulation of BFCNs ($n = 37$) activates the auditory cortex; stimulus-triggered average spectrogram aligned to photostimulation (blue triangles). Color code represents spectral power (dB). **b**, Example of a Burst-BFCN-SB ($n = 16{,}680$ bursts and 50,996 single spikes) strongly synchronized to cortical theta. Left: STAs based on all spikes (solid lines, mean; shading, s.e.m.); middle: STS; right, STS phase demonstrates phase locking in the theta band. **c**, From left to right: average STA for BFCN groups (solid lines, mean; shading, s.e.m.); average STS for Burst-BFCN-SBs, Burst-BFCN-PLs and Reg-BFCNs. **d**, Bursts elicit stronger cortical activation. Left: average STA (solid lines, mean; shading, s.e.m.); middle: average STS for bursts; right: average STS for single spikes. **e**, Synchronous firing elicits stronger cortical activation. Left: average STA (solid lines, mean; shading, s.e.m.); middle: average STS for synchronous (Sync) firing; right: average STS for asynchronous (Async) firing. **f**, Mean spectral power in the theta (top) and gamma band (bottom: black, all spikes, $n = 16$; pink, bursts, $n = 16$; green, single spikes, $n = 16$; dark red, synchronous firing, $n = 9$; blue, asynchronous firing, $n = 9$; $^*P < 0.05$, $^{**}P < 0.01$; theta band, bursts versus single spikes, $P = 0.0437$; synchronous versus asynchronous firing, $P = 0.0391$; gamma-band, bursts versus single spikes, $P = 0.006$; synchronous versus asynchronous firing, $P = 0.008$; two-sided Wilcoxon's signed-rank test).

Burst-BFCNs typically spanned ±25 ms (27.22 ± 5.37, mean ± s.e.m.; maximum 42 ms) and was not restricted to the bursts themselves, because single action potentials of bursting neurons showed similar synchrony (Fig. 4c); thus Burst-BFCNs may share a synchronizing input that differentiates them from other BFCNs, possibly contributing to the bursting phenotype itself.

Cholinergic bursts are coupled to cortical activity. Cholinergic neurons send dense innervation to the cortex, including projections from the nucleus basalis (NB) to auditory cortices[25,30]. These inputs can potently activate cortical circuits, leading to desynchronization and gamma oscillations[31,32], which we confirmed by optogenetic stimulation of NB cholinergic neurons that elicited broad-band activity in the auditory cortical LFPs (Fig. 5a). We reasoned that bursts of cholinergic firing might lead to stronger cortical activation, whereas synchronous activation of ensembles of cholinergic neurons may further increase this effect, providing a finely graded control over cortical activation and thus arousal by the ascending cholinergic system. At the same time, the BF receives cortical feedback[25,33,34] that may be capable of entraining cholinergic neurons, thus establishing an ongoing synchrony between cortical and BF activity, a hypothesis largely under-explored (but see refs. [7,24,35]).

To test these possibilities, we calculated spike-triggered LFP averages and spike-triggered spectrogram averages of auditory cortical LFPs aligned to the action potentials of BFCNs recorded during auditory operant conditioning. We used spike-triggered

averages (STAs) to identify synchronization between BFCN spiking and cortical oscillations, because LFP changes not phase locked with BFCN spikes cancel out[24]. Individual STAs aligned to cholinergic spikes showed prominent oscillations in the theta band (4–12 Hz), suggesting that NB cholinergic activity can synchronize to cortical theta oscillations (Fig. 5b,c). In addition, we often observed strong deflections in cortical LFPs after cholinergic spikes (Extended Data Fig. 7; peak latency, 36.0 ± 13.0 ms; median ± s.e. of median), which may be a signature of cortical activation by cholinergic input. To assess this, we used spike-triggered spectrograms (STSs) to identify evoked responses that are not phase coupled. STS analysis showed high-frequency beta/gamma-band activity after cholinergic spiking (Fig. 5c). Importantly, bursts of BFCNs were associated with stronger LFP responses compared with single spikes (Fig. 5d–f). We note that a small number of single neurons recorded on the stereotrodes implanted in the auditory cortex showed phase locking to local theta, indicating that oscillations recorded in the auditory cortex were at least partially locally generated (Extended Data Fig. 8).

We confirmed that artificial synchrony of BFCNs imposed by optogenetic or electrical stimulation induced cortical desynchronization (Fig. 5a), as shown previously[31,32]. As we have found that synchronous activation of BFCNs also occurred in a physiological setting (see Fig. 4), this raises the question of whether such synchrony indeed leads to stronger cortical impact. To test this, we focused our analysis on the synchronous firing of cholinergic pairs. We found that synchronous events defined by two Burst-BFCNs firing within 10 ms was associated with strong cortical activation compared with asynchronous firing, confirming our prediction that NB signatures of enhanced cholinergic release represent a stronger impact on cortical population activity (Fig. 5e,f).

We observed that bursting cholinergic neurons often showed synchronization to cortical theta-band oscillations (Fig. 5b, left). The presence of high values in the theta band in the average spectral phase (phase domain of STSs; Fig. 5b, right) confirmed this, because it reflects phase locking to LFP oscillations. We reasoned that differential activation of cholinergic cell types by their inputs might underlie differences in synchronizing with cortical oscillations. It is known that frontal cortical projections to the BF synapse on GABAergic neurons[25], likely providing indirect hyperpolarizing input to cholinergic neurons[7]. To model the impact of this circuit on BFCNs, we tested whether Burst-BFCNs and Reg-BFCNs show differential responses to hyperpolarizing current injections in vitro. We found that Burst-BFCNs recovered their spikes with shorter and less variable latency ($n = 4$, 172.3 ± 9.95 ms, median ± s.e. of median than Reg-BFCNs ($n = 6$, 561.25 ± 23.77 ms; 6.47×10^{-44}, two-sided Mann–Whitney *U*-test; Extended Data Fig. 7b,c). This supports the hypothesis that cortically driven indirect inhibition of BFCNs may contribute to their differential coupling to cortical activity.

Synchrony of BFCN spiking with cortical activity predicts behavior during auditory detection. We have demonstrated that bursting and regular rhythmic cholinergic neurons are differentially coupled with the auditory cortex. However, the functional significance of this connection remains unclear. Therefore, we tested whether synchrony between BFCNs and the auditory cortex predicted behavioral performance during auditory conditioning (Fig. 3a). Specifically, we restricted our analysis to 1-s-long windows around auditory cue presentation during the operant auditory detection task[17]. We found that Burst-BFCNs, especially Burst-BFCN-SBs, showed larger STA deflections during hit and false-alarm trials compared with miss and correct-rejection trials (Fig. 6a–c). Therefore, synchronization of Burst-BFCNs with cortical networks predicts mouse responses but not their accuracy, because correct and incorrect responses showed similar STAs. In contrast, we found that large STA deflections for Reg-BFCNs specifically predicted hits; thus, synchronization of Reg-BFCNs and the auditory cortex predicted performance. We did not find similar predictive activity in a 1-s window before the cues, suggesting that predictive synchronization of the BF and auditory cortex was evoked by the cue tones. In summary, we found a behavioral dissociation between the two cholinergic cell types; while cortical coupling of Burst-BFCNs preceded all responses of the animals regardless of performance, Reg-BFCNs specifically predicted correct responses.

The horizontal diagonal band contains few regular cholinergic neurons. We wondered whether the uncovered diversity of cell types is uniform across the basal forebrain; alternatively, differences in the distribution of bursting and regular rhythmic cholinergic neurons may suggest that dedicated cortical areas are differentially regulated by BF cholinergic afferents. The cholinergic neurons we recorded were distributed in the NB (see Fig. 1a) and in the more anterior horizontal limb of the diagonal band of Broca (HDB; Fig. 7a), spanning almost 2 mm rostrocaudal distance. This allowed us to investigate whether BFCN types are differentially distributed along the anteroposterior axis of the BF.

In our in vivo recordings, 27% ($n = 12/45$) of the NB neurons belonged to the regular rhythmic type, whereas this was only 9% ($n = 3/33$) for the HDB (Fig. 7b). When we recorded NB neurons in vitro, 66% ($n = 27/41$) were Reg-BFCNs, whereas only 22% (2/9) Reg-BFCNs were found in the HDB (Fig. 7c). The higher proportion of Burst-BFCNs in our in vivo recordings could be due to better cluster separation because of their somewhat higher firing rates (Fig. 3f) and distinct spike shape (Fig. 2e). Nevertheless, we found that the NB contained three times more regular rhythmic cholinergic neurons both in vivo and in vitro compared with the HDB, which mostly contained the bursting type ($P = 0.0007$, $\chi^2 = 11.37$, χ^2 test). In line with these, the burst index and relative refractory period of cholinergic neurons changed systematically along the anteroposterior axis of the BF (Fig. 7d,e), suggesting that different brain areas may receive different combinations of cholinergic inputs.

Turning to untagged HDB neurons that we recorded in vivo, we found that only 12 of 560 HDB neurons were characterized as regular firing (Extended Data Fig. 9), which confirms both the lack of Reg-BFCNs in the HDB (Fig. 7) and the connection between regular rhythmic phenotype and cholinergic identity (Fig. 1h and Extended Data Fig. 3h).

Discussion

We demonstrated that the cholinergic basal forebrain contains two distinct functional cell types characterized by either burst-firing or rhythmic, non-bursting firing patterns. These types were found both in vivo and in vitro, and bursts could not be elicited from regular firing cholinergic neurons using a range of current injection protocols. Burst-BFCNs fired either discrete bursts of action potentials (Burst-BFCN-SBs) or an irregular pattern of short and long inter-spike intervals resembling a Poisson process (Burst-BFCN-PLs) depending on their membrane potential and strength of depolarization. Their bursts occurred preferentially after behavioral reinforcement, water reward or air-puff punishment, arguing for a separate burst code that selectively represents salient stimuli. Burst-BFCNs showed strong synchrony with each other and cortical oscillations, suggesting that they may have a strong impact on cortical processing. Specifically, synchrony between Burst-BFCNs and the auditory cortex at stimulus presentation predicted response timing. In contrast, coupling between Reg-BFCNs and the auditory cortex was strongest before mice made successful hits, thus predicting behavioral performance. Burst-BFCNs and Reg-BFCNs were differentially represented in the anterior and the posterior basal forebrain. As the anterior and posterior BF have different projection targets[25,36], distinct brain regions receive different proportions of bursting cholinergic input.

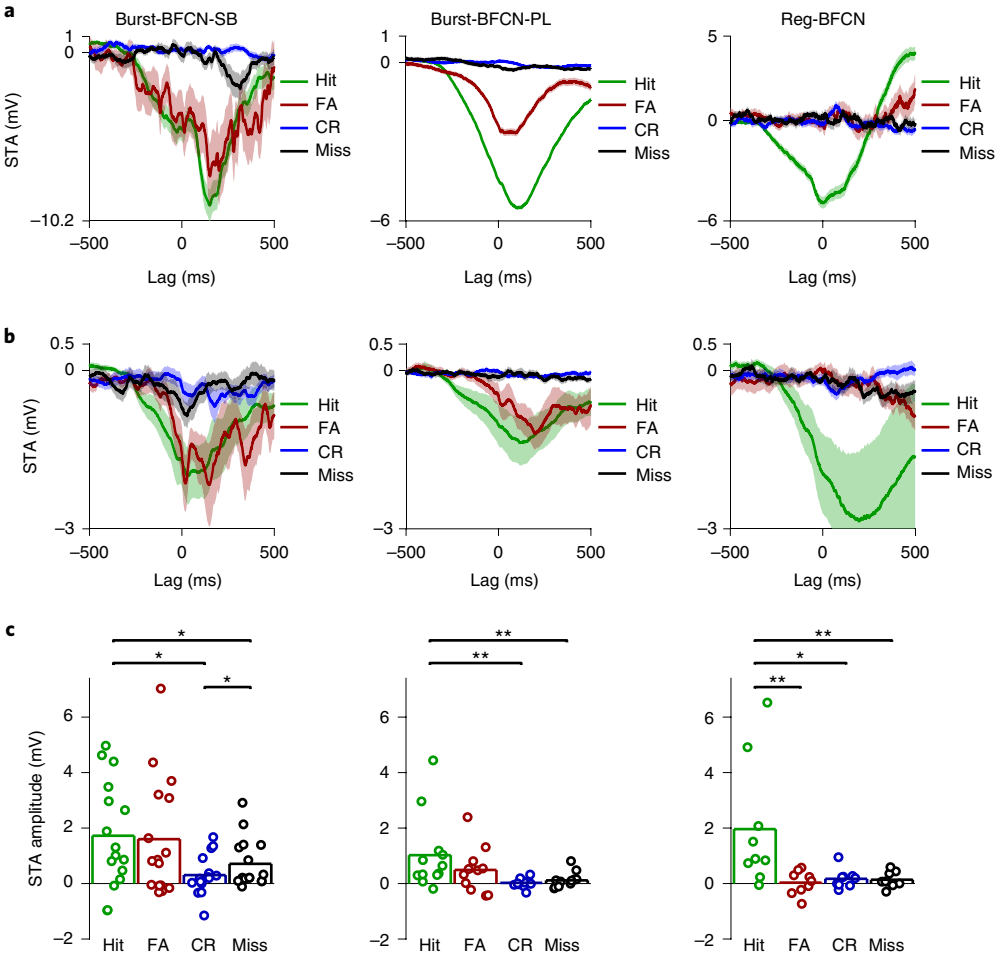

Fig. 6 | Cortex–BFCN synchrony predicts behavior in an auditory detection task. a, Example STAs calculated for spikes of a Burst-BFCN-SB (left), a Burst-BFCN-PL (middle) and a Reg-BFCN (right) restricted to a 1-s-long window around cue tone presentations during auditory detection, separated based on trial outcome. FA, false alarm; CR, correct rejection. Solid lines, mean; shading, s.e.m. **b**, Average STAs calculated for spikes in a 1-s window centered on cue presentations for the Burst-BFCN-SB (left, $n=16$), Burst-BFCN-PL (middle, $n=12$) and Reg-BFCN (right, $n=9$) groups (solid lines, mean; shading, s.e.m.). **c**, Mean absolute STA deflections (*$P<0.05$, **$P<0.01$; left: $n=16$ Burst-BFCN-SB neurons; hit versus FA, $P=0.163$; hit versus CR, $P=0.02$; hit versus miss, $P=0.03$; FA versus CR, $P=0.063$; FA versus miss, $P=0.109$; CR versus miss, $P=0.049$; middle: $n=12$ Burst-BFCN-PLs ; hit versus FA, $P=0.11$, hit versus CR, $P=0.009$; hit versus miss, $P=0.009$; FA versus CR, $P=0.077$; FA versus miss, $P=0.11$; CR versus miss, $P=0.622$; right: $n=9$ Reg-BFCNs; hit versus FA, $P=0.008$; hit versus CR; $P=0.012$; hit versus miss, $P=0.008$; FA versus CR, $P=1$; FA versus miss, $P=0.734$; CR versus miss, $P=0.82$; two-sided Wilcoxon's signed-rank test).

Viewed from the effector side, the cholinergic system has diverse roles at a variety of temporal scales, from slow modulations of the sleep–wake cycle[7] to rapid fluctuations of arousal[8,9,31] to instantaneous reactions to salient events serving learning[6,15,17]. This led to the terminology 'tonic' (seconds to hours) and 'phasic' (subsecond) to describe cholinergic effects, demonstrated by amperometric recording of cholinergic signals[8], as well as recording[17] and imaging[15,16] cholinergic activity. These findings further inspired the hypothesis that different types of BFCNs underlie phasic and tonic effects (Fig. 8a). However, another plausible alternative was that different, phasic-bursting versus tonic firing modes of the same neurons are responsible for controlling the timescale of impact (Fig. 8b)[9,11].

Our results suggest a third, more complex scenario underlying tonic and phasic cholinergic effects (Fig. 8c). We propose that there are two BF cholinergic cell types, demonstrated by our in vivo and in vitro recordings showing clear separation of regular rhythmic and bursting BFCNs (Figs. 1e–i and 2b–k). The same neurons produced Poisson-like or strongly bursting firing patterns depending on their membrane potential and synaptic inputs (Fig. 2k–n) in vitro, showing that Burst-BFCN-SB and Burst-BFCN-PL are different firing modes of the same bursting cell type. This claim was also supported by the fact that the burst index showed a continuum across Poisson-like and strongly bursting firing patterns (Fig. 1i). While Burst-BFCNs and Reg-BFCNs are two separate cell types (Figs. 1 and 2), the firing mode seems crucial to regulating slow and fast cholinergic modulation (Fig. 3). Specifically, single spike firing of both cell types contributes to slow tonic modulation by regular theta-rhythmic (Reg-BFCN) or irregular Poisson-like (Burst-BFCN-PL) firing. Single-spike firing also contributes to fast phasic coding by virtue of surprisingly precise spike timing[17] (Fig. 3c). In stark contrast, bursts of Burst-BFCNs selectively enhance phasic responses to salient events (Fig. 3e), suggestive of a distinct 'burst code' as predicted by theory[37]. Nevertheless, it will be important to examine by what mechanisms these cholinergic responses of different temporal scales influence downstream circuits, including synaptic versus nonsynaptic release[29] and muscarinergic versus nicotinergic effects[6,7,38,39].

Rhythmic Reg-BFCNs beat asynchronously at different frequencies, largely independent of each other and Burst-BFCNs (see Fig. 4)

under our circumstances. The strength of rhythmic firing correlated with the length of the relative refractory period. Refractoriness may itself contribute to rhythmic firing by imposing regular ISIs, which may reflect cell-autonomous mechanisms, whereas extrinsic factors cannot fully be ruled out[40]. Notably, rhythmically firing Reg-BFCNs may share part of the underlying biophysical mechanisms with striatal cholinergic interneurons[40] and regular firing dopaminergic neurons[41]. The similar autofrequencies of Reg-BFCNs in the theta range suggest that they may be capable of theta-rhythmic synchronization in a strongly behavior-dependent manner[24]. This was supported by our finding that strong correlations of Reg-BFCNs and auditory population activities in a specific task phase could predict mouse performance (Fig. 6), which may in part underlie the connection between elevated cortical acetylcholine levels and correct sensory detections[8]. It also suggests that behavior-dependent synchronization may lead to efficient bottom-up information transfer (see Fig. 8d,e). Similar to this result, careful analysis of behavior-dependent frequency coupling led to a new insight in the active sensing field by revealing behavior-dependent theta-frequency synchronization across the hippocampus, respiratory and whisking circuits[42], and prefrontal cortex, suggesting that such theta-frequency binding might be a rather general mechanism.

Unlike Reg-BFCNs, the activity of Burst-BFCNs showed strong synchrony across cholinergic neurons and with the auditory cortex that was less specific to mouse behavior, predicting both correct and incorrect responses but not performance (see Figs. 4–6). This suggests that Burst-BFCNs might convey fast and efficient, although less specific, activation of cortical circuits. It is not yet clear whether this unspecific prediction of animal responses is related to stronger sensory perception, task engagement, arousal or other factors that may influence responsiveness irrespective of accuracy. The Poisson-like firing of Burst-BFCNs might, at least in part, be a hallmark of internal processing or external sensory events not controlled in our experiments. Indeed, supported mathematically by the Poisson limit theorem, the aggregation of many independent discrete events sum up to a Poisson process, with strong implications for Poisson randomness found in spike timing even in primary sensory cortices[43].

In addition, differential rebound response after hyperpolarizing steps in Burst-BFCNs and Reg-BFCNs in vitro suggests that differences in cell-type-specific properties participate in the mechanisms of BF–cerebral cortex synchrony. This is in line with previous studies demonstrating that excitatory cortical feedback targets GABAergic inhibitory neurons in the basal forebrain, arguing for a disynaptic inhibition-triggered rebound mechanism for synchronizing BFCNs with cortical activity[25].

As expected, bursts of Burst-BFCNs were followed by stronger desynchronizations in the cortex and predicted an elevation of beta–gamma band activity compared with single spikes. It is

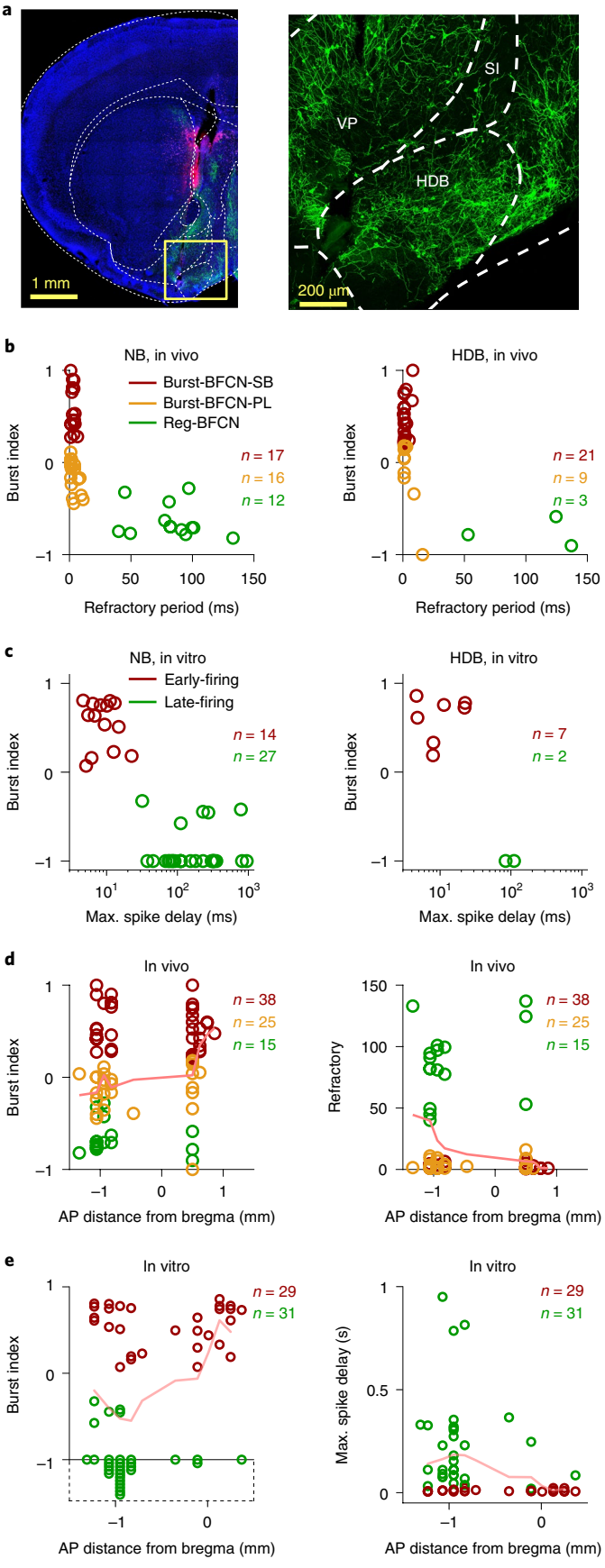

Fig. 7 | The horizontal diagonal band contains few regular firing cholinergic neurons. a, Coronal section showing ChR2 expression (green, eYFP) and tetrode tracks (red, DiI) in the HDB (blue, DAPI staining) (modified from ref. [17]). **b**, Burst index versus relative refractory period for cholinergic neurons recorded in vivo from the NB (left: red, $n=17$ Burst-BFCN-SBs; orange, $n=16$ Burst-BFCN-PLs; green, $n=12$ Reg-BFCNs) and HDB (right: red, $n=21$ Burst-BFCN-SBs; orange, $n=9$ Burst-BFCN-PLs; green, $n=3$ Reg-BFCNs). **c**, Burst index versus maximal spike delay for cholinergic neurons recorded in vitro from the NB (left) and the HDB (right). **d**, Burst index (left) and relative refractory period (right) as a function of anteroposterior (AP) localization in vivo ($n=38$ Burst-BFCN-SBs, $n=25$ Burst-BFCN-PLs, $n=15$ Reg-BFCNs neurons; pink lines, median as a function of the anteroposterior localization, smoothed with a three-point moving average). **e**, Burst index (left) and maximal spike delay (right) as a function of the anteroposterior localization in vitro ($n=31$ late-firing (green), $n=29$ early-firing (red) cholinergic cells; pink lines, median as a function of the anteroposterior localization, smoothed with a three-point moving average; cells with burst indices of −1 were dispersed along the *y* axis to avoid overlapping, marked by the dotted box).

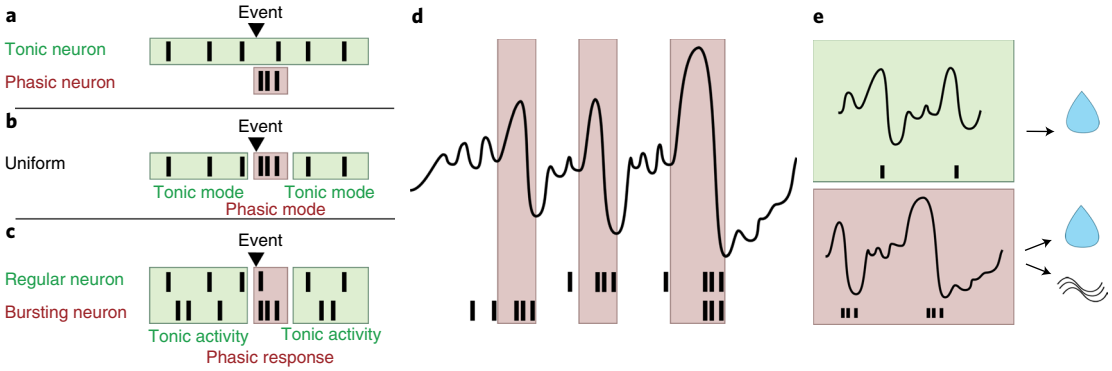

Fig. 8 | Tonic and phasic cholinergic effects. a, Based on heterogeneity found in vitro, it was hypothesized that tonic and phasic responses are mediated by different cell types. Green shading, tonic effects; pink shading, phasic effects through all panels. **b**, Based on homogeneity found in vivo, it was suggested that different firing modes of a uniform cell type mediate tonic and phasic effects. **c**, We found that phasic responses to behaviorally significant events are mediated by phasic single spike and burst firing of Reg-BFCNs and Burst-BFCNs, respectively. **d**, Bursts of BFCNs synchronize with cortical LFPs. Synchronous bursting of Burst-BFCNs is characterized by stronger BF–cortex synchrony. **e**, Synchronization of Reg-BFCNs to cortical LFPs predicts correct detections. Cortical synchronization of Burst-BFCNs precedes both correct and incorrect responses.

tempting to speculate that fast desynchronization after precisely timed cholinergic bursts might be mediated by fast nicotinic receptors, whereas muscarinic receptors are more tuned toward slower ('tonic') changes of cholinergic levels[6–8,38]. Within the nicotinic acetylcholine family, α_7-receptors may be best suited to mediate fast, precise effects due to their fast kinetics, low open probability and fast recovery[38,44,45].

The strongest cortical desynchronization was observed after synchronous firing of cholinergic neurons, also indicating that synchrony detected in our paired recordings was probably part of a larger-scale synchrony of an ensemble of cholinergic neurons[35]. This finding also strengthens a long line of research[31,32], suggesting that synchronous activation of cholinergic neurons leads to strong activation of cortical networks. While previous studies imposed artificial synchrony on the cholinergic system by electrical or optogenetic stimulation, we showed that synchronous cholinergic firing occurs physiologically, and this physiological co-firing is indeed associated with a strong cortical impact.

There have been only a handful of in vivo recordings of identified BF cholinergic neurons and a consensus view has not emerged. In a seminal juxtacellular labeling experiment, Lee and colleagues recorded cholinergic neurons ($n=5$) from the magnocellular preoptic nucleus and substantia innominata, and found that cholinergic neurons fire bursts and can synchronize with theta oscillations in the retrosplenial cortex in head-fixed rats[24]. In contrast, Simon et al. labeled cholinergic neurons ($n=3$) in the medial septum of anesthetized rats, but found different, slow-firing patterns without bursts or any correlation with hippocampal theta oscillations[22]. Similarly, Duque et al. recorded cholinergic neurons ($n=3$) from substantia innominata and NB in anesthetized rats and found slow firing with no synchronization to frontal electroencephalography (EEG; $n=1/3$ BFCN was bursting)[23]. In a novel study, Guo et al. elegantly demonstrated the learning-related activity of optogenetically identified NB cholinergic neurons, while the firing pattern of optotagged units was not specifically analyzed[46]. Using a large in vivo ($n=78$) and in vitro ($n=60$) dataset, we revealed that these seemingly contradictory results can be reconciled by the presence of two distinct types of cholinergic neurons in the basal forebrain, in line with an earlier in vitro study[11]. Burst-BFCNs show strong synchrony with cortical theta oscillations, whereas synchrony is more behavior specific and therefore less apparent for Reg-BFCNs despite their intrinsic theta-rhythmic firing.

The BF cholinergic system shows a roughly topographic projection to the cortex and other structures[25,33,34,36]. The HDB (also known as the Ch3 group) projects to the olfactory bulb, lateral hypothalamus, piriform cortex, entorhinal cortex[25] and prefrontal cortices[36]. In contrast, the NB (part of the Ch4 group, which also includes substantia innominata, sometimes included in the NB) projects to the basolateral amygdala and large parts of the neocortex[25,36]. In particular, it strongly innervates lateral parts of the neocortex such as auditory[46,47], somatosensory and motor cortices, whereas the visual cortex receives its cholinergic innervation from more rostral parts of the BF[36]. We found Reg-BFCNs to constitute about half (one-third to two-thirds) of BFCNs in the NB, whereas the more anterior HDB cholinergic neurons were mostly (80–90%) of the Burst-BFCN type (see Fig. 7), suggesting an anatomical difference along the anteroposterior axis of the basal forebrain. Together with our previous paper demonstrating a gradient of valence coding along the dorsoventral dimension of the NB[17], we uncovered a prominent functional topography of the BF cholinergic system. Added to the large literature of topographical anatomical projections between the BF and the cortex[25,30,33,34,48], this suggests that BF inputs, although largely homogeneous with regard to the events they represent, broadcast different messages to their targets in terms of activation strength, synchrony and behavioral function.

Based on theoretical considerations, it has been suggested that bursts of spikes may represent distinct stimulus features compared with single action potentials[37], proposing the existence of a separate burst code. Such burst codes have been demonstrated in precise place coding of pyramidal cell complex spikes in CA1, sharp tuning of bursts in the visual cortex and visual thalamus or specific coding of complex spikes in Purkinje cells[49,50]. A common theme in these studies is the stronger selectivity, and thus a higher signal-to-noise ratio of encoding by bursts versus single spikes. We strengthen this line of research by showing stronger selectivity to salient events by bursts of BFCNs, suggesting that the above mechanisms and principles generalize to subcortical networks as well. In addition, Kepecs et al. also predicted that bursts readily synchronize to oscillatory inputs, owing to slowly inactivating potassium currents that remain elevated after burst firing[37]. This could serve as a biophysical basis for the stronger synchronization of bursts versus single spikes to cortical theta oscillations.

Online content

Any methods, additional references, Nature Research reporting summaries, source data, extended data, supplementary information, acknowledgements, peer review information; details of author contributions and competing interests; and statements of

data and code availability are available at https://doi.org/10.1038/s41593-020-0648-0.

Received: 18 May 2019; Accepted: 27 April 2020;
Published online: 22 June 2020

References

1. Everitt, B. J. & Robbins, T. W. Central cholinergic systems and cognition. *Annu. Rev. Psychol.* **48**, 649–84 (1997).
2. Hasselmo, M. E. & Sarter, M. Modes and models of forebrain cholinergic neuromodulation of cognition. *Neuropsychopharmacology* **36**, 52–73 (2011).
3. Herman, aM., Huang, L., Murphey, D. K., Garcia, I. & Arenkiel, B. R. Cell type-specific and time-dependent light exposure contribute to silencing in neurons expressing Channelrhodopsin-2. *eLife* **3**, e01481–e01481 (2014).
4. Froemke, R. C., Merzenich, M. M. & Schreiner, C. E. A synaptic memory trace for cortical receptive field plasticity. *Nature* **450**, 425–9 (2007).
5. Chubykin, A. A., Roach, E. B., Bear, M. F. & Shuler, M. G. H. A cholinergic mechanism for reward timing within primary visual cortex. *Neuron* **77**, 723–35 (2013).
6. Gu, Z. & Yakel, J. L. Timing-dependent septal cholinergic induction of dynamic hippocampal synaptic plasticity. *Neuron* **71**, 155–65 (2011).
7. Yang, C., Thankachan, S., McCarley, R. W. & Brown, R. E. The menagerie of the basal forebrain: how many (neural) species are there, what do they look like, how do they behave and who talks to whom? *Curr. Opin. Neurobiol.* **44**, 159–166 (2017).
8. Parikh, V., Kozak, R., Martinez, V. & Sarter, M. Prefrontal acetylcholine release controls cue detection on multiple timescales. *Neuron* **56**, 141–54 (2007).
9. Teles-Grilo Ruivo, L. M. et al. Coordinated acetylcholine release in prefrontal cortex and hippocampus Is associated with arousal and reward on distinct timescales. *Cell Rep.* **18**, 905–917 (2017).
10. Palacios-Filardo, J. & Mellor, J. R. Neuromodulation of hippocampal long-term synaptic plasticity. *Curr. Opin. Neurobiol.* **54**, 37–43 (2019).
11. Unal, C. T., Golowasch, J. P. & Zaborszky, L. Adult mouse basal forebrain harbors two distinct cholinergic populations defined by their electrophysiology. *Front. Behav. Neurosci.* **6**, 21 (2012).
12. López-Hernández, G. Y. et al. Electrophysiological properties of basal forebrain cholinergic neurons identified by genetic and optogenetic tagging. *J. Neurochem.* **142**, 103–110 (2017).
13. Khateb, A. et al. Cholinergic nucleus basalis neurons display the capacity for rhythmic bursting activity mediated by low-threshold calcium spikes. *Neuroscience* **51**, 489–94 (1992).
14. Nyíri, G. et al. GABA B and CB 1 cannabinoid receptor expression identifies two types of septal cholinergic neurons. *Eur. J. Neurosci.* **21**, 3034–3042 (2005).
15. Harrison, T. C., Pinto, L., Brock, J. R. & Dan, Y. Calcium imaging of basal forebrain activity during innate and learned behaviors. *Front. Neural Circuits* **10**, 1–12 (2016).
16. Lovett-Barron, M. et al. Dendritic inhibition in the hippocampus supports fear learning. *Science* **343**, 857–63 (2014).
17. Hangya, B., Ranade, S. P., Lorenc, M. & Kepecs, A. Central cholinergic neurons are rapidly recruited by reinforcement feedback. *Cell* **162**, 1155–1168 (2015).
18. Fries, P. et al. Rhythms for cognition: communication through coherence. *Neuron* **88**, 220–35 (2015).
19. Somogyi, P., Katona, L., Klausberger, T., Lasztóczi, B. & Viney, T. J. Temporal redistribution of inhibition over neuronal subcellular domains underlies state-dependent rhythmic change of excitability in the hippocampus. *Phil. Trans. R. Soc. B Biol. Sci.* **369**, 20120518 (2014).
20. van Dijk, H., Schoffelen, J.-M., Oostenveld, R. & Jensen, O. Prestimulus oscillatory activity in the alpha band predicts visual discrimination ability. *J. Neurosci.* **28**, 1816–23 (2008).
21. Landau, A. N. & Fries, P. Attention samples stimuli rhythmically. *Curr. Biol.* **22**, 1000–1004 (2012).
22. Simon, A. P., Poindessous-Jazat, F., Dutar, P., Epelbaum, J. & Bassant, M. H. Firing properties of anatomically identified neurons in the medial septum of anesthetized and unanesthetized restrained rats. *J. Neurosci.* **26**, 9038–9046 (2006).
23. Duque, A., Balatoni, B., Detari, L. & Zaborszky, L. EEG correlation of the discharge properties of identified neurons in the basal forebrain. *J. Neurophysiol.* **84**, 1627–35 (2000).
24. Lee, M. G., Hassani, O. K., Alonso, A. & Jones, B. E. Cholinergic basal forebrain neurons burst with theta during waking and paradoxical sleep. *J. Neurosci.* **25**, 4365–9 (2005).
25. Zaborszky, L., van den Pol, A. & Gyengesi, E. in *The Mouse Nervous System* (eds Watson, C. et al.) 684–718 (Elsevier, 2012).
26. Royer, S. et al. Control of timing, rate and bursts of hippocampal place cells by dendritic and somatic inhibition. *Nat. Neurosci.* **15**, 769–75 (2012).
27. Buzsáki, G. & Mizuseki, K. The log-dynamic brain: how skewed distributions affect network operations. *Nat. Rev. Neurosci.* **15**, 264–278 (2014).
28. Lin, S.-C. & Nicolelis, Ma. L. Neuronal ensemble bursting in the basal forebrain encodes salience irrespective of valence. *Neuron* **59**, 138–49 (2008).
29. Sarter, M., Parikh, V. & Howe, W. M. Phasic acetylcholine release and the volume transmission hypothesis: time to move on. *Nat. Rev. Neurosci.* **10**, 383–90 (2009).
30. Saper, C. B. Organization of cerebral cortical afferent systems in the rat. II. Magnocellular basal nucleus. *J. Comp. Neurol.* **222**, 313–42 (1984).
31. Buzsaki, G. et al. Nucleus basalis and thalamic control of neocortical activity in the freely moving rat. *J. Neurosci.* **8**, 4007–26 (1988).
32. Pinto, L. et al. Fast modulation of visual perception by basal forebrain cholinergic neurons. *Nat. Neurosci.* **16**, 1857–63 (2013).
33. Gielow, M. R. & Zaborszky, L. The input–output relationship of the cholinergic basal forebrain. *Cell Rep.* **18**, 1817–1830 (2017).
34. Do, J. P. et al. Cell type-specific long-range connections of basal forebrain circuit. *eLife* **5**, 1–17 (2016).
35. Tingley, D., Alexander, A. S., Quinn, L. K., Chiba, A. A. & Nitz, D. A. Cell assemblies of the basal forebrain. *J. Neurosci.* **35**, 2992–3000 (2015).
36. Rye, D. B., Wainer, B. H., Mesulam, M. M., Mufson, E. J. & Saper, C. B. Cortical projections arising from the basal forebrain: a study of cholinergic and noncholinergic components employing combined retrograde tracing and immunohistochemical localization of choline acetyltransferase. *Neuroscience* **13**, 627–43 (1984).
37. Kepecs, A., Wang, X.-J. & Lisman, J. Bursting neurons signal input slope. *J. Neurosci.* **22**, 9053–62 (2002).
38. Arroyo, S., Bennett, C. & Hestrin, S. Nicotinic modulation of cortical circuits. *Front. Neural Circuits* **8**, 1–6 (2014).
39. Urban-Ciecko, J., Jouhanneau, J. S., Myal, S. E., Poulet, J. F. A. & Barth, A. L. Precisely timed nicotinic activation drives SST inhibition in neocortical circuits. *Neuron* **97**, 611–625.e5 (2018).
40. Tanimura, A. et al. Striatal cholinergic interneurons and Parkinson's disease. *Eur. J. Neurosci.* **47**, 1148–1158 (2018).
41. Schiemann, J. et al. K-ATP channels in dopamine substantia nigra neurons control bursting and novelty-induced exploration. *Nat. Neurosci.* **15**, 1272–80 (2012).
42. Moore, J. D. et al. Hierarchy of orofacial rhythms revealed through whisking and breathing. *Nature* **497**, 205–210 (2013).
43. Hires, S. A., Gutnisky, D. A., Yu, J., O'Connor, D. H. & Svoboda, K. Low-noise encoding of active touch by layer 4 in the somatosensory cortex. *eLife* **4**, 1–18 (2015).
44. Bali, Z. K., Nagy, L. V. & Hernádi, I. Alpha7 nicotinic acetylcholine receptors play a predominant role in the cholinergic potentiation of *N*-methyl-D-aspartate evoked firing responses of hippocampal CA1 pyramidal cells. *Front. Cell. Neurosci.* **11**, 1–13 (2017).
45. Pesti, K., Szabo, A. K., Mike, A. & Vizi, E. S. Neuropharmacology kinetic properties and open probability of α7 nicotinic acetylcholine receptors. *Neuropharmacology* **81**, 101–115 (2014).
46. Guo, W., Robert, B. & Polley, D. B. The cholinergic basal forebrain links auditory stimuli with delayed reinforcement to support learning. *Neuron* **103**, 1164–1177 (2019).
47. Letzkus, J. J. et al. A disinhibitory microcircuit for associative fear learning in the auditory cortex. *Nature* **480**, 331–335 (2011).
48. Li, X. et al. Generation of a whole-brain atlas for the cholinergic system and mesoscopic projectome analysis of basal forebrain cholinergic neurons. *Proc. Natl Acad. Sci. USA* **115**, 415–420 (2018).
49. Otto, T., Eichenbaum, H., Wiener, S. I. & Wible, C. G. Learning-related patterns of CA1 spike trains parallel stimulation parameters optimal for inducing hippocampal long-term potentiation. *Hippocampus* **1**, 181–92 (1991).
50. Reinagel, P., Godwin, D., Sherman, S. M. & Koch, C. Encoding of visual information by LGN bursts. *J. Neurophysiol.* **81**, 2558–2569 (1999).

Methods

Animals. Adult (age >2 months) ChAT-Cre ($n=15$, 14/15 male[51]), ChAT-ChR2 ($n=3$, 3/3 male[52]) and PV-Cre ($n=4$, 4/4 male) mice were used for behavioral recording experiments under the protocol approved by the Cold Spring Harbor Laboratory Institutional Animal Care and Use Committee in accordance with the National Institutes of Health regulations. ChAT-Cre mice (male, $n=3$, age >2 months) were used for in vivo and ChAT-Cre mice ($n=12$, 7/12 males, P50-150) were used for in vitro recordings according to the regulations of the European Community's Council Directive of 24 November 1986 (86/609/EEC); experimental procedures were reviewed and approved by the Animal Welfare Committee of the Institute of Experimental Medicine, Budapest and the Committee for Scientific Ethics of Animal Research of the National Food Chain Safety Office. See also Nature Research Reporting Summary.

In vivo electrophysiology and optogenetic tagging experiments. Surgical procedures, viral injection, microdrive construction and implantation, recording, optogenetic tagging and histology have been described previously[17]. Mice were trained on one of two versions of an auditory head-fixed detection task. In the operant version, mice had to detect pure tones in a go/no-go paradigm as described in ref. [17]. In the Pavlovian version, mice responded to reward- and punishment-predicting pure tones with anticipatory licking. In this version, air-puff punishment was delivered in a fixed proportion of trials in each trial type, irrespective of the anticipatory lick response of mice[53].

Analysis of in vivo experiments. Spike sorting was carried out using MClust (A.D. Redish). Only neurons with isolation distance >20 and L-ratio (a cluster quality measure based on Mahalanobis distance; see ref. [54]) <0.15 were included. Optogenetic tagging was verified using the SALT. Putative cholinergic neurons were selected based on hierarchical cluster analysis of punishment response properties (response magnitude, PETH correlation with identified cholinergic neurons and PETH similarity scores with templates derived from groups of all unidentified cells and unidentified cells suppressed after punishment). These analyses have been described in detail previously[17].

ACGs were calculated at 0.5 ms resolution. ACG graphs were smoothed by a 5-point (2.5 ms) moving average for plotting. When plotting all or average ACGs per group, individual ACGs were mean normalized and sorted using burst index (Burst-BFCNs) or refractory period (Reg-BFCNs). The burst index was calculated inspired by the algorithm introduced by the Buzsaki lab[26]: the difference between the maximum ACG for lags of 0–10 ms and the mean ACG for lags of 180–200 ms was normalized by the larger of the two numbers, yielding an index between −1 and 1. The selectivity index for bursts and single spikes was calculated as the burst or single spike number in 20–50 ms relative to 100–250 ms post-event windows. It was not calculated for neurons that did not have bursts/single spikes in these windows due to an insufficient quantity of data. The theta index was calculated as the normalized difference between the mean ACG for a ±25-ms window around the peak between lags of 100 and 200 ms (corresponding to a 5- to 10-Hz theta band) and the mean ACG for lags of 225–275 and 65–85 ms. Normalization was performed similar to that for the burst index. The relative refractory period was defined as a low spiking probability after an AP had been fired, and was calculated by estimating the central gap in the ACG[26]. To estimate the range of delays after an AP at which spiking happened with lower probability, we calculated the maximal bin count of the ACG smoothed by a 10-ms moving average, and took the delay value at which the smoothed ACG first reached half of this value (width at half-height). We note that this definition captures low spike probability and not biophysical partial repolarization, as also used by Royer et al.[26]. As this algorithm allows APs in the 'refractory period', we used the term 'relative refractory period' (lower probability of firing). Nevertheless, this property captured the distinction between regular rhythmic and bursting neurons well (see Fig. 1). Cross-correlations (CCGs) were calculated at 1-ms resolution. Segments (±100 ms) around reinforcement events were excluded to avoid trivial event-driven correlations; 0-ms lag (middle) values were excluded to avoid potential contamination from spike sorting artifacts. When plotting all or average CCGs, individual CCGs were Z-scored and smoothed by a 15-point moving average. Co-activation was considered significant if raw CCGs crossed the 95% confidence limits, calculated by the shift predictor method, for at least two consecutive bins. PETHs were averaged from binned spike rasters and smoothed by a moving average. For comparisons of bursts and single spikes, PETHs were divided by (1 + average baseline PETH). All PETHs were baseline subtracted for visual comparison.

LFP recordings were carried out in the primary auditory cortex (A1) simultaneously with the tetrode recordings using platinum–iridium stereotrodes. LFP traces were Z-scored and averaged in windows centered on the APs of interest for STAs. Positive-deflecting STA traces were inverted before averaging for coherence because the depth of recording was not precisely controlled; therefore, we could not draw conclusions from absolute delta phases. Wavelet calculations were performed using the Morlet wavelet and STSs were calculated from the wavelet power and phase spectra. Individual frequencies were normalized by their averages to give equal weight to spectral components and visualized on a decibel scale. Note that this normalization method may introduce negative STS values.

In vitro recordings. Mice were decapitated under deep isoflurane anesthesia. The brain was removed and placed into an ice-cold cutting solution, which had been bubbled with 95% O_2–5% CO_2 (carbogen gas) for at least 30 min before use. The cutting solution contained the following (in mM): 205 sucrose, 2.5 KCl, 26 $NaHCO_3$, 0.5 $CaCl_2$, 5 $MgCl_2$, 1.25 NaH_2PO_4, 10 glucose. Coronal slices of 300-µm thickness were cut using a Vibratome (Leica VT1000S). After acute slice preparation, slices were placed into an interface-type holding chamber for recovery. This chamber contained standard ACSF solution at 35 °C which gradually cooled down to room temperature. The ACSF solution contained the following (in mM): 126 NaCl, 2.5 KCl, 26 $NaHCO_3$, 2 $CaCl_2$, 2 $MgCl_2$, 1.25 NaH_2PO_4, 10 glucose, saturated with 95% O_2–5% CO_2. Recordings were performed under visual guidance using differential interference contrast microscopy (Nikon FN-1) and a 40× water-dipping objective. Cholinergic neurons expressing ChR2-mCherry were visualized with the aid of a mercury arc lamp and detected with a CCD camera (Hamamatsu Photonics). Patch pipettes were pulled from borosilicate capillaries (with inner filament, thin-walled, outer diameter (OD) 1.5) with a PC-10 puller (Narishige). The composition of the intracellular pipette solution was as follows (in mM): 110 potassium gluconate, 4 NaCl, 20 4-(2-hydroxyethyl)-1-piperazine-ethanesulfonic acid, 0.1 (ethylenebis(oxonitrilo))tetra-acetate, 10 phosphocreatine, 2 ATP, 0.3 GTP, 3 mg ml^{-1} of biocytin adjusted to pH 7.3–7.35 using KOH (285–295 mosmol l^{-1}). Recordings were performed with a Multiclamp 700B amplifier (Molecular Devices), low-pass filtered at 3 kHz, digitized at 10–20 kHz with NI USB-6353, X Series DAQ, and recorded with an in-house data acquisition and stimulus software (courtesy of Attila Gulyás, Institute of Experimental Medicine, Budapest, Hungary). For in vitro light illumination, we used a blue laser diode (447 nm, Roithner LaserTechnik GmbH) attached to a single optic fiber (Thorlabs) positioned above the slice.

Analysis of in vitro experiments. All in vitro data were processed and analyzed off-line using self-developed programs written in Python v.2.7.0 and Delphi v.6.0 by A.I.G. and D.S. Spike delay was defined as the time between the start of the 1-s-long positive current injection step and the peak time of the first following AP. Burst frequency was calculated from the following three ISIs. The membrane potential in Fig. 2f,g was calculated as the average membrane potential of a 1-s-long period preceding the positive current injection step. ACGs for each cell were calculated on spikes evoked by step protocols (see Fig. 2b) and were smoothed by a 5-ms moving average. In the case of Fig. 2n, step protocols form each cell were classified into three groups (see Fig. 2n, inset). Burst indices were calculated in a similar way to the in vivo recordings: the difference between the maximum ACG for lags of 0–15 ms and the mean ACG for lags of 50–300 ms was normalized by the larger of the two numbers, yielding an index between −1 and 1. The average burst index as a function of AP distance from bregma was calculated as a three-section moving average (pink line in Fig. 7e).

Statistics. No statistical methods were used to predetermine sample sizes, but our sample sizes are similar to those reported in previous publications[17,46]. The present study did not involve separate experimental groups; therefore, randomization and blinding across groups were not relevant. Behavioral trials were presented in randomized order. Data analysis was automated, irrespective of neuron identity. Putative single neurons with isolation distance >20 and L-ratio <0.15 were included in the in vivo analysis. These criteria were pre-established based on recommendations and standards of the field[54]. In addition, the selectivity index could not be calculated for neurons that did not show any bursts or single spikes in the analyzed data window. If the number of recorded spikes exceeded 50,000, ACGs, CCGs, STAs and STS analyses were restricted to 50,000 spikes to avoid out-of-memory errors.

We used nonparametric tests for comparing central tendencies of two distributions, because normal distribution of the underlying data could not be determined unequivocally. For unpaired samples, the two-sided Mann–Whitney U-test was applied. For paired samples, we used the two-sided Wilcoxon's signed-rank test. Correlations were calculated using Pearson's correlation and tested using the one-sided F-test. Distributions over categorical variables were compared using the χ^2 test for homogeneity. We tested the significance of optogenetic tagging using the SALT, which is a bootstrap test based on the Jensen–Shannon divergence[55] of spike time distributions with or without stimulation. A full description of the test is provided in ref. [56].

Reporting Summary. Further information on research design is available in the Life Sciences Reporting Summary linked to this article.

Data availability

Statistics source data underlying the figures are provided in Excel format. The datasets analyzed during the current study are available from the corresponding author on reasonable request.

Code availability

Data analysis was performed by built-in and custom written Matlab code (Mathworks) available at: https://github.com/hangyabalazs/nb_sync_subimtted.

References

51. Higley, M. J. et al. Cholinergic interneurons mediate fast vGluT3-dependent glutamatergic transmission in the striatum. *PLoS ONE* **6**, e19155 (2011).
52. Zhao, S. et al. Cell type–specific channelrhodopsin-2 transgenic mice for optogenetic dissection of neural circuitry function. *Nat. Methods* **8**, 745–752 (2011).
53. Solari, N., Sviatkó, K., Laszlovszky, T., Hegedüs, P. & Hangya, B. Open source tools for temporally controlled rodent behavior suitable for electrophysiology and optogenetic manipulations. *Front. Syst. Neurosci.* **12**, 18 (2018).
54. Schmitzer-Torbert, N. et al. Quantitative measures of cluster quality for use in extracellular recordings. *Neuroscience* **131**, 1–11 (2005).
55. Endres, D. M. & Schindelin, J. E. A new metric for probability distributions. *IEEE Trans. Inf. Theory* **49**, 1858–1860 (2003).
56. Kvitsiani, D. et al. Distinct behavioural and network correlates of two interneuron types in prefrontal cortex. *Nature* **498**, 363–366 (2013).

Acknowledgements

We thank J. Szabadics, V. Varga, L. Acsády, N. Hádinger and G. Buzsáki for insightful discussions and comments on the manuscript and K. Sviatkó for help with graphics in Fig. 8. This work was supported by the 'Lendület' Program of the Hungarian Academy of Sciences (LP2015-2/2015), NKFIH KH125294 and the European Research Council Starting (grant no. 715043) to B.H., NKFIH K115441 and KH124345 to A.G., NINDS R01NS088661, R01NS075531 and McKnight Cognitive Disorders Award to A.K., ÚNKP-19-3 New National Excellence Program of the Ministry for Innovation and Technology to P.H., and EFOP-3.6.3-VEKOP-16-2017-00009 to D.S. and T.L. B.H. is a member of the FENS-Kavli Network of Excellence.

Author contributions

B.H. conceived the project, B.H. recorded in vivo data under the supervision of A.K. P.H. recorded in vivo data under the supervision of B.H. D.S. recorded and analyzed in vitro data under the supervision of A.G. and T.F.F. T.L., P.H. and B.H. analyzed in vivo data. B.H., T.L. and D.S. wrote the manuscript, with comments from all authors.

Competing interests

The authors declare no competing interests.

Additional information

Extended data is available for this paper at https://doi.org/10.1038/s41593-020-0648-0.

Supplementary information is available for this paper at https://doi.org/10.1038/s41593-020-0648-0.

Correspondence and requests for materials should be addressed to B.H.

Peer review information *Nature Neuroscience* thanks Anita Disney, Shih-Chieh Lin and the other, anonymous, reviewer(s) for their contribution to the peer review of this work.

Reprints and permissions information is available at www.nature.com/reprints.

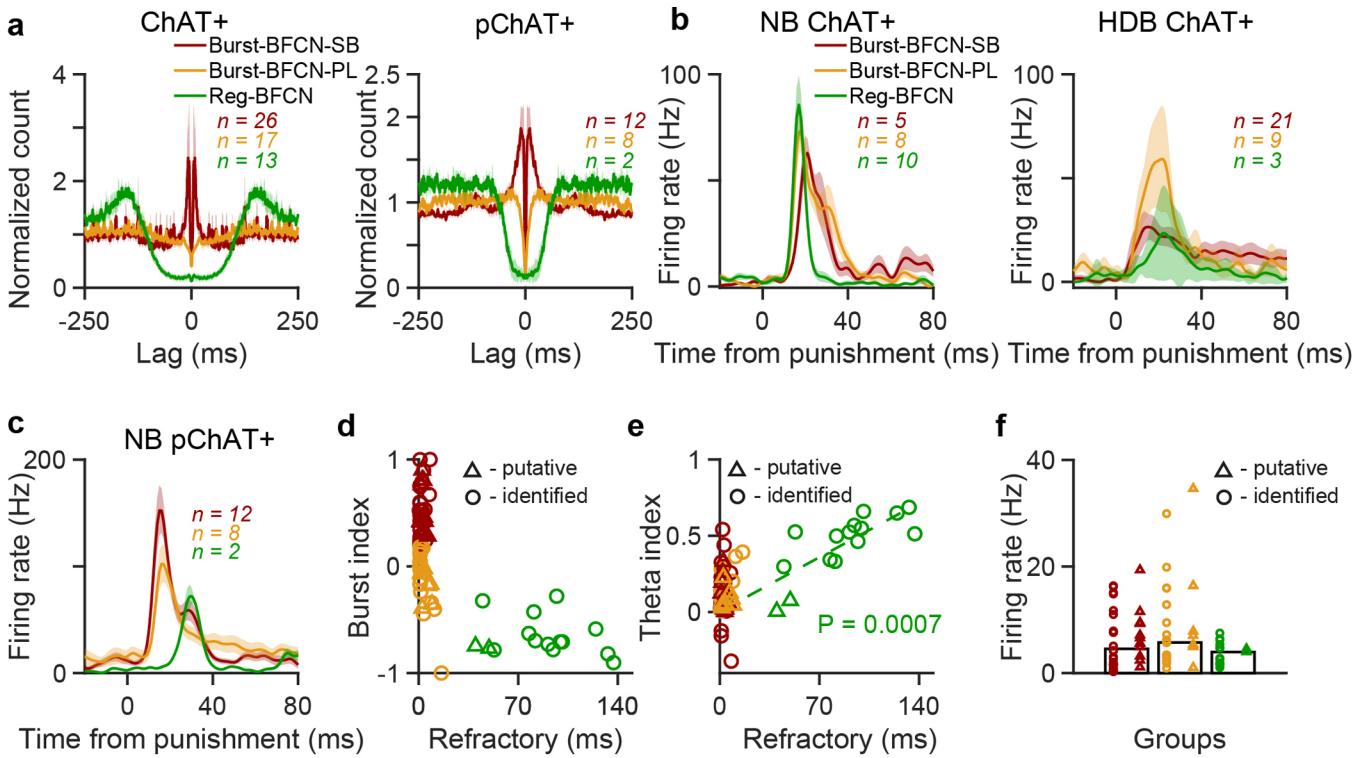

Extended Data Fig. 1 | Optogenetically identified and putative cholinergic neurons behave similarly. a, Average auto-correlogram of Burst-BFCN-SBs (red), Burst-BFCN-PLs (orange) and Reg-BFCNs (green). Left, optogenetically identified; right, putative. While nominal normalized magnitudes may differ due to varying noise levels and moderate sample sizes, the auto-correlation curves are qualitatively similar. Solid lines, mean; shading, s.e.m. **b**, Response to punishment of identified cholinergic neurons (left, identified NB; right, identified HDB). Solid lines, mean; shading, s.e.m. **c**, Response to punishment of putative cholinergic neurons. HDB neurons showed somewhat slower and more variable responses. Note also the longer response latencies of two regular pChAT neurons. Solid lines, mean; shading, s.e.m. **d**, Burst index vs. relative refractory period for identified (circle; red, n = 26 Burst-BFCN-SBs; orange, n = 17 Burst-BFCN-PLs; green, n = 13 Reg-BFCNs) and putative (triangle; red, n = 12 Burst-BFCN-SBs; orange, n = 8 Burst-BFCN-PLs; green, n = 2 Reg-BFCNs) cholinergic neurons. **e**, Pearson's correlation between theta index and relative refractory period. No systematic difference between identified (circle; red, n = 26 Burst-BFCN-SBs; orange, n = 17 Burst-BFCN-PLs; green, n = 13 Reg-BFCNs) and putative (triangle; red, n = 12 Burst-BFCN-SBs; orange, n = 8 Burst-BFCN-PLs; green, n = 2 Reg- BFCNs) cholinergic neurons were detected ($p = 0.0007$ for n = 15 Reg-BFCNs, one-sided F-test, $F(1,13) = 19.67$). **f**, Baseline firing rate did not show systematic differences between identified (circle; red, n = 26 Burst-BFCN-SBs; orange, n = 17 Burst-BFCN-PLs; green, n = 13 Reg-BFCNs) and putative (triangle; red, n = 12 Burst-BFCN-SBs; orange, n = 8 Burst-BFCN-PLs; green, n = 2 Reg-BFCNs) cholinergic neurons.

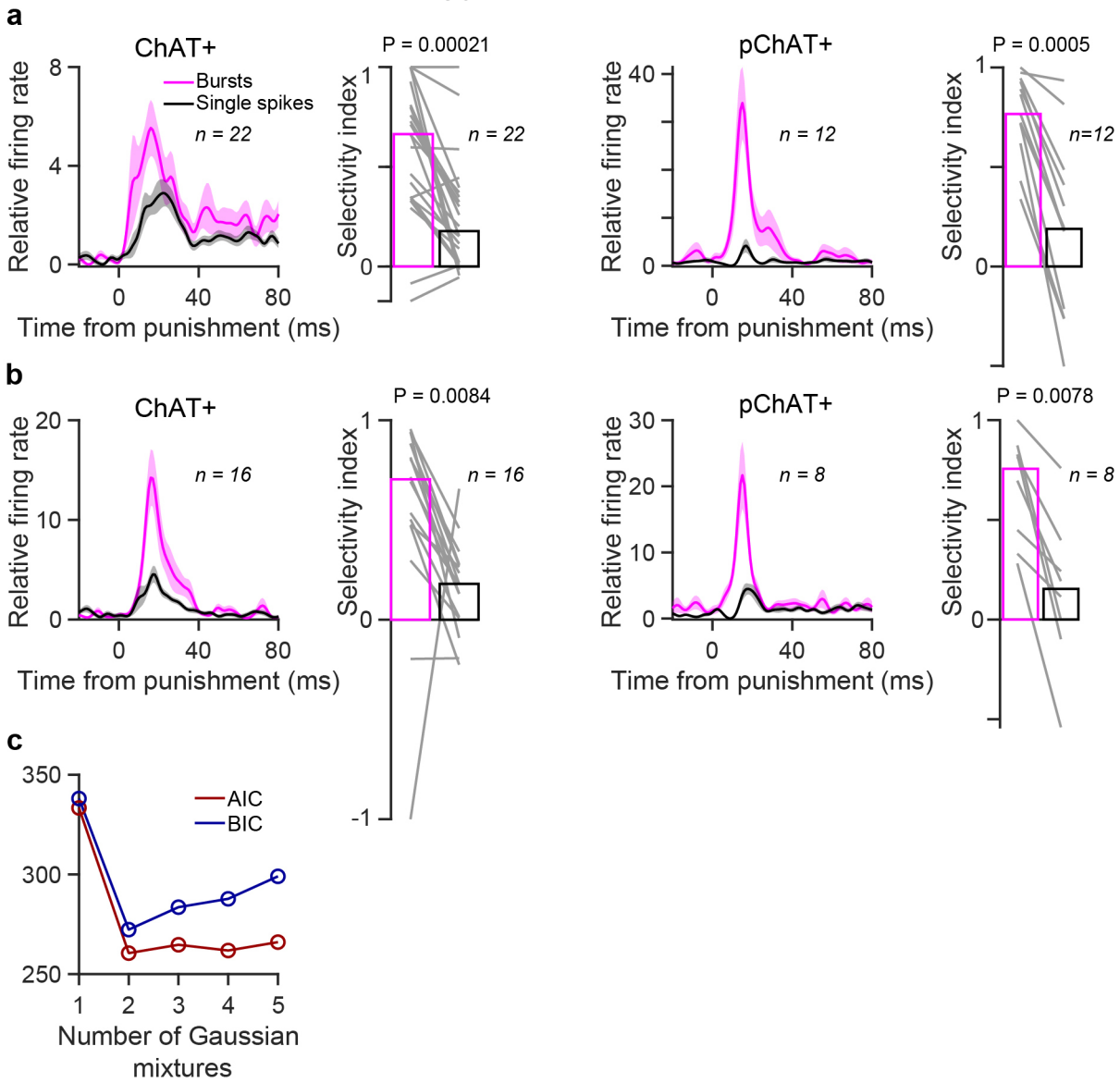

Extended Data Fig. 2 | Burst selectivity and model fitting. a, Identified (left, p = 0.00021, two-sided Wilcoxon signed rank test) and putative (right, p = 0.0005, two-sided Wilcoxon signed rank test) Burst-BFCN-SBs exhibited similar burst selectivity. Solid lines, mean; shading, s.e.m.; bars, median. **b**, The same for Burst-BFCN-PLs (left, identified, p = 0.0084, two-sided Wilcoxon signed rank test; right, putative, p = 0.0078, two-sided Wilcoxon signed rank test). Solid lines, mean; shading, s.e.m.; bars, median. **c**, A mixture of Gaussian distributions from 1 to 5 modes were fitted on the logarithm of refractory period distribution. Refractory period of BFCNs (n = 78) showed bimodal distribution, confirmed by AIC (red) and BIC (blue) model selection measures (lowest value corresponds to best fit model).

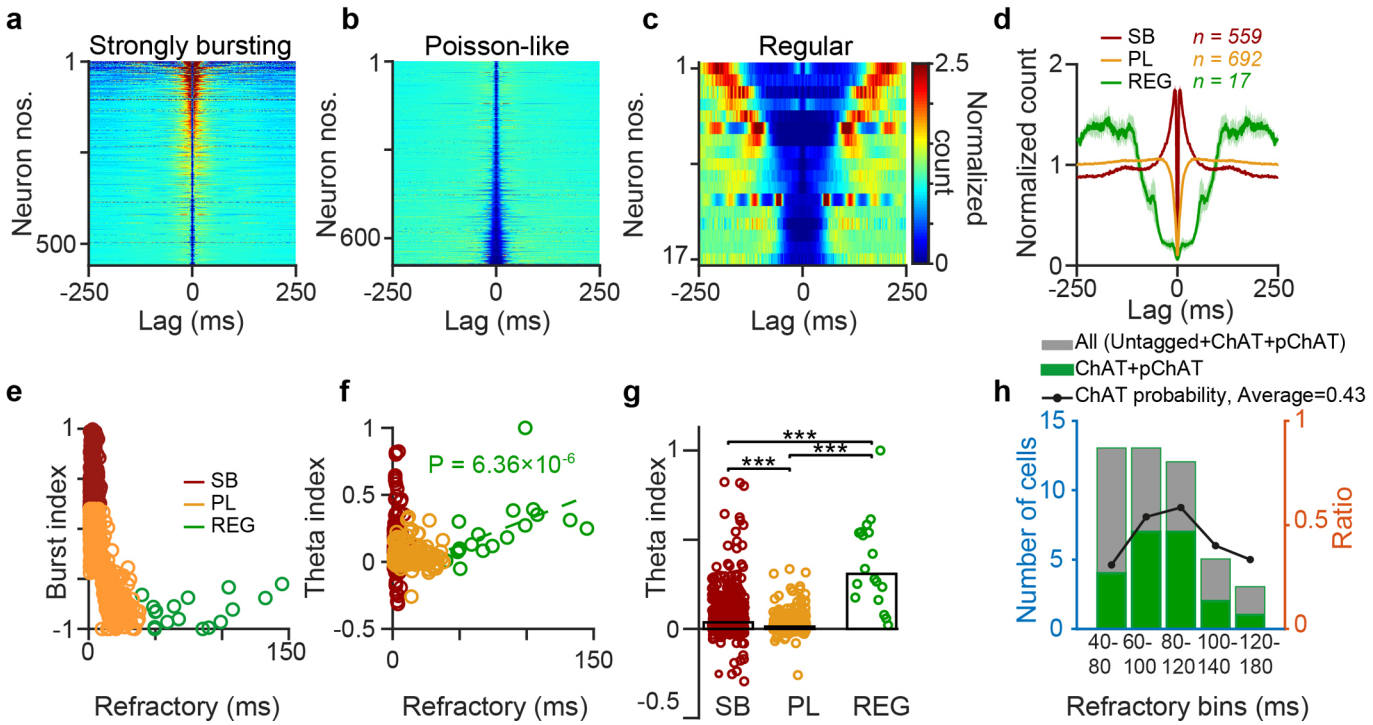

Extended Data Fig. 3 | Many regular rhythmic basal forebrain neurons are cholinergic. a-c, Auto-correlations of untagged bursting (**a**), Poisson-like (**b**), and regular rhythmic (**c**) NB neurons. **d**, Average auto-correlations (red, n = 559 untagged strongly bursting; orange, n = 692 Poisson-like; green, n = 17 regular rhythmic basal forebrain neurons). Solid lines, mean; shading, s.e.m. **e**, Scatter plot showing burst index and refractory period of the same neurons. **f**, Pearson's correlation between refractory period and theta index ($p = 6.36 \times 10^{-6}$ for n = 17 regular rhythmic basal forebrain neurons (green), one-sided F-test, $F(1,15) = 45.77$; red, n = 559 untagged strongly bursting; orange, n = 692 Poisson-like basal forebrain neurons). **g**, Median theta index (red, n = 559 untagged strongly bursting; orange, n = 692 Poisson-like; green, n = 17 regular rhythmic basal forebrain neurons; ***, $p < 0.001$; strongly bursting vs. Poisson-like, $p = 1.99 \times 10^{-24}$; strongly bursting vs. regular rhythmic, $p = 4.41 \times 10^{-8}$; Poisson-like vs. regular rhythmic, 6.04×10^{-11}; two-sided Mann-Whitney U-test). Bars, median. **h**, Predictive value of regular rhythmic firing pattern for cholinergic identity as a function of relative refractory period. Black line and right y-axis correspond to the ratio of (identified or putative) cholinergic neurons to all neurons in the bin.

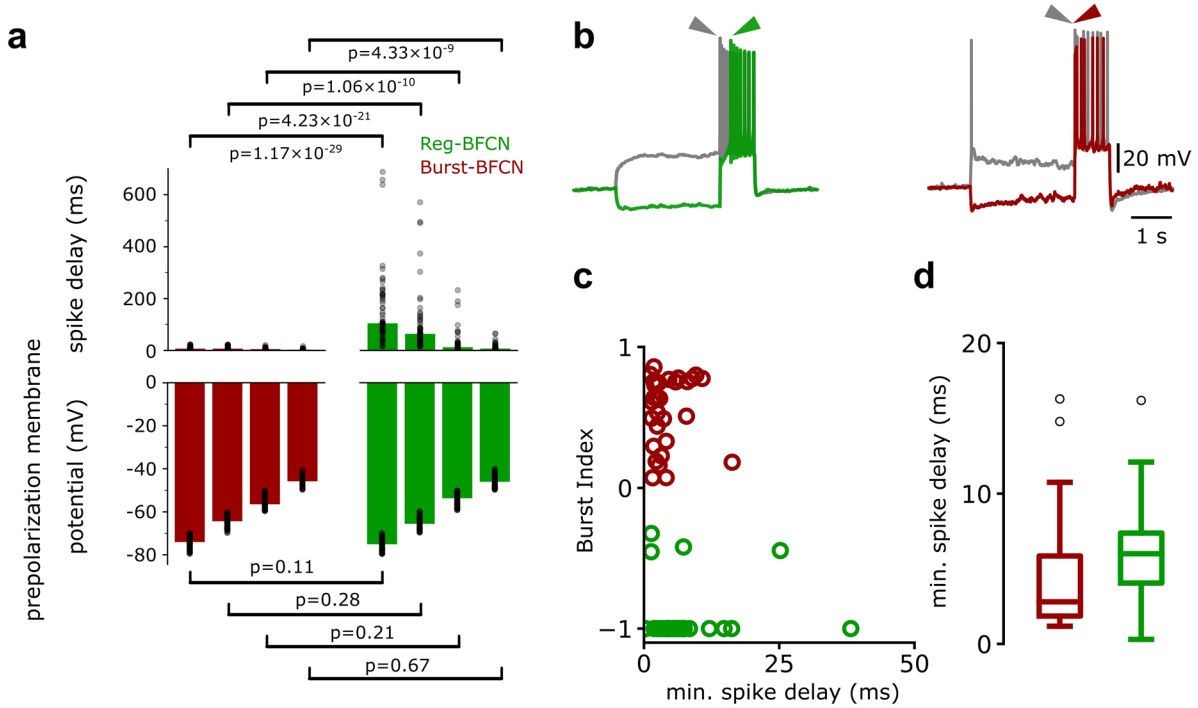

Extended Data Fig. 4 | Similar testing conditions resulted in robust spike delay difference between Burst-BFCNs and Reg-BFCNs, while spike delays were comparable at depolarized membrane potentials. a, Statistical comparison of spike delay as function of pre-polarization membrane potential. To confirm that late spiking property of Reg-BFCNs was not due to different testing conditions, we compared pre-polarization membrane potentials between groups (n = 31 late-firing and n = 29 early firing cholinergic cells, two-sample, two-sided Kolmogorov-Smirnov test). Bars show median. **b,** Example traces of a Reg-BFCN (left) and Burst-BFCN (right) spike response at hyperpolarized and depolarized membrane potentials. Note that the late-firing property of Reg-BFCNs is characteristic to hyperpolarized membrane potentials. **c**, Minimum spike delay of each recorded cell vs. burst index (green, Reg-BFCNs; red, Burst-BFCNs). **d,** Minimum spike delay group statistics (n = 31 late-firing and n = 29 early firing cholinergic cells). Box-whisker plots show median, interquartile range, non-outlier range and outliers.

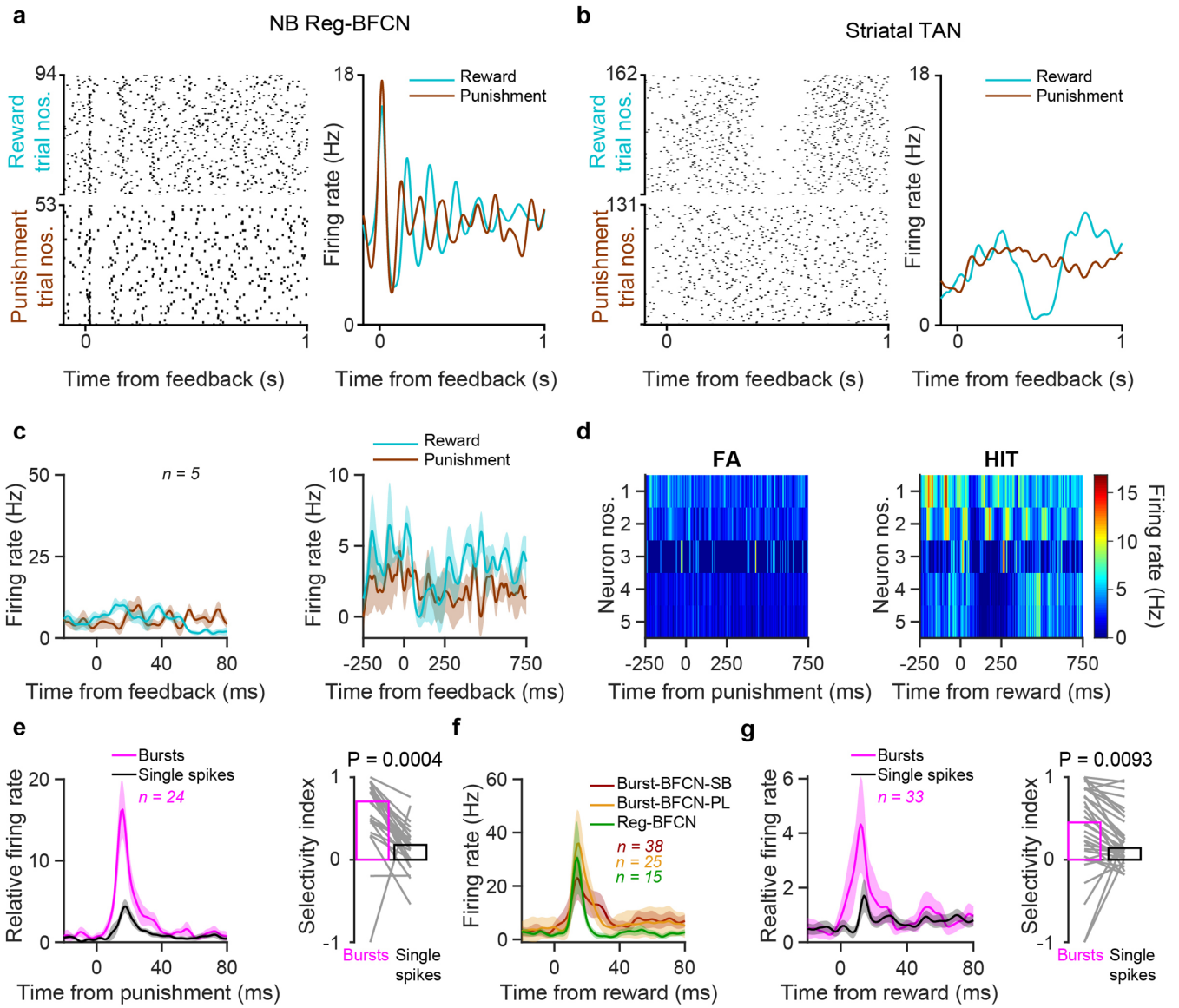

Extended Data Fig. 5 | Cholinergic bursts transmit phasic information about reinforcers. a, Raster plots (left) and corresponding peri-event time histograms (PETH, right) aligned to reward (blue) and punishment (brown) of a Reg-BFCN. After the precise phasic response, the intrinsic theta oscillation resumes. **b**, Raster plots (left) and corresponding PETHs (right) aligned to reward (blue) and punishment (brown) of an optogenetically identified tonically active cholinergic interneuron (TAN) recorded from the nucleus accumbens. Note the lack of precisely timed action potentials after reinforcement. Instead, TANs show well-characterized so-called 'pause-burst' responses after reward. **c**, Average PETH aligned to reward (blue) and punishment (brown) at two different time scales of n = 5 optogenetically identified TANs from caudate putamen (n = 3) and nucleus accumbens (n = 2) Solid lines, mean; shading, s.e.m. **d**, PETHs aligned to punishment (left) and reward (right) for all recorder TANs. **e**, Burst-BFCN-PLs showed similar burst selectivity after punishment as Burst-BFCN-SBs (p = 0.0004, two-sided Wilcoxon signed rank test). Solid lines, mean; shading, s.e.m.; bars, median. **f**, BFCNs responded phasically to reward (red, n = 38 Burst-BFCN-SBs; orange, n = 25 Burst-BFCN-PLs; green, n = 15 Reg-BFCNs). Solid lines, mean; shading, s.e.m. **g**, Bursts of Burst-BFCN-SBs (n = 33) appeared selectively after reward (p = 0.0093, two-sided Wilcoxon signed rank test). Solid lines, mean; shading, s.e.m.; bars, median.

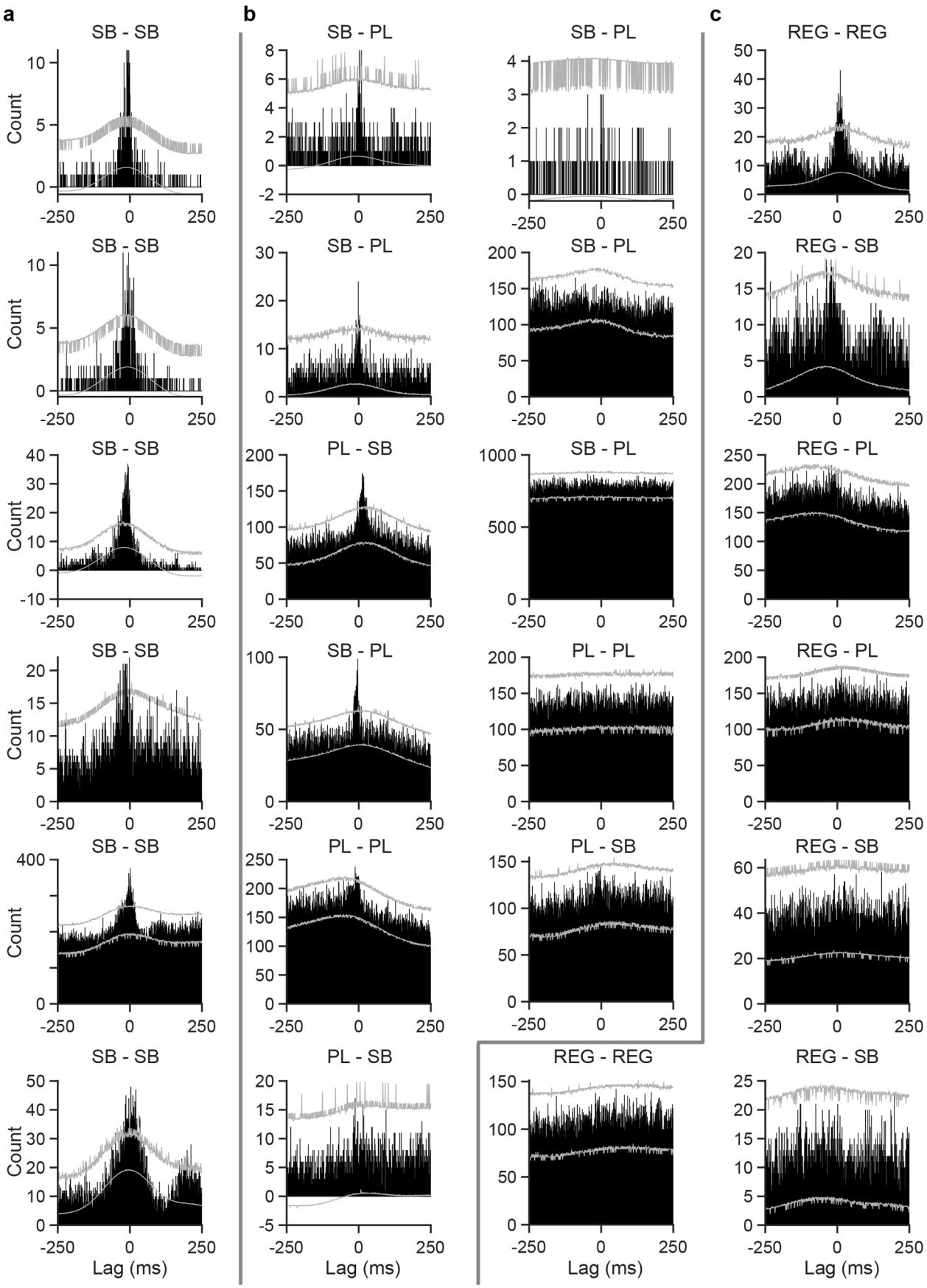

Extended Data Fig. 6 | Individual cross-correlations for all BFCN pairs. a, Pairs of Burst-BFCN-SBs. **b**, Pairs containing Burst-BFCN-PLs and Burst-BFCN-SBs. **c**, Pairs containing Reg-BFCNs. Grey lines indicate 95% bootstrap confidence intervals calculated with the shift predictor method.

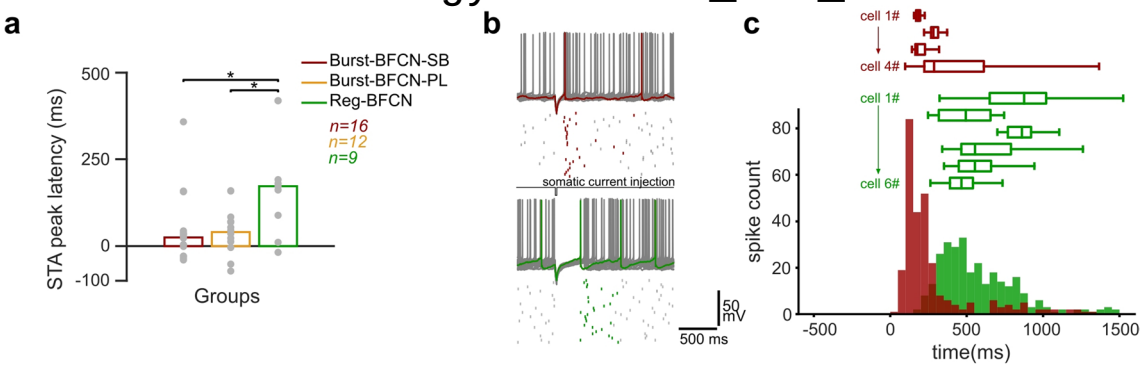

Extended Data Fig. 7 | Bursting and regular rhythmic cholinergic neurons respond differently to hyperpolarization *in vitro*. a, Peak latency statistics of auditory LFP average triggered on BF spikes *in vivo* (see Fig. 5b-c; red, n = 16 Burst-BFCN-SBs; orange, n = 12 Burst-BFCN-PLs; green, n = 9 Reg-BFCNs; *, $p < 0.05$; Burst-BFCN-SBs vs. Burst- BFCN-PLs, $p = 0.546$; Burst-BFCN-SBs vs. Reg-BFCNs, $p = 0.014$; Burst-BFCN-PLs vs. Reg-BFCNs, $p = 0.017$; two-sided Mann-Whitney U-test). Bars, median. **b**, Representative responses of a Burst-BFCN (top, red) and Reg-BFCN (bottom, green) upon short (20 ms) hyperpolarizing somatic current injection *in vitro*. Spike rasters of 30 consecutive current injection sessions are displayed below. **c**, Distribution of the first spike latencies following hyperpolarization. Individual cells (horizontal bar plots) are shown above summary histogram (red, n = 4 Burst-BFCNs, green, n = 6 Reg-BFCNs, $p = 6.47 \times 10^{-44}$, two-sided Mann-Whitney U-test; box plots show median, interquartile range and non-outlier range).

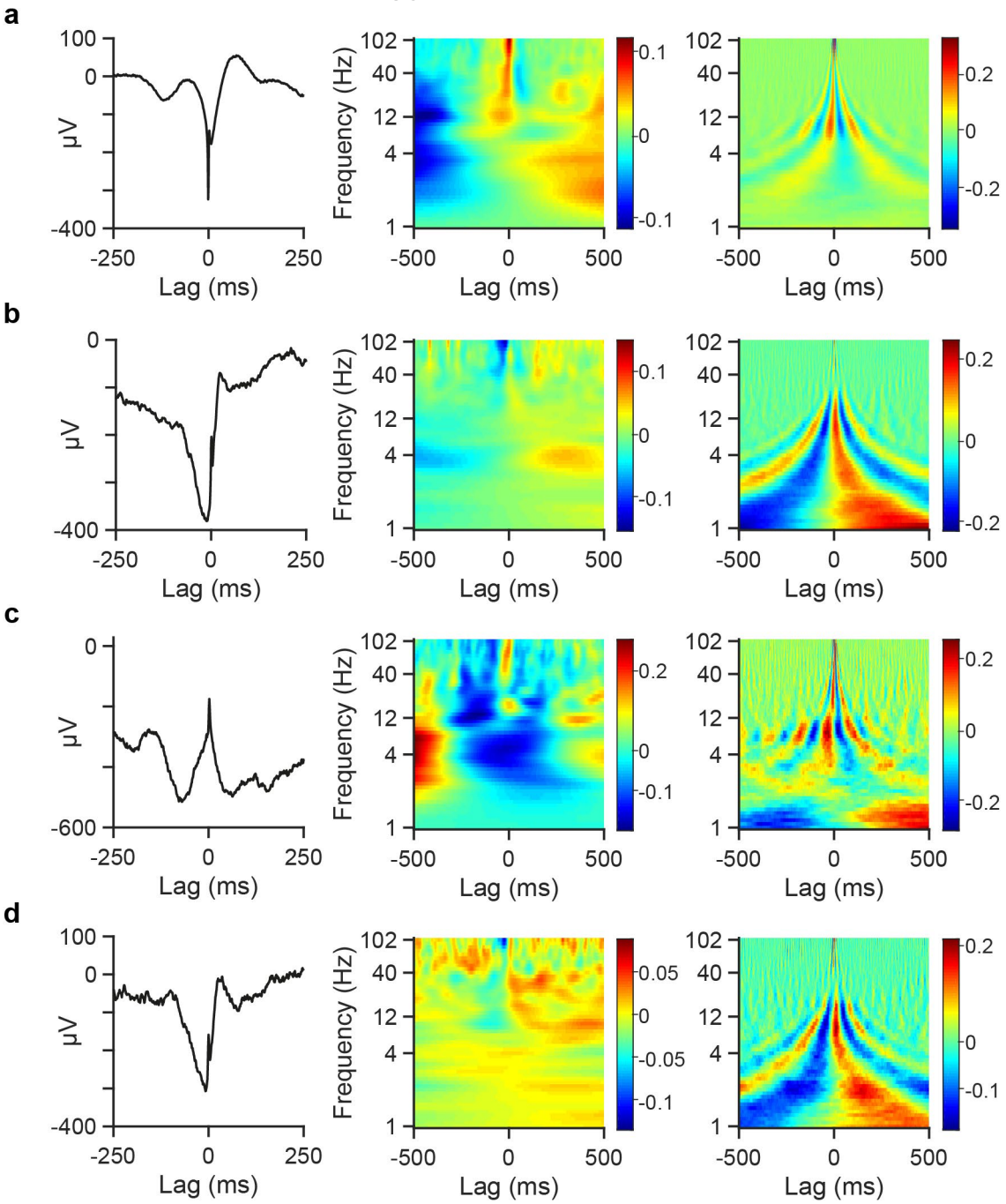

Extended Data Fig. 8 | Some auditory cortical neurons are synchronous with local LFP. a-d, Example cortical neurons that show synchrony with local LFP. Left, STA; middle, STS power; right, STS phase (**a,** n = 50000 spikes; **b,** n = 21765 spikes; **c,** n = 4083 spikes; **d,** n = 7834 spikes). Solid line, mean; shading, s.e.m.

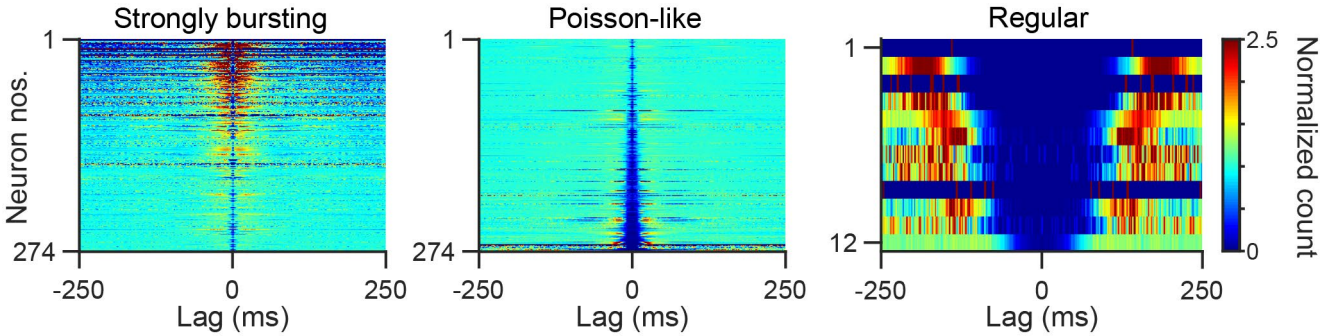

Extended Data Fig. 9 | HDB contains few regular rhythmic neurons. Auto-correlograms of all unidentified HDB neurons (left, bursting, n = 274; middle, Poisson-like, n = 274; right, regular rhythmic, n = 12). HDB had only 12/560 regular rhythmic neurons.

nature research hangya.balazs_256_24

Corresponding author(s): Balázs Hangya

Last updated by author(s): Apr 19, 2020

Reporting Summary

Nature Research wishes to improve the reproducibility of the work that we publish. This form provides structure for consistency and transparency in reporting. For further information on Nature Research policies, see Authors & Referees and the Editorial Policy Checklist.

Statistics

For all statistical analyses, confirm that the following items are present in the figure legend, table legend, main text, or Methods section.

n/a	Confirmed	
☐	☒	The exact sample size (*n*) for each experimental group/condition, given as a discrete number and unit of measurement
☒	☐	A statement on whether measurements were taken from distinct samples or whether the same sample was measured repeatedly
☐	☒	The statistical test(s) used AND whether they are one- or two-sided *Only common tests should be described solely by name; describe more complex techniques in the Methods section.*
☒	☐	A description of all covariates tested
☐	☒	A description of any assumptions or corrections, such as tests of normality and adjustment for multiple comparisons
☐	☒	A full description of the statistical parameters including central tendency (e.g. means) or other basic estimates (e.g. regression coefficient) AND variation (e.g. standard deviation) or associated estimates of uncertainty (e.g. confidence intervals)
☐	☒	For null hypothesis testing, the test statistic (e.g. *F*, *t*, *r*) with confidence intervals, effect sizes, degrees of freedom and *P* value noted *Give P values as exact values whenever suitable.*
☒	☐	For Bayesian analysis, information on the choice of priors and Markov chain Monte Carlo settings
☒	☐	For hierarchical and complex designs, identification of the appropriate level for tests and full reporting of outcomes
☒	☐	Estimates of effect sizes (e.g. Cohen's *d*, Pearson's *r*), indicating how they were calculated

Our web collection on statistics for biologists contains articles on many of the points above.

Software and code

Policy information about availability of computer code

Data collection	In vivo data was collected using custom MATLAB R2016b code and B-control custom behavior control system developed in the Brody lab. In vitro data was collected using software developed in C#.NET and VB.NET.
Data analysis	Data was analyzed using custom MATLAB R2016b, 2018b, Python 2.7.0 and Delphi 6.0 code.

For manuscripts utilizing custom algorithms or software that are central to the research but not yet described in published literature, software must be made available to editors/reviewers. We strongly encourage code deposition in a community repository (e.g. GitHub). See the Nature Research guidelines for submitting code & software for further information.

Data

Policy information about availability of data

All manuscripts must include a data availability statement. This statement should provide the following information, where applicable:

- Accession codes, unique identifiers, or web links for publicly available datasets
- A list of figures that have associated raw data
- A description of any restrictions on data availability

Custom written Matlab codes (Mathworks) generated for this study are available at https://github.com/hangyabalazs/nb_sync_submitted. Raw electrophysiology files, due to their size (multiple terabytes), are available from the corresponding author upon reasonable request.

Field-specific reporting hangya.balazs_256_24

Please select the one below that is the best fit for your research. If you are not sure, read the appropriate sections before making your selection.

☒ Life sciences ☐ Behavioural & social sciences ☐ Ecological, evolutionary & environmental sciences

For a reference copy of the document with all sections, see nature.com/documents/nr-reporting-summary-flat.pdf

Life sciences study design

All studies must disclose on these points even when the disclosure is negative.

Sample size	Sample sizes for non-parametric statistical comparisons of central tendencies were determined according to standards of single cell electrophysiology, typically exceeding minimal statistical requirements.
Data exclusions	Putative single neurons with isolation distance > 20 and L-ratio < 0.15 were included in the in vivo analysis. These criteria were pre-established based on recommendations and standards of the field - see e.g. Schmitzer-Torbert et al., Quantitative measures of cluster quality for use in extracellular recordings. Spike clusters outside these cluster quality ranges cannot be treated as putative single cells according to current definitions in rodent electrophysiology. Additionally, Selectivity Index could not be calculated for neurons that did not show any bursts or single spikes in the analyzed data window. If number of recorded spikes exceeded 50000, ACG, CCG, STA and STS analyses were restricted to 50000 spikes to avoid out-of-memory errors.
Replication	All attempts at replication were successful. Main results were compared, and found to be consistent across multiple mice, two different areas of the basal forebrain (nucleus basalis and nucleus of the horizontal limb of the diagonal band of Broca), two experimenters (BH and PH) and two different laboratories (Cold Spring Harbor Laboratory, US and Institute of Experimental Medicine, Hungary) in in vivo experiments and across in vitro and in vivo preparations.
Randomization	This study did not involve separate experimental groups. Behavioral trials were presented in randomized order.
Blinding	This study did not involve allocating subjects to groups. All data analysis was automated, irrespective of neuron identity.

Reporting for specific materials, systems and methods

We require information from authors about some types of materials, experimental systems and methods used in many studies. Here, indicate whether each material, system or method listed is relevant to your study. If you are not sure if a list item applies to your research, read the appropriate section before selecting a response.

Materials & experimental systems

n/a	Involved in the study
☒	☐ Antibodies
☒	☐ Eukaryotic cell lines
☒	☐ Palaeontology
☐	☒ Animals and other organisms
☒	☐ Human research participants
☒	☐ Clinical data

Methods

n/a	Involved in the study
☒	☐ ChIP-seq
☒	☐ Flow cytometry
☒	☐ MRI-based neuroimaging

Animals and other organisms

Policy information about studies involving animals; ARRIVE guidelines recommended for reporting animal research

Laboratory animals	Adult (over 2 months old) ChAT-Cre (N = 15, 14/15 male, Higley et al., 2011), ChAT-ChR2 (N = 3, 3/3 male, Zhao et al., 2011) and PV-Cre (n = 4, 4/4 male) mice were used for behavioral recording experiments under the protocol approved by Cold Spring Harbor Laboratory Institutional Animal Care and Use Committee in accordance with National Institutes of Health regulations. N = 3 male ChAT-Cre mice (over 2 months old) were used for in vivo and N = 12 ChAT-Cre (7/12 males, P50-150) mice were used for in vitro recordings according to the regulations of the European Community's Council Directive of November 24, 1986 (86/609/EEC); experimental procedures were reviewed and approved by the Animal Welfare Committee of the Institute of Experimental Medicine, Budapest and by the Committee for Scientific Ethics of Animal Research of the National Food Chain Safety Office.
Wild animals	The study did not involve wild animals.
Field-collected samples	The study did not involve samples collected from the field.
Ethics oversight	Adult (over 2 months old) ChAT-Cre (N = 15, 14/15 male, Higley et al., 2011), ChAT-ChR2 (N = 3, 3/3 male, Zhao et al., 2011) and PV-Cre (n = 4, 4/4 male) mice were used for behavioral recording experiments under the protocol approved by Cold Spring Harbor Laboratory Institutional Animal Care and Use Committee in accordance with National Institutes of Health regulations. N =

3 male ChAT-Cre mice (over 2 months old) were used for in vivo and N = 12 ChAT-Cre (7/12 males, P50-150) mice were used for in vitro recordings according to the regulations of the European Community's Council Directive of November 24, 1986 (86/609/EEC); experimental procedures were reviewed and approved by the Animal Welfare Committee of the Institute of Experimental Medicine, Budapest and by the Committee for Scientific Ethics of Animal Research of the National Food Chain Safety Office.

Note that full information on the approval of the study protocol must also be provided in the manuscript.

STAR Protocols

hangya.balazs_256_24

CellPress
OPEN ACCESS

Protocol

Training protocol for probabilistic Pavlovian conditioning in mice using an open-source head-fixed setup

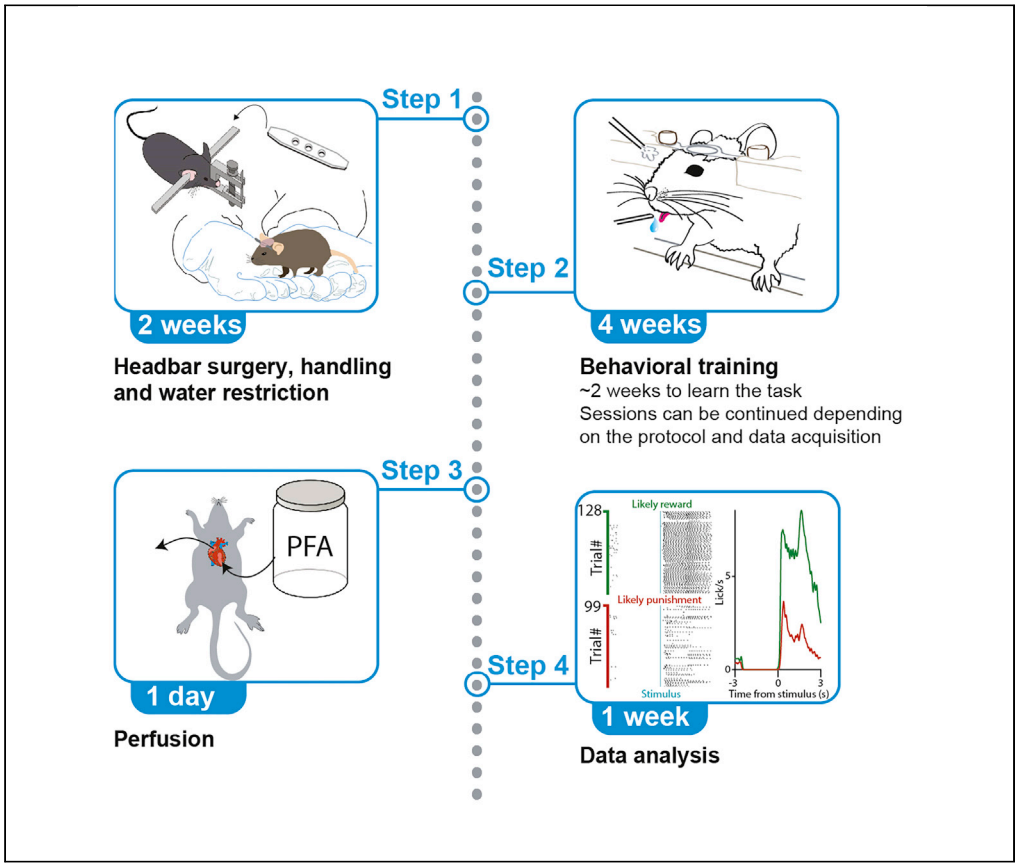

High throughput, temporally controlled, reproducible quantitative behavioral assays are important for understanding the neural mechanisms underlying behavior. Here, we provide a step-by-step training protocol for a probabilistic Pavlovian conditioning task, where two auditory cues predict probabilistic outcomes with different contingencies. This protocol allows us to study the differential behavioral and neuronal correlates of expected and surprising outcomes. It has been tested in combination with chronic *in vivo* electrophysiological recordings and optogenetic manipulations in ChAT-Cre and PV-Cre mouse lines.

Panna Hegedüs, Anna Velencei, Claire-Hélène de Belval, Julia Heckenast, Balázs Hangya

hegedus.panna@koki.hu (P.H.)
hangya.balazs@koki.hu (B.H.)

Highlights

We provide a training protocol for a probabilistic Pavlovian conditioning task in mice

Two auditory cues predict probabilistic outcomes with different contingencies

Possible to combine with chronic *in vivo* electrophysiology and optogenetics

Ideal for testing behavioral and neural correlates of expected and surprising outcomes

Hegedüs et al., STAR Protocols *2*, 100795
September 17, 2021
https://doi.org/10.1016/j.xpro.2021.100795

STAR Protocols

hangya.balazs_256_24

CellPress
OPEN ACCESS

Protocol

Training protocol for probabilistic Pavlovian conditioning in mice using an open-source head-fixed setup

Panna Hegedüs,[1,2,4,*] Anna Velencei,[1,4] Claire-Hélène de Belval,[1,3] Julia Heckenast,[1] and Balázs Hangya[1,5,*]

[1]Lendület Laboratory of Systems Neuroscience, Institute of Experimental Medicine, Budapest, Hungary

[2]János Szentágothai Doctoral School of Neurosciences, Semmelweis University, Budapest, Hungary

[3]Interdisciplinary Masters' in Life Sciences, Ecole Normale Supérieure, Paris, France

[4]Technical contact

[5]Lead contact

*Correspondence: hegedus.panna@koki.hu (P.H.), hangya.balazs@koki.hu (B.H.)
https://doi.org/10.1016/j.xpro.2021.100795

SUMMARY

High throughput, temporally controlled, reproducible quantitative behavioral assays are important for understanding the neural mechanisms underlying behavior. Here, we provide a step-by-step training protocol for a probabilistic Pavlovian conditioning task, where two auditory cues predict probabilistic outcomes with different contingencies. This protocol allows us to study the differential behavioral and neuronal correlates of expected and surprising outcomes. It has been tested in combination with chronic *in vivo* electrophysiological recordings and optogenetic manipulations in ChAT-Cre and PV-Cre mouse lines.

For complete details on the use and execution of this protocol, please refer to Hegedüs et al. (2021).

BEFORE YOU BEGIN

Pavlovian or classical conditioning is an associative learning paradigm. As a hallmark, the outcome does not depend on the actions of the performing agent, as in the case of Ivan Pavlov's famous experiment, in which his dog formed an association between a previously neutral auditory stimulus and food reward (Fanselow and Poulos, 2005). This allows the experimenter to have full control over the outcome contingencies, making this task ideal for probing the neural mechanisms underlying the processing of probabilistic outcomes (Pearce and Hall, 1980; Schultz et al., 1997). This Pavlovian training protocol was tested in combination with extracellular tetrode recordings (Hegedüs et al., 2021) and optogenetic tagging of neurons. We confirmed that it is suitable for optogenetic manipulations and fiber photometry experiments as well. Although not tested, we believe that it would also allow investigation of the effects of pharmacological or chemogenetic manipulations on associative learning. We further envision that, with an addition of a head plate designed for imaging window surgeries, it could be used in combination with two photon imaging. Before presenting the training protocol, we describe the preparatory phase of the experiment including animal welfare, headbar surgery and proper handling of mice.

The training setup

The training apparatus consists of a sound-attenuated training chamber, a head-fixation platform, an open source behavior control unit (Bpod, Sanworks), peripheries for interacting with the animal (lick port, water and air delivery systems, speakers to provide sound stimuli), a camera, optional open

source stimulator unit (PulsePal, Sanworks (Sanders and Kepecs, 2014)) and data acquisition board (Open Ephys (Siegle et al., 2017)), and a PC (Figures 1A and 1B). The custom-built sound-insulated Faraday-cage minimizes environmental noise (Figure 1C) and electric noise during the experiment. In the center of the box, an adjustable platform is placed along with two headbar holders to keep the mice's head in a fixed position during the training sessions. A lick port delivering water reward and a cannula delivering air puff as punishment are adjusted to the animal's position. A camera is placed at the top right corner of the box and speakers for delivering auditory cues are mounted on the side-walls of the box. The behavioral protocol is controlled via an open source closed-loop finite state machine (Bpod, Sanworks, see Figures 1A and 1B). This setup allows us to train mice on high-precision behavioral protocols with temporally controlled stimuli (Figure 1D). Details of this open source multipurpose training platform were published in (Solari et al., 2018).

⚠ CRITICAL: Regularly calibrate valve opening durations to deliver the right amount of water rewards. It is possible to calibrate sound pressure levels of auditory stimuli as well. See (Solari et al., 2018) for details.

Animal welfare

Our experiments were carried out using ChAT-Cre, PV-Cre and 3×Tg-AD Bl6 (Oddo et al., 2003) young adult (3–6 months) and aged (12–21 months) mice of both sexes.

⚠ CRITICAL: Before the experiment, ensure that animal care and all experiments are conducted according to the relevant ethical guidelines, reviewed and approved by your institute's animal welfare and ethical committee, as well as all necessary regulatory agencies.

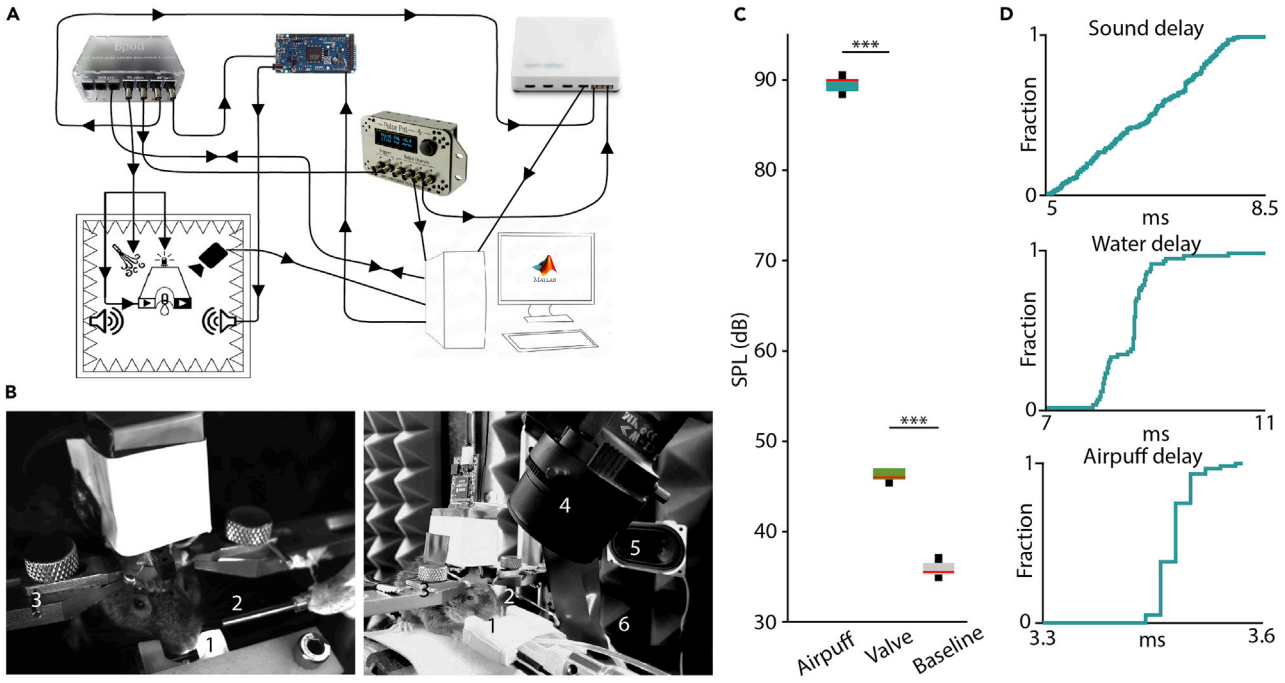

Figure 1. The experimental setup

(A) Schematic diagram of the setup. Modified from (Solari et al., 2018).

(B) Photos of mice performing the auditory Pavlovian conditioning task. 1, lick port; 2, tubing for air puff; 3, headbar holders; 4, camera; 5, speakers; 6, sound absorbing foams.

(C) Sound pressure levels associated with the flow of air at air-puff punishment, the click sound of the solenoid valve at reward presentation and background noise. Box-whisker plots show median, interquartile range and non-outlier range. ***, $p < 0.001$, Mann-Whitney U-test.

(D) Delay measurements for sound cues, water and air puff delivery. Underlying data are from refs. (Solari et al., 2018; Hegedüs et al., 2021).

Headbar surgery

Timing: 1 h + 1 week recovery period

We provide a description of our surgical protocol for mounting a headbar, which is used for head fixation while training mice in the head-fixed setup. We use titanium headbars weighing 0.27 g (dimensions, 19 mm × 3 mm × 1 mm); however, we expect other headfixation systems to provide similar results.

1. Put the mouse on the scale and measure its pre-surgery weight.

2. General anesthesia
   a. Briefly place the mouse in an anesthesia induction chamber (custom-built or commercial) to induce anesthesia by isoflurane inhalation.

   ⚠ CRITICAL: Continuously monitor breathing during the induction.

   b. Inject a mixture of ketamine-xylazine intraperitoneally (83 mg/kg and 17 mg/kg respectively, dissolved in saline).
   c. Confirm the loss of nociceptive reflexes by pinching the paws/tail with surgical tweezers.
   d. Monitor breathing and nociceptive reflexes throughout the surgery.

3. Shave the scalp. It is recommended to apply a small amount of water on the fur before shaving to limit the spread of potential airborne allergens.
4. Disinfect the scalp skin with Betadine.
5. Inject Lidocaine (or other approved local anesthetic) subcutaneously to achieve local anesthesia of the scalp skin and connective tissue.
6. Fix the animal's head in the stereotaxic frame.
7. Cover the eyes with eye ointment (e.g., Corneregel) to protect them from dehydration and strong light.
8. Remove the skin, connective tissue and periosteum from the calvaria using surgical scissors, forceps and scraper. Optionally, make small scratches on the skull with a scalpel to increase the surface for better adhesion of the dental cement.

   ⚠ CRITICAL: Make sure that the skull is perfectly clean and dry. Tissue debris can lead to improper adhesion of the surgical cement and detachment of the implant.

9. Level the skull along both the lateral and antero-posterior axes. We recommend using two symmetrical points over the parietal plates, 2 mm from the sagittal suture for lateral leveling (Király et al., 2020).
10. Cover the calvaria surface with high-adhesive dental cement (e.g., Metabond).

    ⚠ CRITICAL: Most high-adhesive cements should be kept and mixed on ice to aid polymerization.

11. Mount the headbar on the top of the skull by using acrylic powder and liquid resin (e.g., from Lang Dental). We recommend positioning the headbar over or right in front of Bregma. Implanting a small wood stick holder can help positioning the head of the mouse during head-fixation.
12. Once the dental cement is cured, remove the mouse from the stereotax.
13. Place the mouse on the scale and measure its weight, now with the implant mounted.
14. Inject analgesic according to your approved protocol (e.g., buprenorphine, BupaQ).
15. We recommend injecting 0.5 mL saline subcutaneously to prevent dehydration. It is recommended to distribute large amounts to multiple injection sites.

16. Put the mouse in its homecage. Place the cage on a heating pad until the mouse wakes up to prevent hypothermia.

Note: Animals were single-housed from the day of the surgery during the entire course of the experiment to prevent aggression and damage to the implants, and to allow proper control over water intake.

Note: Avoid low cage tops that can block the movement of implanted mice. Cage tops can also be used upside down if they do not leave enough space for the implanted mice.

Handling, water restriction

Timing: 15–20 min / day for 1 week

After surgery, mice are allowed a 1-week recovery period. Handling and water restriction of mice starts 1–2 weeks prior to the training protocol. Animals are handled and habituated to human touch on a daily basis. Below, we provide a short description of our handling protocol (see also Figures 2A–2C).

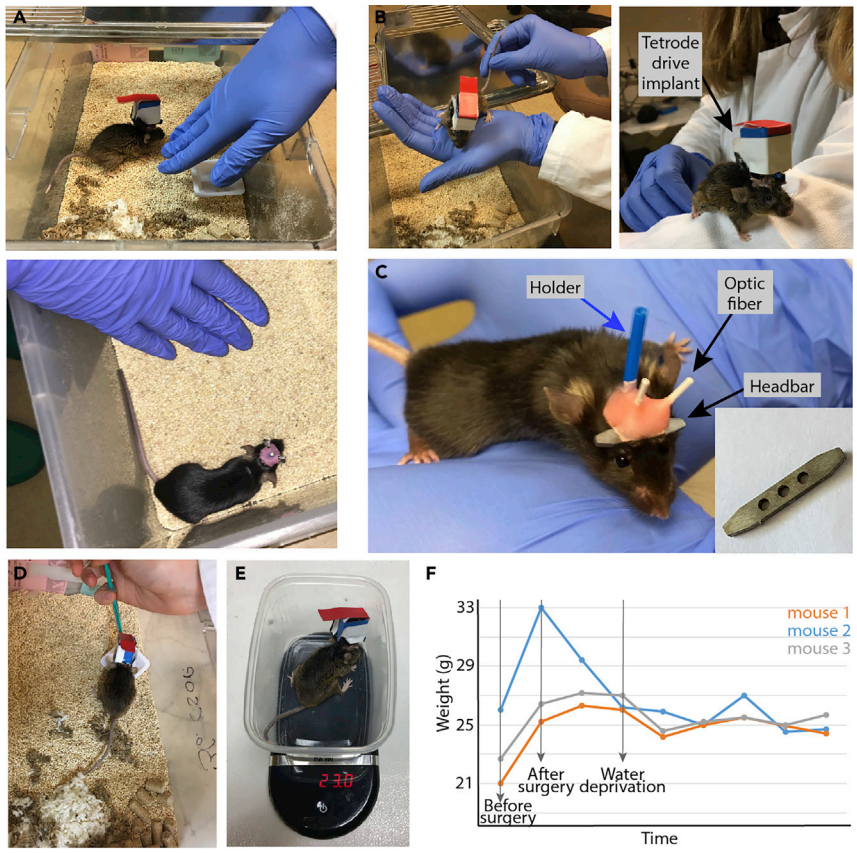

Figure 2. Animal handling

(A–C) Different phases of handling mice: the experimenter putting one hand in the cage (A), lifting the mouse (B) and letting it explore (C). Note that the mouse in panel B was implanted with a moveable tetrode drive besides the headbar, while the mouse in panel C had fixed bilateral optic fiber implants. Note also that lifting the mouse by the tail should be avoided; however, gently holding the tail during lifting can prevent the mouse from falling.

(D) Provide water in a weigh boat or equivalent container.

(E) Measure the weight daily.

(F) Mice drop weight at the beginning of water restriction, but the weight loss should be moderate, and the weight should stabilize after a few days and remain stable throughout the experimental phase.

Pause point: It is possible to include longer delays between headbar surgery and start of handling and water restriction. However, please note that if the training is combined with recording, then extending this delay could result in decreased signal quality.

17. Transport the animals to the behavioral testing room or facility a few days prior to the beginning of handling (typically ~1 week after surgery).
18. The experimenter opens the cage in a way that half of it is still covered by the top and places his/her gloved hand into the cage and allows the mice to sniff it or climb onto it.
19. The experimenter lifts the mouse and places it onto his/her open palm a little above the cage; this way the animal starts to get used to human touch but still has the option to climb off.
20. If the animal is not trying to escape from the experimenter, he/she should lift the mouse and let it explore and sniff the experimenter's hand.
21. Measure the weight of the mouse.
22. Reward the animal with a snack (e.g., sunflower seed) after the handling. We found that mice became used to human touch sooner when the handling process was associated with food reward, in spite of the fact that no food restriction was applied.
23. Water restriction protocol can be started in parallel with handling (Figures 2D–2F). Place a small weigh boat into the cage and fill it with 1 mL of water daily (1–1.5 mL for aged mice), measured with a syringe. Below we provide a list of behavioral and appearance changes that can be signs of dehydration; observing these signs at any time, the daily amount of water should be raised, or the water restriction should be suspended. Signs of severe dehydration in mice:
    a. After pinching the skin over the back, the skin remains bunched up
    b. Mice are weak and having trouble with gripping the cage bar
    c. Mice are curled up in the corner and barely moving or exploring
    d. Shrunken or recessed eyes
    e. Fuzzy facial and back fur

⚠ CRITICAL: The weight of the animals should be measured daily, and their behavior and potential signs of dehydration should be monitored regularly.

KEY RESOURCES TABLE

REAGENT or RESOURCE	SOURCE	IDENTIFIER
Experimental models: organisms/strains		
ChAT-IRES-Cre mice	https://www.jax.org/	Cat#006410
PV-Cre mice	https://www.jax.org/	Cat#008069
3×Tg-AD mice	https://www.mmrrc.org/	Cat#34830-JAX
Software and algorithms		
MATLAB R2016a	https://mathworks.com/	R2016a
Algorithms for behavioral analysis	https://github.com/hangyabalazs/VP_data_analysis	Commit#6308804
Algorithms for closed loop behavioral control	https://github.com/hangyabalazs/Bpod_r0_5	CuedOutComeTask
Code for simple data analysis of lick responses and neural recordings	https://github.com/hangyabalazs/CellBase	ultimate_psth.m
Chemicals, peptides, and recombinant proteins		
Isoflurane	https://vetcentre.com/	N/A
Ketamine	https://vetcentre.com/	N/A
Xylazine	https://vetcentre.com/	N/A
Lidocaine	Local pharmacy	N/A
Betadine	Local pharmacy	N/A
Buprenorphine	http://www.richter-pharma.com/	N/A
Promethazine	https://vetcentre.com/	N/A
Paraformaldehyde	https://taab.co.uk/	Cat#P001

(*Continued on next page*)

Continued

REAGENT or RESOURCE	SOURCE	IDENTIFIER
Other		
Standard surgical scissor	https://www.finescience.com/en-US/	Cat#14060-10
Surgical forceps	https://www.finescience.com/en-US/	Cat#11151-10
Scraper	https://www.finescience.com/en-US/	Cat#10075-16
Jet Set-4 Denture Repair Powder and Liquid	https://www.langdental.com/	N/A
Metabond dental cement	http://www.parkell.com/	Cat#S380
Headbar	Custom made	N/A
Headbar holders	Custom made	N/A
Sound-attenuated training chamber	https://github.com/hangyabalazs/Rodent_behavior_setup/	Commit#85897d1
Lick port	https://www.shapeways.com/	N/A
Infrared sensor and emitter	https://www.digikey.com/	Cat#480-1958-ND and Cat#480-1969-ND
Speakers	https://www.digikey.com/	Cat#668-1447-ND
Camera	https://www.flir.eu/iis/machine-vision/	Cat#FL3-U3-32S2M-CS
Bpod	https://sanworks.io/	Cat#1027
Teensy 3.2	https://www.pjrc.com/teensy/	N/A
PulsePal (if photostimulation is performed)	https://sanworks.io/	Cat#1102
Optogenetics Kit (if photostimulation is performed)	https://www.thorlabs.com/newgrouppage9.cfm?objectgroup_id=6148; light source alternative: laserglow.com	N/A
Data Acquisition System (if recording is performed)	https://open-ephys.org/acquisition-system/starter-kit	Version#2.4
Plastic tubing	https://www.thermofisher.com/	Cat#8001-0102 and Cat#8001-0204
Polyethylene tubing	https://www.warneronline.com/	Cat#64-0755/PE-160
Feeding needle	https://www.finescience.com/en-US/	Cat#18060-20
Bulldog serrefine	https://www.finescience.com/en-US/	Cat#18050-28
Bone rongeour	https://www.finescience.com/en-US/	Cat#16012-12

STEP-BY-STEP METHOD DETAILS

Behavioral training

Timing: 20–60 min / day for 6–8 days for the full training protocol

Timing: 20 min for step 2

Timing: 30 min for step 3

Timing: 40 min for step 4

Timing: 40 min for step 5

Timing: 50 min for step 6

Timing: 60 min for step 7

We provide a detailed description of the training protocol from the beginning to the point when the mice have learned the task (Figures 3A and 3B). We use a 1 training session/day protocol, i.e., each training step we describe here should be performed on consecutive days. The probabilistic training protocol consists of two cues and associated reinforcement; one cue predicts likely reward (80% reward, 10% punishment, 10% omission) and the other cue predicts likely punishment (25% reward, 65% punishment, 10% omission).

Note: These contingencies were calibrated to keep mice motivated on the task. We found that mice often stop licking the water spout when applying a higher ratio of air-puff punishments.

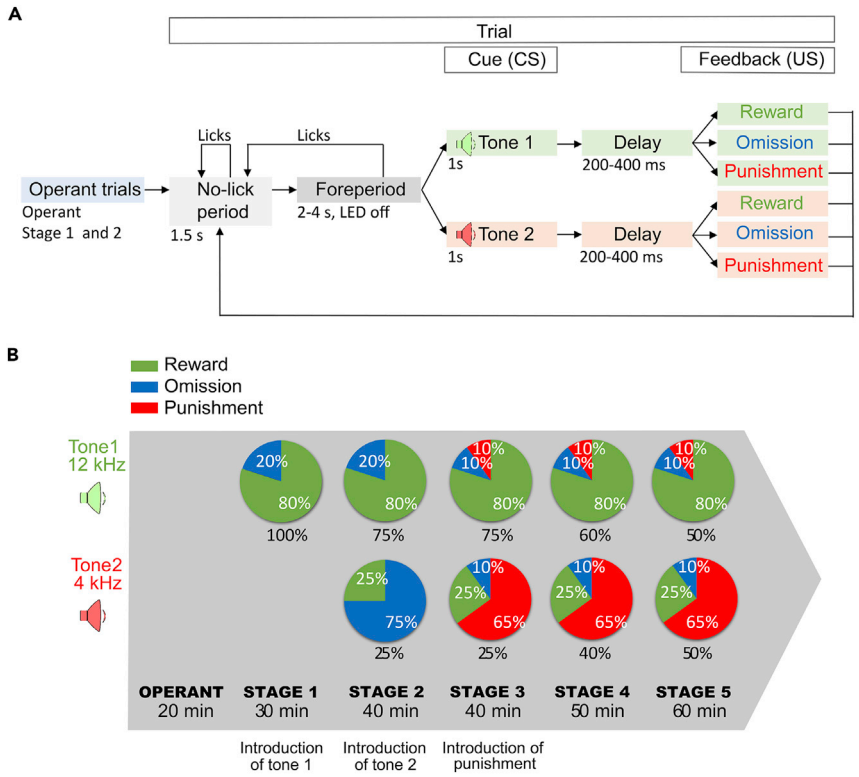

Figure 3. The probabilistic Pavlovian conditioning task

(A) Flowchart indicating the states of the task.

(B) Schematic diagram of reinforcement contingencies during different training phases.

Note: It takes approximately 1 week for young adult animals to reach Stage 5 on the task and then an additional week to achieve stable, good performance. Nevertheless, behavioral sessions of the full task can be continued beyond this period for recording or other purposes based on the experimental design. We observed stable performance for 2–3 months, beyond which we have no experience.

1. Initial steps (perform these before each training session)
   a. Turn on the computer, plug in the speakers, launch Matlab and Bpod. If combined with recording, start the data acquisition system (e.g., Open Ephys; see refs. (Hangya et al., 2015; Laszlovszky et al., 2020)). If combined with optogenetic tagging (Lima et al., 2009; Kvitsiani et al., 2013; Hangya et al., 2015; Széll et al., 2020), turn on the laser.
   b. Make sure that the water tank used for reward is filled.
   c. Clean the head-fixation platform with 70% ethanol.
   d. Remove the air bubbles from the water tube by opening the water valves through Bpod. Make sure to collect the water and thus keep the setup dry.
   e. Put the mouse onto the head-fixation platform of the setup. If combined with recording and/or optogenetics, connect the cables and/or patch chords as appropriate for your system.
   f. Carefully restrain the head of the animal.
   g. Adjust the position of the licking spout with an xyz-stage so that it is close to but not touching the animal's snout.

⚠ CRITICAL: Make sure that the licking spout is well-positioned, within convenient range of the animal's tongue. Too close, too far, and asymmetric positions critically impact behavioral performance. Using a dentist's mirror tool can aid optimal positioning.

⚠ CRITICAL: Make sure that air has been completely removed from the water delivery system.

2. Habituation to head restraint (see problem 1), learning to lick for water (Operant phase)
   a. In a brief operant phase, the mouse receives water reward (3–5 μL) every time it licks the water spout (see problem 2).

⚠ CRITICAL: If the mouse appears distressed, is vocalizing or trying to escape, terminate the protocol and attempt to repeat another time.

3. Introducing the cue that predicts likely reward (Stage 1)
   a. The animal performs 20 operant trials (as in the Operant phase), then the reward predicting cues start.
   b. Each trial starts with a no-lick period, in which the mouse has to withhold licking for 1.5 s. This is followed by a variable foreperiod, randomized between 2 and 4 s.
   c. Then, a 1 s long pure tone is played, followed by a variable 200–400 ms delay (300 ms on average, with uniform distribution), after which the animal receives water reward in 80% of the trials, in a pseudorandomized order.
   d. In this stage, there is no punishment; therefore, the reinforcer is omitted in the other 20% of the trials.

Note: We recommend starting the training with the likely reward cue, since the high probability of reward after the cue motivates mice better during the initial training phase.

Note: If the mouse licks in the foreperiod, the trial is restarted from the no-lick period. This way of enforcing no licking before the stimulus is not critical for forming the cue-reward association. However, it helps interpret the anticipatory lick response of mice (see quantification and statistical analysis). It also helps disentangle neural responses correlated with licking vs. different phases of the trials when concurrent recordings are performed (see problem 3).

⚠ CRITICAL: The variable delay between tone offset and reward delivery is important for the formation of the anticipatory lick response (see quantification and statistical analysis). In our experience, if the reward delivery time is fully predictable, some mice do not develop anticipatory lick responses.

4. Introducing the cue that will predict likely punishment (Stage 2)
   a. The animal performs 5 operant trials before the cued outcome trials. Two pure tones of well-separated pitch (e.g., 4 kHz and 12 kHz) predict likely reward (75% of all trials) or unlikely reward (25% of all trials) in a pseudorandomized order. (The latter cue will predict likely punishment in future training phases.)
   b. There is no punishment in this training phase; therefore, the likely reward cues are followed by reward in 80% and omission in 20% of the cases, whereas the unlikely reward cues are followed by reward in 25% and omission in 75%.

Note: We recommend testing mice with reversed cue-reward contingencies to rule out that the cue tones themselves induce differential behavior or neural activity based on their potential behavioral significance or previous experience of the animals.

5. Introducing punishment (Stage 3)
   a. Operant trials are not included for this phase.
   b. Air puff punishments are introduced in this phase. This modifies the outcome probabilities as follows: the likely reward cues predict 80% reward, 10% punishment, 10% omission and the likely punishment cues predict 25% reward, 65% punishment and 10% omission.

c. These probabilities represent the final task contingencies. The two trial types are pseudorandomly interleaved in a 3:1 ratio, as in the previous phase.

Note: The animals' performance can transiently drop at this stage due to the aversive nature of air puff punishment (see problem 4).

6. Ramping up likely punishment trials (Stage 4)
   a. Likely reward and likely punishment trials are pseudorandomly interleaved in a 6:4 ratio.
7. Final task (Stage 5)
   a. Likely reward and likely punishment trials are pseudorandomly interleaved in a 1:1 ratio.
   b. This is the final phase of the training protocol, and it can be maintained throughout the course of the experiment.

Note: Mice are actively engaged in more trials if they are trained at the beginning of their active (dark) phase (Remmelink et al., 2017; Birtalan et al., 2020), although we had success in training during the light phase as well. Nevertheless, we recommend adjusting the time of training to the light/dark cycle of the animals (see also problem 5).

⚠ CRITICAL: Training should be performed at a consistent time of day, maintained throughout the experiment (Gritton et al., 2012).

Note: When training multiple animals sequentially, keeping the order of mice helps maintain consistency during the experiment and further reducing environmental factors that can lead to poor performance. However, see problem 4.

⚠ CRITICAL: Overtraining animals on intermediate stages slows down or prevents further learning; ideally do not train more than 1 or 2 days on the intermediate stages of the task. Note that aged (over 12 months) mice learn slower and may be trained up to 3 days on intermediate steps.

⚠ CRITICAL: Skipping training days at the initial phase of the training (especially in the first week) can significantly reduce performance and the animal may not be able to learn the task eventually.

⚠ CRITICAL: The cumulative water consumed during the training session should be taken into account when calculating daily water consumption.

⚠ CRITICAL: The daily water should be provided hours after the training session, ideally approximately at the same time every day, to prevent mice from forming an association between water and the end of training.

Perfusion

Timing: 1 h

After concluding the behavioral experiments, animals are anesthetized, and the brain tissue is preserved by transcardial perfusion of 4% paraformaldehyde (PFA) fixative.

Note: This process is performed when the training protocol is combined with neuronal recordings or optogenetic manipulations, to allow histological processing of the brains. However, transcardial perfusion is not necessary for purely behavioral or systemic pharmacological manipulation studies.

8. Put mice in an isoflurane chamber to induce anesthesia.
9. Inject mice with a mixture of ketamine, xylazine and promethazine intraperitoneally (83 mg/kg, 17 mg/kg and 8 mg/kg respectively, dissolved in saline) to achieve deep anesthesia.
10. Wait until the animal does not respond to tail pinch.
11. Restrain the limbs on the perfusion platform.
12. Start the perfusion pump with saline.
13. Make a longitudinal cut on the skin over the abdominal region by using small surgical scissors and tweezers.
14. Hold the xiphoid process with a pair of forceps and cut the diaphragm to open the chest cavity. Carefully avoid piercing the heart.
15. Cut the ribcage on both sides; hold the basis of the sternum and lift it up, exposing the heart.
16. Make a small incision at the apex of the left ventricle and insert a feeding needle (connected to the perfusion pump). Gently push the needle into the aorta. Fix the needle with a small clamp.
17. Make a small cut on the right atrium to drain the blood.
18. Perfuse with saline for ~2 min, then switch to 4% paraformaldehyde fixative for an additional 20 min.
19. Stop the pump and disconnect the feeding needle.
20. Decapitate the animal and remove the brain.

Optional: The brain can be immersed in 4% PFA for enhanced preservation or can be stored in a buffer solution with sodium-azid at 4C°.

EXPECTED OUTCOMES

During successful training, mice form an association between the outcome predicting cues and the reinforcers. They learn the task contingencies, which is expressed by their differential anticipatory licking in response to the likely reward and likely punishment predicting cues (see quantification and statistical analysis). We consider a licking response anticipatory when it happens after the cue onset but before reinforcement delivery (~1.2 s time window from cue onset in the present protocol). Note that for learning outcome probabilities, mice have to integrate rewards over multiple trials. Therefore, this is a harder task than associating specific cues with different reward size, which can be inferred from a single trial (Stephenson-Jones et al., 2020).

QUANTIFICATION AND STATISTICAL ANALYSIS

We suggest that simple behavioral analysis should be performed on each training day to monitor the progress of the animals during training. Mice start licking the water spout after cue presentation in the anticipation of reward. As training progresses and mice start learning the cue contingencies, they develop differential anticipatory licking in response to the cues: they lick more vigorously (with higher frequency) if reward is more likely. We routinely calculate and visualize lick rasters (Figure 4A) and peri-event time histogram of licking activity (Figures 4B and 4C) aligned to cue onset to judge the difference in anticipatory lick rate after the sound cue. Learning curves can be plotted by tracking the changes in anticipatory lick rate across training days (Figure 4D). Reaction times can be measured as the time difference between cue onset and the first lick of the animal (Figure 4E). We use the custom-developed ultimate_psth.m Matlab code for calculating anticipatory lick rates, available at https://github.com/hangyabalazs/CellBase.

LIMITATIONS

This training protocol allows efficient training of mice on a probabilistic Pavlovian task, enabling direct control over outcome contingencies. Nevertheless, it has some limitations.

Training multiple animals in parallel can be time-consuming and labor-intensive, limiting the number of mice. This could be solved by fully automating the training (Qiao et al., 2019; Birtalan et al., 2020); however, that would either require using voluntary head-fixation protocols (Scott et al., 2013; Aoki et al., 2017) or switching to a freely behaving paradigm.

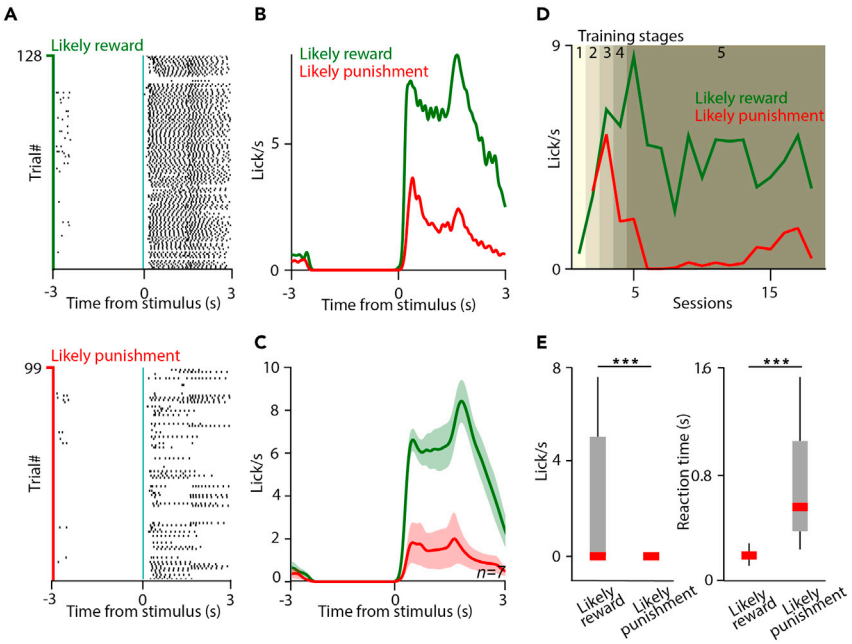

Figure 4. Behavioral analysis

(A) Raster plot of individual licks aligned to cue onset from an example session. Top, licks after the cues predicting likely reward; bottom, licks after the cues predicting likely punishment.

(B) Peri-event time histogram (PETH) of licking frequency aligned to cue onset corresponding to the same example session.

(C) Average PETH of anticipatory licking of n = 7 training sessions. Error shade represents SEM.

(D) Learning curve of an example mouse.

(E) Statistical comparison of lick rate (left) and reaction time (right) after cues predicting likely reward or likely punishment in an example session with n = 165 likely reward trials and n = 165 likely punishment trials. For reaction time comparison, the trials in which mice showed licking were used (n = 80 likely reward trials and n = 8 likely punishment trials). Box-whisker plots show median, interquartile range and non-outlier range. ***, $p < 0.001$, Mann-Whitney U test.

Efficient training requires some level of specific expertise from the experimenter. In our experience, the crucial skill is to learn the proper positioning of the lick port. While the feedback on behavioral performance from the Bpod behavior control system is useful, it is possible that the mouse can perform the task but stops early due to suboptimal positioning of the lick port. If this happens early in training or multiple times, it may influence performance on the long term. This could be improved by including a motorized stage for moving the lick port, which would allow reliable positioning and even enable automating this important step.

In Pavlovian conditioning tasks, the outcome does not depend on the animals' actions, endowing the experimenter with full control over the outcomes. However, as a downside, it is hard to measure the animals' performance and get access to the level of learning. We address this by using the difference in anticipatory lick rate that develops throughout the task (see quantification and statistical analysis). Nevertheless, there is no guarantee that a linear relationship exists between learning outcome probabilities and anticipatory licking, which complicates the interpretation of performance comparisons across mice.

TROUBLESHOOTING

Problem 1

The animal might show signs of strong distress (vocalizing and attempting to escape) at the first session that prevents starting the Operant phase (step 2).

Potential solution

Remove the animal from the setup immediately to prevent further stress. Take a couple more days before the training, and while handling the animal, place it on the setup platform and let it explore.

Consider giving it the daily amount of water on the setup platform as well. This way the experimenter can reduce the anxiety of the animal associated with head restraint.

Problem 2

The animal does not lick for water in the Operant phase (step 2).

Potential solution

Repeat the Operant phase at another time. Do not leave the mouse in the setup for an extended period, which often causes stress.

Problem 3

The animal shows impulsive licking behavior that interferes with the training. If a no-lick period is used in the protocol, this behavior leads to multiple restarting of most trials (step 3).

Potential solution

A brief period of free water before or at the beginning of the training session may help reduce impulsive licking. Counterintuitively, larger reward sizes can lead to impulsive/poor behavior (Kuchibhotla et al., 2019). We suggest starting from a reward size of 5 μL at the beginning of training and decreasing it gradually to 2–3 μL for best performance.

Problem 4

The mouse stops licking upon the introduction of punishment (step 5).

Potential solution

The first introduction of the punishment during training (Stage 3) might cause a setback in the animal's performance. First, repeat Stage 3 on the next day. If the problem persists, it might help training one or two more days at Stage 2; however, overtraining on intermediate phases should generally be avoided. As a rule of thumb, advance the mouse to the next stage as soon as it responds to at least 30% of the likely reward cues.

Problem 5

The animal stops licking early during the training session (step 7).

Potential solution

Allowing some free water by briefly opening the water valve via Bpod might help increase motivation. When training multiple animals sequentially, training at a slightly different time of day by changing the order of mice may help optimize their individual performance. However, try this only if problems occur; otherwise keeping the same order of mice helps develop consistent performance.

RESOURCE AVAILABILITY

Lead contact

Further information and requests for resources and reagents should be directed to and will be fulfilled by the lead contact, Balázs Hangya (hangya.balazs@koki.hu).

Materials availability

This study did not generate new unique reagents.

Data and code availability

MATLAB code developed to analyze the data is available at www.github.com/hangyabalazs/VP_data_analysis. Behavioral data is available from the technical contact upon reasonable request.

ACKNOWLEDGMENTS

We thank Nicola Solari and Katalin Sviatkó for providing data for Figures 1D and 2F, respectively. This work was supported by the ''Lendület'' Program of the Hungarian Academy of Sciences (LP2015-2/2015), NKFIH KH125294, NKFIH K135561, the European Research Council Starting Grant no. 715043, and the Artificial Intelligence National Laboratory Programme of the Ministry of Innovation and Technology to B.H. and the Kerpel-Fronius Talent Support Program of Semmelweis University (EFOP-3.6.3.-VEKOP-16-2017-00009) and the New National Excellence Program of the Ministry of Innovation and Technology (ÚNKP-20-3-II) to P.H. We thank Mackenzie Mathis for open access science art at SciDraw (accessible at https://doi.org/10.5281/zenodo.3925907).

AUTHOR CONTRIBUTIONS

Conceptualization, B.H.; methodology design, B.H. and P.H.; methodology implementation, P.H., J.H., A.V., and C.-H.B.; data analysis and statistical design, B.H. and P.H.; writing—original draft, P.H.; writing—review and editing, P.H., A.V., C.-H.B., J.H., and B.H.; visualization, P.H., C.-H.B., and A.V.; funding acquisition, B.H. and P.H.; supervision, B.H.

DECLARATION OF INTERESTS

The authors declare no competing interests.

REFERENCES

Aoki, R., Tsubota, T., Goya, Y., and Benucci, A. (2017). An automated platform for high-throughput mouse behavior and physiology with voluntary head-fixation. Nat. Commun. *8*, 1196.

Birtalan, E., Bánhidi, A., Sanders, J.I., Balázsfi, D., and Hangya, B. (2020). Efficient training of mice on the 5-choice serial reaction time task in an automated rodent training system. Sci Rep. *10*, 22362.

Fanselow, M.S., and Poulos, A.M. (2005). The neuroscience of mammalian associative learning. Annu. Rev. Psychol. *56*, 207–234.

Gritton, H.J., Kantorowski, A., Sarter, M., and Lee, T.M. (2012). Bidirectional interactions between circadian entrainment and cognitive performance. Learn. Mem. *19*, 126–141.

Hangya, B., Ranade, S.P., Lorenc, M., and Kepecs, A. (2015). Central Cholinergic neurons are rapidly recruited by reinforcement feedback. Cell *162*, 1155–1168.

Hegedüs, P., Heckenast, J., and Hangya, B. (2021). Differential recruitment of ventral pallidal e-types by behaviorally salient stimuli during Pavlovian conditioning. iScience *24*, 102377.

Király, B., Balázsfi, D., Horváth, I., Solari, N., Sviatkó, K., Lengyel, K., Birtalan, E., Babos, M., Bagaméry, G., Máthé, D., et al. (2020). In vivo localization of chronically implanted electrodes and optic fibers in mice. Nat. Commun. *11*, 4686.

Kuchibhotla, K.V., Hindmarsh Sten, T., Papadoyannis, E.S., Elnozahy, S., Fogelson, K.A., Kumar, R., Boubenec, Y., Holland, P.C., Ostojic, S., and Froemke, R.C. (2019). Dissociating task acquisition from expression during learning reveals latent knowledge. Nat. Commun. *10*, 2151.

Kvitsiani, D., Ranade, S., Hangya, B., Taniguchi, H., Huang, J.Z., and Kepecs, A. (2013). Distinct behavioural and network correlates of two interneuron types in prefrontal cortex. Nature *498*, 363–366.

Laszlovszky, T., Schlingloff, D., Hegedüs, P., Freund, T.F., Gulyás, A., Kepecs, A., and Hangya, B. (2020). Distinct synchronization, cortical coupling and behavioral function of two basal forebrain cholinergic neuron types. Nat. Neurosci. *23*, 992–1003.

Lima, S.Q., Hromádka, T., Znamenskiy, P., and Zador, A.M. (2009). PINP: a new method of tagging neuronal populations for identification during in vivo electrophysiological recording. PLoS One *4*, e6099.

Oddo, S., Caccamo, A., Shepherd, J.D., Murphy, M.P., Golde, T.E., Kayed, R., Metherate, R., Mattson, M.P., Akbari, Y., and LaFerla, F.M. (2003). Triple-transgenic model of Alzheimer's disease with plaques and tangles: intracellular Abeta and synaptic dysfunction. Neuron *39*, 409–421.

Pearce, J.M., and Hall, G. (1980). A model for Pavlovian learning: Variations in the effectiveness of conditioned but not of unconditioned stimuli. Psychol. Rev. *87*, 532–552.

Qiao, M., Zhang, T., Segalin, C., Sam, S., Perona, P., and Meister, M. (2019). Mouse academy: high-throughput automated training and trial-by-trial behavioral analysis during learning. bioRxiv, 467878.

Remmelink, E., Chau, U., Smit, A.B., Verhage, M., and Loos, M. (2017). A one-week 5-choice serial reaction time task to measure impulsivity and attention in adult and adolescent mice. Sci. Rep. *7*, 1–13.

Sanders, J.I., and Kepecs, A. (2014). A low-cost programmable pulse generator for physiology and behavior. Front. Neuroeng. *7*, 43.

Schultz, W., Dayan, P., and Montague, P.R. (1997). A neural substrate of prediction and reward. Science *275*, 1593–1599.

Scott, B.B., Brody, C.D., and Tank, D.W. (2013). Cellular Resolution Functional Imaging in Behaving Rats Using Voluntary Head Restraint. Neuron *80*, 371–384.

Siegle, J.H., López, A.C., Patel, Y.A., Abramov, K., Ohayon, S., and Voigts, J. (2017). Open Ephys: an open-source, plugin-based platform for multichannel electrophysiology. J. Neural Eng. *14*, 45003.

Solari, N., Sviatkó, K., Laszlovszky, T., Hegedüs, P., and Hangya, B. (2018). Open source tools for temporally controlled rodent behavior suitable for electrophysiology and optogenetic manipulations. Front. Syst. Neurosci. *12*, 18.

Stephenson-Jones, M., Bravo-Rivera, C., Ahrens, S., Furlan, A., Xiao, X., Fernandes-Henriques, C., and Li, B. (2020). Opposing contributions of GABAergic and glutamatergic ventral pallidal neurons to motivational behaviors. Neuron, 1–13.

Széll, A., Martínez-Bellver, S., Hegedüs, P., and Hangya, B. (2020). OPETH: Open source solution for real-time peri-event time histogram based on open ephys. Front. Neuroinform. *14*, 1–19.

iScience

CellPress
OPEN ACCESS

Article

Cholinergic activity reflects reward expectations and predicts behavioral responses

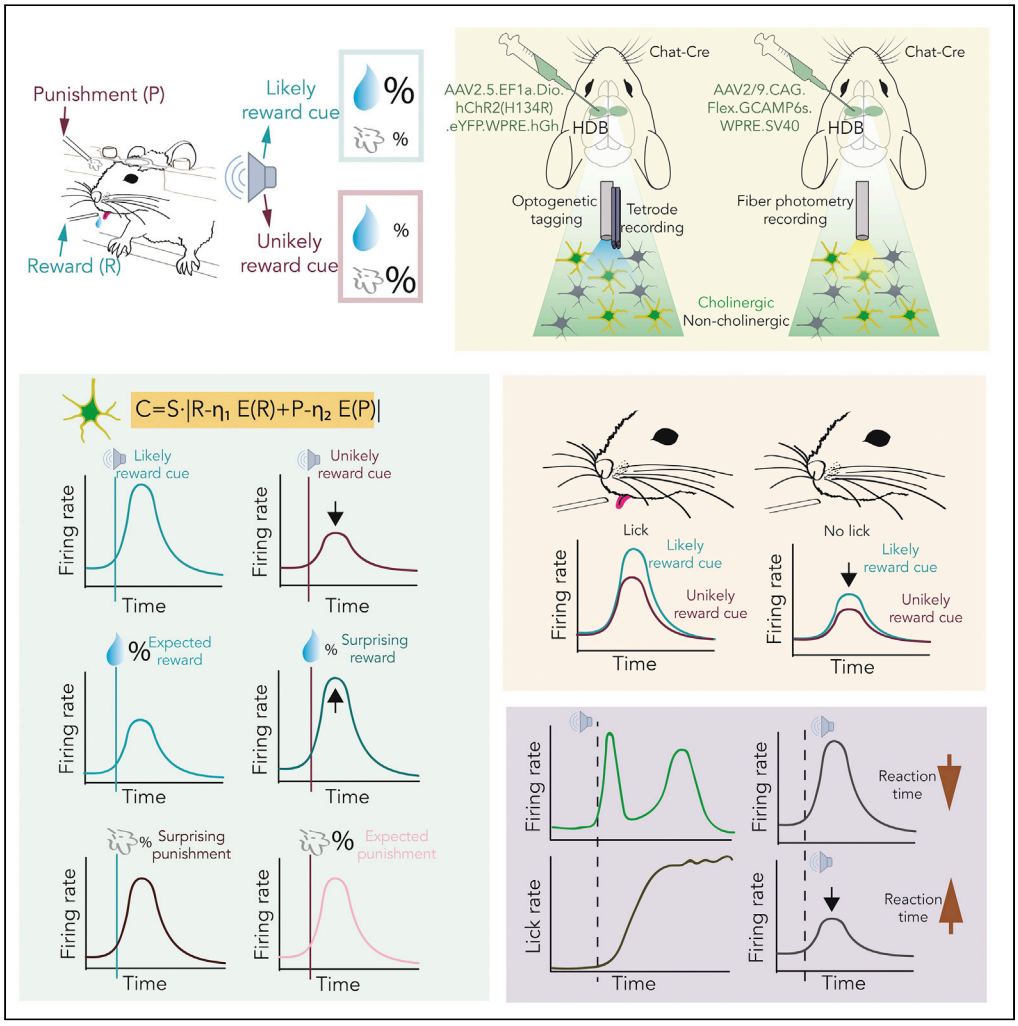

Panna Hegedüs, Katalin Sviatkó, Bálint Király, Sergio Martínez-Bellver, Balázs Hangya

hangya.balazs@koki.hu

Highlights

Predictive strength of sensory cues was controlled in Pavlovian conditioning

BFCNs showed large responses to reward-predicting stimuli and surprising rewards

A reinforcement learning model suggested valence-weighed, unsigned BFCN responses

Cholinergic responses predicted reaction times

Hegedüs et al., iScience 26, 105814
January 20, 2023
https://doi.org/10.1016/j.isci.2022.105814

iScience

CellPress
OPEN ACCESS

Article

Cholinergic activity reflects reward expectations and predicts behavioral responses

Panna Hegedüs,[1,2] Katalin Sviatkó,[1,2] Bálint Király,[1,3] Sergio Martínez-Bellver,[1,4] and Balázs Hangya[1,5,*]

SUMMARY

Basal forebrain cholinergic neurons (BFCNs) play an important role in associative learning, suggesting that BFCNs may participate in processing stimuli that predict future outcomes. However, the impact of outcome probabilities on BFCN activity remained elusive. Therefore, we performed bulk calcium imaging and recorded spiking of identified cholinergic neurons from the basal forebrain of mice performing a probabilistic Pavlovian cued outcome task. BFCNs responded more to sensory cues that were often paired with reward. Reward delivery also activated BFCNs, with surprising rewards eliciting a stronger response, whereas punishments evoked uniform positive-going responses. We propose that BFCNs differentially weigh predictions of positive and negative reinforcement, reflecting divergent relative salience of forecasting appetitive and aversive outcomes, partially explained by a simple reinforcement learning model of a valence-weighed unsigned prediction error. Finally, the extent of cue-driven cholinergic activation predicted subsequent decision speed, suggesting that the expectation-gated cholinergic firing is instructive to reward-seeking behaviors.

INTRODUCTION

Cholinergic neurons of the basal forebrain are important for associative learning. This idea is supported by the selective cholinergic cell loss that parallels cognitive decline in patients with Alzheimer disease.[1,2] Although lesion and pharmacology studies were confirmative,[3–5] they cannot solve how BFCNs exert their control over learning. To address the mechanisms of the contribution of BFCNs to associative learning, it is important to investigate the behavioral correlates of BFCN activity at temporal resolutions comparable to the time scales of behaviorally relevant events animals and humans encounter.[6,7] This has only become possible recently, enabled by the development of optogenetic and imaging tools.[8–11]

Selective cholinergic lesions of the basal forebrain were shown to impair learning in rodents[12–18] and monkeys,[19] and lesions of the basal forebrain in consequence of aneurysm rupture of the anterior cerebral or anterior communicating artery lead to severe learning impairments in humans.[20] Previous studies of the basal forebrain have proposed that responses to behaviorally salient stimuli of cholinergic and/or noncholinergic basal forebrain neurons may underlie the involvement of the basal forebrain in learning.[9–11,21,22] Specifically, cholinergic activation may lead to increased cortical acetylcholine release that induces plastic changes in sensory responses.[23,24] A recent study connected the above pieces of evidence by bulk imaging of BFCNs during auditory fear learning.[11] However, it is not yet known how BFCNs process sensory cues with different predictive features during learning, which could serve as a basis for differential behavioral responses to sensory events that forecast distinct outcomes. Therefore, a comprehensive model of cholinergic neuronal responses that subserve associative learning is also lacking. We set out to fill this knowledge gap by recording cholinergic activity in a probabilistic Pavlovian cued outcome task, which allowed us to directly control outcome probabilities and cue-outcome contingencies during learning.[25] Of note, reward expectation can also be manipulated by reward size.[26,27] However, since we hypothesized that BFCNs are sensitive to the outcome probabilities, we chose to manipulate reward probability instead, despite that this is harder to learn, as animals have to integrate over multiple trials to infer differences in probability, whereas reward size can be learned from a single trial.[28]

We imaged the bulk calcium responses of BFCNs using fiber photometry[29] and recorded the activity of identified basal forebrain cholinergic neurons while mice were performing a head-fixed auditory probabilistic Pavlovian cued outcome task.[25] BFCNs were activated by outcome-predicting stimuli, as well as

[1]Lendület Laboratory of Systems Neuroscience, Institute of Experimental Medicine, H-1083 Budapest, Hungary

[2]János Szentágothai Doctoral School of Neurosciences, Semmelweis University, H-1085 Budapest, Hungary

[3]Department of Biological Physics, Eötvös Loránd University, H-1117 Budapest, Hungary

[4]Department of Anatomy and Human Embryology, Faculty of Medicine and Odontology, University of Valencia, 46010 Valencia, Spain

[5]Lead contact

*Correspondence: hangya.balazs@koki.hu

https://doi.org/10.1016/j.isci.2022.105814

delivery of reinforcement. Reward-predicting stimuli activated cholinergic neurons differentially in correlation with the likelihood of future reward, and subsequent reaction times were predicted by the level of this activation. BFCNs also showed stronger activation after unexpected compared with expected rewards. We show that these findings can be explained by a behavioral model of a stimulus-induced, valence-weighed prediction error, in which outcomes of opposite valence are differentially scaled by the animals. We did not observe robust firing rate changes of BFCNs following omissions of reinforcement, suggesting that the BFCN responses we observed were largely driven by sensory stimuli. Thus, these results suggest that the central cholinergic system broadcasts a stimulus-driven, valence-weighed prediction error signal that can instruct associative learning.

RESULTS

Mice were trained on a probabilistic Pavlovian conditioning task

We trained mice (n = 11) on a head-fixed probabilistic Pavlovian cued outcome task (Figure 1A).[25,28] During this associative learning task, two tones of different pitch (conditioned stimuli) predicted either water reward with 80% chance (10% punishment, 10% omission, "likely reward" cue) or a puff of air on the face with 65% probability (25% reward, 10% omission, "unlikely reward" cue; the contingencies reflect careful calibration to keep mice motivated for the task). Based on the cue that preceded behavioral feedback (unconditioned stimuli), both rewards and punishments could be either expected, or surprising. Mice learned this task, indicated by performing significantly more anticipatory licks after "likely reward" cues (Figures 1B–1E).

BFCN population responses to conditioned and unconditioned stimuli

We expressed GCaMP6s in BFCNs of the horizontal nucleus of the diagonal band of Broca (HDB) by injecting AAV2/9.CAG.Flex.GCAMP6s.WPRE.SV40 in ChAT-Cre mice (n = 7), expressing Cre recombinase driven by the choline acetyltransferase promoter selectively in cholinergic neurons,[10,30,31] and implanted them with an optic fiber in the HDB. We performed bulk calcium imaging of HDB BFCNs while mice were performing the probabilistic Pavlovian task (Figures 2A–2C and S1). An excitation isosbestic wavelength of GCaMP was used to correct for non-calcium-dependent changes in fluorescence (e.g., bleaching and potential movement artifacts).[32] We first asked whether BFCNs as a population responded to auditory cue stimuli that predicted outcomes with different contingencies. Fluorescent dff responses were aligned to cue presentations, revealing BFCN population calcium responses to outcome-predicting cue stimuli (Figures 2D and 2E). These responses were significantly larger for cues that predicted "likely reward" compared with cues predicting "likely punishment" (Figure 2D and 2E, $p = 0.00029$, Wilcoxon signed-rank test, n = 17 sessions). Based on published results of us and others,[8–11] we expected BFCN calcium responses following the delivery of rewards and punishments as well. Indeed, when dff recordings were aligned to reinforcement, we observed robust cholinergic population responses to both water reward and air puff punishment (Figures 2F and 2G). Moreover, we found that BFCN responses to surprising rewards significantly exceeded those to expected rewards, although the observed difference was less than that of the cue responses (Figure 2F, $p = 0.0129$, Wilcoxon signed-rank test, n = 17 sessions). We did not find a significant difference between BFCN calcium responses to surprising vs. expected punishments (Figure 2G, $p = 0.0684$, Wilcoxon signed-rank test, n = 17 sessions).

Optogenetic identification of basal forebrain cholinergic neurons during probabilistic Pavlovian conditioning

Does the spiking of individual BFCNs show similar differential responses to conditioned and unconditioned stimuli according to different outcome expectations? We estimated that a sample of 14–20 identified BFCNs is sufficient to answer such a question with 80% statistical power (assuming a 30%–40% firing rate change corresponding to 0.3–0.4 predicted effect size, detectable in 60% of recorded neurons; the full procedure is available at https://github.com/hangyabalazs/statistical-power; Figure 3A). We expressed channelrhodopsin in BFCNs by injecting AAV.2.5.EF1a.DiO.hChR2(H134R).eYFP.WPRE.hGh in the basal forebrain of ChAT-Cre mice (n = 4) and implanted them with eight moveable tetrode electrodes and an optic fiber (Figures 3B and 3C), to optogenetically tag BFCNs in mice performing the probabilistic Pavlovian task.[10,11] We recorded 25 optogenetically identified, ChAT-expressing BFCNs ($p < 0.01$, stimulus-associated spike latency test[33]) in task-performing mice (Figures 3D–3G, S2, and S3). Cholinergic neurons were recorded at a stage when the animals reached stable behavioral performance. Careful post-hoc histological reconstruction of the location of the recording electrodes showed that 21 of 25 neurons were recorded from HDB, whereas the remaining 4 of 25 neurons were in the medial septum (n = 2) and the

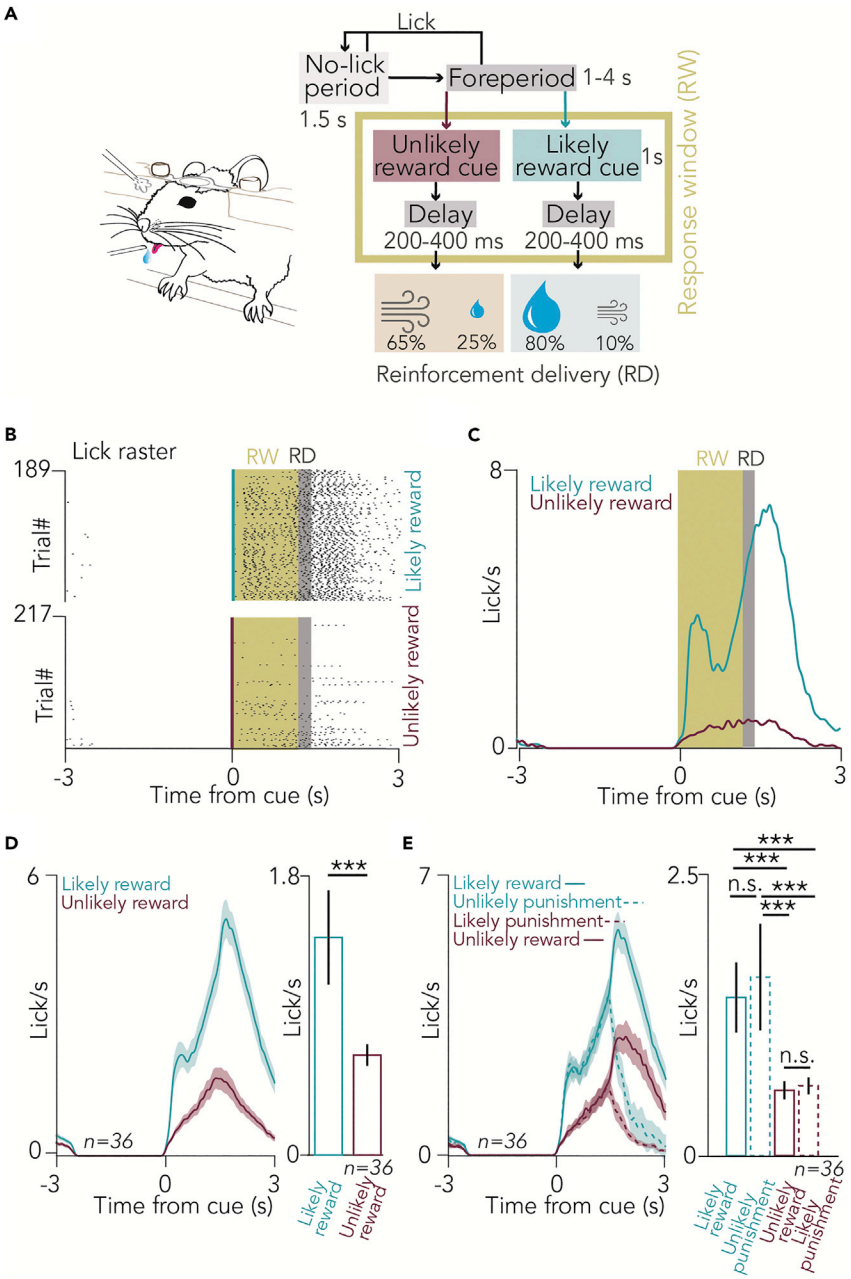

Figure 1. Mice were trained on a probabilistic Pavlovian conditioning task

(A) Schematic illustration of the behavioral training and block diagram of the task. A variable foreperiod, in which the mouse was not allowed to lick, was followed by the presentation of one of two pure tones of well-separated pitch, which predicted reward, punishment, or nothing with different contingencies ("likely reward" and "unlikely reward" cues).

(B) Raster plot of lick responses to the cues predicting likely reward (top) and unlikely reward (bottom) from an example session. Yellow shading, response window (RW); gray shading, reinforcement delivery (RD).

(C) Peri-event time histograms (PETHs) of lick responses aligned to cue onset in the same session.

(D) (Left) Average PETHs of lick responses of all sessions of all animals (n = 36 sessions). (Right) Statistical comparison of anticipatory lick rates in the RW in likely reward and unlikely reward trials (median ± SE of median, n = 36 sessions, $p = 8.7697 \times 10^{-7}$, Wilcoxon signed-rank test; ***$p < 0.001$).

(E) (Left) Average PETHs of lick responses of all sessions of all animals (n = 36 sessions), partitioned based on four possible outcomes: expected or surprising reward, expected or surprising punishment. (Right) Statistical comparison of anticipatory lick rates in the RW for the four possible outcomes (median ±SE of median, n = 36 sessions, from top to bottom, $p = 1.4131 \times 10^{-6}$, $p = 2.6341 \times 10^{-6}$, $p = 0.8628$, $p = 6.8863 \times 10^{-7}$, $p = 1.2065 \times 10^{-6}$, $p = 0.9687$, Wilcoxon signed-rank test; ***$p < 0.001$; n.s., $p > 0.05$).

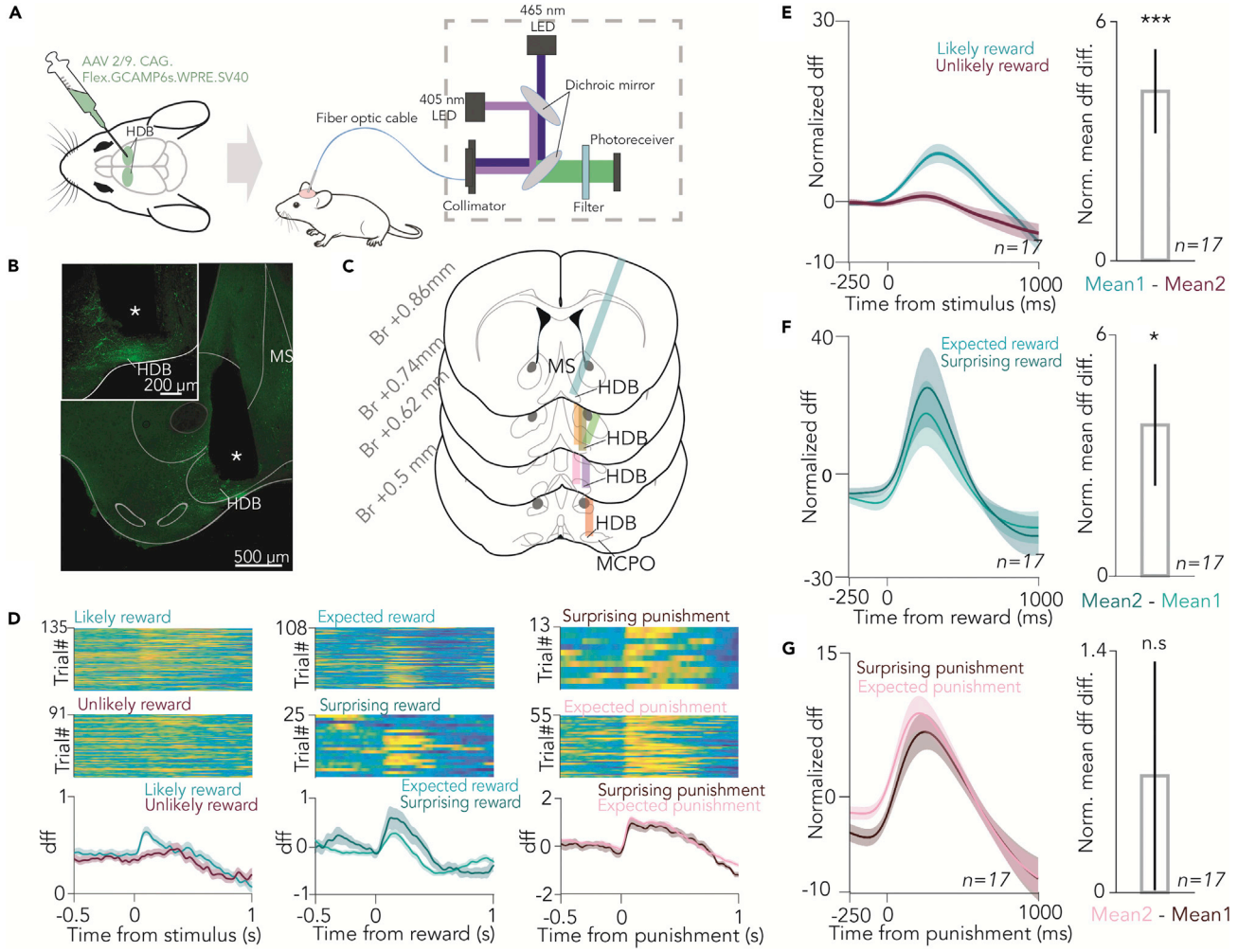

Figure 2. BFCN population responses to conditioned and unconditioned stimuli

(A) Schematic diagram of bulk calcium imaging of HDB BFCNs in behaving mice.

(B) Histological reconstruction of the optic fiber track in the HDB (white asterisk). Scale bar, 500 μm. Inset shows magnified view. Scale bar, 200 μm.

(C) Optical fiber locations in all imaged mice (n = 7). Br, anteroposterior distance from Bregma.

(D) Example session of bulk calcium imaging of cholinergic neurons from the HDB. (Left) dff signals were aligned to outcome-predicting conditioned stimuli. (Top) Trials with likely reward (unlikely punishment) cue; (middle) trials with unlikely reward (likely punishment) cue; (bottom) PETH. (Middle) dff signals were aligned to reward delivery. (Top) Trials with expected reward; (middle) trials with surprising reward; (bottom) PETH. (Right) dff signals were aligned to air puff punishments. (Top) Trials with surprising punishment. (Middle) Trials with expected punishment. (Bottom) PETH.

(E) (Left) Average PETH of Z-scored dff aligned to outcome-predicting conditioned stimuli (n = 17 sessions). (Right) Bar graph of average normalized difference in dff after likely reward and unlikely reward cues. Median ±SE of median, ***$p < 0.001$, $p = 0.00029$, Wilcoxon signed-rank test.

(F) (Left) Average PETH of Z-scored dff aligned to expected and surprising reward (n = 17 sessions). (Right) Bar graph of average normalized difference in dff after surprising and expected reward. Median ±SE of median, *$p < 0.05$, $p = 0.0129$, Wilcoxon signed-rank test.

(G) (Left) Average PETH of Z-scored dff aligned to expected and surprising punishment (n = 17 sessions). (Right) Bar graph of average normalized difference in dff after expected and surprising punishment. Median ±SE of median, n.s., $p > 0.05$, $p = 0.0684$, Wilcoxon signed-rank test. See also Figure S1.

ventral pallidum (n = 2; Figure 3D). Since these neurons exhibited similar responses to conditioned and unconditioned stimuli, they were treated as a single data set for this study; nevertheless, restricting data analyses to the HDB cholinergic neurons yielded similar results.

Large cholinergic responses to reward-predicting cues, surprising rewards, and air puff punishments

We first asked whether individual BFCNs show spiking responses to auditory cue stimuli that predict outcomes with different probabilities. To address this, we aligned BFCN spikes to cue onset and examined raster plots and

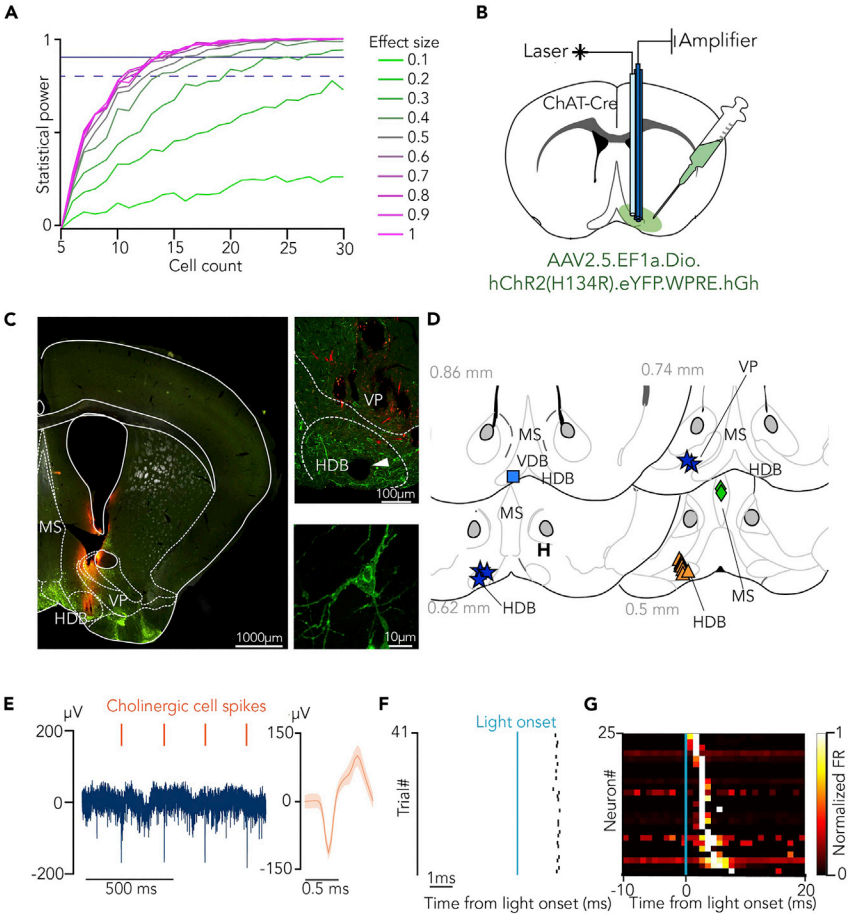

Figure 3. Optogenetic identification of basal forebrain cholinergic neurons during probabilistic Pavlovian conditioning

(A) Statistical power as a function of cell count at different expected effect sizes. Dashed line, 80% power; solid line, 90% power.

(B) Schematic drawing of optogenetic tagging. ChAT-Cre mice were injected with AAV2/5. EF1a.Dio.hChR2(H134R)-eYFP.WPRE.hGH. Eight moveable tetrodes were implanted in the HDB along with an optic fiber.

(C) (Left) Coronal section from a ChAT-Cre mouse showing the distribution of cholinergic neurons (eYFP, green) and the tetrode track (DiI, red). Scale bar, 1000 µm. (Top right) Magnified view of the HDB. The white arrowhead points to the electrolytic lesion marking the tetrode tips. Scale bar, 100 µm. (Bottom right) Confocal image of a cholinergic neuron from the target area. Scale bar, 10 µm.

(D) Reconstructed localization of all identified cholinergic neurons. Different markers correspond to individual mice. Numbers correspond to antero-posterior distance from Bregma, in mm.

(E) (Left) Raw extracellular recording of an identified cholinergic neuron. (Right) Average waveform of the example cholinergic neuron. Orange marks above the recording indicate the cholinergic spikes.

(F) Raster plot of an example cholinergic neuron showing short latency responses to 1-ms blue laser pulses.

(G) Color-coded PETH of all identified cholinergic neurons aligned to laser pulse onset, sorted by response latency (black, no spikes; white, high firing rate). See also Figures S2 and S3.

peri-event time histograms (PETHs) of individual BFCNs (see Figure S4 for a schematic representation of the analysis). We found that BFCNs responded to both auditory cues, with a median peak latency of 133.5 ms for the "likely reward" cue and 422 ms for the "unlikely reward" cue (Figures 4A, 4B, and S5A; interquartile range, 44.5–231 ms and 273–573.5 ms for the two cue types). To cover both peaks, we chose a 500-ms response window (C500), in which we compared BFCN responses to conditioned cue stimuli based on whether they signaled high or low probability of future reward. BFCNs showed 151% stronger responses to the "likely reward" cues based on a comparison of PETH peak responses in the C500 window ($p = 0.0008$, Wilcoxon signed-rank test; Figure 4C; including $n = 14$ neurons where mice encountered >10 surprising reward trials; see Figure S6 for all $n = 25$ neurons), which we also confirmed by spike-number-based statistics ($p = 0.00061$, Wilcoxon signed-rank test on

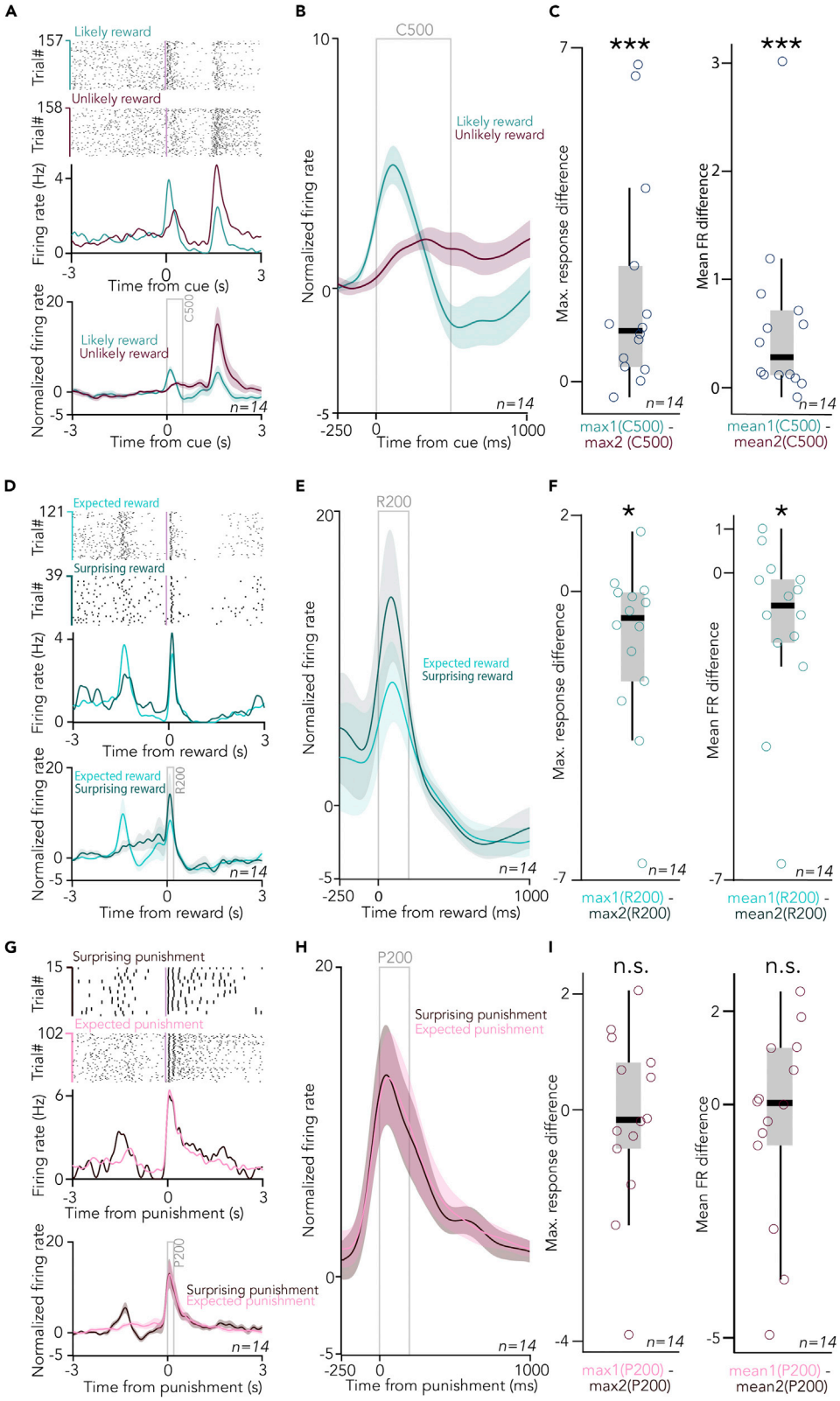
A
Likely reward
Unlikely reward
Trial#
Firing rate (Hz)
Time from cue (s)
Normalized firing rate
C500
n=14
B
C500
Likely reward
Unlikely reward
Normalized firing rate
Time from cue (ms)
n=14
C
***
Max. response difference
Mean FR difference
max1(C500) - max2 (C500)
mean1(C500) - mean2(C500)
D
Expected reward
Surprising reward
Time from reward (s)
E
R200
Time from reward (ms)
F
*
max1(R200) - max2(R200)
mean1(R200) - mean2(R200)
G
Surprising punishment
Expected punishment
Time from punishment (s)
H
P200
Time from punishment (ms)
I
n.s.
max1(P200) - max2(P200)
mean1(P200) - mean2(P200)

Figure 4. Cholinergic neurons respond more to reward-predicting cues and surprising reward

(A) Top, raster plots (top) and PETHs (bottom) of an example BFCN aligned to cue onset, separately for the cues predicting likely reward/unlikely punishment (turquoise) vs. unlikely reward/likely punishment (purple). (Bottom) Average cue-aligned PETHs of identified BFCNs with >10 surprising reward trials (errorshade, mean ± SE; n = 14; see Figure S6 for all n = 25 neurons).

(B) Average cue-aligned PETHs of identified BFCNs enlarged around cue presentations.

(C) (Left) Difference in peak response after cues predicting likely reward and those predicting unlikely reward. ***p < 0.001, p = 0.0008, Wilcoxon signed-rank test, n = 14. (Right) Difference in mean firing rate after cues predicting likely reward and those predicting unlikely reward. ***p < 0.001, p = 0.00061, Wilcoxon signed-rank test, n = 14. Box-whisker plots show median, inter-quartile range, and non-outlier range.

(D) (Top) Raster plots (top) and PETHs (bottom) of the same example BFCN as in (A), aligned to reward delivery, separately for rewards after the cue predicting likely reward (light turquoise, expected reward) vs. after the cue predicting unlikely reward (dark turquoise, surprising reward). (Bottom) Average reward-aligned PETHs of identified BFCNs with >10 surprising reward trials (errorshade, mean ± SE; n = 14; see Figure S6 for all n = 25 neurons).

(E) Average reward-aligned PETHs of identified BFCNs enlarged around reward delivery times.

(F) (Left) Difference in peak response after expected and surprising rewards. *p < 0.05, p = 0.0245, Wilcoxon signed-rank test, n = 14. (Right) Difference in mean firing rate after expected and surprising rewards. *p < 0.05, p = 0.02026, Wilcoxon signed-rank test, n = 14. Box-whisker plots show median, inter-quartile range, and non-outlier range.

(G) (Top) Raster plots (top) and PETHs (bottom) of the same example BFCNs as in (A) and (D), aligned to punishment delivery, separately for punishments after the cue predicting likely reward (dark purple, surprising punishment) vs. after the cue predicting unlikely reward (light purple, expected punishment). (Right) Average punishment-aligned PETHs of identified BFCNs enlarged around punishment delivery times.

(H) Average punishment-aligned PETHs of identified BFCNs with >10 surprising reward trials (errorshade, mean ± SE; n = 14; see Figure S6 for all n = 25 neurons).

(I) (Left) Difference in peak response after expected and surprising punishments. n.s., p > 0.05, p = 0.7869, Wilcoxon signed-rank test, n = 14. (Right) Difference in mean firing rate after expected and surprising punishments. n.s., p > 0.05, p = 0.8393, Wilcoxon signed-rank test, n = 14. Box-whisker plots show median, inter-quartile range, and non-outlier range. See also Figures S4–S7.

BFCN firing rates in the C500 window; Figure 4C). Thus, BFCNs responded more to sensory stimuli that signaled high probability of reward.

Next, we tested whether individual BFCNs responded to the delivery of reward during Pavlovian conditioning, and whether this response depended on previous expectations about reward likelihoods conveyed by the two auditory cues. Therefore, we aligned the spike times of the same BFCNs to the time of reward delivery, again examining raster plots and PETHs (Figures 4D and 4E). We found that reward also elicited large BFCN responses, with a median peak latency of 86.5 and 82.7 ms for expected and surprising rewards, respectively (Figure S5B; interquartile range, 78.13–100.25 ms and 54.5–92.5 ms for expected and surprising rewards). To compare BFCN responses to expected vs. surprising rewards, we defined a 200-ms response window after reward delivery based on the above latency measurements (R200). We found that rewards that were less expected lead to significantly stronger cholinergic firing (69.3%, p = 0.0245, Wilcoxon signed-rank test on R200 response peaks; Figure 4F), also confirmed by firing rate comparison (p = 0.02026, Wilcoxon signed-rank test on BFCN firing rates in the R200 window; Figure 4F). These findings showed that BFCN responses were modulated by the expectation of reward.

We took a similar approach to investigate BFCN responses to the delivery of air puff punishments. BFCNs also responded with firing rate increase to punishment, with remarkably short peak latencies (Figures 4G, 4H, and S6C; median and interquartile range, 24.5 ms and 15.5–36 ms for surprising punishment and 24 ms and 15.5–32 ms for expected punishment), confirming previous results.[8,10,34] When responses to surprising and expected punishments were directly compared in a 200-ms response window (P200), we did not find significant modulation by expectation (p = 0.7869, Wilcoxon signed-rank test on peak responses; Figure 4I; p = 0.8393, Wilcoxon signed-rank test on firing rates). We did not detect significant firing rate changes in either direction after omissions (Figure S7).

Cholinergic responses are explained by a reinforcement learning model of stimulus-driven, valence-weighed, unsigned prediction error

The above-demonstrated differential BFCN responses to conditioned and unconditioned stimuli that reflected outcome expectations were suggestive of prediction error coding.[35] Based on the positive-going BFCN responses following both reward and punishment, we assumed that BFCNs might represent an unsigned prediction error. If an outcome prediction error scaled positive and negative values equally, then it

would track the expectation of reinforcement irrespective of valence. Thus, it would predict identical responses to conditioned cue stimuli that foreshadow reinforcement with a fixed probability, only sensitive to the rate of reinforcement omissions. However, cholinergic neurons showed stronger responses after cues predicting likely reward compared with those predicting unlikely reward but likely punishment. Therefore, our results suggest that BFCNs assign different weights to expected positive and negative outcomes, potentially related to the difference in absolute subjective values of the reinforcers. We did not observe BFCN responses to reinforcement omissions, suggesting that BFCN responses are driven by sensory stimuli, and thus a stimulus-driven, valence-weighed, unsigned prediction error model could explain BFCN spiking dynamics.

To test this, we implemented and fitted a simple three-parameter reinforcement learning (RL) model[35,36] on cholinergic responses:

$$C = S \cdot |R - \eta_1 E(R) + P - \eta_2 E(P)|$$

where C represented cholinergic response, S was a scaling parameter accounting for different mean firing rates of BFCNs, R and P were actual, while $E(R)$ and $E(P)$ were expected reward and punishment determined by task contingencies. To take the assumed difference in the relative sensitivity to water reward and air-puff punishment into account, we introduced two weight parameters, η_1 and η_2 ($0 \leq \eta_1, \eta_2 \leq 1$), which could control how much BFCN responses were influenced by the expectation of positive and negative outcomes, respectively. Taking the absolute value of the sum of reward and punishment prediction error terms ensured positive-going cholinergic responses irrespective of valence, thus resulting in a simple model of unsigned reward prediction error. We found that this model fitted BFCN firing rate changes in response to the different cues and reinforcers defined by the C500, R200, and P200 response windows well (Figures 5A–5C), and significantly better than a control model in which the modeled expectations did not match the task contingencies ($p = 0.0014$ for all $n = 25$ BFCNs recorded; $p = 0.0037$ when only HDB cholinergic neurons were tested; Wilcoxon signed-rank test on the maximum likelihoods of the models; see STAR Methods).

We next simulated spike trains of individual BFCNs based on the best-fit RL models. Baseline firing was modeled by a Poisson process with a frequency matched to the baseline firing rate of the modeled BFCN, and simulated firing responses were added according to Gaussian distributions with a fixed delay after cue and reinforcement events, where the number of added spikes was determined by the best-fit RL model for each BFCN. When applying the same analyses on simulated spike trains as for the real data, we found that simulated PETHs qualitatively reproduced BFCN responses to cues and rewards (Figure 5D). These results further strengthen that the BFCN responses we observed are consistent with the representation of a stimulus-induced, valence-weighed, unsigned prediction error.

The best-fit η_1 values were significantly larger than the best-fit η_2 values, demonstrating stronger sensitivity of BFCN responses to reward than to punishment expectations ($p = 0.0001$, Wilcoxon signed-rank test; median $\pm$SE of median, η_1, 0.61 ± 0.04, η_2, 0.37 ± 0.05). At the same time, the best-fit η_2 values were significantly above 0.2, suggesting that mice learned to predict negative outcomes as well, reflected in their cholinergic responses according to the model ($p = 0.0058$, Wilcoxon signed-rank test). These parameters might reflect potential differences in the internal valuation of water reward and air puff punishment across animals and recording days, and also different sensitivity to reward expectation of individual BFCNs. We hypothesized that they reflect behavioral variability rather than heterogeneity across neurons, which would imply that these parameters show consistency within recording sessions and within individual mice. Indeed, we found smaller within- than across-mice differences in best-fit η_1 parameters ($p = 0.002$, Mann-Whitney U test), and smaller within- than across-session differences in best-fit η_2 parameters ($p = 0.047$, Mann-Whitney U test; $n = 25$; Figure S8). This suggests that best-fit scaling parameters for outcome expectations reflect inter-individual and/or behavioral differences, rather than differential sensitivity of individual BFCNs.

The perceived reward and punishment prediction errors are controlled by η_1 and η_2 in our model; therefore, they together determine the size of the unsigned outcome prediction error represented by BFCNs. If this can drive approach behaviors as previous studies suggested,[21,37–39] then we would expect that the animals' anticipatory licking behavior correlates with these model parameters. Indeed, we found that η_1 as well as the sum of the two parameters ($\eta_1 + \eta_2$), characterizing the cholinergic neurons' sensitivity to momentary outcome prediction, correlates well with behavioral cue differentiation as indexed by anticipatory lick rate difference ($p = 0.012$, $R = 0.52$ and $p = 0.056$, $R = 0.33$ for η_1 and η_2, respectively; $p = 0.007$,

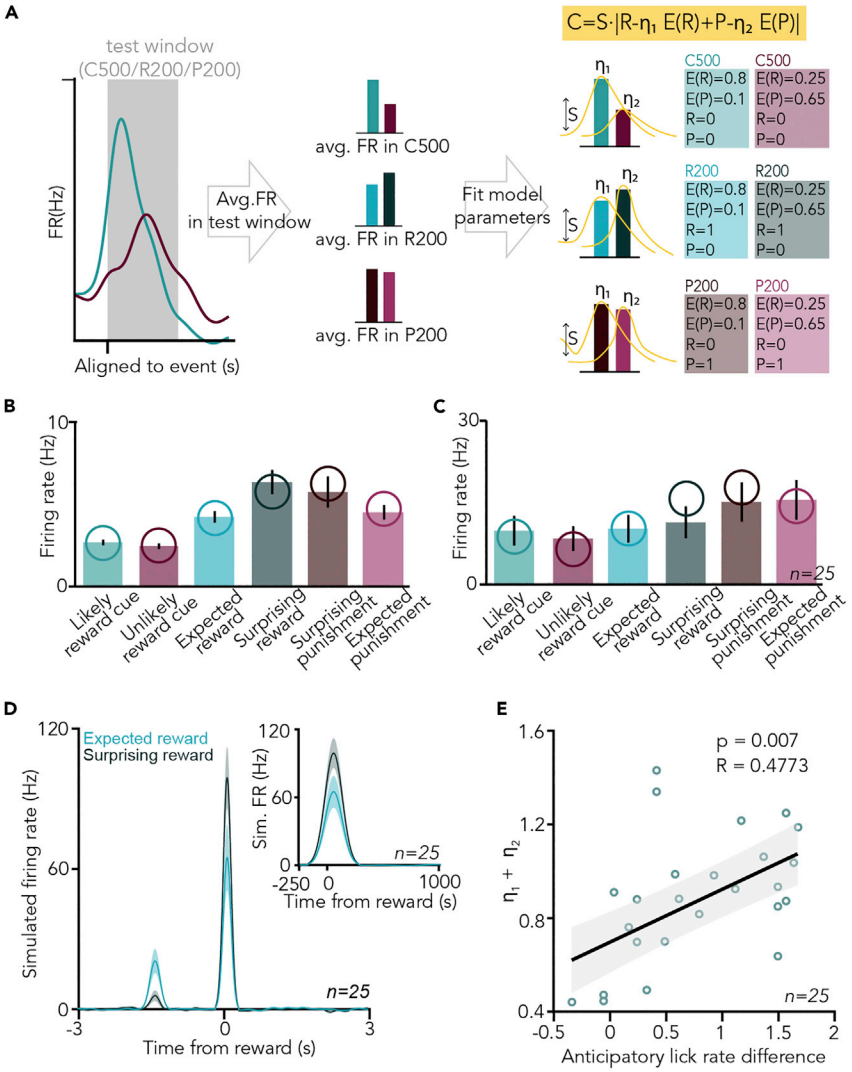

Figure 5. Cholinergic responses are explained by a reinforcement learning model of stimulus-driven, valence-weighed, unsigned prediction error

(A) Schematic illustration of reinforcement learning model fitting on cholinergic neuronal data. Average firing rate (FR) values were fit by a three-parameter RL model incorporating task contingencies.

(B) Firing rates of an example BFCN in 500-ms response windows after cue presentations and 200-ms response windows after reward or punishment, separated by trial type. Bar graphs represent mean ± SE over trials. Hypothetical firing rates corresponding to a best-fit RL model are overlaid, indicated by open circles.

(C) Average firing rates of all identified BFCNs (n = 25) in the same response windows. Bar graphs represent mean ± SE over neurons. Average modeled firing rates are indicated by open circles.

(D) Spike responses were simulated based on the best-fit RL models for each BFCN (see STAR Methods). PETHs were calculated the same way as for the real data and averaged over the modeled responses (n = 25).

(E) The sum of the two model parameters that controls the differential sensitivity to reward and punishment expectations ($\eta_1 + \eta_2$) was correlated with the difference in anticipatory lick rate after likely reward vs. unlikely reward-predicting cues (R = 0.4773, Pearson's correlation coefficient; p = 0.007, linear regression, F-test). See also Figure S8.

R = 0.48 for $\eta_1 + \eta_2$; n = 25; Figures 5E and S8; p = 0.0013 and R = 0.78 when calculated for the n = 14 neurons with >10 surprising reward trials; Pearson's correlation coefficient, linear regression and one-sided F-test).

Cholinergic responses predict reaction time

The correlation of model parameters quantifying the animals' sensitivity to outcome expectations with behavioral performance prompted us to further assess whether BFCN responses could predict animal

behavior. BFCN responses to outcome-predicting cues consistently preceded the animals' first licks (Figures 6A and 6B). When we aligned cholinergic spikes to the last lick before the foreperiod during which mice were not allowed to lick, cholinergic activity peaked before licking with a similar time course as during cue-related licking activity (Figure S9). These findings excluded that a potential "lick-driven" cholinergic activity could confound the results and instead indicated that cholinergic activity had the potential to influence behavioral responses of mice performing the task. Indeed, we found that larger cholinergic cue responses were followed by faster reactions ($p = 0.00073$ and $p = 0.05108$ for "likely reward" and "unlikely reward" cues, respectively; Wilcoxon signed-rank test; Figure 6C). In accordance, cholinergic cue responses were larger when mice were licking after the cue ($p = 0.048$ and $p = 0.023$ for "likely reward" and "unlikely reward" cues, respectively; Wilcoxon signed-rank test; Figure 6D). Since lick responses can be taken as an indication of mice expecting reward, these results are consistent with cholinergic reward expectation coding. Next, we divided the trials into four quartiles according to mice's reaction times after cue onset. In line with the above results, we found that faster lick responses were preceded by stronger cholinergic firing (Figure 6E, $p = 0.0314$, one-way ANOVA). This was also reflected in a significant negative trial-by-trial correlation of BFCNs' firing rate after the reward-predicting cue and animal reaction time ($R = -0.45$, $p = 0.034$; Pearson's correlation coefficient, linear regression and one-sided F-test). In sum, these results indicate that cue responses of BFCNs predict reaction times, suggesting that cholinergic outcome prediction coding affects behavioral responses.

DISCUSSION

Cholinergic neurons of the basal forebrain respond to behaviorally salient events.[8–11,22,34,40,41] To better understand the nature of these responses, we investigated whether activity patterns elicited by outcome-predictive stimuli and behavioral feedback are consistent with a prediction error hypothesis. By investigating the responses of BFCN populations using bulk calcium imaging and of individual BFCNs by optogenetic tagging in a probabilistic Pavlovian cued outcome task, we found that BFCNs showed strong activation after reward-predicting stimuli, and larger responses to surprising than to expected rewards. These results were consistent with a simple RL model of a stimulus-driven, valence-weighed, unsigned reward prediction error. The model also demonstrated that while BFCNs responded with firing rate increase to events of both positive and negative valence, they also reflected different behavioral sensitivity to positive and negative expectations. Finally, BFCN responses were found to likely influence behavioral performance, as mice showed faster responses after stronger cholinergic activation.

Temporal difference reinforcement learning (TDRL) models were successful in explaining the reward prediction errors represented by the dopaminergic system.[35,36,42] The presence of a reward response modulated by expectation and responsiveness to reward-predicting sensory stimuli suggested that cholinergic signals may also be related to prediction errors; however, consistently positive-going responses for punishment indicated that this prediction error signal may be unsigned. A model that puts the same positive weight on both aversive and appetitive outcomes tracks the expectation of a reinforcement irrespective of its valence; therefore, it would predict identical responses for reward- and punishment-predicting cues if omission rate is constant. However, BFCNs clearly preferred reward-predicting stimuli, suggesting differential representation of rewards and punishments. Therefore, we implemented an RL model and fitted parameters capturing differential weighing based on valence. We found that this model reliably predicted average BFCN responses to cues, rewards, and punishments. It also reproduced larger BFCN responses to cues that foreshadowed rewards with high probability, as well as to surprising, when compared with expected rewards. The best-fit model indicated non-zero weights for both reward and punishment expectation, suggesting the behavioral anticipation of both types of outcomes, but with a significantly larger weight on the expectation of reward, suggesting that the outcome prediction error cholinergic neurons represented was indeed unequally weighed.

What may be the function of this fast prediction error signal? The cholinergic system has long been known to strongly influence cortical plasticity.[3,43–47] A line of studies has demonstrated that pairing auditory stimuli with cholinergic stimulation reorganizes cortical sensory representations, known by the term "receptive field plasticity."[23,24] Furthermore, recent studies showed that cholinergic inputs may even endow primary sensory cortices with non-sensory representations not expected previously.[48,49] In particular, Liu et al. showed that optogenetic activation of cholinergic fibers in the visual cortex entrained neural responses that mimicked behaviorally conditioned reward timing activity.[50] It was also demonstrated that the cholinergic system exerts a rapid, fine-balanced control over plasticity at millisecond timescales, stressing the importance of timing

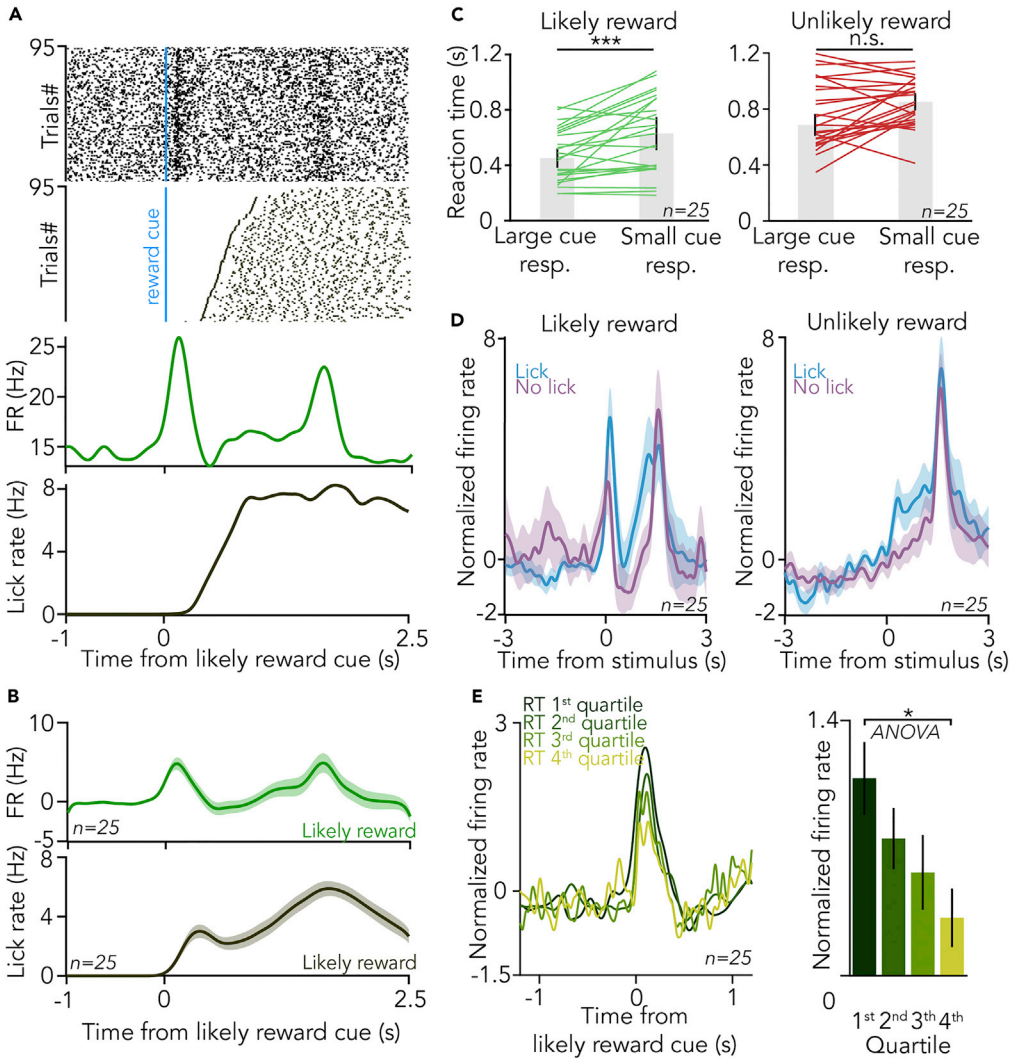

Figure 6. Cholinergic responses predict reaction time

(A) (Top) Spike raster of cholinergic firing (top) and lick responses of the animal (bottom) aligned to the likely reward cues from an example session. (Bottom) Corresponding PETH of the cholinergic response (top) and licking activity (bottom).

(B) Average PETH of cholinergic firing (top) and lick response (bottom) after the reward-predicting cue (n = 25 BFCNs).

(C) Reaction time after large and small cue responses to the likely reward (left) and unlikely reward cue (right). Cue responses were divided by a median split. ***$p < 0.001$, $p = 0.00073$ and n.s., $p > 0.05$, $p = 0.05108$, Wilcoxon signed-rank test, n = 25. Bar graphs represent median ±SE of median.

(D) Average PETH of cholinergic responses to the likely reward and unlikely reward cue, separated based on the presence or absence of anticipatory lick response of the animal.

(E) Stronger cholinergic response to the reward-predicting cue predicted faster reaction time. (Left) Average PETH of responses to the likely reward cue, partitioned to reaction time quartiles (1st quartile corresponds to shortest reaction time, in dark green). (Right) Bar graphs (mean ± SE) of the peak responses to the likely reward cue as a function of reaction time quartiles. *$p < 0.05$, $p = 0.0314$, one-way ANOVA. See also Figure S9.

even for neuromodulatory systems.[51–53] This effect on plasticity might have a fundamental impact on associative learning at the behavioral level,[54] also suggested by recent advances in the fear learning field.[11,22,55,56]

Indeed, we found that the best-fit model parameters were correlated with the difference in the animals' anticipatory lick rate indicating learning performance. Moreover, cholinergic responses to reward-predicting cues predicted behavioral responses and reaction time, fitting in a more general scheme of basal forebrain control over response speed to motivationally salient stimuli.[21,37,45] Therefore, we propose that a

rapid acetylcholine-mediated cortical activation, scaled by unsigned outcome prediction error, tunes synaptic plasticity in the service of behavioral learning. This idea is supported by strong theories that associated prediction errors and cholinergic activity with learning and memory.[57–59] Nevertheless, the functions of cholinergic effects probably go beyond learning, and BFCNs may control many aspects of behavior including arousal or alertness,[21,31,40,45,60–64] attention,[3,54,65–67] and vigilance.[68–70]

The activity of cholinergic neurons shares strong similarities with dopaminergic neurons in response to reward and reward-predicting cues.[35,71–73] Reward-predicting cues evoke an increase in firing rate, which is stronger for more likely rewards. Reward itself also elicits cholinergic firing, but less so if the reward is more expected. However, cholinergic neurons differ from dopaminergic neurons in their response to punishment. Dopaminergic neurons can respond to aversive stimuli with either increased or decreased firing,[74–76] whereas cholinergic neurons consistently respond with a fast, precisely timed response to air puffs. Therefore, the positive-going response of BFCNs irrespective of valence, sensitive to outcome probabilities for cues and rewards, suggests that compared with the reward prediction error signal dopaminergic neurons encode, BFCNs represent an unsigned outcome prediction error. Importantly, bursting basal forebrain neurons with similar coding properties have been uncovered in primates,[39] suggesting that at least part of those neurons might be cholinergic.

Cholinergic neurons appeared to respond faster than dopaminergic neurons; however, response timing may depend on seemingly subtle details of the behavioral paradigm. Altogether, BFCNs appear to provide a faster but less specific response to salient stimuli, which is likely broadcasted to large cortical areas innervated by cholinergic fibers.[77,78] In contrast, calculations related to value that are represented in the dopaminergic system may require more processing time and result in somewhat delayed, albeit more specific representations. Nevertheless, direct comparisons of cholinergic and dopaminergic neurons in the same experiment will be necessary to reveal the differential functions of these major neuromodulatory systems.

Limitations of the study

A valence-weighed unsigned prediction error hypothesis predicts stronger response to unexpected than to expected punishment; the larger the weight of the punishment, the stronger the difference. We did not find a significant difference, which could be due to the lower weight of punishment that decreased statistical power, or a theoretical deviation from a full-fledged outcome prediction error.

Additionally, an unsigned prediction error signal predicts a firing rate increase after omitted reward. Note that unsigned prediction error variables only take non-negative values, and thus all unexpected changes in state value result in increased values due to the absolute value operator; however, different models that predict a firing rate decrease after omission are also conceivable. We tested an alternative model that included omission-related activity (see STAR Methods), but we found that this model was statistically indistinguishable from our original model based on our data set, suggesting that larger amounts of data are required to resolve this question. Also, given the phasic nature of cholinergic reinforcement responses comprising often very few (sometimes only one) but precisely timed action potentials,[10] it is expected that an omission response, where there is no sensory stimulus to align to, is very hard to detect in single neurons. Indeed, a recent study demonstrated positive-going omission responses in HDB cholinergic neurons using fiber photometry.[41] Alternatively, the cholinergic system may be sensitive to external sensory stimuli but not to absence of an expected stimulus, in line with its strong bottom-up anatomical inputs conveying sensory signals,[79] likely gated via local inhibitory neurons that may relay expectation information.[80] A recent study demonstrated topographic variations in cholinergic responses to salient events,[41] which could also contribute to these ambiguities.

STAR★METHODS

Detailed methods are provided in the online version of this paper and include the following:

- KEY RESOURCES TABLE
- RESOURCE AVAILABILITY
  - Lead contact
  - Materials availability
  - Data and code availability
- EXPERIMENTAL MODEL AND SUBJECT DETAILS

SUPPLEMENTAL INFORMATION

Supplemental information can be found online at https://doi.org/10.1016/j.isci.2022.105814.

ACKNOWLEDGMENTS

We thank Katalin Lengyel for technical assistance in anatomical methods, Annal Velencei and Victoria Lyakhova for assistance in behavioral training, the FENS-Kavli Network of Excellence for fruitful discussions and Dr. Janos Szabadics for helpful comments on the manuscript. This work was supported by the "Lendület" Program (LP2015-2/2015), NAP3.0 and NKM 2019-25 of the Hungarian Academy of Sciences; the European Union project RRF-2.3.1-21-2022-00004 within the framework of the Artificial Intelligence National Laboratory; NKFIH KH125294, NKFIH K135561, SPIRITS 2020 of Kyoto University, and the European Research Council Starting Grant no. 715043 to B.H.; the ÚNKP-21-3 New National Excellence Program of the Ministry for Innovation and Technology to P.H.; ÚNKP-19-3, ÚNKP-20-3, and ÚNKP 21-3 New National Excellence Program of the Ministry for Innovation and Technology from the source of the National Research, Development and Innovation Fund to B.K.; and the Generalitat Valenciana Postdoctoral Fellowship Program (APOSTD/2019/003) to S.M.-B. We acknowledge the help of the Nikon Center of Excellence at the Institute of Experimental Medicine (IEM), Nikon Europe, Nikon Austria, and Auro-Science Consulting for kindly providing microscopy support and the supportive help of the Central Virus Laboratory of IEM. We thank Mackenzie Mathis for open access science art at SciDraw (accessible at https://doi.org/10.5281/zenodo.3925907).

AUTHOR CONTRIBUTIONS

P.H. and B.H. conceived the study; P.H. and K.S. performed the recording experiments; P.H. and S.M.-B. conducted the fiber photometry experiments; P.H., B.H., and B.K. analyzed the data; P.H. prepared the figures, B.H. and P.H. wrote the manuscript with inputs from all authors.

DECLARATION OF INTERESTS

The authors declare no competing interests.

INCLUSION AND DIVERSITY

We support inclusive, diverse, and equitable conduct of research.

Received: September 30, 2021
Revised: October 22, 2022
Accepted: December 12, 2022
Published: January 20, 2023

REFERENCES

1. Mesulam, M.M., and Bigl, V. (1986). Alzheimer plaques and cortical cholinergic innervation. Neuroscience *17*, 275–276. https://doi.org/10.1016/0306-4522(86)90242-3.

2. Whitehouse, P.J., Price, D.L., Struble, R.G., Clark, A.W., Coyle, J.T., and Delon, M.R. (1982). Alzheimer's disease and senile dementia: loss of neurons in the basal forebrain. Science *215*, 1237–1239. https://doi.org/10.1126/science.7058341.

3. Hasselmo, M.E., and Sarter, M. (2011). Modes and models of forebrain cholinergic neuromodulation of cognition. Neuropsychopharmacology *36*, 52–73. https://doi.org/10.1038/npp.2010.104.

4. Everitt, B.J., and Robbins, T.W. (1997). Central cholinergic systems and cognition. Annu. Rev. Psychol. *48*, 649–684. https://doi.org/10.1146/annurev.psych.48.1.649.

5. Wrenn, C.C., and Wiley, R.G. (1998). The behavioral functions of the cholinergic basalforebrain : lessons from 192 IgG-SAPORIN. Int. J. Dev. Neurosci. *16*, 595–602. https://doi.org/10.1016/S0736-5748(98)00071-9.

6. Sviatkó, K., and Hangya, B. (2017). Monitoring the right collection: the central cholinergic neurons as an instructive example. Front. Neural Circ. *11*, 31. https://doi.org/10.3389/fncir.2017.00031.

7. Solari, N., Sviatkó, K., Laszlovszky, T., Hegedüs, P., and Hangya, B. (2018). Open source tools for temporally controlled rodent behavior suitable for electrophysiology and optogenetic manipulations. Front. Syst. Neurosci. *12*, 18. https://doi.org/10.3389/fnsys.2018.00018.

8. Lovett-Barron, M., Kaifosh, P., Kheirbek, M. a, Danielson, N., Zaremba, J.D., Reardon, T.R., Turi, G.F., Hen, R., Zemelman, B.V., and Losonczy, A. (2014). Dendritic inhibition in the hippocampus supports fear learning. Science *343*, 857–863. https://doi.org/10.1126/science.1247485.

9. Harrison, T.C., Pinto, L., Brock, J.R., and Dan, Y. (2016). Calcium imaging of basal forebrain activity during innate and learned behaviors. Front. Neural Circ. *10*, 36. https://doi.org/10.3389/fncir.2016.00036.

10. Hangya, B., Ranade, S.P., Lorenc, M., and Kepecs, A. (2015). Central cholinergic neurons are rapidly recruited by reinforcement feedback. Cell *162*, 1155–1168. https://doi.org/10.1016/j.cell.2015.07.057.

11. Guo, W., Robert, B., and Polley, D.B. (2019). The cholinergic basal forebrain links auditory stimuli with delayed reinforcement to support learning. Neuron *103*, 1164–1177.e6. https://doi.org/10.1016/j.neuron.2019.06.024.

12. Dalley, J.W., Theobald, D.E., Bouger, P., Chudasama, Y., Cardinal, R.N., and Robbins, T.W. (2004). Cortical cholinergic function and deficits in visual attentional performance in rats following 192 IgG-saporin-induced lesions of the medial prefrontal cortex. Cerebr. Cortex *14*, 922–932. https://doi.org/10.1093/cercor/bhh052.

13. Berger-Sweeney, J., Heckers, S., Mesulam, M.M., Wiley, R.G., Lappi, D.A., and Sharma, M. (1994). Differential effects on spatial navigation of immunotoxin-induced cholinergic lesions of the medial septal area and nucleus basalis magnocellularis. J. Neurosci. *14*, 4507–4519. https://doi.org/10.1523/JNEUROSCI.14-07-04507.1994.

14. Bailey, A.M., Rudisill, M.L., Hoof, E.J., and Loving, M.L. (2003). 192 IgG-saporin lesions to the nucleus basalis magnocellularis (nBM) disrupt acquisition of learning set formation. Brain Res. *969*, 147–159. https://doi.org/10.1016/S0006-8993(03)02294-7.

15. Conner, J.M., Culberson, A., Packowski, C., Chiba, A.A., and Tuszynski, M.H. (2003). Lesions of the basal forebrain cholinergic system impair task acquisition and abolish cortical plasticity associated with motor skill learning. Neuron *38*, 819–829. https://doi.org/10.1016/S0896-6273(03)00288-5.

16. McGaughy, J., Koene, R. a, Eichenbaum, H., and Hasselmo, M.E. (2005). Cholinergic deafferentation of the entorhinal cortex in rats impairs encoding of novel but not familiar stimuli in a delayed nonmatch-to-sample task. J. Neurosci. *25*, 10273–10281. https://doi.org/10.1523/JNEUROSCI.2386-05.2005.

17. Ross, R.S., McGaughy, J., and Eichenbaum, H. (2005). Acetylcholine in the orbitofrontal cortex is necessary for the acquisition of a socially transmitted food preference. Learn. Mem. *12*, 302–306. https://doi.org/10.1101/lm.91605.

18. McGaughy, J., Dalley, J.W., Morrison, C.H., Everitt, B.J., and Robbins, T.W. (2002). Selective behavioral and neurochemical effects of cholinergic lesions produced by intrabasalis infusions of 192 IgG-saporin on attentional performance in a five-choice serial reaction time task. J. Neurosci. *22*, 1905–1913. https://doi.org/10.1523/JNEUROSCI.22-05-01905.2002.

19. Fine, A., Hoyle, C., Maclean, C.J., Levatte, T.L., Baker, H.F., and Ridley, R.M. (1997). Learning impairments following injection of a selective cholinergic immunotoxin, ME20.4 IgG-saporin, into the basal nucleus of Meynert in monkeys. Neuroscience *81*, 331–343. https://doi.org/10.1016/S0306-4522(97)00208-X.

20. Damasio, A.R., Graff-Radford, N.R., Eslinger, P.J., Damasio, H., and Kassell, N. (1985). Amnesia following basal forebrain lesions. Arch. Neurol. *42*, 263–271. https://doi.org/10.1001/archneur.1985.04060030081013.

21. Lin, S.-C., and Nicolelis, M. a L. (2008). Neuronal ensemble bursting in the basal forebrain encodes salience irrespective of valence. Neuron *59*, 138–149. https://doi.org/10.1016/j.neuron.2008.04.031.

22. Crouse, R.B., Kim, K., Batchelor, H.M., Girardi, E.M., Kamaletdinova, R., Chan, J., Rajebhosale, P., Pittenger, S.T., Role, L.W., Talmage, D.A., et al. (2020). Acetylcholine is released in the basolateral amygdala in response to predictors of reward and enhances the learning of cue-reward contingency. Elife *9*, e57431. https://doi.org/10.7554/eLife.57335.

23. Froemke, R.C., Merzenich, M.M., and Schreiner, C.E. (2007). A synaptic memory trace for cortical receptive field plasticity. Nature *450*, 425–429. https://doi.org/10.1038/nature06289.

24. Kilgard, M.P., and Merzenich, M.M. (1998). Cortical map reorganization enabled by nucleus basalis activity. Science *279*, 1714–1718. https://doi.org/10.1126/science.279.5357.1714.

25. Hegedüs, P., Velencei, A., Belval, C.H.d., Heckenast, J., and Hangya, B. (2021). Training protocol for probabilistic Pavlovian conditioning in mice using an open-source head-fixed setup. STAR Protoc. *2*, 100795. https://doi.org/10.1016/j.xpro.2021.100795.

26. Eshel, N., Tian, J., Bukwich, M., and Uchida, N. (2016). Dopamine neurons share common response function for reward prediction error. Nat. Neurosci. *19*, 479–486. https://doi.org/10.1038/nn.4239.

27. Stephenson-Jones, M., Bravo-Rivera, C., Ahrens, S., Furlan, A., Xiao, X., Fernandes-Henriques, C., and Li, B. (2020). Opposing contributions of GABAergic and glutamatergic ventral pallidal neurons to motivational behaviors. Neuron *105*, 921–933.e5. https://doi.org/10.1016/j.neuron.2019.12.006.

28. Hegedüs, P., Heckenast, J., and Hangya, B. (2021). Differential recruitment of ventral pallidal e-types by behaviorally salient stimuli during Pavlovian conditioning. iScience *24*, 102377. https://doi.org/10.1016/j.isci.2021.102377.

29. Kim, C.K., Yang, S.J., Pichamoorthy, N., Young, N.P., Kauvar, I., Jennings, J.H., Lerner, T.N., Berndt, A., Lee, S.Y., Ramakrishnan, C., et al. (2016). Simultaneous fast measurement of circuit dynamics at multiple sites across the mammalian brain. Nat. Methods *13*, 325–328. https://doi.org/10.1038/nmeth.3770.

30. Higley, M.J., Gittis, A.H., Oldenburg, I. a, Balthasar, N., Seal, R.P., Edwards, R.H., Lowell, B.B., Kreitzer, A.C., and Sabatini, B.L. (2011). Cholinergic interneurons mediate fast VGluT3-dependent glutamatergic transmission in the striatum. PLoS One *6*, e19155. https://doi.org/10.1371/journal.pone.0019155.

31. Eggermann, E., Kremer, Y., Crochet, S., and Petersen, C.C.H. (2014). Cholinergic signals in mouse barrel cortex during active whisker sensing. Cell Rep. *9*, 1654–1660. https://doi.org/10.1016/j.celrep.2014.11.005.

32. Lerner, T.N., Shilyansky, C., Davidson, T.J., Evans, K.E., Beier, K.T., Zalocusky, K.A., Crow, A.K., Malenka, R.C., Luo, L., Tomer, R., and Deisseroth, K. (2015). Intact-brain analyses reveal distinct information carried by SNc dopamine subcircuits. Cell *162*, 635–647. https://doi.org/10.1016/j.cell.2015.07.014.

33. Kvitsiani, D., Ranade, S., Hangya, B., Taniguchi, H., Huang, J.Z., and Kepecs, A. (2013). Distinct behavioural and network correlates of two interneuron types in prefrontal cortex. Nature *498*, 363–366. https://doi.org/10.1038/nature12176.

34. Laszlovszky, T., Schlingloff, D., Hegedüs, P., Freund, T.F., Gulyás, A., Kepecs, A., and Hangya, B. (2020). Distinct synchronization, cortical coupling and behavioral function of two basal forebrain cholinergic neuron types. Nat. Neurosci. *23*, 992–1003. https://doi.org/10.1038/s41593-020-0648-0.

35. Schultz, W., Dayan, P., and Montague, P.R. (1997). A neural substrate of prediction and reward. Science *275*, 1593–1599. https://doi.org/10.1126/science.275.5306.1593.

36. Kim, H.R., Malik, A.N., Mikhael, J.G., Bech, P., Tsutsui-Kimura, I., Sun, F., Zhang, Y., Li, Y., Watabe-Uchida, M., Gershman, S.J., and Uchida, N. (2020). A unified framework for dopamine signals across timescales. Cell *183*, 1600–1616.e25. https://doi.org/10.1016/j.cell.2020.11.013.

37. Avila, I., and Lin, S.-C. (2014). Motivational salience signal in the basal forebrain is coupled with faster and more precise decision speed. PLoS Biol. *12*, e1001811. https://doi.org/10.1371/journal.pbio.1001811.

38. Ahrens, A.M., Ferguson, L.M., Robinson, T.E., and Aldridge, J.W. (2018). Dynamic encoding of incentive salience in the ventral pallidum: dependence on the form of the reward cue. eNeuro *5*. ENEURO.0328-17.2018. https://doi.org/10.1523/ENEURO.0328-17.2018.

39. Zhang, K., Chen, C.D., and Monosov, I.E. (2019). Novelty, salience, and surprise timing are signaled by neurons in the basal forebrain. Curr. Biol. *29*, 134–142.e3. https://doi.org/10.1016/j.cub.2018.11.012.

40. Teles-Grilo Ruivo, L.M., Baker, K.L., Conway, M.W., Kinsley, P.J., Gilmour, G., Phillips, K.G., Isaac, J.T.R., Lowry, J.P., and Mellor, J.R. (2017). Coordinated acetylcholine release in prefrontal cortex and Hippocampus is associated with arousal and reward on distinct timescales. Cell Rep. *18*, 905–917. https://doi.org/10.1016/j.celrep.2016.12.085.

41. Robert, B., Kimchi, E.Y., Watanabe, Y., Chakoma, T., Jing, M., Li, Y., and Polley, D.B. (2021). A functional topography within the cholinergic basal forebrain for encoding sensory cues and behavioral reinforcement outcomes. Elife *10*, e69514–e69528. https://doi.org/10.7554/eLife.69514.

42. Gershman, S.J., and Uchida, N. (2019). Believing in dopamine. Nat. Rev. Neurosci. *20*, 703–714. https://doi.org/10.1038/s41583-019-0220-7.

43. Gasselin, C., Hohl, B., Vernet, A., Crochet, S., and Petersen, C.C.H. (2021). Cell-type-specific nicotinic input disinhibits mouse barrel cortex during active sensing. Neuron *109*, 778–787.e3. https://doi.org/10.1016/j.neuron.2020.12.018.

44. Gombkoto, P., Gielow, M., Varsanyi, P., Chavez, C., and Zaborszky, L. (2021). Contribution of the basal forebrain to corticocortical network interactions. Brain Struct. Funct. *226*, 1803–1821. https://doi.org/10.1007/s00429-021-02290-z.

45. Lin, S.C., Brown, R.E., Hussain Shuler, M.G., Petersen, C.C.H., and Kepecs, A. (2015). Optogenetic dissection of the basal forebrain neuromodulatory control of cortical activation, plasticity, and cognition. J. Neurosci. *35*, 13896–13903. https://doi.org/10.1523/JNEUROSCI.2590-15.2015.

46. Leão, R.N., Mikulovic, S., Leão, K.E., Munguba, H., Gezelius, H., Enjin, A., Patra, K., Eriksson, A., Loew, L.M., Tort, A.B.L., and Kullander, K. (2012). OLM interneurons differentially modulate CA3 and entorhinal inputs to hippocampal CA1 neurons. Nat. Neurosci. *15*, 1524–1530. https://doi.org/10.1038/nn.3235.

47. Palacios-Filardo, J., and Mellor, J.R. (2019). Neuromodulation of hippocampal long-term synaptic plasticity. Curr. Opin. Neurobiol. *54*, 37–43. https://doi.org/10.1016/j.conb.2018.08.009.

48. Chubykin, A.A., Roach, E.B., Bear, M.F., and Shuler, M.G.H. (2013). A cholinergic mechanism for reward timing within primary visual cortex. Neuron *77*, 723–735. https://doi.org/10.1016/j.neuron.2012.12.039.

49. Shuler, M.G., and Bear, M.F. (2006). Reward timing in the primary visual cortex. Science *311*, 1606–1609. https://doi.org/10.1126/science.1123513.

50. Liu, C.-H., Coleman, J.E., Davoudi, H., Zhang, K., and Hussain Shuler, M.G. (2015). Selective activation of a putative reinforcement signal conditions cued interval timing in primary visual cortex. Curr. Biol. *25*, 1551–1561. https://doi.org/10.1016/j.cub.2015.04.028.

51. Gu, Z., and Yakel, J.L. (2011). Timing-dependent septal cholinergic induction of dynamic hippocampal synaptic plasticity. Neuron *71*, 155–165. https://doi.org/10.1016/j.neuron.2011.04.026.

52. Berg, D.K. (2011). Timing is everything, even for cholinergic control. Neuron *71*, 6–8. https://doi.org/10.1016/j.neuron.2011.06.029.

53. Urban-Ciecko, J., Jouhanneau, J.S., Myal, S.E., Poulet, J.F.A., and Barth, A.L. (2018). Precisely timed nicotinic activation drives SST inhibition in neocortical circuits. Neuron *97*, 611–625.e5. https://doi.org/10.1016/j.neuron.2018.01.037.

54. Pinto, L., Goard, M.J., Estandian, D., Xu, M., Kwan, A.C., Lee, S.-H., Harrison, T.C., Feng, G., and Dan, Y. (2013). Fast modulation of visual perception by basal forebrain cholinergic neurons. Nat. Neurosci. *16*, 1857–1863. https://doi.org/10.1038/nn.3552.

55. Letzkus, J.J., Wolff, S.B.E., Meyer, E.M.M., Tovote, P., Courtin, J., Herry, C., and Lüthi, A. (2011). A disinhibitory microcircuit for associative fear learning in the auditory cortex. Nature *480*, 331–335. https://doi.org/10.1038/nature10674.

56. Jiang, L., Kundu, S., Lederman, J.D., López-Hernández, G.Y., Ballinger, E.C., Wang, S., Talmage, D.A., and Role, L.W. (2016). Cholinergic signaling controls conditioned fear behaviors and enhances plasticity of cortical-amygdala circuits. Neuron *90*, 1057–1070. https://doi.org/10.1016/j.neuron.2016.04.028.

57. Rouhani, N., and Niv, Y. (2021). Signed and unsigned reward prediction errors dynamically enhance learning and memory. Elife *10*, e61128. https://doi.org/10.7554/eLife.61077.

58. Rouhani, N., Norman, K.A., and Niv, Y. (2018). Dissociable effects of surprising rewards on learning and memory. J. Exp. Psychol. Learn. Mem. Cogn. *44*, 1430–1443. https://doi.org/10.1037/xlm0000518.

59. Zannone, S., Brzosko, Z., Paulsen, O., and Clopath, C. (2018). Acetylcholine-modulated plasticity in reward-driven navigation: a computational study. Sci. Rep. *8*, 9486. https://doi.org/10.1038/s41598-018-27393-2.

60. Nelson, A., and Mooney, R. (2016). The basal forebrain and motor cortex provide convergent yet distinct movement-related inputs to the auditory cortex. Neuron *90*, 635–648. https://doi.org/10.1016/j.neuron.2016.03.031.

61. Metherate, R., Cox, C.L., and Ashe, J.H. (1992). Cellular bases of neocortical activation: modulation of neural oscillations by the nucleus basalis and endogenous acetylcholine. J. Neurosci. *12*, 4701–4711. https://doi.org/10.1523/JNEUROSCI.12-12-04701.1992.

62. Buzsaki, G., Bickford, R.G., Ponomareff, G., Thal, L.J., Mandel, R., and Gage, F.H. (1988). Nucleus basalis and thalamic control of neocortical activity in the freely moving rat. J. Neurosci. *8*, 4007–4026. https://doi.org/10.1523/JNEUROSCI.08-11-04007.1988.

63. Richardson, R.T., and DeLong, M.R. (1991). Electrophysiological studies of the functions of the nucleus basalis in primates. In Advances in experimental medicine and biology, pp. 233–252. https://doi.org/10.1007/978-1-4757-0145-6_12.

64. Zhang, H., Lin, S.-C., and Nicolelis, M.A.L. (2011). A distinctive subpopulation of medial septal slow-firing neurons promote hippocampal activation and theta oscillations. J. Neurophysiol. *106*, 2749–2763. https://doi.org/10.1152/jn.00267.2011.

65. Parikh, V., Kozak, R., Martinez, V., and Sarter, M. (2007). Prefrontal acetylcholine release controls cue detection on multiple timescales. Neuron *56*, 141–154. https://doi.org/10.1016/j.neuron.2007.08.025.

66. Disney, A.A., Aoki, C., and Hawken, M.J. (2007). Gain modulation by nicotine in macaque v1. Neuron *56*, 701–713. https://doi.org/10.1016/j.neuron.2007.09.034.

67. Harris, K.D., and Thiele, A. (2011). Cortical state and attention. Nat. Rev. Neurosci. *12*, 509–523. https://doi.org/10.1038/nrn3084.

68. Lee, M.G., Hassani, O.K., Alonso, A., and Jones, B.E. (2005). Cholinergic basal forebrain neurons burst with theta during waking and paradoxical sleep. J. Neurosci. *25*, 4365–4369. https://doi.org/10.1523/JNEUROSCI.0178-05.2005.

69. Duque, A., Balatoni, B., Detari, L., and Zaborszky, L. (2000). EEG correlation of the discharge properties of identified neurons in the basal forebrain. J. Neurophysiol. *84*, 1627–1635. https://doi.org/10.1152/jn.2000.84.3.1627.

70. Xu, M., Chung, S., Zhang, S., Zhong, P., Ma, C., Chang, W.-C., Weissbourd, B., Sakai, N., Luo, L., Nishino, S., and Dan, Y. (2015). Basal forebrain circuit for sleep-wake control. Nat. Neurosci. *18*, 1641–1647. https://doi.org/10.1038/nn.4143.

71. Schultz, W. (2015). Neuronal reward and decision signals: from theories to data. Physiol. Rev. *95*, 853–951. https://doi.org/10.1152/physrev.00023.2014.

72. Cohen, J.Y., Haesler, S., Vong, L., Lowell, B.B., and Uchida, N. (2012). Neuron-type-specific signals for reward and punishment in the

ventral tegmental area. Nature *482*, 85–88. https://doi.org/10.1038/nature10754.

73. Lak, A., Stauffer, W.R., and Schultz, W. (2016). Dopamine neurons learn relative chosen value from probabilistic rewards. Elife *5*, e18119. https://doi.org/10.7554/eLife.18044.

74. Matsumoto, M., and Hikosaka, O. (2009). Two types of dopamine neuron distinctly convey positive and negative motivational signals. Nature *459*, 837–841. https://doi.org/10.1038/nature08028.

75. Menegas, W., Akiti, K., Amo, R., Uchida, N., and Watabe-Uchida, M. (2018). Dopamine neurons projecting to the posterior striatum reinforce avoidance of threatening stimuli. Nat. Neurosci. *21*, 1421–1430. https://doi.org/10.1038/s41593-018-0222-1.

76. Tsutsui-Kimura, I., Matsumoto, H., Akiti, K., Yamada, M.M., Uchida, N., and Watabe-Uchida, M. (2020). Distinct temporal difference error signals in dopamine axons in three regions of the striatum in a decision-making task. Elife *9*, e62439. https://doi.org/10.7554/ELIFE.62390.

77. Gielow, M.R., and Zaborszky, L. (2017). The input-output relationship of the cholinergic basal forebrain. Cell Rep. *18*, 1817–1830. https://doi.org/10.1016/j.celrep.2017.01.060.

78. Zaborszky, L., Csordas, A., Mosca, K., Kim, J., Gielow, M.R., Vadasz, C., and Nadasdy, Z. (2015). Neurons in the basal forebrain project to the cortex in a complex topographic organization that reflects corticocortical connectivity patterns: an experimental study based on retrograde tracing and 3D reconstruction. Cerebr. Cortex *25*, 118–137. https://doi.org/10.1093/cercor/bht210.

79. Zaborszky, L., van den Pol, A., and Gyengesi, E. (2012). The basal forebrain cholinergic projection system in mice. In The Mouse Nervous System, C. Watson, G. Paxinos, and L. Puelles, eds. (Elsevier), pp. 684–718. https://doi.org/10.1016/B978-0-12-369497-3.10028-7.

80. Zaborszky, L., Gaykema, R.P., Swanson, D.J., and Cullinan, W.E. (1997). Cortical input to the basal forebrain. Neuroscience *79*, 1051–1078. https://doi.org/10.1016/S0306-4522(97)00049-3.

81. Pi, H.-J., Hangya, B., Kvitsiani, D., Sanders, J.I., Huang, Z.J., and Kepecs, A. (2013). Cortical interneurons that specialize in disinhibitory control. Nature *503*, 521–524. https://doi.org/10.1038/nature12676.

82. Najafi, F., Giovannucci, A., Wang, S.S.H., and Medina, J.F. (2014). Coding of stimulus strength via analog calcium signals in Purkinje cell dendrites of awake mice. Elife *3*, e03663. https://doi.org/10.7554/eLife.03663.

83. Siegle, J.H., López, A.C., Patel, Y.A., Abramov, K., Ohayon, S., and Voigts, J. (2017). Open Ephys: an open-source, plugin-based platform for multichannel electrophysiology. J. Neural. Eng. *14*, 045003. https://doi.org/10.1088/1741-2552/aa5eea.

84. Széll, A., Martínez-Bellver, S., Hegedüs, P., and Hangya, B. (2020). OPETH: open source solution for real-time peri-event time histogram based on open ephys. Front. Neuroinf. *14*, 21. https://doi.org/10.3389/fninf.2020.00021.

85. Endres, D.M., and Schindelin, J.E. (2003). A new metric for probability distributions. IEEE Trans. Inf. Theor. *49*, 1858–1860. https://doi.org/10.1109/TIT.2003.813506.

86. Fraser, G.W., and Schwartz, A.B. (2012). Recording from the same neurons chronically in motor cortex. J. Neurophysiol. *107*, 1970–1978. https://doi.org/10.1152/jn.01012.2010.

87. Franklin, K.B., and Paxinos, G. (2007). The Mouse Brain in Stereotaxic Coordinates, Third Edition (Academic Press).

88. Schmitzer-Torbert, N., Jackson, J., Henze, D., Harris, K., and Redish, a D. (2005). Quantitative measures of cluster quality for use in extracellular recordings. Neuroscience *131*, 1–11. https://doi.org/10.1016/j.neuroscience.2004.09.066.

STAR★METHODS

KEY RESOURCES TABLE

REAGENT or RESOURCE	SOURCE	IDENTIFIER
Bacterial and virus strains		
AAV2/5.EF1a.DiO.hChR2(H134R).eYFP.WPRE.hGh	https://www.addgene.org/	20298-AAV5
AAV2/9.CAG.Flex.GCAMP6s.WPRE.SV40	https://www.addgene.org/	100842-AAV9
Chemicals, peptides, and recombinant proteins		
Isoflurane	https://vetcentre.com/	N/A
Ketamine	https://vetcentre.com/	N/A
Xylazine	https://vetcentre.com/	N/A
Buprenorphine	http://www.richter-pharma.com/	N/A
Neomycin	Local pharmacy	N/A
Lidocaine	Local pharmacy	N/A
Betadine	Local pharmacy	N/A
Promethazine	https://vetcentre.com/	N/A
Paraformaldehyde	https://taab.co.uk/	Cat#P001
Fluorescent dye (1,1′-Dioctadecyl-3,3,3′,3′-Tetramethylindocarbocyanine Perchlorate, DiI)	https://www.thermofisher.com	Cat#D282
Aqua-Poly/Mount mounting medium	https://www.polysciences.com	Cat#18606
Metabond dental cement	http://www.parkell.com/	Cat#S380
Jet Set-4 Denture Repair Powder and Liquid	https://www.langdental.com/	N/A
Eye ointment	https://www.laboratoires-thea.com	N/A
Deposited data		
Electrophysiology and fiber photometry	https://doi.org/10.5061/dryad.p5hqbzkrv	https://doi.org/10.5061/dryad.p5hqbzkrv
Experimental models: Organisms/strains		
ChAT-Cre Bl6 mice	https://www.jax.org/	#006410
Software and algorithms		
Matlab 2016a	https://mathworks.com/	N/A
Algorithms for behavioral analysis	https://github.com/hangyabalazs/cholinergic_Pavlovian_analysis	N/A
Algorithms for closed loop behavioral control	https://github.com/hangyabalazs/Bpod_r0_5	CuedOutcomeTask
Code for simple data analysis of lick responses and neural recordings	https://github.com/hangyabalazs/CellBase	N/A
OPETH	https://github.com/hangyabalazs/opeth	SCR_018022
MClust 3.5	https://redishlab.umn.edu/mclust	v. 3.5.
Other		
Surgical forceps	https://www.finescience.com/en-US/	11151–10
Standard surgical scissors	https://www.finescience.com/en-US/	14060–10
Scraper	https://www.finescience.com/en-US/	10075–16
Headbar	Custom made	N/A
Headbar holders	Custom made	N/A

(*Continued on next page*)

Continued

REAGENT or RESOURCE	SOURCE	IDENTIFIER
Lick port	https://www.shapeways.com/	N/A
Infrared sensor and emitter	https://www.digikey.com/	480-1958-ND and 480-1969-ND
Speaker	https://www.digikey.com/	668-1447-ND
Camera	https://www.flir.eu/iis/machine-vision/	FL3-U3-32S2M-CS
Bpod	https://sanworks.io/	1027
Teensy 3.2	https://www.pjrc.com/teensy/	N/A
Plastic tubing	https://www.thermofisher.com/	Cat#8001–0102 and Cat#8001–0204
Polyimide tubing	https://www.warneronline.com/	Cat#64–0755/PE-160
Feeding needle	https://www.finescience.com/en-US/	18060–20
Bulldog serrefine	https://www.finescience.com/en-US/	18050–28
Bone rongeour	https://www.finescience.com/en-US/	16012–12
Fiber Photometry System	https://neuro.doriclenses.com/	N/A
Data Acquisition System	https://openephys.org/acquisition-system/	Version#2.4
RHD 32-channel headstage	https://intantech.com	Part#C3314
RHD standard SPI interface cable	https://intantech.com	Part#3206
Ø400 µm Core, 0.50 NA FC/PC to Ø1.25 mm Ferrule Patch Cable, 1 m Long	https://www.thorlabs.de/	M127L01
Vibratome	https://www.leicabiosystems.com	2100S
Confocal microscope	https://www.microscope.healthcare.nikon.com/	C2
Stimulus isolator	https://www.superte.ch/	IBP-7c

RESOURCE AVAILABILITY

Lead contact

Further information and requests for resources should be directed to and will be fulfilled by the lead contact, Balázs Hangya (hangya.balazs@koki.hu).

Materials availability

This study did not generate new unique reagents.

Data and code availability

- Electrophysiology and fiber photometry data have been deposited to a Dryad repository at https://doi.org/10.5061/dryad.p5hqbzkrv.
- MATLAB codes generated for this study are available at https://github.com/hangyabalazs/cholinergic_Pavlovian_analysis.
- Any additional information required to reanalyze the data reported in this paper is available from the lead contact upon request.

EXPERIMENTAL MODEL AND SUBJECT DETAILS

Adult (over two months old) male ChAT-Cre mice (The Jackson Laboratory, RRID: IMSR_JAX:006410) were used (n = 11). All experiments were approved by the Animal Care and Use Committee of the Institute of Experimental Medicine and the Committee for Scientific Ethics of Animal Research of the National Food Chain Safety Office (PE/EA/675–4/2016; PE/EA/1212–5/2017; PE/EA/864–7/2019) and were performed according to the guidelines of the institutional ethical code and the Hungarian Act of Animal Care and Experimentation (1998; XXVIII, section 243/1998, renewed in 40/2013) in accordance with the European Directive 86/609/CEE and modified according to the Directive 2010/63/EU.

METHOD DETAILS

Tetrode implantation surgery

Mice were implanted using standard stereotaxic surgery techniques with miniaturized microdrives housing 8 tetrodes and an optic fiber.[10,33,81] Briefly, mice were anesthetized by a mixture of ketamine and xylazine (83 and 17 mg/kg, respectively, dissolved in 0.9% saline). The skin was shaved and disinfected with Betadine, subcutaneous tissues were infused with Lidocaine, eyes were protected with eye ointment (Laboratories Thea) and mice were placed in a stereotaxic frame (Kopf Instruments). The skull was cleaned, and a craniotomy was drilled above the horizontal diagonal band of Broca (HDB, antero-posterior 0.75 mm, lateral 0.60 mm; n = 4) or the medial septum (MS, antero-posterior 0.90 mm, lateral 0.90 mm, 10 degrees lateral angle; n = 1). Virus injection (AAV2/5.EF1a.Dio.hChR2(H134R)-eYFP.WPRE.hGH; HDB, dorso-ventral 5.00 and 4.70 mm, 300 nL at each depth; MS, dorsoventral 3.95, 4.45 and 5.25 mm, 200 nL at each depth) and drive implantation was performed according to standard techniques.[10,33] Ground and reference electrodes were implanted to the bilateral parietal cortex. Mice received analgesics (Buprenorphine, 0.1 mg/kg), local antibiotics (Neomycin) and were allowed 10 days of recovery before starting behavioral training.

Optical fiber implantation surgery

Mice (n = 7) were implanted using standard stereotactic surgery techniques described in the previous section. Following virus injection (AAV2/9.CAG.Flex.GCAMP6s.WPRE.SV40; HDB, 300 nL each side, antero-posterior 0.75 mm, lateral 0.60 mm; dorso-ventral 5.00 and 4.7 mm), 400 μm core diameter optic fibers with ceramic ferrules were implanted bilaterally (HDB, antero-posterior 0.75 mm, lateral 0.60 mm; 0 and 20 degrees lateral angle on the two sides). Optical fiber implantation was performed similarly to tetrode drive implantation. Mice received analgesics (Buprenorphine, 0.1 mg/kg), local antibiotics (Neomycin) and were allowed 10 days of recovery before starting behavioral training.

Behavioral training

Mice were trained on a head-fixed probabilistic auditory Pavlovian conditioning task[28] in a custom-built behavioral setup that allowed millisecond precision of stimulus and reinforcement delivery (described in[7]). Mice were water restricted before training and worked for small amounts of water reward (5 μL) during conditioning. Pure tones of one second duration predicted likely reward/unlikely punishment or unlikely reward/likely punishment based on their pitch (12 kHz tone predicted 80% water reward, 10% air-puff punishment, 10% omission; 4 kHz tone predicted 25% water reward, 65% air-puff punishment, 10% omission in n = 6 mice; opposite cue contingencies were used in n = 5 mice, see Figures S1 and S3; 50–50% of the two cue tones were mixed randomly; all cue tone intensities were set at 50 dB sound pressure level). The animal was free to lick a waterspout after tone onset and individual licks were detected by the animal's tongue breaking an infrared photobeam. After an additional 200–400 ms post-stimulus delay, the animal received water reward, air-puff punishment or omission, pseudorandomized according to the above contingencies. The next trial started after the animal stopped licking for at least 1.5 s. The stimulus was preceded by a 1–4 s foreperiod according to a truncated exponential distribution, in order to prevent temporal expectation of stimulus delivery. If the mouse licked in the foreperiod, the trial was restarted. We used the open source Bpod behavioral control system (Sanworks LLC, US) for operating the task. Behavioral performance of the task did not depend on the identity (frequencies) of the conditioned stimuli (Figure S1).

The aversive quality of air-puffs depends on the exact experimental settings. We applied 200 ms long puffs at 15 psi pressure (within the range of parameters used for eyeblink conditioning[82]). We demonstrated that mice consistently choose water without air-puff over water combined with air-puff, showing that air-puffs are aversive under these circumstances (see Figures 2C and 2D in [10]). We also demonstrated that water and air-puff are accompanied by different auditory signals in our setup, thus making sensory response generalization unlikely to explain BFCN responses (see Figure S2A in [28]).

Fiber photometry imaging

Bilateral fluorescent calcium imaging was performed using a dual fiber photometry setup (Doric Neuroscience) and visualized during training sessions using Doric Studio Software. Two LED light sources (465 nm, 405 nm) were channeled in fluorescent Mini Cubes (iFMC4, Doric Neuroscience). Light was amplitude-modulated by the command voltage of the two-channel LED driver (LEDD_2, Doric Neuroscience, the 465 nm wavelength light was modulated at 208 Hz and 405 nm wavelength was modulated at 572 Hz). Light was channeled into 400 μm diameter patch cord fibers and was connected to optical fiber implants during training sessions.

The same optical fibers were used to collect the bilateral emitted fluorescence signal, which were detected with 500–550 nm fluorescent detectors integrated in the Mini Cubes. Emitted signals were sampled at 12 kHz, decoded in silico and saved in a *.csv format.

Chronic extracellular recording

We used the open ephys data acquisition system[83] for spike data collection. A 32-channels Intan headstage (RHD2132) was connected to the Omnetics connector on the custom-built microdrive. Data was transferred through digital SPI cables (Intan) to the Open Ephys board and saved by the Open Ephys software, digitized at 30 kHz.

Optogenetic tagging

The custom microdrives were equipped with a 50 μm core optic fiber (Thorlabs) that ended in an FC connector (Precision Fiber Products). This was connected with an FC-APC patch chord during recording. For optogenetic tagging, 1 ms laser pulses were delivered (473 nm, Sanctity) at 20 Hz for 2 seconds, followed by 3 seconds pause, repeated 20–30 times. Light-evoked spikes and potential artifacts were monitored online using the OPETH plugin (SCR_018022)[84] and laser power was adjusted as necessary to avoid light-induced photoelectric artifacts and population spikes that could mask individual action potentials. Significance of photoactivation was assessed during offline analyses by the SALT test based spike latency distributions after light pulses, compared to a surrogate distribution using Jensen-Shannon divergence (information radius).[33,85] Neurons with $p < 0.01$ were considered light-activated, and thus cholinergic. Cholinergic neurons recorded on the same tetrode within 200 μm dorso-ventral distance were compared by waveform correlation and autocorrelogram similarity,[28,86] and similar units were counted towards the sample size only once.

Histology

After the last behavioral session, mice were deeply anesthetized with ketamine/xylazine and we performed an electrolytic lesion to aid electrode localization (5 μA current for ~5s on 2 leads/tetrode), Supertech, IBP-7c). Mice were perfused transcardially, starting with a 2-minute washout period with saline, followed by 4% paraformaldehyde solution for 20 minutes. After the perfusion, mice were removed from the platform and decapitated. The brain was carefully removed and postfixed overnight in 4% PFA. A block containing the full extent of the HDB was prepared and 50 μm thick sections were cut using a Leica 2100S vibratome. All attempts were made to section parallel to the canonical coronal plane to aid track reconstruction efforts. All sections that contained the electrode tracks were mounted on slides in Aquamount mounting medium. Fluorescent and dark field confocal images of the sections were taken with a Nikon C2 confocal microscope. During track reconstruction, it is important to convert the logged screw turns (20 μm for each one eights of a full turn, allowed by a 160 μm pitch custom precision screw, Easterntec, Shanghai) that were performed throughout the experiment into brain atlas coordinates with maximal possible precision. To this end, dark field and bright field images of the brain sections were morphed onto the corresponding atlas planes[87] using Euclidean transformations only. The aligned atlas images were carried over to fluorescent images of the brain sections showing the DiI-labelled electrode tracks (red) and green fluorescent labeling (cholinergic neurons labelled by the AAV2.5-EF1a-Dio-hChR2(H134R)-eYFP.WPRE.hGh virus) in the target area. The entry points, electrode tips and lesion sites were localized with respect to the atlas coordinates maximizing the combined information of the structural (dark/bright field), DiI track and ChAT-labelling fluoromicrographs. Recording location of each section was interpolated based on the above coordinates, using the screw turn logs and the measured protruding length of the tetrodes after the experiments (also described in[10]). If the track spanned multiple sections, special care was taken to precisely reconstruct the part of the track where the recordings took place within the target area. This procedure minimizes the localization errors that may arise from differences between the recorded and the reference brain coordinates and eliminates the effect of tissue distortions caused by the fixation process. Only those recordings that were convincingly localized to the basal forebrain were analyzed in this study.

QUANTIFICATION AND STATISTICAL ANALYSIS

Data processing and analysis was carried out in Matlab R2016a (Mathworks, Natick).

Data analysis

Fiber photometry signals were preprocessed according to Lerner et al. (2015). In case of bilateral data acquisition, fiber photometry signal of the side with the better signal-to-noise ratio was chosen for further

analysis. Briefly, the fluorescence signals were filtered below 20 Hz using a low-pass Butterworth digital filter to remove high frequency noise. To calculate dff, a least-squares linear fit was applied to the isosbestic 405 nm signal to align its baseline intensity to that of the calcium-dependent 465 nm (f465) signal. The fitted 405 nm signal ($f_{405,fitted}$) was used to normalize the 465 nm signal as follows:

$$dff = \frac{f_{465} - f_{405,fitted}}{f_{405,fitted}} * 100$$

to remove the effect of motion and autofluorescence. Slow decay of the baseline activity was filtered out with an 0.2 Hz high pass Butterworth digital filter. Finally, the dff signal was triggered on cue and feedback times, Z-scored by the mean and standard deviation of a baseline window (1s before cue onset) and averaged across trials.

Tetrode recording channels were digitally referenced to a common average reference, filtered between 700-7000 Hz with Butterworth zero-phase filter and spikes were detected using a 750 μs censoring period. Spike sorting was carried out in MClust 3.5 software (A .D. Redish). Autocorrelations were inspected for refractory period violations and putative units with insufficient refractory period were not included in the data set. Cluster separation was measured using Isolation Distance and L-ratio calculated on the basis of two features, the full spike amplitude and the first principle component of the waveform.[88] Putative single neurons exceeding Isolation Distance (ID) of 20 and below L-ratio of 0.15 were automatically included (n = 20 cholinergic neurons and n = 452 untagged neurons recorded in the same sessions). Additionally, spike sorting was aided by the information provided by light-evoked spike shapes[81] in n = 5 cholinergic neurons, resulting in a data set of n = 25 optogenetically identified cholinergic neurons (L-ratio of cholinergic neurons, 0.0511 ± 0.0133, median ± SE; ID of cholinergic neurons, 30.0809 ± 6.4121, median ±SE; n = 17, 5, 2, 1 cells in the four mice). Spike shape correlations between spontaneous and light-induced spikes were calculated for all cholinergic neurons. Correlation coefficient exceeded R = 0.85 in all and R = 0.9 in 22/25 optotagged neurons (0.98 ± 0.01, median ±SE; range, 0.87 - 1.0), confirming cholinergic identity.[72]

We did not find any systematic differences in our analyses based on anatomical location; thus, we analyzed the 25 neurons as one dataset. First, we calculated event-aligned raster plots and peri-event time histograms (PETHs) for all neurons. To calculate average PETHs, neuronal responses were triggered on cue and feedback times, Z-scored by the mean and standard deviation of a baseline window (1s before cue onset) and averaged across trials. Response latency and jitter to optogenetic stimulation and behaviorally relevant events were determined based on activation peaks in the peri-event time histograms.[10] Behavioral performance was tested by comparing the anticipatory lick rate after reward and punishment predicting stimuli in a 1.2 s time window after stimulus onset. Reaction time was determined as the latency of the first lick after stimulus presentation.

We would like to note that an initial analysis of a part of this data set was presented in a bioRxiv preprint (https://www.biorxiv.org/content/10.1101/2020.02.17.953141v1).

Model fitting

Firing rates of cholinergic neurons were calculated in 500 ms response windows after cue presentation and 200 ms response windows after reinforcement presentation, to include the full firing response based on the observed time course of cholinergic activation (Figure 4). Firing rates were fitted by the following modified temporal difference RL model of cholinergic activity *(C)*.

$$C = S \cdot |R - \eta_1 E(R) + P - \eta_2 E(P)|$$

In this equation, $R - \eta_1 E(R)$ stands for reward prediction error (RPE). RPE classically takes the formula of $R - E(R)$, where $E(R)$ is expected, and R is actual amount of reward at a given time point. This was modified by the η_1 parameter, allowing potential differences in sensitivity to reward expectation across animals, sessions and neurons. Similarly, $P - \eta_2 E(P)$ represents the difference of expected and encountered punishment, referred to as 'punishment prediction error' hereafter. The two terms sum up to a full outcome prediction error, rendered 'unsigned' by the absolute value operator. The scaling factor S accounts for differences in baseline firing rate of cholinergic neurons. Of note, we found a variable mean firing rate of cholinergic neurons with an average of 8.22 ± 11.39 (SD) Hz during Pavlovian conditioning. We allowed the model to account for this difference with a scalar factor. This implicitly assumes response magnitudes proportional to 'baseline' firing rate, as in a multiplicative gain model, similar to what was found for

dopamine neurons.[26] The temporal discounting factor inherent to TDRL models was omitted from the equation, as it leads to only negligible firing rate differences within the few seconds of time that spans a behavioral trial. We note that another way of incorporating differential responsiveness to reward and punishment expectations would be by adding classical learning rates in the form of

$$C = S \cdot \alpha_1 |R - E(R)| + \alpha_2 |P - E(P)|$$

We fitted this alternative model as well; however, this model failed to capture the relative ratios of cue and outcome responses of cholinergic neurons and thus resulted in worse fits than the model presented in Figure 5.

The model was evaluated for the time of the cue, reward and punishment presentations. At the time of cues, $R = P = 0$, therefore the model takes the form of

$$C = S \cdot [\eta_1 E(R) + \eta_2 E(P)]$$

Since no omission responses were observed in cholinergic recordings (Figure S7), we dropped the negative expectation term of the omitted reinforcer at the time of reinforcement (e.g. omitted reward response at the time of punishment), leading to

$$C = S \cdot [R - \eta_1 E(R)]$$

at reward ($P = 0$) and

$$C = S \cdot [P - \eta_2 E(P)]$$

at punishment ($R = 0$) delivery. Nevertheless, keeping the omission responses in the model resulted in fits that were statistically indifferentiable ($p = 0.86$, Wilcoxon signed-rank test of model errors), suggesting that our data were not sufficient to differentiate between RL models with or without omission responses. The $E(R)$ and $E(P)$ expectation terms were set according to the task contingencies ($E(R) = 0.8$ or 0.25 and $E(P) = 0.1$ or 0.65 for the likely reward and unlikely reward cues, respectively). As a control model, we ran the same fitting process after these contingencies for reward and punishment expectations were swapped ($E(R) = 0.25$ or 0.8 and $E(P) = 0.65$ or 0.1 for the likely reward and unlikely reward cues, respectively). Fitting error was estimated by the maximum likelihood method and minimized by using the fminsearch built-in Matlab function employing the Nelder-Mead simplex algorithm. Models were statistically compared by Wilcoxon signed-rank test on the maximum likelihoods. Note that the compared models had equal complexity and number of parameters; therefore, a punishment term for free parameters was not required. Correlation between model parameters and anticipatory lick rate difference was calculated using the built-in robust regression algorithm of Matlab. Confidence intervals were derived using the polypredci.m function (Star Strider, https://www.mathworks.com/matlabcentral/fileexchange/57630-polypredci, MATLAB Central File Exchange, retrieved December 30, 2020).

Spike trains were simulated as Poisson-processes matched to each recorded cholinergic neuron in frequency ($n = 25$). Cholinergic responses to cue, reward and punishment were simulated as additional spikes drawn from a Gaussian distribution with fixed latency after the events. The number of 'evoked spikes' was based on the best-fit RL model corresponding to each neuron. Peri-event time histograms were generated from simulated spike trains the same way as applied for real data.

Statistics

We estimated the sample size before conducting the study based on previous publications, mostly Hangya et al. (2015),[10] as reported in the Results. Firing rates and other variables were compared across conditions using non-parametric tests, as normality of the underlying distributions could not be determined. Two-sided Wilcoxon signed-rank test was applied for paired, and two-sided Mann-Whitney U-test was applied for non-paired samples. Correlations were estimated by the Pearson's correlation coefficient, and their significance were judged by using a standard linear regression approach (one-sided F-test, in accordance with the asymmetric null hypothesis of linear regression). The relationship between BFCN firing rate and reaction time quartiles was also assessed by one-way ANOVA. Model fits were compared by negative log likelihood. Since the models compared had equal number of parameters, this is mathematically equivalent with model selection approaches using information criteria (e.g. Akaike and Bayesian Information Criterion). Peri-event time histograms show mean $\pm$ SE. Box-whisker plots show median, interquartile range and non-outlier range, with all data points overlaid.

iScience, Volume *26*

Supplemental information

Cholinergic activity reflects reward expectations and predicts behavioral responses

Panna Hegedüs, Katalin Sviatkó, Bálint Király, Sergio Martínez-Bellver, and Balázs Hangya

Supplemental figures

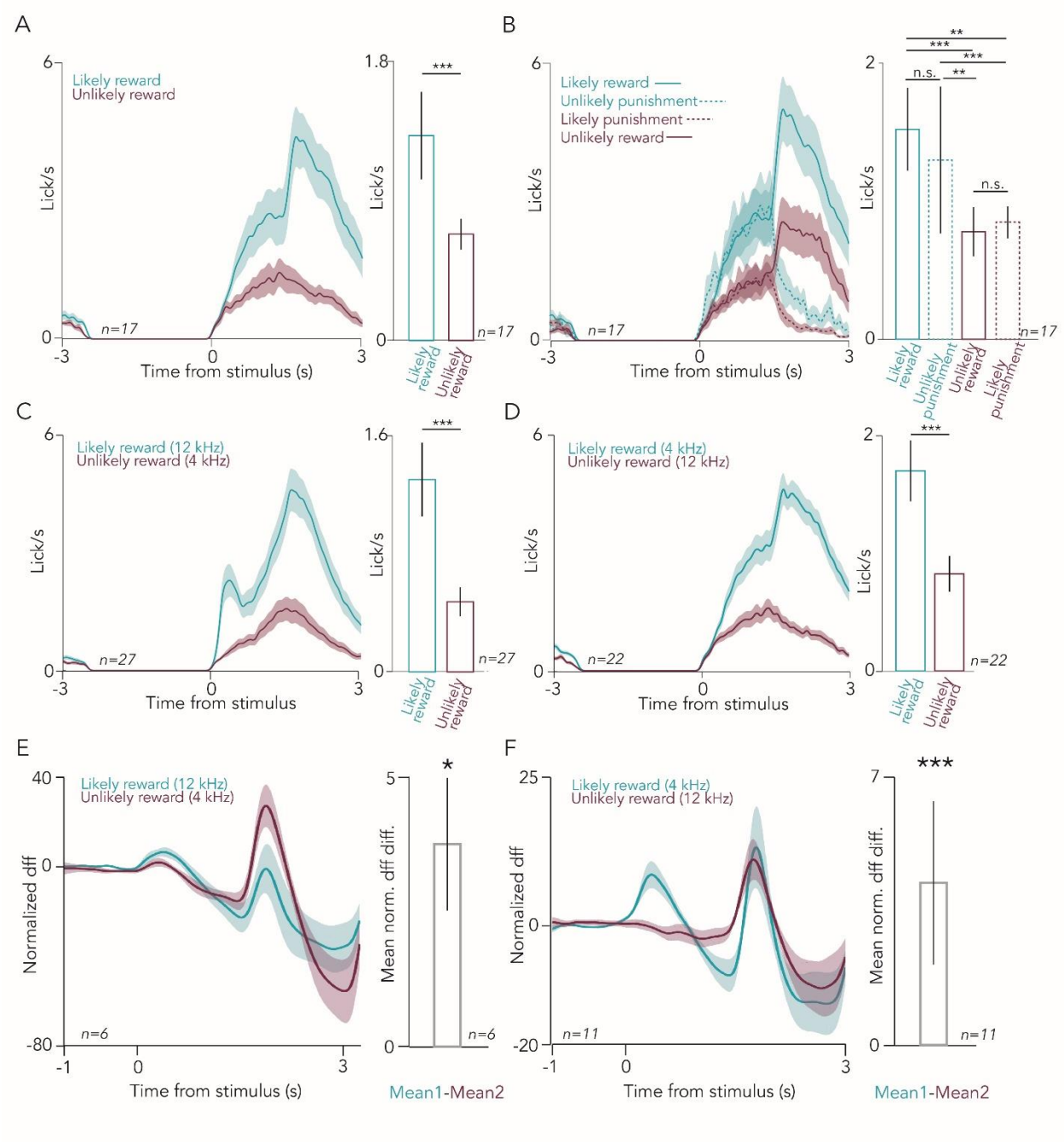

Figure S1. Behavioral performance during bulk calcium imaging of cholinergic neurons, Related to Figure 2. (A) Left, average PETHs of lick responses of all sessions during fiber photometry imaging (n = 17 sessions). Right, statistical comparison of anticipatory lick rates in the RW in likely reward and unlikely reward trials (n = 17 sessions, median ± SE of median, ***, $p < 0.001$, $p = 0.00042$, Wilcoxon signed-rank test). (B) Left, average PETHs of lick responses of all sessions of all animals (n = 17 sessions), partitioned

based on the four possible outcomes: expected or surprising reward, expected or surprising punishment. Right, statistical comparison of anticipatory lick rates in the RW with respect to the four possible outcomes (n = 17 sessions, median ± SE of median, **, $p < 0.01$, ***, $p < 0.001$, n.s., $p > 0.05$; from top to bottom, $p = 0.00118$, $p = 0.00085$, $p = 0.00042$, $p = 0.7226$, $p = 0.0012$, $p = 0.9811$, Wilcoxon signed-rank test). (C) Left, average PETHs of lick responses in sessions where likely reward (unlikely punishment) was predicted by a 12 kHz tone and unlikely reward (likely punishment) was predicted by a 4 kHz tone (n = 27 sessions, all sessions with full task contingencies were included). Right, statistical comparison of anticipatory lick rates in the RW in likely reward and unlikely reward trials (n = 27 sessions, median ± SE of median, ***, $p < 0.001$, $p = 2.91 \times 10^{-5}$, Wilcoxon signed-rank test). (D) The same as C, but with opposite contingencies (n = 22 sessions, all sessions with full task contingencies were included; median ± SE of median, ***, $p < 0.001$, $p = 0.00033$, Wilcoxon signed-rank test). (E) Left, average PETH of Z-scored dff aligned to outcome-predicting conditioned stimuli, where likely reward (unlikely punishment) was predicted by a 12 kHz tone and unlikely reward (likely punishment) was predicted by a 4 kHz tone (n = 6 sessions). Right, bar graph of average normalized difference in dff after likely reward and unlikely reward cues. Median ± SE of median, *, $p < 0.05$, $p = 0.03125$, Wilcoxon signed-rank test. (F) The same as E, but with opposite contingencies (n = 11 sessions, median ± SE of median, ***, $p < 0.001$, $p = 0.00098$, Wilcoxon signed-rank test).

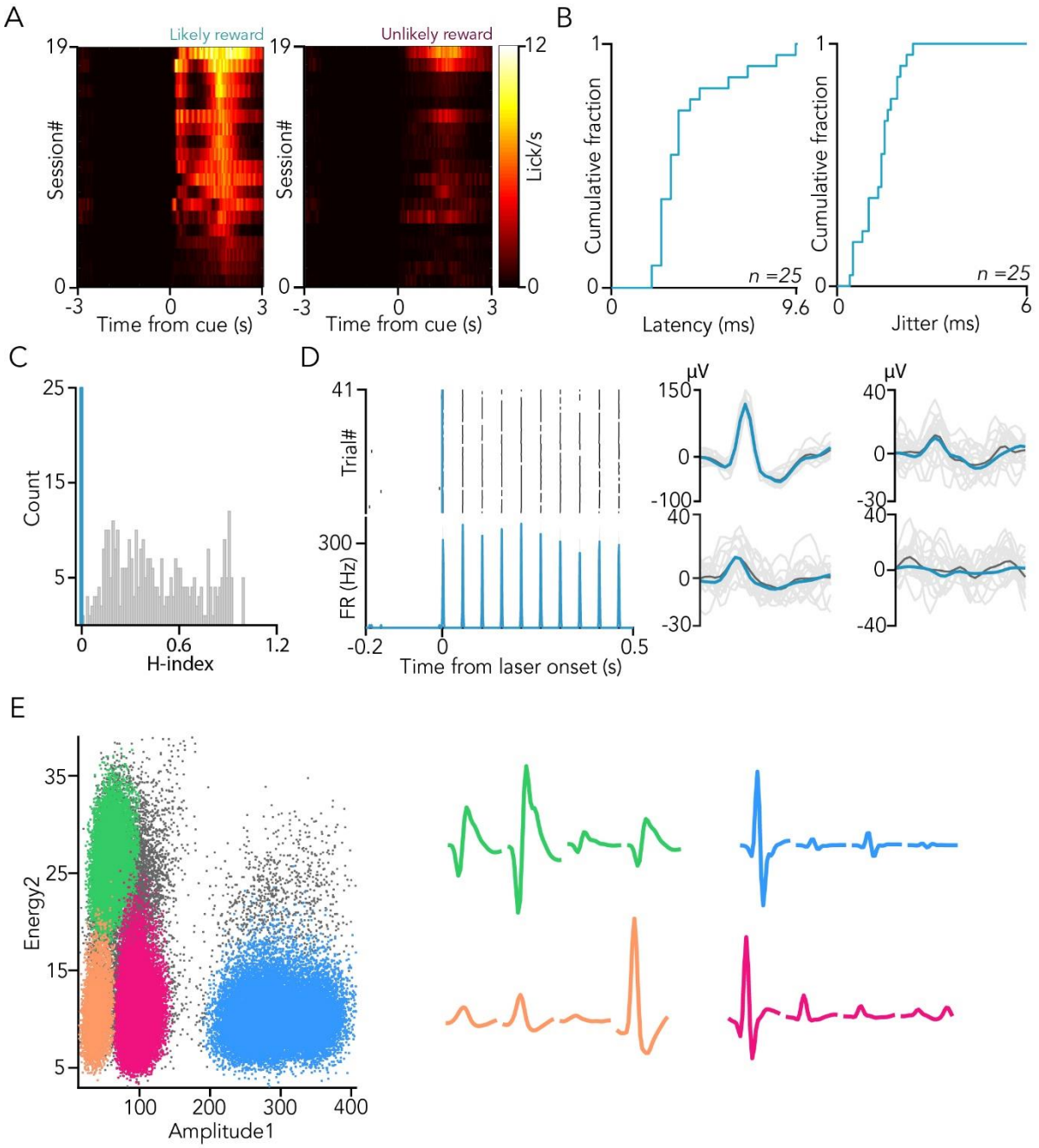

Figure S2. Optogenetic tagging of cholinergic neurons, Related to Figure 3. (A) Color-coded PETHs of lick responses of all sessions in which cholinergic neurons were recorded (n = 19 sessions; black, no licks; white, maximal lick response). (B) Left, cumulative histogram of the peak response latency of BFCNS after optogenetic stimulation. Right, cumulative histogram of the jitter of cholinergic spike responses after optogenetic stimulation. (C) Distribution of the significance values of the SALT statistical test (H-index) for

all recorded neurons (blue, $p < 0.01$, tagged cholinergic neurons; grey, $p > 0.01$, untagged neurons). (D) Left, example spike raster (top) and PETH (bottom) of an optogenetically tagged BFCN responding to 20 Hz blue laser light stimulation. Right, average spike waveform of the same BFCN on the four tetrode channels (blue, average light-evoked spikes; black, average spontaneous spikes; grey, all spikes). (E) Left, example of spike clusters plotted in feature space from a recording session. Right, average spike waveform of the recorded neurons on each tetrode channel.

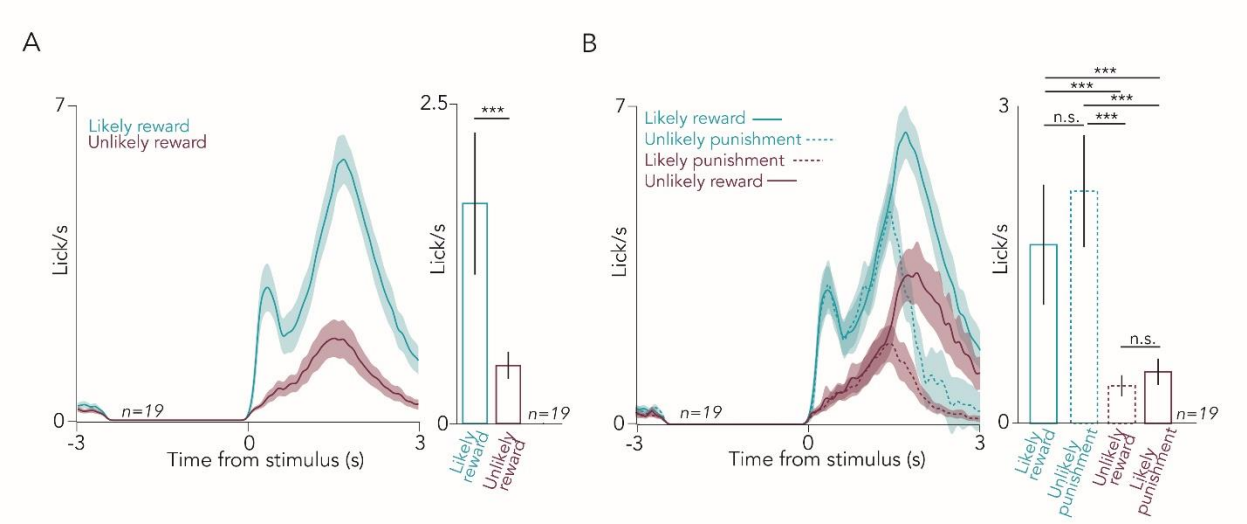

Figure S3. Behavioral performance during tetrode recordings, Related to Figure 3. (A) Left, average PETHs of lick responses of all sessions of all animals (n = 19 sessions). Right, statistical comparison of anticipatory lick rates in the response window (RW) in likely reward and unlikely reward trials (median ± SE of median, n = 19 sessions; ***, $p < 0.001$, $p = 0.00034$, Wilcoxon signed-rank test). (B) Left, average PETHs of lick responses of all sessions of all animals (n = 19 sessions), partitioned based on the four possible outcomes: expected or surprising reward, expected or surprising punishment. Right, statistical comparison of anticipatory lick rates in the RW, with respect to the four possible outcomes (median ± SE of median, n = 19 sessions; ***, $p < 0.001$, n.s., $p > 0.05$; from top to bottom, $p = 0.00034$, $p = 0.00084$, $p = 0.00021$, $p = 0.8721$, $p = 0.00025$ and $p = 0.9512$, Wilcoxon signed-rank test).

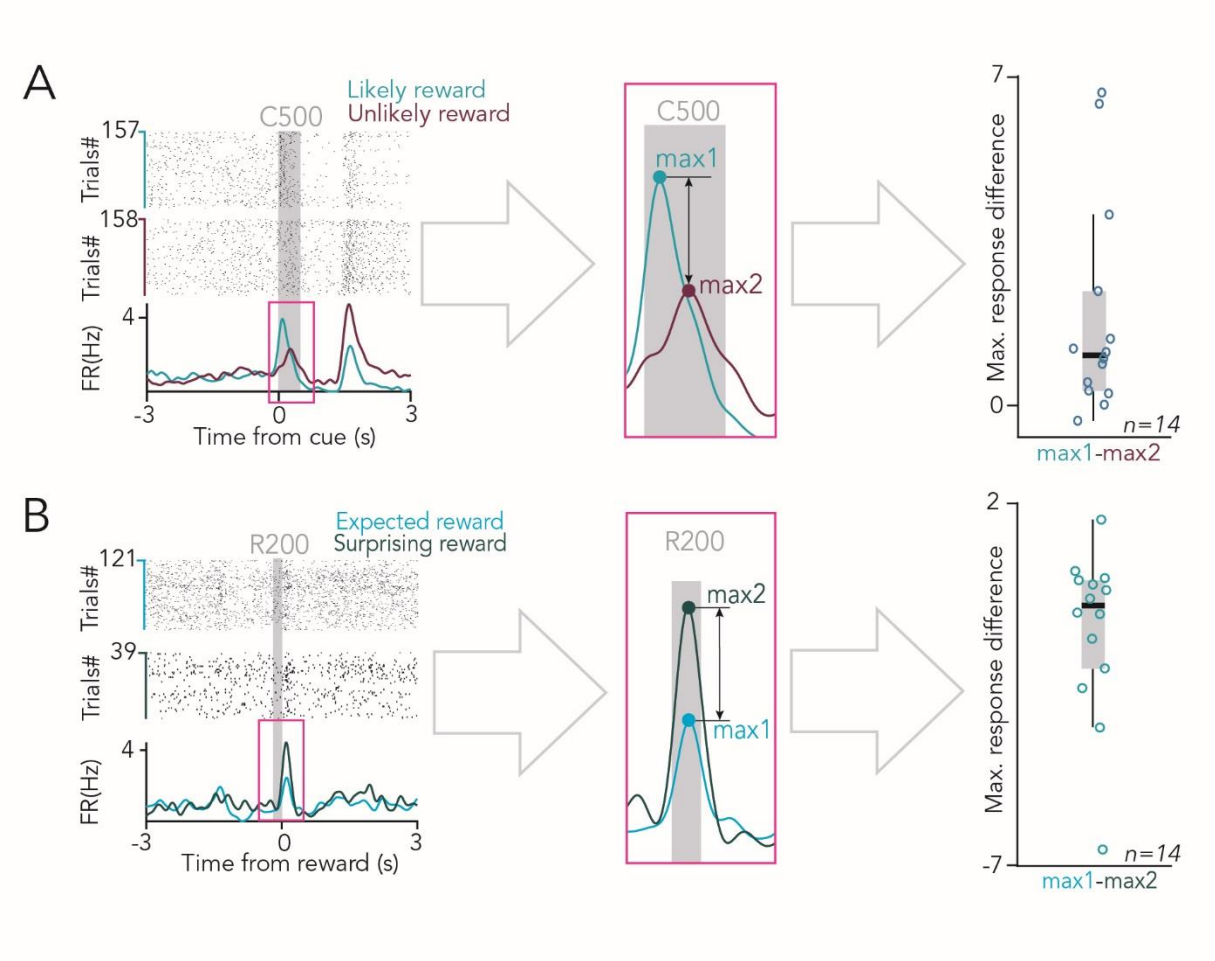

Fig S4. Schematic illustration of quantifying neuronal responses, Related to Figure 4. (A) Schematic illustration of quantifying neuronal response to conditioned stimuli. Peak firing rate of the PETH and total spike number were calculated in a 500 ms window after cue presentation (C500), based on the range of response latencies (see Results). (B) Schematic illustration of quantifying neuronal responses to reward. Peak firing rate of the PETH and total spike number were calculated in a 200 ms window after reward delivery (R200), based on the range of response latencies (see Results). Both maximal response and average firing rate (FR) were statistically compared using Wilcoxon signed-rank test. Box-whisker plots show median, inter-quartile range and non-outlier range.

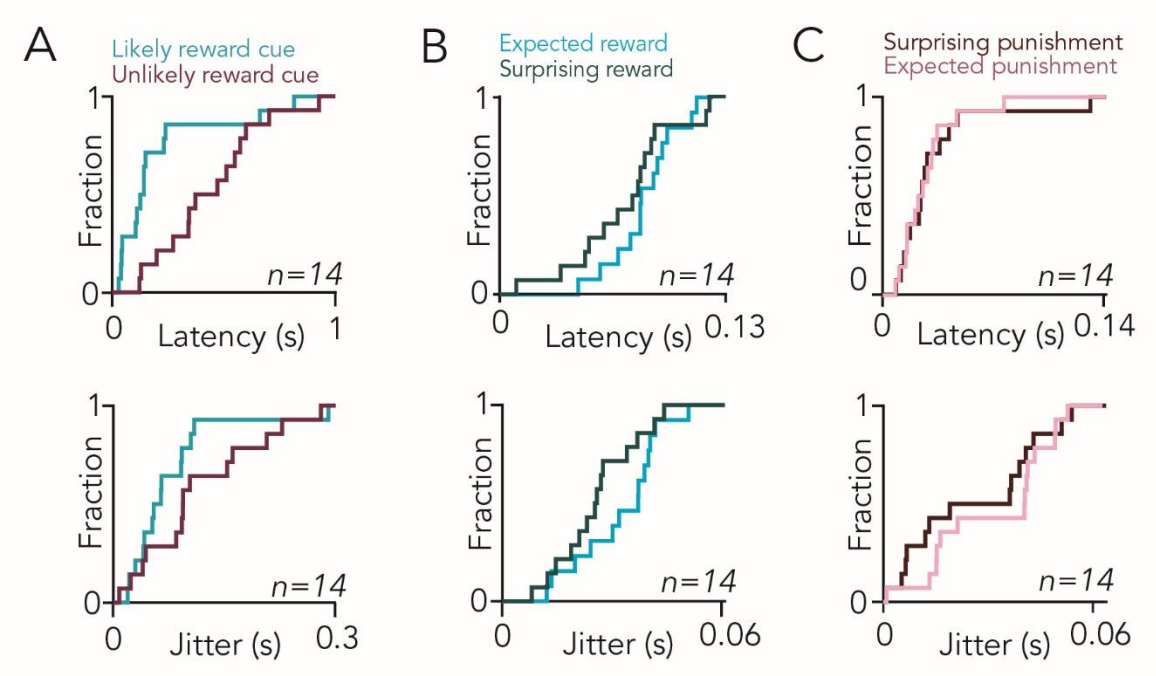

Fig S5. Latency and jitter of identified cholinergic neurons, Related to Figure 4. (A) Top, Cumulative histogram of the peak response latencies of BFCNs (n = 14) after cue presentation. Bottom, Cumulative histogram of the jitter of cholinergic spike responses after cue presentation (n = 14 BFCNs). (B) Top, Cumulative histogram of the peak response latencies of BFCNs (n = 14) after reward. Bottom, Cumulative histogram of the jitter of cholinergic spike responses after reward (n = 14 BFCNs). (C) Top, Cumulative histogram of the peak response latencies of BFCNs (n = 14) after punishment. Bottom, Cumulative histogram of the jitter of cholinergic spike responses after punishment (n = 14 BFCNs).

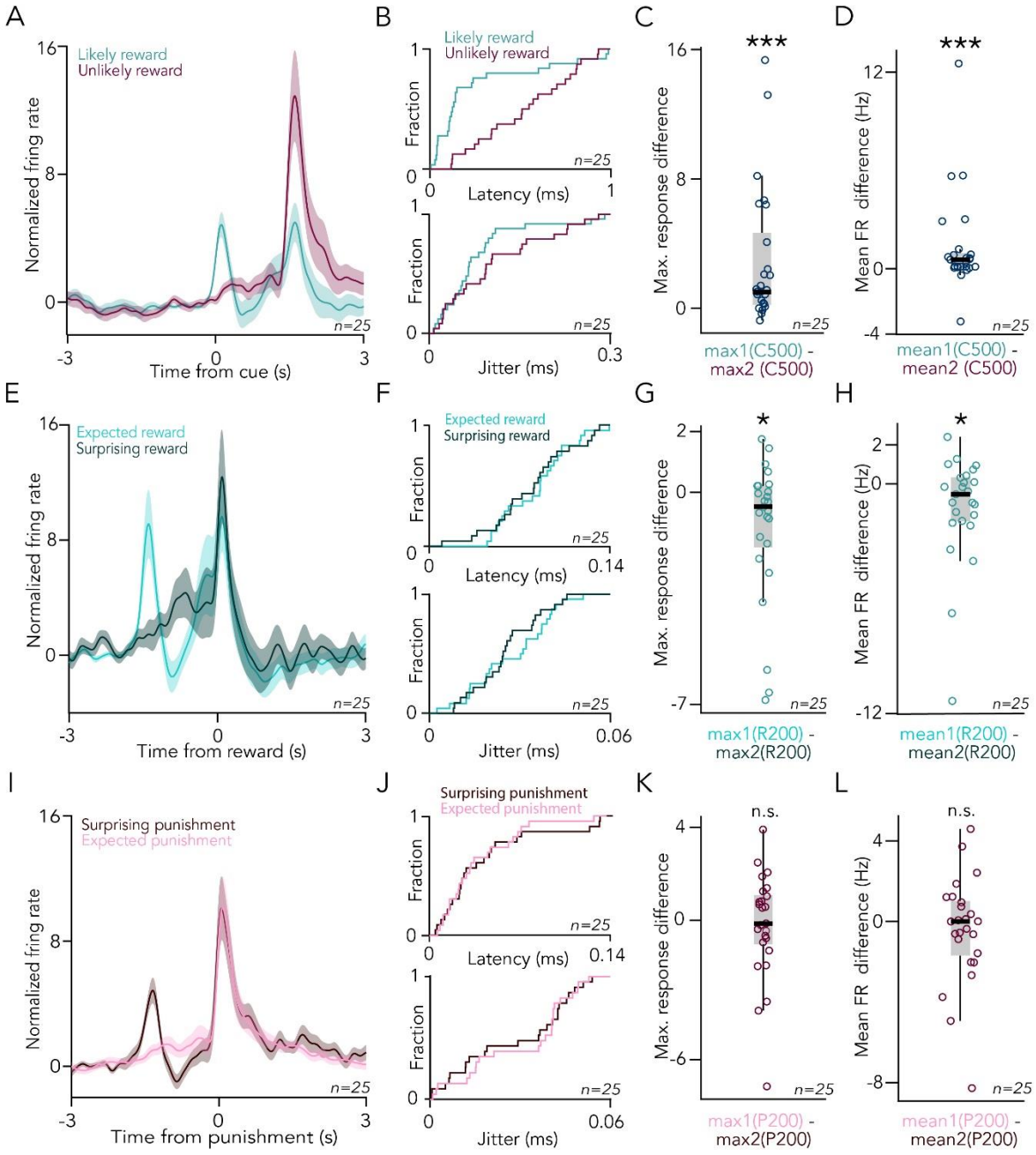

Figure S6. Cholinergic neurons respond more to reward-predicting cues and surprising reward, Related to Figure 4. (A) Average cue-aligned PETHs of identified BFCNs (errorshade, mean ± SE; n = 25), aligned to cue onset, separately for the cues predicting likely reward (turquoise) vs. unlikely reward (purple). (B) Top, Cumulative histogram of the peak response latencies of BFCNs (n = 25) after cue presentation. Bottom, Cumulative histogram of the jitter of cholinergic spike responses after cue presentation (n = 25 BFCNs).

(C) Difference in peak response after cues predicting likely reward and those predicting unlikely reward. ***, $p < 0.001$, $p = 0.0001743$, Wilcoxon signed-rank test, $n = 25$. (D) Difference in mean firing rate after cues predicting likely reward and those predicting unlikely reward. ***, $p < 0.001$, $p = 0.000664$, Wilcoxon signed-rank test, $n = 25$. (E) Average reward-aligned PETHs of identified BFCNs (errorshade, mean ± SE; $n = 25$), separately for rewards after the cue predicting likely reward (light turquoise, expected reward) vs. after the cue predicting unlikely reward (dark turquoise, surprising reward). (F) Top, Cumulative histogram of the peak response latencies of BFCNs ($n = 25$) after reward delivery. Bottom, Cumulative histogram of the jitter of cholinergic spike responses after reward delivery ($n = 25$ BFCNs). (G) Difference in peak response after expected and surprising rewards. *, $p < 0.05$, $p = 0.02465$, Wilcoxon signed-rank test, $n = 25$. (H) Difference in mean firing rate after expected and surprising rewards. *, $p < 0.05$, $p = 0.03704$, Wilcoxon signed-rank test, $n = 25$. (I) Average punishment-aligned PETHs of identified BFCNs (errorshade, mean ± SE; $n = 25$), separately for punishments after the cue predicting likely reward (dark purple, surprising punishment) vs. after the cue predicting unlikely reward (light purple, expected punishment). (J) Top, Cumulative histogram of the peak response latencies of BFCNs ($n = 25$) after punishment delivery. Bottom, Cumulative histogram of the jitter of cholinergic spike responses after punishment delivery ($n = 25$ BFCNs). (K) Difference in peak response after expected and surprising punishments. n.s., $p > 0.05$, $p = 0.94637$, Wilcoxon signed-rank test, $n = 25$. (L) Difference in mean firing rate after expected and surprising punishments. n.s., $p > 0.05$, $p = 0.54851$, Wilcoxon signed-rank test, $n = 25$. All box-whisker plots in the figure show median, inter-quartile range and non-outlier range.

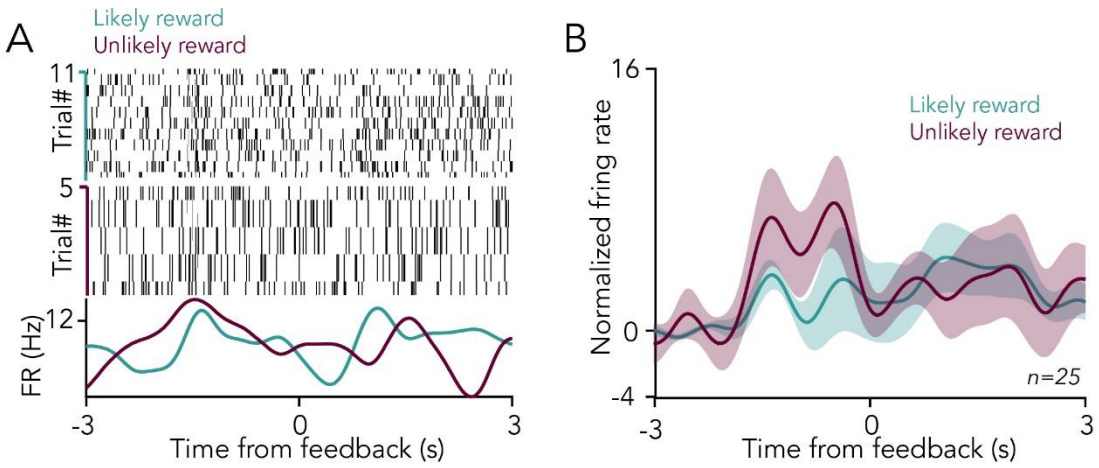

Figure S7. Cholinergic neurons do not respond to outcome omissions, Related to Figure 4. (A) Example spike raster and PETH of a BFCN aligned to the expected time of omitted feedback. **(B)** Average PETH of all BFCNS (errorshade, mean ± SE; n = 25) with the same alignment.

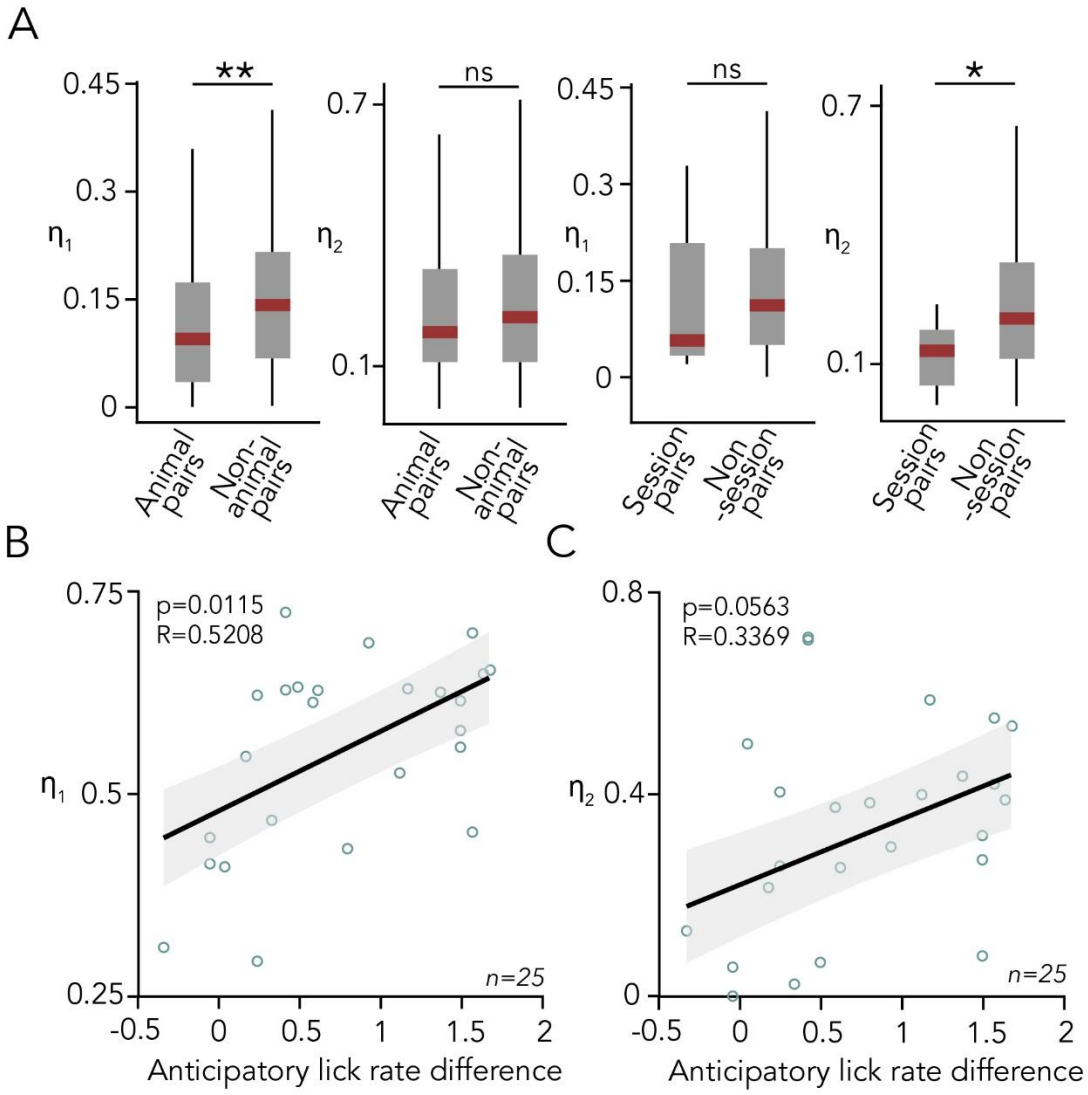

Figure S8. Prediction error parameters reveal behavioral correlations, Related to figure 5. (A) Left, difference of best-fit η_1 and η_2 parameters between BFCNs recorded in the same animal vs. in different mice. Right, difference of best-fit η_1 and η_2 parameters between BFCNs recorded in the same recording session vs. in different sessions. *, $p < 0.05$; **, $p < 0.01$, n.s., $p > 0.05$, Mann-Whitney U-test, n = 147 animal pairs, n = 153 non-animal pairs, n = 7 session pairs, n = 293 non-session pairs; exact p values, p = 0.00199, p = 0.2496, p = 0.5725, p = 0.04677, respectively. Box-whisker plots show median, inter-quartile range and non-outlier range. **(B)** Correlation between the best-fit η_1 parameter and the difference in anticipatory lick rate after likely reward vs. unlikely reward cues (R = 0.5208, Pearson's correlation coefficient; p = 0.0115, linear regression, F-test). Correlation between the best-fit η_2 parameter and the

difference in anticipatory lick rate after likely reward vs. unlikely reward cues (R = 0.3369, Pearson's correlation coefficient; p = 0.0563, linear regression, F-test).

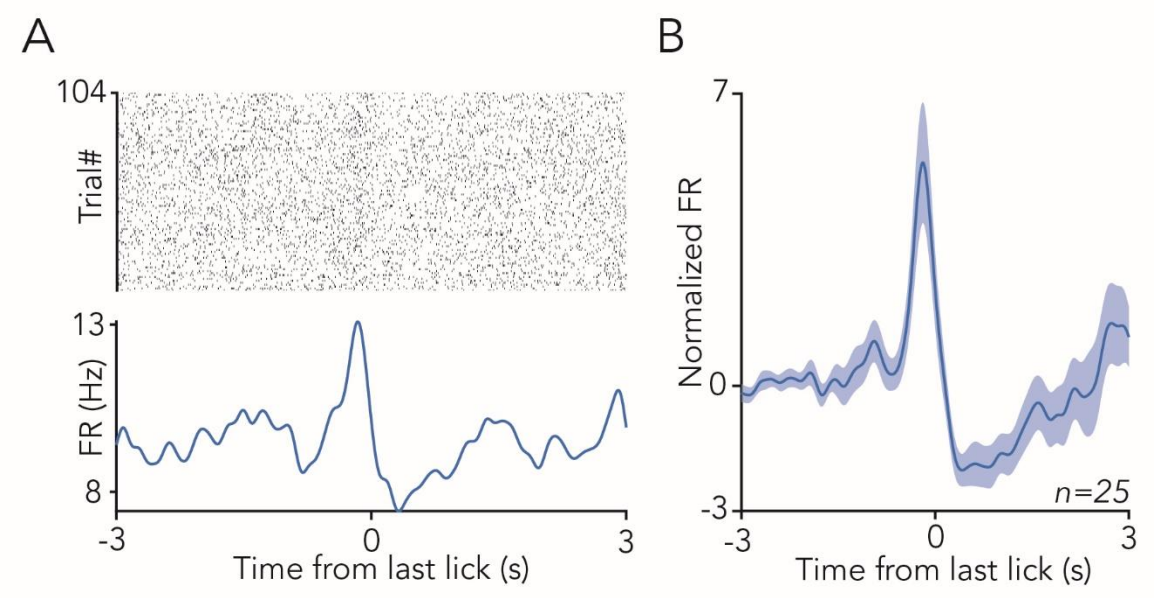

Figure S9. Cholinergic activity aligned to the last lick before the foreperiod, Related to Figure 6. (A) Raster plot (top) and PETHs (bottom) of an example cholinergic neuron aligned to the last lick before the foreperiod. (B) Average PETH of all cholinergic neurons (errorshade, mean ± SE, n = 25) aligned to the last lick before the foreperiod. FR, firing rate.

nature communications hangya.balazs_256_24

Article

https://doi.org/10.1038/s41467-024-48755-7

Parvalbumin-expressing basal forebrain neurons mediate learning from negative experience

Received: 17 April 2023

Accepted: 11 May 2024

Published online: 07 June 2024

Check for updates

Panna Hegedüs[1,2,4], Bálint Király[1,4], Dániel Schlingloff[1,4], Victoria Lyakhova[1,2], Anna Velencei[1], Írisz Szabó[1], Márton I. Mayer[3], Zsofia Zelenak[1], Gábor Nyiri[3] & Balázs Hangya[1]

Parvalbumin (PV)-expressing GABAergic neurons of the basal forebrain (BFPVNs) were proposed to serve as a rapid and transient arousal system, yet their exact role in awake behaviors remains unclear. We performed bulk calcium measurements and electrophysiology with optogenetic tagging from the horizontal limb of the diagonal band of Broca (HDB) while male mice were performing an associative learning task. BFPVNs responded with a distinctive, phasic activation to punishment, but showed slower and delayed responses to reward and outcome-predicting stimuli. Optogenetic inhibition during punishment impaired the formation of cue-outcome associations, suggesting a causal role of BFPVNs in associative learning. BFPVNs received strong inputs from the hypothalamus, the septal complex and the median raphe region, while they synapsed on diverse cell types in key limbic structures, where they broadcasted information about aversive stimuli. We propose that the arousing effect of BFPVNs is recruited by aversive stimuli to serve crucial associative learning functions.

Basal forebrain (BF) nuclei in the ventral part of the forebrain are defined by the presence of cholinergic projection neurons (BFCNs)[1–3]. However, there are approximately five times more GABAergic than cholinergic neurons in the BF[4–6], of which the parvalbumin-expressing population was shown to project to several cortical and subcortical target areas[7–9].

These BFPVNs were shown to be important regulators of cortical gamma oscillations[10,11] and to promote wakefulness and arousal through their local[12] and distant projections[13]. However, a number of observations point to the direction that BFPVNs might also play a role in awake behaviors, and associative learning in particular. First, similarly to BFCNs, degeneration of BFPVNs was also linked to cognitive decline in Alzheimer's disease[14] and during physiological aging[15–17]. Second, non-selective lesions of the BF revealed a more substantial attentional and learning deficit in rodents compared to selective cholinergic lesions[18–21] and a study of selective BF GABAergic ablation revealed a deficit in eyeblink conditioning[22]. Third, a line of studies demonstrated that non-cholinergic BF neurons responded phasically to behaviorally salient stimuli irrespective of their valence[23], where stronger responses[24] or higher pre-stimulus activity[25] predicted faster and more precise decision speed during operant conditioning. These studies raise the possibility that BFPVNs might also play a role in associative learning.

To address this question, we performed in vivo electrophysiological recordings with optogenetic tagging and bulk calcium measurements by fiber photometry of PV-expressing neurons of the rostral HDB nucleus of the BF (referred to as BFPVNs hereinafter), while mice were performing a probabilistic Pavlovian conditioning

[1]Lendület Laboratory of Systems Neuroscience, HUN-REN Institute of Experimental Medicine, H-1083 Budapest, Hungary. [2]János Szentágothai Doctoral School of Neurosciences, Semmelweis University, H-1085 Budapest, Hungary. [3]Laboratory of Cerebral Cortex Research, HUN-REN Institute of Experimental Medicine, H-1083 Budapest, Hungary. [4]These authors contributed equally: Panna Hegedüs, Bálint Király, Dániel Schlingloff.
e-mail: hangya.balazs@koki.hun-ren.hu

task[26]. We found that BFPVNs showed rapidly rising, brief (i.e., phasic) responses to punishment, whereas rewards, as well as sensory stimuli that predicted reward or punishment, elicited comparably smaller and delayed responses. These observations revealed that BFPVN activity correlated with behavioral reinforcement, and punishment in particular, suggesting that these neurons signaled negative behavioral outcome to other parts of the brain. In accordance, optogenetic inhibition of BFPVNs during punishments in a Pavlovian conditioning task impaired the ability of mice to form stimulus-outcome associations, demonstrating that HDB BFPVNs encode outcome-related information crucial for associative learning.

We performed cell type-specific anterograde and monotranssynaptic retrograde tracing experiments to reveal long-range afferent and efferent connections of HDB BFPVNs. We demonstrated that they received dense inputs from the lateral hypothalamus, the septal complex and the median raphe nucleus, and innervated important nodes of the limbic system crucial for contextual learning, including the medial septum, the hippocampal formation and the retrosplenial cortex[27–32]. They synapsed on a range of cell types including cholinergic and PV-expressing neurons in the BF, as well as interneuron types of the neocortex and hippocampus, as revealed by light- and electron microscopy and in vitro acute slice recordings. Finally, by performing bulk calcium measurements of HDB BFPVN fibers in target areas, we demonstrated that these neurons broadcast outcome-related information to multiple downstream areas. These data suggest that BFPVNs of the HDB mediate learning from negative reinforcement.

Results

Identified BFPVNs of the HDB show phasic responses to punishment

We trained PV-Cre mice ($n = 4$) on an auditory probabilistic Pavlovian conditioning task (Hegedüs et al., 2021) to examine how HDB BFPVNs respond to cues predicting reward or punishment with different probabilities and to the reinforcement itself. Mice were head restrained and two tones of different pitches were presented in a randomized order (Fig. 1a); Cue 1 predicted reward with higher probability (water drop; 80% reward, 10% punishment, 10% omission), whereas Cue 2 predicted punishment with higher probability (air puff; 65% punishment, 25% reward, 10% omission). This experimental design enabled us to examine how BFPVNs respond to surprising and expected reward or punishment (unconditioned stimuli, US) as well as their predicting cues (conditioned stimuli, CS). Mice learned these task contingencies, demonstrated by significantly higher anticipatory lick rate in response to Cue 1 that predicted likely reward (Fig. 1b–e).

To examine how individual BFPVNs responded to conditioned and unconditioned stimuli, we injected AAV2.5-EF1a-DiO-hChR2(H134R)-eYFP.WPRE.hGh into the HDB region of PV-Cre mice and performed extracellular multiple single-cell recordings combined with optogenetic tagging of HDB BFPVNs ($n = 36$) by implanting a head-mounted micro-drive housing moveable tetrode electrodes and an optical fiber (Fig. 1f–j, Fig. S1; specific expression verified in ref. 33, Fig. S15). Electrode placement in the HDB was verified by histological reconstruction at the end of the experiment (Fig. 1f, g). We found that BFPVNs responded with a gradual, ramp-like activation to cue onset ($n = 12/36$, 33%; Fig. 2a, b) irrespective of the predictive value of the cues (Fig. S2) and with a small but significant activation to the delivery of water reward ($n = 14/36$, 39%; Fig. 2c, d). In contrast, they responded to punishment with fast, phasic activation, homogeneously detectable in most ($n = 27/36$, 75%) identified BFPVNs (Fig. 2e, f, Table S4). BFPVN punishment responses showed adaptation, as they decreased in magnitude as a function of repeated air puff presentations; however, they remained present in late trials of the training sessions (Fig. 2g–i). BFPVN responses to reward and punishment were not modulated by surprise (Fig. S2), unlike what we found in the case of reward-elicited responses of BFCNs in the same task[34,35].

An unbiased clustering approach applied on the response patterns of $n = 685$ HDB neurons revealed two clusters of neurons ($n = 134$ and 193) exhibiting strong punishment and smaller reward responses similar to the identified HDB BFPVNs, which indeed largely fell in these clusters (29/36, 80%; Fig. S3). A distinct group ($n = 97/685$, 14%) showed suppression of firing after reinforcement, while one cluster ($n = 48/685$, 7%) corresponded to putative cholinergic neurons based on their fast responses to air puffs[25,36] and slower responses to rewards and reward-predicting stimuli[35], completed with a mostly non-responsive cluster of cells ($n = 213/685$, 31%).

We also contrasted HDB BFPVNs with another prominent GABAergic population of the basal forebrain, the somatostatin-expressing neurons (BFSOMNs), by performing bulk calcium measurements from the HDB of task-performing SOM-Cre mice injected with AAV2/9.CAG.Flex.GCaMP6s.WPRE.SV40 (Fig. S4). BFSOMNs showed distinct responses compared to BFPVNs, with comparable responses to reward and punishment modulated by outcome expectations, and a phasic response to reward-predicting stimuli.

We examined the electrophysiological properties of punishment responsive BFPVNs and found that half of these neurons were burst firing. Both burst spikes and single spikes were time-locked to punishment presentation, but bursting BFPVNs were more punishment-activated ($n = 17/18$, 94%) than non-bursters ($n = 10/18$, 56%; Fig. S5).

HDB BFPVNs respond to aversive stimuli across sensory modalities

We asked whether HDB BFPVNs respond to aversive stimuli in multiple sensory modalities. Therefore, we tested their responses to air puffs characterized by tactile sensation and loud noise[26] as well as foot shock and predator (fox) odor by performing bulk calcium measurements from the HDB of mice expressing GCaMP6s in BFPVNs. Since these stimuli are innately aversive to mice, we expected that they evoke neural responses already at first encounters, similar to what we found previously in BFCNs[25].

BFPVNs responded to air puffs as early as during training sessions when punishments were introduced, and even when only the first punished trials were considered (Fig. 3a). Like air puffs, foot shocks and the presence of fox odor also potently activated BFPVNs, suggesting that they convey information that generalizes over different aversive events (Fig. 3b, c). These responses also occurred already at the first encounter. Activation by air puffs, electrical shocks and predator odor indicate that BFPVN responses to aversive stimuli are multimodal, and not solely driven by a single sensory modality.

Optogenetic inhibition of HDB BFPVNs during punishment impairs association learning

To assess whether the robust responses of BFPVNs to punishment represent an aversive signal that induces avoidance behavior, we tested whether optogenetic activation of BFPVNs elicited conditioned place aversion. We injected either AAV2.5-EF1a-DiO-hCHR(H134R)-eYFP.WPRE.hGh (n = 8) or AAV2.5-EF1a-DiO-eYFP.WPRE.hGh ($n = 10$ used as controls) viral vectors into the HDB of PV-Cre mice and performed a conditioned place aversion test. Mice were placed in an arena, the two sides of which were separated by a small open gate and differentiated by dotty and striped sidewall patterns. After habituation, BFPVNs were optogenetically stimulated in one side of the arena and different behavioral parameters such as total distance traveled, speed, time spent on either side of the arena, grooming, digging, freezing, and rearing were recorded and analyzed. We found that stimulation of HDB BFPVNs did not elicit aversive (or appetitive) behavior, as channelrhodopsin-expressing mice did not avoid the stimulated side, nor did they express any other behavioral differences

https://doi.org/10.1038/s41467-024-48755-7

hangya.balazs_256_24

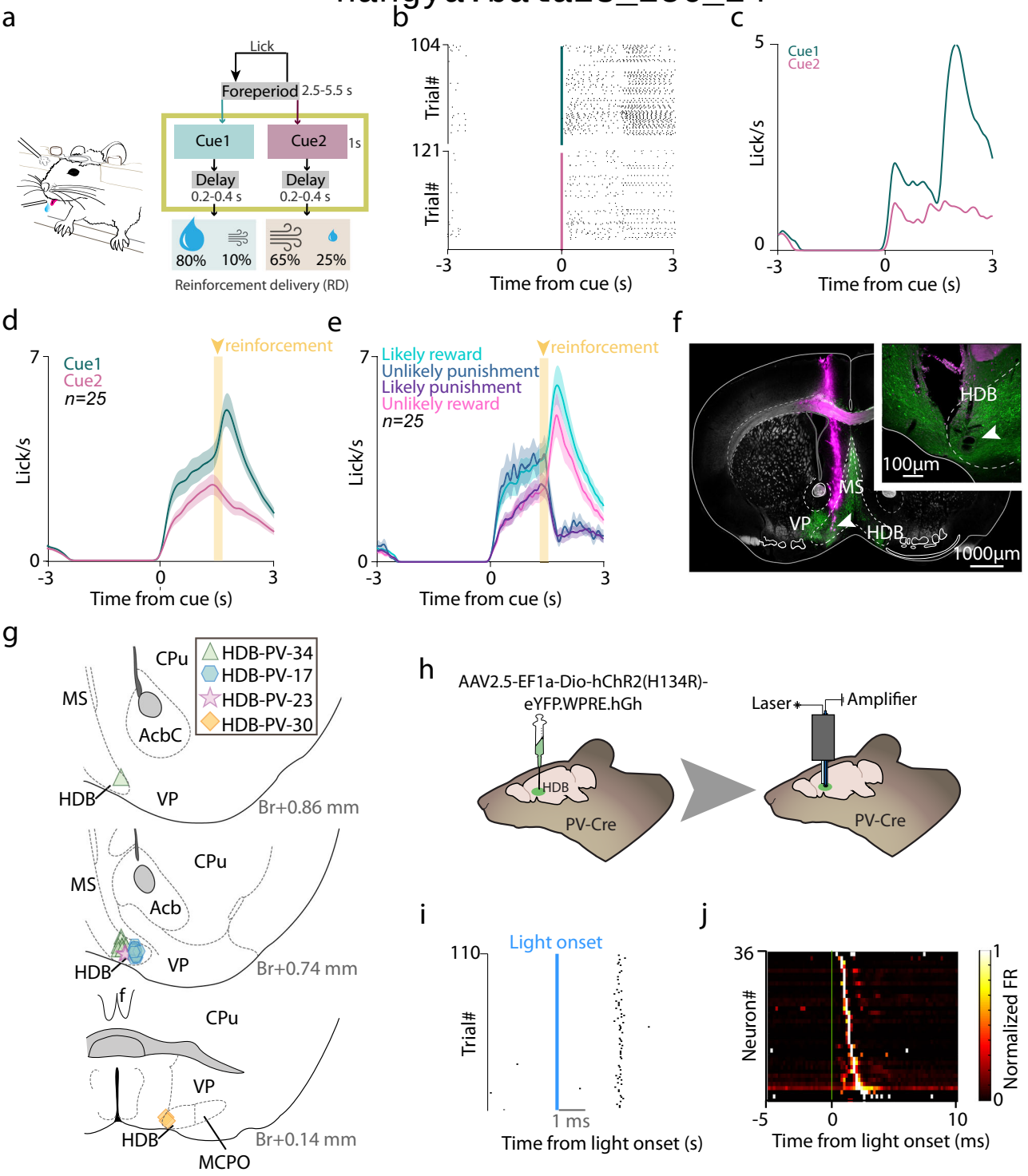

compared to control animals, and they did not show behavioral signs of stress (Fig. S6).

Next, to causally test the behavioral function of the punishment-elicited HDB BFPVN response in learning, we tested whether the optogenetic suppression of BFPVNs during the time of air puff delivery affected the learning ability of mice. We injected the HDB of PV-Cre mice bilaterally with AAV2.9-CAG-Flex-ArchT-GFP ($n = 6$, ArchT group) or AAV2.9-CAG-Flex -GFP ($n = 8$, control group; Fig. 4a). A one-second-long continuous laser pulse was applied to HDB BFPVNs through bilaterally implanted optic fibers starting at the same time as punishment presentation while mice were trained on the auditory Pavlovian conditioning task. Both ArchT-expressing and control mice developed anticipatory licking in response to the conditioned stimuli. However, while control mice learned to suppress licking after Cue 2 which signaled likely punishment (similar to our initial cohort, see Fig. 1b–e), lick rates of ArchT-expressing mice remained high after both cues (Fig. S7) and thus they did not show differential anticipatory licking after the CS (Fig. 4b, c). Receiver operating characteristic analysis (ROC; see Methods) revealed a significant difference between ArchT-expressing and control mice in a half-second window before reinforcement delivery (from about 0.6 to 1.1 s after cue onset, Fig. 4b, c, Fig. S7). Control mice not only responded with a higher anticipatory lick rate to Cue 1 predicting likely reward, but their responses were significantly faster compared to those after Cue 2 predicting likely punishment.

Fig. 1 | Head-fixed probabilistic Pavlovian conditioning combined with tetrode recording and optogenetic tagging. a Schematic diagram of the task protocol. After a variable foreperiod, in which the animals were not allowed to lick, they were presented with two cues, either predicting likely reward or likely punishment; reinforcement was preceded by a short, variable delay period. Created using Mathis, M. (2020), Classical Conditioning Mouse, Zenodo, https://doi.org/10.5281/zenodo.3925907, under Creative Commons 4.0 license (https://creativecommons.org/licenses/by/4.0/). The original image was not modified. **b** Raster plot of mouse licking times aligned to stimulus (cue) onset from an example session, showing higher anticipatory lick rate in response to the reward-predicting cue (Cue 1). **c** Lick rates (peri-event time histograms, PETH) aligned to stimulus onset from the same example session. **d** Average lick rates of all recording sessions in which BFPVNs were identified ($n = 25$ sessions; errorshade, SEM). **e** Average lick rates of the same $n = 25$ sessions as in (**d**), partitioned according to the four possible outcomes (errorshade, SEM). **f** Histological reconstruction of the tetrode track in the HDB. Green, ChR2-eYFP; magenta, DiI. Top right, magnified image of the electrolytic lesion site (white arrowhead) from a different section, indicating the tip of the electrodes. MS, medial septum; VP, ventral pallidum. Repeated in $n = 4$ mice. **g** Locations of the recorded BFPVNs based on histological reconstruction. Different markers correspond to different mice. Numbers show antero-posterior positions relative to Bregma. **h** Schematic illustration of viral injections, extracellular tetrode recordings and optogenetic tagging in mice. Created using Kennedy, A. (2020), Mouse brain silhouette, Zenodo, https://doi.org/10.5281/zenodo.3925919, under Creative Commons 4.0 license (https://creativecommons.org/licenses/by/4.0/). The original image was modified by adding illustrations of a syringe and an electrophysiological drive as well as additional legends. **i**, Example raster plot of spike times aligned to photostimulation pulses of an optogenetically identified BFPVN. **j** Firing rate (color-coded PETH) of all optogenetically identified BFPVNs aligned to photostimulation onset.

This reaction time difference was also abolished by suppressing HDB BFPVNs in the ArchT group of mice (Fig. 4d, e). Thus, optogenetic suppression of HDB BFPVNs prevented mice from associating higher value with the cue that predicted likely reward.

BFPVNs of the HDB receive inputs from aversion-coding nuclei and send projections to the limbic system

We used mono-transsynaptic rabies tracing to identify brain areas and cell types that provide synaptic input to HDB BFPVNs. We injected Cre-dependent helper virus and G protein-deleted EnvA-pseudotyped rabies virus into the HDB of PV-Cre mice ($n = 3$; Fig. 5). Long-range input cells were distributed throughout the whole brain, suggesting a high level of input convergence onto HDB BFPVNs (Table S1.). The hypothalamus provided the most inputs (lateral hypothalamus, 33.1%, fraction of total input neurons; preoptic area, 7.6%), followed by the lateral septum (13.8%). Neighboring areas of the basal forebrain, such as the medial septum (MS, 10.8%) and the vertical limb of the diagonal band of Broca (VDB, 6.4%) also contained substantial number of input cells, together with the nucleus accumbens (3.5%), while the median raphe region (MRR) provided the highest number of synaptic inputs from the brainstem (3.9%, Fig. 5e). In case of one mouse, we performed unilateral helper and rabies virus injection to the HDB. In this animal, the presynaptic neurons were predominantly ipsilateral (93.7%) to the starter population, and the pattern of anatomical connectivity was similar for ipsilateral and contralateral projections.

Because MRR has an important role in mediating negative experience, we further investigated its cell types that provided inputs to HDB BFPVNs. MRR vesicular glutamate transporter 2 (vGluT2) expressing cells that are key regulators of negative experience are known to target BFPVNs[37]. However, MRR has several other types of cells including serotonergic (5HT) neurons, vGluT3-expressing glutamatergic neurons, those that express both serotonin and vGluT3, and GABAergic neurons as well[38]. We found that most of the input cells of BFPVNs were vGluT3-expressing glutamatergic neurons (59%, $n = 2$ mice) and out of these cells only a small fraction was serotonergic as well (5-HT-immunopositive, 2% of all inputs from MRR, Fig. 5f, g). We found no input cells that were only 5HT-immunopositive. The rest (41%) of the input cells (that were immunonegative for both vGluT3 and 5-HT) included vGluT2 cells that are known to target BFPVNs and may also include some MRR GABAergic neurons. These suggest that MRR targets BFPVNs with both vGluT2- and vGluT3-expressing glutamatergic neurons, both of which play a key role in the brainstem control of negative experience[37,39].

Next, we examined the downstream targets of HDB BFPVNs by performing a series of anterograde tracing experiments. We injected AAV2.9-CAG-Flex-eGFP viral vectors bilaterally in the HDB of PV-Cre mice to visualize HDB BFPVN axons using fluorescent microscopy ($n = 3$; Fig. 6a). We found that the majority of the projecting axons targeted the medial septum−diagonal band of Broca area, the hippocampus and the retrosplenial cortex (RSC; Fig. 6a), which are important regions of the limbic system. Additionally, other limbic structures such as the medial mammillary nucleus, the supramammillary nucleus and the paratenial thalamus were also targeted by HDB BFPVNs. A smaller extent of projections was received by the prefrontal cortex (medial orbital and infralimbic cortices), the lateral septum and the MRR. By using correlated electron and light microscopy, we demonstrated that HDB BFPVNs established symmetrical synaptic contacts with PV-expressing and cholinergic neurons in the medial septum, with calretinin-expressing (CR+) and PV-expressing neurons in the hippocampal CA1 region and with PV-expressing neurons in the retrosplenial cortex (Fig. 6b–d).

HDB BFPVNs broadcast negative reinforcement signals to multiple downstream targets

Finally, we tested whether HDB BFPVNs send signals upon aversive US in a target-specific manner or distribute similar information to multiple downstream areas. To address this, we expressed GCaMP6s in PV-Cre mice ($n = 12$) by injecting AAV2/9.CAG.Flex.GCaMP6s.WPRE.SV40 bilaterally in the HDB and recorded their bulk calcium signals both at the cell body level within the HDB and in axonal projections in their main target areas such as the MS, the hippocampal CA1 and the retrosplenial cortex (Fig. 7a). We recorded bulk calcium signals via fiber photometry while mice performed the Pavlovian conditioning task.

First, we confirmed that somatic calcium concentrations showed similar responses to air puff punishments to what we observed when single neuron spiking responses of BFPVNs were analyzed (Fig. 7b, c, Fig. S8). Next, we found that BFPVN projections showed phasic punishment responses in all three target areas investigated (Fig. 7d–i), arguing for a widespread broadcast-type function of HDB BFPVNs.

Next, to test the physiological impact of these BFPVN projections on target neurons, we performed channelrhodopsin-assisted circuit mapping experiments in the dorsal CA1, medial septum and retrosplenial cortex (Fig. 8a–c). These experiments confirmed all connections revealed by EM (PV+ cells in RSC, CA1 and MS, CR+ in the hippocampus and ChAT+ cells in the MS; Fig. 8d–f). Furthermore, we found that BFPVN inhibitory inputs to the RSC showed smaller amplitude compared to the MS and CA1 as well as longer latency to peak and slower rise time (Fig. 8g). Importantly, when we examined the short-term synaptic plasticity of BFPVN inputs, we found that inputs to the RSC neurons were characterized by short-term synaptic facilitation, while MS and CA1 neurons showed strong short-term synaptic depression in a frequency-dependent manner (Fig. 8h, i). These results

https://doi.org/10.1038/s41467-024-48755-7

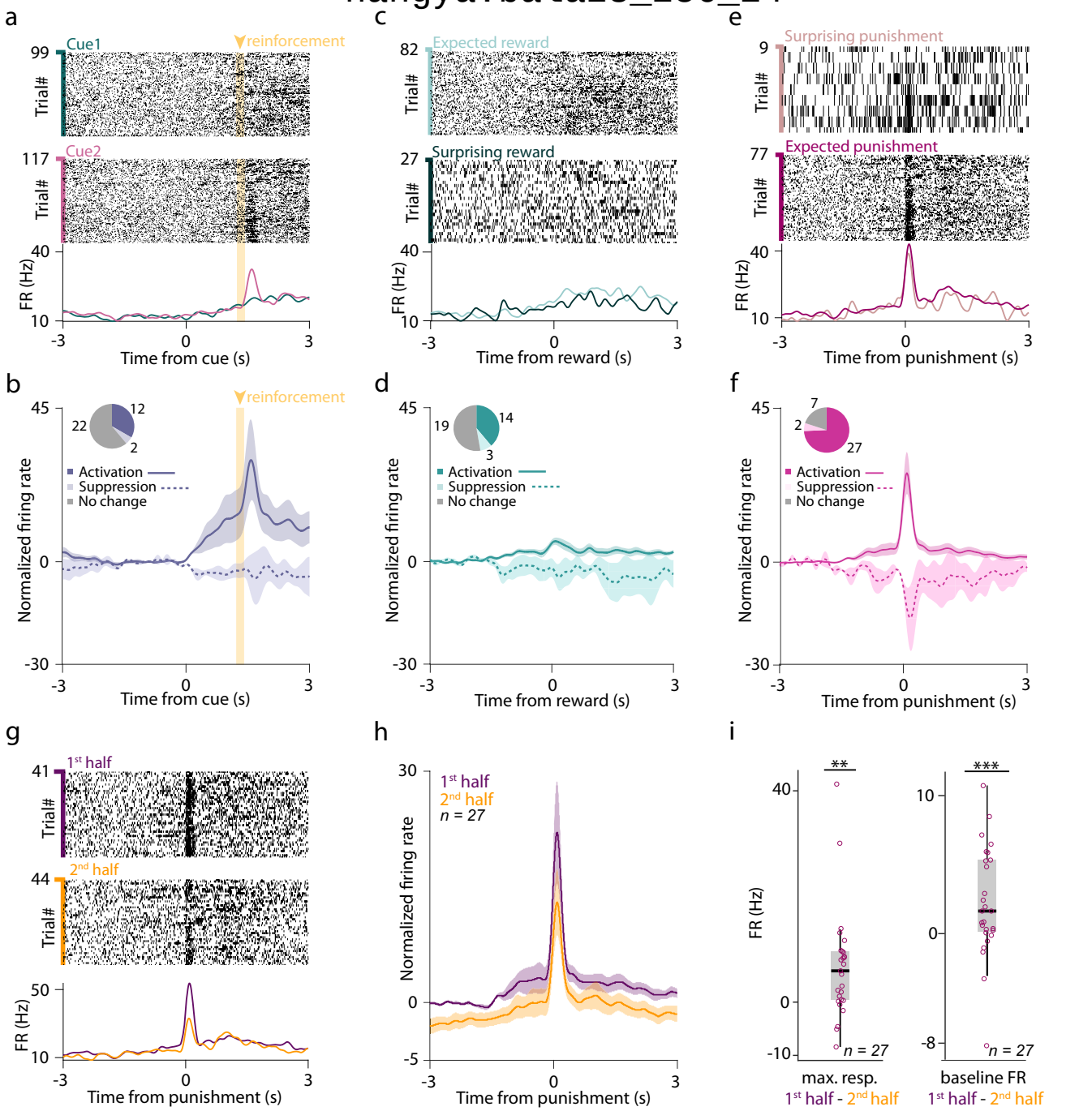

Fig. 2 | BFPVNs of the HDB show strong responses to punishment. a Raster plots and PETHs of the spike times aligned to cue onset of an example BFPVN. Trials are partitioned by the cue types (Cue 1 predicting likely reward / unlikely punishment, top, green; Cue 2 predicting likely punishment / unlikely reward, middle, purple). **b** Average PETH of BFPVN activity aligned to cue onset (activation, $n = 12$, solid line; inhibition, $n = 2$, dashed line; see inset for distribution of responses; errorshade, SEM). **c** Example PETH of the same BFPVN as in (**a**) aligned to reward delivery. Trials are partitioned into expected (following Cue 1) and surprising (following Cue 2) reward trials. **d** Average PETH of BFPVN activity aligned to reward delivery (activation, $n = 14$, solid line; inhibition, $n = 3$, dashed line; see inset for distribution of responses; errorshade, SEM). **e** Example PETH of the same BFPVN as in (**a**) aligned to punishment delivery. Trials are partitioned to surprising (following Cue 1) and expected (following Cue 2) punishment trials. **f** Average PETH of BFPVN activity aligned to punishment delivery (activation, $n = 27$, solid line; inhibition, $n = 2$, dashed line; see inset for distribution of responses; errorshade, SEM). **g** Spike raster plots and PETH aligned to punishment delivery for an example BFPVN. Top, trials in the first half of the session; middle, trials in the second half of the session; bottom, PETH. **h** Average PETH of BFPVN activity aligned to punishment delivery ($n = 27$ punishment-activated BFPVNs). Purple, first half of the session; mustard, second half of the session (errorshade, SEM). **i** Left, difference in peak punishment response between the first and second half of the session (**$p < 0.01$, $p = 0.00458$, two-sided Wilcoxon signed-rank rest; $n = 27$ punishment-activated BFPVNs). Right, difference in baseline firing rate between the first and second half of the session (***$p < 0.001$, $p = 0.00071$, two-sided Wilcoxon signed-rank test; $n = 27$ punishment-activated BFPVNs). Boxes and whiskers show median, interquartile range and non-outlier range. Source data are provided as a Source Data file.

https://doi.org/10.1038/s41467-024-48755-7

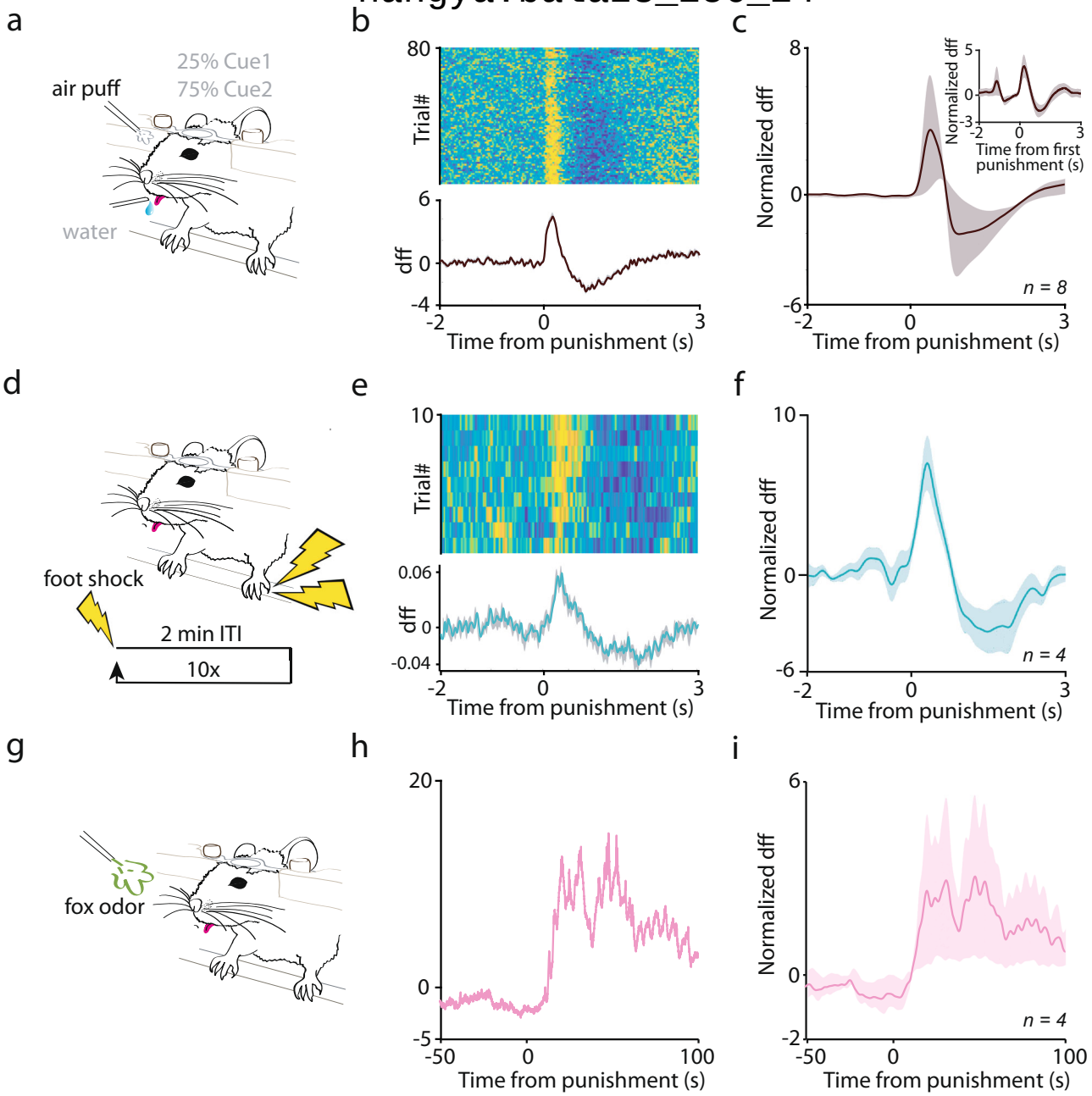

Fig. 3 | BFPVNs respond to aversive stimuli of different modality (air puff, foot shock, fox odor) in naïve mice. a Schematic diagram of introducing punishment during the Pavlovian conditioning task. **b** Example of a session when punishment was first introduced to the mouse. Top, PETH of individual trials; bottom, average ($n = 80$ trials; errorshade, SEM). **c** Average PETH of sessions when punishment was first introduced ($n = 8$ sessions from n = 8 mice). Inset, average BFPVN response to the first air puff presentation ($n = 8$ trials from n = 8 mice; errorshade, SEM). **d** Schematic diagram of foot shock presentation. **e** PETH aligned to foot shocks in an example session ($n = 10$ trials; errorshade, SEM). **f** Average PETH of foot shock response ($n = 4$ animals; 10 sessions each; errorshade, SEM). **g** Schematic diagram of fox odor presentation. **h** PETH aligned to fox odor presentation in an example session. **i** Average PETH of fox odor response in PVBFNs. ($n = 4$ animals; 1 session each; errorshade, SEM; note the longer time scale). PETHs were smoothed with a Gaussian kernel (width, 100 ms). (**a**), (**d**) and (**g**) panels were created using Mathis, M. (2020), Classical Conditioning Mouse, Zenodo, https://doi.org/10.5281/zenodo.3925907, under Creative Commons 4.0 license (https://creativecommons.org/licenses/by/4.0/). The original image was modified by removing illustrations of tubing and introducing additional legends and symbols.

suggest that BFPVN outputs to their prominent target regions might undergo reconfiguration depending on their firing rate, which varies with behavioral context.

Discussion

We demonstrated that PV-expressing long-range inhibitory neurons in the HDB nucleus of the basal forebrain respond strongly and homogeneously to punishments, broadcast this activity to multiple downstream targets in the limbic system, and that this activity aids the learning of stimulus-outcome associations. These results suggest that basal forebrain PV-expressing neurons are important for learning from negative experiences.

The BF contains a substantial GABAergic population that is approximately five times larger than its cholinergic population according to stereological estimates in rodents[4,6]. Lesions of BF GABAergic neurons lead to learning deficits[22,40,41], and their gradual age-associated degeneration is linked to cognitive decline during healthy aging and Alzheimer disease[15–17], suggesting they have

https://doi.org/10.1038/s41467-024-48755-7

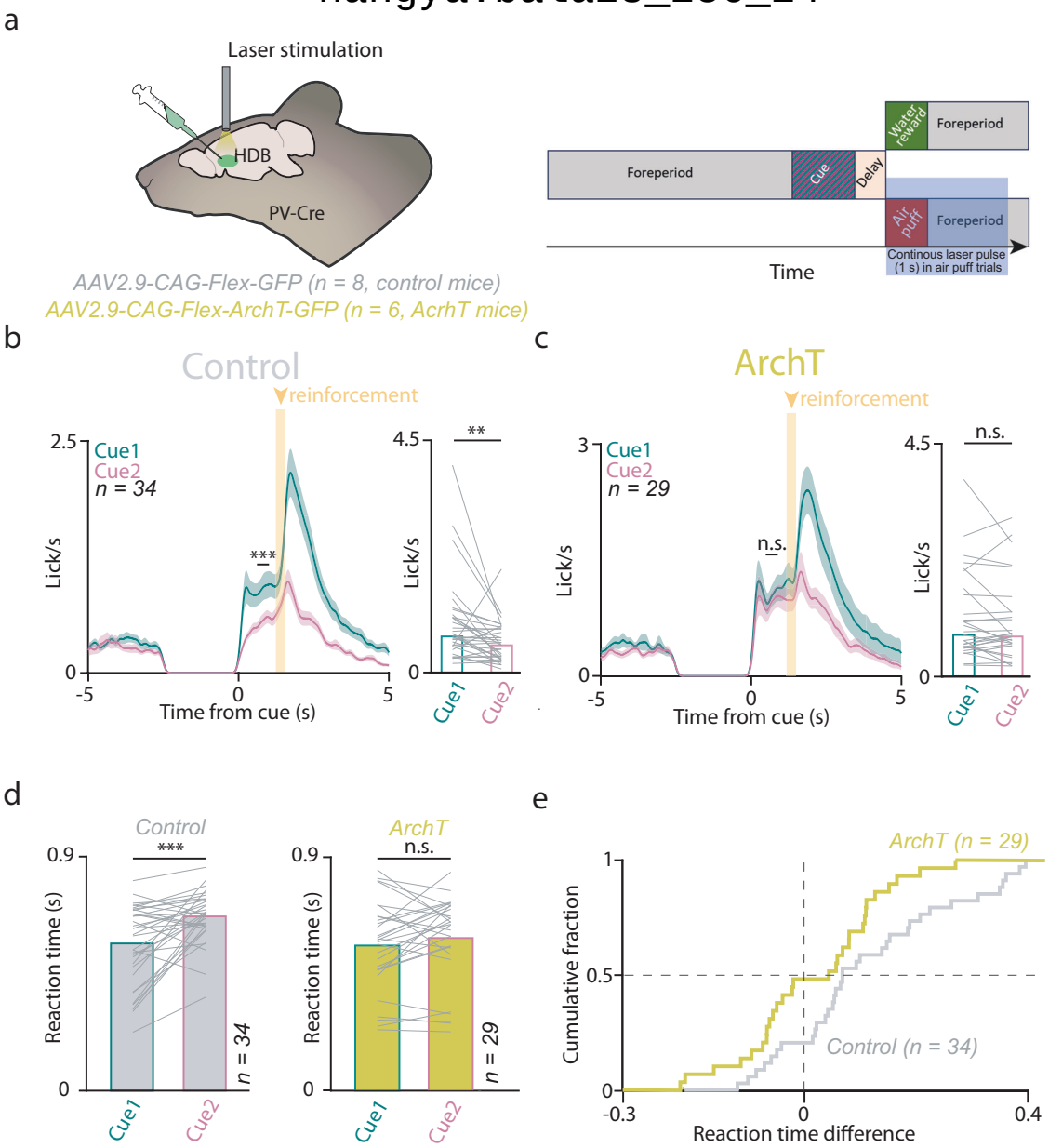

Fig. 4 | Optogenetic suppression of HDB BFPVN punishment responses disrupts learning cue contingencies during Pavlovian conditioning. a Left, schematic illustration of optogenetic suppression of BFPVNs in PV-Cre mice during air puff punishments. Created using Kennedy, A. (2020), Mouse brain silhouette, Zenodo, https://doi.org/10.5281/zenodo.3925919, under Creative Commons 4.0 license (https://creativecommons.org/licenses/by/4.0/). The original image was modified by adding labels and illustrations of a syringe and an optic fiber. Right, timeline of optogenetic suppression. **b** Left, average lick rate of control mice in the final training stage of the task ($n = 34$ sessions; errorshade, SEM). ***$p < 0.001$, ROC analysis with permutation test (see Methods). Right, bar graph showing mean lick rate before reinforcement (0.6–1.1 s window from cue onset, see ROC analysis in Fig. S7). Lines correspond to individual sessions. **$p < 0.01$, $p = 0.001517$, two-sided Wilcoxon signed-rank test. **c**, Left, average lick rate of ArchT-expressing mice in the final training stage of the task ($n = 29$ sessions; errorshade, SEM). n.s., $p > 0.05$, ROC analysis. Right, bar graph showing mean lick rate in a 0.6–1.1 s window from cue onset. n.s., $p > 0.05$, $p = 0.40513$, two-sided Wilcoxon signed-rank test. **d** Left, reaction time difference between lick responses to Cue 1 and Cue 2 in control animals. ***$p < 0.001$, $p = 0.000472$, two-sided Wilcoxon signed-rank test. Right, same for the ArchT group. n.s., $p > 0.05$, $p = 0.15668$, two-sided Wilcoxon signed-rank test. **e** Cumulative histogram of reaction time differences (Cue 2–Cue 1) of ArchT (yellow, $n = 29$ sessions) and control (gray, $n = 34$ sessions) animals. Source data are provided as a Source Data file.

important functions in attention, learning and memory processes[6,10,42,43]. This inhibitory population contains a significant long-range projecting neuron pool, many of which express parvalbumin[7,8,42,44–46]. These projections include target areas implicated in cognitive processing, including frontal cortices and hippocampus[8,10,46].

We therefore asked whether the PV-expressing population of BF GABAergic projection neurons, the BFPVNs, are essential for associative learning. We focused on the rostral portion of the horizontal nucleus of the diagonal band of Broca (HDB) and used bulk calcium recording via fiber photometry and tetrode recordings combined with optogenetic tagging to measure BFPVN activity in the HDB. We first tested whether BFPVNs responded to behaviorally salient events during classical conditioning, while mice learned to associate previously neutral pure tone stimuli (CS) with water rewards and air puff punishments (US). Previous studies showed that a bursting

https://doi.org/10.1038/s41467-024-48755-7

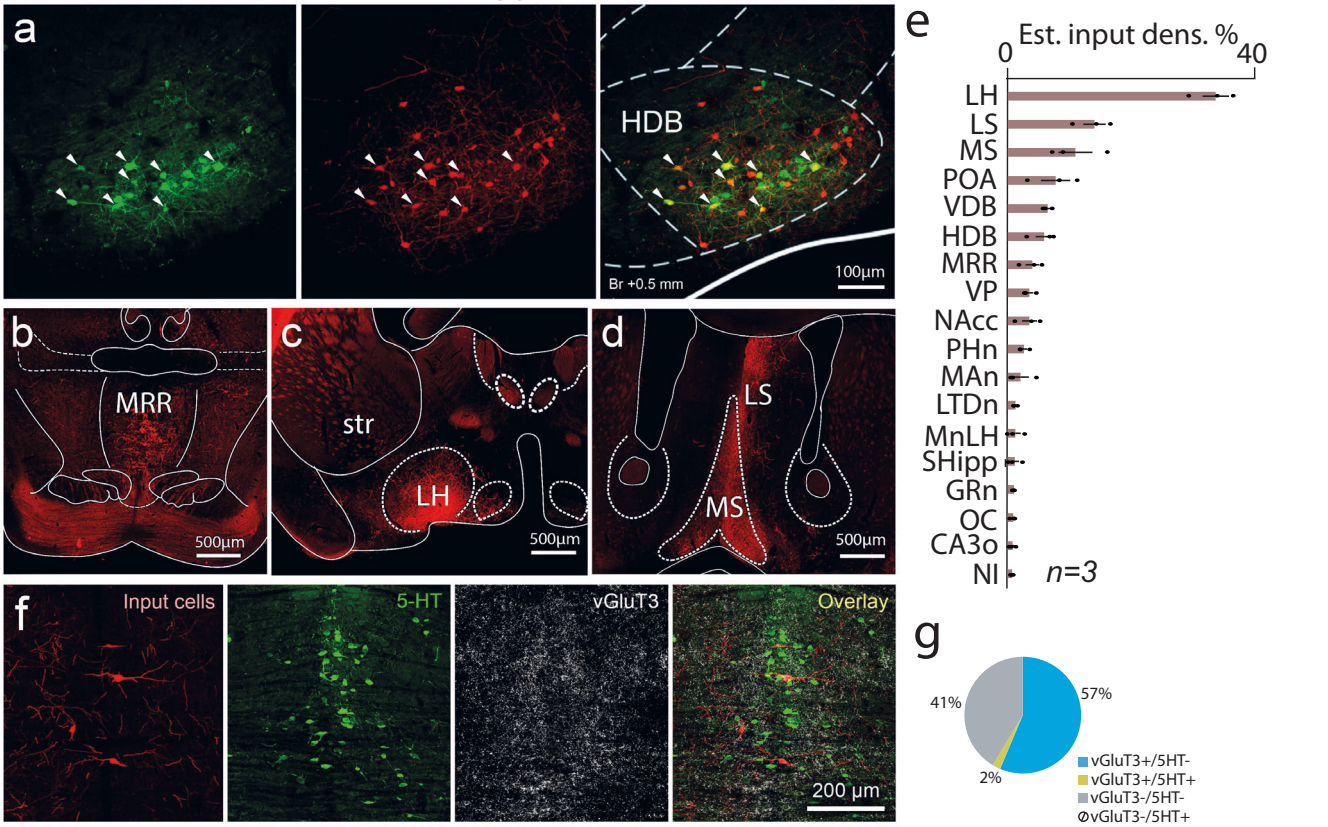

Fig. 5 | BFPVNs of the HDB receive inputs from aversion-coding nuclei. **a** Retrograde tracing, using pseudotyped rabies virus. Green, helper virus (left); red, pseudotyped rabies virus (middle); yellow, colocalizaton (right). Starter cells in the HDB are indicated by white arrowheads. **b** Coronal fluoromicrograph showing input cells in the MRR (red fluorescence). **c** Coronal fluoromicrograph showing input cells in the lateral hypothalamus (red fluorescence). **d** Coronal fluoromicrograph showing input cells in the medial septum (red fluorescence). **e** Estimated input density (% of all input cells) in different input brain regions. Bars and errorbars indicate the mean ± SEM from n = 3 mice. **f** Immunohistochemical staining of input neurons (red), serotonergic neurons (5-HT, green) and vGluT3+ glutamatergic neurons (vGluT3, far red visualized in white) in the MRR. **g** Proportion of neurons in the MRR that target BFPVNs. LH lateral hypothalamus, LS lateral septum, MS medial septum, POA preoptic area, VDB vertical limb of the diagonal band of Broca, HDB horizontal limb of the diagonal band of Broca, MRR median raphe region, VP ventral pallidum, NAcc nucleus accumbens, PHn posterior hypothalamic nucleus, MAn medial amygdaloid nucleus, LTDn laterodorsal tegmental nucleus, MnLH magnocellular nucleus of the lateral hypothalamus, SHipp septohippocampal nucleus, GRn gigantocellular reticular nucleus, OC orbital cortex, CA3o CA3 stratum oriens, NI nucleus incertus. Source data are provided as a Source Data file.

population of BF non-cholinergic neurons responded to behaviorally relevant events irrespective of their valence during associative learning[23,24]. We also found that BFPVNs responded to salient events including cue tones, reward and punishment; however, in contrast with Lin and colleagues, we demonstrated a preference of HDB BFPVNs towards responding to the aversive US, with only weaker and less consistent responses to CS and reward, suggesting that HDB BFPVNs constitute a specialized subpopulation of non-cholinergic BF neurons. We also found that BFPVNs markedly differed from cholinergic BF neurons, the BFCNs, in their responses: our previous studies revealed outcome prediction coding of BFCNs both following CS and US[25,34–36], absent in HDB BFPVNs. We also found that HDB BFPVNs were responsive to electrical shock and predator odor, demonstrating that BFPVN responses to aversive stimuli are multimodal.

BFPVN responses to air puffs showed a gradual decrease during the recording sessions. This could indicate that the aversive quality of the air puffs decreased with repeated exposure; however, other potential contributing sources like decreasing motivation, stimulus novelty, and fatigue cannot be excluded.

An unbiased clustering of HDB neuron responses to behaviorally relevant events in the probabilistic Pavlovian conditioning task grouped most BFPVNs in two clusters that together covered 48% of the recorded HDB cells. Non-tagged neurons in these clusters could represent both undetected BFPVNs due to limitations of viral infection and photoactivation, and, based on cluster size, likely also other HDB neuron types activated after reinforcement[4,6]. A smaller cluster contained cells that showed suppression of firing after punishment and to a lesser extent after reward. These responses mirrored BFPVN response profiles, suggesting that some of these neurons might be locally inhibited by the GABAergic BFPVNs. Such connections were found to be rare by circuit mapping studies[6,12], and in accordance, this group contained only 14% of HDB neurons.

The basal forebrain contains another prominent GABAergic cell type that expresses somatostatin (SOM). These BFSOMNs inhibit BFCNs, BFPVNs and BF glutamatergic neurons[12] via GABAergic synapses. In addition, SOM itself presynaptically inhibits glutamate and GABA release onto BFCNs[2]. BFSOMNs receive excitatory inputs from local glutamatergic neurons as well as BFCNs via nicotinic ACh receptors, while muscarinic receptors convey slower hyperpolarizing inputs[6]. Many of these cells are sleep-active and sleep promoting, suggesting that BFSOMNs potently suppress all wake-promoting BF cell types during non-REM sleep[12]. At the same time, specific activity of BFSOMNs during behavior was not known. By performing bulk calcium recordings of these neurons, we found that BFSOMNs responded to rewards, punishments, and reward-predicting auditory cues. This activity pattern differentiated them from BFPVNs that were most active after punishments and was

https://doi.org/10.1038/s41467-024-48755-7

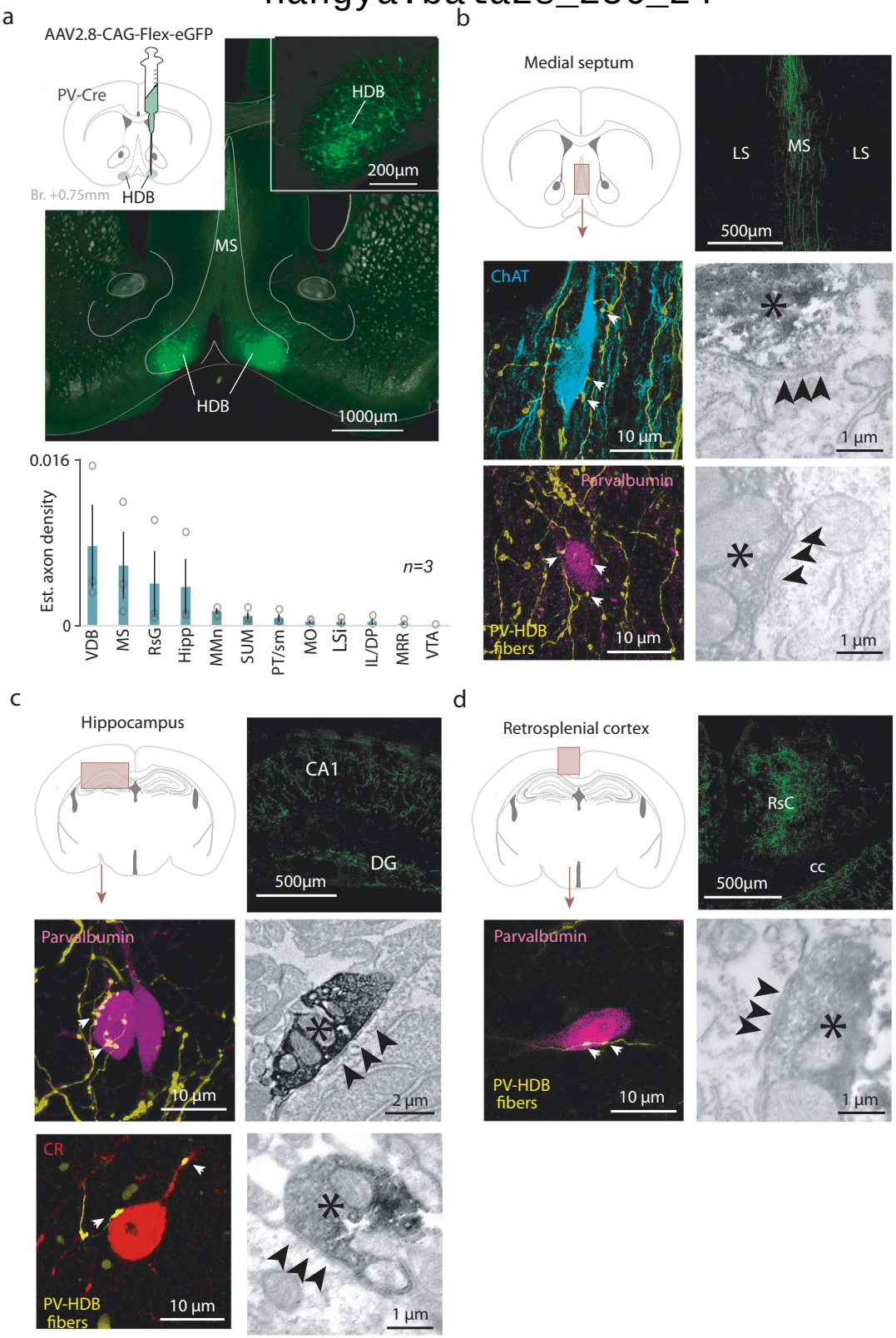

remarkably similar to BFCN calcium responses[35]. However, no overlap was found between SOM- and ChAT-expressing neurons in the HDB (Fig. S4c), as reported before[6]. Additionally, BFSOMNs showed higher activity after surprising than after expected rewards, similar to BFCNs and unlike BFPVNs. However, this higher activity occurred on the background of higher calcium levels at times of surprising reward delivery, due to a suppression of the calcium signal following the activation induced by the reward-predicting cue (not observed for BFCNs[35]), complicating the interpretation of this difference.

Thus, BFSOMNs responded to the same behaviorally salient events as BFPVNs but differed in relative response magnitudes (e.g. large reward responses for BFSOMNs) and coding properties (differential response to surprising and expected outcomes in BFSOMNs). We propose that BFSOMNs might provide negative feedback onto

Fig. 6 | BFPVNs of the HDB innervate the limbic system. a Top left, schematic illustration of cell-type specific anterograde tracer virus injection into the HDB. Top right and middle, fluorescent image of the injection site (green, eGFP). Bottom, normalized BFPVN axon density in target brain areas. Bars and errorbars indicate the mean ± SEM from $n = 3$ mice. **b** Top left, schematic illustration of the medial septum on a coronal atlas image. Top right, fluoromicrograph of labeled axons in the MS (repeated in $n = 3$ mice). Middle and bottom left, fluorescent images of ChAT+ and PV+ target neurons in the medial septum (white arrowheads indicate plausible contact sites). Right, electronmicrographs of synaptic contacts established by BFPVNs with the target cell types shown in the left panels (different examples). HDB BFPVN axons are labeled by DAB precipitate (black asterisk); black arrows indicate synaptic contacts. **c**, Top left, schematic illustration of the hippocampus on a coronal atlas image. Top right, fluoromicrograph of labeled axons in the CA1 (repeated in $n = 3$ mice). Middle and bottom left, fluorescent images of CR+ and PV+ target neurons in the hippocampus. Middle and bottom right, electronmicrographs of synaptic contacts established by BFPVNs with the target cell types shown in the left panels. **d** Top left, schematic illustration of the retrosplenial cortex (RSC) on a coronal atlas image. Top right, fluoromicrograph of labeled axons in the RSC (repeated in $n = 3$ mice). Bottom left, fluorescent images of a PV+ target neuron in the retrosplenial cortex. Bottom right, electronmicrograph of a synaptic contact established by BFPVNs with the target cell type shown on the left. VDB ventral limb of the diagonal band of Broca, MS medial septum, RsG retrosplenial cortex, granular part, Hipp hippocampus, MMn meidal mamillary nucleus, SUM supramamillary nucleus, PT/sm paratenial thalamic nucleus/stria medullaris, MO medial orbital cortex, LSi lateral septum, intermediate part, IL/DP inflalimbic cortex/dorsal peduncular cortex, MRR median raphe region, VTA ventral tegmental area. Source data are provided as a Source Data file.

BFCNs, both inhibiting their outputs (via GABA release) and decoupling them from their inputs (via SOM release), thereby limiting the duration of their activation. Previous recording studies showing fast and precise activation of BFCNs support this notion[25,35,36], suggesting that a fast bottom-up activation of the cholinergic system might recruit negative BFSOMN feedback via nicotinic receptors[6].

Information about aversive outcomes has multiple relevance for the animals, likely involving partly overlapping, but partly divergent circuits. First, aversive outcomes typically (but not mandatorily, see ref. 47) evoke avoidance behavior, engaging effector circuits and eventually muscles. A number of nuclei and cell types (mostly glutamatergic) have been shown to be involved in active avoidance[37,48–51]. Second, animals have to learn from aversive information, e.g. form stimulus-outcome associations that will then be stored in memory[50]. Third, aversive information also leads to arousal, attention and increased vigilance. These are different processes induced by aversive sensory information; therefore, it is expected that they be mediated by at least partially separable circuits. For example, basal forebrain cholinergic neurons respond rapidly and reliably to aversive stimuli including shocks and air puffs, but their stimulation evokes neither avoidance nor approach[25,52]. Indeed, they are thought to contribute to the learning aspects of outcomes by controlling cortical plasticity[25,53–56]. Being part of the same anatomical structure, BFPVNs are likely also involved in cognitive processing rather than direct motor effector functions. In line with this, they were hypothesized to contribute to arousal on both slower and faster timescales[6,10,12,13]. The lack of place avoidance after photostimulation of BFPVNs combined with impaired learning caused by their photoinhibition confirmed this hypothesis. We propose that HDB BFPVNs might specifically increase attention for aversive learning, thus mediating associative learning processes through increasing cortical excitability at specific target areas, probably by disinhibition.

Optogenetic inhibition of HDB BFPVNs during air puff punishments prevented mice from forming differential representation of CS cues based on their valence, demonstrated by a lack of differential anticipatory lick responses in optogenetically manipulated mice within the course of training. This lack of difference in CS-elicited licking was apparently due to an impaired inhibition of licking after Cue 2 that predicted likely punishment, in line with a previous study in which ibotenic acid injected to the BF of rats, preferentially destroying non-cholinergic neurons, lead to an increased false alarm rate in a visual detection task[18].

What may be the input that conveys aversive information to HDB BFPVNs? To address this question, we mapped the input neurons to HDB BFPVNs by mono-transsynaptic retrograde tracing using rabies vectors. We found that the input patterns of HDB BFPVNs only partially overlapped with those of a broader PV-expressing population[8]; most importantly, the lateral hypothalamus showed the largest density of input neurons, known to transmit nociceptive information that it receives via direct monosynaptic connections from nociceptive neurons of the spinal cord and periaqueductal gray[57–59]. HDB BFPVNs receive inputs from different BF nuclei including the medial septum and the ventral pallidum, which may also transmit punishment-related signals[2,25,60–62]. Furthermore, the median raphe was also sending monosynaptic inputs to BFPVNs, raising the possibility of a direct brainstem source of aversive information[37,63,64]. This was supported by our finding that MRR input cells consisted mostly of vGluT2- and vGluT3-expressing glutamatergic neurons, known to play important roles in the brainstem control of negative experience[37,39]. Importantly, the remaining major inputs to HDB BFPVNs were the lateral septum and the nucleus accumbens, thought to be important regulators of affect[65]. The potential convergence of aversive/affective information on BFPVNs revealed by rabies-based input mapping suggests that these neurons may act as an integrating and processing hub for aversive information. Nonetheless, we cannot rule out the possibility that one of these inputs dominates over the others, and we have limited knowledge on whether other HDB neurons participate in this process through local connections onto BFPVNs. Of note, lateral hypothalamic inputs dominated over striatal inputs to HDB BFPVNs, while these two sources were balanced in a broader PV-expressing population[8], which may underlie the robust punishment responses of HDB BFPVNs in comparison to reward-related activity.

We tested by anterograde tracing, fluorescence and electron microscopy to what target areas and neurons this aversive information was transmitted. HDB BFPVNs were projecting to neighboring BF nuclei, the vertical limb of the diagonal band of Broca and the medial septum (MS-VDB), where they synapsed on cholinergic and PV-expressing GABAergic neurons. They also sent dense projections to the hippocampus, where they formed synaptic contacts on PV-expressing and calretinin-expressing hippocampal interneurons. Of note, this innervation pattern was similar to what had been found for the septohippocampal GABAergic projection[44,66]. A third major target of HDB BFPVNs was the retrosplenial cortex, interfacing multimodal sensory and limbic information[67,68]. Previous studies suggested that long-range projecting GABAergic BF neurons may be mostly disinhibitory[69–74], which we confirmed in the CA1 and in the retrosplenial cortex, where we demonstrated HDB BFPVN synapses on PV-expressing interneurons; however, potential contacts onto pyramidal neurons could not be reliably tested. Further targets of HDB BFPVNs included other limbic structures like the mammillary and supramammillary nuclei and the paratenial thalamic nucleus, and to a lesser extent areas of the frontal cortex. This innervation pattern showed considerable differences from the projection pattern of a broader PV-expressing BF population[8], while it was remarkably similar to subcortical projections of HDB GABAergic neurons[7], suggesting that the PV-expressing population might provide a substantial fraction of the BF inhibitory projections[6,10,75], while it may show strong topography, similar to other BF cell types[2,76,77]. We note that while we found relatively sparse connections to frontal areas like medial orbital and infralimbic cortices, caudal portion of the HDB may show denser

https://doi.org/10.1038/s41467-024-48755-7

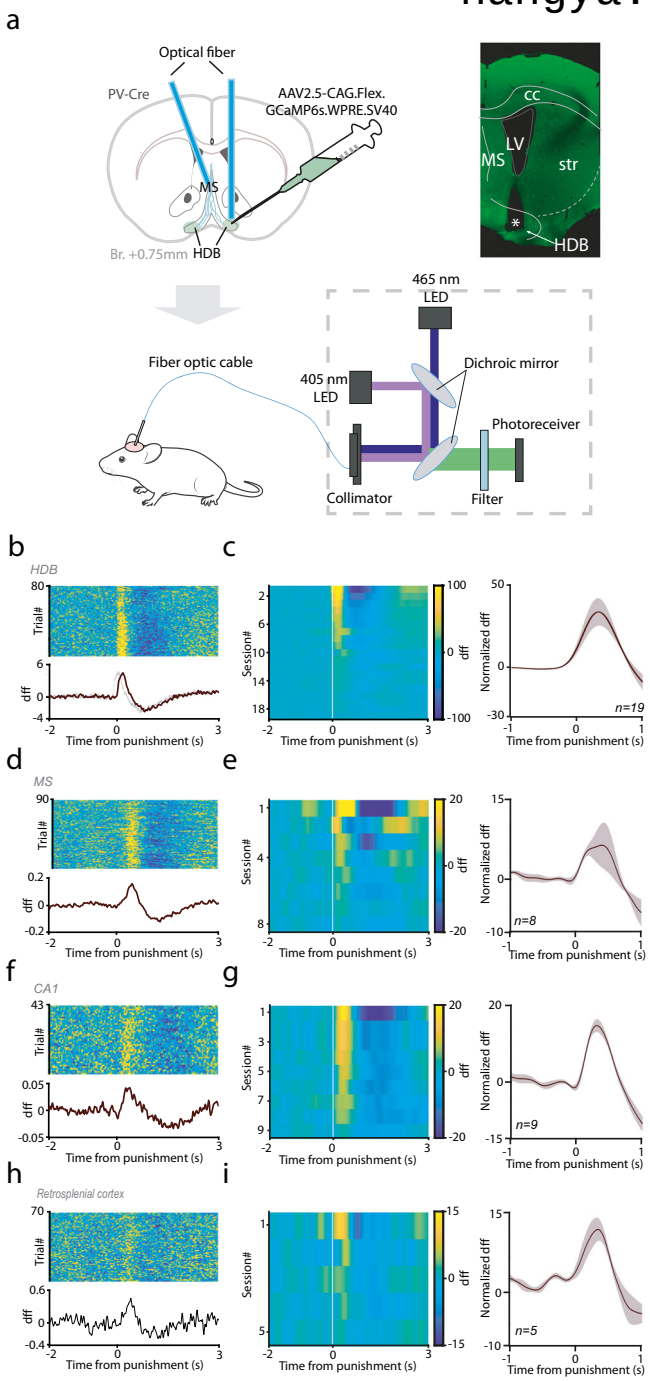

Fig. 7 | HDB BFPVNs broadcast negative feedback information to multiple limbic target regions. a Schematic illustration of bulk calcium measurements of BFPVN activity in the HDB and in the main target areas. Top left, injection of GCaMP6s-expressing viral vector; top right, fluoromicrograph of an optical fiber track (green, GCaMP6s; asterisk, tip of the optical fiber). Bottom, schematic of bulk calcium recording. Created using Tyler, E., & Kravitz, L. (2020), Mouse, Zenodo, https://doi.org/10.5281/zenodo.3925901, under Creative Commons 4.0 license (https://creativecommons.org/licenses/by/4.0/). The original image was modified by adding illustrations of an optic cable and photometry recording system. **b**, **c** Fiber photometry recordings of HDB BFPVN somata. **b** Example session recorded in the HDB. Top, single trial dff traces; bottom, average PETH aligned to air puff punishments (n = 80 trials; errorshade, SEM). **c** Left, all single sessions of HDB recordings, sorted according to descending amplitudes. Right, mean PETH of all sessions (n = 19; errorshade, SEM). **d**–**i** Fiber photometry recordings of HDB BFPVN projections. **d** Example session recorded in the medial septum. Top, single trial dff traces; bottom, average PETH aligned to air puff punishments (n = 90 trials; errorshade, SEM). **e** Left, all single sessions of medial septum recordings, sorted according to descending amplitudes. Right, mean PETH of all sessions (n = 8; errorshade, SEM). **f** Example session recorded in the hippocampal CA1 region. Top, single trial dff traces; bottom, average PETH aligned to air puff punishments (n = 43 trials; errorshade, SEM). **g** Left, all single sessions of CA1 recordings, sorted according to descending amplitudes. Right, mean PETH of all sessions (n = 9; errorshade, SEM). **h** Example session recorded in the retrosplenial cortex. Top, single trial dff traces; bottom, average PETH aligned to air puff punishments (n = 70 trials; errorshade, SEM). **i** Left, all single sessions of retrosplenial cortex recordings, sorted according to descending amplitudes. Right, mean PETH of all sessions (n = 5; errorshade, SEM). PETHs were smoothed with a Gaussian kernel (width, 100 ms).

frontal cortical projections[10]. Importantly, the innervation pattern revealed by the tracing indicates a broad targeting of the limbic system by HDB BFPVNs, multiple areas of which were shown to be necessary for learning from aversive experience[49,78–84].

Calcium recording of HDB BFPVN projections performed at three major termination zones, the medial septum, the CA1 of the hippocampus and the retrosplenial cortex revealed that all HDB BFPVN projections exhibited similar response properties to what was observed at the cell body level. Specifically, all three projections showed prominent activation by air puff punishments. Although some quantitative differences could be observed, it was not possible to dissect whether it was due to differences in axon density or differential response strength at the projection level. Altogether, the qualitatively similar response profiles suggest a broadcast function of HDB BFPVNs, sending similar message to broad areas of the limbic system.

At the same time, in vitro electrophysiology recordings revealed substantial differences in processing inputs from BFPVNs in target neurons: inhibitory synaptic responses of CA1 hippocampal interneurons were relatively large and fast and showed prominent short-term depression, while inputs on RSC neurons were smaller in amplitude, had longer latency to peak as well as rise time, and showed frequency-dependent short-term facilitation. In the MS, where BFPVNs synapsed on PV-expressing and cholinergic neurons, the synaptic properties showed intermediate values. Thus, the impact of BFPVN activity across target areas could dynamically change with varying behavioral and brain states.

Although theoretically possible, it is unlikely that BFPVNs would exert their effects through local connections within the HDB, since they do not innervate local BFCNs or BFSOMNs, and provide only weak and sparse connections to local glutamatergic neurons[6,12]. In line with this, Kim et al. found that the BFPVNs impact cortical gamma oscillations independent of BFCNs[10].

BFPVNs have been shown to control cortical gamma oscillations[6,9–11] and were suggested to participate in mediating arousal at different timescales, including brief and rapidly changing microarousals[6,9,12]. Relatedly, they were proposed to control changing levels of attention through cortical activation[6,9,25]. BFPVNs were also suggested to activate the default mode network, which is likely responsible for maintaining global oscillatory activity necessary for higher cognitive functions and conscious experience in humans, determining the significance of which will require future studies[85,86]. Combining these and our results, we speculate that BFPVNs may rapidly disinhibit limbic areas upon aversive stimuli to facilitate learning from negative experience. Thus, at least for aversive stimuli, BFPVNs might be the physical substrate of the 'attention for learning' concept[9,87].

Methods

Animals

Adult (over two months old) male Pvalb-IRES-Cre (PV-IRES-Cre or PV-Cre; n = 60, The Jackson Laboratory, RRID: IMSR_JAX:017320) and SOM-IRES-Cre (also known as Sst-IRES-Cre; n = 4, The Jackson Laboratory, RRID: IMSR_JAX:013044) mice were used for recording,

https://doi.org/10.1038/s41467-024-48755-7

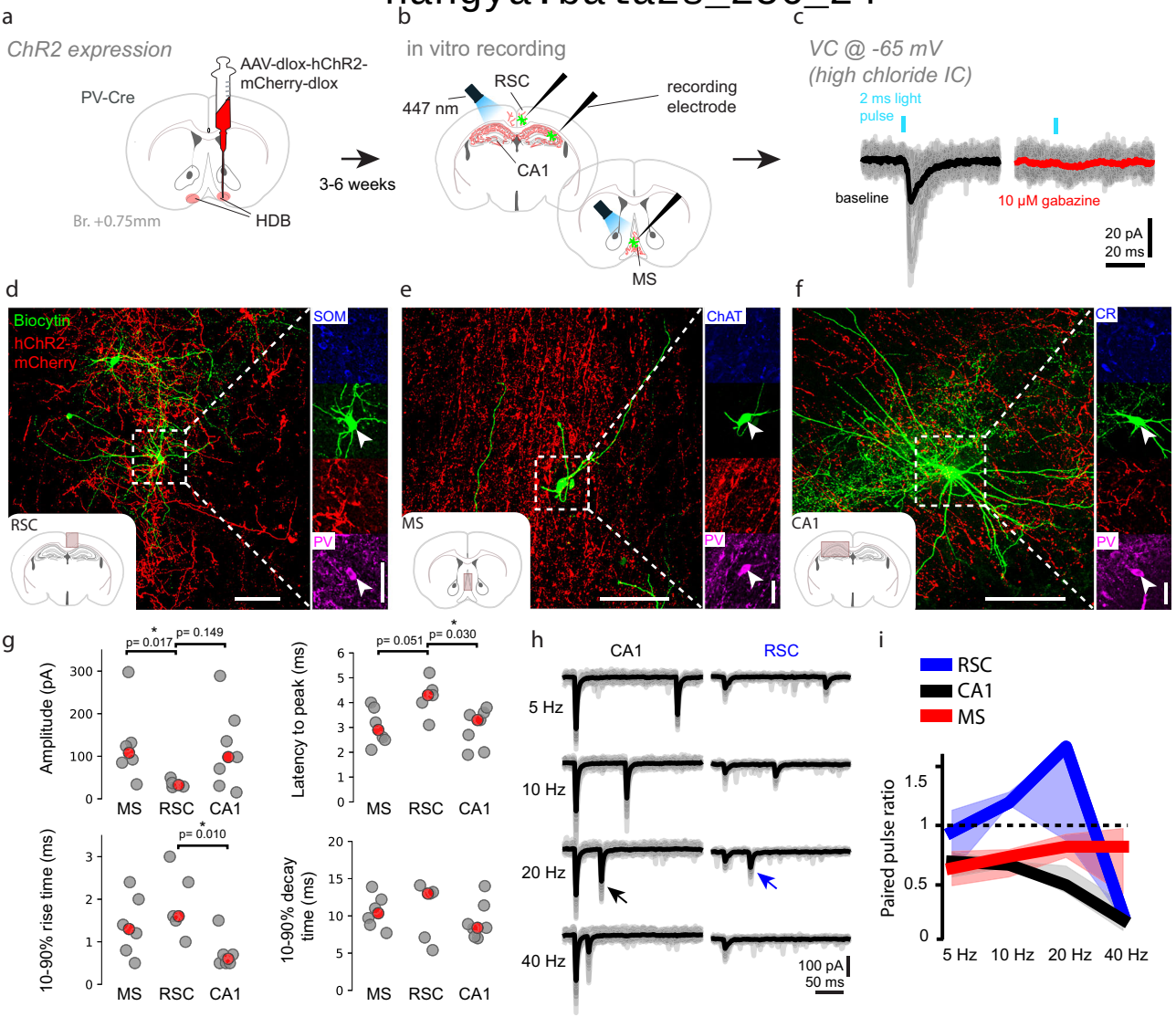

Fig. 8 | Functional synaptic contacts of BFPVNs show target area specific short-term plasticity. a PV-Cre mice ($n = 7$) were injected with AAV to express ChR2 in BFPVN axonal projections. **b** Acute slice electrophysiology recordings were performed from the retrosplenial cortex (RSC), CA1 area of the dorsal hippocampus and the medial septum (MS). **c** Left, representative example of postsynaptic inhibitory currents recorded from a neuron in response to the optogenetic stimulation of BFPVN fibers. Right, the inhibitory response was eliminated in the presence of $GABA_A$ blocker gabazine (10 µM). **d**–**f** Representative confocal images of responsive cells from the RSC, MS, and CA1, respectively (green, recorded cells; red, BFPVN axonal projections; scale bars: 100, 30 µm). Post-hoc immunohistochemistry shows functional contacts on PV+ cells in RSC, CA1 and MS. ($n = 4/7$ patched cells were PV+ in the CA1; $n = 2/5$ in the MS; $n = 2/5$ in the RSC). **g** Top left, optogenetically evoked IPSCs were significantly smaller on RSC neurons ($n = 5$) compared to MS neurons ($n = 6$) and showed a tendentious difference compared to CA1 neurons ($n = 7$; RSC vs. MS, $p = 0.017$; RSC vs. CA1, $p = 0.149$). Latency to peak was higher in the RSC compared to the other two regions (RSC vs. MS, $p = 0.051$; RSC vs. CA1, $p = 0.030$). In line with these, 10–90% rise-time was shortest in the CA1 (RSC vs. CA1, $p = 0.010$). We found no differences in 90–10% decay time. Statistical comparisons were performed using two-sided Mann–Whitney U test. **h** We delivered two consecutive light pulses at different frequencies to calculate paired-pulse ratios (PPR). Responses from representative CA1 and RSC neurons are shown. Note the prominent short-term synaptic depression of the BFPVN input onto the CA1 cell (black arrow), and the short-term facilitation up to 20 Hz of the BFPVN input onto the RSC cell (blue arrow). **i** Summary data of PPR at different frequencies in the three brain areas (RSC vs. CA1 @ 10 Hz, $p = 0.008$, RSC vs. MS @ 10 Hz, $p = 0.030$, RSC vs. CA1 @ 20 Hz, $p = 0.051$, two-sided Mann–Whitney U test). Source data are provided as a Source Data file.

optogenetic activation and inhibition, bulk calcium recording and for immunohistochemistry, and 30-60 days old PV-IRES-Cre mice were used for acute slice electrophysiology ($n = 7$, males) according to the regulations of the Hungarian Act of Animal Care and Experimentation (1998; XXVIII, section 243/1998, renewed in 40/2013) in accordance with the European Directive 86/609/CEE and modified according to the Directive 2010/63/EU. Experimental procedures were reviewed and approved by the Animal Welfare Committee of the Institute of Experimental Medicine, Budapest and by the Committee for Scientific Ethics of Animal Research of the National Food Chain Safety Office of Hungary (PE/EA/675-4/2016; PE/EA/1212-5/2017; PE/EA/864-7/2019; PE/EA/1003-7/2021). Animals were housed individually in 36 × 20 × 15 cm cages under a standard 12-h light-dark cycle (lights on at 8 a.m.) with food available ad libitum. During behavioral training, mice were water-restricted to 1 ml per day. Temperature and humidity were kept at 21 ± 1 °C and 50–60%, respectively.

Tetrode implantation surgery

Mice were implanted with microdrives housing 8 tetrodes and a 50 µm core optic fiber[25,88,89]. Mice were anesthetized with a ketamine-xylazine

solution (83 mg/kg ketamine and 17 mg/kg xylazine, dissolved in 0.9% saline). The scalp was shaved and disinfected with Betadine, the skin and subcutaneous tissues were topically anesthetized with Lidocaine spray, and mice were placed in a stereotaxic frame (Kopf Instruments). Eyes were protected with eye ointment (Corneregel, Bausch & Lomb). The skin was opened with a single sagittal incision made by a surgical scalpel, the skull was cleaned, and a craniotomy was drilled above the horizontal limb of the diagonal band of Broca (HDB, antero-posterior 0.75 mm, lateral 0.60 mm; $n = 4$). Virus injection (AAV2/5.EF1a.-Dio.hChR2(H134R)-eYFP.WPRE.hGH, Addgene, titer $\geq 1 \times 10^{13}$ vg/mL; HDB, dorso-ventral 5.00 and 4.70 mm, 300 nl at each depth) and drive implantation was performed using the stereotaxic frame and a programmable nanoliter injector (Drummond Nanoject III). Ground and reference electrodes were implanted to the bilateral parietal cortex. The microdrive was secured in place using dental cement (Lang Dental). When the dental cement was cured, mice were transferred from the stereotaxic frame into their homecage and received analgesics (Buprenorphine, 0.1 mg/kg), and local antibiotics (Gentamycin). Mice were closely monitored after surgery and were allowed 10-14 days of recovery before starting behavioral training.

Anterograde tracing surgery

PV-IRES-Cre mice were injected with AAV2/8.CAG.Flex.eGFP (Addgene, titer $\geq 1 \times 10^{13}$ vg/mL) anterograde tracing virus in the HDB (antero-posterior, 0.75 mm; lateral, 0.60 mm; dorso-ventral, 5.00 mm and 4.9 mm; 50 nl each side, injecting 25–25 nl each depth) using standard stereotaxic surgery techniques described in the previous section. Following bilateral virus injection, craniotomies were closed with Vaseline, and scalp skin was sutured using standard surgical needle and thread (Dafilon). Postoperative care was applied as described above. The virus injection was followed by a 4-week virus expression period. Mice were then transcardially perfused (as described in details below) and their brains were processed for further immunohistology experiments.

Retrograde tracing surgery

PV-IRES-Cre mice were anesthetized with 2% isoflurane followed by an intraperitoneal injection of a ketamine-xylazine anesthetic mixture (83 mg/kg ketamine and 17 mg/kg xylazine, dissolved in 0.9% saline), then mounted in a stereotaxic frame (David Kopf Instruments). After exposing the skull surface, 20 nl of the Cre-dependent helper virus was injected into the HDB (bilateral, $n = 2$; unilateral, $n = 1$) using a Nanoliter 2010 microinjection pump (World Precision Instruments). The injection coordinates were defined by a stereotaxic atlas (Paxinos and Franklin, 2012) and were the following given in mm for the anteroposterior, mediolateral and dorsoventral axes, respectively: +0.75 (from Bregma), ±0.60 (from Bregma, unilateral in case of Mouse 3), −5.0 (from brain surface). After 3 weeks of survival, mice were injected with 20 nl of the G protein-deleted EnvA-pseudotyped rabies virus at the same coordinates. After 9 days of survival, mice were prepared for perfusion.

Optical fiber implantation surgery for optogenetic activation, inhibition and fiber photometry recordings

PV-IRES-Cre or SOM-IRES-Cre (also known as Sst-IRES-Cre) mice were implanted using standard stereotactic surgery techniques described in the previous section. Following virus injection (for optogenetic activation: AAV2/5.EF1a.Dio.hChR2(H134R)-eYFP.WPRE.hGH, Addgene, titer $\geq 1 \times 10^{13}$ vg/mL or AAV2/5.EF1a-eYFP.WPRE.hGH, Addgene, titer $\geq 7 \times 10^{12}$ vg/mL as control virus, 70 nl each side; for optogenetic inhibition: AAV2.9-CAG-Flex-ArchT-GFP, Addgene, titer $\geq 1 \times 10^{13}$ vg/mL or AAV2.9-CAG-Flex-GFP, Addgene, titer $\geq 1 \times 10^{13}$ vg/mL as control virus, 100 nl each side; for fiber photometry: AAV2/9.CAG.Flex.GCaMP6s.WPRE.SV40, Addgene, titer $\geq 1 \times 10^{13}$ vg/mL; HDB, antero-posterior 0.75 mm, lateral 0.60 mm; dorso-ventral 5.00 and 4.7 mm). Following virus injection, optical fibers were implanted (for optogenetic activation: 200 μm core fiber was implanted unilaterally into HDB, antero-posterior 0.75 mm, lateral 0.60 mm; for optogenetic inhibition: 400 μm core fibers were implanted bilaterally in 0- and 20-degree angle into HDB; for fiber photometry: 400 μm core fibers were implanted into HDB and MS, antero-posterior 0.75 mm, lateral 1.2 mm, 20-degrees lateral angle; CA1 region of the hippocampus, antero-posterior −2.3 mm, lateral 1.4 mm, dorso-ventral 1.2 mm; retrospelnial cortex, antero-posterior −2.3 mm, lateral 0.5 mm, dorso-ventral 0.2 mm respectively). Mice received post-surgery care as described above in the *Tetrode implantation surgery* section and allowed 10–14 days of recovery before starting behavioral training.

Probabilistic Pavlovian conditioning

PV-IRES-Cre or SOM-IRES-Cre mice were trained on an auditory Pavlovian conditioning task[26] in a head-fixed behavioral setup that allowed millisecond precision of stimulus and reinforcement delivery[90]. On the first day of training, water restricted mice[26] were head-fixed and given access to water reward whenever they licked a waterspout. Individual licks were detected by the animal's tongue breaking an infrared photobeam. The following day, a 50 dB pure tone cue of one second duration was introduced that predicted likely reward (5 μl of water). After each cue presentation, water reward was delivered with 0.8 probability with a 200–400 ms delay, while the rest of the outcomes were omissions. The next trial started after the animal stopped licking for at least 1.5 s. The stimulus was preceded by a 1–4 s foreperiod according to a truncated exponential distribution, in order to prevent temporal expectation of stimulus delivery[91]. If the mouse licked in the foreperiod, the trial was restarted. We used the open source Bpod behavioral control system (Sanworks LLC, US) for operating the task.

Next, a second pure tone cue of well-separated pitch was introduced that predicted low probability reward (0.25). Next, air puff punishment (200 ms, 15 psi) was introduced in the following session with the final outcome contingencies (likely reward trials, 80% reward, 10% punishment, 10% omission; likely punishment trials, 25% reward, 65% punishment, 10% omission). These contingencies reflect careful calibration to keep mice motivated for the task. Different trial types (likely reward and likely punishment) and outcomes (water reward, air puff punishment and omission) were presented in a pseudorandomized order following the described outcome contingencies. Mice learned the task in approximately one week and consistently demonstrated reward anticipation by differential lick rate in response to the cues from the second week.

Auditory stimuli were calibrated using a precision electret condenser microphone (EMM-6, Daytonaudio) connected to a preamplifier digital converter (AudioBox iOne, PreSonus) and sound pressure levels were measured by the TrueRTA software[90]. Cue tone intensities were well above the hearing threshold for both sounds (20-30 dB for 4 and 12 kHz pure tones) but not as loud as to cause a startle reflex (around 70 dB)[25,92]. Mice in this study underwent the same training protocol for consistency; however, we have reported that behavioral performance of the task did not depend on the identity (frequencies) of the conditioned stimuli (Figure S1 in ref. 35).

The aversive quality of air puffs depends on the exact experimental settings. We applied 200 ms long puffs at 15 psi pressure (within the range of parameters used for eyeblink conditioning[93]). We demonstrated that mice consistently choose water without air puff over water combined with air puff, showing that air puffs are aversive under these circumstances (see Figs. 2C and 2D in ref. 25).

Optogenetic inhibition of BFPVNs

A set of PV-IRES-Cre animals injected with AAV2.9-CAG-Flex-ArchT-GFP (Addgene, titer $\geq 1 \times 10^{13}$ vg/mL, $n = 6$, ArchT group) or AAV2.9-CAG-

Flex-GFP (Addgene, titer ≥ 1×10^{13} vg/mL, $n = 8$, Control group) were trained for a two-week period on the probabilistic Pavlovian conditioning task according to the training protocol described above[26]. Starting at the time of punishment presentation, a one-second-long yellow laser pulse (593 nm wavelength, Sanctity Laser) was delivered to the HDB bilaterally via optical fibers (400 μm core) to achieve optogenetic silencing of BFPVNs, introduced already at the first air puff delivery. Anticipatory lick rate (licking between cue onset and reinforcement delivery) was recorded in each (ArchT and Control) group.

Conditioned place aversion task

PV-IRES-Cre animals injected with AAV2/5.EF1a.Dio.hChR2(H134R)-eYFP.WPRE.hGH (Addgene, titer ≥ 1×10^{13} vg/mL, $n = 8$, ChR group) or AAV2/5.EF1a-eYFP.WPRE.hGH (Addgene, titer ≥ 7×10^{12} vg/mL, $n = 10$, Control group) were placed in an arena with two sides, which were separated by a wall but connected with an open gate on the wall. The two sides of the arena were marked by different wall patterns (dotty or striped). In the arena, a center part (one third of the size of the arena) and a peripheral part was differentiated. The conditioning protocol took two days; on the first day, animals were placed into the chamber and were allowed to move freely for 5 min (habituation phase). The next day (test phase), mice were place into the chamber again and received 20 Hz laser light stimulation (473 nm wavelength, Sanctity Laser) on one of the sides. The stimulation side was assigned pseudorandomly across animals. Time spent in the center and peripheral part of the arena (in seconds or in % of total time spent in the arena), time spent on each side (in seconds or in % of total time spent in the arena), side crosses (number of crosses), velocity (cm/s) and different behavioral components (rearing, grooming, freezing, exploration) were measured.

Presentation of mild foot shocks and fox odor

Mild foot shocks (~0.5–1 mA, 200 ms, 10 times, @1 min interval) were delivered 20 times with 1-min interstimulus intervals, using a Supertech Ltd. (Pécs, Hungary) BioStim STI-4a computer interface connected to a STE-8a stimulus isolator end-stage. To evoke innate fear, a threat-relevant odor 2-methyl-2-thiazoline (10 μl of 2MT, Santa Cruz Biotechnology, Inc., Dallas, US), a synthetic derivative of a fox anogenital product was delivered in front of the animal on a filter paper after a baseline recording period.

Tetrode recording

Extracellular recordings were performed with custom-built microdrives consisting of 8 movable nichrome tetrode electrodes (diameter, 12.7 μm; Sandvik) and a 50 μm core optical fiber (Thorlabs)[25,88]. Microdrive screws were specifically designed to precisely control the descent of the tetrodes and the optic fiber into the brain; the pitch of the threading was 160 μm, therefore one eighths of a turn with the screw corresponded to 20 μm descent (M0.6 stainless steel flat head screw, 12 mm length; Easterntec, Shanghai, China). Before the tetrode surgery, we measured the protruding length of the electrodes on each microdrive with a micro-ruler (Olympus SZ61 stereomicroscope; micro-ruler, Electron Microscopy Tools). The electrodes were gold-plated (PEG was dissolved in DI water to create 1 g/l concentration, then 1.125 ml of PEG-solution was mixed with 0.375 ml gold plating solution, Neuralynx, see also Ferguson et al., 2009)[94] to impedances of 30-100 kΩ measured at 1 kHz (NanoZ) and dipped in DiI (ThermoFischer Scientific) red fluorescent dye to aid later track reconstruction efforts.

Before each recording session, the microdrive was connected (Omnetics) to a 32-channel RHD headstage (Intan). Data were digitized at 30 kHz and transferred from the headstage to a data acquisition board (Open Ephys) via a Serial Peripheral Interface cable (Intan). The tetrodes were advanced 0–100 μm after each recording session. The descent of the tetrodes was logged each recording day. Throughout the experiments, detailed notes of the assumed brain coordinates during each recording session were taken based on the length of the tetrodes measured before the surgery, stereotaxic information from the surgery and controlled screw turns on the microdrive.

Optogenetic tagging

The optic fiber of the microdrive (see above) ended in an FC connector (Precision Fiber Products). The optic fiber was connected with an FC-APC patch chord during recording. Before the training session began, to optogenetically tag BFPVNs, 1 ms laser pulses were applied (473 nm, Sanctity) at 20 Hz for 2 seconds, followed by 3 seconds pause, repeated 20-30 times. Light-evoked spikes and incidental artifacts were monitored online using the OPETH plugin (SCR_018022)[95] for Open Ephys and when light-induced photoelectric artifacts or population spikes were observed, laser power was adjusted as necessary to avoid masking of individual action potentials. The significance of photoactivation was assessed with offline data analysis by applying the SALT test, which compares spike latency distributions after light pulses to a surrogate distribution based on Jensen-Shannon divergence (information radius)[88,96]. Neurons with $p < 0.01$ were considered light-activated, and thus BFPVNs. BFPVNs recorded on the same tetrode within 200 μm dorso-ventral distance were compared by waveform correlation and autocorrelogram similarity[60,97], and similar units were counted towards the sample size only once.

Fiber photometry

A dual fiber photometry setup (Doric Neuroscience) was used to perform bilateral fluorescent calcium measurements. Recording sessions were visualized using Doric Studio Software. Two LED light sources (465 nm, 405 nm) were amplitude-modulated by the command voltage of the two-channel LED driver (LEDD_2, Doric Neuroscience, the 465 nm wavelength light was modulated at 208 Hz and 405 nm wavelength was modulated at 572 Hz) and were channeled into fluorescent Mini Cubes (iFMC4, Doric Neuroscience). Light was delivered into the HDB, MS, CA1 or retrosplenial cortex via 400 μm core patch cord fibers that were connected to optical fiber implants during training sessions. The same optical fibers were used to collect the emitted fluorescence signal from the target areas. The emitted fluorescent signal was detected with 500–550 nm fluorescent detectors integrated into the Mini Cubes. The sampling rate of emitted signals was set to 12 kHz, decoded in silico and saved in a *.csv format.

Perfusion

Mice were anesthetized with 2% isoflurane followed by an intraperitoneal injection of a mixture of ketamine-xylazine and promethazinium-chloride (83 mg/kg, 17 mg/kg and 8 mg/kg, respectively). After achieving deep anesthesia, mice were perfused transcardially (by placing the cannula into the ascending part of the aorta via an incision placed on the left ventricle wall) with saline for 2 min, followed by 4% paraformaldehyde (PFA) solution for 40 min, then saline for 10 min. After perfusion, mice were decapitated, and brains were carefully removed from the skull and postfixed in PFA overnight. Brains were then washed in PBS and cut into 50 μm thick coronal sections using a vibrating microtome (Leica VT1200S). Sections were thoroughly rinsed in 0.1 M PB (3 × 10 min) and used for further immunohistochemical experiments.

Acute slice electrophysiology

Animals. PV-IRES-Cre animals ($n = 7$ males, P30-60 days) were injected into the HDB (antero-posterior 0.75 mm, lateral 0.60 mm; dorso-ventral 5.00 mm) bilaterally with 70 nl AAV5-EF1a-DIO-ChR2-mCherry (UNC Vector Core, US) or ssAAV-9/2-hEF1α-dlox-hChR2(H134R)-mCherry-dlox-WPRE-hGHp(A) (VVF-Zürich, Switzerland) to enable channelrhodopsin-assisted circuit mapping. After 3–6 weeks of expression time, acute brain slices were prepared for electrophysiology experiments.

Slice preparation. Mice were decapitated under deep isoflurane anesthesia. The brain was removed and placed into an ice-cold cutting solution, which had been carbogenated (95% O_2–5% CO_2) for at least 30 min before use. The cutting solution contained the following (in mM): 205 sucrose, 2.5 KCl, 26 NaHCO3, 0.5 CaCl2, 5 MgCl2, 1.25 NaH2PO4, 10 glucose. Coronal slices of 300 μm thickness were cut using a Vibratome (Leica VT1200S). After acute slice preparation, slices were placed into an interface-type holding chamber for at least 1 h of recovery time. This chamber contained standard ACSF solution at 35 °C which gradually cooled down to room temperature. The ACSF solution contained the following (in mM): 126 NaCl, 2.5 KCl, 26 $NaHCO_3$, 2 $CaCl_2$, 2 $MgCl_2$, 1.25 NaH_2PO_4, 10 glucose, saturated with carbogen gas as above.

In vitro electrophysiology recordings. Recordings were performed under visual guidance using Nikon Eclipse FN1 microscope with infrared differential interference contrast (DIC) optics. The flow rate of the ACSF was 4–5 ml/min at 30–32 °C (Supertech Instruments, Pecs, Hungary). Patch pipettes were pulled from borosilicate capillaries (with inner filament, thin-walled, outer diameter (OD) 1.5) with a PC-10 puller (Narishige, Tokyo, Japan). Pipette resistances were 3–6 MΩ when filled with intrapipette solution. The composition of the intracellular pipette solution was as follows (in mM): 54 d-gluconic acid potassium salt, 4 NaCl, 56 KCl, 20 Hepes, 0.1 EGTA, 10 phosphocreatine di(tris) salt, 2 ATP magnesium salt and 0.3 GTP sodium salt; with 0.2 % biocytin; adjusted to pH 7.3 using KOH and with osmolarity of ~295 mOsm/l. Recordings were performed with a Multiclamp 700B amplifier (Molecular Devices, San Jose, US), digitized at 20 kHz with Digidata analog-digital interface (Molecular Devices), and recorded with pClamp11 Software suite (Molecular Devices). For slice illumination, we used a blue LED light source (Prizmatix Ltd., Holon, Israel) integrated into the optical light path of the microscope. 2 ms long light pulses were delivered @ 5-10-20-40 Hz. To record optogenetically evoked IPSCs, cells were clamped to −65 mV, in the presence of fast excitatory synaptic transmission blockers 2,3-dihydroxy-6-nitro-7-sulfamoyl-benzo(f)quinoxaline-2,3-dione (NBQX, 20 μM) and 2-amino-5-phosphonopentanoic acid (AP-5, 50 μM).

Immunohistochemical identification of in vitro recorded cells. After acute slice electrophysiology experiments, brain sections were fixed overnight in 4% PFA. Sections were extensively washed in 0.1 M PB and TBS and blocked in 1% human serum albumin (HSA; Sigma-Aldrich) solution for 1 h. Then, sections were incubated in primary antibodies against PV, SOM, CR or ChAT (see Table S2) for 48–60 h. This step was followed by thorough rinse with TBS (3 × 10 min) and overnight incubation with a mixture of secondary antibodies (see Table S3) and streptavidin-A488 (Invitrogen, 1:1000). We used 0.1% Triton-X detergent through every incubation step due to the thickness of the brain section. Finally, sections were washed in TBS and PB, mounted on microscopy slides and covered with Vectashield (Vector Laboratories Inc, US) and imaged with a Nikon A1R confocal laser scanning microscope.

Histological track reconstruction

After tetrode recording and fiber photometry experiments, animals were anesthetized with an intraperitoneal injection of ketamine-xylazine (83 mg/kg and 17 mg/kg, respectively) and underwent an electrolytic lesioning protocol (30 μA for 5 s on two leads of two selected tetrodes, where opto-tagged BFPVNs were recorded; stimulator from Supertech, Pecs, Hungary). Twenty-to-thirty minutes after the electrolytic lesion, mice were perfused transcardially as described above. Microdrives and/or optical fibers were extracted and the brain was gently removed from the skull. The brain was postfixed in 4% PFA overnight and then washed in 0.1 M phosphate buffer (3 × 10 min). The explanted microdrives were examined under stereomicroscope and the protruding length of the electrodes were measured and compared to the depth registrations made during the recording sessions.

Coronal sections of 50 μm thickness were cut by a vibratome (Leica VT1200S). Special care was taken to section the brain perpendicular to brain surface, so that resulting sections could be easily aligned with coronal atlas images. The sections were thoroughly washed in phosphate buffer 3 times (10 min each) and mounted on microscopy slides in Aquamount mounting resin. Fluorescent micrographs of the sections were taken using a Nikon C2 confocal microscope. Four times four large field-of-view dark-field images, red and green fluorescent images were taken at 10x magnification in order to capture the whole sections.

Confocal microscopic images were further analyzed to reconstruct in vivo recording locations. The recording locations were referenced to atlas coordinates[98]. By referencing recording location to atlas coordinates, individual size differences of mouse brains compared to the atlas reference and slight deviations from the vertical direction during electrode descent were accounted for. Dark-field whole-section brain images aided atlas alignment, since they provided a detailed contrast for white and gray matter. By using Euclidean transformations, atlas images of coronal sections were morphed on the corresponding dark-field brain images, to verify area boundaries and determine the coronal plane of the section. If the brain section was non-uniformly distorted during histological processing, special care was taken to accurately map the vicinity of the electrode tracks within the target areas. Next, green fluorescent images of the same sections were transformed similarly as the dark-field images to verify PV expression within the boundaries of anatomical structures corresponding to the atlas images. In the case of tetrode recordings, aligned atlas images were superimposed on red fluorescent images of the same field of view, which showed the DiI-labeled electrode tracks. Coordinates of electrode entry points and deepest points in the brain were marked by DiI tracks and the tip of the electrode was localized using small electrolytic lesions. Coordinates of electrode endpoints were read from the atlas image and were used to interpolate the recording locations referenced to the atlas coordinates, based on experimental logs of the protrusion of the electrode. Based on this interpolation procedure, antero-posterior, lateral and dorso-ventral coordinates and an atlas-defined brain area were assigned to each recording session and thus to each recorded neuron.

Sections from mice implanted with optic fibers were processed similarly; dark-field whole section brain images were used for atlas alignment, while green fluorescent images verified the expression of ChR2, ArchT or GCaMP6s. Optic fiber locations were reconstructed based on the tissue track caused by the fiber.

Anterograde tracing

Sections were washed in PB (0.1 M) and immersed in 30% sucrose solution overnight, then freeze-thawed over liquid nitrogen three times. Sections were extensively washed in 0.1 M PB and TBS and blocked in 1% human serum albumin (HSA; Sigma-Aldrich) solution for 1 h. Then, sections were incubated in primary antibodies against choline-acetyltransferase (ChAT) or parvalbumin (PV) or calretinin (CR) together with anti-EGFP antibody (see Table S2) for 48–60 h. Sections were rinsed 3 times for 10 min in TBS; secondary fluorescent antibodies (see Table S3) were applied overnight. Sections were rinsed in TBS and 0.1 M PB and mounted on slides in Aquamount mounting medium (BDH Chemicals Ltd). Next, fluorescent images were taken with a Nikon A1R Confocal Laser Scanning Microscope. In target areas of BFPVNs, fluorescent images of 10x magnification were taken. The axon densities of BFPVN projections were estimated by the mean pixel brightness value in each region.

Retrograde tracing

Sections were washed in 0.1 M PB, incubated in 30% sucrose overnight for cryoprotection, then freeze-thawed over liquid nitrogen three times for antigen retrieval. Sections were subsequently washed in PB and Tris-buffered saline (TBS) and blocked in 1% HSA in TBS, then

incubated in a mixture of primary antibodies for 48–72 h. This was followed by extensive washes in TBS, and incubation in the mixture of appropriate secondary antibodies overnight. Then, sections were washed in TBS and PB, dried on slides and covered with Aquamount.

The combinations and specifications of the primary and secondary antibodies used are listed in Tables S2 and S3. The specificities of the primary antibodies were extensively tested, using knock-out mice if possible. Secondary antibodies were tested for possible cross-reactivity with the other antibodies used, and possible background labeling without primary antibodies was excluded.

Sections were imaged using a Nikon Ni-E Eclipse epifluorescent microscope system equipped with a 10× air objective and a Nikon DS-Fi3 camera. Fifty µm thick coronal sections spaced at 300 µm were prepared, so that approximately one-sixth of the whole brain was sampled to measure and estimate the number of transsynaptically labeled input cells.

Correlated light an electron microscopic analysis

Sections from the anterograde tracing experiments (see above) were imaged with Nikon A1R confocal laser scanning microscope for axon density measurements and for imaging target cell types. First, sections from anterograde tracing experiments were used for immunohistochemical staining against markers of possible target cell types (PV; VIP, vasoactive intestinal peptide; CB, calbindin; CR, calretinin; ChAT). A subset of sections were mounted in Aquamount mounting medium and imaged at 60× magnification and oil immersion with A1R Nikon Confocal laser scanning microscope. Sections from at least 3 animals were examined for possible contact sites between BFPVN projecting axons (labeled by eGFP) and target cell types. When possible terminal contacts were observed with a target cell type, another subset of sections from the same immunohistochemical experiment were mounted on slides in 0.1 M PB and were imaged similarly as described above. Possible terminal contacts were photographed at multiple magnifications (60×, 20×, 10×, and 4×) and surrounding landmarks blood vessels, location of ventricles, corpus callosum and other white matter tracts, tears at the edge of the section) were marked. After imaging, the sections were demounted from the slides to perform a second immunohistochemical staining to label eGFP (labeling BFPVNs and their projections) with 3,3′-Diaminobenzidine (DAB) as chromogen. Sections were rinsed extensively in TBS (3 × 10 min), then anti-chicken biotinylated secondary antibody was applied (in order to label eGFP-containing fibers, which were previously recognized by a chicken anti-eGFP primary antibody, see above) overnight. This step was followed by incubation in avidin–biotinylated horseradish peroxidase complex overnight (Elite ABC; 1:500; Vector Laboratories); the immunoperoxidase reaction was developed using DAB (Sigma-Aldrich) chromogen. Next, sections were mounted on slides in PB and light microscopic imaging (Nikon C2) was performed to reveal BFPVN axons. Next, light microscopic images were taken and aligned with former fluorescent images based on previously marked landmarks to determine the precise location of possible contact sites between BFPVN axons and target cell types on the light microscopic images. After this, sections were incubated with 0.5% osmium tetroxide in 0.1 M PB on ice and they were dehydrated using ascending alcohol series and acetonitrile, and finally incubated in 1% uranylacetate in 70% ethanol and embedded in Durcupan resin (ACM; Fluka). Brain regions containing the possible contact sites were re-embedded into resin blocks and 70 nm thick sections were cut with an ultra-microtome (Leica EM UC 6). Electron microscopic images were taken either with a Hitachi H-7100 transmission electron microscope or a FEI series electron microscope to reveal synaptic contacts between BFPVNs and target cell types in the MS, CA1 and retrosplenial cortex.

Data analysis

Analysis of extracellular recordings. Data analysis was carried out using custom written Matlab code (R2016a, Mathworks). Tetrode recording channels were digitally referenced to a common average reference, filtered between 700 and 7000 Hz with Butterworth zero-phase filter and spikes were detected using a 750 µs censoring period. Action potentials were sorted into putative single neurons manually by using MClust 3.5 (A.D Redish, University of Minnesota). Autocorrelations were examined for refractory period violations and only putative units with sufficient refractory period were included in the data set. Neurons with $p < 0.01$ significance values of the SALT statistical test (H-index) were considered light-activated, therefore BFPVNs (see above). Spike shape correlations between light-induced and spontaneous spikes were calculated for all BFPVNs. The correlation coefficient exceeded R = 0.84 in all and R = 0.9 in 22/36 optotagged neurons (0.96 ± 0.0085, median ± SE; range, 0.8427–0.9989, see also Cohen et al.[99]). Only those BFPVNs with high cluster quality (isolation distance > 20 and L-ratio <0.15 calculated based on full spike amplitude and first principal component of the waveform) were included in the final dataset for further analysis[25,100].

After spike sorting, the activity of individual neurons was aligned to cue presentation, reward and punishment delivery. Statistics were carried out on each neuronal unit; baseline activity was defined by taking a 1 s window before the cue, then firing rate in the baseline window was compared to firing rate in the test window (0–0.5 s after the event). One-sided hypotheses of firing rate increase and decrease were tested by Mann–Whitney U test ($p < 0.001$; for cue-evoked activity, separately for likely reward and likely punishment cue). Neurons were sorted into different groups based on their statistically significant responses to the behaviorally relevant events (e.g. activated by cue, inhibited by reward, etc.).

We calculated event-aligned raster plots and peri-event time histograms of spike times (PETHs) for all neurons, and lick times for all recording sessions, aligned to both behavioral events and/or photostimulation pulses. PETHs were smoothed with a Gaussian kernel. To calculate average PETHs, individual PETHs were Z-scored by the mean and standard deviation of a baseline window (1 s before cue onset) and averaged across neurons. Response latency and jitter to optogenetic stimulation and behavioral events were determined based on activation peaks in the PETHs. We performed K-means clustering of Z-scored PETHs (similar to ref. 99) aligned to the auditory cues for n = 685 well-isolated neurons recorded from the HDB of task-performing mice. We defined five separate clusters based on the first 3 principal components of the PETHs triggered on the two auditory cues. We ordered the clusters according to the percentage of tagged BFPVNs they contained and sorted the neurons within the clusters according to the principal components.

Autocorrelograms (ACG) were calculated at a 0.5 ms resolution. Burst index (BI) was calculated by the normalized difference between maximum ACG for 0-10 ms lags and mean ACG for 180–200 ms lags, where the normalizing factor was the greater of the two numbers, yielding an index between −1 and 1[101]. A neuron with a BI > 0.3 and a refractory period <2 ms was considered bursting, confirmed by the presence of burst shoulders on average ACG in the bursting group and the complete lack of burst shoulders on the average ACG in the non-bursting group. To examine burst coding in BFPVNs, analysis of neuronal responses to punishment were also carried out when only burst spikes or single spikes were considered for a neuron. A burst was detected whenever an inter-spike interval (ISI) was <10 ms and subsequent spikes were considered as part of the burst as long as the ISI remained <15 ms. Data were Z-score normalized with their surrogate mean and standard deviation to plot average ACG. The surrogates were generated according to ref. 102.

Fiber photometry signal processing. Fiber photometry signals were preprocessed according to refs. 103. Briefly, the recorded fluorescence signals were filtered using a low-pass Butterworth digital filter below 20 Hz to remove high-frequency noise. To calculate dff, a least-squares linear fit was applied to the isosbestic 405 nm signal to align its

baseline intensity to that of the calcium-dependent 465 nm (f_{465}) signal. The fitted 405 nm signal ($f_{405,\text{fitted}}$) was used to normalize the 465 nm signal as follows:

$$\text{dff} = \frac{f_{465} - f_{405,\text{fitted}}}{f_{405,\text{fitted}}} * 100 \quad (1)$$

to remove the effect of motion and autofluorescence. A 0.2 Hz high pass Butterworth digital filter was used to filter out the slow decrease of the baseline activity observed during the recording session. Finally, the dff signal was aligned to cue and reinforcement times, smoothed with a Gaussian kernel (width, 100 ms), Z-scored by the mean and standard deviation of a baseline window (1 s before cue onset) and averaged across sessions.

Statistics. Firing rates and other variables were compared across conditions using non-parametric tests (normality of the underlying distributions could not be determined unequivocally). For non-paired samples, Mann–Whitney *U* test was used; for paired samples, Wilcoxon signed-rank test was applied (two-sided unless stated otherwise). Pearson's correlation coefficient was used to estimate correlations between variables, and a standard linear regression approach was used to judge their significance (one-sided F-test, in accordance with the asymmetric null hypothesis of linear regression). Peri-event time histograms (PETHs) show mean ± SE. Box-whisker plots show median, interquartile range and non-outlier range, with all data points overlaid. Bar graphs show mean and all data points overlaid.

ROC analysis was performed to test if the anticipatory lick rate difference between Cue 1 and Cue 2 trials was different between control and ArchT groups in the optogenetic inhibition experiment. First, average PETH of lick rates were calculated for control and ArchT groups in a 1.1 s long time window from cue onset (from cue to reinforcement), then values at every 10 ms of the time window were taken. Next, area under the ROC curve (auROC) based on the cumulative density functions of lick rate differences in control and ArchT groups were calculated for each time point. The significance of the auROC was tested with a bootstrap permutation test with 200 resamplings.

Reporting summary

Further information on research design is available in the Nature Portfolio Reporting Summary linked to this article.

Data availability

The in vivo electrophysiology, fiber photometry and behavioral data generated in this study have been deposited at https://doi.org/10.6084/m9.figshare.22776776.v1, https://doi.org/10.6084/m9.figshare.25403350 and https://doi.org/10.6084/m9.figshare.25403593. Source data are provided with this paper.

Code availability

MATLAB codes generated for this study are available at https://github.com/hangyabalazs/PV_Pavlovian_analysis and also https://doi.org/10.5281/zenodo.10808341.

References

1. Mesulam, M.-M., Mufson, E. J., Levey, A. I. & Wainer, B. H. Cholinergic innervation of cortex by the basal forebrain: Cytochemistry and cortical connections of the septal area, diagonal band nuclei, nucleus basalis (Substantia innominata), and hypothalamus in the rhesus monkey. *J. Comp. Neurol.* **214**, 170–197 (1983).
2. Zaborszky, L., van den Pol, A. & Gyengesi, E. in *The Mouse Nervous System* (eds. Watson, C., Paxinos, G. & Puelles, L.) 684–718 (Elsevier, 2012). https://doi.org/10.1016/B978-0-12-369497-3.10028-7.
3. Lehmann, J., Nagy, J. I., Atmadja, S. & Fibiger, H. C. The nucleus basalis magnocellularis: the origin of a cholinergic projection to the neocortex of the rat. *Neuroscience* **5**, 1161–1174 (1980).
4. Gritti, I. et al. Stereological estimates of the basal forebrain cell population in the rat, including neurons containing choline acetyltransferase, glutamic acid decarboxylase or phosphate-activated glutaminase and colocalizing vesicular glutamate transporters. *Neuroscience* **143**, 1051–1064 (2006).
5. Gritti, I., Manns, I. D., Mainville, L. & Jones, B. E. Parvalbumin, calbindin, or calretinin in cortically projecting and GABAergic, cholinergic, or glutamatergic basal forebrain neurons of the rat. *J. Comp. Neurol.* **458**, 11–31 (2003).
6. Yang, C., Thankachan, S., McCarley, R. W. & Brown, R. E. The menagerie of the basal forebrain: how many (neural) species are there, what do they look like, how do they behave and who talks to whom? *Curr. Opin. Neurobiol.* **44**, 159–166 (2017).
7. Agostinelli, L. J., Geerling, J. C. & Scammell, T. E. Basal forebrain subcortical projections. *Brain Struct. Funct.* **224**, 1097–1117 (2019).
8. Do, J. P. et al. Cell type-specific long-range connections of basal forebrain circuit. *Elife* **5**, 1–17 (2016).
9. Maness, E. B. et al. Role of the locus coeruleus and basal forebrain in arousal and attention. *Brain Res. Bull.* **188**, 47–58 (2022).
10. Kim, T. et al. Cortically projecting basal forebrain parvalbumin neurons regulate cortical gamma band oscillations. *Proc. Natl Acad. Sci.* **112**, 3535–3540 (2015).
11. Király, B. et al. The medial septum controls hippocampal supratheta oscillations. *Nat. Commun.* **14**, 6159 (2023).
12. Xu, M. et al. Basal forebrain circuit for sleep-wake control. *Nat. Neurosci.* **18**, 1641–1647 (2015).
13. McKenna, J. T. et al. Basal forebrain parvalbumin neurons mediate arousals from sleep induced by hypercarbia or auditory stimuli. *Curr. Biol.* **30**, 2379–2385.e4 (2020).
14. Etter, G. et al. Optogenetic gamma stimulation rescues memory impairments in an Alzheimer's disease mouse model. *Nat. Commun.* **10**, 1–11 (2019).
15. Stanley, E. M., Fadel, J. R. & Mott, D. D. Interneuron loss reduces dendritic inhibition and GABA release in hippocampus of aged rats. *Neurobiol. Aging* **33**, 431.e1–431.e13 (2012).
16. Bañuelos, C. et al. Cognitive aging and the primate basal forebrain revisited: disproportionate GABAergic vulnerability revealed. *J. Neurosci.* **43**, 8425–8441 (2023).
17. Chaves-Coira, I., García-Magro, N., Zegarra-Valdivia, J., Torres-Alemán, I. & Núñez, Á. Cognitive deficits in aging related to changes in basal forebrain neuronal activity. *Cells* **12**, 1477 (2023).
18. Burk, J. & Sarter, M. Dissociation between the attentional functions mediated via basal forebrain cholinergic and GABAergic neurons. *Neuroscience* **105**, 899–909 (2001).
19. McGaughy, J., Dalley, J. W., Morrison, C. H., Everitt, B. J. & Robbins, T. W. Selective behavioral and neurochemical effects of cholinergic lesions produced by intrabasalis infusions of 192 IgG-Saporin on attentional performance in a five-choice serial reaction time task. *J. Neurosci.* **22**, 1905–1913 (2002).
20. Roßner, S. Cholinergic immunolesions by 192IgG-saporin—a useful tool to simulate pathogenic aspects of alzheimer's disease. *Int. J. Dev. Neurosci.* **15**, 835–850 (1997).
21. Muir, J. L., Page, K. J., Sirinathsinghji, D. J. S., Robbins, T. W. & Everitt, B. J. Excitotoxic lesions of basal forebrain cholinergic neurons: effects on learning, memory and attention. *Behav. Brain Res.* **57**, 123–131 (1993).
22. Roland, J. J., Janke, K. L., Servatius, R. J. & Pang, K. C. H. GABAergic neurons in the medial septum-diagonal band of Broca (MSDB) are important for acquisition of the classically conditioned eyeblink response. *Brain Struct. Funct.* **219**, 1231–1237 (2014).

23. Lin, S.-C. & Nicolelis, M. A. L. Neuronal ensemble bursting in the basal forebrain encodes salience irrespective of valence. *Neuron* **59**, 138–149 (2008).
24. Avila, I. & Lin, S.-C. Motivational salience signal in the basal forebrain is coupled with faster and more precise decision speed. *PLoS Biol.* **12**, e1001811 (2014).
25. Hangya, B., Ranade, S. P., Lorenc, M. & Kepecs, A. Central cholinergic neurons are rapidly recruited by reinforcement feedback. *Cell* **162**, 1155–1168 (2015).
26. Hegedüs, P. et al. Training protocol for probabilistic Pavlovian conditioning in mice using an open-source head-fixed setup. *STAR Protoc.* **2**, 100795 (2021).
27. Trask, S. & Helmstetter, F. J. Unique roles for the anterior and posterior retrosplenial cortices in encoding and retrieval of memory for context. *Cereb. Cortex* **32**, 3602–3610 (2022).
28. Stepanichev, M., Lazareva, N., Tukhbatova, G., Salozhin, S. & Gulyaeva, N. Transient disturbances in contextual fear memory induced by Aβ(25-35) in rats are accompanied by cholinergic dysfunction. *Behav. Brain Res.* **259**, 152–157 (2014).
29. Tsai, T. C., Yu, T. H., Hung, Y. C., Fong, L. I. & Hsu, K. S. Distinct contribution of granular and agranular subdivisions of the retrosplenial cortex to remote contextual fear memory retrieval. *J. Neurosci.* **42**, 877–893 (2022).
30. Mitsushima, D., Sano, A. & Takahashi, T. A cholinergic trigger drives learning-induced plasticity at hippocampal synapses. *Nat. Commun.* **4**, 1–10 (2013).
31. Pan, T. T. et al. Retrosplenial cortex effects contextual fear formation relying on dysgranular constituent in rats. *Front. Neurosci.* **16**, 1–10 (2022).
32. Tronson, N. C. et al. Segregated populations of hippocampal principal CA1 neurons mediating conditioning and extinction of contextual fear. *J. Neurosci.* **29**, 3387–3394 (2009).
33. Kocsis, B. et al. Huygens synchronization of medial septal pacemaker neurons generates hippocampal theta oscillation. *Cell Rep.* **40**, 111149 (2022).
34. Sturgill, J. F. et al. Basal forebrain-derived acetylcholine encodes valence-free reinforcement prediction error. *bioRxiv* https://doi.org/10.1101/2020.02.17.953141. (2020).
35. Hegedüs, P., Sviatkó, K., Király, B., Martínez-Bellver, S. & Hangya, B. Cholinergic activity reflects reward expectations and predicts behavioral responses. *iScience* **26**, 105814 (2023).
36. Laszlovszky, T. et al. Distinct synchronization, cortical coupling and behavioral function of two basal forebrain cholinergic neuron types. *Nat. Neurosci.* **23**, 992–1003 (2020).
37. Szőnyi, A. et al. Median raphe controls acquisition of negative experience in the mouse. *Science* **366**, eaay8746 (2019).
38. Sos, K. E. et al. Cellular architecture and transmitter phenotypes of neurons of the mouse median raphe region. *Brain Struct. Funct.* **222**, 287–299 (2017).
39. Varga, V. et al. Fast synaptic subcortical control of hippocampal circuits. *Science* **326**, 449–453 (2009).
40. Yoder, R. M. & Pang, K. C. H. Involvement of GABAergic and cholinergic medial septal neurons in hippocampal theta rhythm. *Hippocampus* **15**, 381–392 (2005).
41. Dwyer, T. A., Servatius, R. J. & Pang, K. C. H. Noncholinergic lesions of the medial septum impair sequential learning of different spatial locations. *J. Neurosci.* **27**, 299–303 (2007).
42. McKenna, J. T. et al. Distribution and intrinsic membrane properties of basal forebrain GABAergic and parvalbumin neurons in the mouse. *J. Comp. Neurol.* **521**, 1225–1250 (2013).
43. Calandreau, L., Jaffard, R. & Desmedt, A. Dissociated roles for the lateral and medial septum in elemental and contextual fear conditioning. *Learn. Mem.* **14**, 422–429 (2007).
44. Freund, T. F. & Antal, M. GABA-containing neurons in the septum control inhibitory interneurons in the hippocampus. *Nature* **336**, 403–405 (1988).
45. Freund, T. F. GABAergic septohippocampal neurons contain parvalbumin. *Brain Res.* **478**, 375–381 (1989).
46. Tian, J. et al. Dissection of the long-range projections of specific neurons at the synaptic level in the whole mouse brain. *Proc. Natl Acad. Sci.* **119**, 1–10 (2022).
47. Yawata, Y. et al. Mesolimbic dopamine release precedes actively sought aversive stimuli in mice. *Nat. Commun.* **14**, 2433 (2023).
48. Faget, L. et al. Opponent control of behavioral reinforcement by inhibitory and excitatory projections from the ventral pallidum. *Nat. Commun.* **9**, 849 (2018).
49. Stephenson-Jones, M. et al. Opposing contributions of GABAergic and glutamatergic ventral pallidal neurons to motivational behaviors. *Neuron* **105**, 921–933.e5 (2020).
50. Manning, E. E., Bradfield, L. A. & Iordanova, M. D. Adaptive behaviour under conflict: Deconstructing extinction, reversal, and active avoidance learning. *Neurosci. Biobehav. Rev.* **120**, 526–536 (2021).
51. Barbano, M. F. et al. Lateral hypothalamic glutamatergric inputs to VTA glutamatergric neurons mediate prioritization of innate defensive behavior over feeding. *IBRO Neurosci. Rep.* **15**, S935–S936 (2023).
52. McKenna, J. T. et al. Characterization of basal forebrain glutamate neurons suggests a role in control of arousal and avoidance behavior. *Brain Struct. Funct.* **226**, 1755–1778 (2021).
53. Kilgard, M. P. & Merzenich, M. M. Cortical map reorganization enabled by nucleus basalis activity. *Science* **279**, 1714–1718 (1998). (80-.).
54. Froemke, R. C., Merzenich, M. M. & Schreiner, C. E. A synaptic memory trace for cortical receptive field plasticity. *Nature* **450**, 425–429 (2007).
55. Seol, G. H. et al. Neuromodulators control the polarity of spike-timing-dependent synaptic plasticity. *Neuron* **55**, 919–929 (2007).
56. Gu, Z. & Yakel, J. L. Timing-dependent septal cholinergic induction of dynamic hippocampal synaptic plasticity. *Neuron* **71**, 155–165 (2011).
57. Kai, Y., Oomura, Y. & Shimizu, N. Responses of rat lateral hypothalamic neurons to periaqueductal gray stimulation and nociceptive stimuli. *Brain Res.* **461**, 107–117 (1988).
58. Berthoud, H.-R. & Münzberg, H. The lateral hypothalamus as integrator of metabolic and environmental needs: From electrical self-stimulation to opto-genetics. *Physiol. Behav.* **104**, 29–39 (2011).
59. Burstein, R., Cliffer, K. & Giesler, G. Direct somatosensory projections from the spinal cord to the hypothalamus and telencephalon. *J. Neurosci.* **7**, 4159–4164 (1987).
60. Hegedüs, P., Heckenast, J. & Hangya, B. Differential recruitment of ventral pallidal e-types by behaviorally salient stimuli during Pavlovian conditioning. *iScience* **24**, 102377 (2021).
61. Zhang, G.-W. et al. A non-canonical reticular-limbic central auditory pathway via medial septum contributes to fear conditioning. *Neuron* **97**, 406–417.e4 (2018).
62. Ang, S. T. et al. GABAergic neurons of the medial septum play a nodal role in facilitation of nociception-induced affect. *Sci. Rep.* **5**, 15419 (2015).
63. Cohen, J. Y., Amoroso, M. W. & Uchida, N. Serotonergic neurons signal reward and punishment on multiple timescales. *Elife* **4**, 06346 (2015).
64. Ranade, S. P. & Mainen, Z. F. Transient firing of dorsal raphe neurons encodes diverse and specific sensory, motor, and reward events. *J. Neurophysiol.* **102**, 3026–3037 (2009).

65. Sheehan, T. P., Chambers, R. A. & Russell, D. S. Regulation of affect by the lateral septum: implications for neuropsychiatry. *Brain Res. Rev.* **46**, 71–117 (2004).
66. Rocamora, N. et al. Expression of NGF and NT3 mRNAs in Hippocampal Interneurons Innervated by the GABAergic Septohippocampal Pathway. *J. Neurosci.* **16**, 3991–4004 (1996).
67. Solari, N. & Hangya, B. Cholinergic modulation of spatial learning, memory and navigation. *Eur. J. Neurosci.* **48**, 2199–2230 (2018).
68. Miller, A. M. P., Vedder, L. C., Law, L. M. & Smith, D. M. Cues, context, and long-term memory: the role of the retrosplenial cortex in spatial cognition. *Front. Hum. Neurosci.* **8**, 1–15 (2014).
69. Borhegyi, Z., Varga, V., Szilagyi, N., Fabo, D. & Freund, T. F. Phase segregation of medial septal GABAergic neurons during hippocampal theta activity. *J. Neurosci.* **24**, 8470–8479 (2004).
70. Villar, P. S., Hu, R. & Araneda, R. C. Long-range GABAergic inhibition modulates spatiotemporal dynamics of the output neurons in the olfactory bulb. *J. Neurosci.* **41**, 3610–3621 (2021).
71. Gracia-Llanes, F. J. et al. GABAergic basal forebrain afferents innervate selectively GABAergic targets in the main olfactory bulb. *Neuroscience* **170**, 913–922 (2010).
72. Salib, M. et al. GABAergic medial septal neurons with low-rhythmic firing innervating the dentate gyrus and hippocampal area CA3. *J. Neurosci.* **39**, 4527–4549 (2019).
73. Viney, T. J. et al. Shared rhythmic subcortical GABAergic input to the entorhinal cortex and presubiculum. *Elife* **7**, 1–35 (2018).
74. McDonald, A. J., Muller, J. F. & Mascagni, F. Postsynaptic targets of GABAergic basal forebrain projections to the basolateral amygdala. *Neuroscience* **183**, 144–159 (2011).
75. Freund, T. F. & Meskenaite, V. Gamma-aminobutyric acid-containing basal forebrain neurons innervate inhibitory interneurons in the neocortex. *Proc. Natl Acad. Sci.* **89**, 738–742 (1992).
76. Zaborszky, L. et al. Neurons in the basal forebrain project to the cortex in a complex topographic organization that reflects corticocortical connectivity patterns: an experimental study based on retrograde tracing and 3D reconstruction. *Cereb. Cortex* **25**, 118–137 (2015).
77. Gielow, M. R. & Zaborszky, L. The input-output relationship of the cholinergic basal forebrain. *Cell Rep.* **18**, 1817–1830 (2017).
78. Jiang, L. et al. Cholinergic signaling controls conditioned fear behaviors and enhances plasticity of cortical-amygdala circuits. *Neuron* **90**, 1057–1070 (2016).
79. Záborszky, L. et al. Specific basal forebrain–cortical cholinergic circuits coordinate cognitive operations. *J. Neurosci.* **38**, 9446–9458 (2018).
80. Staib, J. M., Della Valle, R. & Knox, D. K. Disruption of medial septum and diagonal bands of Broca cholinergic projections to the ventral hippocampus disrupt auditory fear memory. *Neurobiol. Learn. Mem.* **152**, 71–79 (2018).
81. Marks, W. D., Yokose, J., Kitamura, T. & Ogawa, S. K. Neuronal ensembles organize activity to generate contextual memory. *Front. Behav. Neurosci.* **16**, 1–16 (2022).
82. Wulff, A. B., Tooley, J., Marconi, L. J. & Creed, M. C. Ventral pallidal modulation of aversion processing. *Brain Res.* **1713**, 62–69 (2019).
83. Farrell, M. R. et al. Ventral pallidum GABA neurons mediate motivation underlying risky choice. *J. Neurosci.* **41**, 4500–4513 (2021).
84. Fournier, D. I., Monasch, R. R., Bucci, D. J. & Todd, T. P. Retrosplenial cortex damage impairs unimodal sensory preconditioning. *Behav. Neurosci.* **134**, 198–207 (2020).
85. Lozano-Montes, L. et al. Optogenetic stimulation of basal forebrain parvalbumin neurons activates the default mode network and associated behaviors. *Cell Rep.* **33**, 108359 (2020).
86. Aguilar, D. D. & McNally, J. M. Subcortical control of the default mode network: Role of the basal forebrain and implications for neuropsychiatric disorders. *Brain Res. Bull.* **185**, 129–139 (2022).
87. Lewthwaite, R. & Wulf, G. Optimizing motivation and attention for motor performance and learning. *Curr. Opin. Psychol.* **16**, 38–42 (2017).
88. Kvitsiani, D. et al. Distinct behavioural and network correlates of two interneuron types in prefrontal cortex. *Nature* **498**, 363–366 (2013).
89. Pi, H.-J. et al. Cortical interneurons that specialize in disinhibitory control. *Nature* **503**, 521–524 (2013).
90. Solari, N., Sviatkó, K., Laszlovszky, T., Hegedüs, P. & Hangya, B. Open source tools for temporally controlled rodent behavior suitable for electrophysiology and optogenetic manipulations. *Front. Syst. Neurosci.* **12**, 18 (2018).
91. Janssen, P. & Shadlen, M. N. A representation of the hazard rate of elapsed time in macaque area LIP. *Nat. Neurosci.* **8**, 234–241 (2005).
92. Ralls, K. Auditory sensitivity in mice: peromyscus and Mus musculus. *Anim. Behav.* **15**, 123–128 (1967).
93. Najafi, F., Giovannucci, A., Wang, S. S. H. & Medina, J. F. Coding of stimulus strength via analog calcium signals in Purkinje cell dendrites of awake mice. *Elife* **3**, e03663 (2014).
94. Ferguson, J. E., Boldt, C. & Redish, A. D. Creating low-impedance tetrodes by electroplating with additives. *Sens. Actuators A: Phys.* **156**, 388–393 (2009).
95. Széll, A., Martínez-Bellver, S., Hegedüs, P. & Hangya, B. OPETH: open source solution for real-time peri-event time histogram based on open Ephys. *Front. Neuroinform.* **14**, 1–19 (2020).
96. Endres, D. M. & Schindelin, J. E. A new metric for probability distributions. *IEEE Trans. Inf. Theory* **49**, 1858–1860 (2003).
97. Fraser, G. W. & Schwartz, A. B. Recording from the same neurons chronically in motor cortex. *J. Neurophysiol.* **107**, 1970–1978 (2012).
98. Paxinos, G. & Franklin, K. B. J. *The Mouse Brain in Stereotaxic Coordinates* 2nd ed. (Academic Press, 2001).
99. Cohen, J. Y., Haesler, S., Vong, L., Lowell, B. B. & Uchida, N. Neuron-type-specific signals for reward and punishment in the ventral tegmental area. *Nature* **482**, 85–88 (2012).
100. Schmitzer-Torbert, N., Jackson, J., Henze, D., Harris, K. & Redish, A. D. Quantitative measures of cluster quality for use in extracellular recordings. *Neuroscience* **131**, 1–11 (2005).
101. Royer, S. et al. Control of timing, rate and bursts of hippocampal place cells by dendritic and somatic inhibition. *Nat. Neurosci.* **15**, 769–775 (2012).
102. Fujisawa, S., Amarasingham, A., Harrison, M. T. & Buzsáki, G. Behavior-dependent short-term assembly dynamics in the medial prefrontal cortex. *Nat. Neurosci.* **11**, 823–833 (2008).
103. Lerner, T. N. et al. Intact-brain analyses reveal distinct information carried by SNc dopamine subcircuits. *Cell* **162**, 635–647 (2015).

Acknowledgements

The authors thank Katalin Lengyel for technical assistance in anatomical methods, Ilka Jakab and Melinda Szabó for assistance in behavioral training and Dr. Norbert Hájos for helpful comments on the manuscript. We thank the FENS-Kavli Network of Excellence for fruitful discussions. This work was supported by the "Lendület" Program (LP2015-2/2015), NKFIH K135561, NKFIH K147097 and the European Research Council Starting Grant no. 715043 to B.H.; the Hungarian Brain Research Program

NAP3.0 (NAP2022-I-1/2022) by the Hungarian Academy of Sciences and the European Union project RRF-2.3.1-21-2022-00004 within the framework of the Artificial Intelligence National Laboratory to B.H. and G.N.; Frontline Research Excellence Programme by the Hungarian National Research, Development and Innovation Office (NRDI Fund 133837) and the European Union project RRF-2.3.1-21-2022-00011 within the framework of the Translational Neuroscience National Laboratory to GN; ÚNKP-21-3 New National Excellence Program of the Ministry for Innovation and Technology and the Kerpel Scholarship of Semmelweis University to P.H; ÚNKP-23-4-II New National Excellence Program of the Ministry for Culture and Innovation from the source of the National Research, Development and Innovation Fund to D.S. We acknowledge the help of the Nikon Center of Excellence at the HUN-REN Institute of Experimental Medicine (IEM), Nikon Europe, Nikon Austria, and Auro-Science Consulting for kindly providing microscopy support and the supportive help of the Central Virus Laboratory and the Behavioral Unit of IEM. We thank István Katona for kindly providing access to an in vitro electrophysiology setup. We thank Mackenzie Mathis, Ann Kennedy and Ethan Tyler for open access science art at SciDraw.

Author contributions

P.H. and B.H. conceived the study; P.H. performed the immunohistological experiments, fluorescent and electron microscopic imaging; M.M and G.N. performed the retrograde tracing experiments; P.H., I.S., A.V., and Z.Z. performed the recording and optogenetic activation experiments; P.H., A.V. and V.L. conducted the fiber photometry and optogenetic inhibition experiments; D.S. conducted the in vitro electrophysiology experiments; P.H., B.K., D.S. and V.L. analyzed the data; P.H., B.K., D.S., M.M., and G.N. prepared the figures; B.H. and P.H. wrote the manuscript with inputs from all authors.

Competing interests

The authors declare no competing interests.

Additional information

Supplementary information The online version contains supplementary material available at https://doi.org/10.1038/s41467-024-48755-7.

Correspondence and requests for materials should be addressed to Balázs Hangya.

Peer review information : *Nature Communications* thanks Shih-Chieh Lin and the other, anonymous, reviewer(s) for their contribution to the peer review of this work. A peer review file is available.

Parvalbumin-expressing basal forebrain neurons mediate learning from negative experience

Hegedüs, Király & Schlingloff et al.

Supplementary Information

Supplementary Figures

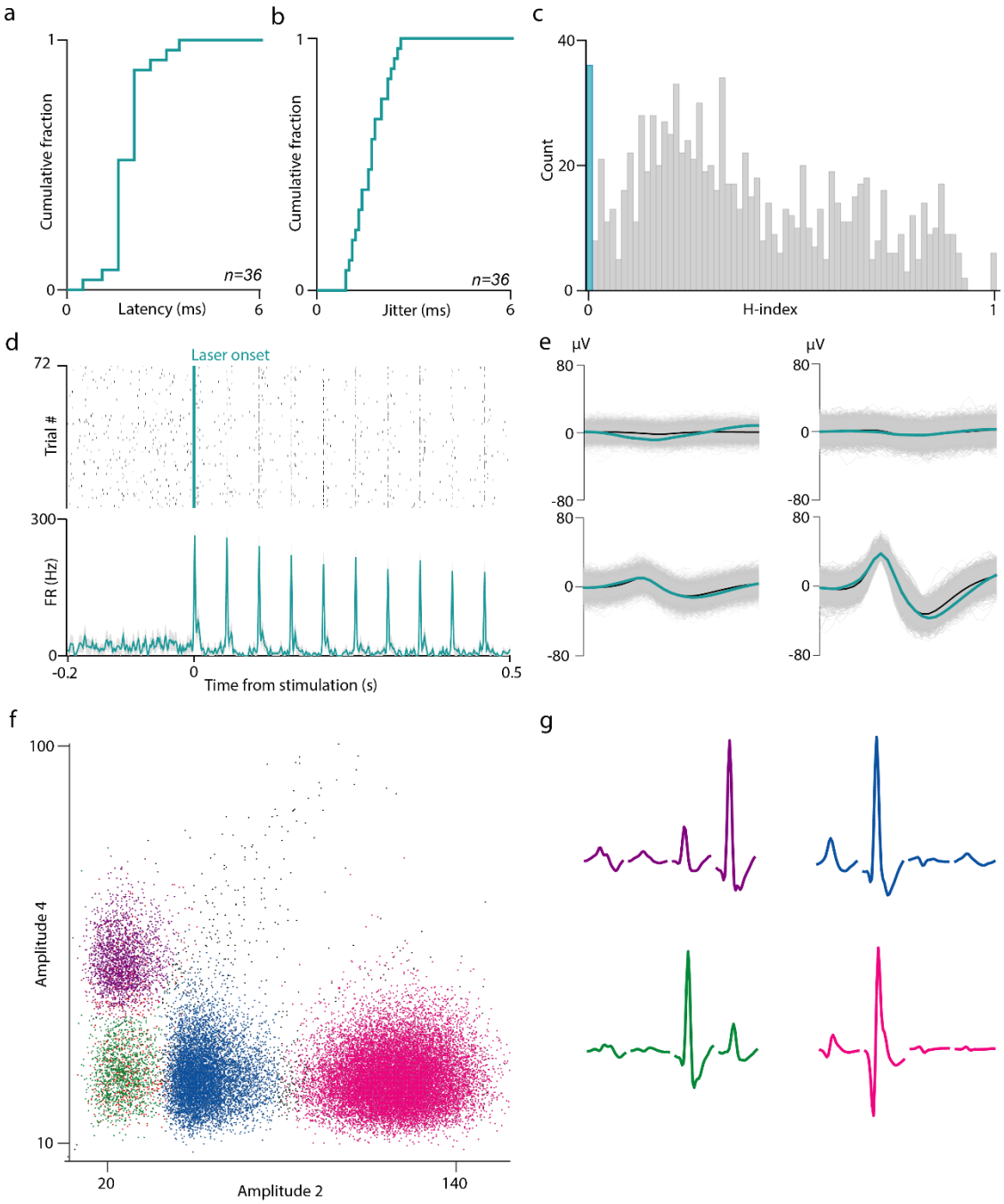

Figure S1. Optogenetic tagging of HDB BFPVNs. a, Cumulative histogram of the peak response latency of BFPVNs after optogenetic stimulation (n = 36). **b,** Cumulative histogram of the jitter of BFPVN spike responses after optogenetic stimulation (n = 36). **c,** Distribution of the significance values of the SALT statistical test (H-index) for all recorded neurons (blue, $p < 0.01$, tagged BFPVNs; grey, $p > 0.01$, untagged neurons). **d,** Example spike raster and PETH of an optogenetically tagged BFPVN responding to 20 Hz blue laser light stimulation. **e,**

Average spike waveform of the same BFPVN on the four tetrode channels (blue, average light-evoked spikes; black, average spontaneous spikes; grey, all spikes). **f,** Spike clusters plotted in feature space from an example recording session. **g,** Average spike waveforms of the recorded neurons on each tetrode channel from the same session.

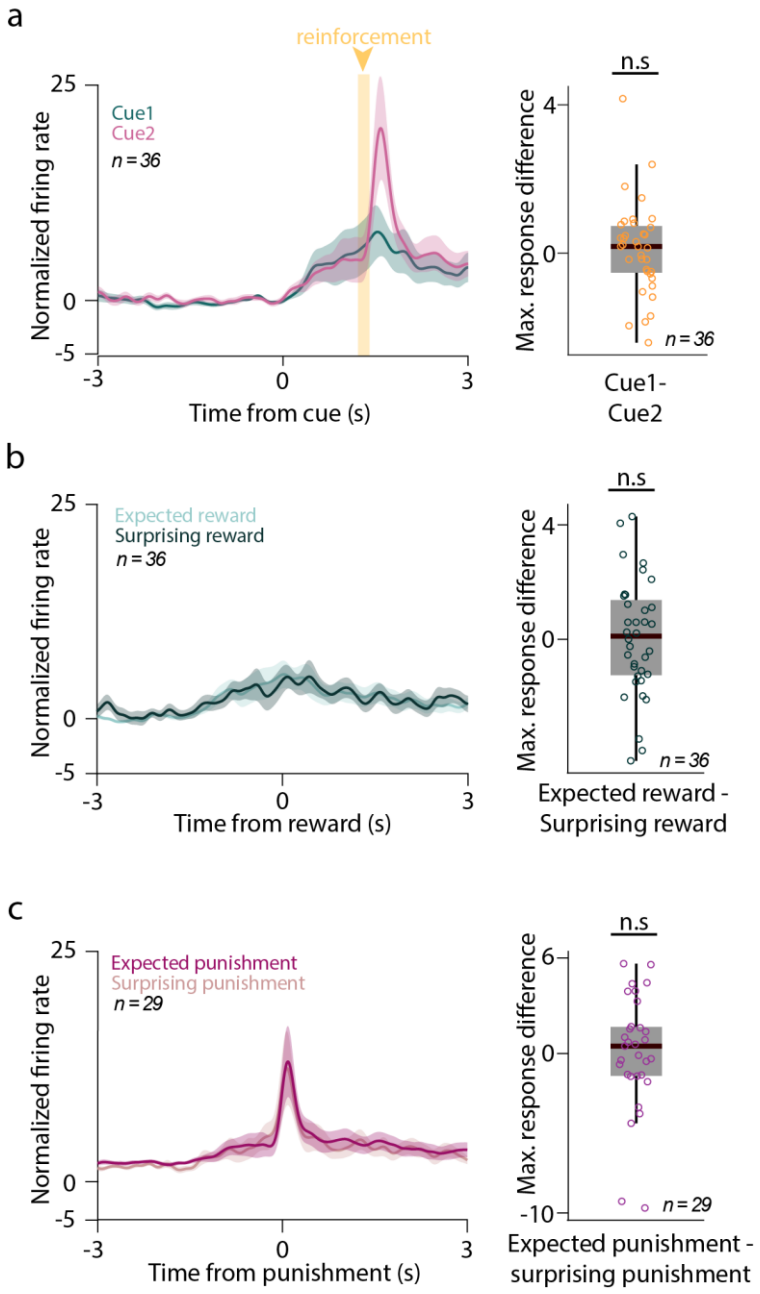

Figure S2. HDB BFPVNs are not modulated by outcome expectation. a, Left, average PETH of BFPVNs aligned to cue onset (n = 36). Right, difference of peak response to Cue 1 and Cue 2 (in a 0-0.5s time window from cue onset). n.s., $p > 0.05$, $p = 0.6151$, two-sided Wilcoxon signed-rank test. **b,** Left, average PETH of BFPVNs aligned to expected and surprising reward (n = 36). Right, difference of peak response to expected and surprising reward. n.s., $p > 0.05$, $p = 0.8628$, two-sided Wilcoxon signed-rank test. **c,** Left, average PETH of BFPVNs aligned to expected and surprising punishment (n = 29, 7 neurons excluded from this analysis because there were only 5 or less surprising punishments in the session). Right, difference of peak response to expected and surprising punishment. n.s., $p > 0.05$, $p = 0.5566$, two-sided Wilcoxon signed-rank test. Source data are provided as a Source Data file.

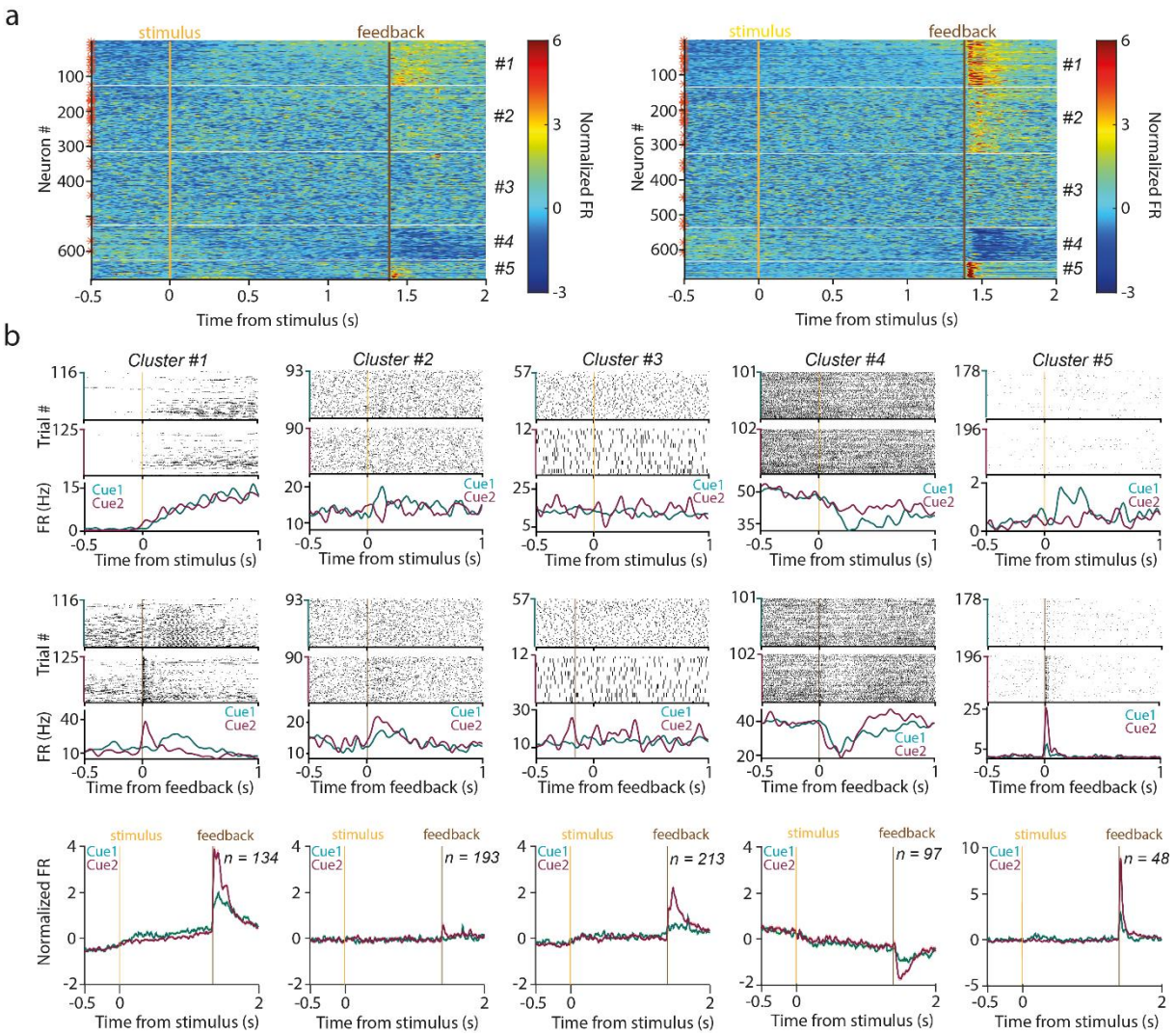

Figure S3. K-means clustering of BF neuronal responses reveals groups of neurons with distinct firing patterns. a, Color-coded, Z-scored PETHs of all neurons aligned to Cue 1 (left) and Cue 2 (right; n = 685). Red asterisks indicate tagged BFPVNs. The clusters were ordered according to percentage of tagged neurons. **b,** Top and middle, PETH of example neurons aligned to stimulus (top) and reinforcement (middle). Bottom, Average, Z-scored PETH of each cluster.

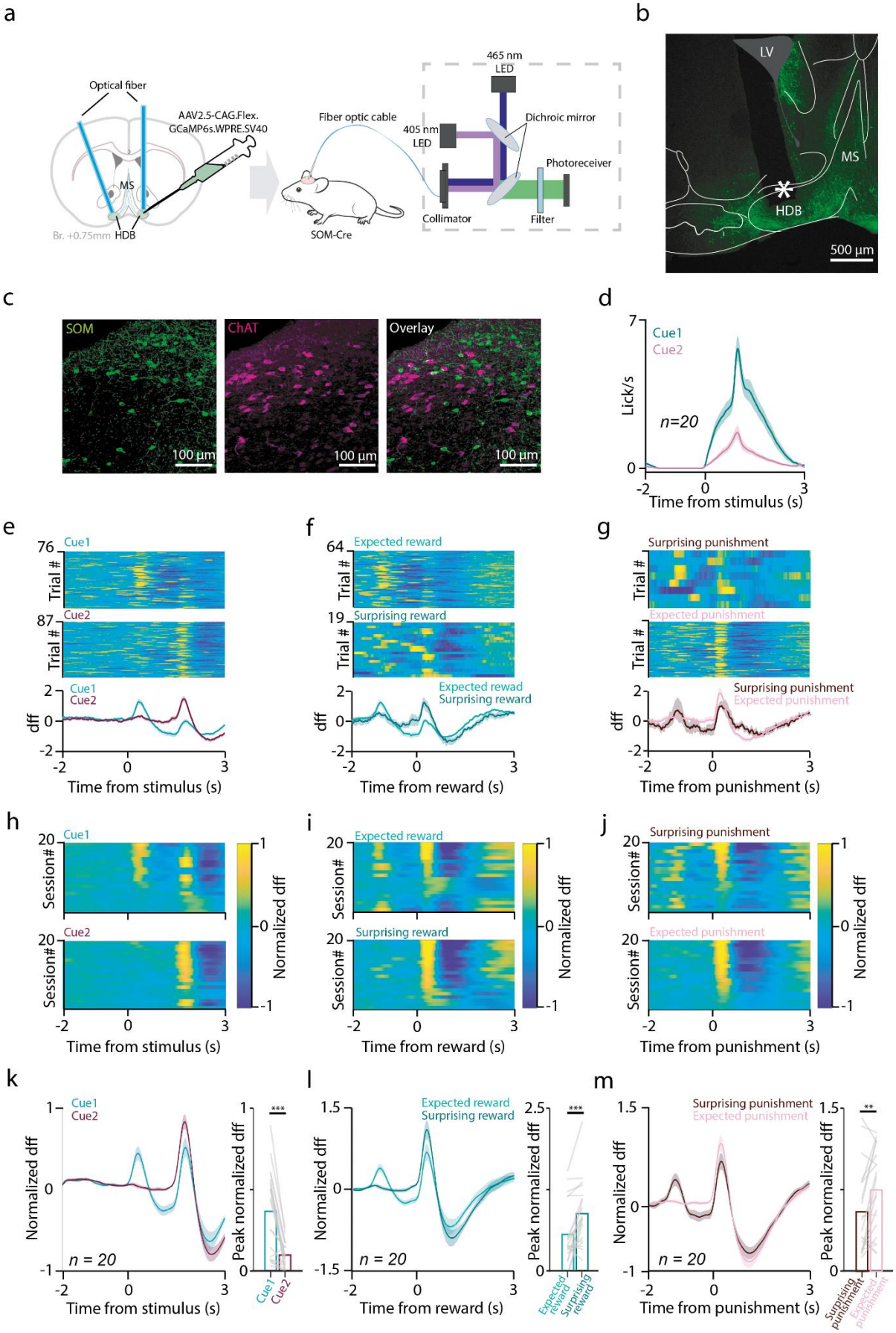
a
Optical fiber
AAV2.5-CAG.Flex.
GCaMP6s.WPRE.SV40
MS
Br. +0.75mm HDB
Fiber optic cable
SOM-Cre
465 nm
LED
405 nm
LED
Dichroic mirror
Photoreceiver
Collimator
Filter
b
LV
MS
HDB
500 µm
c
SOM
ChAT
Overlay
100 µm
d
Cue1
Cue2
Lick/s
n=20
Time from stimulus (s)
e
Cue1
Cue2
Trial #
dff
Time from stimulus (s)
f
Expected reward
Surprising reward
Expected rewad
Surprising reward
Time from reward (s)
g
Surprising punishment
Expected punishment
Time from punishment (s)
h
Session#
Normalized dff
Time from stimulus (s)
i
Time from reward (s)
j
Time from punishment (s)
k
n = 20
Peak normalized dff
***
l
m
**

Figure S4. BFSOMNs respond to reward, punishment, and reward-predictive auditory cues. a, Schematic diagram of bulk calcium measurements of BFSOMNs. Created using Tyler, E., & Kravitz, L. (2020). mouse, Zenodo, https://doi.org/10.5281/zenodo.3925901, under Creative Commons 4.0 license (https://creativecommons.org/licenses/by/4.0/). The original image was modified by adding illustrations of optic cable and photometry recording system. **b**, Fluoromicrograph of an optical fiber track (green, GCaMP6s; asterisk, tip of the optical fiber). **c**, Immunohistochemical staining of the HDB shows no overlap between BFSOMNs and BFCNs (green, SOM; magenta, ChAT; 8 out of 392 SOM cells (~ 2%) expressed ChAT, n = 5 animals). **d,** SOM-Cre mice have learned the task indicated by higher anticipatory lick rate to the reward predicting cue. **e-g,** PETHs of bulk-calcium recording of BFSOMNs aligned to cue (left), reward (middle) and punishment (right) in an example session (top, trial-by-trial data; bottom, session average). **h-j,** Color-coded PETH showing all recorded training sessions where animals have acquired the task contingencies, aligned to cue (left), reward (middle) and punishment (right). **k-m,** Average PETHs of BFSOMN response during the task, aligned to cue (left), reward (middle) and punishment (right). PETHs were smoothed with a Gaussian kernel (width, 100 ms). Bar plots represent the mean of the peak response distribution. Errorshades on all PETHs indicate SEM. Two-sided Wilcoxon signed-rank test; **, $p \leq 0.01$; ***, $p \leq 0.001$. Cue responses, $p = 0.000189$; reward responses, $p = 0.000681$; punishment responses, $p = 0.01$. Source data are provided as a Source Data file.

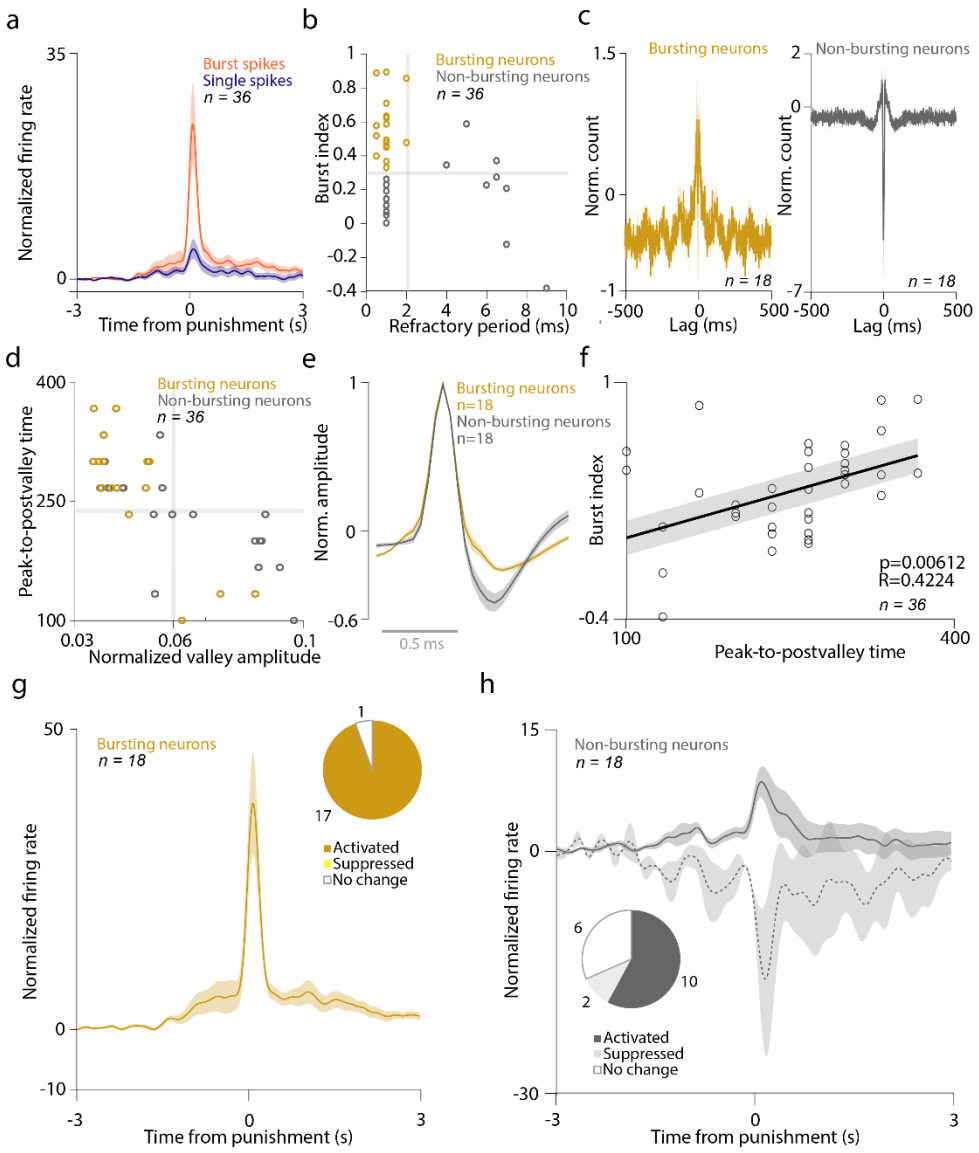

Figure S5. Electrophysiological properties of HDB BFPVNs. a, Average PETH of burst spikes and single spikes aligned to punishment onset (n = 36; errorshade, SEM). **b,** BFPVNs were partitioned based on burst index and refractory period. Neurons with high (> 0.3) burst index and short (< 2 ms) refractory period were considered as bursting neurons. Neurons with low burst index and/or long refractory period were considered non-bursting. **c,** Average autocorrelogram of bursting (left) and non-bursting (right) neurons (errorshade, SEM). **d,** Spike shape features of BFPVNs (peak-to-post-valley time and post-valley magnitude, normalized to the integral). Most bursting neurons had smaller valley and longer peak-to-post-valley time. **e,** Average spike shape of bursting and non-bursting neurons (errorshade, SEM). **f,** Correlation of burst index and peak-to-post-valley time. **g,** Average PETH of bursting BFPVNs aligned to punishment (errorshade, SEM). Pie chart showing activation, suppression or no response to

punishment of bursting BFPVNs (n = 18). **h,** Average PETH of non-bursting BFPVNs aligned to punishment (errorshade, SEM). Pie chart showing activation, suppression, or no response to punishment of non-bursting BFPVNs (n = 18). Source data are provided as a Source Data file.

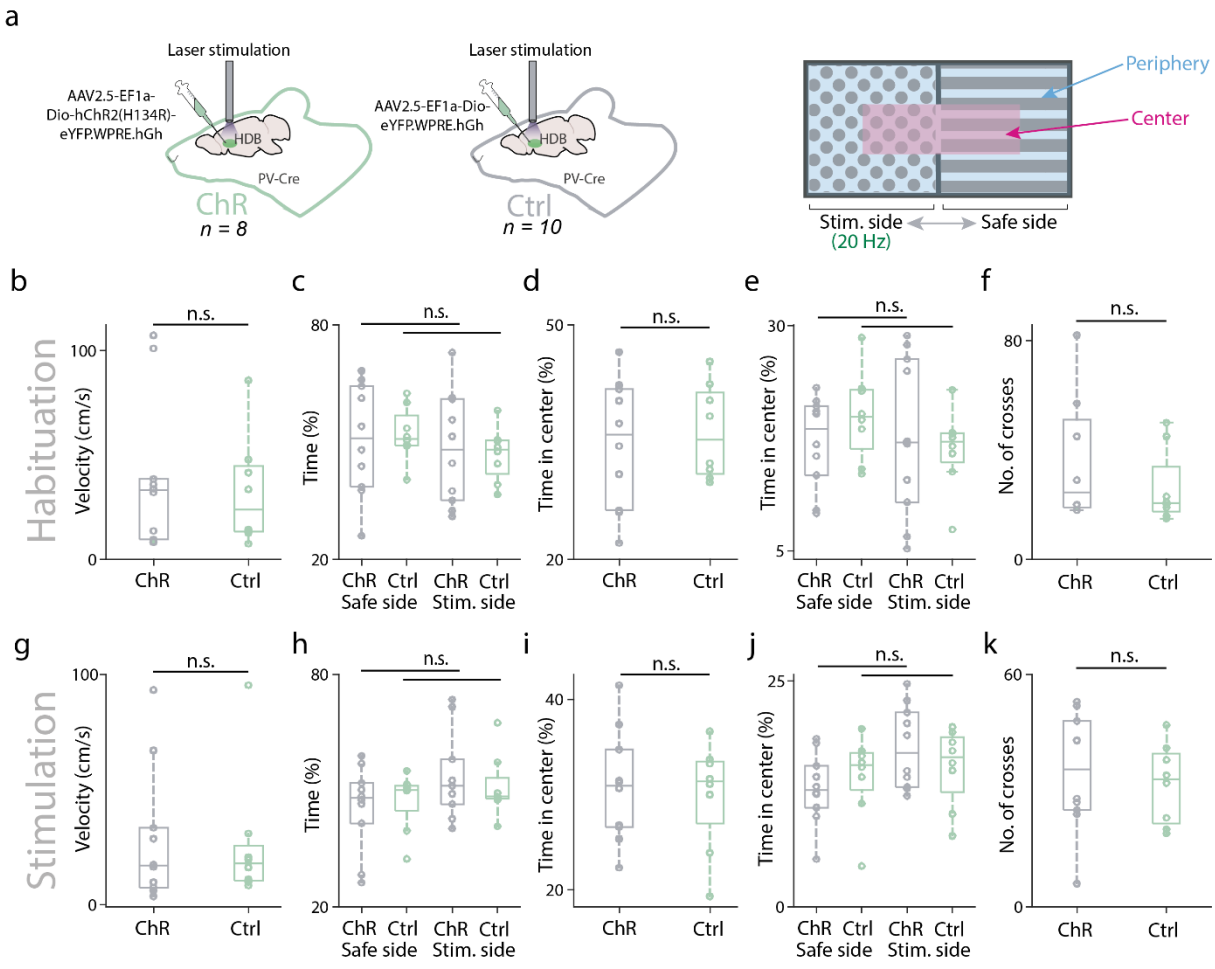

Fig S6. Conditioned place aversion. a, Schematic illustration of the experiment (for further details, see Methods). ChR, channelrhodopsin; Ctrl, control; Stim. side, stimulated side. Created using Kennedy, A. (2020) Mouse brain silhouette, Zenodo, https://doi.org/10.5281/zenodo.3925919, under Creative Commons 4.0 license (https://creativecommons.org/licenses/by/4.0/). The original image was modified by adding illustrations of a syringe and an optic fiber as well as modifying colors. **b,** Velocity of channelrhodopsin-expressing (ChR, n = 8) and control (Ctrl, n = 10) animals during habituation (n.s., p > 0.05, p = 0.4557, Mann-Whitney U-test). Box plots indicate median and interquartile range; whiskers indicate the non-outlier range in all graphs in this figure. **c,** Proportion of time spent on the safe (non-stimulated) and stimulated side during habituation (n.s., p > 0.05, p = 0.9591 and p = 0.6454, Mann-Whitney U-test). **d,** Overall proportion of time spent in the center area during habituation (n.s., p > 0.05, p = 0.8673, Mann-Whitney U-test). **e,** Proportion of time spent in center area on the stimulated and safe sides during habituation (n.s., p > 0.05, p = 0.2134 and p = 0.7643, Mann-Whitney U-test). **f,** Number of side crosses during habituation (n.s., p > 0.05, p = 0.4538, Mann-Whitney U-test). **g-k,** Same as in b-f, but during the

stimulation phase (n.s., $p > 0.05$, $p = 0.6334$, $p = 0.7985$, $p = 0.995$, $p = 0.6734$, $p = 0.4352$, $p = 0.2452$, $p = 0.3955$, respectively, Mann-Whitney U-test). Source data are provided as a Source Data file.

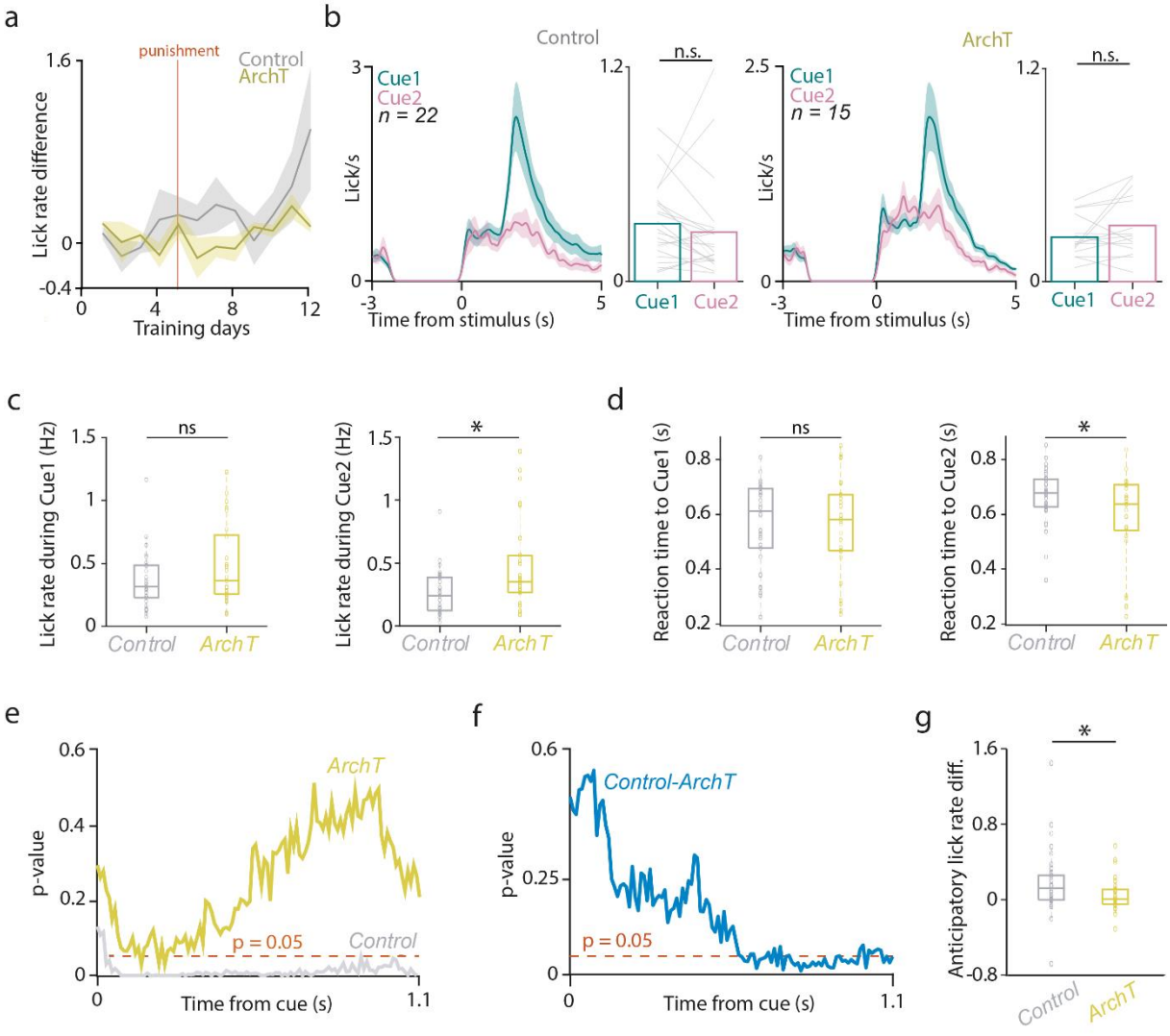

Fig S7. Differential learning in Control and ArchT-inhibited mice. a Learning curve of Control and ArchT animals (anticipatory lick rate difference plotted as a function of training days; errorshade, SEM). **b**, PETH and bar graph showing no anticipatory lick rate difference between Control and ArchT mice at an earlier training stage (before introducing punishment; two-sided Wilcoxon signed-rank test; p = 0.101 for Control and p = 0.173 for ArchT; n.s., p > 0.05; errorshade, SEM). **c**, Lick rate during Cue1 and Cue2 presentation in Control and ArchT mice. *, p < 0.05, p = 0.373 for Cue1, p = 0.013 for Cue2, two-sided Mann-Whitney U-test. Box-whisker plots indicate median, interquartile range and non-outlier range. **d**, Reaction time to Cue1 and Cue2 in Control and ArchT mice. *, p < 0.05, p = 0.715 for Cue1, p = 0.0128 for Cue2, two-sided Mann-Whitney U-test. Box-whisker plots indicate median, interquartile range and non-outlier range. **e**, Statistical significance of cue-specific anticipatory lick rate difference as a function of time from cue onset (ROC analysis, see Methods). **f,** Statistical significance of the cue-related anticipatory lick rate difference between the ArchT and the control group as a

function of time from cue onset (ROC analysis, see Methods). The difference reached statistical significance around the middle of the response window due to large variability in reaction times. **g,** Anticipatory lick rate difference in control (left) and ArchT (right) groups in a 0.6-1.1 s window from cue onset. *, $p < 0.05$, $p = 0.03669$, two-sided Mann-Whitney U-test**.** Box-whisker plot indicates median, interquartile range and non-outlier range. Source data are provided as a Source Data file.

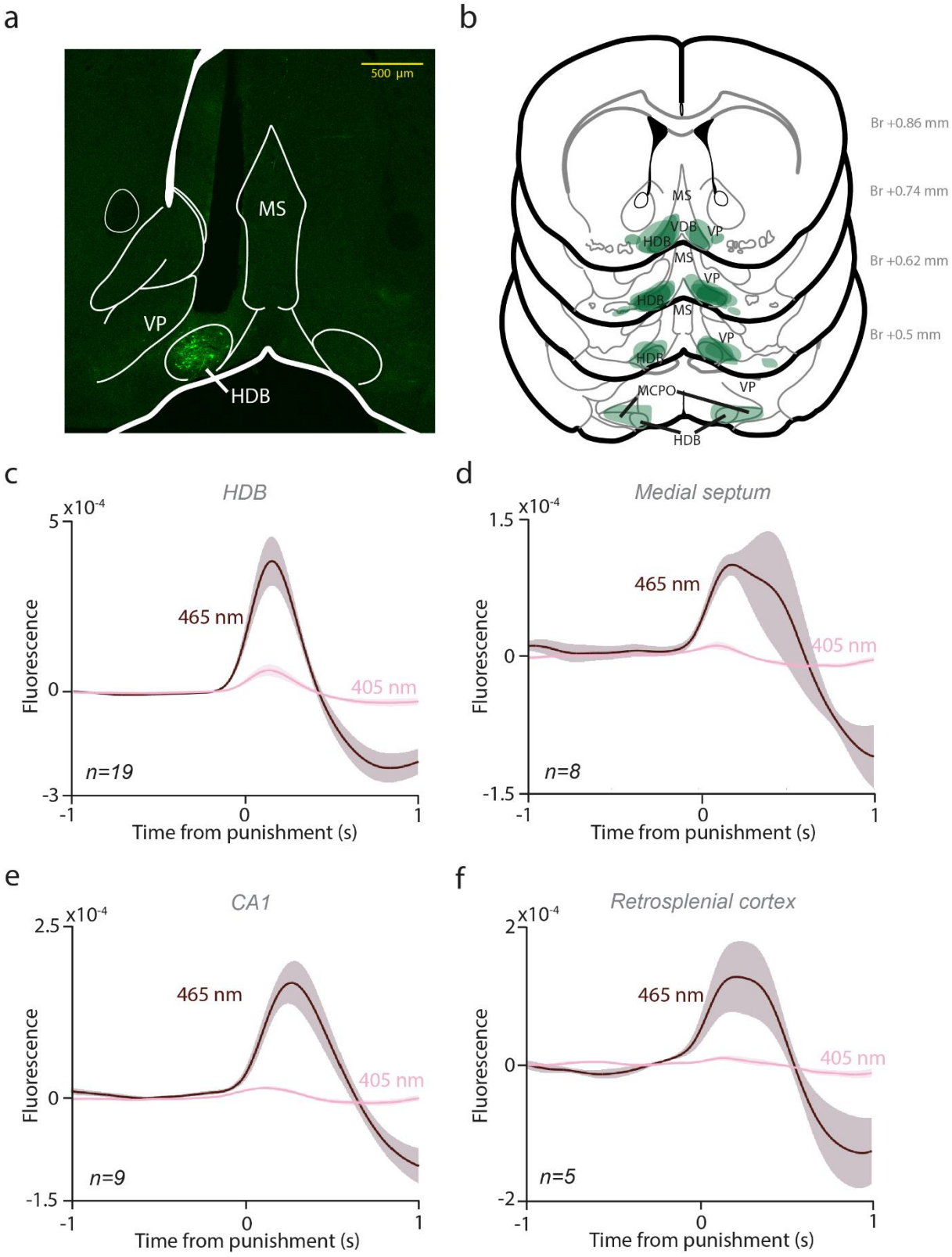

Fig S8. Track reconstruction and isosbestic channels of fiber photometry recordings. a, Representative fluoromicrograph of a GCaMP6s injection in a PV-Cre mouse (repeated in n = 12 mice). **b**, Reconstruction of all injection sites in the HDB. **c,** PETH of 465 nm and 405 nm wavelength fluorescent signals aligned to punishment, recorded in the HDB (n = 19 sessions;

errorshade, SEM). **d,** PETH of 465 nm and 405 nm wavelength fluorescent signals aligned to punishment, recorded in the MS (n = 8 sessions; errorshade, SEM). **e,** PETH of 465 nm and 405 nm wavelength fluorescent signals aligned to punishment, recorded in the CA1 hippocampus (n = 9 sessions; errorshade, SEM). **f,** PETH of 465 nm and 405 nm wavelength fluorescent signals aligned to punishment, recorded in the RSC (n = 5 sessions; errorshade, SEM). PETHs were smoothed with a Gaussian kernel (width, 100 ms).

Brain areas	Fraction of total input neurons
Lateral hypothalamus	33.09
Lateral septum	13.81
intermediate part	10.18
dorsal part	2.89
ventral part	0.74
Medial septum	10.77
Vertical limb of the diagonal band	6.37
Preoptic area	7.62
lateral preoptic area	5.96
medial preoptic area	1.66
Horizontal limb of the diagonal band	5.81
Median raphe region	3.93
paramedian raphe nucleus	2.52
median raphe nucleus	1.41
Ventral pallidum	3.47
Nucelus accumbens	3.46
shell part	2.23
core part	1.23
Posterior hypothalamic nucleus	2.59
Medial amygdaloid nucleus	2.04
Laterodorsal tegmental nucleus	1.26
Magnocellular nucl. of the lat. hypothalamus	1.23
Septohippocampal nucleus	1.14
Gigantocellular reticular nucleus	1.01
Orbital cortex	0.90
CA3 stratum oriens	0.78
Nucleus incertus	0.72
TOTAL	100%

Table S1. Fraction of total inputs to HDB BFPVNs.

Antigen	Host	Dilution	Source	Catalog number	Specificity	Characterized in
eGFP	Chicken	1:2000	Thermo Fisher Scientific	A10262	No staining in mice not injected with eGFP-expressing virus.	Information of the distributor.
mCherry	Chicken	1:1000	Abcam	ab205402	Validated for WB, ICC/IF. Positive control: Lysate of HEK293 cells transfected with pFin-EF1-mCherry vector, HEK293 cells transfected with pFin-EF1-mCherry vector.	Information of the distributor.
mCherry	Rabbit	1:2000	BioVision	5993-100	No staining in mice not injected with mCherry-expressing virus.	Information of the distributor.
vGluT3	Guinea pig	1:1000	Frontier Institute	AF510321	Immunoblot detects a single protein band at 60-62 kDa.[1] Antibody to VGLUT3, (1 µg/mL) were absorbed to the whole fusion protein (30 µg/mL), which eliminated all labelling, indicating specificity.[2]	[1]Information of the distributor. [2] PMID: 14984406
RFP	Rat	1:2000	Chromotek	5F8	No staining in mice not injected with mCherry-expressing virus.	Information of the distributor.
5-HT	Rabbit	1:10000	Immunostar	20080	KO verified.	[104]
Chat	rabbit	1:1000 or 1:500	Synaptic Systems	297013	Specific for rat and mouse Chat.	Information of the distributor.
SOM	rabbit	1:500	Origene	AP-33464SU-N	Specificity: Recognizes Somatostatin-14	PMID:37205047
Chat	goat	1:1000	Merck	AB-144P	Specific for Chat in mouse among other species.	Information of the distributor.
PV	mouse	1:2000	Swant	PV235	Reacts specifically with parvalbumin in tissue originating from human, monkey, rabbit, rat, mouse, chicken and fish.	Information of the distributor.
PV	rabbit	1:1000	Swant	PV27	KO verified.	Information of the distributor.
CR	rabbit	1:10000	Swant	7697	KO verified.	Information of the distributor.

Table S2. Primary antibodies used in immunhistochemical experiments.

Raised in	Raised against	Conjugated with	Dilution	Source	Catalog number
Goat	Rabbit	Alexa 405	1:500	Invitrogen	A31556
Donkey	Chicken	Alexa 488	1:1000	Jackson Immunoresearch	703-545-155
Donkey	Rabbit	Alexa 594	1:500	Thermo Fisher Scientific	A21207
Goat	Chicken	Alexa 594	1:500	Abcam	Ab150172
Donkey	Guinea pig	Alexa 647	1:500	Jackson Immunoresearch	706-605-148
Donkey	Mouse	Alexa 647	1:500	Jackson Immunoresearch	715-605-150
Donkey	Rat	Alexa 594	1:500	Thermo Fisher Scientific	A21209
Donkey	Rabbit	Alexa 488	1:1000	Thermo Fisher Scientific	A21206
Donkey	Chicken	Biotin-SP	1:1000	Jackson Immunoresearch	703-065-155
Donkey	Goat	Alexa 594	1:1000	Thermo Fisher Scientific	A-11058

Table S3. Secondary antibodies used in immunohistochemical experiments.

Cellid	Baseline firing rate (Hz)	Peak firing rate after punishment (Hz)	Peak latency (ms)
'HDB17_170720a_4.2'	13.16	29.38	119
'HDB17_170723a_7.1'	11.14	22.89	20
'HDB17_170724a_7.2'	10.10	27.45	85
'HDB17_170725a_5.2'	21.93	47.88	91
'HDB17_170805a_5.1'	20.47	60.61	105
'HDB17_170807a_5.2'	18.24	34.08	158
'HDB17_170810a_3.1'	30.95	48.78	89
'HDB17_170810a_5.1'	26.10	89.49	83
'HDB17_170811a_3.2'	26.15	43.48	74
'HDB17_170812a_4.1'	12.48	21.06	73
'HDB17_170904a_4.2'	20.14	104.48	87
'HDB17_170904a_6.2'	2.78	33.08	19
'HDB17_170906a_6.3'	1.62	11.35	70
HDB17_170912a_6.1'	7.69	13.29	21
'HDB17_170928a_2.1'	4.36	36.47	86
'HDB17_170928a_4.1'	17.67	99.99	90
'HDB17_170928a_4.2'	8.05	14.62	16
'HDB17_171010a_2.1'	4.13	53.05	81
'HDB23_180221a_3.2'	28.38	39.83	15
'HDB23_180223a_3.1'	14.71	22.74	12
'HDB23_180223a_5.3'	4.26	22.80	66
'HDB34_190113a_7.1'	18.18	30.28	182
'HDB34_190115a_5.1'	16.53	40.53	15
'HDB34_190117a_4.1'	2.91	5.46	33
'HDB34_190118a_4.1'	4.25	8.39	97
'HDB34_190207a_8.1'	14.87	28.86	197
'HDB30_181002a_2.2'	2.85	8.52	95
HDB17_170811a_4.2'	11.62		
'HDB17_170812a_3.1'	23.68		
'HDB17_170912a_4.1'	35.32		
'HDB23_180225a_3.1'	16.24		
'HDB34_190115a_4.2'	4.73		
'HDB34_190123a_2.1'	53.69		
'HDB34_190127a_2.1'	18.92		
'HDB34_190207a_6.1'	17.97		
'HDB30_181002a_2.1'	5.26		
Average ± standard error	**15.32 ± 1.84**	**36.99 ± 5.24**	**77.0 ± 9.52**

Table S4. Baseline firing rate for all identified BFPVNs (n = 36) and punishment-evoked peak firing rate of punishment-activated BFPVNs (n = 27) along with peak latency of punishment response.

Article

Cell Reports

Huygens synchronization of medial septal pacemaker neurons generates hippocampal theta oscillation

Graphical abstract

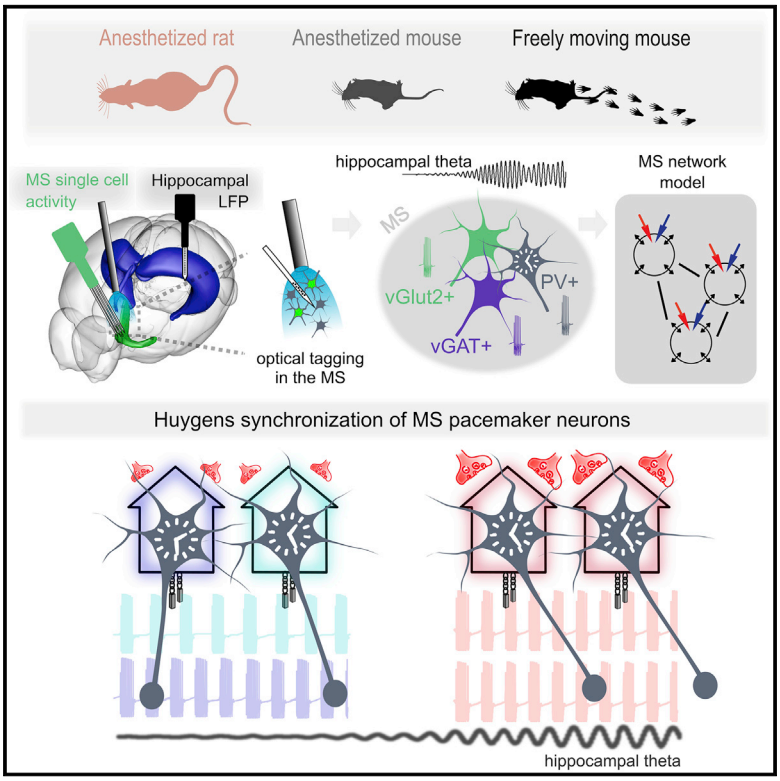

Highlights

- MS pacemakers show Huygens synchronization
- MS pacemakers are parvalbumin-expressing GABAergic neurons
- MS glutamatergic neurons provide tonic excitation sufficient to induce theta
- A network model of a homogeneous GABAergic population reproduces experimental data

Authors

Barnabás Kocsis, Sergio Martínez-Bellver, Richárd Fiáth, ..., Szabolcs Káli, Viktor Varga, Balázs Hangya

Correspondence

hangya.balazs@koki.hu

In brief

How medial septal (MS) neurons synchronize to generate hippocampal theta oscillation is not well understood. Kocsis et al. find that MS GABAergic neurons synchronize their individual rhythmicity frequencies, similar to coupled pendulum clocks, while MS glutamatergic neurons provide tonic excitatory drive to the pacemaker network sufficient to induce theta.

Kocsis et al., 2022, Cell Reports *40*, 111149
August 2, 2022
https://doi.org/10.1016/j.celrep.2022.111149

CellPress

Cell Reports

CellPress
OPEN ACCESS

Article

Huygens synchronization of medial septal pacemaker neurons generates hippocampal theta oscillation

Barnabás Kocsis,[1,2,3] Sergio Martínez-Bellver,[1,4] Richárd Fiáth,[2,5] Andor Domonkos,[6] Katalin Sviatkó,[1,7] Dániel Schlingloff,[1] Péter Barthó,[8] Tamás F. Freund,[6] István Ulbert,[2,5] Szabolcs Káli,[6] Viktor Varga,[6,9] and Balázs Hangya[1,10,*]

[1]Lendület Laboratory of Systems Neuroscience, Institute of Experimental Medicine, 1083 Budapest, Hungary
[2]Institute of Cognitive Neuroscience and Psychology, Research Centre for Natural Sciences, 1117 Budapest, Hungary
[3]Roska Tamás Doctoral School of Sciences and Technology, Faculty of Information Technology and Bionics, Pázmány Péter Catholic University, 1083 Budapest, Hungary
[4]Department of Anatomy and Human Embryology, Faculty of Medicine and Odontology, University of Valencia, 46010 Valencia, Spain
[5]Faculty of Information Technology and Bionics, Pázmány Péter Catholic University, 1083 Budapest, Hungary
[6]Cerebral Cortex Research Group, Institute of Experimental Medicine, 1083 Budapest, Hungary
[7]János Szentágothai Doctoral School of Neurosciences, Semmelweis University, 1085 Budapest, Hungary
[8]Sleep Oscillations Research Group, Research Centre for Natural Sciences, 1117 Budapest, Hungary
[9]Subcortical Modulation Research Group, Institute of Experimental Medicine, 1083 Budapest, Hungary
[10]Lead contact
*Correspondence: hangya.balazs@koki.hu
https://doi.org/10.1016/j.celrep.2022.111149

SUMMARY

Episodic learning and memory retrieval are dependent on hippocampal theta oscillation, thought to rely on the GABAergic network of the medial septum (MS). To test how this network achieves theta synchrony, we recorded MS neurons and hippocampal local field potential simultaneously in anesthetized and awake mice and rats. We show that MS pacemakers synchronize their individual rhythmicity frequencies, akin to coupled pendulum clocks as observed by Huygens. We optogenetically identified them as parvalbumin-expressing GABAergic neurons, while MS glutamatergic neurons provide tonic excitation sufficient to induce theta. In accordance, waxing and waning tonic excitation is sufficient to toggle between theta and non-theta states in a network model of single-compartment inhibitory pacemaker neurons. These results provide experimental and theoretical support to a frequency-synchronization mechanism for pacing hippocampal theta, which may serve as an inspirational prototype for synchronization processes in the central nervous system from Nematoda to Arthropoda to Chordate and Vertebrate phyla.

INTRODUCTION

Exploratory behaviors are accompanied by a 4–12 Hz theta oscillation in the hippocampus of rodents, carnivores, and primates, including humans (Buzsáki, 2002; Buzsáki and Moser, 2013; Kahana et al., 1999; Rutishauser et al., 2010). This theta oscillation provides a temporal reference signal for hippocampal networks, which is crucial for episodic learning and memory retrieval (Buzsáki, 2006). GABAergic neurons of the medial septum (MS) have been identified as putative pacemakers of hippocampal theta rhythms (Freund and Antal, 1988; Hangya et al., 2009; Petsche et al., 1962; Yoder and Pang, 2005). However, the mode of theta-frequency synchronization within the septal GABAergic network has not been tested experimentally.

Theoretical studies proposed that individual pacemaker neurons may oscillate at different frequencies and synchronize in the frequency domain upon increased depolarizing input (Ujfalussy and Kiss, 2006; Wang, 2002), a mechanism termed ''Huygens synchronization'' in the physics of coupled oscillators (Oliveira and Melo, 2015; Ramirez et al., 2016). Two influential models assumed the presence of two separate GABAergic populations that inhibit each other through a so-called ping-pong mechanism, either within the MS network (Cutsuridis and Poirazi, 2015; Ujfalussy and Kiss, 2006) or involving the hippocampo-septal GABAergic projection neurons (Wang, 2002). Theta amplitude modulation through increased MS firing rates was proposed as a direct layer of control (Bland et al., 1996; Denham and Borisyuk, 2000; Tokuda et al., 2019), whereas a change in MS bursting patterns could also impact theta generation (Joshi et al., 2017; Simon et al., 2006; Sotty et al., 2003). The role of the hyperpolarization-activated and cyclic nucleotide-gated (HCN) channels was emphasized as a part of the potential underlying ionic mechanisms (Kocsis and Li, 2004; Varga et al., 2008). However, beside frequency synchronization, other mechanisms are also plausible, including synchronization in the phase domain without changes in oscillation frequency (Borhegyi et al., 2004; Ujfalussy and Kiss, 2006). Additionally, little is known about the exact role of different MS cell types in theta generation (Lee et al., 1994; Robinson et al., 2016; Vandecasteele et al., 2014).

Therefore, we investigated potential theta generation mechanisms experimentally by recording single neurons from the medial septum, with concurrent local field potentials (LFP) from the hippocampus using multichannel silicon electrode arrays. To address the generality of results across theta oscillations observed in awake or anesthetized rodents (Kramis et al., 1975; Stewart and Fox, 1989), we obtained three datasets: from urethane-anesthetized rats, urethane-anesthetized mice, and awake, drug-free mice. We found that hippocampal theta onset was accompanied by Huygens (frequency) synchronization of MS pacemaker neurons otherwise rhythmic at more distinct frequencies in the theta range. We confirmed the pacemaker role of parvalbumin (PV)-expressing GABAergic neurons (Freund and Antal, 1988; Hangya et al., 2009; Varga et al., 2008) by optogenetic tagging (Kvitsiani et al., 2013; Lima et al., 2009), whereas glutamatergic neurons showed strong firing rate increase during theta without much rhythmicity, suggesting they may contribute to the theta-associated increase of tonic drive to the pacemakers (Ford et al., 1989; Green and Arduini, 1954; Oddie et al., 1996; Vandecasteele et al., 2014; Yang et al., 2014). Indeed, optogenetic stimulation of MS glutamatergic neurons induced theta oscillation in the CA1. These results were consistent with a circuit model of the MS in which a network of inhibitory neurons was capable of synchronizing and desynchronizing in the frequency domain upon changing levels of tonic excitatory input.

RESULTS

Recording MS and hippocampal data in three rodent models of theta oscillations

Hippocampal theta oscillations have been investigated in both urethane-anesthetized and awake rodents (Borhegyi et al., 2004; Buzsáki, 2002; Klausberger and Somogyi, 2008; Kramis et al., 1975; Mikulovic et al., 2018; Stewart and Fox, 1989). To explore the commonalities and differences across different theta model systems, we collected three independent datasets (Figure 1). We recorded multiple single neurons from the MS using silicon probes from anesthetized rats (n = 903 neurons from n = 7 rats; 416 and 636 neurons active during both theta and non-theta states or at least one of them, respectively; Figure S1A), anesthetized mice (n = 1,155 neurons from n = 11 mice; 617 and 950 active during both or at least one of the states; Figures 1A–1D) and awake mice (n = 312 neurons from n = 4 mice; 265 and 289 active during both or at least one of the states; Figure S1B). Simultaneously, we recorded LFP from all layers of the dorsal CA1 area of the hippocampus using linear silicon probe electrodes (Figure 1E). We detected the hippocampal layers based on combined information from histology and theta phase reversal (Buzsáki, 2006; Buzsaki et al., 1986; Green et al., 1960) and used the large amplitude stratum radiatum/lacunosum-moleculare signal for detecting theta epochs (Figure S1C) (Buzsáki, 2002). Theta frequency boundaries were defined specifically for the three types of recordings based on LFP spectra, confirming the known observation of slower oscillations under urethane anesthesia (Borhegyi et al., 2004; Varga et al., 2008) (Figure 1F). Theta segments were detected based on the theta/delta spectral ratio (McNamara et al., 2014; Wikenheiser and Redish, 2013) (Figures 1G and 1H).

Putative pacemaker neurons show constitutive theta-rhythmic activity

We developed an unbiased method to identify functional MS neuron classes based on their rhythmic firing properties. Theta and delta rhythmicity indices were defined by the normalized autocorrelation peak in the respective frequency bands, and significant rhythmic activity was tested against bootstrap distributions generated from simulated Poisson neurons that were matched with MS neurons in their firing rates ($p < 0.05$, bootstrap test; Figure S2; STAR Methods).

We found that a subpopulation of MS neurons showed theta-rhythmic bursting activity both when theta oscillation was present and when it was absent in the CA1 (Figure 2A). These neurons showed prominent theta oscillations in their autocorrelograms (Figures 2B–2D) and strong phase locking to CA1 theta oscillation, but no strong phase relationship with hippocampal delta band activity during non-theta episodes (Figures 2E–2G). This constitutively theta-rhythmic population, often considered as "putative pacemaker neurons" of theta oscillation (Borhegyi et al., 2004; Ford et al., 1989; Hangya et al., 2009; Stewart and Fox, 1989; Varga et al., 2008) was found in anesthetized rats (n = 29/416), anesthetized mice (n = 47/617), and freely moving mice (n = 35/265; note that these numbers represent conservative estimates based on significant rhythmicity) (Figure S3, Figure S4).

We confirmed the presence of two separate clusters of neurons that showed anti-phase preference to hippocampal theta in anesthetized rats (Akaike information criterion values for the unimodal, bimodal, and trimodal distributions were 109.08, 103.19, and 108.98, respectively; Bayesian information criterion values were 111.81, 110.03, and 119.92), as reported previously (Borhegyi et al., 2004; Varga et al., 2008). Although a similar tendency could be observed in mice, we did not find statistical support for a bimodal distribution based on our samples (see STAR Methods; Table S1).

Putative "follower," theta-skipping, and tonically active MS neurons

A considerable MS population reflected (followed) the ongoing activity of the septo-hippocampal network. These neurons were theta-rhythmic during hippocampal theta oscillation but not when it was absent, often phase locked to both theta and delta band oscillations. In anesthetized rats, many of these neurons showed slow rhythmic activity at delta frequencies in the absence of hippocampal theta (Figure 3; Figure S5), while in mice, these follower neurons were mostly non-rhythmic or slow firing in non-theta states ("theta follower neurons") (Figures S6–S8; Table S1). Some neurons exhibited follower activity only in the non-theta state, remaining non-rhythmic or silent during hippocampal theta.

A subpopulation of MS neurons, identified previously as "theta-skipping," showed slow rhythmic activity regardless of whether theta oscillation was present in CA1 (Figure S9). While some of these neurons doubled their rhythmic frequency at theta onset (but still in the delta range), many cells of this population maintained a constant slow rhythmicity, often firing regularly in every second theta cycle. Interestingly, while this group was rather prominent in anesthetized rats, these cells were only rarely

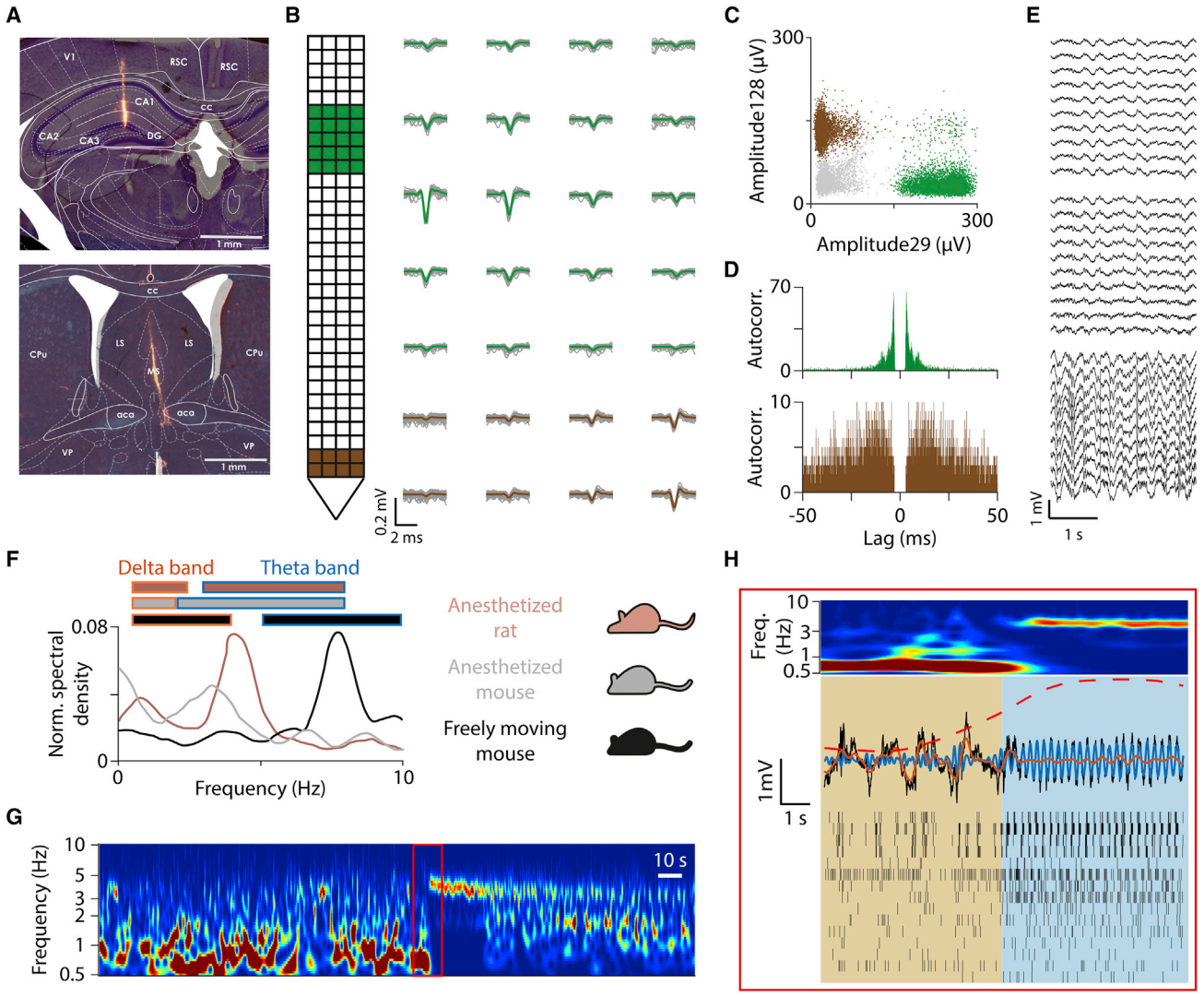

Figure 1. Dual recording of hippocampal LFP and single neuron activity from the medial septum

(A) Histology of the silicon probe tracks in the mouse hippocampus (top) and medial septum (bottom). Nissl-staining; red, DiI. See also Figure S1 for histology in rats.

(B) MS single units were collected using a 128-channel silicon probe in anesthetized mice (see STAR Methods). Example spike waveforms for two neurons are shown for the channels marked on the schematic representation of the probe (green and brown, average waveforms; grey, 100 randomly selected individual spikes).

(C) Amplitudes (peak-to-valley) on selected channels show clear separation of the example cells.

(D) Autocorrelograms of the example neurons.

(E) Hippocampal LFP was collected concurrently using a linear silicon probe. A 3-second-long example recording is shown (two broken channels were removed).

(F) We collected data from three rodent models of theta oscillations: urethane-anesthetized rats (brown), urethane-anesthetized mice (grey), and freely moving mice (black). Representative Fourier spectra of hippocampal LFP recordings from the three model systems. Theta and delta band boundaries were determined based on Fourier spectra of hippocampal LFPs for each model separately, indicated by color-coded horizontal bars on top.

(G) Representative hippocampal LFP wavelet spectrogram from an anesthetized rat recording.

(H) Top, theta onset is enlarged from (G). Middle, raw LFP (black), LFP filtered in the theta (blue) and delta frequency band (orange), and theta-delta power ratio (dashed line). Bottom, raster plot of individual units (n = 15) recorded from the medial septum concurrently. Note the change in network activity at theta onset.

found in mice, revealing species-specific differences in the MS theta generation network (anesthetized rats, 48/416; anesthetized mice, 4/617; freely moving mice, 1/265; Table S1).

Finally, a group of MS cells showed regular rhythmic firing patterns resembling those of striatal cholinergic interneurons (Inokawa et al., 2010); therefore, we called this MS group "tonically active neurons" (Figures S10A–S10D). Although these neurons fired rhythmically with a frequency in the theta band (Figures S10E–S10I), they showed little to no overall phase locking to hippocampal activity (Figures S10J–S10K), typically exhibiting rhythmicity at slightly higher frequencies than ongoing CA1 theta oscillation (based on autocorrelation peak, median ± standard

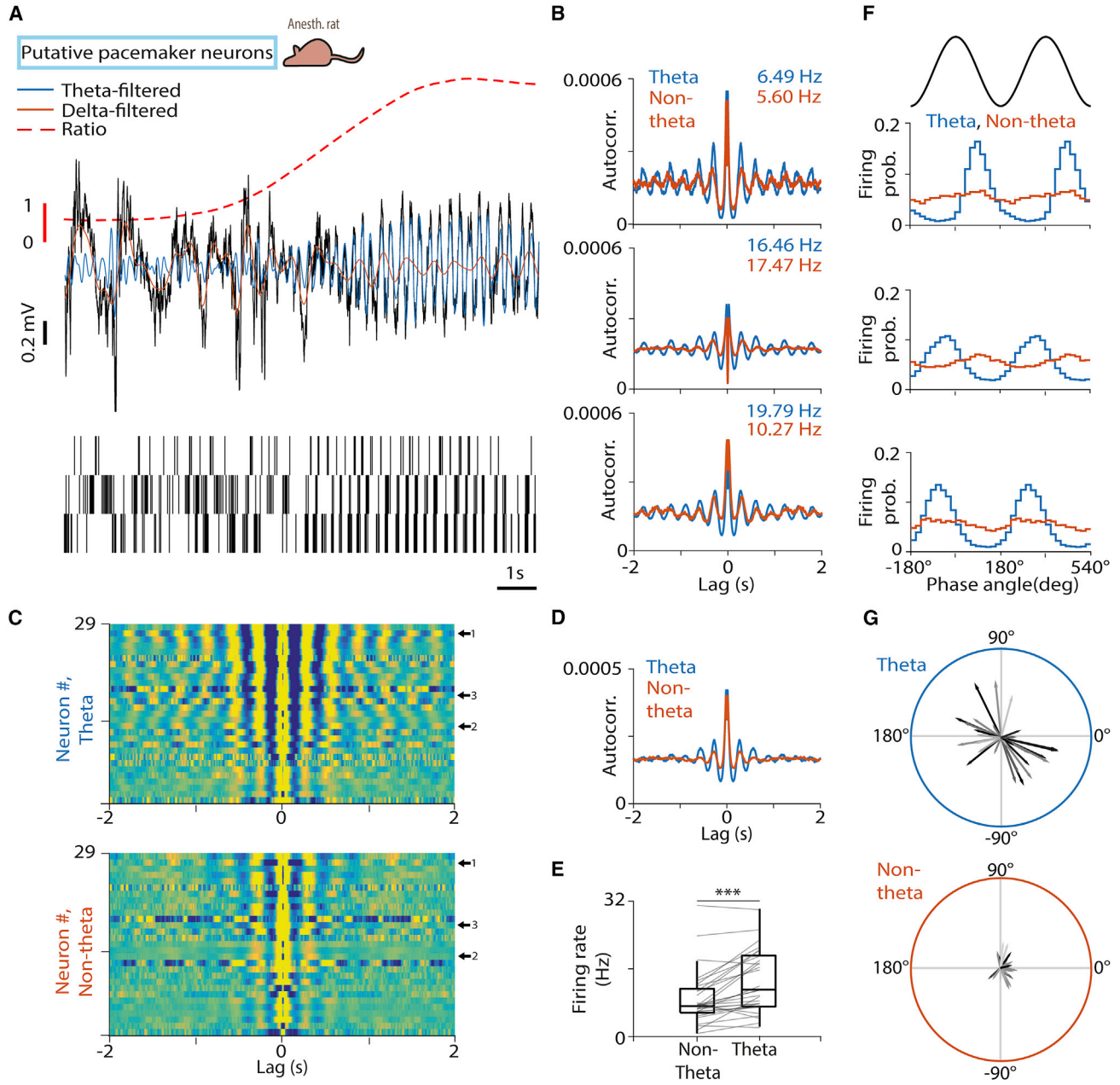

Figure 2. Putative pacemaker neurons of the MS

(A) Top, black, raw LFP from the CA1 shows a delta-to-theta state transition. Orange, LFP filtered in the delta band; blue, LFP filtered in the theta band; dashed, theta-delta amplitude ratio. Bottom, spike raster of three examples of putative pacemaker neurons from the same recording session. Recordings are from urethane-anesthetized rats; see Figures S3 and S4 for the anesthetized and awake mouse recordings.

(B) Autocorrelograms of the three example neurons in (A). Numbers indicate average firing rates during theta and non-theta segments.

(C) Autocorrelograms of all putative pacemaker neurons during theta (top) and non-theta (bottom) segments. Arrows indicate the example neurons.

(D) Average autocorrelogram of all putative pacemaker neurons.

(E) Firing rates of putative pacemaker neurons during non-theta and theta segments. Boxes and whiskers represent interquartile ranges and non-outlier ranges, respectively. Lines correspond to individual neurons. Firing rate was significantly higher during theta (***$p < 0.001$; $p = 1.04 \times 10^{-4}$, $W = 397$, $n = 29$, Wilcoxon signed-rank test).

(F) Phase histogram of the example neurons in (A) relative to delta (orange) and theta (blue) oscillations. Two oscillatory cycles are shown.

(G) Phase-locking of all putative pacemaker neurons to theta (top) and delta (bottom) oscillation in polar coordinates. Angle, circular phase; length, mean vector length; greyscale corresponds to average firing rate (black, higher firing rate). Note that neurons formed two opposite phase clusters during theta, whereas phase-locking strength to delta oscillations was low for putative pacemaker neurons.

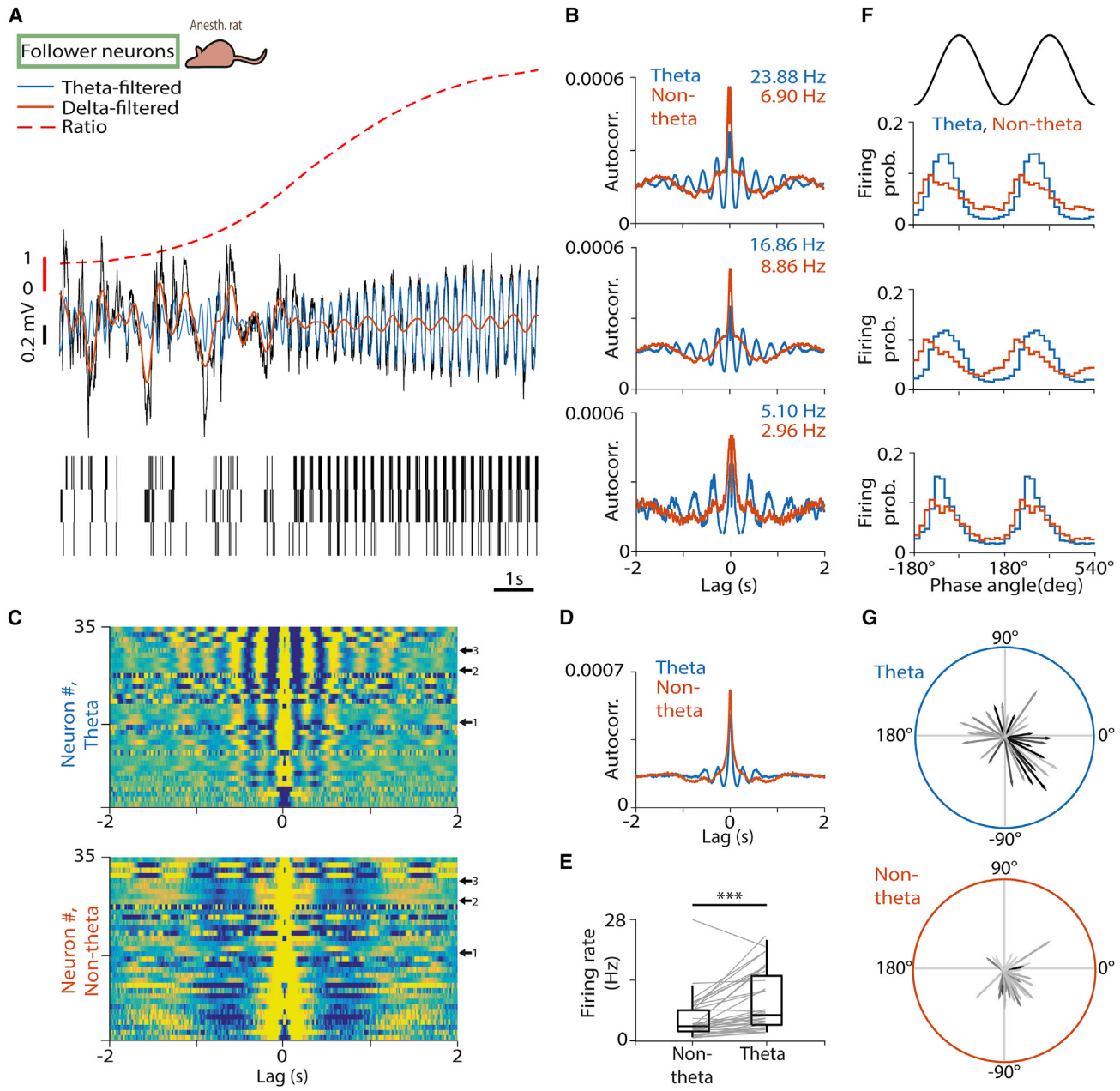

Figure 3. Follower MS neurons

(A) Top, black, raw LFP from the CA1 shows a delta-to-theta state transition. Orange, LFP filtered in the delta band; blue, LFP filtered in the theta band; dashed, theta-delta amplitude ratio. Bottom, spike raster of three example neurons from the same recording session. Follower neurons showed delta-rhythmic activity during non-theta epochs and theta-rhythmic activity during theta epochs in urethane-anesthetized rats. See Figure S6 for mouse recordings.

(B) Autocorrelograms of the three example neurons in (A). Numbers indicate average firing rates during theta and non-theta segments.

(C) Autocorrelograms of all follower neurons during theta (top) and non-theta (bottom) segments. Arrows indicate the example neurons.

(D) Average autocorrelogram of all follower neurons.

(E) Firing rates of follower neurons during non-theta and theta segments. Boxes and whiskers represent interquartile ranges and non-outlier ranges, respectively. Lines correspond to individual neurons. Firing rate was significantly higher during theta (***$p < 0.001$; $p = 1.65 \times 10^{-5}$, $W = 578$, $n = 35$, Wilcoxon signed-rank test).

(F) Phase histogram of the example neurons in (A) relative to delta (orange) and theta (blue) oscillations. Two oscillatory cycles are shown.

(G) Phase locking of all follower neurons to theta (top) and delta (bottom) oscillation in polar coordinates. Angle, circular phase; length, mean vector length; greyscale corresponds to average firing rate (black, higher firing rate). Many of these neurons were phase-locked to both hippocampal oscillations.

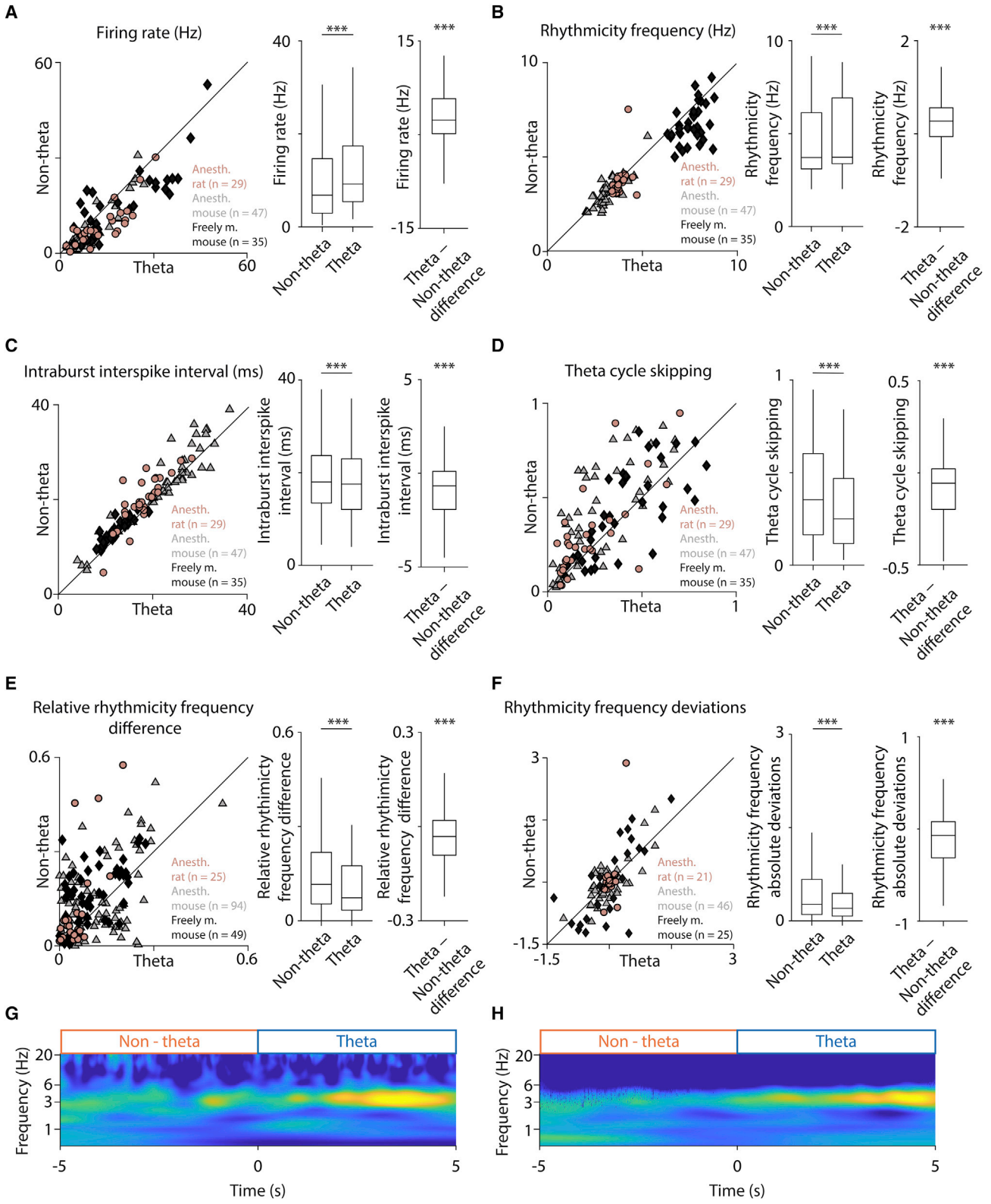

Figure 4. Septal pacemakers synchronize their burst frequencies

(A) Firing rates of MS putative pacemakers were higher during theta oscillation then during non-theta segments. Left, scatter plot shows the firing rate of all putative pacemaker neurons, color coded according to the rodent theta models. Middle and right, box-whisker plots showing statistics on pooled data

(legend continued on next page)

error of the median, 5.68 ± 0.34, 4.29 ± 0.41, and 8.40 ± 0.37 Hz during theta segments in anesthetized rats, anesthetized mice, and freely moving mice, respectively). They did not show the long bursts with 20- to 50-ms interspike intervals (ISIs) known to be characteristic of the putative pacemaker group, but some of them occasionally fired short, fast bursts of action potentials (ISI < 15 ms; Figures S10A–S10D). They were found in all three rodent theta models tested (anesthetized rats, 18/416; anesthetized mice, 49/617; freely moving mice, 8/265) (Figures S11 and S12A–S12G). These neurons also showed a firing rate change during theta oscillation. Interestingly, however, while their firing rate decreased at theta onset in rats (15/18 neurons), previously coined as a "theta-OFF" pattern (Ford et al., 1989) (Figure S10I), they exhibited a theta-associated firing rate increase in mice, both anesthetized (34/49 neurons) and awake (8/8 neurons) (Figures S11E and S12E; Table S1).

Together with those cells that did not exhibit any rhythmic activity according to our conservative rhythmicity analysis, the above-described groups of MS neurons constitute the entire MS population (Figure S12H; Table S2).

Septal pacemakers synchronize their burst frequencies

To gain information on the neural synchronies between the above-described groups, we calculated pairwise cross-correlations for pairs of MS cells (n = 527 pairs in anesthetized rats). We found that during non-theta segments, follower neurons showed strong synchrony within each other, but also with putative pacemaker neurons (Figure S13). This remained consistent across theta and non-theta segments, while the putative pacemaker neurons became the most synchronous group in theta state. Tonically active neurons showed lower levels of synchrony within each other and with putative pacemakers, while they expressed moderate correlations with follower neurons. Therefore, we reasoned that theta-rhythmic putative pacemaker and follower neurons likely participate in the MS theta generating mechanisms, unlike tonically active neurons.

We found that, during CA1 theta, putative pacemakers showed an increased firing rate and somewhat higher rhythmicity frequency as measured by the first peak in their autocorrelograms, arguing for a stronger excitatory drive during theta (Figures 4A and 4B). Interestingly, we only found moderate changes in burst parameters, suggesting that the bursting mechanisms of MS pacemakers are mostly intrinsic and show only slight modulation with changing network states (Figure 4C). Since the change in burst parameters and rhythmicity frequency seemed too small to account for the observed elevated firing rate, we argued that putative pacemakers should be skipping more theta cycles during non-theta states. We confirmed this by calculating the proportion of cycles skipped during non-theta and theta activity (Figure 4D).

Next, we analyzed the pairs of putative pacemakers further to address how the synchrony of these neurons changes during hippocampal theta oscillation. Based on theoretical work, we hypothesized that pacemaker neurons may synchronize their frequencies, thus increasing constructive interference across individual oscillators, providing a stronger theta-rhythmic output toward the hippocampus (Ramirez et al., 2016; Ujfalussy and Kiss, 2006; Wang, 2002; Willms et al., 2017). This would imply that pairwise differences in the rhythmicity frequency of putative pacemakers decrease during theta oscillation compared with non-theta episodes. Indeed, we found smaller differences in individual theta frequencies when hippocampal theta was present when we pooled all pacemaker pairs from the three datasets (Figure 4E). This difference was significant for anesthetized rats and freely moving mice, and marginally significant when only anesthetized mice were considered (Table S3). This frequency synchronization was detected after normalizing the relative frequency difference to the individual frequencies of the tested neurons; thus, a change in the individual theta frequencies could not account for this effect.

If differences across rhythmicity frequencies decrease during theta, one also expects rhythmicity frequencies across the putative pacemaker population to converge to a tighter distribution. We tested this by comparing the absolute deviation of rhythmicity frequencies from their mean during theta and non-theta segments and found a larger spread in non-theta state (Figure 4F). Additionally, we visualized the pacemaker synchronization process by calculating wavelet coherence among putative

(***$p < 0.001$; $p = 1.402 \times 10^{-9}$, W = 5166, n = 111, Wilcoxon signed-rank test). See Table S3 for statistics on the three datasets separately. All box-whisker plots show median, interquartile range and non-outlier range in this figure.

(B) Left, scatter plot of rhythmicity frequency of putative pacemakers measured by the time lag of the first autocorrelation peak in the theta band. Middle and right, statistics on pooled data indicated higher rhythmicity frequency during hippocampal theta (***$p < 0.001$; $p = 2.64 \times 10^{-7}$, W = 4857.5, n = 111, Wilcoxon signed-rank test).

(C) Left, scatter plot of average intraburst ISIs for putative pacemaker neurons. Middle and right, the moderate decrease of ISIs during theta oscillation indicates a slight elevation of intraburst frequency (***$p < 0.001$; $p = 7.336 \times 10^{-5}$, W = 1275.5, n = 111, Wilcoxon signed-rank test).

(D) Left, scatter plot of the ratio of skipped theta cycles of putative pacemakers during non-theta and theta segments. Middle and right, statistics on pooled data indicated that putative pacemaker neurons skipped more theta cycles during non-theta segments (***$p < 0.001$; $p = 3.021 \times 10^{-6}$, W = 1521, n = 111, Wilcoxon signed-rank test).

(E) Left, scatter plot of relative frequency difference of individual pacemaker neurons for simultaneously recorded pairs, normalized to the larger of the frequencies. Middle and right, statistics on pooled data indicated that individual pacemakers became more similar in frequency during theta oscillation (***$p < 0.001$; $p = 3.17 \times 10^{-6}$, W = 4156, n = 168, Wilcoxon signed-rank test).

(F) Left, deviation from the session mean rhythmicity frequency during theta vs. non-theta segments for putative pacemaker neurons (sessions in which at least two putative pacemakers were co-recorded are included). Middle and right, statistics on pooled data indicated that the absolute deviation from the mean rhythmicity frequency was significantly larger during non-theta segments (***$p < 0.001$; $p = 4.189 \times 10^{-4}$, W = 1233, n = 92, Wilcoxon signed-rank test).

(G) Mean wavelet coherence spectrogram of an example putative pacemaker neuron pair (spike trains were convolved with a 50-ms Gaussian window, from anesthetized rat) averaged around non-theta to theta transitions.

(H) Mean wavelet coherence spectrogram averaged across pairs of putative pacemaker neurons recorded in urethane-anesthetized rats (time 0 corresponds to non-theta to theta transitions; sessions in which at least two putative pacemakers were co-recorded are included, n = 25 pairs).

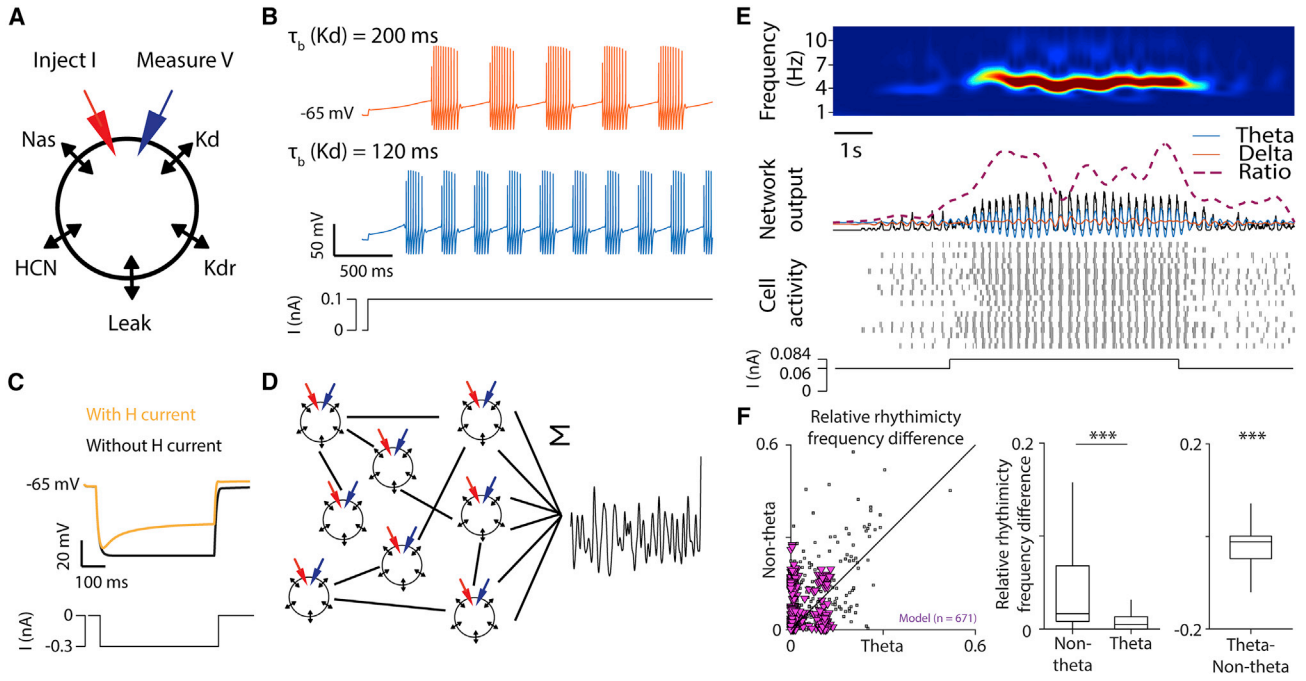

Figure 5. A simple conductance-based network model of the MS pacemaker circuit is capable of theta-synchronization upon tonic excitation

(A) Schematic of the single-compartment model neuron. The inhibitory neuron was equipped with transient sodium (Nas), slowly inactivating D-type potassium (Kd), delayed rectifier potassium (Kdr), HCN channels and passive leak channels. An electrode delivering current is attached to the cell.

(B) Rhythmicity frequency of the model neuron can be controlled by the τ_b(Kd) inactivation time constant. Slower inactivation (200 ms) also increases burst length.

(C) Adding H current caused a sag response to hyperpolarizing current, similar to MS GABAergic neurons reported in the literature (see, e.g., Figure 1C in Xu et al. [2004]). The moderate rebound effect did not induce rebound spikes.

(D) Schematics of the network. Twenty model cells were connected with simulated GABA-A-mediated inhibitory synapses. Spike trains were summed and convolved with a 50-ms Gaussian window to model network output.

(E) Simulation of network behavior (60% connection rate; 7-ms synaptic delay, 3-nS mean synaptic strength; 2-ms synaptic decay; 10% variance for the latter three synaptic parameters; 60-pA mean baseline stimulation with 10% variance). Neurons synchronized in the theta frequency band in response to a tonic increase of stimulation and desynchronized when stimulation was reset to baseline. (Increased excitation was applied with jittered onset latency to avoid synchronous phase reset; see STAR Methods.) Top, wavelet spectrogram of network output. Middle, network output (black, raw; blue, filtered in the theta band; orange, filtered in the delta band; dashed, theta-delta ratio) and simulated spike raster. Bottom, injected current.

(F) Left, scatter plot of relative frequency difference of simultaneous pairs of pacemaker neurons, normalized to the larger of the frequencies; real data in black (three datasets pooled, see Figure 4E), model data overlaid in magenta. Middle and right, statistics indicated that individual model pacemakers became more similar in frequency during theta (***$p < 0.001$; $p = 2.20 \times 10^{-30}$, W = 51519, n = 671, Wilcoxon signed-rank test). Box-whisker plots show median, interquartile range and non-outlier range.

pacemaker pairs. This analysis also indicated greater coherence in a narrow frequency band among putative pacemakers during theta (Figures 4G and 4H). Thus, these analyses confirmed our prediction that the theta-rhythmic population converges to a tighter rhythmicity frequency distribution after theta onset.

Network model of the medial septum confirms frequency (Huygens) synchronization mechanism

Our neural data suggested that increased tonic excitation led to higher firing rates and frequency synchronization in putative pacemakers that resulted in a strong theta-modulated output. To test if a simple network model of a homogeneous MS pacemaker population could produce these dynamics, we simulated MS neurons based on a minimalistic single-compartment conductance-based model constructed to produce fast spiking burst dynamics (Golomb et al., 2007) (Figure 5A). The model neuron expressed rhythmic discharges upon current injection with a rhythmicity frequency in the delta-theta range, controlled by the inactivation time constant of a slowly inactivating D-type potassium channel (Figure 5B). Septal pacemaker neurons are known to express strong H-currents (Kocsis and Li, 2004; Xu et al., 2004); hence, we also included an HCN channel in the model, which successfully reproduced the previously reported H-current characteristics (Figure 5C).

Next, we built a network model by connecting the neurons with inhibitory synapses, simulating GABA-A receptor kinetics with a reversal potential at −70 mV that triggered fast inhibitory postsynaptic currents. All neurons received a non-rhythmic (“tonic”) somatic excitatory current to mimic the changing excitatory drive to the septal pacemaker population. To model the impact of the MS output on the hippocampal LFP, we convolved the averaged septal firing with a Gaussian kernel (Figure 5D). We found that, at low tonic excitation levels, the modelled septal output showed irregular activity with low levels of theta oscillation. Increasing

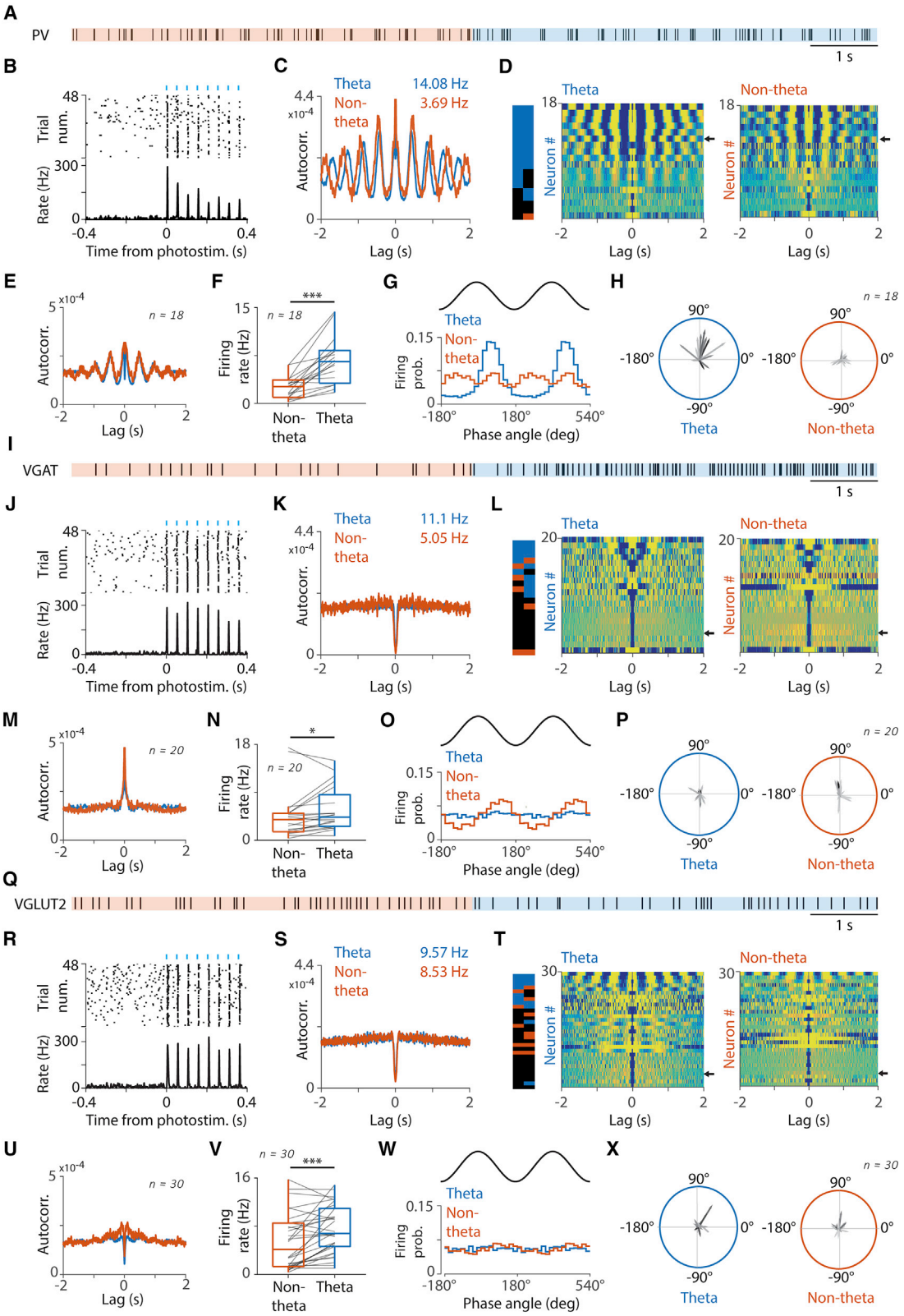

(legend on next page)

the tonic drive resulted in a strong theta oscillatory output, which returned to the irregular activity when the tonic current was decreased (Figure 5E). Thus, the level of non-rhythmic excitation could toggle the model pacemaker network between theta and non-theta output, as suggested earlier (Bland et al., 1996; Hajszan et al., 2004) and consistent with our neural recordings.

To test the robustness and parameter dependence of this finding, we systematically explored the parameter space (Figures S14A–S14E). We found a discrete maximum of the model's synchronization capabilities at a mean baseline excitation of around 60 pA, which was largely independent of the connectivity rate. Interestingly, very strong baseline excitation could result in a mirrored activity (decreased theta synchronization upon increased excitation owing to switching to a continuously firing mode, indicated by a synchronization score <0.5), sometimes also observed in anesthetized preparations. Fixing the baseline tonic excitation at the optimum, the model network was capable of synchronizing at a range of mean synaptic strength levels and connection rates.

This model allowed us to test whether a network of interconnected, minimalistic inhibitory MS units, without introducing specialized subpopulations and biased connectivity, exhibits the same frequency synchronization properties as we found in the septal network *in vivo*. To address this, we repeated the same battery of analyses on the model that we ran on the neural data (Figures S14F–S14K). We found that model neurons increased their firing rate in theta state (Figure S14F), accompanied by a slight increase in rhythmicity frequency (Figure S14G) and a strong decrease in theta skipping (Figure S14I), with a consistent but relatively small change in burst properties (Figure S14H). When we compared pairwise differences in pacemaker frequencies, we found a significant theta-associated decrease (Figure 5F), accompanied by a tightening of the rhythmicity frequency distribution (Figure S14K), suggesting the presence of a frequency synchronization mechanism.

Since a subset of putative pacemaker pairs showed stable anti-phasic firing patterns in urethane-anesthetized rats (Figures S14L–S14M), we tested whether the model also generated anti-phasic firing patterns. The analysis of pairwise cross-correlograms showed that in-phase synchrony dominated in most of the parameter space (Figures S14N–S14O), whereas we also found examples of anti-phasic synchronization (Figures S14P–S14S). This suggests that anti-phasic synchronization can occur in the model, although it is not necessary for theta synchronization, in accordance with Huygens synchronization theory.

Thus, the model behaved similarly to the rodent theta-generating networks, confirming that Huygens-type frequency synchronization might be a general mechanism operating in brain networks, similar to many mechanical systems.

Most PV-expressing GABAergic neurons are theta rhythmic, whereas MS glutamatergic neurons are "tonic theta ON"

Finally, to investigate the genetic and neurotransmitter identity of MS neurons, we performed optogenetic tagging in urethane-anesthetized mice in a separate set of experiments (Figures S15A–S15I). Theta oscillation was induced by tail pinch, and we performed theta detection and rhythmicity-based classification of MS neurons as above. We performed optogenetic stimulation in PV-Cre (n = 2), vesicular GABA transporter (VGAT)-Cre (n = 2) or VGluT2-Cre (n = 3) mice transduced by a Cre-dependent Channelrhodopsin (ChR2) construct injected in the MS to identify PV-expressing, GABAergic, and glutamatergic MS neurons, respectively (Gritti et al., 2006; Sotty et al., 2003).

We found that many PV-expressing neurons were theta rhythmic (Figures 6A–6H), and 9 of 18 neurons were characterized as putative pacemakers (Figure S15J). Surprisingly, GABAergic neurons as a population contained few theta-rhythmic neurons; instead, most VGAT+ MS neurons were non-rhythmic (Figures 6I–6P and S15J; n = 2/20 putative pacemakers). Anatomical studies showed that a subset of GABAergic MS neurons express PV (Gritti et al., 2003; Kiss et al., 1990; Unal et al., 2015; Yang et al., 2017; Zaborszky et al., 1999, 2012), suggesting that the subset of VGAT+ MS neurons that were rhythmic may have been PV expressing. These results suggest that PV expression marks the theta-generating population, confirming previous studies (Borhegyi et al., 2004; Freund, 1989; Varga et al., 2008). When we calculated the theta-associated change in relative frequency differences between pairs of putative pacemakers where at least one of the cells was tagged as PV+ (Figure S15K), we found similar frequency synchronization as shown for unlabeled pairs of putative pacemakers in Figure 4E and for model pacemaker neurons in Figure 5F.

Figure 6. Optogenetic identification of MS neuron types in anesthetized mice

(A) Example spike raster of a PV-expressing MS neuron during non-theta (orange) and theta (blue) segments.

(B) Raster plot (top) and corresponding peri-stimulus time histogram (bottom) of an example PV-expressing light-sensitive MS neuron aligned to the onset of 20 Hz photostimulation (blue ticks).

(C) Autocorrelograms of the example neuron during non-theta (orange) and theta (blue) segments. Numbers in the top right corner indicate average firing rate during non-theta (orange) and theta (blue).

(D) Autocorrelograms of all identified PV-expressing MS neurons, sorted by rhythmicity index. Left, color bar indicates significant theta-rhythmicity (blue) and delta-rhythmicity (orange) during theta (left) and non-theta (right) segments. Middle, autocorrelograms during theta segments. Right, autocorrelograms during non-theta segments. The arrows indicate the example neuron. Most PV-positive MS neurons were constitutively theta-bursting putative pacemakers.

(E) Average autocorrelogram of all identified PV-expressing MS neurons.

(F) Firing rate change between non-theta and theta segments of all identified PV-expressing MS neurons (***$p < 0.001$; $p = 2.33 \times 10^{-4}$, W = 170, n = 18, Wilcoxon signed-rank test).

(G) Phase-locking of the example neuron to delta (orange) and theta (blue) oscillations.

(H) Phase-locking of all identified PV-expressing MS neurons to theta (left) and delta (right) oscillations. Greyscale indicates average firing rate.

(I–P) Same as (A–H), but for VGAT-expressing MS neurons. In (N), *$p < 0.05$; $p = 3.66 \times 10^{-2}$, W = 161, n = 20, Wilcoxon signed-rank test.

(Q–X) Same as in (A–H), but for VGLUT2-expressing MS neurons. In (V), ***$p < 0.001$; $p = 8.94 \times 10^{-4}$, W = 394, n = 30, Wilcoxon signed-rank test.

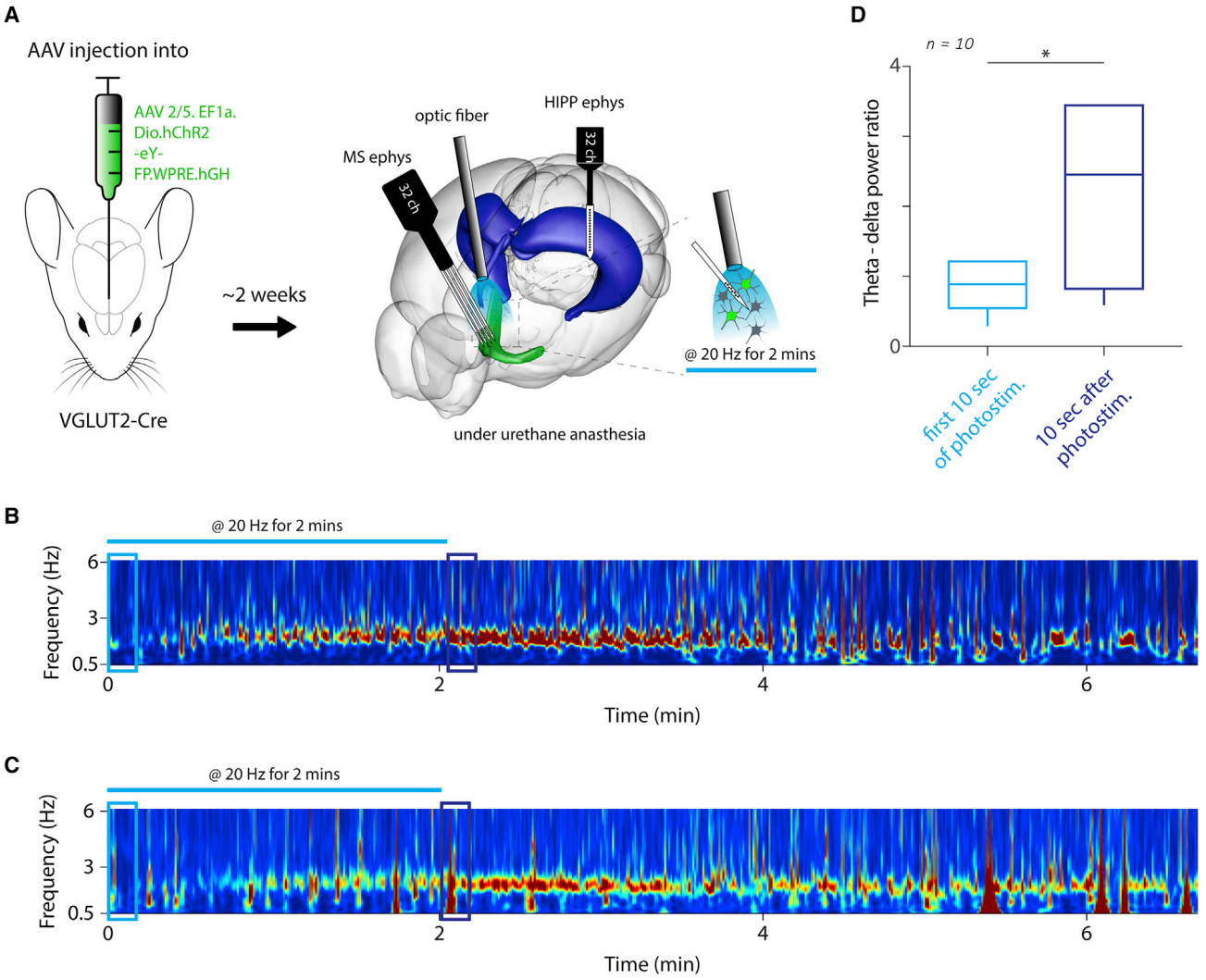

Figure 7. Optogenetic stimulation of MS glutamatergic neurons at 20 Hz generates theta oscillations in CA1

(A) Schematic of the experiment. VLGUT2-Cre mice were injected with AAV2/5.EF1a.Dio.hChR2-eYFP.WPRE.hGh in the MS and implanted with an optic fiber in the MS and silicon probes in the MS and CA1 in acute anesthetized experiments. Three-dimensional mouse brain adopted from Bakker et al. (2015).

(B) Wavelet spectrogram of an example CA1 LFP segment during and after 20-Hz stimulation of MS glutamatergic neurons. The photostimulation induced lasting theta oscillation. (Note the lower frequency of theta typical under anesthesia).

(C) Average of all recording sessions (n = 10) of 20 Hz glutamatergic stimulation).

(D) Box-whisker plot showing significant increase in theta-delta ratio upon glutamatergic stimulation. Median, interquartile range and non-outlier range are shown (*$p < 0.05$; $p = 3.71 \times 10^{-2}$, W = 7, n = 10, Wilcoxon signed-rank test).

The majority of optogenetically identified MS glutamatergic neurons showed a strong increase in the firing rate (fold increase median ± standard error of the median, 1.42 ± 0.34) without any theta rhythmicity during hippocampal theta state (Figures 6Q–6X, Figure S15J). Few glutamatergic neurons were theta-rhythmic, with 3 of 30 characterized as pacemakers. This identifies the MS glutamatergic population as tonic theta ON neurons (Ford et al., 1989).

Thus, local glutamatergic neurons may contribute to the increased excitatory drive to the MS pacemaker neurons during theta synchronization. To directly test this prediction, we analyzed CA1 LFP after 20 Hz stimulation of MS glutamatergic neurons in urethane-anesthetized VGLUT2-Cre mice (Figure 7A). Optogenetic stimulation induced hippocampal theta oscillation in most cases, reflected in the appearance of theta frequencies in the wavelet spectrogram of CA1 LFP recordings (Figures 7B and 7C), and a significant increase in the theta-delta ratio upon photostimulation (Figure 7D).

DISCUSSION

We categorized MS neurons based on their rhythmic properties. Putative pacemaker neurons showed constitutive theta rhythmic activity and synchronized their frequencies during

hippocampal theta oscillations in different rodent theta model systems. This mechanism, known as Huygens synchronization, was reproduced by a network model of minimalistic theta-rhythmic inhibitory MS units, demonstrating that a homogeneous group of pacemakers can synchronize and desynchronize via inhibitory connections upon changing levels of tonic excitatory drive. Optogenetic tagging confirmed that pacemaker neurons are PV-expressing GABAergic cells, while non-PV GABAergic neurons likely do not participate in rhythm genesis. Glutamatergic septal neurons were of tonic theta ON type, which suggests that they contribute to the non-rhythmic excitatory control of the pacemaker rhythm generator network. In line with this prediction, optogenetic activation of MS glutamatergic neurons at 20 Hz induced theta oscillation in CA1.

We first performed an unbiased physiological characterization of MS units, extending previous electrophysiology studies (Apartis et al., 1998; Borhegyi et al., 2004; Duque et al., 2000; Ford et al., 1989; Hassani et al., 2009; Simon et al., 2006; Stewart and Fox, 1989; Varga et al., 2008). Bland and colleagues characterized MS neurons as theta-on versus theta-off based on their firing rate changes, and phasic (theta bursting) versus tonic (non-rhythmic) based on their firing patters. Petsche et al. (1962) described A- and B-units, where B-units were phase locked to theta with a stable phase relationship. Many studies have since investigated B-units (Apartis et al., 1998; Borhegyi et al., 2004; Joshi et al., 2017; King et al., 1998; Stewart and Fox, 1989), but A-units received less attention. Other studies indicated the presence of lower frequency rhythms, including "slow oscillations" and rhythmic activity related to breathing (Buzsaki et al., 1986; Tsanov, 2015; Tsanov et al., 2014; Wolansky et al., 2006). In accordance, we also observed rhythmic activity in the delta frequency band, especially in urethane-anesthetized rats. Therefore, we characterized MS neurons based on their rhythmicity during hippocampal theta and non-theta episodes as non-rhythmic, delta-rhythmic or theta-rhythmic. While this resulted in nine theoretical combinations, most MS neurons belonged to a few characteristic types.

Stewart and Fox (1989) found that, after eliminating theta oscillation in the hippocampus of urethane-anesthetized rats using atropine, a subset of MS neurons remained theta rhythmic. In another study, 15% of septal neurons were found phasic bursting even during non-theta epochs under anesthesia (Ford et al., 1989). We identified putative pacemaker neurons that fired theta-rhythmic bursts regardless of whether theta oscillation was present in CA1. This group comprised 13% of MS neurons in freely moving mice; however, we found a lower percentage of rhythmic bursting neurons in anesthetized rodents, in line with some previous reports (King et al., 1998; Stewart and Fox, 1989). The differences in percentage of pacemakers across reports may stem both from biased sampling, as the MS can be identified during recording based on the presence of theta-rhythmic activity, as well as from strictness of definitions for rhythmicity. We applied relatively conservative inclusion criteria for significant rhythmicity (Figure S2) to ensure data quality necessary for analyzing mechanisms of rhythmic synchronization, which may have resulted in a lower percentage of putative pacemakers in our datasets. These results also suggest that some MS neurons may be identified as putative pacemakers under awake but not in anesthetized conditions.

The expression of PV and HCN, the channel protein that underlies the H-current, has been associated with rhythmic pacemaking properties of MS GABAergic neurons (Borhegyi et al., 2004; Kocsis and Li, 2004; Varga et al., 2008; Xu et al., 2004). However, other studies suggested that rhythmic MS glutamatergic or cholinergic neurons may act as pacemakers (Manseau et al., 2005; Mysin et al., 2015; Smythe et al., 1992; Ujfalussy and Kiss, 2006; but see Vandecasteele et al., 2014). Here, we confirmed by optogenetic identification of multiple MS cell types that PV-expressing GABAergic neurons probably constitute most of the constitutive theta-rhythmic group. At the same time, we found that GABAergic neurons as a population contained only few theta-rhythmic neurons, suggesting that their subset that were rhythmic may have been PV expressing. We confirmed that septal pacemakers formed two groups with opposing phase preference with respect to the hippocampal theta oscillation in urethane-anesthetized rats, as reported previously (Borhegyi et al., 2004; Joshi et al., 2017; Varga et al., 2008).

We referred to MS neurons only showing theta-rhythmic bursting when hippocampal theta was present as follower neurons; their firing patterns tended to correspond with hippocampal network states. However, this property does not exclude them from participating in theta genesis. Indeed, these neurons tended to strongly synchronize with each other and putative pacemaker neurons both during theta and non-theta states, and optogenetic tagging experiments revealed an enrichment of both putative pacemaker and follower neurons in the PV+ GABAergic group (Figure S15J), suggesting that this functional distinction based on rhythmicity may occur within the anatomically defined PV-expressing group.

In the seventeenth century, Christiaan Huygens observed that two pendulum clocks, coupled through a house beam, tended to synchronize over time, which he referred to as "sympathy of two clocks" (Huygens, 1673; Oliveira and Melo, 2015; Ramirez et al., 2016; Willms et al., 2017). Such synchronization of coupled oscillators, where individual oscillators become closer to each other in their frequency and period time, has been found in many dynamical systems (Equihua and Ramirez, 2018; Ramirez et al., 2016). We identified this mechanism among MS pacemaker neurons, suggesting that a Huygens synchronization mechanism underlies the generation of a strong theta rhythmic output transmitted to the hippocampus. The two dominant oscillatory behaviors that emerge in coupled oscillators during Huygens synchronization are in-phase and anti-phase synchronization (Korteweg, 1906; Ramirez et al., 2014), and either one can sufficiently underlie frequency synchronization (Czolczynski et al., 2011; Ramirez et al., 2014, 2016). This may, at least in part, explain the observation of anti-phase firing in the MS of urethane-anesthetized rats. Experiments and modeling studies also observed less common modes of Huygens synchronization, including partial synchronization, when oscillators synchronize with a phase difference of less than 180°; "quenching," when the two oscillators suppress each other; "beating death," in which one oscillator is suppressed but remains oscillatory owing to the influence of the other; and amplitude modulation, a consequence of mutual influence (Ramirez et al., 2014). It will be

exciting to study whether and how the broad theory behind Huygens synchronization, often investigating limit behavior of complex non-linear ordinary differential equation systems, can be applied to neural circuits. For instance, "modulating" behavior can theoretically be related to forms of cross-frequency coupling (Buzsáki and Wang, 2012; Lisman and Jensen, 2013), whereas quenching and beating death can be viewed as synchronization failures, which may be relevant to oscillopathies, e.g. gamma oscillation failures in patients with schizophrenia (Hunt et al., 2017). Theoretical studies may explain how and why the output oscillation period may differ from the eigenperiods of the coupled individual oscillators (Dilão, 2009; Ramirez et al., 2016), also observed in the context of neuronal oscillations, possibly serving as a basis for phase precession (Geisler et al., 2007; O'Keefe and Recce, 1993; Zutshi et al., 2018).

Previous models of the septal pacemaker network either explored GABAergic (Denham and Borisyuk, 2000; Ujfalussy and Kiss, 2006; Wang, 2002) or glutamatergic (Ujfalussy and Kiss, 2006) pacing mechanisms. These previous works already contained indirect reference to potential Huygens synchronization mechanisms. For instance, Wang suggested that desynchronized septal pacemaker units may oscillate at different frequencies (see Figure 4 in Wang, 2002). Additionally, Ujfalussy et al. wrote that "blocking the GABAergic synapses in our ping-pong model causes desynchronization of these neurons but the cells remain theta periodic." However, Huygens synchronization has neither been experimentally tested nor directly modelled, and previous models mostly focused on exploring the ways different oscillator networks may interplay, such as two GABAergic MS groups with opposing firing phase (Ujfalussy and Kiss, 2006), MS and CA1 GABAergic groups (Denham and Borisyuk, 2000; Wang, 2002; Zou et al., 2011), or MS GABAergic and glutamatergic neurons (Mysin et al., 2015). Thus, in previous ping pong models, the synchronization mechanism required the presence of at least two dedicated inhibitory groups, with biased, non-random connectivity between the groups. In contrast, we found that even a minimalistic, homogeneous network of MS GABAergic pacemakers was sufficient to generate coherent theta-rhythmic output upon increased tonic excitation. While desynchronization of the MS network was rarely addressed in previous theoretical work, we also found that our MS model network showed rapid spontaneous desynchronization when tonic excitation was decreasing. This MS model network could recapitulate multiple features of the *in vivo* synchronization process, including Huygens synchronization, increased firing rate, faster rhythmic firing, decreased theta skipping, and a slight increase in intra-burst firing frequency.

We found a substantial increase in the firing rates in MS pacemaker neurons upon theta onset. This finding is in line with previous studies suggesting that an increased tonic excitatory drive can switch the MS network into theta state (Korvasová et al., 2021; Lu et al., 2011; Müller and Remy, 2018; Oddie et al., 1996; Ujfalussy and Kiss, 2006). Multiple cell types and pathways were proposed to contribute to this excitatory drive, including MS cholinergic, glutamatergic, and ascending brainstem inputs (Hajszan et al., 2004; Leranth and Frotscher, 1989; Müller and Remy, 2018; Oddie and Bland, 1998; Zaborszky et al., 2012). We found that MS glutamatergic neurons strongly and non-rhythmically increased their firing rates at the onset of CA1 theta, suggesting they may be the dominant relay that conveys changing levels of tonic excitation to the MS pacemaker network, in agreement with anatomical findings showing that local excitatory neurons provide the majority of excitatory inputs to MS GABAergic neurons (Hajszan et al., 2004).

In line with this, the optogenetic activation of MS glutamatergic neurons induced theta oscillation in the CA1. Importantly, we evoked theta rhythm by using a stimulation frequency of 20 Hz well above the theta range, demonstrating that VGLUT2-expressing MS neurons are capable of theta induction not only when stimulated at theta-range frequencies (Robinson et al., 2016). These results are also consistent with the growing body of evidence showing that these neurons are involved in conveying locomotion-related activation to other cell types of the MS and beyond (Fuhrmann et al., 2015; Justus et al., 2017; Korvasová et al., 2021; Oddie et al., 1996; Teitelbaum et al., 1975).

Previous studies demonstrated theta-skipping behavior of rhythmic neurons both in the entorhinal cortex (EC) (Brandon et al., 2013; Jeffery et al., 1995) and in the MS (Kay et al., 2020; King et al., 1998; Varga et al., 2008). Theta skipping was characterized by rhythmic activity with one-half the frequency of ongoing hippocampal theta, by neurons firing rhythmically in every second theta cycle. It has been demonstrated that MS input was necessary for theta-skipping behavior in the EC in rats (Brandon et al., 2013), and that theta-skipping behavior in the EC may rely on inhibitory rebound mechanisms, potentially crucial to the formation of characteristic grid cell firing fields (Hasselmo, 2014). We confirmed the presence of theta-skipping neurons in the MS of urethane-anesthetized rats. While some of these neurons fired regularly in every second cycle, other neurons showed a less regular pattern, occasionally skipping more than one cycle. Interestingly, we found very few theta-skipping neurons in anesthetized and freely moving mice. Therefore, theta-skipping in the MS may not be necessary for grid pattern formation in mice.

We found a group of tonically active neurons both in rats and mice, which may be cholinergic, since (1) their firing patterns resemble cholinergic neurons in previous publications (Brazhnik and Fox, 1997; Mamad et al., 2015; Tsanov, 2015), (2) we identified cholinergic neurons with similar rhythmic and synchronization properties from other basal forebrain structures (Laszlovszky et al., 2020), and (3) rhythmic basal forebrain cholinergic neurons were not phase locked to hippocampal theta in a former study (Lee et al., 2005), as we also found for the tonically active group. Theta-rhythmic cholinergic neurons may be more linked with a neocortical theta oscillation that can be recorded from the posterior cingulate cortex (Destrade and Ott, 1982; Lee et al., 2005), and we have also reported behavior-specific synchronization of nucleus basalis cholinergic neurons with theta-band activity in the auditory cortex (Laszlovszky et al., 2020). This would confirm that the role of MS cholinergic neurons in hippocampal theta generation is mostly indirect through GABAergic neurons, controlling theta amplitude but not participating in rhythmic theta pacing (Dannenberg et al., 2015; Lee et al., 1994; Yang et al., 2014, 2017). We expect that it

will be one of the most exciting future directions to better understand how multiple theta rhythms interact dynamically in the brain, including synchronization with active sensing processes (Moore et al., 2013; Ranade et al., 2013; Semba and Komisaruk, 1984), entraining local pacemaker groups (Manseau et al., 2008) and interacting with cellular resonance properties (Zemankovics et al., 2010).

Limitations of the study

Although we demonstrated that a homogeneous group of MS inhibitory neurons may be capable of pacing hippocampal theta, this does not rule out the possibility of other contributing neuronal populations including the hippocampo-septal feedback projection (Katona et al., 2017; Manseau et al., 2008; Toth et al., 1993; Wang, 2002) and subcortical areas such as the supramammillary nucleus (Farrell et al., 2021; Pan and McNaughton, 2002; Vertes and Kocsis, 1997) and the nucleus incertus (Ma et al., 2009; Martínez-Bellver et al., 2015; Szőnyi et al., 2019). Nevertheless, recent studies demonstrated that intraseptal connections are necessary for CA1 theta oscillations to emerge (Korvasová et al., 2021) and that the nucleus incertus may not provide but rather receive theta-rhythmic signals from the MS (Trenk et al., 2022).

An alternative mechanism to frequency synchronization is phase synchronization without concurrent change in rhythmicity frequency, defined generally as changes in the phase relationship of coupled oscillators (Rosenblum et al., 1996, 2001). Such mechanisms are known to operate between synchronizing brain regions and are thought to underlie changes in the efficacy of information transfer (Fell and Axmacher, 2011). As a special case of phase synchronization, a decrease in phase difference between individual pacemaker units may lead to a larger amplitude rhythmic output. In contrast, we demonstrated a convergence of rhythmicity frequencies during synchronization. Although this change in frequencies can be accompanied by a change in relative firing phases, it is hard to interpret whether this is a necessary consequence of the frequency synchronization, or a parallel, separate phase synchronization process also takes place (Rosenblum et al., 1996).

We found a strong consistency of rhythmic MS cell types and synchronization mechanisms across urethane-anesthetized rats, urethane-anesthetized mice and feely moving mice, while we did not obtain data from freely moving rats. This argues for common mechanisms of septo-hippocampal theta-rhythmic synchronization. However, we also noted some differences. Part of them may stem from known distinctions of urethane- and atropine-sensitive theta oscillations (Kramis et al., 1975; Li et al., 2007), with different underlying mechanisms (Losonczy et al., 2010; Mikulovic et al., 2018; Nicola and Clopath, 2019; Winterer et al., 2019). Anesthetized rats showed strong hippocampal rhythmicity in the delta band during non-theta episodes, mostly absent in mice. In accordance, we found delta-rhythmic and theta-skipping MS neurons in rats but very few in mice. Tonically active neurons showed a theta-associated firing rate decrease in rats but increase in mice. While we speculated that this group might be cholinergic, the lack of optogenetic identification of cholinergic MS neurons is another limitation of this study.

Marder and colleagues observed that often the rhythmic firing activities are controlled and not the exact underlying ion channel constellations, leading to unexpected variability in channel abundance with stable oscillatory parameters (Alonso and Marder, 2019). It is possible that, similar to this principle, the theta-rhythmic activity of the septo-hippocampal system is evolutionarily conserved, with a larger variance in the exact implementation (Payne et al., 2021). Further experiments and modeling will help gauge the significance of this variability.

STAR★METHODS

Detailed methods are provided in the online version of this paper and include the following:

- KEY RESOURCES TABLE
- RESOURCE AVAILABILITY
  - Lead contact
  - Materials availability
  - Data and code availability
- EXPERIMENTAL MODEL AND SUBJECT DETAILS
- METHOD DETAILS
  - Surgery and electrophysiological recordings
  - Histological verification of the recording location
  - Immunostaining
- QUANTIFICATION AND STATISTICAL ANALYSIS
  - Hippocampal state detection
  - Spike sorting of septal neurons
  - Rhythmicity indices of MS neurons
  - Theta-burst index
  - Analysis of phase-coupling
  - Crosscorrelation
  - Pacemaker synchronization
  - Wavelet coherence
  - Data analysis of the optogenetic tagging experiments
  - Analysis of photostimulation impact
  - MS pacemaker neuron model
  - Modeling the MS pacemaker network
  - Exploring the parameter space of the pacemaker network model
  - Model network synchronization
  - Statistical testing

SUPPLEMENTAL INFORMATION

Supplemental information can be found online at https://doi.org/10.1016/j.celrep.2022.111149.

ACKNOWLEDGMENTS

The authors thank Katalin Lengyel for technical assistance and Drs. Tim Viney and Peter Somogyi for helpful comments on the manuscript. This work was supported by the "Lendület" Program of the Hungarian Academy of Sciences (LP2015-2/2015), NKFIH KH125294, NKFIH K135561, the ERC Starting Grant no. 715043 and SPIRITS 2020 of Kyoto University to B.H.; the NRDI Office of Hungary within the framework of the Artificial Intelligence National Laboratory Program (RRF-2.3.1-21-2022-00004) to B.H., V.V., and S.K.; NKFIH K119650 to P.B.; National Brain Research Program 1.2.1-NKP-2017-00002 to P.B., R.F., and I.U.; NKFIH PD124175 and PD134196 to R.F.; NKFIH TUDFO/51757-1/2019-ITM, ELKH KEP-4/5/2021, and ELKH KÖ-39/2021 to I.U.; the

ÚNKP-20-3 New National Excellence Program of the Ministry for Innovation and Technology to B.K.; and the Generalitat Valenciana Postdoctoral Fellowship Program (APOSTD/2019/003) to S.M.B. We acknowledge the help of the Nikon Center of Excellence at the Institute of Experimental Medicine (IEM), Nikon Europe, Nikon Austria, and Auro-Science Consulting for kindly providing microscopy support and the supportive help of the Central Virus Laboratory of IEM. We thank Luigi Petrucco for open access science art at SciDraw (https://doi.org/10.5281/zenodo.3925903).

AUTHOR CONTRIBUTIONS

B.H. developed the idea and conceptualized the manuscript. S.M.B., R.F., A.D., B.H., and P.B. performed the experiments, supervised by T.F.F., I.U., V.V., and B.H. B.K., S.M.B., and P.B. performed the data analysis. B.K., K.S., and D.S. generated the figures. D.S. performed immunocytochemistry. B.K. performed the modeling, supervised by S.K. B.H. wrote the manuscript with input from all authors.

DECLARATION OF INTERESTS

The authors declare no competing financial interests.

Received: January 22, 2021
Revised: May 6, 2022
Accepted: July 7, 2022
Published: August 2, 2022

REFERENCES

Adler, A., Zhao, R., Shin, M.E., Yasuda, R., and Gan, W.-B. (2019). Somatostatin-expressing interneurons enable and maintain learning-dependent sequential activation of pyramidal neurons. Neuron *102*, 202–216.e7.

Akaike, H. (1973). Information theory and an extension of the maximum likelihood principle. In 2nd International Symposium on Information Theory, pp. 267–281.

Alonso, L.M., and Marder, E. (2019). Visualization of currents in neural models with similar behavior and different conductance densities. Elife *8*, e42722.

Apartis, E., Poindessous-Jazat, F.R., Lamour, Y.A., and Bassant, M.H. (1998). Loss of rhythmically bursting neurons in rat medial septum following selective lesion of septohippocampal cholinergic system. J. Neurophysiol. *79*, 1633–1642.

Bakker, R., Tiesinga, P., and Kötter, R. (2015). The scalable brain atlas: instant web-based access to public brain atlases and related content. Neuroinformatics *13*, 353–366.

Barthó, P., Hirase, H., Monconduit, L., Zugaro, M., Harris, K.D., and Buzsáki, G. (2004). Characterization of neocortical principal cells and interneurons by network interactions and extracellular features. J. Neurophysiol. *92*, 600–608.

Bland, B.H., Trepel, C., Oddie, S.D., and Kirk, I.J. (1996). Intraseptal microinfusion of muscimol: effects on hippocampal formation theta field activity and phasic Theta-ON cell discharges. Exp. Neurol. *138*, 286–297.

Borg-Graham, L.J. (1999). Models of cortical circuits. In Interpretations of Data and Mechanisms for Hippocampal Pyramidal Cell Models (Springer), pp. 19–138.

Borhegyi, Z., Varga, V., Szilágyi, N., Fabo, D., and Freund, T.F. (2004). Phase segregation of medial septal GABAergic neurons during hippocampal theta activity. J. Neurosci. *24*, 8470–8479.

Brandon, M.P., Bogaard, A.R., Schultheiss, N.W., and Hasselmo, M.E. (2013). Segregation of cortical head direction cell assemblies on alternating theta cycles. Nat. Neurosci. *16*, 739–748.

Brazhnik, E.S., and Fox, S.E. (1997). Intracellular recordings from medial septal neurons during hippocampal theta rhythm. Exp. Brain Res. *114*, 442–453.

Brewer, M.J., Butler, A., and Cooksley, S.L. (2016). The relative performance of AIC, AIC C and BIC in the presence of unobserved heterogeneity. Methods Ecol. Evol. *7*, 679–692.

Buzsáki, G., Czopf, J., Kondákor, I., and Kellényi, L. (1986). Laminar distribution of hippocampal rhythmic slow activity (RSA) in the behaving rat: current-source density analysis, effects of urethane and atropine. Brain Res. *365*, 125–137.

Buzsáki, G. (2002). Theta oscillations in the hippocampus. Neuron *33*, 325–340.

Buzsáki, G. (2006). Rhythms of the Brain (Oxford University Press).

Buzsáki, G., and Mizuseki, K. (2014). The log-dynamic brain: how skewed distributions affect network operations. Nat. Rev. Neurosci. *15*, 264–278.

Buzsáki, G., and Moser, E.I. (2013). Memory, navigation and theta rhythm in the hippocampal-entorhinal system. Nat. Neurosci. *16*, 130–138.

Buzsáki, G., and Wang, X.-J. (2012). Mechanisms of gamma oscillations. Annu. Rev. Neurosci. *35*, 203–225.

Carnevale, N.T., and Hines, M.L. (2006). The NEURON Book (Cambridge University Press).

Cummings, K.A., and Clem, R.L. (2020). Prefrontal somatostatin interneurons encode fear memory. Nat. Neurosci. *23*, 61–74.

Cutsuridis, V., and Poirazi, P. (2015). A computational study on how theta modulated inhibition can account for the long temporal windows in the entorhinal-hippocampal loop. Neurobiol. Learn. Mem. *120*, 69–83.

Czolczynski, K., Perlikowski, P., Stefanski, A., and Kapitaniak, T. (2011). Huygens' odd sympathy experiment revisited. Int. J. Bifurcation Chaos *21*, 2047–2056.

Dannenberg, H., Pabst, M., Braganza, O., Schoch, S., Niediek, J., Bayraktar, M., Mormann, F., and Beck, H. (2015). Synergy of direct and indirect cholinergic septo-hippocampal pathways coordinates firing in hippocampal networks. J. Neurosci. *35*, 8394–8410.

Denham, M.J., and Borisyuk, R.M. (2000). A model of theta rhythm production in the septal-hippocampal system and its modulation by ascending brain stem pathways. Hippocampus *10*, 698–716.

Destrade, C., and Ott, T. (1982). Is a retrosplenial (cingulate) pathway involved in the mediation of high frequency hippocampal rhythmical slow activity (theta)? Brain Res. *252*, 29–37.

DiCarlo, J.J., Lane, J.W., Hsiao, S.S., and Johnson, K.O. (1996). Marking microelectrode penetrations with fluorescent dyes. J. Neurosci. Methods *64*, 75–81.

Dilão, R. (2009). Antiphase and in-phase synchronization of nonlinear oscillators: the Huygens's clocks system. Chaos *19*, 023118.

Duque, A., Balatoni, B., Detari, L., and Zaborszky, L. (2000). EEG correlation of the discharge properties of identified neurons in the basal forebrain. J. Neurophysiol. *84*, 1627–1635.

Equihua, G.G.V., and Ramirez, J.P. (2018). Synchronization of hindmarsh-rose synchronization of hindmarsh-rose synchronization of hindmarsh-rose neurons huygens-like coupling synchronization of hindmarsh-rose neurons huygens-like coupling huygens-like coupling. IFAC-PapersOnLine *51*, 186–191.

Farrell, J.S., Lovett-Barron, M., Klein, P.M., Sparks, F.T., Gschwind, T., Ortiz, A.L., Ahanonu, B., Bradbury, S., Terada, S., Oijala, M., et al. (2021). Supramammillary regulation of locomotion and hippocampal activity. Science *374*, 1492–1496.

Fell, J., and Axmacher, N. (2011). The role of phase synchronization in memory processes. Nat. Rev. Neurosci. *12*, 105–118.

Fiáth, R., Raducanu, B.C., Musa, S., Andrei, A., Lopez, C.M., van Hoof, C., Ruther, P., Aarts, A., Horváth, D., and Ulbert, I. (2018). A silicon-based neural probe with densely-packed low-impedance titanium nitride microelectrodes for ultrahigh-resolution in vivo recordings. Biosens. Bioelectron. *106*, 86–92.

Fiáth, R., Márton, A.L., Mátyás, F., Pinke, D., Márton, G., Tóth, K., and Ulbert, I. (2019). Slow insertion of silicon probes improves the quality of acute neuronal recordings. Sci. Rep. *9*, 111.

Fisher, N.I. (1993). Statistical Analysis of Circular Data (Cambridge University Press).

Ford, R.D., Colom, L.V., and Bland, B.H. (1989). The classification of medial septum-diagonal band cells as σ-on or σ-off in relation to hippocampal EEG states. Brain Res. *493*, 269–282.

Freund, T.F. (1989). GABAergic septohippocampal neurons contain parvalbumin. Brain Res. *478*, 375–381.

Freund, T.F., and Antal, M. (1988). GABA-containing neurons in the septum control inhibitory interneurons in the hippocampus. Nature *336*, 170–173.

Fuhrmann, F., Justus, D., Sosulina, L., Kaneko, H., Beutel, T., Friedrichs, D., Schoch, S., Schwarz, M.K., Fuhrmann, M., and Remy, S. (2015). Locomotion, theta oscillations, and the speed-correlated firing of hippocampal neurons are controlled by a medial septal glutamatergic circuit. Neuron *86*, 1253–1264.

Geisler, C., Robbe, D., Zugaro, M., Sirota, A., and Buzsáki, G. (2007). Hippocampal place cell assemblies are speed-controlled oscillators. Proc. Natl. Acad. Sci. USA *104*, 8149–8154.

Golomb, D., Donner, K., Shacham, L., Shlosberg, D., Amitai, Y., and Hansel, D. (2007). Mechanisms of firing patterns in fast-spiking cortical interneurons. PLoS Comput. Biol. *3*, e156.

Green, J.D., and Arduini, A.A. (1954). Hippocampal electrical activity in arousal. J. Neurophysiol. *17*, 533–557.

Green, J.D., Maxwell, D.S., Schindler, W.J., and Stumpf, C. (1960). Rabbit eeg "theta" rhythm: its anatomical source and relation to activity in single neurons. J. Neurophysiol. *23*, 403–420.

Gritti, I., Manns, I.D., Mainville, L., and Jones, B.E. (2003). Parvalbumin, calbindin, or calretinin in cortically projecting and GABAergic, cholinergic, or glutamatergic basal forebrain neurons of the rat. J. Comp. Neurol. *458*, 11–31.

Gritti, I., Henny, P., Galloni, F., Mainville, L., Mariotti, M., and Jones, B.E. (2006). Stereological estimates of the basal forebrain cell population in the rat, including neurons containing choline acetyltransferase, glutamic acid decarboxylase or phosphate-activated glutaminase and colocalizing vesicular glutamate transporters. Neuroscience *143*, 1051–1064.

Hajszan, T., Alreja, M., and Leranth, C. (2004). Intrinsic vesicular glutamate transporter 2-immunoreactive input to septohippocampal parvalbumin-containing neurons: novel glutamatergic local circuit cells. Hippocampus *14*, 499–509.

Hangya, B., Borhegyi, Z., Szilágyi, N., Freund, T.F., and Varga, V. (2009). GABAergic neurons of the medial septum lead the hippocampal network during theta activity. J. Neurosci. *29*, 8094–8102.

Hassani, O.K., Lee, M.G., Henny, P., and Jones, B.E. (2009). Discharge profiles of identified GABAergic in comparison to cholinergic and putative glutamatergic basal forebrain neurons across the sleep-wake cycle. J. Neurosci. *29*, 11828–11840.

Hasselmo, M.E. (2014). Neuronal rebound spiking, resonance frequency and theta cycle skipping may contribute to grid cell firing in medial entorhinal cortex. Philos. Trans. R. Soc. Lond. B Biol. Sci. *369*, 20120523.

Hunt, M.J., Kopell, N.J., Traub, R.D., and Whittington, M.A. (2017). Aberrant network activity in schizophrenia. Trends Neurosci. *40*, 371–382.

Huygens, C. (1673). Horologium Oscillatorium: sive de motu pendulorum ad horologia aptato demonstrationes geometricae (F. Muguet).

Inokawa, H., Yamada, H., Matsumoto, N., Muranishi, M., and Kimura, M. (2010). Juxtacellular labeling of tonically active neurons and phasically active neurons in the rat striatum. Neuroscience *168*, 395–404.

Jeffery, K.J., Donnett, J.G., and O'Keefe, J. (1995). Medial septal control of theta-correlated unit firing in the entorhinal cortex of awake rats. Neuroreport *6*, 2166–2170.

Joshi, A., Salib, M., Viney, T.J., Dupret, D., and Somogyi, P. (2017). Behavior-dependent activity and synaptic organization of septo-hippocampal GABAergic neurons selectively targeting the hippocampal CA3 area. Neuron *96*, 1342–1357.e5.

Justus, D., Dalügge, D., Bothe, S., Fuhrmann, F., Hannes, C., Kaneko, H., Friedrichs, D., Sosulina, L., Schwarz, I., Elliott, D.A., et al. (2017). Glutamatergic synaptic integration of locomotion speed via septoentorhinal projections. Nat. Neurosci. *20*, 16–19.

Kahana, M.J., Sekuler, R., Caplan, J.B., Kirschen, M., and Madsen, J.R. (1999). Human theta oscillations exhibit task dependence during virtual maze navigation. Nature *399*, 781–784.

Káli, S., and Zemankovics, R. (2012). The effect of dendritic voltage-gated conductances on the neuronal impedance: a quantitative model. J. Comput. Neurosci. *33*, 257–284.

Katona, L., Micklem, B., Borhegyi, Z., Swiejkowski, D.A., Valenti, O., Viney, T.J., Kotzadimitriou, D., Klausberger, T., and Somogyi, P. (2017). Behavior-dependent activity patterns of GABAergic long-range projecting neurons in the rat hippocampus. Hippocampus *27*, 359–377.

Kay, K., Chung, J.E., Sosa, M., Schor, J.S., Karlsson, M.P., Larkin, M.C., Liu, D.F., and Frank, L.M. (2020). Constant sub-second cycling between representations of possible futures in the Hippocampus. Cell *180*, 552–567.e25.

Kim, T., Thankachan, S., McKenna, J.T., McNally, J.M., Yang, C., Choi, J.H., Chen, L., Kocsis, B., Deisseroth, K., Strecker, R.E., et al. (2015). Cortically projecting basal forebrain parvalbumin neurons regulate cortical gamma band oscillations. Proc. Natl. Acad. Sci. USA *112*, 3535–3540.

King, C., Recce, M., and O'Keefe, J. (1998). The rhythmicity of cells of the medial septum/diagonal band of Broca in the awake freely moving rat: relationships with behaviour and hippocampal theta. Eur. J. Neurosci. *10*, 464–477.

Kiss, J., Patel, A.J., Baimbridge, K.G., and Freund, T.F. (1990). Topographical localization of neurons containing parvalbumin and choline acetyltransferase in the medial septum-diagonal band region of the rat. Neuroscience *36*, 61–72.

Klausberger, T., and Somogyi, P. (2008). Neuronal diversity and temporal dynamics: the unity of hippocampal circuit operations. Science *321*, 53–57.

Kocsis, B., and Li, S. (2004). In vivo contribution of h-channels in the septal pacemaker to theta rhythm generation. Eur. J. Neurosci. *20*, 2149–2158.

Konishi, S., and Kitagawa, G. (2008). Information Criteria and Statistical Modeling (Springer).

Korteweg, D. (1906). Les horloges sympathiques de Huygens. Arch. Neerl. Des Sci. Exactes Nat. *11*, 273–296.

Korvasová, K., Ludwig, F., Kaneko, H., Sosulina, L., Tetzlaff, T., Remy, S., and Mikulovic, S. (2021). Locomotion induced by medial septal glutamatergic neurons is linked to intrinsically generated persistent ring. Preprint at bioRxiv. https://doi.org/10.1101/2021.04.23.441122.

Kramis, R., Vanderwolf, C.H., and Bland, B.H. (1975). Two types of hippocampal rhythmical slow activity in both the rabbit and the rat: relations to behavior and effects of atropine, diethyl ether, urethane, and pentobarbital. Exp. Neurol. *49*, 58–85.

Kvitsiani, D., Ranade, S., Hangya, B., Taniguchi, H., Huang, J.Z., and Kepecs, A. (2013). Distinct behavioural and network correlates of two interneuron types in prefrontal cortex. Nature *498*, 363–366.

Laszlovszky, T., Schlingloff, D., Hegedüs, P., Freund, T.F., Gulyás, A., Kepecs, A., and Hangya, B. (2020). Distinct synchronization, cortical coupling and behavioral function of two basal forebrain cholinergic neuron types. Nat. Neurosci. *23*, 992–1003.

Lee, M.G., Chrobak, J.J., Sik, A., Wiley, R.G., and Buzsáki, G. (1994). Hippocampal theta activity following selective lesion of the septal cholinergic system. Neuroscience *62*, 1033–1047.

Lee, M.G., Hassani, O.K., Alonso, A., and Jones, B.E. (2005). Cholinergic basal forebrain neurons burst with theta during waking and paradoxical sleep. J. Neurosci. *25*, 4365–4369.

Leranth, C., and Frotscher, M. (1989). Organization of the septal region in the rat brain: cholinergic-GABAergic interconnections and the termination of hippocampo-septal fibers. J. Comp. Neurol. *289*, 304–314.

Li, S., Topchiy, I., and Kocsis, B. (2007). The effect of atropine administered in the medial septum or hippocampus on high- and low-frequency theta rhythms in the hippocampus of urethane anesthetized rats. Synapse *61*, 412–419.

Lima, S.Q., Hromádka, T., Znamenskiy, P., and Zador, A.M. (2009). PINP: a new method of tagging neuronal populations for identification during in vivo electrophysiological recording. PLoS One *4*, e6099.

Lisman, J.E., and Jensen, O. (2013). The theta-gamma neural code. Neuron *77*, 1002–1016.

Losonczy, A., Zemelman, B.V., Vaziri, A., and Magee, J.C. (2010). Network mechanisms of theta related neuronal activity in hippocampal CA1 pyramidal neurons. Nat. Neurosci. *13*, 967–972.

Lu, C.B., Ouyang, G., Henderson, Z., and Li, X. (2011). Induction of theta-frequency oscillations in the rat medial septal diagonal band slice by metabotropic glutamate receptor agonists. Neuroscience *177*, 1–11.

Ma, S., Olucha-Bordonau, F.E., Hossain, M.A., Lin, F., Kuei, C., Liu, C., Wade, J.D., Sutton, S.W., Nuñez, A., and Gundlach, A.L. (2009). Modulation of hippocampal theta oscillations and spatial memory by relaxin-3 neurons of the nucleus incertus. Learn. Mem. *16*, 730–742.

Mamad, O., McNamara, H.M., Reilly, R.B., and Tsanov, M. (2015). Medial septum regulates the hippocampal spatial representation. Front. Behav. Neurosci. *9*, 166–216.

Manseau, F., Danik, M., and Williams, S. (2005). A functional glutamatergic neurone network in the medial septum and diagonal band area. J. Physiol. *566*, 865–884.

Manseau, F., Goutagny, R., Danik, M., and Williams, S. (2008). The hippocamposeptal pathway generates rhythmic firing of GABAergic neurons in the medial septum and diagonal bands: an investigation using a complete septohippocampal preparation in vitro. J. Neurosci. *28*, 4096–4107.

Martínez-Bellver, S., Cervera-Ferri, A., Martínez-Ricós, J., Ruiz-Torner, A., Luque-García, A., Luque-Martinez, A., Blasco-Serra, A., Guerrero-Martínez, J., Bataller-Mompeán, M., and Teruel-Martí, V. (2015). Regular theta-firing neurons in the nucleus incertus during sustained hippocampal activation. Eur. J. Neurosci. *41*, 1049–1067.

McNamara, C.G., Tejero-Cantero, Á., Trouche, S., Campo-Urriza, N., and Dupret, D. (2014). Dopaminergic neurons promote hippocampal reactivation and spatial memory persistence. Nat. Neurosci. *17*, 1658–1660.

Migliore, M., and Migliore, R. (2012). Know your current I(h): interaction with a shunting current explains the puzzling effects of its pharmacological or pathological modulations. PLoS One *7*, e36867.

Mikulovic, S., Restrepo, C.E., Siwani, S., Bauer, P., Pupe, S., Tort, A.B.L., Kullander, K., and Leão, R.N. (2018). Ventral hippocampal OLM cells control type 2 theta oscillations and response to predator odor. Nat. Commun. *9*, 3638.

Moldestad, O., Karlsen, P., Molden, S., and Storm, J.F. (2009). Tracheotomy improves experiment success rate in mice during urethane anesthesia and stereotaxic surgery. J. Neurosci. Methods *176*, 57–62.

Moore, J.D., Deschênes, M., Furuta, T., Huber, D., Smear, M.C., Demers, M., and Kleinfeld, D. (2013). Hierarchy of orofacial rhythms revealed through whisking and breathing. Nature *497*, 205–210.

Morris, N.P., Fyffe, R.E.W., and Robertson, B. (2004). Characterisation of hyperpolarization-activated currents (Ih) in the medial septum/diagonal band complex in the mouse. Brain Res. *1006*, 74–86.

Müller, C., and Remy, S. (2018). Septo–hippocampal interaction. Cell Tissue Res. *373*, 565–575.

Mysin, I.E., Kitchigina, V.F., and Kazanovich, Y. (2015). Modeling synchronous theta activity in the medial septum: key role of local communications between different cell populations. J. Comput. Neurosci. *39*, 1–16.

Nicola, W., and Clopath, C. (2019). A diversity of interneurons and Hebbian plasticity facilitate rapid compressible learning in the hippocampus. Nat. Neurosci. *22*, 1168–1181.

O'Keefe, J., and Recce, M.L. (1993). Phase Relationship between Hippocampal Place Units and the EEG Theta Rhythm. Hippocampus *3*, 317–330.

Oddie, S.D., and Bland, B.H. (1998). Hippocampal formation theta activity and movement selection. Neurosci. Biobehav. Rev. *22*, 221–231.

Oddie, S.D., Stefanek, W., Kirk, I.J., and Bland, B.H. (1996). Intraseptal procaine abolishes hypothalamic stimulation-induced wheel-running and hippocampal theta field activity in rats. J. Neurosci. *16*, 1948–1956.

Oliveira, H.M., and Melo, L.V. (2015). Huygens synchronization of two clocks. Sci. Rep. *5*, 11548–11612.

Pachitariu, M., Steinmetz, N., Kadir, S., Carandini, M., and Harris, K.D. (2016). Kilosort: realtime spike-sorting for extracellular electrophysiology with hundreds of channels. Preprint at bioRxiv. https://doi.org/10.1101/061481.

Pan, W.-X., and McNaughton, N. (2002). The role of the medial supramammillary nucleus in the control of hippocampal theta activity and behaviour in rats. Eur. J. Neurosci. *16*, 1797–1809.

Paxinos, G., Franklin, K.B.J., and Franklin, K.B.J. (2001). The Mouse Brain in Stereotaxic Coordinates (Academic Press).

Payne, H.L., Lynch, G.F., and Aronov, D. (2021). Neural representations of space in the hippocampus of a food-caching bird. Science *373*, 343–348.

Petsche, H., Stumpf, C., and Gogolak, G. (1962). The significance of the rabbit's septum as a relay station between the midbrain and the hippocampus I. The control of hippocampus arousal activity by the septum cells. Electroencephalogr. Clin. Neurophysiol. *14*, 202–211.

Peña Ramirez, J., Fey, R.H.B., Aihara, K., and Nijmeijer, H. (2014). An improved model for the classical Huygens ' experiment on synchronization of pendulum clocks. J. Sound Vib. *333*, 7248–7266.

Ramirez, J.P., Olvera, L.A., Nijmeijer, H., and Alvarez, J. (2016). The sympathy of two pendulum clocks: beyond Huygens' observations. Sci. Rep. *6*, 1–16.

Ranade, S., Hangya, B., and Kepecs, A. (2013). Multiple modes of phase locking between sniffing and whisking during active exploration. J. Neurosci. *33*, 8250–8256.

Robinson, J., Manseau, F., Ducharme, G., Amilhon, B., Vigneault, E., El Mestikawy, S., and Williams, S. (2016). Optogenetic activation of septal glutamatergic neurons drive hippocampal theta rhythms. J. Neurosci. *36*, 3016–3023.

Rosenblum, M., Pikovsky, A., Kurths, J., Schäfer, C., and Tass, P.A. (2001). Phase synchronization: from theory to data analysis. Handb. Biol. Phys. *4*, 279–321.

Rosenblum, M.G., Pikovsky, A.S., and Kurths, J. (1996). Phase synchronization of chaotic oscillators. Phys. Rev. Lett. *76*, 1804–1807.

Rossant, C., Kadir, S.N., Goodman, D.F.M., Schulman, J., Hunter, M.L.D., Saleem, A.B., Grosmark, A., Belluscio, M., Denfield, G.H., Ecker, A.S., et al. (2016). Spike sorting for large, dense electrode arrays. Nat. Neurosci. *19*, 634–641.

Rutishauser, U., Ross, I.B., Mamelak, A.N., and Schuman, E.M. (2010). Human memory strength is predicted by theta-frequency phase-locking of single neurons. Nature *464*, 903–907.

Semba, K., and Komisaruk, B.R. (1984). Neural substrates of two different rhythmical vibrissal movements in the rat. Neuroscience *12*, 761–774.

Simon, A.P., Poindessous-Jazat, F., Dutar, P., Epelbaum, J., and Bassant, M.H. (2006). Firing properties of anatomically identified neurons in the medial septum of anesthetized and unanesthetized restrained rats. J. Neurosci. *26*, 9038–9046.

Smythe, J.W., Colom, L.V., and Bland, B.H. (1992). The extrinsic modulation of hippocampal theta depends on the coactivation of cholinergic and GABA-ergic medial septal inputs. Neurosci. Biobehav. Rev. *16*, 289–308.

Sotty, F., Danik, M., Manseau, F., Laplante, F., Quirion, R., and Williams, S. (2003). Distinct electrophysiological properties of glutamatergic, cholinergic and GABAergic rat septohippocampal neurons: novel implications for hippocampal rhythmicity. J. Physiol. *551*, 927–943.

Stewart, M., and Fox, S.E. (1989). Two populations of rhythmically bursting neurons in rat medial septum are revealed by atropine. J. Neurophysiol. *61*, 982–993.

Széll, A., Martínez-Bellver, S., Hegedüs, P., and Hangya, B. (2020). OPETH: open source solution for real-time peri-event time histogram based on open Ephys. Front. Neuroinf. *14*, 21.

Szőnyi, A., Sos, K.E., Nyilas, R., Schlingloff, D., Domonkos, A., Takács, V.T., Pósfai, B., Hegedüs, P., Priestley, J.B., Gundlach, A.L., et al. (2019). Brainstem nucleus incertus controls contextual memory formation. Science *364*, eaaw0445.

Teitelbaum, H., Lee, J.F., and Johannessen, J.N. (1975). Behaviorally evoked hippocampal theta waves: a cholinergic response. Science *188*, 1114–1116.

Tokuda, K., Katori, Y., and Aihara, K. (2019). Chaotic dynamics as a mechanism of rapid transition of hippocampal local field activity between theta and non-theta states. Chaos *29*, 113115.

Tóth, K., Borhegyi, Z., and Freund, T.F. (1993). Postsynaptic targets of GABAergic hippocampal neurons in the medial septum-diagonal band of Broca complex. J. Neurosci. *13*, 3712–3724.

Trenk, A., Walczak, M., Szlaga, A., Pradel, K., Blasiak, A., and Blasiak, T. (2022). Bidirectional communication between the pontine nucleus incertus and the medial septum is carried out by electrophysiologically-distinct neuronal populations. J. Neurosci. *42*, 2234–2252.

Tsanov, M. (2015). Septo-hippocampal signal processing: breaking the code. Prog. Brain Res. *219*, 103–120.

Tsanov, M., Chah, E., Reilly, R., and O'Mara, S.M. (2014). Respiratory cycle entrainment of septal neurons mediates the fast coupling of sniffing rate and hippocampal theta rhythm. Eur. J. Neurosci. *39*, 957–974.

Ujfalussy, B., and Kiss, T. (2006). How do glutamatergic and GABAergic cells contribute to synchronization in the medial septum? J. Comput. Neurosci. *21*, 343–357.

Umbriaco, D., Watkins, K.C., Descarries, L., Cozzari, C., and Hartman, B.K. (1994). Ultrastructural and morphometric features of the acetylcholine innervation in adult rat parietal cortex: an electron microscopic study in serial sections. J. Comp. Neurol. *348*, 351–373.

Unal, G., Joshi, A., Viney, T.J., Kis, V., and Somogyi, P. (2015). Synaptic targets of medial septal projections in the Hippocampus and extrahippocampal cortices of the mouse. J. Neurosci. *35*, 15812–15826.

Vandecasteele, M., Varga, V., Berényi, A., Papp, E., Barthó, P., Venance, L., Freund, T.F., and Buzsáki, G. (2014). Optogenetic activation of septal cholinergic neurons suppresses sharp wave ripples and enhances theta oscillations in the hippocampus. Proc. Natl. Acad. Sci. USA *111*, 13535–13540.

Varga, V., Hangya, B., Kránitz, K., Ludányi, A., Zemankovics, R., Katona, I., Shigemoto, R., Freund, T.F., and Borhegyi, Z. (2008). The presence of pacemaker HCN channels identifies theta rhythmic GABAergic neurons in the medial septum. J. Physiol. *586*, 3893–3915.

Vertes, R.P., and Kocsis, B. (1997). Brainstem-diencephalo-septohippocampal systems controlling the theta rhythm of the hippocampus. Neuroscience *81*, 893–926.

Viney, T.J., Salib, M., Joshi, A., Unal, G., Berry, N., and Somogyi, P. (2018). Shared rhythmic subcortical GABAergic input to the entorhinal cortex and presubiculum. Elife *7*, 1–35.

Wang, X.-J. (2002). Pacemaker neurons for the theta rhythm and their synchronization in the septohippocampal reciprocal loop. J. Neurophysiol. *87*, 889–900.

Wikenheiser, A.M., and Redish, A.D. (2013). The balance of forward and backward hippocampal sequences shifts across behavioral states. Hippocampus *23*, 22–29.

Willms, A.R., Kitanov, P.M., and Langford, W.F. (2017). Huygens' clocks revisited. R. Soc. Open Sci. *4*, 170777.

Winterer, J., Lukacsovich, D., Que, L., Sartori, A.M., Luo, W., and Földy, C. (2019). Single-cell RNA-Seq characterization of anatomically identified OLM interneurons in different transgenic mouse lines. Eur. J. Neurosci. *50*, 3750–3771.

Wolansky, T., Clement, E.A., Peters, S.R., Palczak, M.A., and Dickson, C.T. (2006). Hippocampal slow oscillation: a novel EEG state and its coordination with ongoing neocortical activity. J. Neurosci. *26*, 6213–6229.

Xu, C., Datta, S., Wu, M., and Alreja, M. (2004). Hippocampal theta rhythm is reduced by suppression of the H-current in septohippocampal GABAergic neurons. Eur. J. Neurosci. *19*, 2299–2309.

Yang, C., McKenna, J.T., Zant, J.C., Winston, S., Basheer, R., and Brown, R.E. (2014). Cholinergic neurons excite cortically projecting basal forebrain GABAergic neurons. J. Neurosci. *34*, 2832–2844.

Yang, C., Thankachan, S., McCarley, R.W., and Brown, R.E. (2017). The menagerie of the basal forebrain: how many (neural) species are there, what do they look like, how do they behave and who talks to whom? Curr. Opin. Neurobiol. *44*, 159–166.

Yoder, R.M., and Pang, K.C.H. (2005). Involvement of GABAergic and cholinergic medial septal neurons in hippocampal theta rhythm. Hippocampus *15*, 381–392.

Zaborszky, L., Pang, K., Somogyi, J., Nadasdy, Z., and Kallo, I. (1999). The basal forebrain corticopetal system revisited. Ann. N. Y. Acad. Sci. *877*, 339–367.

Zaborszky, L., van den Pol, A., and Gyengesi, E. (2012). The basal forebrain cholinergic projection system in mice. In The Mouse Nervous System, C. Watson, G. Paxinos, and L. Puelles, eds. (Elsevier), pp. 684–718.

Zemankovics, R., Káli, S., Paulsen, O., Freund, T.F., and Hájos, N. (2010). Differences in subthreshold resonance of hippocampal pyramidal cells and interneurons: the role of h-current and passive membrane characteristics. J. Physiol. *588*, 2109–2132.

Zou, X., Coyle, D., Wong-Lin, K., and Maguire, L. (2011). Computational study of Hippocampal-septal theta rhythm changes due to Beta-Amyloid-Altered ionic channels. PLoS One *6*, e21579.

Zutshi, I., Brandon, M.P., Fu, M.L., Donegan, M.L., Leutgeb, J.K., and Leutgeb, S. (2018). Hippocampal neural circuits respond to optogenetic pacing of theta frequencies by generating accelerated oscillation frequencies. Curr. Biol. *28*, 1179–1188.e3.

STAR★METHODS

KEY RESOURCES TABLE

REAGENT or RESOURCE	SOURCE	IDENTIFIER
Antibodies		
Primary antibody against PV	https://www.swant.com	PV 27
Primary antibody against Cre recombinase	https://www.biolegend.com	Cat#908002
Primary antibody against GFP	https://www.thermofisher.com	Cat#A10262
Primary antibody against choline-acetyltransferase	Umbriaco et al. (1994)	ChAT-17
Secondary antibody solution containing Alexa 488 conjugated goat anti-chicken	https://www.thermofisher.com	Cat#A11039
Secondary antibody solution containing Alexa 594 conjugated donkey anti-rabbit	https://www.jacksonimmuno.com	Cat#711585152
Secondary antibody solution containing Alexa 647 conjugated donkey anti-rabbit	https://www.jacksonimmuno.com	Cat#711605152
Bacterial and virus strains		
pAAV-EF1a-double floxed-hChR2(H134R)-EYFP-WPRE-HGHpA	https://www.addgene.org	Cat#20298
pAAV-Ef1a-DIO SwiChRca-TS-EYFP	https://www.addgene.org	Cat#55631
Chemicals, peptides, and recombinant proteins		
Urethane	https://vetcentre.com/	N/A
Fluorescent dye (1,1-Dioctadecyl-3,3,3′,3′-Tetramethylindocarbocyanine Perchlorate, DiI)	https://www.thermofisher.com	Cat#D282
Isoflurane	https://vetcentre.com/	N/A
Ketamine	https://vetcentre.com/	N/A
Xylazine	https://vetcentre.com/	N/A
Ringer's lactate solution	Local pharmacy	N/A
Betadine	Local pharmacy	N/A
Lidocaine	Local pharmacy	N/A
OptiBond XTR	https://www.kerrdental.com	N/A
Buprenorphine	http://www.richter-pharma.com/	N/A
Artificial dura	www.cambridgeneurotech.com	N/A
Eye ointment	https://www.laboratoires-thea.com	N/A
Neomycin	Local pharmacy	N/A
Paraformaldehyde	https://taab.co.uk/	Cat#P001
Xylene	Sigma-Aldrich	Cat#XX0020
DePex mounting medium	https://www.serva.de/	Cat#18243
Aqua-Poly/Mount mounting medium	https://www.polysciences.com	Cat#18606
Experimental models: Organisms/strains		
Wild type mice (C57BL/6)	https://www.jax.org/	Cat#000664
Wistar rats	https://rgd.mcw.edu/rgdweb/report/strain/main.html?id=13508588	RGD_13508588
Sst-IRES-Cre mice (C57BL/6J)	https://www.jax.org/	Cat#028864
PV-IRES-Cre mice (FVB/AntFx)	https://www.jax.org/	Cat#008069
VGAT-IRES-Cre mice (Bl6Fx)	https://www.jax.org/	Cat#016962
Vglut2-IRES-Cre (C57BL/6J)	https://www.jax.org/	Cat#028863
Software and algorithms		
OPETH	https://github.com/hangyabalazs/opeth	SCR_018022
MATLAB 2016a	https://mathworks.com	R2016a
MATLAB 2020a	https://mathworks.com	R2020a
Klustakwik spike sorting software	http://github.com/klusta-team	SCR_014480

(*Continued on next page*)

Continued

REAGENT or RESOURCE	SOURCE	IDENTIFIER
Kilosort spike sorting software	https://github.com/MouseLand/Kilosort	SCR_016422
Phy GUI	https://github.com/cortex-lab/phy	N/A
NEURON simulation environment	https://www.neuron.yale.edu/neuron/download	SCR_005393
Matlab and NEURON codes for analysis and modeling	https://github.com/hangyabalazs/ms_sync_analysis	https://doi.org/10.5281/zenodo.6798310
Matlab codes for optical tagging	https://github.com/hangyabalazs/CellBase	N/A
Matlab codes for circular statistics	https://github.com/hangyabalazs/Hangya-Matlab-code	N/A
Other		
Heating pad for rats	https://superte.ch	Cat#AHP-2
Heating pad for mice	https://superte.ch	Cat#AHP-1
Dual Ultra Precise Small Animal Stereotaxic Instrument	https://kopfinstruments.com	Cat#962
Robot Stereotaxic instrument – StereoDrive (Motorized manipulator)	https://neurostar.de	N/A
32 channel linear silicon probe	https://www.neuronexus.com	Cat#A1x32-6mm-50-177
32-channels, 4-shank Buzsáki-type acute silicon probe	https://www.neuronexus.com	Cat#Buzsaki32-A32
32-channels, 4-shank Buzsáki-type chronic silicon probe	https://www.neuronexus.com	Cat#Buzsaki32-CM32
128-channels single-shank high-density silicon probe	Fiáth et al. (2018)	N/A
DAQ module for acute rat recordings	https://www.ni.com/	Cat#PCI-6259
DAQ module for chronic mouse recordings	http://www.amplipex.com	Cat#KJE-1001
Open Ephys Acquisition Board for acute mouse recordings	https://open-ephys.org	N/A
RHD2000 Recording System	https://intantech.com	N/A
RHD USB Interface Board	https://intantech.com	Part#3100
RHD 32-channel headstage	https://intantech.com	Part#C3314
RHD 64-channel headstage	https://intantech.com	Part#C3315
RHD 6-ft (1.8 m) standard SPI interface cable	https://intantech.com	Part#3206
Optic fiber (200 μm core)	https://www.thorlabs.com	Cat#FT200UMT
Leica VT1200 vibratome	https://www.leicabiosystems.com	SCR_018453
Leica Light microscope	https://www.leica-microsystems.com	Cat#DM2500
Leica illumination force	https://www.leica-microsystems.com	Cat#SFL4000
Olympus Digital Camera (DP70)	https://americanlaboratorytrading.com	Cat#22272
Olympus Digital Camera (DP73)	https://biocompare.com	Cat#DP73

RESOURCE AVAILABILITY

Lead contact

Further information and requests for resources should be directed to and will be fulfilled by the lead contact, Balázs Hangya (hangya.balazs@koki.hu).

Materials availability

This study did not generate new unique reagents.

Data and code availability

- Electrophysiology data reported in this paper will be shared by the lead contact upon reasonable request.
- All original code has been deposited at Zenodo and is publicly available as of the date of publication. DOIs are listed in the key resources table. The GitHub repository of the code is available at https://github.com/hangyabalazs/ms_sync_analysis.
- Any additional information required to reanalyze the data reported in this paper is available from the lead contact upon request.

EXPERIMENTAL MODEL AND SUBJECT DETAILS

Wild type C57BL/6 mice (N = 11; 27.4 g ± 4.9 g, 7 males) were used for acute mouse recordings; Wistar rats (N = 7; 200–400 g; males) were used for acute rat recordings; Sst-IRES-Cre mice with C57BL/6J genetic background (N = 4; 28–30 g; males) were used for the chronic mouse recordings; 4 PV-IRES-Cre males (genetic background FVB/AntFx), 4 VGAT-IRES-Cre males (genetic background Bl6Fx) and 5 Vglut2-IRES-Cre male and female mice (genetic background C57BL/6J) were used for optogenetic tagging. All experiments were performed according to the EC Council Directive of September 22, 2010 (2010/63/EU), with all procedures being reviewed and approved by the Animal Care Committee of the Research Centre for Natural Sciences or the Institutional Animal Care and Use Committee of the Institute of Experimental Medicine and by the National Food Chain Safety Office of Hungary.

METHOD DETAILS

Surgery and electrophysiological recordings

Acute rat recordings

Rats were anesthetized with an intraperitoneal injection of urethane (40%; dose, 0.37 mL/100 g). A homeothermic heating pad connected to a rectal probe held body temperature constant (36°C). The top of the head was shaved, the rat was placed in a stereotaxic frame (David Kopf Instruments, Tujunga, US), the skin and the connective tissue above the calvaria were removed and the skull was cleared. A craniotomy was opened over the medial septum and another one over the right hippocampus. A 32-channels linear silicon probe (A1x32-6mm-50-177; NeuroNexus Technologies, Ann Arbor, US) was lowered into the right CA1 (anterior-posterior (AP): −4.5 mm and medial-lateral (ML): 3 mm) and a 32-channels Buzsaki-type silicon probe (Buzsaki32; NeuroNexus Technologies, Ann Arbor, US) was lowered to the top of the medial septum (AP: 0.4 mm and ML: −1.6 mm, 15° angle in the coronal plane). The silicon probes were dipped in red fluorescent dye (1,1′-Dioctadecyl-3,3,3′,3′-Tetramethylindocarbocyanine Perchlorate, DiI) before insertion to aid later histological reconstruction. The ground electrode was secured in the nuchal muscles.

Neural signals were acquired by two National Instruments PCI-6259 cards, amplified (2000 times) and digitized at 20 kHz. After allowing 30 min for the brain tissue around the electrode to stabilize, a 30-min recording was conducted. Theta oscillation was induced by temporarily placing an insulated clip on the tail for 1 min, repeated 3 times. After the recording, the septal probe was moved 100 μm ventrally, and the procedure was repeated. Recording sessions were conducted as long as theta oscillation could be detected via audio feedback; correct positioning of the probe in the MS was later confirmed by both histological reconstruction (Figure S1A) and the presence of theta-rhythmic neurons in the recordings.

Acute mouse recordings

Implantations were performed under general anesthesia. Mice received an intraperitoneal injection of urethane (∼1.3 mg/g). If necessary, an additional dose of urethane was injected intramuscularly to maintain the depth of the anesthesia during surgery and recordings. The body temperature of the animals was maintained during the experiments at 37°C using a thermostatically regulated heating pad (Supertech, Pécs, Hungary). Mice were placed in a stereotaxic frame (David Kopf Instruments, Tujunga, US), then the skin and the connective tissue were removed from the top of the skull. Next, two small circular craniotomies (1 mm diameter) were made on the skull with a dental drill, one for the recording probe inserted into the MS and one for the probe inserted into the hippocampus (CA1). Stereotaxic coordinates were used to determine the septal and hippocampal locations for recording (MS, AP: 0.6 mm and ML: 0.5 mm; CA1, AP: −2.2 mm and ML: 1.5 mm from the Bregma) (Paxinos et al., 2001). For post-mortem histological verification of the recording location of the probes, the backside of the silicon shank was coated with red-fluorescent dye (DiI, D-282, ∼10% in ethanol, Thermo Fischer Scientific, Waltham, US) before insertion (DiCarlo et al., 1996; Fiáth et al., 2019). The septal probe was a high-density single-shank silicon probe with 128 square-shaped recording sites (Fiáth et al., 2018). The 8-mm-long shank of the probe had a cross-section of 100 μm × 50 μm (width × thickness). The closely spaced recording sites (20 μm × 20 μm) were arranged in a 32 × 4 array with 2.5 μm spacing between the edge of electrodes. The probe was mounted on a motorized micromanipulator (Robot Stereotaxic, Neurostar, Tübingen, Germany) and inserted at a slow speed (2 μm/s) into the brain tissue to increase the single unit yield by decreasing the tissue damage (Fiáth et al., 2019). The probe was tilted at an angle of 8° from vertical in the coronal plane to have better access to the medial septum. Since the effective vertical recording area of the probe (∼0.7 mm) was smaller than the dorsoventral extent of the MS (∼1.5 mm), to obtain the spiking activity of as many septal neurons as possible, recordings were performed in three, slightly overlapping (∼0.2 mm) depths. (Unit clusters recorded twice due this overlap, based on waveform similarity and autocorrelograms, were counted only once, see below.) The hippocampal probe was a linear silicon probe with 32 recording sites and with a shank thickness of 50 μm (A1x32-6mm-50-177, NeuroNexus Technologies, Ann Arbor, US). The recording sites of the device had a diameter of 15 μm and an interelectrode distance of 50 μm. The probe was attached to a manual micromanipulator, then inserted at a speed of ∼10 μm/s to a dorsoventral depth of 2 mm. The two recording probes were connected to an electrophysiological recording system (RHD2000, Intan Technologies, Los Angeles, CA, USA) equipped with 32-channel and 64-channel headstages.

Wideband brain electrical activity (0.1–7500 Hz) was recorded on 160 channels with 16-bit resolution and at 20 kHz/channel sampling rate. A stainless-steel wire inserted into the neck muscle of the animal served as the reference and ground electrode during

recordings. Room temperature physiological saline solution was regularly dropped into the craniotomy to prevent dehydration of the brain tissue. Recordings were conducted for 15 min each, consisting of 5 min baseline period, 5 min tail-pinch-induced theta oscillation, and 5 min recovery from stimulation.

Chronic mouse recordings

Sst-IRES-Cre male mice of C57BL/6J genetic background underwent bilateral injection of AAV2/5-Ef1a-DIO-ChR2-YFP-WPRE (N = 2) or AAV5-Ef1a-DIO-SwiChRca-TS-EYFP-WPRE (N = 2) into the dorsal hippocampi (coordinates: AP -2.1 and −2.5 mm and ML ±1.5 and 1.6 mm from Bregma with tip at DV -1.2 mm from brain surface; 2 × 150–200 nL on both sides) using standard surgery techniques. Silicon probes for multichannel electrophysiological recordings were implanted above the medial septum and into the dorsal hippocampus 40–83 days after the virus injection. The surgery was performed under isoflurane anesthesia induced by ketamine-xylazine (4:1) combination diluted 6× in Ringer's lactate solution (intraperitoneal injection, dose 0.01 mL/1 g body weight). Mice were head-fixed in a stereotaxic frame (David Kopf Instruments, Tujunga, US) and their body temperature and respiratory rate were continuously monitored. After local disinfection (Betadine) and analgesia (10% Lidocaine-spray), the cranium was exposed and cleaned for application of adhesive agent (OptiBond XTR, Kerr Corporation, Orange, US). Craniotomies were performed for stereotaxis-guided implantation of a 32-channels linear type and a 32-channels, 4-shank Buzsáki-type silicon probe into the dorsal hippocampus (coordinates: AP -2.5 mm and ML + 2 mm from Bregma with tip at DV -2.1 mm from brain surface) and above the medial septum (AP +0.9 mm and ML +0.9 mm, at an angle of 12°, and with tip at DV -2.8 mm from brain surface), respectively. Both probes were mounted on a custom-made, adjustable micro-drive. The probes were coated with red fluorescent DiI for later histological confirmation of the recording site. After the recovery from the surgery, the tip of the septal probe was lowered in steps of 75–150 micrometers per day to reach the zone of cells with theta-modulated firing pattern. Within this zone, the probe was advanced in steps of 45 micrometers per day as long as the theta-modulated firing pattern was still present. In case of SwiChR-transfected animals, each shank of the septal probe was equipped with an optical fiber (50 micrometers core diameter, 0.22 NA) with tip positioned 75–100 micrometers above the uppermost recording site and glued by optical adhesive. In case of ChR2-transfected animals, one optical fiber (105 micrometers core diameter, 0.22 NA) was implanted to illuminate the fimbria, independently from the septal silicon probe. In one animal, a Buzsáki-type silicon probe was implanted into the hippocampus, instead of the linear probe. In this case, the probe was advanced stepwise to reach the pyramidal layer of the dorsal hippocampus after the post-surgery recovery period. The craniotomies were sealed with artificial dura (Cambridge NeuroTech Ltd, Cambridge, UK). The probe-micro-drive assemblies were shielded by copper mesh preventing the contamination of the recordings by environmental electric noise. The mesh was covered by dental acrylate. Two stainless steel wires inserted above the cerebellum served as ground and reference for the electrophysiological recordings. Before finishing the surgery, Buprenorphine (dose: 0.045 μg/1 g body weight) was injected subcutaneously. Recordings were started after a one-week-long post-surgery recovery and habituation to connectorization.

The electrophysiological activity was registered by a multiplexing data acquisition system (KJE-1001, Amplipex Ltd, Szeged, Hungary) at 20 kHz sampling rate. The position of the animal was tracked by a marker-based, high speed (120 frame/s) motion capture system and reconstructed in 3D (Motive, OptiTrack, NaturalPoint Inc, Corvallis, US). Recordings were conducted both in the animals' home cage (dominated by sleep) and while mice were placed on a linear track (dominated by active movement). Home cage and linear track recordings were concatenated for data analysis to include sufficient amount of time spent in theta and non-theta states. Thus, the majority of theta segments originated from movement epochs, while non-theta segments represented both quiet wakefulness and sleep. As the main focus was on general oscillatory mechanisms, these states were not subdivided further. The septal probe was lowered 45 micrometers after the recordings each day, through a total of 8–35 days of recording.

Optogenetic manipulations were carried out separately. Only the control recordings were analyzed in the present study. The Sst-IRES-Cre mouse line and the above AAV constructs were used in a large number of studies without reporting adverse phenotypic changes, and results of these studies were interpreted as general for mice and not specific for the particular strain (Adler et al., 2019; Cummings and Clem, 2020; Kim et al., 2015; Kvitsiani et al., 2013; Viney et al., 2018). Therefore, we do not consider using this particular mouse line a significant limitation of our study.

Optogenetic tagging in mice

4 PV-IRES-Cre males (genetic background FVB/AntFx), 4 VGAT-IRES-Cre males (genetic background Bl6Fx) and 5 Vglut2-IRES-Cre males and females (genetic background C57BL/6J) were used to assess the neurochemical nature of MS cells; 2 PV-Cre (n = 17, 1), 2 VGAT-Cre (n = 17, 3) and 3 VGLUT2-Cre (n = 15, 9, 6) mice yielded tagged neurons (numbers in brackets). Mice were anesthetized with an i.p. injection of ketamine-xylazine (0.166 and 0.006 mg/kg, respectively). After shaving and disinfecting (Betadine) the scalp, local anesthetic was applied (Lidocaine). Animals were positioned in the stereotaxic frame and the eyes were protected with eye ointment (Laboratories Thea). After opening the skin, the skull was cleaned and the head of the animal was leveled using Bregma, Lambda and a pair of lateral points equidistant from the sagittal suture.

A trephine hole was drilled in order to access the MS with a 10° lateral angle (MS 10°, antero-posterior +0.90 mm, lateral, 0.90 mm). An adeno-associated virus vector allowing Cre-dependent expression of channelrhodopsin2 [AAV 2/5. EF1a.Dio.hChR2(H134R)-eYFP.WPRE.hGH] was injected into the MS at 3.95, 4.45 and 5.25 mm depth from skull surface (200 nL at each depth, 100 nL at 25 nL s^{-1} and 100 nL at 5 nL s^{-1}). After the viral injections, the skin was sutured and local antibiotics (Neomycin) and analgesics (Buprenorphine 0.1 mg kg-1, s.c.) were applied.

Around two weeks after the virus injection, the animals were anesthetized with an i.p. injection of 20% urethane (Sigma-Aldrich, 0.007 mL g^{-1} body weight). The depth of anesthesia was evaluated by pinching the paw, tail, or ear of the animal, and by checking

the ocular reflex. When no reflexes were elicited, the throat was shaved, and topical lidocaine was applied. A heating pad was used to keep constant body temperature of the animals. A tracheotomy was performed in order to sustain a constant airflow (Moldestad et al., 2009). The animals were placed in a stereotaxic frame and, after opening the skin and leveling the skull, a cranial window was made above the MS (silicon probe MS 10°, antero-posterior, +0.90 mm, lateral, 0.90 mm; optic fiber MS 5° contralateral, antero-posterior, +0.90 mm, lateral, −0.50 mm), the hippocampus (silicon probe HPC, antero-posterior, −2.20 mm, lateral, 1.50 mm) and two above the cerebellum for reference electrode placement. A Neuronexus A1x32-6mm-50-177-CM32 silicon probe was placed in the hippocampus at 2.20 mm depth from skull surface. A Neuronexus Buzsaki32-H32_21 mm probe was lowered to the dorsal boundary of the MS at a 10° lateral angle (3.95 mm from skull surface). Reference electrodes for both probes were placed in the cerebellum, and a ground electrode was placed in the spinotrapezius muscle. A 200 μm core optic fiber (Thorlabs) was lowered 500 μm above the shanks of the MS probe. The MS probe and the optic fiber were lowered in consecutive recordings (100 μm steps for the probe; 50 μm steps for the optic fiber), spanning the entire depth of the MS. Extracellular data were collected by the Open Ephys data acquisition system, digitized at 30 kS/s. Each recording session consisted of an optical tagging period of two minutes, followed by a baseline period of five minutes of spontaneous activity. Three consecutive repetitions of one-minute tail pinch induced theta activity followed by one-minute control recording were applied, finishing the recording session with another two-minute-long optical tagging period. For optimizing the probability of finding tagged cells, we used the Online Peri-Event Time Histogram (OPETH) Open Ephys compatible plugin that allowed us to visualize the direct effect of the optogenetic activation at the cell population level. OPETH (Széll et al., 2020) allowed us to reduce recording time by more efficient 'hunting' for light responsive neurons in the MS and to reduce light-triggered artifacts in our recordings, improving data quality and further analysis.

Histological verification of the recording location

To detect the tracks of the silicon probes in the brain tissue, we used a histological procedure similar to that described previously (Borhegyi et al., 2004; Fiáth et al., 2018, 2019). In brief, the animal was deeply anesthetized after the recordings, then transcardially perfused with physiological saline solution followed by a fixative solution containing 4% paraformaldehyde in 0.1 M phosphate buffer (PB, pH = 7.4). Next, the fixed brain was gently removed from the skull and stored at 4°C in the fixative solution until processed further. Histological processing started by cutting 60-μm-thick coronal sections with a vibratome (Leica VT1200, Leica Microsystems, Wetzlar, Germany). Then, the brain sections were washed in 0.1 M PB, mounted onto microscopic slides and air dried. To identify brain sections containing fluorescent marks of DiI corresponding to the probe track, the slides were examined under a light microscope (Leica DM2500, Leica Microsystems) equipped with a fluorescence LED illumination source (SFL4000, Leica; Zeiss, Oberkochen, Germany in case anesthetized rats) and with a digital camera (DP70 or DP73, Olympus, Tokyo, Japan). Relevant sections from the anesthetized mouse experiments were processed for cresyl violet (Nissl) staining, dehydrated in xylene and coverslipped with DePex (SERVA Electrophoresis, Heidelberg, Germany); sections from the anesthetized rat experiments were stained for choline-acetyltransferase (ChAT; mouse monoclonal anti-ChAT (Umbriaco et al., 1994)) to visualize the MS; no staining for sections from the awake mouse experiments was performed. Finally, to verify the recording location based on the stereotaxic mouse brain atlas (Paxinos et al., 2001), sections containing the track of the silicon probe were photographed under the microscope.

Immunostaining

To verify the specificity of the ChR2 expression in targeted neuronal types in the optogenetic tagging experiments, 3 animals from each mouse strain (PV-Cre, VGAT-Cre, VGLUT2-Cre) were sacrificed 2–3 weeks after virus injection into the MS (see details in the 'Optogenetic tagging in mice' section). First, animals were anesthetized with an intraperitoneal injection of ketamine-xylazine (0.166 and 0.006 mg/kg, respectively), followed by transcardial perfusion with saline for 2 min and 4% para-formaldehyde (PFA) for 20 min. After sectioning 50 μm thick slices of the brain tissue, sections containing the MS were washed in 0.1M phosphate buffer (PB) and tris-buffered saline (TBS), then incubated in blocking medium (1% human serum albumin + 0.1% Triton-X detergent) for 1 h. Then, sections derived from PV-Cre mice were incubated in primary antibody against PV (PV 27, Swant, Switzerland), while sections from VGLUT2- and VGAT-Cre mice were incubated in primary antibody against Cre recombinase (Biologend, USA, cat#908002, 1:500) in each case mixed with primary antibody against GFP (Thermofisher Scientific, USA, cat#A10262, 1:1000) in TBS at 4°C for two days. After an extensive wash in TBS, the sections were incubated in a secondary antibody solution containing Alexa 488 conjugated goat anti-chicken (Thermofisher Scientific, USA, Cat#A11039, 1:1000), Alexa 594 conjugated donkey anti-rabbit (Jackson ImmunoResearch Europe Ltd., UK, cat#711585152, 1:500) or Alexa 647 conjugated donkey anti-rabbit (Jackson ImmunoResearch Europe Ltd., UK, cat#711605152, 1:500) antibodies at 4°C overnight. Finally, sections were mounted on slides in aqua-Poly/Mount mounting medium (cat#18606, Polysciences, Inc., USA) and images were taken with a Nikon A1R confocal microscope.

QUANTIFICATION AND STATISTICAL ANALYSIS

All signal processing codes were implemented in MATLAB 2016a and 2020a (Mathworks, Natick, US).

Hippocampal state detection

Pyramidal layer was detected from linear silicon probe recordings based on the documented phase reversal of hippocampal theta oscillation below the pyramidal layer and verified based on histological reconstruction (Figure S1C) (Buzsáki, 2006; Buzsaki et al.,

1986; Green et al., 1960). Theta detection was performed on a single channel from the stratum radiatum (400 μm below the detected pyramidal layer in rats and 250 μm below the pyramidal layer in mice), since theta amplitude was largest in this layer, allowing the most robust detection (Buzsáki, 2002, 2006). In one chronically implanted mouse, a Buzsaki-type probe was used in the hippocampus; in this case, the deepest channel was used for LFP analysis, which appeared to be below the pyramidal layer based on theta phase reversal, thus providing phase values consistent with other recordings. The appropriate theta and delta frequency band boundaries were defined separately for the three different rodent models based on the Fourier spectra of the recordings (Figure 1F). Our observations confirmed known spectral differences between urethane-anesthetized and awake rodents (frequency boundaries in anesthetized rats, delta, 0.5–2.5 Hz; theta, 3–8 Hz; in anesthetized mice, delta, 0.5–2 Hz, theta, 2–8 Hz; in awake mice, delta, 0.5–4 Hz, theta, 5–10; in optogenetic experiments, frequency boundaries were optimized for each mouse individually). Raw LFP traces were resampled at 1 kHz and bandpass filtered in the theta and delta bands using the built-in finite impulse response filter (fir1.m) with zero-phase-lag filtering (built-in filtfilt.m function). The filtered traces were Hilbert-transformed and the instantaneous amplitude and phase values were calculated as the magnitude and phase of the complex Hilbert-transform. A simple artifact removal was performed on the theta/delta ratio by clamping values exceeding 10-fold difference. Next, the theta/delta amplitude ratio was smoothed with a moving average (window size, 5 s for anesthetized and 3 s for awake recordings; the difference in window size was due to the observed faster and more frequent state transitions in awake recordings). Theta segments were defined where the theta/delta ratio exceeded an empirically defined threshold, optimized for each dataset separately (1 for anesthetized mouse and rat recordings, 2 for awake mouse recordings and 1.5 in the optogenetic experiments); all other segments were defined as non-theta. Brief interruptions of theta or non-theta segments were not considered state switches (<5 s in anesthetized and <3 s in awake recordings; the difference was due to the observed faster and more frequent state transitions in awake recordings). In some optogenetic tagging experiments (n = 8 recordings), only a part of the recording was analyzed due to electrical artifacts in other segments.

Spike sorting of septal neurons

The mouse MS recordings were fed to the Kilosort software (Pachitariu et al., 2016). Clustering was initialized with the desired number of clusters set to twice the number of channels. The Kilosort output was curated manually in the Phy template-gui graphical user interface module. We examined any potential violations of the refractory periods, slow electrode drifts, spatial distributions of action potential (AP) energies among neighboring channels, AP shapes and amplitudes and the principal components (PC) of the AP shapes. In case of noisy autocorrelograms and multiple subclusters in the PC space, we considered manual splitting of the automatically assigned cluster. The high similarity of clusters as well as lack of co-firing ('mutual refractoriness') in crosscorrelograms could imply that two automatically determined clusters belonged to the same neuron, in which case the clusters were merged. Finally, we calculated objective cluster quality measures based on the interspike interval histograms and cluster isolation distances, to verify putative single neuron clusters. Kilosort execution time was reduced by running on an Nvidia Geforce GTX 1080 graphic card with the Matlab Parallel Computing Toolbox. The anaesthetized rat recordings were clustered automatically in KlustaKwik (Rossant et al., 2016) (available at http://github.com/klusta-team) and curated manually based on auto- and crosscorrelograms similar to the mouse recordings, as described previously (Bartho et al., 2004).

In case of acute mouse recordings, the size of the probe resulted in potential overlap between subsequent recordings. Therefore, putative overlapping units were excluded by using a semi-automated method (Figure S1D). First, we calculated average spike waveforms for all clusters by averaging ±2 ms windows around all individual spike times separately for all channels. Average waveforms were aligned to zero on each channel by subtracting their mean (across time). Next, the integral of the absolute value of mean waveforms were taken for all channels as a measure of channel magnitudes. Overlapping channels from consecutive recordings were 500 μm from each other, resulting in an 88-channel displacement of the overlapping clusters due to the arrangement of the probe (4 channels in a row with 22.5 μm longitudinal separation). If two clusters shared at least 9 out of their 16 top amplitude channels, we considered them duplication candidates. Mean waveform profiles and autocorrelations were compared visually by an expert experimenter for all pairs that had been marked as duplication candidates for final decision.

Rhythmicity indices of MS neurons

Theta- and delta-rhythmicity of MS neurons was judged based on rhythmicity indices derived from autocorrelograms. First, autocorrelation of the spike train was computed in a ±3 s window at 1 ms resolution; the central peak corresponding to the total spike number was removed and the autocorrelogram was smoothed by a 20-ms moving average and normalized to an integral of 1. Next, theta and delta peaks were determined between time lags corresponding to theta and delta frequency bands. 'Peak values' were averaged from the autocorrelograms in the ±20 ms neighborhoods of the peaks. 'Baseline values' were averaged from the ±20 ms neighborhoods around the lags corresponding to half and one and a half times the peak location (assumed troughs). Finally, the difference between the peak and baseline values was normalized to the larger of the two, yielding a Theta Index and a Delta Index between −1 and 1:

$$\text{Rhythmicity Index} = (\text{peak} - \text{baseline})/\max(\text{peak}, \text{baseline})$$

Rhythmicity indices were calculated separately for hippocampal theta and non-theta segments (Figures S2A and S2B). Cells with insufficient number of spikes (<2 spikes/autocorrelogram bin on average) were excluded from later analysis.

To assess statistical significance of rhythmicity in the theta and delta frequency bands, we simulated a dataset of neurons exhibiting spiking generated by a Poisson-process. We determined the λ parameter of the Poisson-process individually for each simulated cell so that they matched the firing rate of an actual MS neuron. Rhythmicity Index was calculated for the simulated neurons using the same procedure as for the biological recordings, then Rhythmicity Index thresholds were determined corresponding to $p < 0.05$ significance levels based on this bootstrap null distribution. If both Rhythmicity Indices exceeded the threshold, rhythmicity was determined by the larger of the two Rhythmicity Indices (normalized to their respective thresholds) (Figures S2C and S2D).

Theta-burst index

To differentiate between tonically active and putative pacemaker neurons, a Theta-burst Index (TBI) was introduced, quantifying the characteristic long theta-bursts putative pacemakers fire during individual theta cycles (Borhegyi et al., 2004; Varga et al., 2008). Average autocorrelograms between lags corresponding to a pre-defined window spanning the intraburst interspike intervals (anesthetized rats, 20–40 ms; anesthetized mice, 20–50 ms and 20–40 ms in optogenetic tagging experiments, see below; freely moving mice, 10–30 ms) were normalized to the average autocorrelation, similar to the Rhythmicity Indices, providing a TBI between −1 and 1. The above windows were determined based on variations of theta frequencies across datasets. Using a traditional 20–50 ms window for all datasets altered the classification of only a few neurons and did not change the main results. Tonically active neurons were defined as those having a TBI <0 (Figures S10A–S10D).

Analysis of phase-coupling

Selected LFP channels were filtered in the theta and delta frequency bands, as described above. The filtered signals were Hilbert-transformed, and the instantaneous phase values of the analytical signal were computed. Spike phases were determined by taking the instantaneous phase values corresponding to the spike times. To quantify phase-locking, mean phase and mean resultant length (measure of phase-locking strength) were calculated as the angle and magnitude of the first trigonometric moment of spike phases. Phase value distributions for individual neurons were visualized as phase histograms, and distributions over groups of neurons were visualized as polar plots, in which each neuron was represented by a vector pointing to its mean phase, with a length corresponding to its mean resultant length and color corresponding to its firing rate in greyscale.

Crosscorrelation

Crosscorrelations of simultaneously recorded pairs of MS neurons were calculated in ±3 s windows at 1 ms resolution, smoothed by a 20-ms moving average and normalized to an integral of 1. Crosscorrelograms were aligned to their peaks between ±1.5 s and averaged both within and across rhythmicity groups.

We quantified crosscorrelation strength by taking the squared integral of mean-subtracted individual crosscorrelograms and statistically compared crosscorrelation strength within and across the major rhythmicity groups in urethane-anesthetized rats.

Pacemaker synchronization

To test how putative pacemakers synchronize during theta segments, we calculated a number of parameters and performed comparisons during theta vs. non-theta episodes. (i) Firing rates were calculated as the ratio of spike number and total segment length. (ii) Rhythmicity frequencies were estimated from the peak locations of autocorrelograms, smoothed by a 20-ms moving average (see above). (iii) Theta-bursts were defined by interspike intervals falling in the theta-burst windows defined for the TBI (see above) and average intraburst interspike intervals were computed. (iv) To estimate theta cycle skipping, an event vector was built from first spikes of bursts and single spikes. Theta cycle length was calculated for each neuron based on its rhythmicity frequency (see above), and an edge vector was defined with uniform spacing according to theta cycle length. Events were binned by the edge vector and skipping was quantified as the ratio of empty to all cycles. Although the edge vector was only based on neuronal rhythmicity and thus could not account for individual cycle variabilities, this approach likely provides a good approximation of theta cycle skipping. Since we aimed to define this metric for both theta and non-theta segments, we had to move away from LFP-based cycle definitions for this analysis. (v) Difference in rhythmicity frequency was calculated between concurrently recorded pairs of putative pacemaker neurons and normalized to the greater of the two frequencies. (vi) We compared the standard deviation of pacemaker frequency distributions during theta and non-theta segments. First, we took the difference of rhythmicity frequencies of individual putative pacemaker neurons and mean rhythmicity frequency of the recording session, to remove the variance stemming from differences in the exact theta frequency in each model (see Figure 1). We compared the absolute deviation from the mean across these normalized distributions by Wilcoxon signed-rank test.

Wavelet coherence

Spike trains of the pacemaker neurons were convolved with a 50 ms Gaussian kernel to obtain a continuous signals. Magnitude-squared wavelet coherence spectrograms of the signals were calculated around non-theta to theta transitions, where each of the segments were at least 7 s long, using the analytic Morlet wavelet.

Data analysis of the optogenetic tagging experiments

Hippocampal state detection was performed on a single channel from the stratum radiatum (~250 μm below the pyramidal layer). The LFP signal was resampled at 1 kHz. Theta and delta frequency band boundaries were determined based on spectral components (theta: 1.5–4 Hz; 1–4 and 1.5–6 Hz in 1–1 mice; delta: 0.5–1.5 Hz, 0.5–1 Hz in one mouse). Theta/delta amplitude ratio was smoothed with a 5 s window and a 1.5 threshold (1 in one mouse) was applied for theta detection. Additionally, theta amplitude was required to surpass the median value of the theta-filtered signal. Less than 5-second-long epochs were not considered as state transitions. In 8 recordings, only a part of the recording was analyzed due to electrical artifacts in other segments.

MS units were sorted in Kilosort as described above. MS neurons that had sufficient number of spikes (>500 in total and median interspike interval <500 ms) were further analyzed. Note that these spike number criteria were less stringent compared to other datasets (see above) due to generally shorter recordings. Significant photoactivation ($p < 0.01$) was determined using the stimulus-associated spike latency test (SALT) based on specific spike timing after light flashes (Kvitsiani et al., 2013). After removing the phototagging segments from the recordings, rhythmicity indices and TBI (with [20,40] ms window) were computed as described above.

Analysis of photostimulation impact

To assess the effect of phtostimulation of MS glutamatergic neurons in VGLUT2-Cre mice on CA1 oscillations, spectral power was calculated from the wavelet spectrograms for delta and theta frequency bands by averaging across within-band frequencies. Spectral power values were then averaged for the first 10 s of photostimulation and the first 10 s after photostimulation, and the theta-delta power ratio was visualized and compared statistically using Wilcoxon signed-rank test.

MS pacemaker neuron model

The model was implemented in NEURON (Carnevale and Hines, 2006). We used a fixed time step of 0.025 ms. The neuron network parameters were defined, and the simulation results were processed by Matlab scripts.

We based our model on a fast spiking single compartment neuron model by Golomb et al. (Golomb et al., 2007). This choice was motivated by the model's simplicity and its desirable firing properties, capable of high-frequency tonic firing but also rhythmic bursting, characteristic of MS pacemaker neurons. This model included a transient sodium channel (nas) that is necessary for action potential generation, the delayed rectifier potassium channel (kdr) for repolarization during fast spiking and the slowly inactivating d-type potassium channel (kd) for bursting behavior through controlling the duration of the after-hyperpolarization. We added the HCN-channel (hcn) responsible for the hyperpolarization-activated H-current, which was reported to be responsible for sag responses in MS neurons (Kocsis and Li, 2004; Morris et al., 2004; Sotty et al., 2003; Varga et al., 2008; Xu et al., 2004). We could reproduce this sag response by including the H-current (Figure 5C); we note, however, that the presence of the H-current was not a prerequisite of rhythmic bursting in the present model. Further electrophysiology data and modeling should clarify the exact channel properties of MS pacemaker neurons. Nevertheless, the present model was capable of reproducing the characteristic rhythmic bursting of MS pacemaker neurons in the range of biologically plausible rhythmicity frequencies upon current injection, serving the modeling purposes of this study.

Potential change across the cell membrane was described by the following equation.

$$C\frac{dV}{dt} = -I_{Na}(V,m,h) - I_{Kdr}(V,n) - I_{Kd}(V,a,b) - I_H(V,x) - g_L(V - V_L) + I_{app}$$

where $C = 1\mu F/cm^2$ is the membrane capacitance, $g_L = 0.1$ mS/cm^2 is the passive conductance, $V_L = -60$ mV is the equilibrium potential for leakage and I_{app} is the injected current in μA/cm^2. The lower g_L and higher V_L compared to the Golomb-model ($g_L = 0.25$ mS/cm^2, $V_L = -70$ mV) were introduced to facilitate the characteristic sag response mediated by the HCN channels. The total surface of the neuron was 5000 μm^2. The applied point source input current amplitude varied between 40 and 80 pA in the network simulations (below).

Transient Na current I_{Na} was governed by the following equations.

$$I_{Na}(V,m,h) = g_{Na}m^3h(V - V_{Na})$$

where the maximal conductance of the channels was $g_{Na} = 112.5$ mS/cm^2, the reversal potential of sodium ion was $V_{Na} = 50$ mV and the dynamics of the three activation gates m and one inactivation gate h were given by

$$\frac{dm}{dt} = [m_\infty(V) - m]/\tau_m$$

$$\frac{dh}{dt} = [h_\infty(V) - h]/\tau_h(V)$$

The time constant of the m gate was $\tau_m = 0.01$ ms and the voltage-dependent steady-state activation and inactivation variables m_∞, h_∞ and time constant of the h gate τ_h were

$$m_\infty(V) = \{1 + \exp[-(V - \theta_m)/\sigma_m]\}^{-1}$$

$$h_\infty(V) = \{1+\exp[-(V-\theta_h)/\sigma_h]\}^{-1}$$

$$\tau_h(V) = 0.5+14\times\{1+\exp[-(V-\theta_{th})/\sigma_{th}]\}^{-1}$$

where $\theta_m = -24$ mV, $\sigma_m = 11.5$ mV, $\theta_h = -58.3$ mV, $\sigma_h = -6.7$ mV, $\theta_{th} = -60$ mV and $\sigma_{th} = -12$ mV.

The delayed rectifier K current I_{Kdr} was governed by

$$I_{Kdr}(V,n) = g_{Kdr}n^2(V)(V-V_K)$$

where the maximal conductance of the channels was $g_{Kdr} = 225$ mS/cm^2, the reversal potential of potassium ions was $V_K = -90$ mV and the dynamics of the two activation gates n were defined by

$$\frac{dn}{dt} = [n_\infty(V) - n]/\tau_n(V)$$

The voltage-dependent steady-state activation variable n_∞ and time constant of the n gates τ_n were

$$n_\infty(V) = \{1+\exp[-(V-\theta_n)/\sigma_n]\}^{-1}$$

$$\tau_n(V) = \left\{0.087 + 11.4\times\left\{1+\exp\left[\frac{V+14.6}{8.6}\right]\right\}^{-1}\right\} \times \left\{0.087 + 11.4\times\left\{1+\exp\left[\frac{-(V-1.3)}{18.7}\right]\right\}^{-1}\right\}$$

where $\theta_n = -12.4$ mV, $\sigma_n = 6.8$ mV.

The slowly inactivating d-type K current I_{Kd} was governed by

$$I_{Kd}(V,a,b) = g_{Kd}a^3b(V-V_K)$$

where the maximal conductance of the channels was $g_{Kd} = 1.8$ mS/cm^2 and the dynamics of the three activation gates a and one inactivation gate b were defined by

$$\frac{da}{dt} = [a_\infty(V) - a]/\tau_a$$

$$\frac{db}{dt} = [b_\infty(V) - b]/\tau_b$$

The time constant of the activation gate was $\tau_a = 2$ ms and that of the inactivation gate was $\tau_b = 120$ ms. The voltage-dependent steady-state activation and inactivation variables a_∞ and b_∞ were

$$a_\infty(V) = \{1+\exp[-(V-\theta_a)/\sigma_a]\}^{-1}$$

$$b_\infty(V) = \{1+\exp[-(V-\theta_b)/\sigma_b]\}^{-1}$$

where $\theta_a = -50$ mV, $\sigma_a = 20$ mV, $\theta_b = -60$ mV, $\sigma_b = -6$ mV.

We introduced smaller τ_b compared to the Golomb-model (where τ_b was 150 ms), which resulted in faster rhythmicity that was within the delta-theta frequency range. We used a θ_b of -60 mV that enabled the characteristic sag response by the H-current.

To define the HCN channel, we started from a generic HCN model by Kali and Zemankovics (Káli and Zemankovics, 2012) which used an alternative parameterization of the Hodgkin-Huxley type model as described by Borg-Graham (Borg-Graham, 1999). Next, parameters of our model were tuned to match the dynamical properties of the H-current in MS neurons (Migliore and Migliore, 2012; Xu et al., 2004). The final I_H current was defined by

$$I_H(V,x) = g_Hx(V-V_H)$$

where the maximal conductance of the channels was $g_H = 0.1$ mS/cm^2 and the reversal potential of the cations was $V_x = -30$ mV. The open probability of the activation gate x evolved as

$$\frac{dx}{dt} = [x_\infty(V) - x]/\tau_x(V)$$

where the voltage-dependent steady-state activation variable x_∞ and time constant τ_x were

$$x_\infty(V) = \{1 + exp[-(V - \theta_x)/\sigma_x]\}^{-1}$$

$$\tau_x(V) = \left\{ G_x exp\left[\frac{\gamma_x(V - \theta_x)}{\sigma_x}\right] + G_x exp\left[\frac{(\gamma_x - 1)(V - \theta_x)}{\sigma_x}\right] \right\}^{-1} + \tau_{x0}$$

where rate coefficient was G_x = 1.2353 1/ms, asymmetry parameter was γ_x = 0.81, half activation was θ_x = −98 mV, σ_x = −6.73 mV, τ_{x0} = 130 ms.

Modeling the MS pacemaker network

The neuron network parameters were defined, and the simulation results were processed in Matlab. In our network simulations, 20 inhibitory pacemaker neurons were connected at an average connection rate (CR) varied between 0 and 100% (randomly chosen connections were deleted from a fully connected graph). Inhibitory synapses were implemented with the built-in Netcon() and ExpSyn() point processes of the NEURON environment. Netcon() implements a presynaptic source object with threshold, delay and weight parameters. The threshold parameter was fixed at 0 mV. Synaptic delays between 1 and 15 ms (1, 4, 7, 11, 15 ms) were tested (Figures S14A–S14E), fixed at 7 ms with 10% variance for simulations shown in Figure 5 and S14F–S14K. Expsyn() modelled the postsynaptic effect with a discontinuous change in conductance after each incoming spike event (which was initiated by Netcon() when the presynaptic membrane potential crossed the spike detection threshold), followed by an exponential decay with time constant τ:

$$I(t, V) = g(t) \times (V - e)$$

$$g(t) = weight \times \exp(-t/\tau)$$

where I (in nA) was the current transmitted to the postsynaptic cell, g (in μS) was the actual conductance, *weight* (in μS) was the maximal conductance or synaptic strength, e (in mV) was the reversal potential, which was set to −70 mV and τ (in ms) was the exponential decay factor, which was set to 2 ms with 10% variance.

The network simulations were implemented by NEURONS's built-in IClamp() function, which simulated an electrode delivering current pulses of a given duration, amplitude and delay. Every neuron received three electrodes at their somata, delivering a sequence of three current pulses implementing weak, strong (1.4-fold), and weak tonic excitation in this order, with variable stimulus onset latency uniformly dispersed over a one-second-long interval to avoid synchronous phase reset across the population. The extent of increase in excitation strength was based on the average firing rate increase of MS glutamatergic neurons (Figure 6V), the main excitatory input to MS GABAergic cells (Hajszan et al., 2004), determined by our optogenetic tagging experiments. During each simulation, synaptic and stimulation parameters were drawn from normal distributions with given mean and variance.

We modeled the theoretical output signal of the simulated pacemaker network as a proxy for the septal input to the hippocampus. Spike trains (i.e. the events when the simulated membrane potential reached the 0 mV spike generation threshold) were convolved with a 50 ms Gaussian window and averaged across all neurons. State detection was executed similarly as described for real data above with the following parameters: resampling rate, 1 kHz; theta band, 4–6 Hz; delta band, 0.5–4 Hz; theta-delta ratio was smoothed, and short segments (<0.5 s) were handled as above; theta-delta ratio threshold, 2.

Exploring the parameter space of the pacemaker network model

To study the network dynamics and its dependence on key parameters, we performed a series of simulations. In each run, we simulated a 5-second-long baseline period, followed by a 10-second-long 'expected theta' period when a stronger excitatory current was injected to all pacemaker neurons (1.4-fold of baseline), followed by a 5-second-long 'expected non-theta' period when tonic excitation was reverted to baseline (with varied stimulus onset latency, see above). We systematically varied the connection rate (0–100% in increments of 20%), mean synaptic delay (1, 4, 7, 11, 15 ms), mean absolute synaptic strength (1, 3, 6, 9, 12 nS), mean (40–80 pA in increments of 10 pA) and variance (0–20% in increments of 5%) of baseline stimulation strength. The variance of synaptic weights, delays and decay times was kept at 10%.

We performed three sets of simulations. First, the variance of baseline stimulation was fixed at 10% and the synaptic delay at 7 ms, while all combinations of connection rates, stimulation strength and synaptic weight were tested (Figures S14A–S14C). Second, stimulation strength was fixed at 60 pA, synaptic weight at 3 nS and stimulation variance at 10%, while all possible combinations of connection rate and synaptic delay were tested (Figure S14D). Third, stimulation strength was fixed at 60 pA, synaptic weight at 3 nS and synaptic delay at 7 ms, while all possible combinations of connection rate and variance of stimulation strength were tested (Figure S14E). We repeated each simulation for a given parameter arrangement 10 times by redrawing parameters from the same distributions, performing 1800, 300 and 300 runs in the first, second and third set of simulations, respectively. We evaluated the simulated models by calculating a simple synchronization score, which quantified the ratio of the total simulation time the network spent in the expected state based on the state detection described above.

Model network synchronization

Based on the exploration of the network model parameter space, we fixed mean baseline excitation at 60 pA with 10% variance, connectivity rate at 60%, mean synaptic strength at 3 nS and mean synaptic delay at 7 ms. We performed a series of simulations (n = 60) of 60-second-long segments, with 20 s of baseline, followed by 20 s of increased excitation (with varied stimulus onset latency, see above), followed by 20 s of returning to baseline excitation levels to enable large scale analysis of pacemaker synchronization (Figures 5F and S14F–S14K). Rhythmicity indices, TBI (theta-burst interspike interval window, 20–40 ms), significant modulations, phase preference (with respect to the theoretical population output) and pacemaker synchronization were computed as described for the biological data.

We detected anti-phasic firing based on the peak location distributions of pairwise cross-correlations between pacemaker neurons in the model, since anti-phasic firing results in the over-representation of cross-correlation peaks around half of the cycle length of theta. We ran a parameter search to detect such over-representations by defining an in-phase and an anti-phase sync score for each simulation. Crosscorrelogram peaks during the stronger tonic input period (6–15 s) were detected in the −300 to 300 ms range of lags, looking for peaks at least 166.7 ms apart (corresponding to maximal theta frequency). Crosscorrelogram 'offset' was defined as the lag corresponding to the peak that was closest to zero. Next, histograms of absolute offsets were calculated using a bin size of 25 ms. The 'in-phase' score was defined as the value of the first offset bin, while the 'anti-phase' value was defined as the fourth offset bin, corresponding to anti-phase crosscorrelation lags.

Statistical testing

Significant rhythmic firing rate modulation was determined by a bootstrap permutation test at a $p = 0.05$ significance level as described above. This provides a conservative threshold for rhythmicity, constrained by the sample size (number of recorded action potentials per neurons), as indicated by the apparent presence of rhythmic modulation beyond the thresholds in Figure S2D. Please note that this is only apparent in the Rhythmicity Index-sorted images that allow pattern-detection across multiple neurons.

We used non-parametric tests for comparing central tendencies of distributions: Mann-Whitney U-test for non-paired and Wilcoxon signed-rank test for paired samples. We report W+ test statistic (ranksum for theta- > delta-related measures for theta-delta comparisons). Nonparametric tests are ideally suited when no assumptions on underlying distributions are made. We avoided statistical tests that require normal distribution of the underlying random variables, since statistical tests for normality may reject the null hypothesis of the Gaussian distribution of data, but the lack of significance does not prove normality, and their statistical power strongly depends on sample size. Additionally, firing rates are positive random variables known to deviate from normal distribution (Buzsáki and Mizuseki, 2014). Significance was determined at $p < 0.05$ (*), $p < 0.01$ (**) and $p < 0.001$ (***), as also indicated in the figure legends.

We considered multiple circular statistical models to explain the distribution of mean theta phase values of the putative pacemaker neurons. These models were mixtures of one to five von Mises distributions (circular analog of the Gaussian distribution), corresponding to unimodal, bimodal, trimodal, etc. distributions on the circle (Fisher, 1993). To assess which model described the data best, we performed model selection by calculating Akaike Information Criterion (AIC) and Bayesian Information Criterion (BIC) for these models. The model with the lowest value corresponded to the best fitting model (Akaike, 1973; Brewer et al., 2016; Konishi and Kitagawa, 2008). The information criteria did not support models with more than three modes; therefore, we focus on the unimodal, bimodal and trimodal phase distributions below. For the anesthetized rat recordings, we found that AIC values for the unimodal, bimodal and trimodal distributions were 109.08, 103.19 and 108.98, respectively. The BIC values were 111.81, 110.03 and 119.92; thus, both information criteria indicated that the bimodal phase distribution described the data best. This was further confirmed by a parametric bootstrap approach (Fisher, 1993), which statistically tested whether a unimodal or a bimodal model can be rejected based on the data. The unimodal hypothesis was rejected at $p = 0.02$, while the bimodal hypothesis could not be rejected ($p = 0.91$). The mean phases of the best fitting mixture of two von Mises distributions were 147.28° and 342.57° (referenced to pyramidal layer theta). Model selection results in mice favored either a unimodal (AIC in freely moving mice: 111.17, 113.11, 111.67; BIC in freely moving mice: 114.28, 120.89, 124.11; BIC in anesthetized mice, 171.09, 180.66, 175.92 for the unimodal, bimodal and trimodal distributions, respectively) or a more complex trimodal (AIC in anesthetized mice: 167.39, 171.41, 161.12 for the unimodal, bimodal and trimodal distributions, respectively) phase model.

Cell Reports, Volume *40*

Supplemental information

Huygens synchronization of medial septal pacemaker neurons generates hippocampal theta oscillation

Barnabás Kocsis, Sergio Martínez-Bellver, Richárd Fiáth, Andor Domonkos, Katalin Sviatkó, Dániel Schlingloff, Péter Barthó, Tamás F. Freund, István Ulbert, Szabolcs Káli, Viktor Varga, and Balázs Hangya

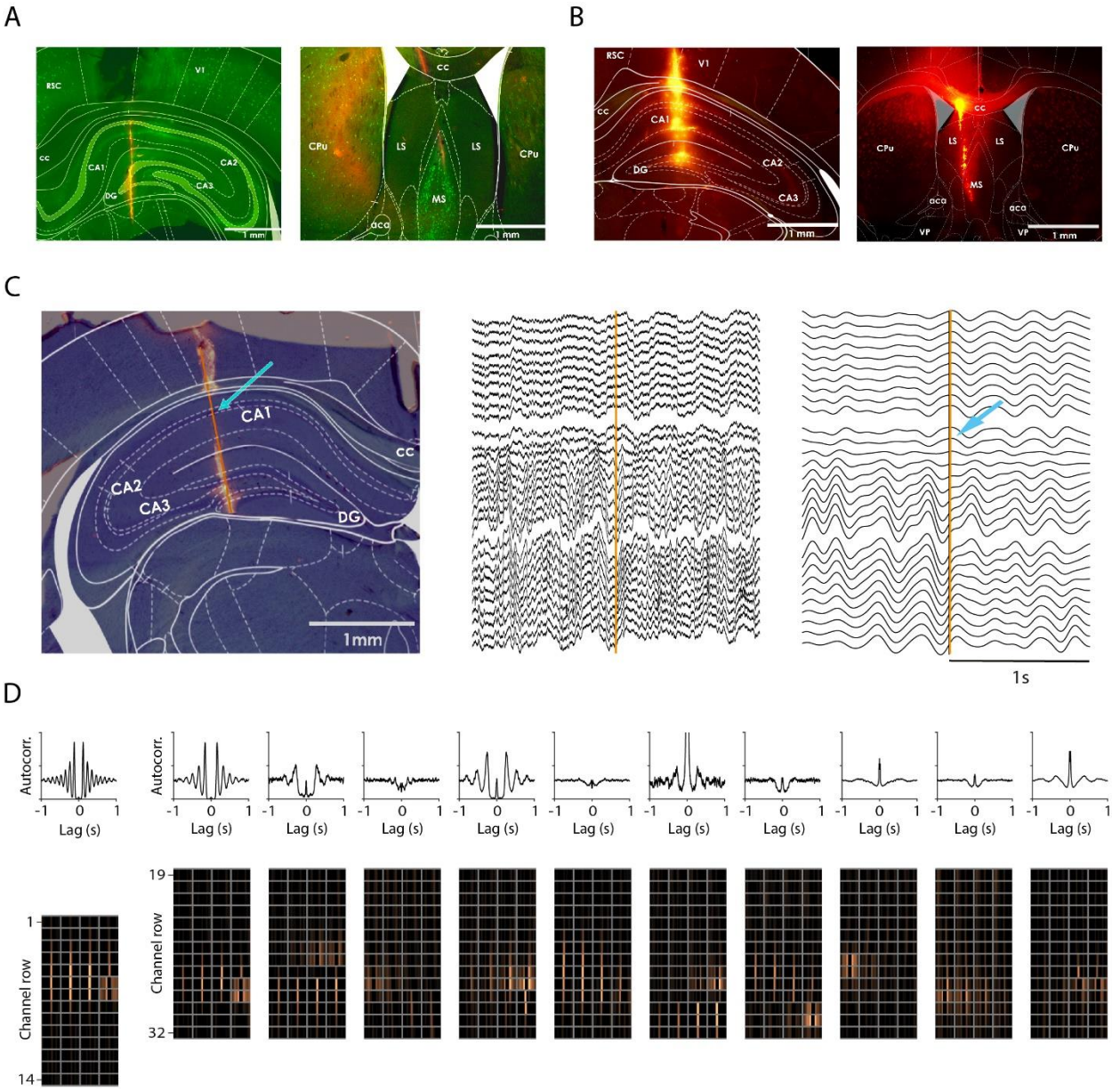

Figure S1. Histological track reconstruction in mice and rats. Phase reversal of hippocampal theta oscillation. Identification of putative overlapping units across recordings in urethane-anesthetized mice. Related to Figure 1 and STAR Methods. (A) Left, fluorescent images of a silicon probe track in the hippocampus. Green, ChAT staining; red, DiI. Right, silicon probe track in the medial septum. Acute rat recording. (B) Left, silicon probe track in the hippocampus. Red, DiI. Right, silicon probe track in the medial septum. Chronic mouse recording. See also Figure 1A for track reconstruction after an acute mouse experiment. aca, anterior commissure; CA, cornu ammonis; cc, corpus callosum; CPu, caudate putamen; DG, dentate gyrus; LS, lateral septum; MS, medial septum; RSC, retrosplenial cortex; V1, primary visual

cortex; VP, ventral pallidum. (C) Left, fluorescent image of the silicon probe track in the hippocampus from an acute mouse experiment. An estimated 10% of tissue shrinkage during perfusion and histological processing was taken into account. Middle, raw 32-channel LFP recording from the same experiment (two broken channels were removed). Right, LFP channels filtered in the theta band. Theta phase reversal, known to occur just below the pyramidal layer, is indicated by cyan arrow. Left, the reconstructed position of the corresponding electrode contact site is marked by cyan arrow. (D) Left, example cluster from the second recording session of a urethane-anesthetized mouse recording, after 500 μm descent of the recording electrode array, corresponding to a displacement of 22 channel rows on the silicon probe. Top, autocorrelation; bottom, spatial waveform profile on the silicon probe. Right, candidates for potentially overlapping units from the first recording session (top, autocorrelation; bottom, spatial waveform profile). We decided to exclude the example cluster in the left panel because of the high similarity to the first candidate in the right panel.

hangya.balazs_256_24

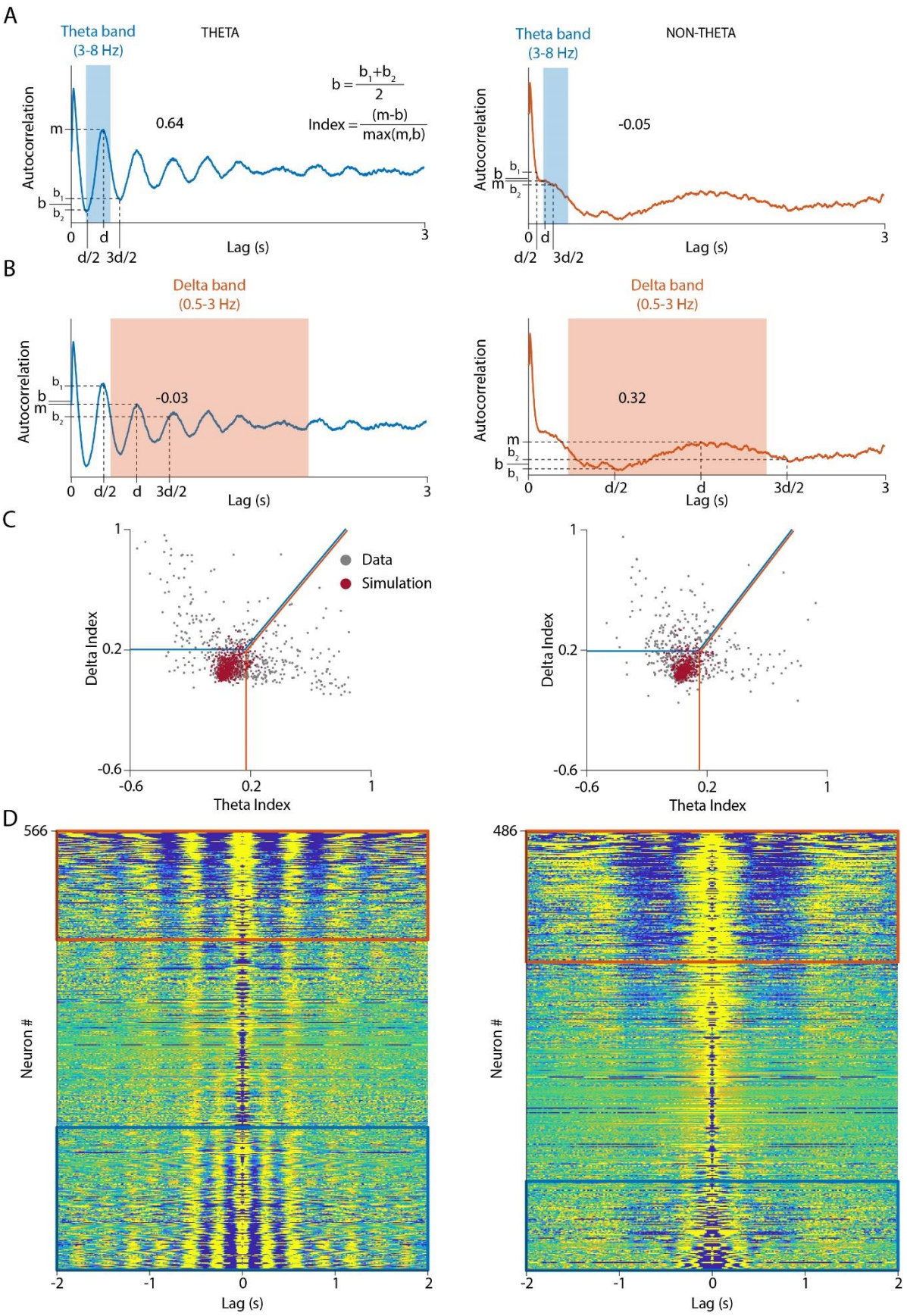

Figure S2. Determining theta and delta rhythmicity. Related to STAR Methods. (A) Theta Index was calculated based on autocorrelograms for theta and non-theta segments by normalizing the theta-band autocorrelation peak with the average of pre- and post-peak troughs (see STAR Methods). The number above the trace indicates the calculated value of the rhythmicity index for the example. (B) Delta Index was calculated using a similar algorithm for the delta band. (C) Theta and Delta Index was calculated for all recorded neurons during theta (left) and non-theta segments (right; grey, recordings from urethane-anesthetized rats are shown) and for simulated Poisson-neurons with matching firing rate (red). Significant rhythmicity was defined by the 0.05 percentile of the Theta and Delta Index distributions of the Poisson-neurons (vertical and horizontal lines). If both indices exceeded the threshold, rhythmicity was determined by the larger of the two Rhythmicity Indices (normalized to their respective thresholds). (D) Autocorrelograms (left, theta segments; right, non-theta segments) for all neurons with sufficient firing rate (see STAR Methods), sorted by the larger of the two Rhythmicity Indices (normalized to their respective thresholds): delta-rhythmic on top and theta-rhythmic on bottom; significantly delta- and theta-modulated neurons are above and below the respective colored lines.

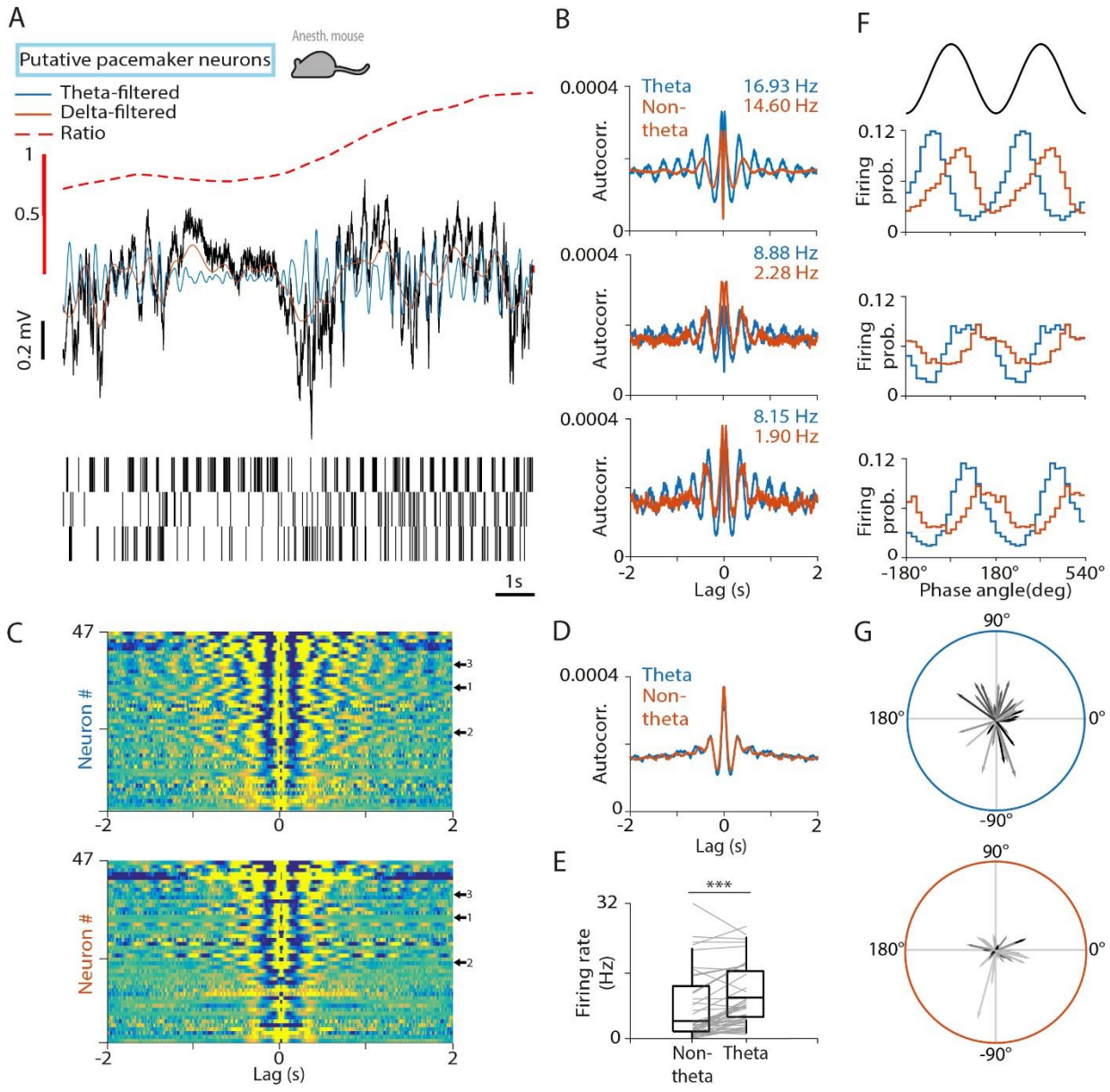

Figure S3. Putative pacemaker neurons of the MS in urethane-anesthetized mice. Related to Figure 2. (A) Top, black, raw LFP from the CA1 shows a delta-to-theta state transition. Orange, LFP filtered in the delta band; blue, LFP filtered in the theta band; dashed, theta-delta amplitude ratio. Bottom, spike raster of three examples of putative pacemaker neurons from the same recording session. Recordings are from urethane-anesthetized mice. (B) Autocorrelograms of the three example neurons in panel (A). Numbers indicate average firing rates during theta and non-theta segments. (C) Autocorrelograms of all putative pacemaker neurons during theta (top) and non-theta (bottom) segments. Arrows indicate the example neurons. (D) Average autocorrelogram of all putative pacemaker neurons. (E) Firing rates of putative pacemaker neurons during non-theta and theta segments. Boxes and whiskers represent interquartile

ranges and non-outlier ranges, respectively. Lines correspond to individual neurons. Firing rate was significantly higher during theta (***, $p < 0.001$; $p = 7.98 \times 10^{-6}$, $W = 986$, $n = 47$, Wilcoxon signed-rank test). (F) Phase histogram of the example neurons in panel (A) relative to delta (orange) and theta (blue) oscillations. Two oscillatory cycles are shown. (G) Phase-locking of all putative pacemaker neurons to theta (top) and delta (bottom) oscillation in polar coordinates. Angle, circular phase; length, mean vector length; greyscale corresponds to average firing rate (black, higher firing rate). Phase-locking strength to delta oscillation was low for most putative pacemaker neurons.

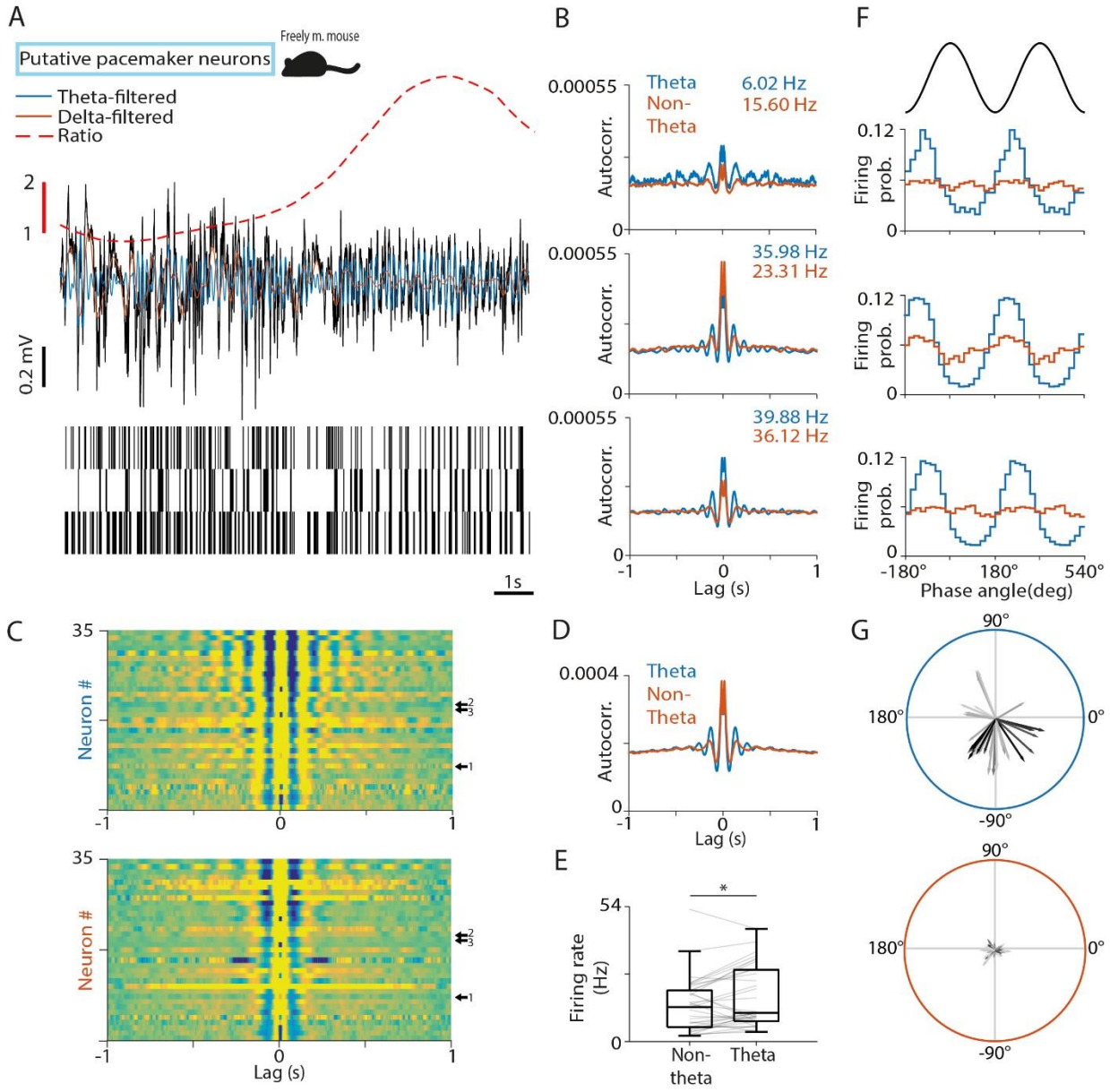

Figure S4. Putative pacemaker neurons of the MS in freely moving mice. Related to Figure 2. (A) Top, black, raw LFP from the CA1 shows a delta-to-theta state transition. Orange, LFP filtered in the delta band; blue, LFP filtered in the theta band; dashed, theta-delta amplitude ratio. Bottom, spike raster of three examples of putative pacemaker neurons from the same recording session. Recordings are from drug-free mice. (B) Autocorrelograms of the three example neurons in panel (A). Numbers indicate average firing rates during theta and non-theta segments. (C) Autocorrelograms of all putative pacemaker neurons during theta (top) and non-theta (bottom) segments. Arrows indicate the example neurons. (D) Average autocorrelogram of all putative pacemaker neurons. (E) Firing rates of putative pacemaker neurons during non-theta and theta segments. Boxes and whiskers represent interquartile ranges and non-outlier ranges,

respectively. Lines correspond to individual neurons. Firing rate was significantly higher during theta (*, $p < 0.05$; $p = 1.34 \times 10^{-2}$, W = 466, n = 35, Wilcoxon signed-rank test). (F) Phase histogram of the example neurons in panel (A) relative to delta (orange) and theta (blue) oscillations. Two oscillatory cycles are shown. (G) Phase-locking of all putative pacemaker neurons to theta (top) and delta (bottom) oscillation in polar coordinates. Angle, circular phase; length, mean vector length; greyscale corresponds to average firing rate (black, higher firing rate). Phase-locking strength to delta oscillation was low for putative pacemaker neurons.

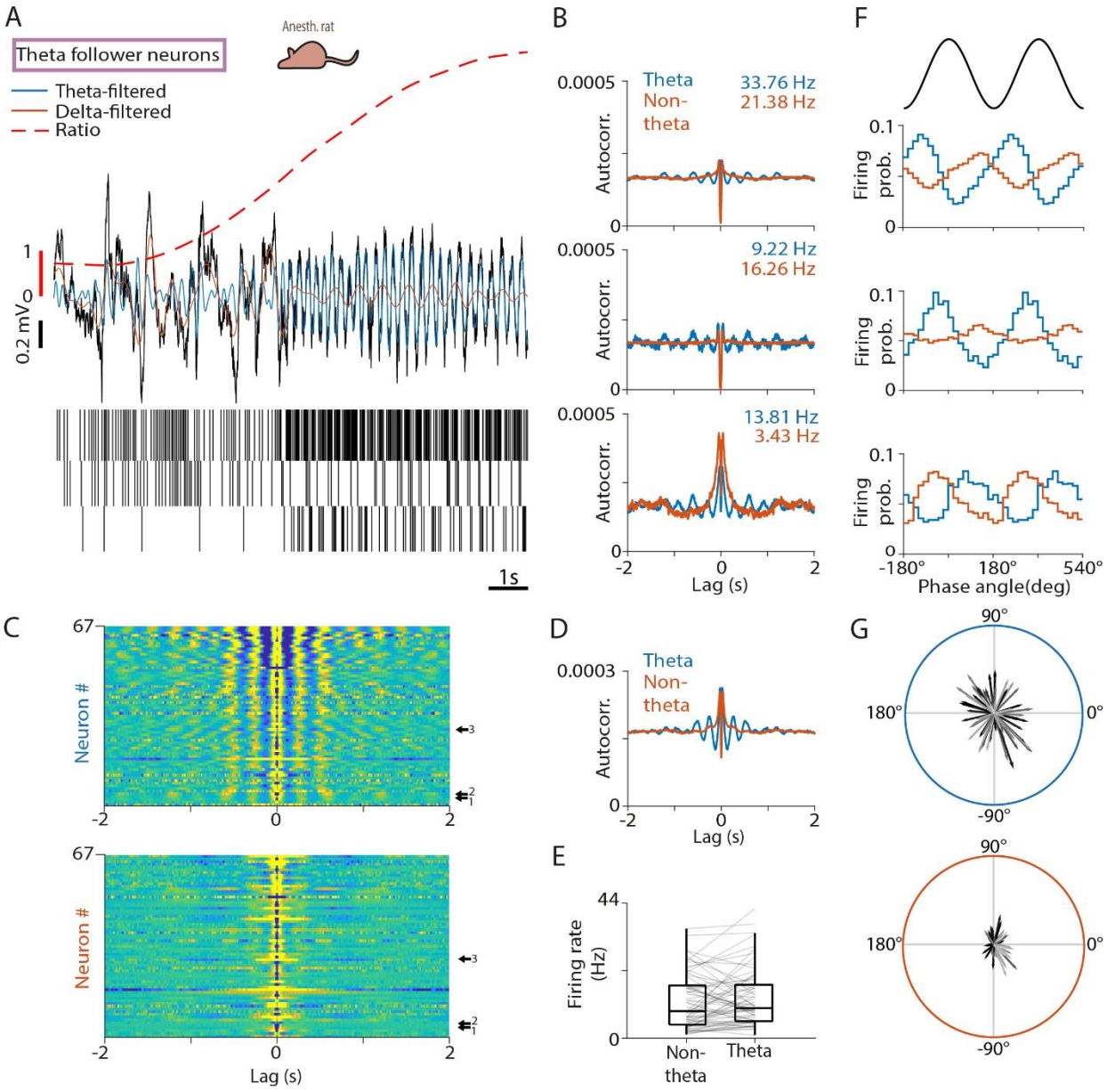

Figure S5. Theta follower neurons in the MS of urethane-anesthetized rats. Related to Figure 3. (A) Top, black, raw LFP from the CA1 shows a delta-to-theta state transition. Orange, LFP filtered in the delta band; blue, LFP filtered in the theta band; dashed, theta-delta amplitude ratio. Bottom, spike raster of three example neurons from the same recording session. 'Theta follower' neurons showed non-rhythmic activity during non-theta epochs and theta-rhythmic activity during theta epochs in urethane-anesthetized rats. See Figure S7 and Figure S8 for the anesthetized and awake mouse recordings. (B) Autocorrelograms of the three example neurons in panel (A). Numbers indicate average firing rates during theta and non-theta segments. (C) Autocorrelograms of all theta follower neurons during theta (top) and non-theta (bottom) segments. Arrows indicate the example neurons. (D) Average autocorrelogram of all

neurons. (E) Firing rates of neurons during non-theta and theta segments. Boxes and whiskers represent interquartile ranges and non-outlier ranges, respectively. Lines correspond to individual neurons. No systematic firing rate change was found ($p = 0.2026$, $W = 1343$, $n = 67$, Wilcoxon signed-rank test). (F) Phase histogram of the example neurons in panel (A) relative to delta (orange) and theta (blue) oscillations. Two oscillatory cycles are shown. (G) Phase-locking of all theta follower neurons to theta (top) and delta (bottom) oscillation in polar coordinates. Angle, circular phase; length, mean vector length; greyscale corresponds to average firing rate (black, higher firing rate). Many of these neurons were phase-locked to both hippocampal oscillations.

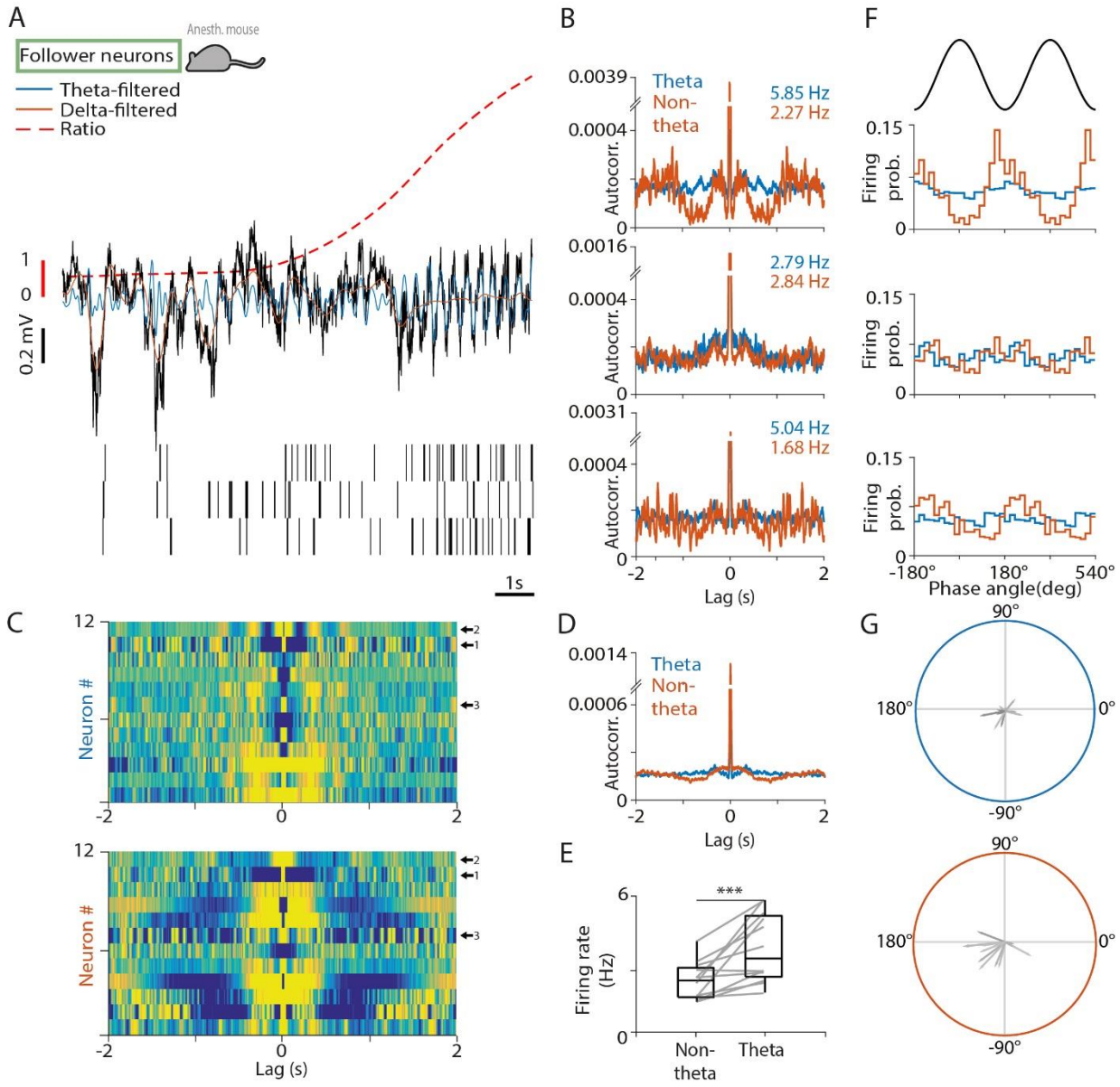

Figure S6. Follower MS neurons in urethane-anesthetized mice. Related to Figure 3. (A) Top, black, raw LFP from the CA1 shows a delta-to-theta state transition. Orange, LFP filtered in the delta band; blue, LFP filtered in the theta band; dashed, theta-delta amplitude ratio. Bottom, spike raster of three example neurons from the same recording session. 'Follower' neurons showed delta-rhythmic activity during non-theta epochs and theta-rhythmic activity during theta epochs. (B) Autocorrelograms of the three example neurons in panel (A). Numbers indicate average firing rates during theta and non-theta segments. (C) Autocorrelograms of all follower neurons during theta (top) and non-theta (bottom) segments. Arrows indicate the example neurons. (D) Average autocorrelogram of all follower neurons. (E) Firing rates of follower neurons during non-theta and theta segments. Boxes and whiskers represent interquartile

ranges and non-outlier ranges, respectively. Lines correspond to individual neurons. Firing rate was significantly higher during theta (***, $p < 0.001$; $p = 9.77 \times 10^{-4}$, $W = 77$, $n = 12$, Wilcoxon signed-rank test). (F) Phase histogram of the example neurons in panel (A) relative to delta (orange) and theta (blue) oscillations. Two oscillatory cycles are shown. (G) Phase-locking of all follower neurons to theta (top) and delta (bottom) oscillation in polar coordinates. Angle, circular phase; length, mean vector length; greyscale corresponds to average firing rate (black, higher firing rate).

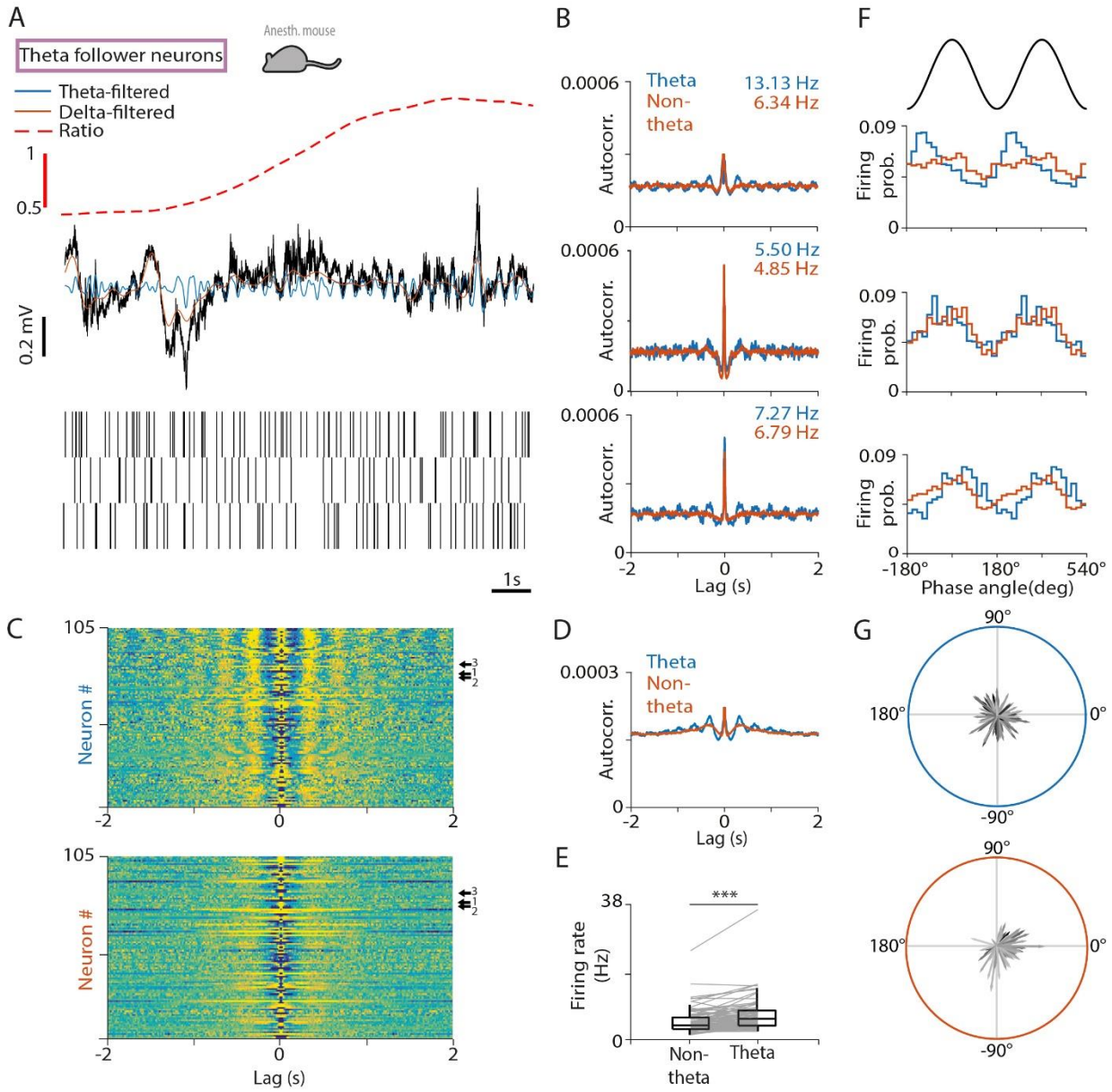

Figure S7. Theta follower neurons in the MS of urethane-anesthetized mice. Related to Figure 3. (A) Top, black, raw LFP from the CA1 shows a delta-to-theta state transition. Orange, LFP filtered in the delta band; blue, LFP filtered in the theta band; dashed, theta-delta amplitude ratio. Bottom, spike raster of three example neurons from the same recording session. 'Theta follower' neurons showed non-rhythmic activity during non-theta epochs and theta-rhythmic activity during theta epochs. (B) Autocorrelograms of the three example neurons in panel (A). Numbers indicate average firing rates during theta and non-theta segments. (C) Autocorrelograms of all theta follower neurons during theta (top) and non-theta (bottom) segments. Arrows indicate the example neurons. (D) Average autocorrelogram of all neurons. (E) Firing rates of neurons during delta and theta oscillation. Boxes and whiskers represent interquartile

ranges and non-outlier ranges, respectively. Lines correspond to individual neurons. Firing rate was significantly higher during theta (***, $p < 0.001$; $p = 5.08 \times 10^{-13}$, $W = 5042$, $n = 105$, Wilcoxon signed-rank test). (F) Phase histogram of the example neurons in panel (A) relative to delta (orange) and theta (blue) oscillations. Two oscillatory cycles are shown. (G) Phase-locking of all theta follower neurons to theta (top) and delta (bottom) oscillation in polar coordinates. Angle, circular phase; length, mean vector length; greyscale corresponds to average firing rate (black, higher firing rate).

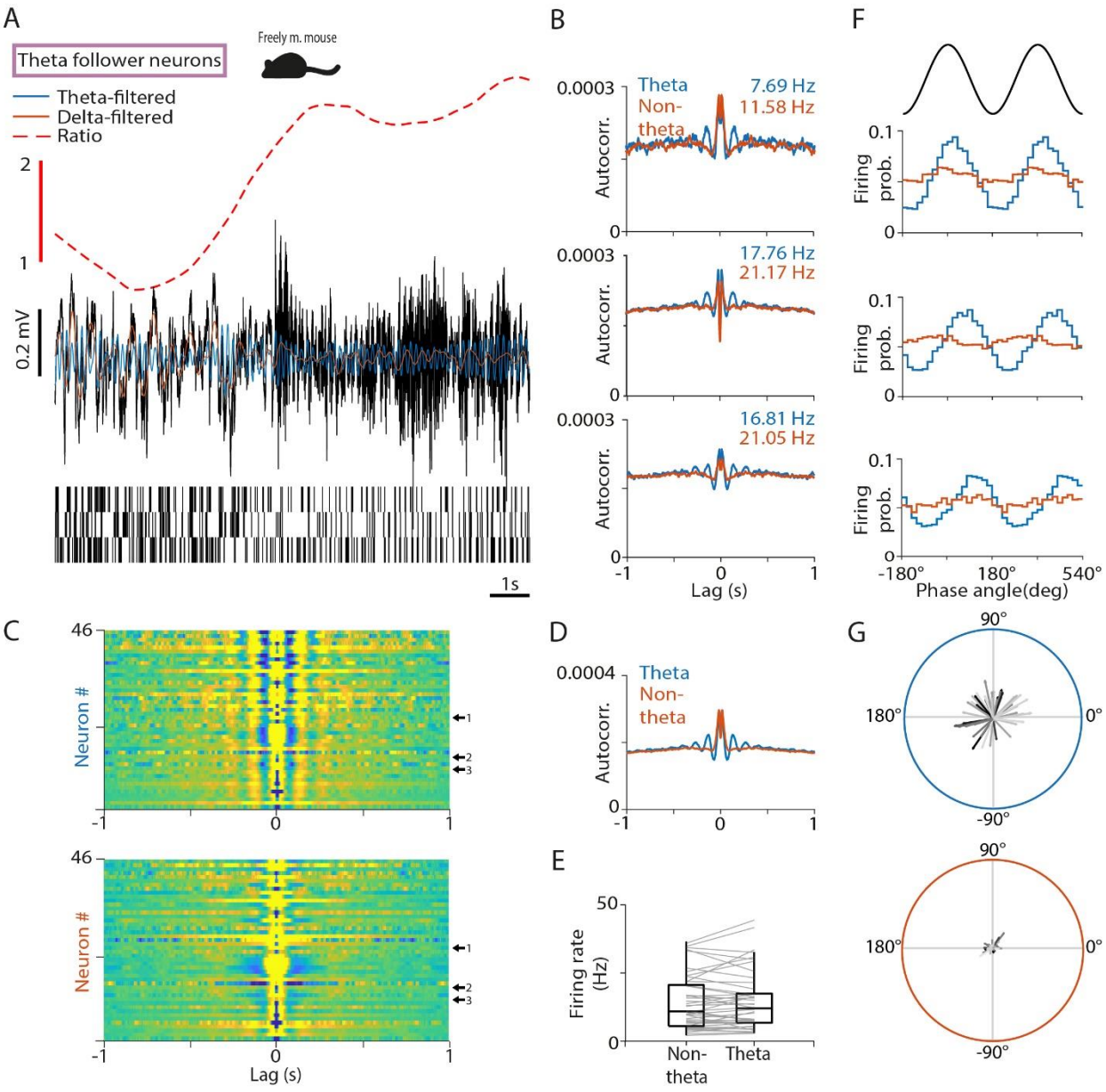

Figure S8. Theta follower neurons in the MS of freely moving mice. Related to Figure 3. (A) Top, black, raw LFP from the CA1 shows a delta-to-theta state transition. Orange, LFP filtered in the delta band; blue, LFP filtered in the theta band; dashed, theta-delta amplitude ratio. Bottom, spike raster of three example neurons from the same recording session. Theta follower neurons showed non-rhythmic activity during non-theta epochs and theta-rhythmic activity during theta epochs. (B) Autocorrelograms of the three example neurons in panel (A). Numbers indicate average firing rates during theta and non-theta segments. (C) Autocorrelograms of all theta follower neurons during theta (top) and non-theta (bottom) segments. Arrows indicate the example neurons. (D) Average autocorrelogram of all neurons. (E) Firing rates of neurons during non-theta and theta segments. Boxes and whiskers represent interquartile ranges and

non-outlier ranges, respectively. Lines correspond to individual neurons. No systematic firing rate change was found ($p = 0.8398$, $W = 559$, $n = 46$, Wilcoxon signed-rank test). (F) Phase histogram of the example neurons in panel (A) relative to delta (orange) and theta (blue) oscillations. Two oscillatory cycles are shown. (G) Phase-locking of all theta follower neurons to theta (top) and delta (bottom) oscillation in polar coordinates. Angle, circular phase; length, mean vector length; greyscale corresponds to average firing rate (black, higher firing rate).

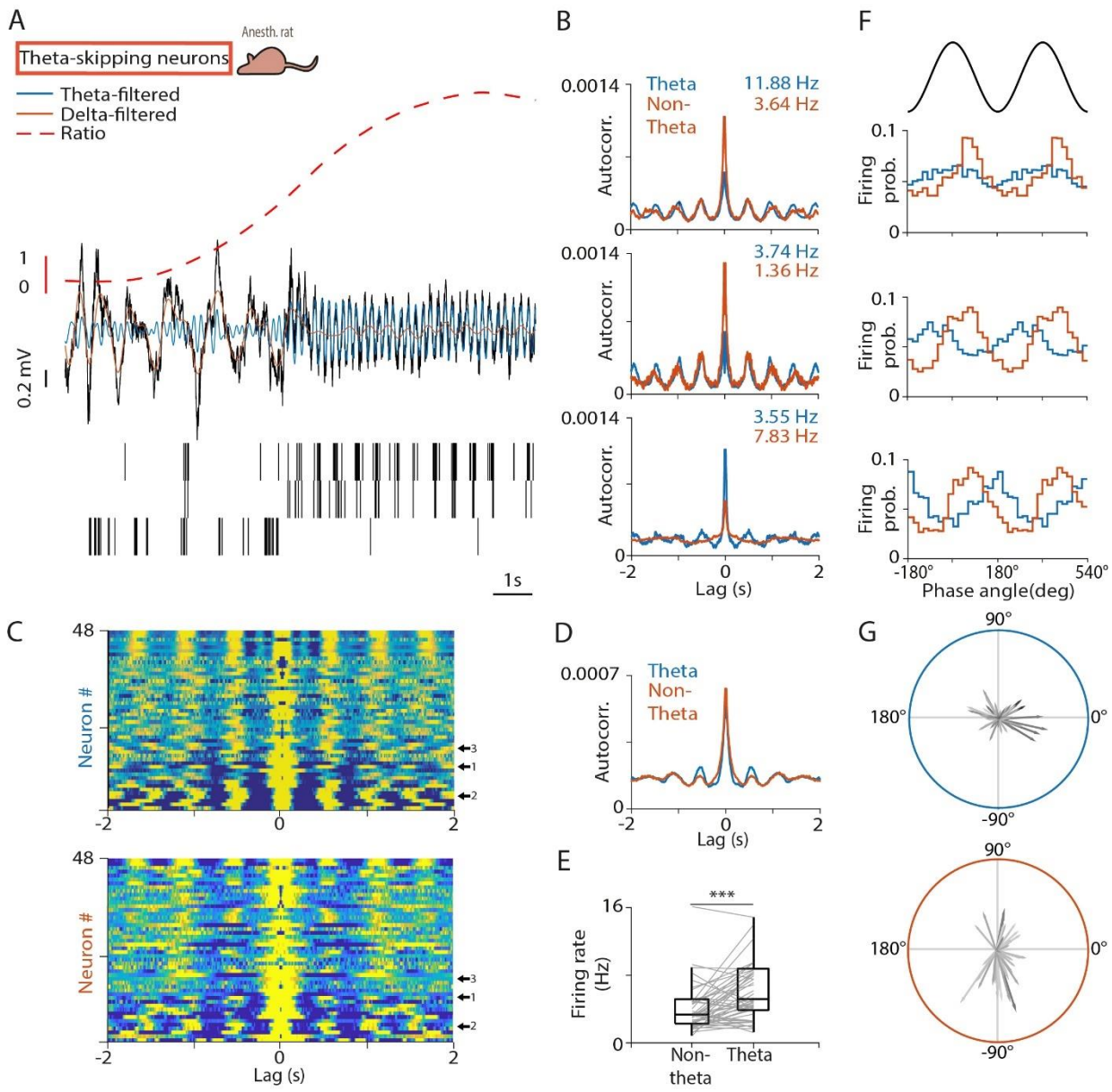

Figure S9. Theta-skipping neurons of the MS. Related to Figure 3. (A) Top, black, raw LFP from the CA1 shows a delta-to-theta state transition. Orange, LFP filtered in the delta band; blue, LFP filtered in the theta band; dashed, theta-delta amplitude ratio. Bottom, spike raster of three examples of theta-skipping neurons from the same recording session. Recordings are from urethane-anesthetized rats. (B) Autocorrelograms of the three example neurons in panel (A). Numbers indicate average firing rates during theta and non-theta segments. (C) Autocorrelograms of all theta-skipping neurons during theta (top) and non-theta (bottom) segments. Arrows indicate the example neurons. (D) Average autocorrelogram of all theta-skipping neurons. (E) Firing rates of theta-skipping neurons during non-theta and theta segments. Boxes and whiskers represent interquartile ranges and non-outlier ranges, respectively. Lines correspond

to individual neurons. Firing rate was significantly higher during theta (***, $p < 0.001$; $p = 2.83 \times 10^{-4}$, W = 942, n = 48, Wilcoxon signed-rank test). (F) Phase histogram of the example neurons in panel (A) relative to delta (orange) and theta (blue) oscillations. Two oscillatory cycles are shown. (G) Phase-locking of all theta-skipping neurons to theta (top) and delta (bottom) oscillation in polar coordinates. Angle, circular phase; length, mean vector length; greyscale corresponds to average firing rate (black, higher firing rate).

hangya.balazs_256_24

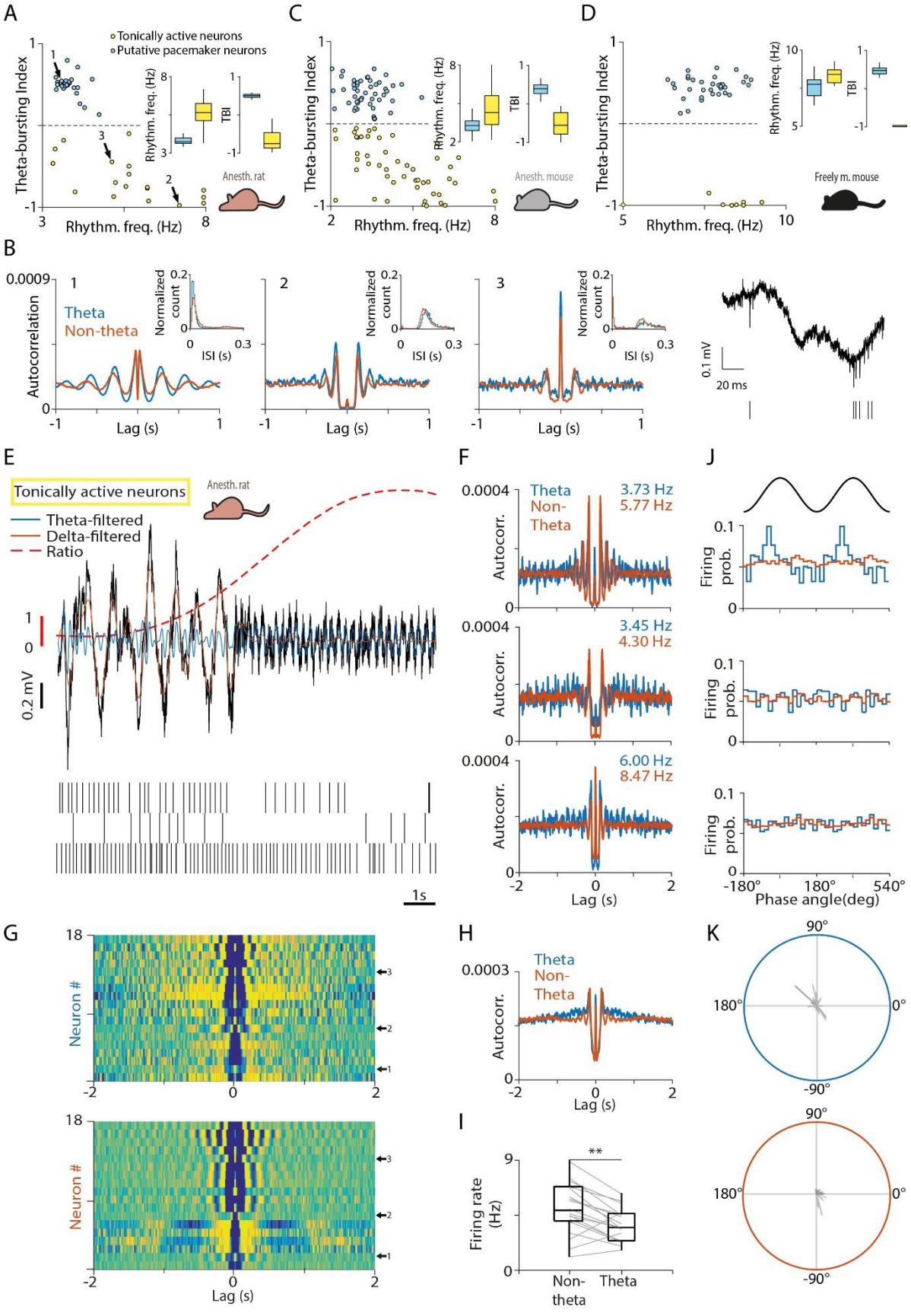

Figure S10. Separating theta-bursting and tonically active neurons. Tonically active MS neurons. Related to Figure 2, Figure 3 and STAR Methods. (A) Theta-bursting Index (TBI; see STAR Methods) and rhythmicity frequency revealed a theta-rhythmic population that showed theta-bursting and a separate one that did not, in anesthetized rats. The former corresponded to putative pacemakers (Figure 2), while the latter formed the group of 'tonically active' neurons. (B) Left, autocorrelogram and interspike interval (ISI) histogram (inset) of three example neurons, marked by arrows in panel (A). Example 1 is a theta-bursting putative pacemaker; examples 2 and 3 are tonically active neurons. Right, raw data (top) and spike raster (bottom) of example 3. Note the fast-bursting phenotype, different from the slower theta-bursting observed in putative pacemakers. (C-D) The same distinction was observed in anesthetized (C) and freely moving mice (D). Box-whisker plots show median, interquartile range and non-outlier range. (E) Top, black, raw LFP from the CA1 shows a delta-to-theta state transition. Orange, LFP filtered in the delta band; blue, LFP filtered in the theta band; dashed, theta-delta amplitude ratio. Bottom, spike raster of three examples of tonically active neurons from the same recording session. Recordings are from urethane-anesthetized rats; see Figure S11 and Figure S12 for the anesthetized and awake mouse recordings. (F) Autocorrelograms of the three example neurons in panel (E). Numbers indicate average firing rates during theta and non-theta segments. (G) Autocorrelograms of all tonically active neurons during theta (top) and non-theta (bottom) segments. Arrows indicate the example neurons. (H) Average autocorrelogram of all tonically active neurons. (I) Firing rates of tonically active neurons during non-theta and theta epochs. Boxes and whiskers represent interquartile ranges and non-outlier ranges, respectively. Lines correspond to individual neurons. Firing rate was significantly higher during non-theta (**, $p < 0.01$; $p = 5.68 \times 10^{-3}$, $W = 22$, $n = 18$, Wilcoxon signed-rank test). (J) Phase histogram of the example neurons in panel (E) relative to delta (orange) and theta (blue) oscillations. Two oscillatory cycles are shown. (K) Phase-locking of all tonically active neurons to theta (top) and delta (bottom) oscillation in polar coordinates. Angle, circular phase; length, mean vector length; greyscale corresponds to average firing rate (black, higher firing rate). These neurons did not show strong phase-locking to hippocampal oscillations.

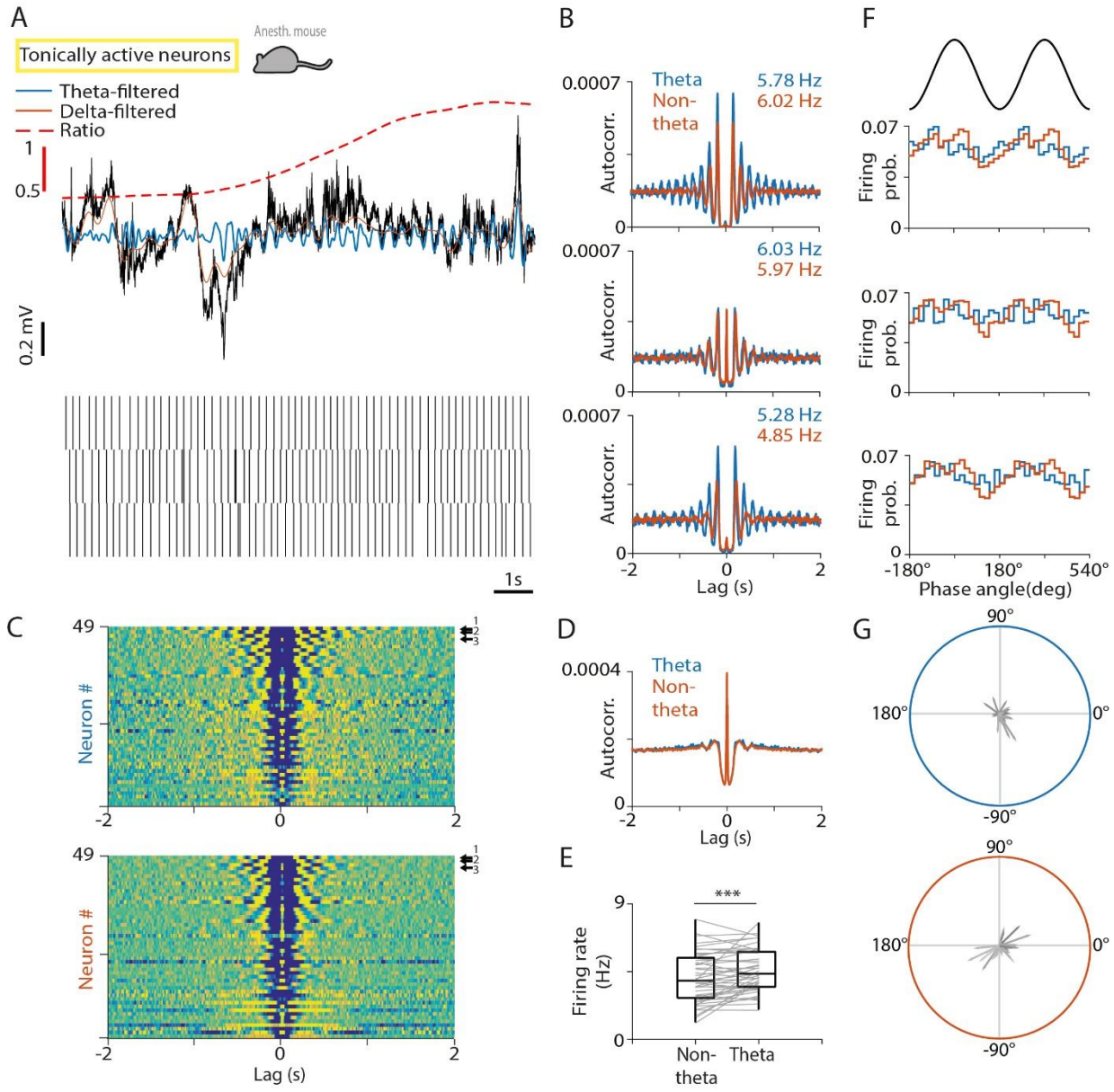

Figure S11. Tonically active MS neurons in urethane-anesthetized mice. Related to Figure 3. (A) Top, black, raw LFP from the CA1 shows a delta-to-theta state transition. Orange, LFP filtered in the delta band; blue, LFP filtered in the theta band; dashed, theta-delta amplitude ratio. Bottom, spike raster of three examples of tonically active neurons from the same recording session. Recordings are from urethane-anesthetized mice. (B) Autocorrelograms of the three example neurons in panel (A). Numbers indicate average firing rates during theta and non-theta segments. (C) Autocorrelograms of all tonically active neurons during theta (top) and non-theta (bottom) segments. Arrows indicate the example neurons. (D) Average autocorrelogram of all tonically active neurons. (E) Firing rates of tonically active neurons during

non-theta and theta segments. Boxes and whiskers represent interquartile ranges and non-outlier ranges, respectively. Lines correspond to individual neurons. Firing rate was significantly higher during theta (***, $p < 0.001$; $p = 3.23 \times 10^{-4}$, $W = 974$, $n = 49$, Wilcoxon signed-rank test). (F) Phase histogram of the example neurons in panel (A) relative to delta (orange) and theta (blue) oscillations. Two oscillatory cycles are shown. (G) Phase-locking of all tonically active neurons to theta (top) and delta (bottom) oscillation in polar coordinates. Angle, circular phase; length, mean vector length; greyscale corresponds to average firing rate (black, higher firing rate). These neurons did not show strong phase-locking to hippocampal oscillations.

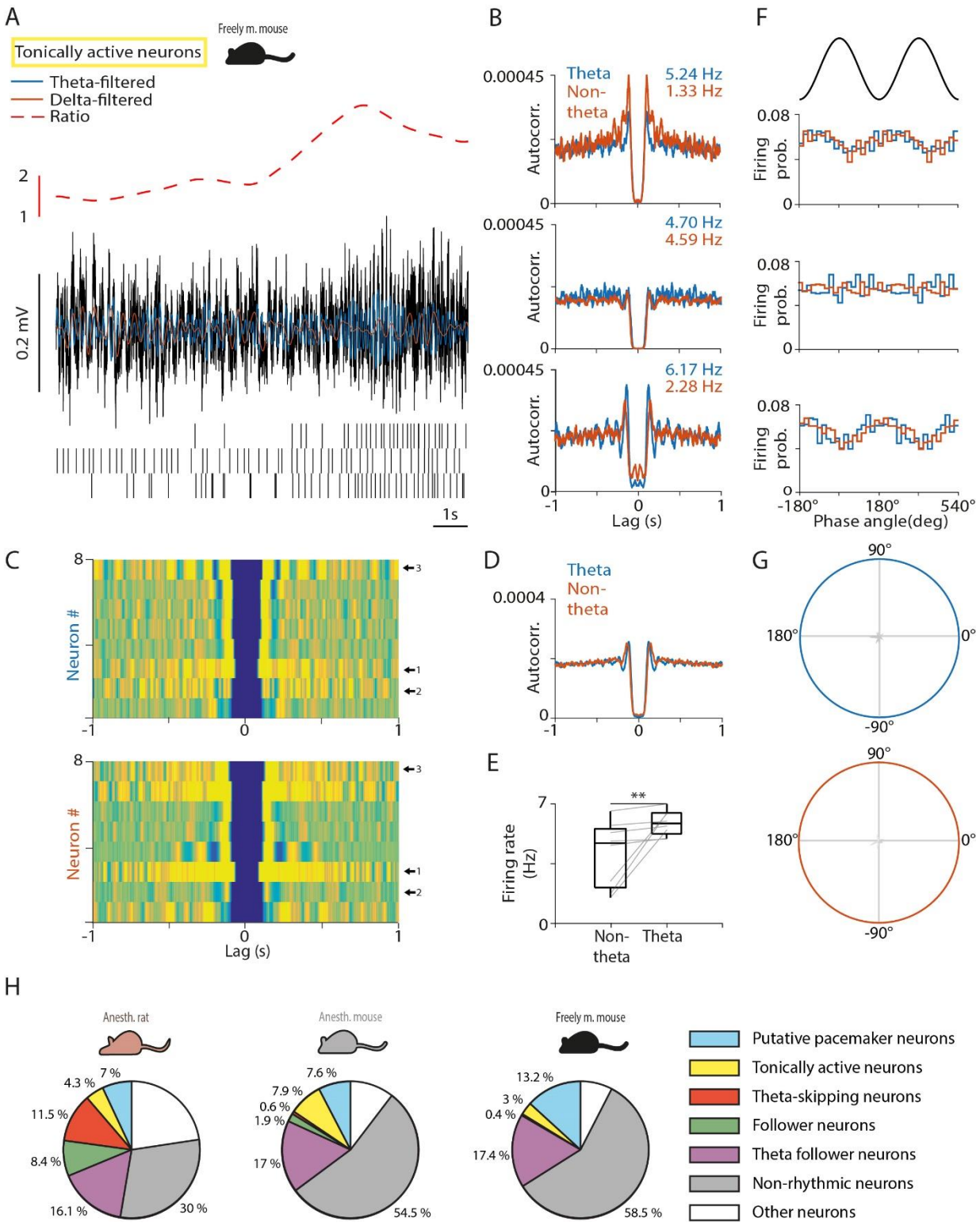

Figure S12. Tonically active MS neurons in freely moving mice. Rhythmicity groups in the MS. Related to Figure 3. (A) Top, black, raw LFP from the CA1 shows a delta-to-theta state transition. Orange, LFP filtered in the delta band; blue, LFP filtered in the theta band; dashed, theta-delta amplitude ratio.

Bottom, spike raster of three examples of tonically active neurons from the same recording session. Recordings are from freely moving mice. (B) Autocorrelograms of the three example neurons in panel (A). Numbers indicate average firing rates during theta and non-theta segments. (C) Autocorrelograms of all tonically active neurons during theta (top) and non-theta (bottom) segments. Arrows indicate the example neurons. (D) Average autocorrelogram of all tonically active neurons. (E) Firing rates of tonically active neurons during none-theta and theta segments. Lines correspond to individual neurons. Firing rate was significantly higher during theta (**, $p < 0.01$; $p = 7.82 \times 10^{-3}$, $W = 36$, $n = 8$, Wilcoxon signed-rank test). (F) Phase histogram of the example neurons in panel (A) relative to delta (orange) and theta (blue) oscillations. Two oscillatory cycles are shown. (G) Phase-locking of all tonically active neurons to theta (top) and delta (bottom) oscillation in polar coordinates. Angle, circular phase; length, mean vector length; greyscale corresponds to average firing rate (black, higher firing rate). These neurons did not show strong phase-locking to hippocampal oscillations. (H) Proportions of MS neurons in the different rhythmicity groups in anesthetized rats (left), anesthetized mice (middle) and freely moving mice (right).

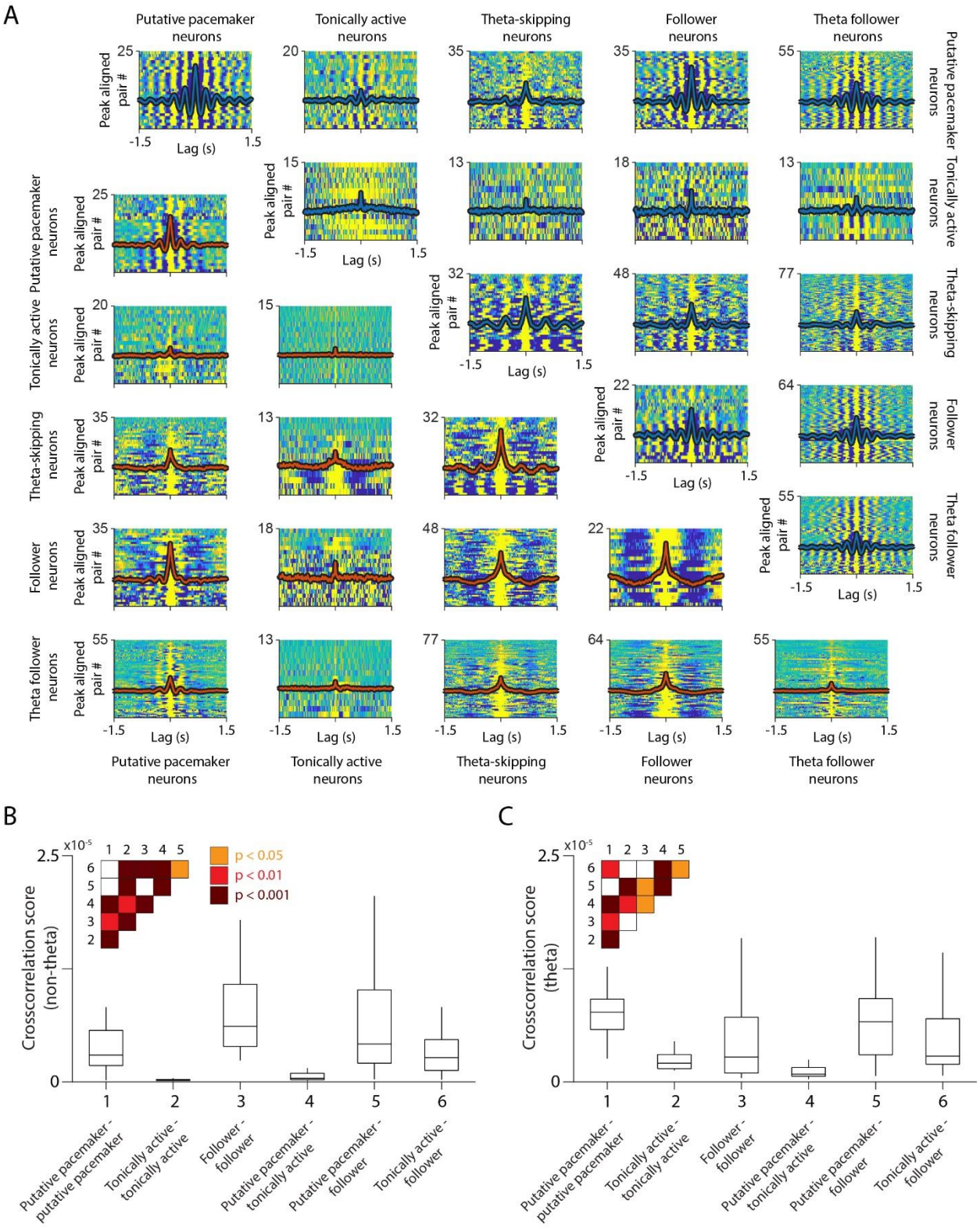

Figure S13. Crosscorrelation within and between MS rhythmicity groups. Related to Figure 4 and STAR Methods. (A) Crosscorrelations of all rhythmic cell pairs recorded in anesthetized rats were sorted by

rhythmicity categories. Individual crosscorrelations are shown color coded (small values are blue) and average crosscorrelations are overlaid (red, during non-theta, lower left triangle; blue, during theta, upper right triangle). (B) Distributions of crosscorrelation scores (mean squared integral of the mean-subtracted crosscorrelograms, see STAR Methods) within and across rhythmicity groups during non-theta segments. Box-whisker plots show median, inter-quartile range and non-outlier range. The inset indicates statistically significant differences across the crosscorrelation score distributions (Mann-Whitney U-test). (C) Same as in panel B for theta segments.

hangya.balazs_256_24

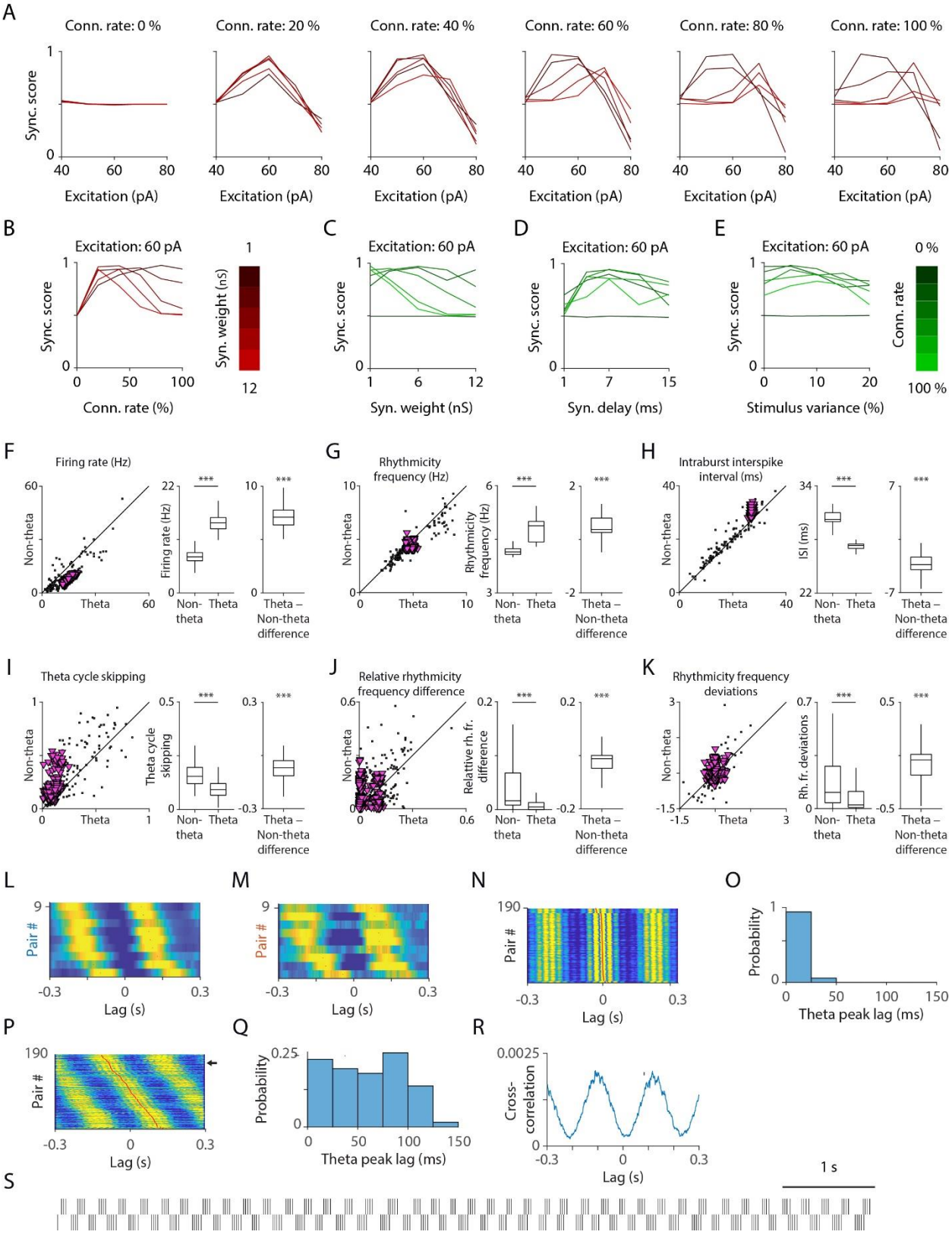

Figure S14. Parameter-dependence of the synchronization of the network model. The pacemaker network model reproduces Huygens-synchronization properties of the MS neural circuit. In-phase versus anti-phase synchronization in the rat MS and in the MS network model. Related to Figure 4 and Figure 5. (A) We systematically varied the parameters of the network model to explore the synchronization of the modelled pacemaker circuit with respect to the parameter space. The parameters of the network model were the connection rate (Conn. rate), the mean inhibitory synaptic strength (Syn. weight), the synaptic delay (Syn. delay) and the mean baseline excitation level and its variance. The synchronization score (Sync. score) quantified the proportional time the network spent in the expected network state (non-theta state during baseline excitation and theta state during increased excitation). By systematically varying mean excitation (variance fixed at 10%), connection rate and synaptic strength (synaptic delay was fixed to 7 ms), we found a discrete peak in synchronization score around 50-70 pA, largely independent of the connection rate. (B, C) Varying the connection rate and the synaptic weight indicated an inverse relationship, demonstrating that sparsely connected networks could only synchronize with stronger synapses, while densely connected networks required small inhibitory weights. (D) The model tolerated a range of synaptic delays, while very short delays did not result in stable synchrony. (E) The model was relatively insensitive to the variance of tonic excitation strength, although high variance tended to destabilize the network. We used a moderate 10% variance in the final simulations. (F) Firing rates of model pacemaker neurons were higher during theta oscillation than during non-theta segments. Left, scatter plot; real data in black (three data sets pooled, see Figure 4), model data overlaid in magenta. Middle and right, box-whisker plots showing statistics for the simulated data (***, $p < 0.001$; $p = 8.50 \times 10^{-50}$, W = 43071, n = 293, Wilcoxon signed-rank test). All box-whisker plots show median, interquartile range and non-outlier range in this figure. (G) Left, scatter plot of rhythmicity frequency measured by the time lag of the first autocorrelation peak in the theta band; real data in black (three data sets pooled, see Figure 4), model data overlaid in magenta. Middle and right, Wilcoxon signed-rank test on model neuron data indicated higher rhythmicity frequency during theta (***, $p < 0.001$; $p = 6.35 \times 10^{-41}$, W = 40489.5, n = 293, Wilcoxon signed-rank test). (H) Left, scatter plot of average intraburst interspike intervals; real data in black (three data sets pooled, see Figure 4), model data overlaid in magenta. Middle and right, the theta-associated decrease of interspike intervals in model neurons indicated a moderate elevation of intraburst frequency (***, $p < 0.001$; $p = 7.60 \times 10^{-50}$, W = 0, n = 293, Wilcoxon signed-rank test). (I) Left, scatter plot of the ratio of skipped theta cycles; real data in black (three data sets pooled, see Figure 4), model data overlaid in magenta. Middle and right, statistics indicated that model pacemaker neurons skipped more theta cycles during non-theta segments (***, $p < 0.001$; $p = 3.47 \times 10^{-45}$, W = 1060, n = 293,

Wilcoxon signed-rank test). (J) Left, scatter plot of relative frequency difference of individual pacemaker neurons for simultaneously simulated pairs, normalized to the larger of the frequencies. Middle and right, statistics indicated that individual model pacemakers became more similar in frequency during theta (***, $p < 0.001$; $p = 2.20 \times 10^{-30}$, W = 51519, n = 671, Wilcoxon signed-rank test). (K) Left, deviation from the mean rhythmicity frequency during theta vs. non-theta segments for model pacemaker neurons. Middle and right, statistics on pooled data indicated that the absolute deviation from the mean rhythmicity frequency was significantly larger during non-theta segments (***, $p < 0.001$; $p = 1.46 \times 10^{-13}$, W = 10808, n = 293, Wilcoxon signed-rank test). (L) Pairs of putative pacemaker neurons recorded in anesthetized rats that show anti-phasic firing, based on the peak of their crosscorrelogram showing an offset above 50 ms during hippocampal theta. Crosscorrelograms during theta segments were color coded (blue, low correlation; yellow, high correlation; each row corresponds to a pair of neurons). (M) Crosscorrelograms of the same pairs during non-theta segments. The similarity of crosscorrelograms across theta and non-theta segments indicates stable anti-phasic firing across hippocampal states. (N) Crosscorrelograms of pairs of putative pacemaker model neurons in a realization of the model that showed in-phase synchronization. Crosscorrelograms during synchronous segments were color coded (blue, low correlation; yellow, high correlation; each row corresponds to a pair of model neurons). (O) Histogram of lags corresponding to the crosscorrelogram peaks show that most crosscorrelograms peaked around zero, indicating in-phase synchrony. (P) Crosscorrelograms of pairs of putative pacemaker model neurons in a realization of the model where anti-phasic firing occurred. Parameters: CR, 20%; baseline excitation, 70 pA with 10% variance; synaptic delay, 7 ms; synaptic weight, 1 nS. (Q) The histogram of lags corresponding to the crosscorrelogram peaks shows an over-representation of peak lags around 100 ms, corresponding to half of the theta oscillation period time. (R) Crosscorrelogram of an example pair of putative pacemaker model neurons (marked by an arrow in panel P). (S) Spike raster of the example pair with stable anti-phasic spiking.

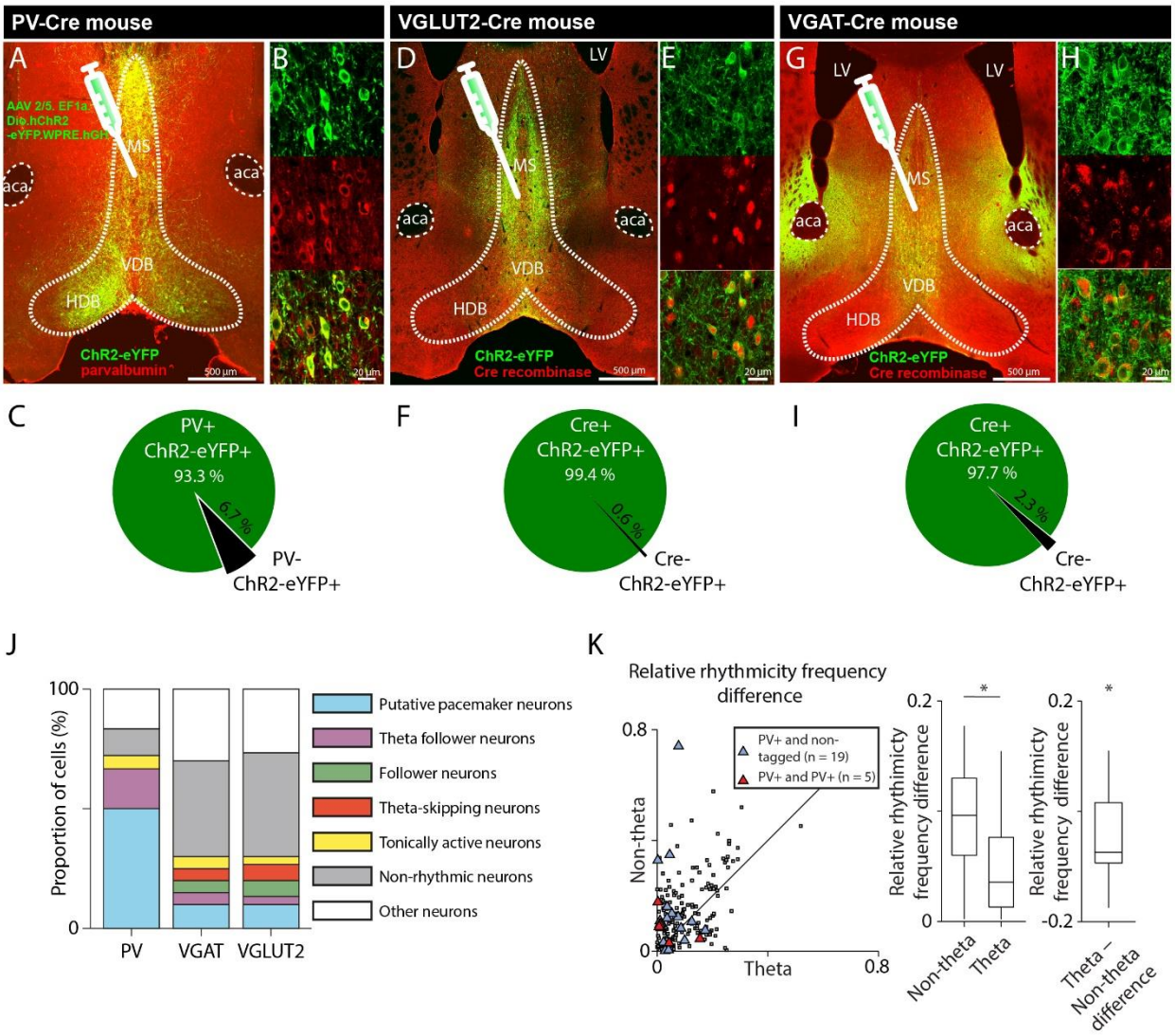

Figure S15. Channelrhodospin-2 expression is confined to targeted PV+, VGLUT2+ and VGAT+ neuronal populations. PV+ MS neurons show frequency synchronization. Related to Figure 6. (A) Confocal image of ChR2-eYFP (green) and PV (red) expression in the MS of a PV-Cre mouse injected with AAV2/5.EF1a.DIO.hChR2-eYFP-WPRE-hGH. (B) High magnification images of ChR2-eYFP expression in the MS (top) along with PV expression (middle). Composite image shown on the bottom support strong specificity of ChR2 expression in PV+ cells. (C) 93.25 percent of cells expressing ChR2-eYFP were positive for PV (n = 267 cells from 3 animals). (D) Expression of ChR2-eYFP (green) and Cre recombinase (red) in the MS of a VGLUT2-Cre mouse injected with AAV2/5.EF1a.DIO.hChR2-eYFP-WPRE-hGH. (E) High magnification images of ChR2-eYFP expression in the MS (top) along with Cre expression in VGLUT2-cre mouse line (middle). Composite image is shown on the bottom. (F) 99.43 percent of cells expressing eYFP

were positive for Cre recombinase (n = 529 cells from 3 animals). (G) Image of ChR2-eYFP (green) and Cre recombinase (red) expression in the MS of a VGAT-Cre mouse injected with AAV2/5.EF1a.DIO.hChR2-eYFP-WPRE-hGH. (H) High magnification images of ChR2-eYFP expression in the MS (top) along with Cre expression in VGAT-Cre mouse line (middle). Composite image is shown on the bottom. (I) 97.65 percent of cells expressing eYFP were positive for Cre recombinase (n = 256 cells from 3 animals), supporting the high specificity of the viral targeting of ChR2 in GABAergic cells. (J) Proportion of rhythmicity types within identified PV+, GABAergic VGAT+ and glutamatergic VGLUT2+ neurons. (K) Left, relative rhythmicity frequency difference of putative pacemaker MS neurons during theta vs. non-theta segments. Red triangles, pairs of two optogenetically identified PV+ neurons. Blue tringles, pairs of an identified PV+ and an untagged putative pacemaker neuron. Black squares, pooled data from the anesthetized rat, anesthetized mouse and awake mouse experiments, see Figure 4E. Middle and right, the relative frequency difference of pairs containing at least one identified PV+ neuron significantly decreased during theta oscillation compared to non-theta segments (*, $p < 0.05$; $p = 1.293 \times 10^{-2}$, $W = 63$, $n = 24$ pairs containing at least one PV+ neuron, Wilcoxon signed-rank test).

urethane-anesthetized rats	**urethane-anesthetized mice**	**freely moving mice**
delta-rhythmic activity dominates in non-theta state	non-rhythmic activity dominates in non-theta state	non-rhythmic activity dominates in non-theta state
substantial number of theta-skipping neurons	few theta-skipping neurons	few theta-skipping neurons
tonically active neurons decrease their firing rate upon theta onset	tonically active neurons increase their firing rate upon theta onset	tonically active neurons increase their firing rate upon theta onset
statistically significant anti-phase groups within putative pacemakers	no strong support for two anti-phasic putative pacemaker groups	no strong support for two anti-phasic putative pacemaker groups

Table S1. Major differences among rodent models of hippocampal theta oscillation. Related to Figure 2 and Figure 3.

Activity during theta	Activity during non-theta	Anesth. rat (#,%)		Anesth. mouse (#,%)		Freely m. mouse (#,%)		
theta-rhythmic	theta-rhythmic	29	7.0%	47	7.6%	35	13.2%	**Putative pacemakers (theta-bursting)**
		18	4.3%	49	7.9%	8	3.0%	**Tonically active neurons**
	delta-rhythmic	35	8.4%	12	1.9%	0	0.0%	**Follower neurons**
	non-rhythmic	67	16.1%	105	17.0%	46	17.4%	**Theta follower neurons**
delta-rhythmic	theta-rhythmic	6	1.4%	2	0.3%	1	0.4%	**Hypothetical 'inverse' neurons**
	delta-rhythmic	48	11.5%	4	0.6%	1	0.4%	**Theta-skipping neurons**
	non-rhythmic	31	7.5%	12	1.9%	5	1.9%	
non-rhythmic	theta-rhythmic	21	5.0%	36	5.8%	2	0.8%	**Probably part of the pacemaker circuit**
	delta-rhythmic	36	8.7%	14	2.3%	12	4.5%	**Delta follower neurons**
	non-rhythmic	125	30.0%	336	54.5%	155	58.5%	**Non-rhythmic neurons**
Total		**416**	**100.0%**	**617**	**100.0%**	**265**	**100.0%**	

Table S2. Number of neurons in different rhythmicity groups in the MS. Related to Figure 2 and Figure 3. Theta-rhythmic neurons were separated to theta-bursting MS neurons reported in previous studies and tonically active neurons that show rhythmic firing in the theta band but do not exhibit rhythmic bursting properties and show little synchrony with ongoing theta activity (see Figure S10). Follower neurons reflected theta versus non-theta state of the network. For part of neurons, this type of activity was only confirmed statistically for either of these states (theta followers and delta followers). Neurons that were delta-rhythmic during theta oscillation were identified as theta-skipping neurons. (Figure S9 focuses on those cells that were delta-rhythmic during both states.) Neurons that were theta-rhythmic during non-theta segments but found non-rhythmic during theta segments may be part of the pacemaker group, where the amount of data (number of spikes and length of identified theta segments) may have been insufficient for statistical detection of rhythmicity during theta. It is theoretically possible that some MS neurons would be theta-rhythmic in non-theta state but delta-rhythmic in theta state. However, this group was negligible in all three data sets.

	Anesth. rat	Anesth. mouse	Freely m. mouse	Pooled	Figure	Model	Figure
Firing rate (Hz)	1.04×10^{-4}	7.98×10^{-6}	1.34×10^{-2}	$\mathbf{1.40 \times 10^{-9}}$	Fig. 4A	8.50×10^{-50}	Fig. S14F
Rhythmicity frequency (Hz)	1.37×10^{-3}	1.53×10^{-1}	2.21×10^{-5}	$\mathbf{2.64 \times 10^{-7}}$	Fig. 4B	6.35×10^{-41}	Fig. S14G
Intraburst interspike interval (ms)	2.95×10^{-3}	3.30×10^{-1}	1.95×10^{-4}	$\mathbf{7.34 \times 10^{-5}}$	Fig. 4C	7.60×10^{-50}	Fig. S14H
Theta cycle skipping	2.06×10^{-3}	4.41×10^{-5}	4.61×10^{-1}	$\mathbf{3.02 \times 10^{-6}}$	Fig. 4D	3.47×10^{-45}	Fig. S14I
Relative rhythmicity frequency difference	4.53×10^{-3}	5.61×10^{-2}	1.48×10^{-5}	$\mathbf{3.17 \times 10^{-6}}$	Fig. 4E	2.20×10^{-30}	Fig. 5F Fig S14J
Rhythmicity frequency deviations	3.70×10^{-3}	4.61×10^{-1}	2.47×10^{-3}	4.19×10^{-4}	Fig. 4F	1.46×10^{-13}	Fig. S14K

Table S3. Statistics for synchronization analysis in individual data sets. Related to Figure 4. Since all three data sets showed similar results, Figure 4 displays pooled results. This table provides p-values (two-sided Mann-Whitney U-test for unpaired samples and two-sided Wilcoxon signed-rank test for paired samples) for the three data sets separately and pooled. Corresponding statistical tests on simulated data are also indicated.

nature communications hangya.balazs_256_24

Article

https://doi.org/10.1038/s41467-023-41746-0

The medial septum controls hippocampal supra-theta oscillations

Received: 27 July 2022

Accepted: 15 September 2023

Published online: 10 October 2023

Check for updates

Bálint Király[1,2], Andor Domonkos[3], Márta Jelitai[3], Vítor Lopes-dos-Santos[4], Sergio Martínez-Bellver[1,5], Barnabás Kocsis[1,6], Dániel Schlingloff[1], Abhilasha Joshi[7], Minas Salib[7], Richárd Fiáth[6,8], Péter Barthó[8], István Ulbert[6,8], Tamás F. Freund[9], Tim J. Viney[7], David Dupret[4], Viktor Varga[3] & Balázs Hangya[1]

Hippocampal theta oscillations orchestrate faster beta-to-gamma oscillations facilitating the segmentation of neural representations during navigation and episodic memory. Supra-theta rhythms of hippocampal CA1 are coordinated by local interactions as well as inputs from the entorhinal cortex (EC) and CA3 inputs. However, theta-nested gamma-band activity in the medial septum (MS) suggests that the MS may control supra-theta CA1 oscillations. To address this, we performed multi-electrode recordings of MS and CA1 activity in rodents and found that MS neuron firing showed strong phase-coupling to theta-nested supra-theta episodes and predicted changes in CA1 beta-to-gamma oscillations on a cycle-by-cycle basis. Unique coupling patterns of anatomically defined MS cell types suggested that indirect MS-to-CA1 pathways via the EC and CA3 mediate distinct CA1 gamma-band oscillations. Optogenetic activation of MS parvalbumin-expressing neurons elicited theta-nested beta-to-gamma oscillations in CA1. Thus, the MS orchestrates hippocampal network activity at multiple temporal scales to mediate memory encoding and retrieval.

Hippocampal theta oscillations (4–12 Hz) of the local field potential (LFP) reflect rhythmic inputs that orchestrate neuronal firing, occurring typically during exploratory or memory-guided behaviors or rapid eye movement (REM) sleep, and have been linked to learning and memory[1–9]. Previous studies revealed an important diversity of theta cycles along different dimensions, including length[10–13] and shape[14] of the cycles or the presence of phase-coupled oscillations in the beta (12-30 Hz) and gamma (30-140 Hz) frequency bands[15–22]. Importantly, in rodents performing memory tasks, cycle-by-cycle variations with differential contributions to memory processes were found based on theta-nested spectral components (tSCs), related to distinct spiking dynamics of CA1 pyramidal neurons[15,23].

The medial septum has a broad role in coordinating hippocampal rhythmic activity through cholinergic, GABAergic and glutamatergic projections[12,24–33]. Importantly, the MS has long been proposed as a key nucleus in the generation of hippocampal theta oscillations[30,34–38], while the roles of other subcortical structures including the supramammillary nucleus[39–41] and the nucleus incertus[42–46] are increasingly recognized. Parvalbumin-expressing (PV) GABAergic neurons of the MS, targeting the inhibitory neurons of the CA1, CA3 and dentate gyrus areas[24,47,48], have been suggested to play a pivotal role in controlling

[1]Lendület Laboratory of Systems Neuroscience, Institute of Experimental Medicine, Budapest, Hungary. [2]Department of Biological Physics, Institute of Physics, Eötvös Loránd University, Budapest, Hungary. [3]Subcortical Modulation Research Group, Institute of Experimental Medicine, Budapest, Hungary. [4]Medical Research Council Brain Network Dynamics Unit, Nuffield Department of Clinical Neurosciences, University of Oxford, Oxford, UK. [5]Department of Anatomy and Human Embryology, Faculty of Medicine and Odontology, University of Valencia, Valencia, Spain. [6]Faculty of Information Technology and Bionics, Pázmány Péter Catholic University, Budapest, Hungary. [7]Department of Pharmacology, University of Oxford, Oxford, UK. [8]Institute of Cognitive Neuroscience and Psychology, Research Centre for Natural Sciences, Budapest, Hungary. [9]Laboratory of Cerebral Cortex Research, Institute of Experimental Medicine, Budapest, Hungary. e-mail: hangya.balazs@koki.hu

hippocampal theta rhythm[49–52]. Theta waves entrain faster, supra-theta oscillations of the beta and gamma bands, thought to be routed from different areas representing distinct memory processes[15,18,22,53,54]. According to the current models, these oscillations are generated by different extra- and intrahippocampal sources, mainly through inputs from the CA3 (slow gamma, 30–50 Hz), the entorhinal cortex (mid-gamma, 50–100 Hz) or local CA1 networks (fast gamma, 100–140 Hz)[19,53–60]. However, the burst structure of MS neurons suggests the septal presence of beta/gamma-band spectral components[61–63]. Indeed, entorhinally projecting Orchid neurons of the MS can couple to CA1 mid-gamma oscillations[64], and low-rhythmic MS neurons, projecting to CA3 and dentate gyrus, can couple to slow- and mid-gamma bands in dorsal CA1[47]. This raises the question whether hippocampal theta-nested beta and gamma oscillations couple to MS activities.

To address whether supra-theta oscillations in the CA1 are mediated by the MS, we recorded CA1 LFP and MS single neuron activity simultaneously in freely moving mice as well as urethane-anesthetized mice and rats. We uncovered a wide-spread presence of beta/gamma band spectral components in the MS, which showed transient coherence with CA1 spectra at the time of MS neuron bursts. In the CA1, we identified distinct tSCs representing beta (tSC1), slow gamma (tSC2), mid-gamma (tSC3 and tSC4) and fast gamma (tSC5) oscillations[15,53,54,57–59]. We found that firing rates and theta-coupling of MS neurons changed with the occurrence of distinct CA1 tSCs, suggesting that tSCs are also represented in MS network states. Furthermore, the majority of MS neurons, including most constitutively theta-rhythmic cells, showed strong phase-coupling to one or more CA1 tSCs. To better understand the causal relations in the reciprocally connected septo-hippocampal circuit, we determined that most MS neurons best locked to phase values of the tSC signals occurring at a small temporal delay, i.e., activity changes of most MS neurons anticipated correlated changes in hippocampal tSCs. Next, we investigated anatomically defined MS Orchid, Teevra and Low-rhythmic Neurons[47,48,64] with known projection targets, which revealed the coupling of entorhinal-projecting, parvalbumin-expressing MS Orchid cells to mid-gamma components and CA3-projecting MS cells to slow gamma components, suggesting that indirect pathways between the MS and CA1 via EC vs. CA3 mediate different gamma components. These results encouraged us to test whether MS GABAergic neurons are capable of evoking theta-nested beta and gamma oscillations, by optogenetically stimulating PV-expressing MS neurons with theta-modulated bursts of laser light, mimicking physiological tSCs. We found that MS PV stimulation elicited artificial tSCs in the CA1 that resembled their physiological counterparts in spectral content and laminar distribution, demonstrating that the MS GABAergic network can mediate supra-theta hippocampal oscillations. In contrast with previous models, these results raise the possibility that the MS has a hitherto overlooked role in CA1 oscillation genesis beyond the theta frequency range.

Results

Supra-theta spectral components are present in the MS and the CA1 of freely moving mice

To test whether MS neuronal activity correlates with hippocampal theta-nested beta and gamma oscillations, we analyzed dual silicon probe recordings from mice ($n = 6$) moving along a linear track, monitoring CA1 local field potentials (LFPs) concurrently with MS neuronal spiking ($n = 365$ neurons; Fig. 1a). Many MS neurons fired bursts of action potentials, with inter-spike intervals corresponding to beta/gamma band activity (Fig. 1a, b). In accordance, spectral analysis revealed strong beta/gamma band activities besides theta-rhythmicity of MS single neurons (Fig. 1c). We tested whether these beta/gamma band spectral components were coherent with CA1 LFP and found an increase in MS-CA1 coherence in the supra-theta bands after the burst onset of individual MS units lasting ~50 ms, likely corresponding to bursts of action potentials (Fig. 1d).

Next, to decompose the CA1 LFP recorded from the radiatum layer into theta and supra-theta components, we applied single-cycle spectral profiling using empirical mode decomposition (EEMD), an adaptive unsupervised spectral decomposition technique well-suited for non-stationary signals[65]. By performing independent component analysis (ICA) on the supra-theta spectral content of the theta cycles, we confirmed the presence of five different theta-nested spectral components[15] (tSCs; Fig. 1e) that consistently occurred across individual theta cycles, but remained hidden when only the average spectral signature of all theta cycles was considered (Fig. 1f). Each tSC attributed large weights to different characteristic frequency components in the frequency range spanning beta to fast gamma bands (Fig. 1g and Supplementary Fig. 1a, peak frequencies of the average power spectra across all recordings: tSC1: 20 Hz, tSC2: 32 Hz, tSC3: 50 Hz, tSC4: 74 Hz, tSC5: 179 Hz). All five tSCs were robustly detected across mice ($n = 6$) and recordings ($n = 31$) and an average of 30% of all theta cycles contained at least one strong tSC (see Methods).

We asked whether the presence of strong tSCs was correlated with other parameters in which theta cycles showed diversity. First, we found that theta cycles strongly expressing a tSC had a higher theta frequency than those containing no strong tSCs (up to >1 Hz difference on average) and cycles with gamma frequency tSCs (tSC2-5) had higher theta frequency than tSC1-expressing cycles (Fig. 1h and Supplementary Fig. 1b, repeated measures ANOVA with Tukey's test for post hoc analysis, $p < 0.001$). We also found a positive correlation between the strength of each tSC and theta frequency (Supplementary Fig. 1d, Spearman correlation, $p < 0.001$, tSC4 strength was the most correlated). Second, we investigated whether cycles during long (>30 s) continuous theta-dominant periods differed from those during shorter periods or near theta segment boundaries. During long theta epochs, tSCs were more frequent, and each tSC was detected in similar proportions of theta cycles (similarly to ref. 15). In contrast, both during short theta epochs and non-theta-to-theta transitions, tSC1-expressing cycles were overrepresented and gamma frequency tSCs (tSC2-5) were underrepresented (Fig. 1i).

Since hippocampal theta and gamma oscillations are correlated with movement and velocity, we tested the expression of tSCs as a function of animal speed. In line with previous studies[66], we found that mice were significantly faster during theta cycles with strong gamma tSCs (tSC2-5) compared to tSC1-expressing cycles or cycles with no tSC (repeated measures ANOVA with Tukey's test for post hoc analysis, $p < 0.01$, Fig. 1j and Supplementary Fig. 1c). The strength of gamma tSC expression was positively correlated with animal speed (Supplementary Fig. 1e, Spearman correlation, $p < 0.001$, strongest correlation for tSC4). In contrast, tSC1 expression showed a weak negative correlation with speed. Since theta frequency also correlated with animal speed, we calculated partial correlations among tSC strength, theta frequency and velocity. All correlations remained strongly significant ($p < 0.001$) and decreased only slightly by removing the effect of the third variable, demonstrating that these correlations occurred independently (Supplementary Fig. 1f). Overall, these data confirmed the presence of distinct theta-nested spectral components in mouse CA1 LFP recordings.

MS single neuron firing is correlated with hippocampal tSCs

To test whether MS neurons' activity patterns are linked to hippocampal tSCs, we first examined changes in the firing rate of MS single units across theta cycles with different tSCs ($n = 198$ MS neurons with firing rate > 3 Hz and stable spike amplitude). We found that MS neurons were more active during theta cycles expressing tSCs than during those without strong tSC presence (Figs. 2a and 2b left, repeated measures ANOVA with Tukey's test for post hoc analysis, $p < 0.01$). Furthermore, the occurrence of gamma frequency tSCs, particularly

https://doi.org/10.1038/s41467-023-41746-0

hangya.balazs_256_24

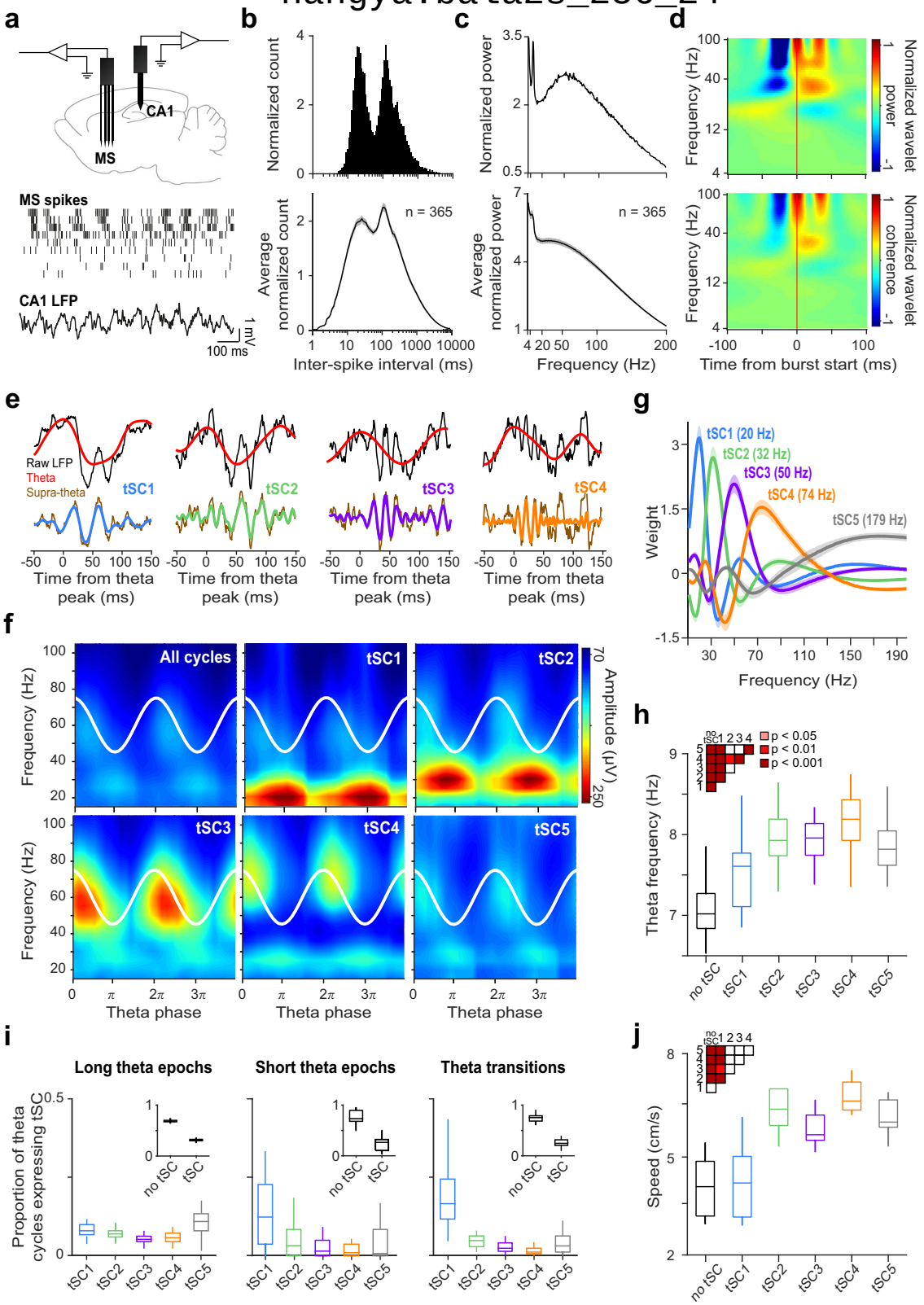

tSC4 in the mid-gamma range, were associated with the highest MS firing rates (82%, 163/198 neurons were most active during theta cycles with gamma-band tSCs, Figs. 2a and 2b, repeated measures ANOVA with Tukey's test for post hoc analysis, $p < 0.05$, example neurons #1 and #2). However, there was a subset of MS neurons (14%, 27/198) that were the most active during cycles expressing the beta range tSC1 component (Figs. 2a and 2b right, example neuron #3).

Many MS neurons show phase-coupling to hippocampal theta oscillation[63,67]. We hypothesized that a possible association between hippocampal tSCs and MS activity might also be reflected in differential theta-phase coupling properties of MS neurons. Therefore, we tested whether MS neurons phase-coupled to hippocampal theta (91%, 181/198; Rayleigh's test for circular uniformity, $p < 0.01$) changed their preferred theta phase (mean angle) and phase-coupling strength

Fig. 1 | Supra-theta spectral components in the MS and the hippocampal CA1 radiatum layer of freely moving mice. a Top, schematic of dual silicon probe recordings from the hippocampal CA1 region and the MS. Bottom, example of synchronously recorded CA1 LFPs and MS extracellular spike rasters. **b** Inter-spike interval histogram of an example MS neuron (top) and average of all recorded MS neurons (bottom, $n = 365$ neurons from 6 awake mice). **c** Power spectrum of an example MS neuron (top) and average of all recorded MS neurons (bottom, $n = 365$). **d** Top, normalized average wavelet spectrogram of an example MS spike train (convolved by a Gaussian window, see Methods) triggered on first spikes of bursts. Bottom, average coherence between MS spiking and CA1 LFP triggered on first spikes of bursts of an example MS neuron. Spectrograms were normalized by the mean power for each frequency, thus visualizing the spectral changes around the triggering event. **e** Example theta cycles dominated by different tSCs. Black, raw LFP signal; red, theta band signal; brown, supra-theta signal extracted by EEMD. Blue, green, purple and orange lines show the dominant tSCs in each example cycle. **f** Mean amplitude of supra-theta spectral components as a function of theta phase was computed from the raw LFP of an example session, for all cycles (top left) and for cycles strongly expressing a given tSC. Two theta cycles are shown, indicated by white cosine curves. **g** Average power spectrum of tSCs across all sessions. Peak frequencies are shown in the brackets. Error shades show the standard error of the mean. **h** Frequency of theta cycles expressing different tSCs. **i** Average proportion of theta cycles expressing each tSC during long theta periods (left), short theta epochs (middle) and around theta segment boundaries (right). Insets show the proportion of theta cycle expressing any of the tSCs. **j** Speed of mice during theta cycles expressing different tSCs. Box-whisker plots show median, interquartile range and non-outlier range in panels **h**–**j**. Differences were tested with two-sided repeated measures ANOVA and Tukey's post hoc test and significant differences are indicated by the color-coded matrices in (**h** and **j**). Source data are provided as a Source Data file.

(mean resultant length) according to the presence of hippocampal tSCs. Indeed, we found many examples of MS neurons showing different phase-coupling strength (Fig. 2a), and sometimes even different preferred theta phase (example neuron #2) depending on which tSC was present. On average, theta-coupling was strongest in theta cycles expressing gamma frequency tSCs, particularly mid-gamma tSC4 (repeated measures ANOVA with Tukey's test for post hoc analysis, $p < 0.001$), and weakest in cycles expressing the beta range tSC1 ($p < 0.01$, Fig. 2c and d). The majority of theta-coupled MS neurons fired at an earlier phase in tSC1-expressing cycles compared to other theta cycles, most prominently in comparison with tSC4-expressing cycles (60%, 108/181, Fig. 2e; largest difference in preferred phase was found for the neurons most active during tSC1 cycles; Supplementary Fig. 2).

MS neurons often show phase-locked rhythmic bursting activity during hippocampal theta oscillations[48,50,68,69]. Furthermore, constitutively bursting (CB) MS neurons, which express theta-rhythmic burst firing both in the presence and absence of CA1 theta rhythms, have been proposed to be important part of the theta-generating subcortical network (referred to as putative pacemakers by some studies)[48–50,61,63]. To test whether this rhythmicity property is correlated with the tSC-related firing behavior of MS neurons, we classified MS neurons based on their rhythmicity during hippocampal theta and non-theta periods[52] (Supplementary Fig. 3, see also Methods). Along with the putative pacemaker constitutively bursting neurons (10% of all recorded MS units, Supplementary Fig. 3a–d), we identified two additional special subpopulations based on their rhythmic properties. Theta-associated bursting neurons (12%) were theta-rhythmic but only when theta oscillation was detected in the hippocampus (Supplementary Fig. 3e-h). Tonically active neurons (3%) showed regular rhythmic activity with little to no phase coupling to hippocampal LFP (Supplementary Fig. 3i–l). Constitutively bursting and theta-associated bursting populations showed increased firing rate and theta coupling in theta cycles with gamma-band tSCs, especially tSC4 (Supplementary Figs. 2g, h and 4b, c), similarly to the entire population of theta-coupled MS neurons (Fig. 2b–d). Interestingly, tonically active MS neurons were also firing more in theta cycles with gamma-band tSCs compared to those expressing tSC1, despite their lack of phase coupling to theta (Supplementary Fig. 4d, repeated measures ANOVA with Tukey's test for post hoc analysis, $p < 0.05$).

Finally, we tested whether burst properties such as intra-burst frequency, intra-burst spike number or theta-cycle skipping[47,70,71] showed tSC-associated differences. We found that while intra-burst frequencies of theta-coupled MS neurons were higher in cycles with strong tSCs (except for tSC5 cycles, Fig. 2f, repeated measures ANOVA with Tukey's test for post hoc analysis, $p < 0.05$), burst parameters were otherwise surprisingly stable across different types of theta cycles (Supplementary Fig. 4a-c).

Most MS neurons are phase-coupled to beta-gamma band hippocampal tSCs

In the previous section we demonstrated that the firing of MS single units was robustly modulated on a theta cycle basis according to the presence of different tSCs. To directly test whether MS neurons' spiking correlated with hippocampal tSCs on shorter time scales, we first calculated hippocampal LFP averages triggered on the spikes of each medial septal neuron (spike triggered LFP average, STA; Fig. 3a, top). This analysis allows visualizing the average hippocampal local field activity around MS action potentials. Beyond the well-documented phase locking of septal firing to hippocampal theta cycles, these STA calculations often revealed additional faster oscillatory components, indicating that MS neurons may phase lock to supra-theta hippocampal frequency bands as well (Fig. 3a top, black arrowheads). To confirm this, we next calculated average LFP spectrograms triggered on MS action potentials (spike triggered LFP spectrograms, STS; Fig. 3a). Analogous to STA, this analysis shows the average LFP spectral amplitude and phase around MS spikes. We normalized these spectrograms for each individual frequency, revealing those spectral components that change near MS firing. This normalization removed the stationary theta-frequency component from the STS power and clearly revealed spectral increases associated with MS firing in the beta and gamma bands (Fig. 3a, middle and bottom).

This prompted us to test whether individual MS neurons showed phase-coupling to hippocampal tSCs. Indeed, we found many examples where MS spikes were coupled to tSC phases (Fig. 3b and Supplementary Fig. 5). Neurons phase-coupled to locally or distantly recorded oscillatory activity often show a temporal offset between the two signals, which can be estimated by calculating the phase-locking strength as a function of possible time lags and localizing the maximum of this function (Z-shift method)[49,72]. To estimate and account for these offsets, we calculated Rayleigh's Z-statistic for each MS neuron, quantifying phase-locking strength, with temporal shifts added to the spikes in the −100 ms – 100 ms range. We found that 51% of all recorded MS neurons were phase-coupled to at least one tSC (Fig. 3c; $p < 0.05$ at any of the temporal shifts, Rayleigh's test for circular uniformity, type I errors were controlled with Storey's false discovery rate method[73]; no robust phase coupling to tSC5 were found). This was not explained by theta-phase correlations of tSCs and MS spikes, since shuffling spikes across theta cycles reduced coupling strength in 93% of cases (Supplementary Fig. 6a) and removed most of the significant phase-coupling of MS neurons to tSCs (72, 95, 100 and 95% for tSC1, 2, 3 and 4, respectively; Supplementary Fig. 6b). Moreover, a closer look at intra-burst spike timing revealed a subset of MS neurons showing correlations of MS intra-burst frequencies with the concurrent tSCs (Supplementary Fig. 7). The preferred

https://doi.org/10.1038/s41467-023-41746-0

hangya.balazs_256_24

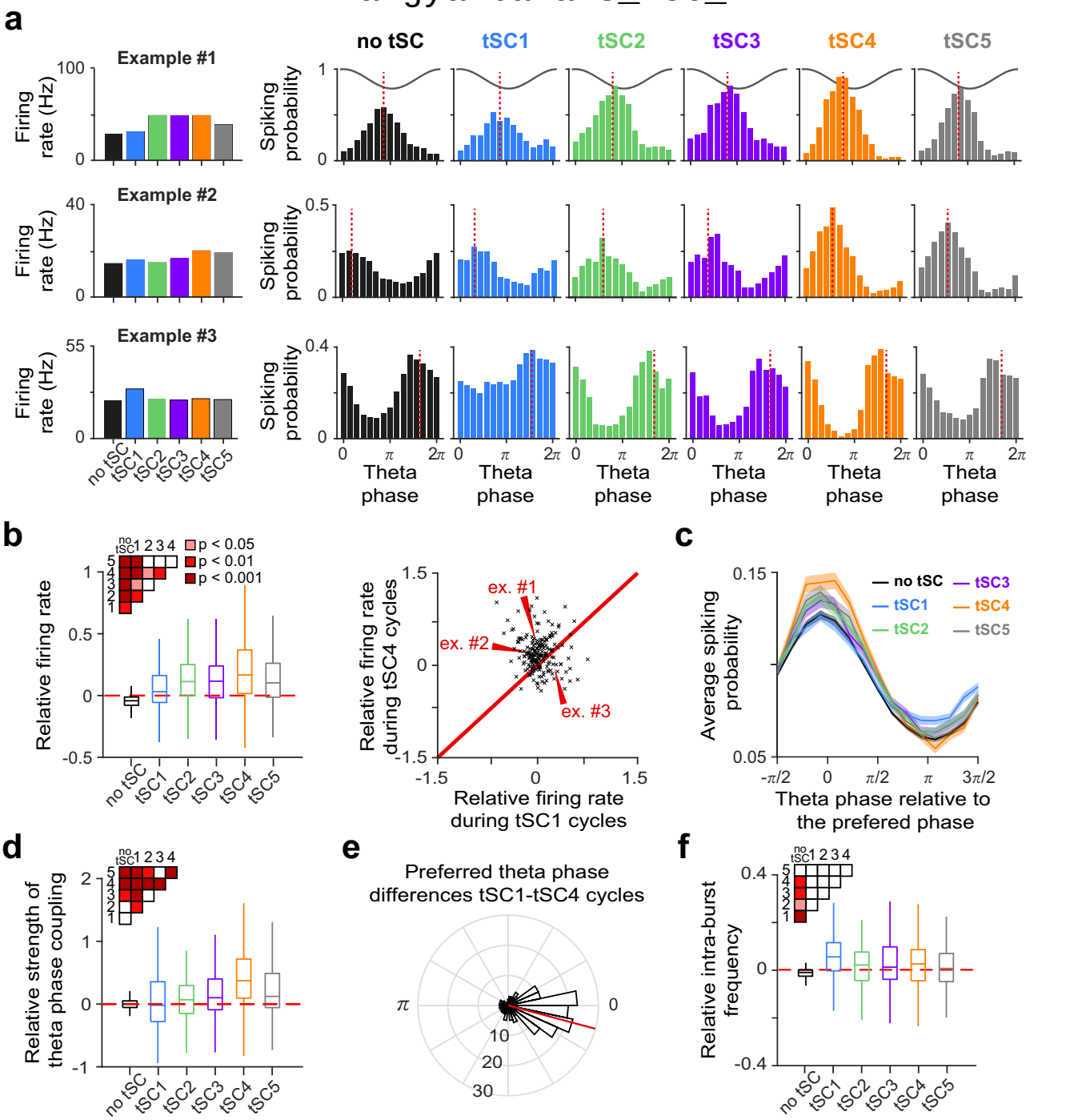

Fig. 2 | MS single neuron firing is correlated with hippocampal tSCs. a Three example neurons' average firing rate (left) and theta phase histogram (right) during theta cycles expressing different tSCs. Cosine curves indicate the theta phase; red dashed lines show the preferred phase. **b** Left, firing rate distribution of MS neurons ($n = 198$) as a function of tSC presence, relative to the average firing rate over all cycles (red dashed line). Boxes and whiskers show median, interquartile range and non-outlier range. Differences were statistically tested with two-sided repeated measures ANOVA, followed by Tukey's test for post hoc comparison. Significant differences are indicated by the color-coded matrix in the inset. Right, relative firing rate of MS neurons during tSC1-expressing theta cycles vs. tSC4-expressing cycles. Example neurons from panel **a** are marked by red arrowheads. **c** Average theta phase histogram (relative to the preferred phase) of theta-phase-coupled MS neurons' ($n = 181$) firing during theta cycles with different tSCs. Error shades show the standard error of the mean. **d** Phase coupling strength distribution of theta-coupled MS neurons ($n = 181$) measured by the mean resultant length over cycles expressing a particular tSC, relative to the average coupling strength over all cycles (red dashed line). Boxes and whiskers show median, interquartile range and non-outlier range. Differences were statistically tested with two-sided repeated measures ANOVA, followed by Tukey's test for post hoc comparison. Significant differences are indicated by the color-coded matrix in the inset. **e** Phase histogram of differences between the preferred phase of theta-phase-coupled MS neurons in tSC1 and tSC4 cycles. The red line indicates the mean difference. **f** Intra-burst frequency distribution of theta-coupled MS neurons ($n = 181$) as a function of tSC expression, relative to the average intra-burst frequency over all cycles (red dashed line). Boxes and whiskers show median, interquartile range and non-outlier range. Differences were statistically tested with two-sided repeated measures ANOVA, followed by Tukey's test for post hoc comparison. Significant differences are indicated by the color-coded matrix in the inset. Source data are provided as a Source Data file.

https://doi.org/10.1038/s41467-023-41746-0

hangya.balazs_256_24

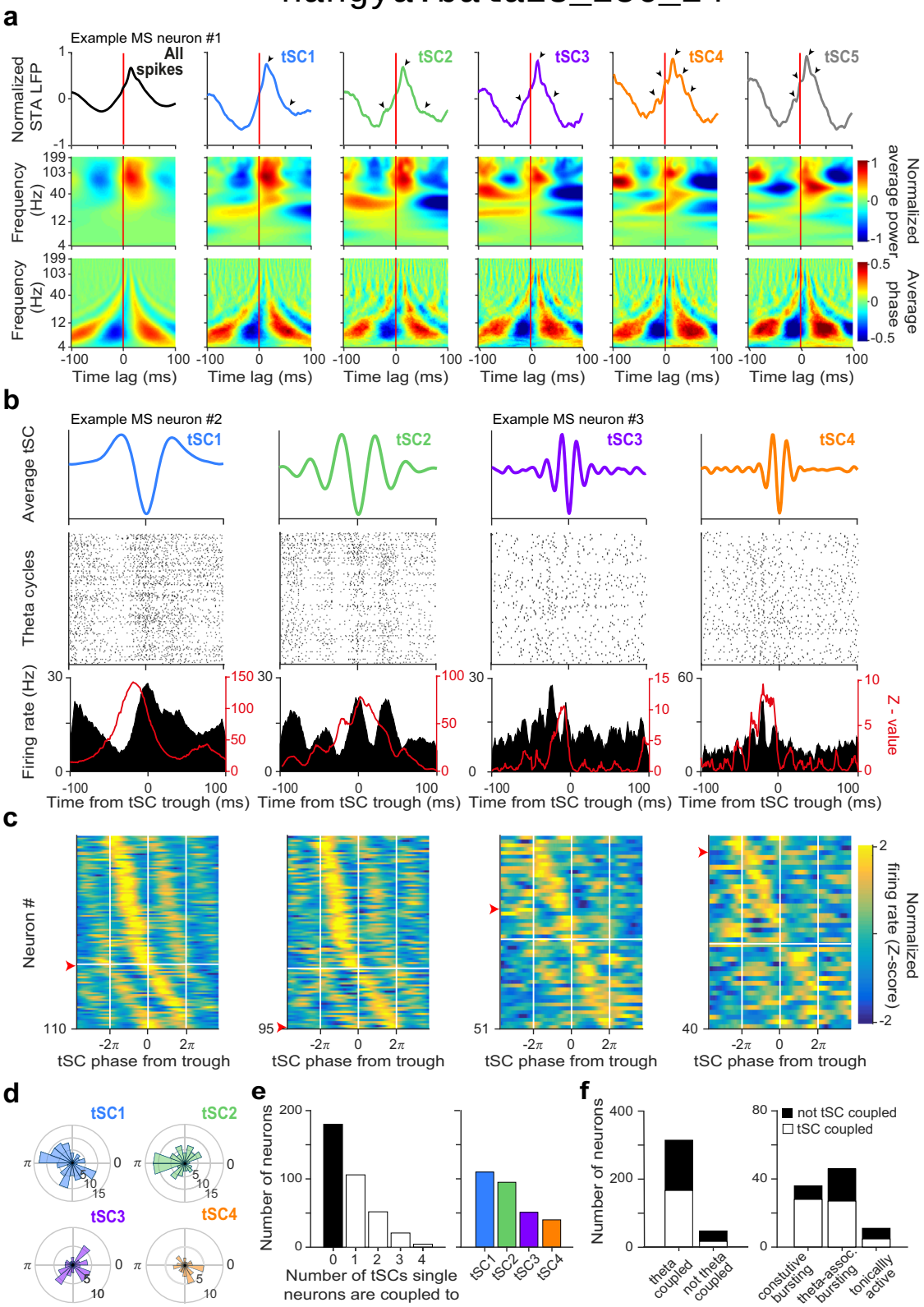

phase of MS neurons covered the entire tSC cycles, albeit not uniformly in case of tSC1 and tSC2 (Fig. 3d, Rayleigh-test; tSC1, $p = 0.0446$; tSC2, $p = 0.0024$). Several neurons were coupled to more than one tSC and coupling to slower tSCs was more frequent than to faster tSCs (Fig. 3e and Supplementary Fig. 5). Phase-locking to tSCs was more common among cells phase-coupled to hippocampal theta as well (53% vs. 35% in the non-theta-coupled subpopulation), and tSC-coupled MS neurons showed higher firing rate, stronger theta-coupling, longer bursts and more gamma-band inter-spike intervals than MS neurons not significantly coupled to tSCs (Supplementary Fig. 8). Interestingly, the majority of constitutively bursting (78%) and theta-associated bursting (59%) neurons were strongly coupled to tSCs, while 5 of 11 tonically active neurons showed tSC coupling (Fig. 3f).

Fig. 3 | MS neurons show phase coupling to hippocampal tSCs. a Top, spike triggered averages (STA) of the raw CA1 LFPs of an example MS neuron. Theta cycles were sorted by tSC expression (from left to right, all cycles included, theta cycles expressing tSC1 to tSC5). Arrowheads indicate tSC peaks. Middle, spike triggered spectral power images (STS power) of the CA1 LFP for the same example neuron. Bottom, corresponding spike triggered spectral phase images (STS phase) of the same MS neuron. **b** Firing pattern of two tSC-coupled example MS neurons (example neuron #2 to tSC1 and tSC2, example neuron #3 to tSC3 and tSC4). Top, average tSC signals. Middle, raster plots of spike times aligned to the most negative trough of the tSC signal within each theta cycle. Bottom, peri-event time histograms (PETHs) corresponding to each spike raster (black; y-axis on the left) and Rayleigh's *Z*-value as a function of temporal offset between hippocampal tSCs and MS spike trains (red; y-axis on the right). **c** *Z*-scored phase histograms of all tSC-coupled MS neurons, sorted into four groups based on the tSC they are coupled to (blue, low firing rate; yellow, high firing rate). Zero phase corresponds to tSC troughs (white vertical lines). Cells within each group are sorted by their preferred phase in two blocks: top, cells with maximum firing rate before the most negative tSC trough; bottom, cells with maximal firing after the most negative tSC trough. Red arrowheads mark the example neurons from panel (**b**). **d** Histograms of preferred tSC phases for all tSC-coupled MS neurons, sorted into four groups based on the tSC they are coupled to. **e** Left, histogram of the number of tSCs single MS neurons are coupled to. Right, number of neurons phase-coupled to each tSC. **f** Stacked bar chart showing the proportion of tSC-coupled neurons (empty bars) as a function of their theta-coupling (left) and rhythmic firing properties (right). Source data are provided as a Source Data file.

MS neurons temporally lead hippocampal beta-gamma band activity

To determine the direction of possible causal relationships between MS and hippocampal activity, we investigated whether MS activity changes consistently anticipated or lagged correlated changes in hippocampal tSCs. For that, we quantified the coupling strength (Rayleigh's Z-value) between MS firing and hippocampal tSCs as a function of a temporal lag, similar to a crosscorrelation analysis. Peak coupling strength in the negative domain indicated that the MS neuron best coupled to the future of the hippocampal tSC, thus temporally led hippocampal population activity. We examined the distribution of the optimal lags that provided the strongest coupling, and the average of the normalized *Z*-value functions for tSC-coupled MS neurons (Fig. 4). We found that the majority of the tSC-coupled MS neurons preceded the corresponding hippocampal tSCs, indicated by (i) negative optimal lags in 58% of the neurons (tSC1, 65%; tSC2, 52%; tSC3, 55%; tSC4, 56%; median optimal lags, tSC1, −8 ms; tSC2, −1 ms; tSC3, −6 ms; tSC4, −9 ms), (ii) negative peak locations of the average Z-value functions (tSC1, −8 ms; tSC2, −4 ms; tSC3, −8 ms; tSC4, −9 ms), and (iii) larger area under the average Z-value function in the negative vs. the positive half-plane (the lags splitting the area under the curve to two equal halves: tSC1, −6 ms; tSC2, −5 ms; tSC3, −6 ms; tSC4, −7 ms). Furthermore, the vast majority (81%) of tSC-coupled constitutively bursting neurons were preceding tSCs (tSC1, 96%; tSC2, 71%; tSC3, 73%; tSC4, 71%; Supplementary Fig. 9), with a significantly larger lag compared to the rest of the coupled population ($p = 0.0024$, one-tailed Mann-Whitney U-test; the lags splitting the areas to equal halves: tSC1, −13 ms; tSC2, −11 ms; tSC3, −9 ms; tSC4, −5 ms). Theta-associated bursting MS neurons showed similar temporal properties for tSC1 and tSC2 (Supplementary Fig. 10, $p = 0.033$, one-tailed Mann-Whitney U-test; preceding neurons: tSC1, 83%; tSC2, 65%; lags splitting the areas to equal halves: tSC1, −11 ms; tSC2, −8 ms).

Revealing the optimal lag between spike timing of each tSC-coupled MS neuron and the concurrent tSCs allowed us to align MS spikes with the corresponding tSC cycles, which enabled further refinement of the correlation analysis between MS intra-burst spike timing and tSCs. We found systematic tSC cycle length variations, with cycles around the largest trough being slower than flanking cycles. This slowing of tSCs was reflected in longer time intervals between corresponding troughs and peaks of MS firing rate changes (Supplementary Fig. 11). These correlations between MS intra-burst spike timing and concurrent tSCs suggest that the MS might be closely integrated into the hippocampal gamma generation mechanisms.

Differential coupling of anatomically identified MS cells to CA1 tSCs

Several kinds of neurons in the MS have been defined based on their combined firing patterns, neurochemical profile, and cortical projection targets[47,48,64] (Fig. 5a). Based on the differential engagement of CA1 inputs in theta-nested slow, mid and fast gamma oscillations[21,22,54,59], we reasoned that these defined MS cells may participate differently in CA1 tSCs of distinct frequencies, in correlation with their projections to CA1 input regions. To test this, we analyzed MS neurons recorded and labeled juxtacellularly in awake mice, with concurrent recordings of CA1 LFP, from three studies[47,48,64] (Fig. 5b).

GABAergic MS Teevra cells fire short-duration theta-rhythmic bursts, project mainly to the CA3 (some of them also to CA1 to a lesser degree), target PV+ axo-axonic and CCK+ interneurons, and are themselves PV-expressing[48]. We analyzed $n = 9$ Teevra cells from 9 mice and found that they mostly couple to beta/slow-gamma tSC1 ($n = 5/9$) and tSC2 ($n = 4/9$), while no coupling to faster tSCs was detected (Fig. 5c, d).

MS Orchid cells fire longer duration theta-bursts, send projections to the entorhinal cortex, the dorsal presubiculum and the retrosplenial cortex, target PV+ and nNOS+ interneurons, and are themselves PV-expressing[64]. We analyzed $n = 7$ Orchid cells from different mice and found that these neurons could couple to both low- and mid-gamma tSCs (Fig. 5c and Supplementary Fig. 5c, tSC1, $n = 7/7$; tSC2, $n = 6/7$; tSC3, $n = 4/6$; tSC4, $n = 3/6$; one neuron could not be tested for tSC3 and 4 due to insufficient data, see Methods).

Low rhythmic neurons (LRNs) form a group of MS cells that fire with a lower degree of rhythmicity, are suppressed during CA1 sharp-wave ripples and mostly lack detectable PV immunoreactivity, with common projections mainly to CA3 and the dentate gyrus[47]. By analyzing $n = 10$ LRNs from separate awake mice (Fig. 5c), we found that they showed coupling to the beta-band tSC1 ($n = 6/10$), and only occasional coupling to other tSCs (tSC2, $n = 3/10$; tSC3, $n = 0/10$; tSC4, $n = 1/8$; two neurons could not be tested for tSC4 due to insufficient data, see Methods). LRN neurons coupled to tSC1 or tSC2 but not to tSC4 were projecting to CA3 ($n = 3/3$, no projection data for two neurons). Interestingly, the only tSC4-coupled LRN neuron (MS104e) was a remarkable outlier sharing some properties of Orchid neurons: it was coupled to both tSC1 and tSC2, expressed PV, projected to the CA1, retrosplenial cortex, dorsal subiculum and dorsal presubiculum via the fornix and did not project to CA3 or dentate gyrus. The group of LRNs coupled only to tSC1 (cells MS16d, TV77q, TV78l) comprised the PV-negative Calbindin-negative subpopulation of LRNs[47].

Next, we visualized the distribution of preferred phases of these anatomically identified MS neurons relative to the different tSCs (Fig. 5d). We observed a non-uniform distribution of phase preference in case of tSC1 and tSC2, similar to our previous, unlabeled cell data (Fig. 3d), with different identified MS neuron types exhibiting tendencies of firing at distinct tSC phases (Fig. 5d bottom). We also tested whether Teevra, Orchid and LRN neurons preceded or followed CA1 tSC activity by repeating the time-shifted phase coupling analysis (Fig. 4) and found a clear temporal antecedence in case of the Orchid neurons (Fig. 5e and Supplementary Fig. 5c). Finally, we found that intra-burst frequencies of MS PV+ neurons showed a correlation with concurrent tSCs (Supplementary Fig. 12) based on average inter-spike interval histograms, similar to what we found for a subset of unidentified MS neurons (Supplementary Fig. 7).

https://doi.org/10.1038/s41467-023-41746-0

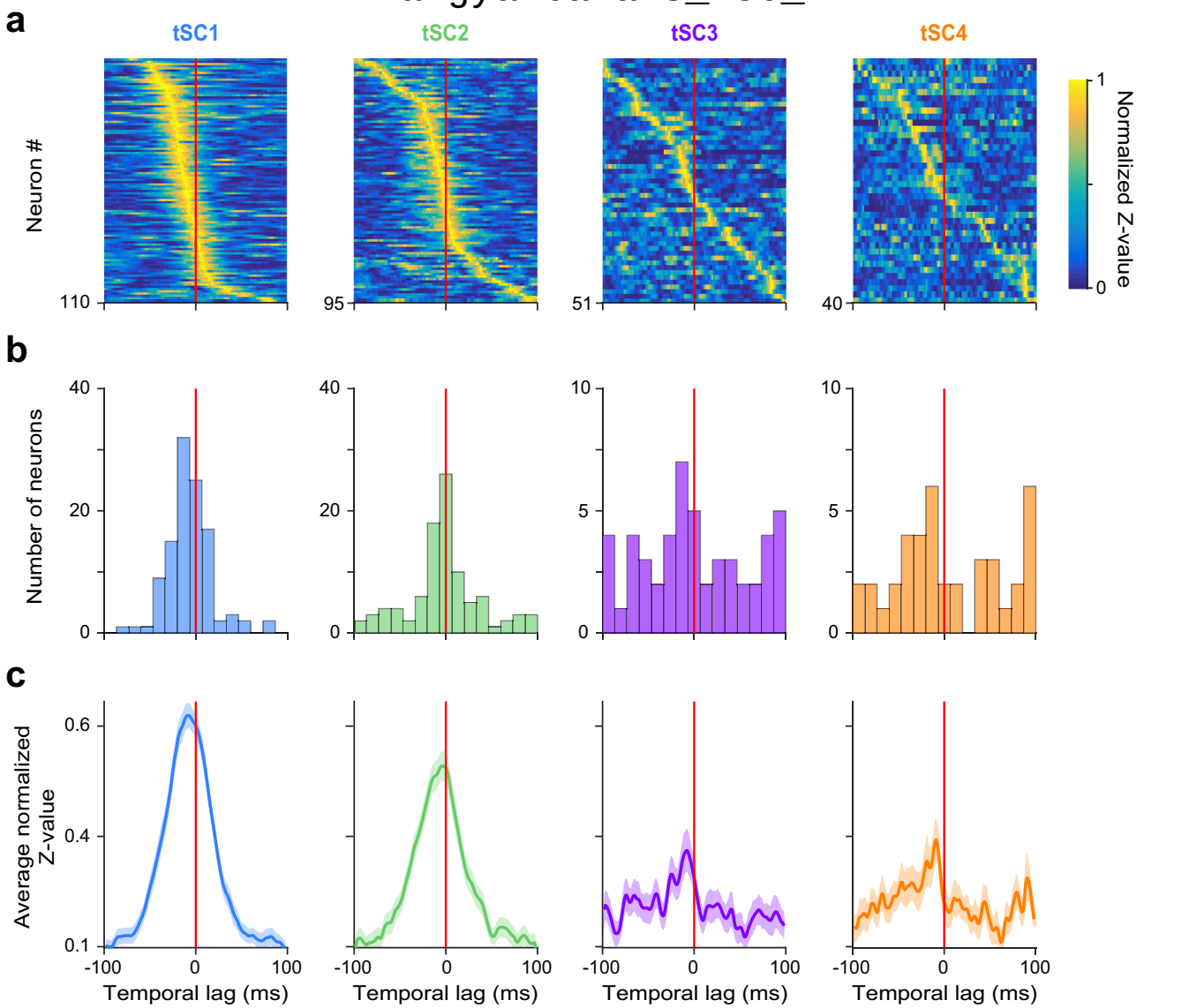

Fig. 4 | Firing of most MS neurons predicts tSCs signals. a Normalized Rayleigh's *Z*-value as a function of temporal lag between hippocampal tSCs and MS spike trains. All MS neurons coupled to the given tSC are shown. *Z*-values at negative lags quantify how well MS signals predict future tSC values. **b** Histograms showing the distribution of time lags across MS neurons that realize the maximal phase locking as quantified by the *Z*-values, separately for each tSC. **c** Average normalized *Z*-value of tSC-coupled MS neurons as a function of time lag. Error shade represents SEM. Source data are provided as a Source Data file.

Thus, two anatomically identified, theta-rhythmic PV-expressing MS GABAergic cell types exhibited strong correlations with CA1 tSCs, the CA3-projecting Teevra cells being locked to beta/low-gamma, and the entorhinal-projecting Orchid cells coupled to beta to mid-gamma tSCs, in line with the assumed role of their projection targets in the control of distinct gamma oscillations of the CA1.

Optogenetic stimulation of PV-expressing MS neurons evokes tSC-like CA1 activities

The finding that MS firing anticipated hippocampal tSCs raised the possibility that the MS has a role in tSC expression. Putative theta pacemaker MS neurons, previously suggested to express PV[48,52,63,74], were most prominently predicting tSCs in the CA1 (Fig. 5e and Supplementary Fig. 9). In accordance, we also demonstrated that $n = 10/14$ identified PV-expressing MS neurons showed coupling to more than one tSC ($n = 1/8$ PV-negative neurons, Fig. 5c) and the PV-expressing Orchid cell group consistently anticipated hippocampal tSCs.

Therefore, we focused on PV-expressing MS neurons and tested whether they are capable of evoking theta-nested beta and gamma oscillations. First, we performed in vitro whole-cell patch clamp recordings from acute hippocampal slices of PV-Cre mice ($n = 6$) injected with an AAV vector containing Cre-dependent ChR2-eYFP in the MS and confirmed a direct connection from MS PV+ neurons to PV+ and somatostatin-expressing (SOM+) interneurons in the dorsal CA1 and CA3 (Supplementary Fig. 13a-d). We performed photostimulation of MS PV+ fibers with theta-modulated bursts of laser light pulses (theta-modulated stimulation, tmS1-4), mimicking physiological tSC1-4 rhythms, and found that most hippocampal interneurons were capable of following the tmS1-3 burst stimulation patters with IPSCs, IPSPs and rebound spikes (Supplementary Fig. 13e–g).

Next, we performed acute optogenetic stimulation experiments in awake PV-IRES-Cre mice injected with AAV2/5.DIO.h-ChR2.eYFP ($n = 7$, see Supplementary Fig. 14 for histological track reconstruction and viral expression in PV cells) or with the AAV2/5.DIO.eYFP control virus ($n = 3$). We stimulated channelrhodopsin2-expressing MS PV neurons with tmS1-4 stimulation patterns, and recorded LFP and single unit activities from CA1 concurrently (Fig. 6a). We observed high amplitude stimulation-evoked tSC-like

https://doi.org/10.1038/s41467-023-41746-0

hangya.balazs_256_24

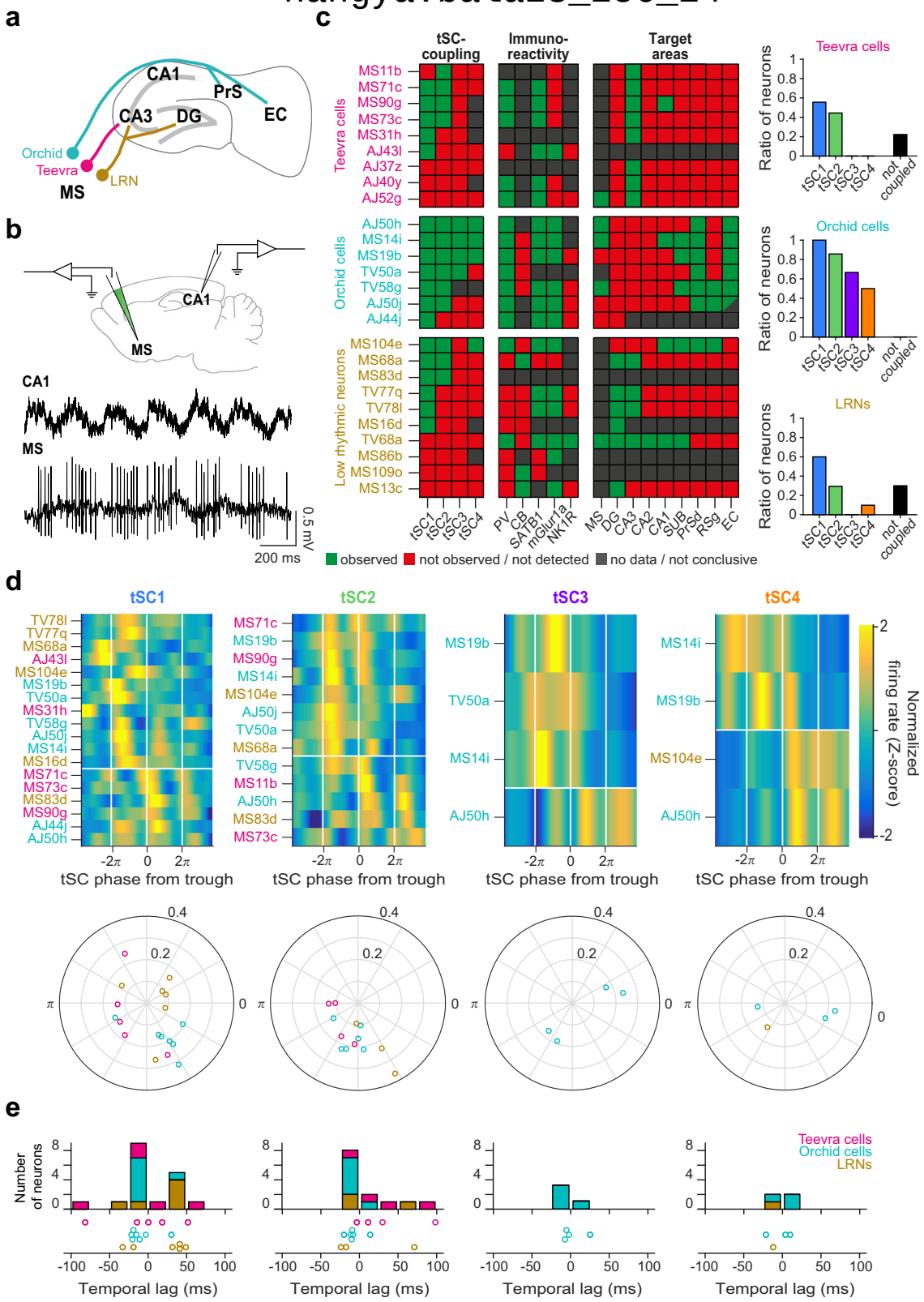

oscillations from CA1 in all channelrhodopsin2-expressing animals but not in control mice. These oscillations largely followed the stimulation frequency and resembled physiological tSCs in spectral content (Fig. 6a, b and Supplementary Fig. 15). We also found stimulus-evoked tSC-associated firing of single CA1 neurons, with some putative CA1 interneurons robustly following the stimulation frequency from tmS1 to tmS4 (Fig. 6c and Supplementary Fig. 16). In sum, these experiments demonstrated that MS PV neurons are capable of evoking tSC-like activity in the CA1 network.

We next examined the laminar profiles of both spontaneous and stimulation-induced tSCs to examine their layer-specific sources. Therefore, we performed current-source density (CSD) analysis with electrode arrays spanning the full somato-dendritic axis of CA1 pyramidal neurons ($n = 4$ mice for spontaneous and $n = 4$ mice for

Fig. 5 | Anatomically identified MS cells show differential coupling to CA1 tSCs. **a** Main projection targets of Teevra, Orchid and low rhythmic (LRN) MS neurons (MS, medial septum; DG, dentate gyrus; PrS, presubiculum; EC, entorhinal cortex)[47,48,64]. **b** Top, schematic of the juxtacellular labeling and recording experiment with concurrent recordings from CA1 pyramidal layer in awake mice. Bottom, example of simultaneously recorded CA1 LFPs and MS spikes. **c** Left, tSC-coupling, immunoreactivity and projection targets of identified MS neurons. Cells were sorted based on the fastest tSC they were coupled to. Right, number of Teevra, Orchid and LRN neurons phase-coupled to each tSC. PV, parvalbumin; CB, calbindin; mGluR1a, metabotropic glutamate receptor 1a; NK1R, neurokinin 1 receptor; SUB, dorsal subiculum; PrSd, dorsal presubiculum; RSg, granular retrosplenial cortex. AJ50j is a putative EC-projecting neuron, as its main axon faded just rostral to caudo-dorsal EC. **d** Top, *Z*-scored phase histograms of all identified tSC-coupled MS neurons, sorted into four groups based on the tSC they are coupled to (blue, low firing rate; yellow, high firing rate). Zero phase corresponds to tSC troughs (white vertical lines). Cells within each group were sorted by their preferred phase in two blocks: top, cells with maximum firing rate before the most negative tSC trough; bottom, cells with maximal firing after the most negative tSC trough. Bottom, polar plot showing the phase preference (angle) and coupling strength (radius) of different MS neuron types for each tSC. **e** Distribution of time lags across different MS neuron types that realize the maximal phase locking as quantified by Rayleigh's *Z*-values, separately for each tSC. Source data are provided as a Source Data file.

stimulation-induced tSCs). We examined the frequency – theta phase relationship of the CSD signal, allowing us to specifically compare currents related to the different tSCs. In line with previous studies[15,22,55,58,59], spontaneous fast gamma signals (tSC5) were dominant in the pyramidal layer, while slower oscillations emerged from deeper layers (Fig. 6d and Supplementary Fig. 17). Spontaneous mid-gamma oscillations (tSC3 and tSC4) were characterized by prominent currents in stratum lacunosum moleculare, while tSC1 and tSC2 signals were most distinct from mid-gamma signals in stratum radiatum. Examining laminar profiles of the stimulation-induced theta cycles revealed similar spatial current source density distributions. The pyramidal layer CSD was dominated by fast gamma components regardless of the intra-burst frequency of the stimulation. Meanwhile, stimulation-evoked tSCs following the stimulation frequencies in the beta to mid-gamma range had strong currents in the deeper layers, most prominently in stratum lacunosum moleculare (Fig. 6e).

GABAergic septo-hippocamal feedback suppresses tSC generation

The MS not only sends GABAergic projections to the hippocampus, but also receives inputs from hippocampal somatostatin-expressing (SOM+) GABAergic neurons forming a reciprocally connected inhibitory circuit[75–79]. To fully explore the role of this circuit in the generation of the supra-theta oscillations, we performed optogenetic suppression experiments using SwiChR in 4 of the freely moving SOM-IRES-Cre mice used in this study (Fig. 6f). Mice underwent bilateral injections of AAV5-Ef1a-DIO-SwiChRca-TS-EYFP in the dorsal CA1. To enable the inhibition of the hippocampo-septal projections, each shank of the septal silicon probes in these animals were equipped with an optical fiber. Four additional mice were injected with AAV5-Ef1a-DIO-EYFP control virus and implanted with 2 optical fibers bilaterally.

These experiments revealed that the proportion of theta cycles strongly expressing tSCs significantly increased during the inhibition of these feedback projections compared to control periods without stimulation (paired, two-sided Wilcoxon signed rank test, $p = 0.0015$, Fig. 6g; no effect observed in control animals, $p = 0.7422$, Supplementary Fig. 18a). These results suggest that this inhibitory feedback loop may play a role in suppressing the septo-hippocampal generator of supra-theta oscillations.

Next, we examined the impact of optogenetic suppression of SOM+ hippocampo-septal projections in the MS on tSC-coupled and non-coupled MS neurons. More tSC-coupled than non-coupled MS neurons showed a >10% firing rate increase during stimulation (tSC-coupled, 20%; non- coupled, 13%). These neurons were likely directly targeted by the hippocampo-septal pathway and thus disinhibited upon inhibition of the hippocampo-septal GABAergic fibers. We also found MS neurons that showed firing rate suppression, possibly via the disinhibited neurons. We found that less tSC-coupled MS neurons were suppressed than non-coupled neurons (tSC-coupled, 32%; non-coupled, 39%; Supplementary Fig. 18b).

We also tested the effect of 20 Hz optogenetic stimulation of SOM + fibers in the Fimbria of channelrhodopsin-expressing SOM-Cre mice ($n = 2$) on tSC-coupled and non-coupled MS neurons. Many MS neurons showed firing rate suppression, which might be due to direct targeting of these cells by the hippocampo-septal inhibitory pathway. Some MS neurons showed firing rate increase, possibly disinhibited through the suppressed group. This population was more numerous among the not tSC-coupled MS neurons compared to the tSC-coupled ones (tSC-coupled, 6%; non-coupled, 18%; Supplementary Fig. 18c).

We found a significantly higher proportion of tSC-coupled neurons among the MS neurons activated upon SwiChR-mediated inhibition of hippocampo-septal GABAergic fibers then among the suppressed ones (65% vs. 48%, chi-squared test, $p = 0.0322$). This difference was due to a larger percentage of 'follower' neurons (ones with positive lags in the Z-shift analysis, demonstrating activity changes following/lagging CA1 activity changes) in the activated group (Supplementary Fig. 18d). In accordance, during optogenetic stimulation of the hippocampo-septal pathway, we found the lowest proportion of tSC-coupled neurons among the activated group, which was significantly less compared to the non-reactive neurons (31% vs, 63%, chi-squared test, $p = 0.0428$, Supplementary Fig. 18d). These results may indicate that there might be more tSC-coupled neurons among MS neurons directly targeted by the hippocampo-septal feedback.

MS neurons couple to tSCs in anesthetized mice and rats

To test whether these findings can be generalized across theta rhythms in awake and anesthetized rodents and across mice and rats[10,11], we attempted to discriminate different types of theta cycles from the LFP recorded from the CA1 radiatum layer of urethane-anesthetized rats ($n = 6$) and mice ($n = 5$) using a similar approach. The EEMD algorithm successfully detected tSCs in urethane-anesthetized rodents (Fig. 7a, b and Supplementary Fig. 19a, b). However, these were substantially less common than in awake mice (24% of all theta cycles both in rats and mice, Fig. 7c and Supplementary Fig. 19c). They were also described by slower characteristic frequencies, consistent with a general slowing of many oscillatory patterns during anesthesia including theta[80–83]. Additionally, they showed a weaker separation in theta phase across tSCs, arguing for potential mechanistic differences in oscillation genesis under anesthesia.

To test the potential contribution of the MS, we examined whether concurrently recorded MS neurons showed phase-coupled firing to tSCs in anesthetized rodents, too. Indeed, we found significant phase-locking in 33% and 35% of MS neurons recorded from urethane-anesthetized rats and mice, respectively (Rayleigh's test, $p < 0.05$, type I errors were controlled with Storey's false discovery rate method[73], Fig. 7c and Supplementary Fig. 19d). These data indicate that the MS network may contribute to theta-gamma coordination in the CA1 even in the absence of sensory inputs.

Theta-nested spectral components are present in the ventral CA1

Finally, running EEMD analysis on a public dataset[84] revealed beta-gamma band tSCs in ventral hippocampus recordings (Supplementary Fig. 20). Distinct tSCs followed the same characteristic frequencies in

https://doi.org/10.1038/s41467-023-41746-0

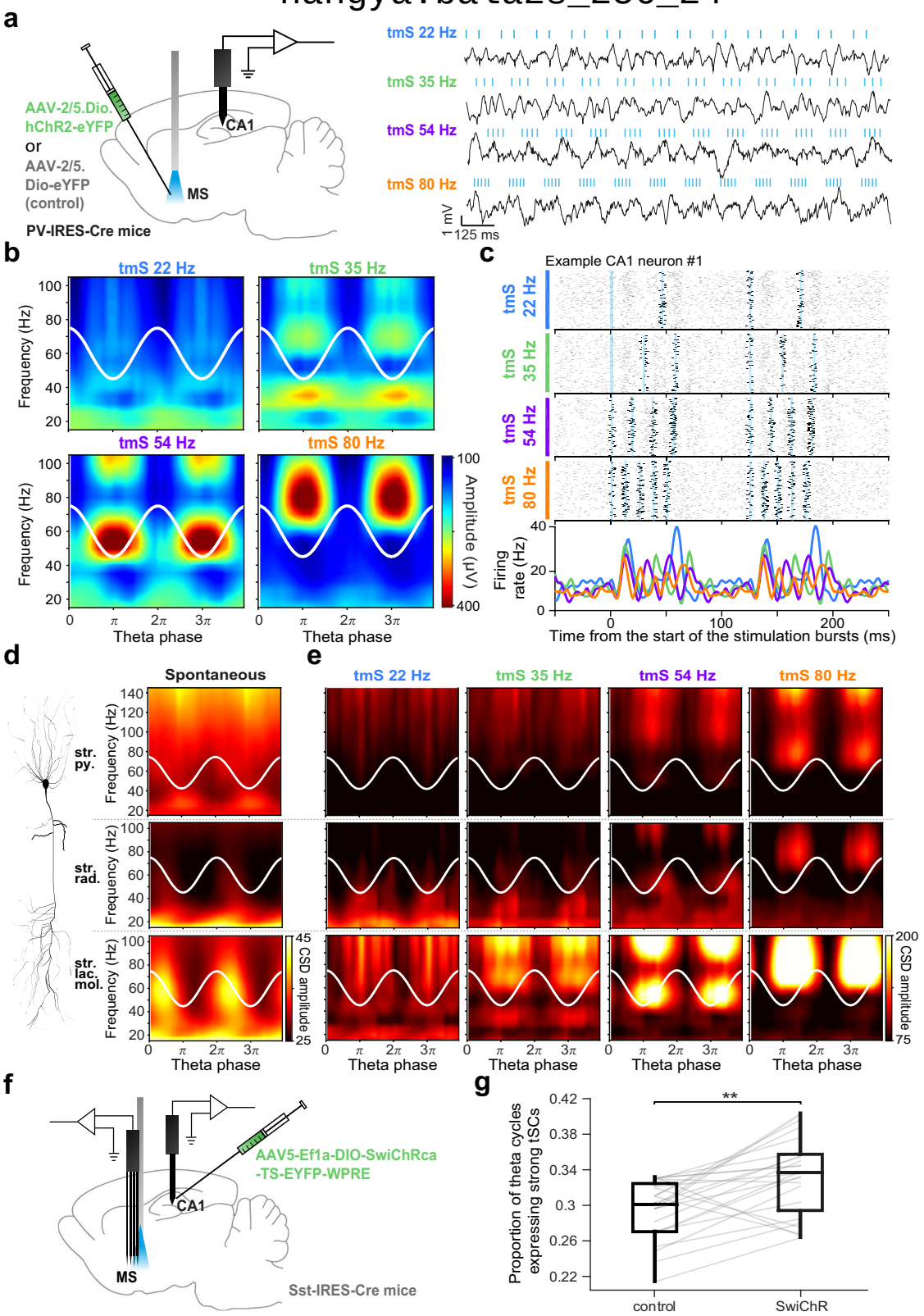

the beta to mid-gamma range as in the dorsal CA1, with largely similar theta-gamma phase-amplitude coupling. In contrast, tSC5 measured in the ventral CA1 was typically slower (with a peak around 80–90 Hz) and preferred the same phase as the mid-gamma components. Thus, while tSC5 in dorsal CA1 is thought to reflect local processing[19,55], ventral hippocampal tSC5 might rather reflect conceptually different network mechanisms, possibly controlled by external inputs similarly to mid-gamma components. Observing dorso-ventral similarities in tSCs1-4 may reflect similar oscillation mechanisms across the CA1.

Discussion

Hippocampal network activities of different time scales are not independent but interact in specific ways. The momentary phase of the 4–12 Hz theta oscillation modulates the fluctuating spectral power of

Fig. 6 | Optogenetic stimulation of PV-expressing MS neurons evokes tSC-like activity patterns in the CA1. a Left, schematic of the acute experiment with optogenetic stimulation of PV-expressing MS neurons in awake mice. Right, raw LFPs recorded from the CA1 radiatum layer (black) during photostimulation of MS PV-expressing neurons. Blue ticks mark 2 ms laser pulses. Stimulation was performed in theta-modulated bursts of laser pulses (tmS) mimicking the different frequencies of physiological tSCs (22 Hz, 35 Hz, 54 Hz, 80 Hz). **b** Mean amplitude of supra-theta spectral components as a function of theta phase during the different tmS protocols. Two theta cycles are shown, indicated by the white cosine curves. **c** Spike rasters and peri-stimulus time histograms of a putative CA1 interneuron aligned to the onset of each tmS sorted by stimulation frequency (blue lines, photostimulation). Note the brief initial suppression of spiking upon photostimulation before the firing rate increase (see also Supplementary Fig. 16). **d** Laminar profile of currents related to spontaneous tSCs. Left, schematic of a pyramidal cell showing CA1 layers (str. py., stratum pyramidale; str. rad., stratum radiatum; str. lac. mol., stratum lacunosum moleculare). Stoyo, Karamihalev. (2020). CA1 pyramidal neuron. Zenodo. https://doi.org/10.5281/zenodo.4312494. Right, mean amplitude of supra-theta CSD signals as a function of theta phase from an example session of a freely moving mouse (see also Supplementary Fig. 17 for the same analysis on cycles strongly expressing a particular tSC). Note that the upper limit of the y-axis is extended in the stratum pyramidale panel to visualize fast gamma-bands. White cosine curves, two theta cycles are shown. **e** Mean amplitude of supra-theta CSD signals as a function of theta phase during different tmS protocols, showing the laminar profile of currents related to photostimulation-evoked tSCs. White cosine curves indicate the theta phase defined from the radiatum layer LFP. **f** Schematic of the experiment using SwiChR injected into the CA1 and an optic fiber implanted into the MS. **g** Proportion of theta cycles expressing tSCs during inhibition and control periods. Data points belonging to the same recording session ($n = 23$) are connected with gray lines. Box-whisker plots show median, interquartile range and non-outlier range. $^{**}p = 0.0015$, two-sided Wilcoxon signed-rank test. Source data are provided as a Source Data file.

faster, beta/gamma band oscillations[85–88]. This so-called cross-frequency coupling has been shown to be important for cognitive functions such as working memory[89,90]. Medial septal GABAergic neurons have a central role in orchestrating theta oscillations; however, whether they also participate in regulating faster, supra-theta oscillations of the hippocampus is unclear. While phase coupling to entorhinal or hippocampal gamma oscillations has been demonstrated for some MS cell types[47,64], hippocampal gamma oscillations are typically interpreted without including the MS in the gamma generating network[17,53]. We challenge this view by demonstrating that MS firing correlates with, predicts changes of and is capable of generating theta-nested beta/gamma band oscillations in the CA1.

Early accounts of CA1 oscillatory activity revealed cross-frequency coupling between theta and gamma oscillations[91–93], giving rise to the concept of theta-nested gamma bouts[94–96]. A landmark discovery of functionally distinct CA1 oscillatory patterns within the gamma band suggested the parallel presence of multiple fast-scale network mechanisms organized by theta phase[21,22,54]. Recent studies revealed that individual theta cycles can be reliably categorized by their beta/gamma content, and these distinct theta-nested spectral components also segregate at the network and functional levels[15,97]. This strengthens the prevailing view that theta cycles can be considered as individual processing units that organize spatial processing[7,98–100], episodic memory encoding and retrieval[70,101], by temporal arrangement of information routing from distinct sources[9,22,54].

Medial septal GABAergic neurons, particularly their parvalbumin-expressing subpopulation, have been implicated in the genesis of CA1 theta oscillations. MS PV neurons project to the hippocampal formation and innervate GABAergic interneurons[24,74,102–105]. They were proposed to pace the theta rhythm through providing rhythmic disinhibition of pyramidal neurons via their interneuron targets[49,51,63,67,106,107], probably as part of a wider theta synchronization network that includes other MS populations[47,48,50,52,64,108,109], the supramammillary nucleus[39–41], the nucleus incertus[42–46,110] and the raphe nuclei[111,112]. Additionally, previous studies suggested the presence of higher frequency spectral elements in the MS[47,64], which we also confirmed (Fig. 1b, c). However, while the involvement of cholinergic mechanisms in theta-gamma coupling has been demonstrated[33], the role of the MS GABAergic projection in controlling hippocampal gamma rhythms is less explored[17]. Since basal forebrain PV neurons that project to the neocortex can control gamma rhythms in the frontal cortices[113,114], we hypothesized that MS PV neurons projecting to the hippocampus may exert a similar influence on CA1 supra-theta oscillations.

First, we confirmed the presence of tSC components in the CA1 of mice moving freely on a linear track, which appeared in coherence with MS bursts with beta-gamma band intra-burst spike frequencies[61–63]. In line with former results[15], we reliably detected five distinct theta-nested spectral components well-separated in frequency and preferred theta phase. One or more of these tSCs were strongly expressed in nearly one third of all theta cycles. The identified tSCs exhibited different characteristic frequencies spanning the beta to fast gamma range, resembling supra-theta oscillations reported in previous studies[15,21,53,54,58,59]. For instance, tSC2 matched the frequency of slow gamma oscillations, thought to promote memory retrieval driven by CA3[19,54,57], whereas tSC3 and tSC4 were characterized by mid-gamma frequencies suggested to originate from the medial entorhinal cortex[57]. We confirmed that the strength of most tSCs (tSC2-tSC5) positively correlated with animal speed[15,66], while interestingly, tSC1 showed a significant negative correlation. Faster locomotion is accompanied by higher theta frequencies; this might be related to place coding, which is probably a strong organizing factor while collecting episodic memories during movement[115]. Theta frequency was gradually increasing with the frequency of the spectral component nested in the theta cycle for tSC1-tSC4, likely reflecting that mid-gamma components are related to memory encoding processes[17,54]. Interestingly, theta frequency during theta cycles expressing tSC5 components, which are thought to reflect internal processing in CA1, did not follow this trend. We found an over-representation of tSC1, corresponding to beta band oscillations, in short theta epochs and during non-theta-to-theta transitions. In line with this, a recent study found that theta-nested hippocampal beta oscillations rapidly increase at the onset of exploratory behavior, after which they gradually adapt and fade, not explained by locomotion alone. The presence of these beta bouts predicted subsequent performance in an object location test[116]. Other studies found that hippocampal beta oscillations are related to odor sampling[117] and originate from the olfactory bulb[118]; thus, these results together suggest that tSC1-dominated theta cycles may be hallmarks of olfactory exploration and reflect a transient increase in the synchrony between the olfactory system and the hippocampus. We further propose that tSC1-dominated cycles interspersed in longer theta episodes may also reflect increased odor processing subserving exploration, planning and memory, providing a window on the information routing process of the hippocampal network.

Most MS neurons showed higher firing rate and stronger theta phase coupling during theta cycles in which tSC4 was present, corresponding to mid-gamma oscillations that have been associated with entorhinal inputs[22]. More place cells phase-lock to this gamma band than to other supra-theta oscillations[54], and this activity pattern might be particularly important for memory encoding and long-term potentiation. In accordance, Lopes-dos-Santos et al.[15] found that the tSC4 component strongly increased and predicted subsequent performance during learning in a crossword maze[15]. Our results indicate that the MS is strongly involved in the regulation of these learning-related theta cycles, reflected in higher activity levels and stronger

https://doi.org/10.1038/s41467-023-41746-0

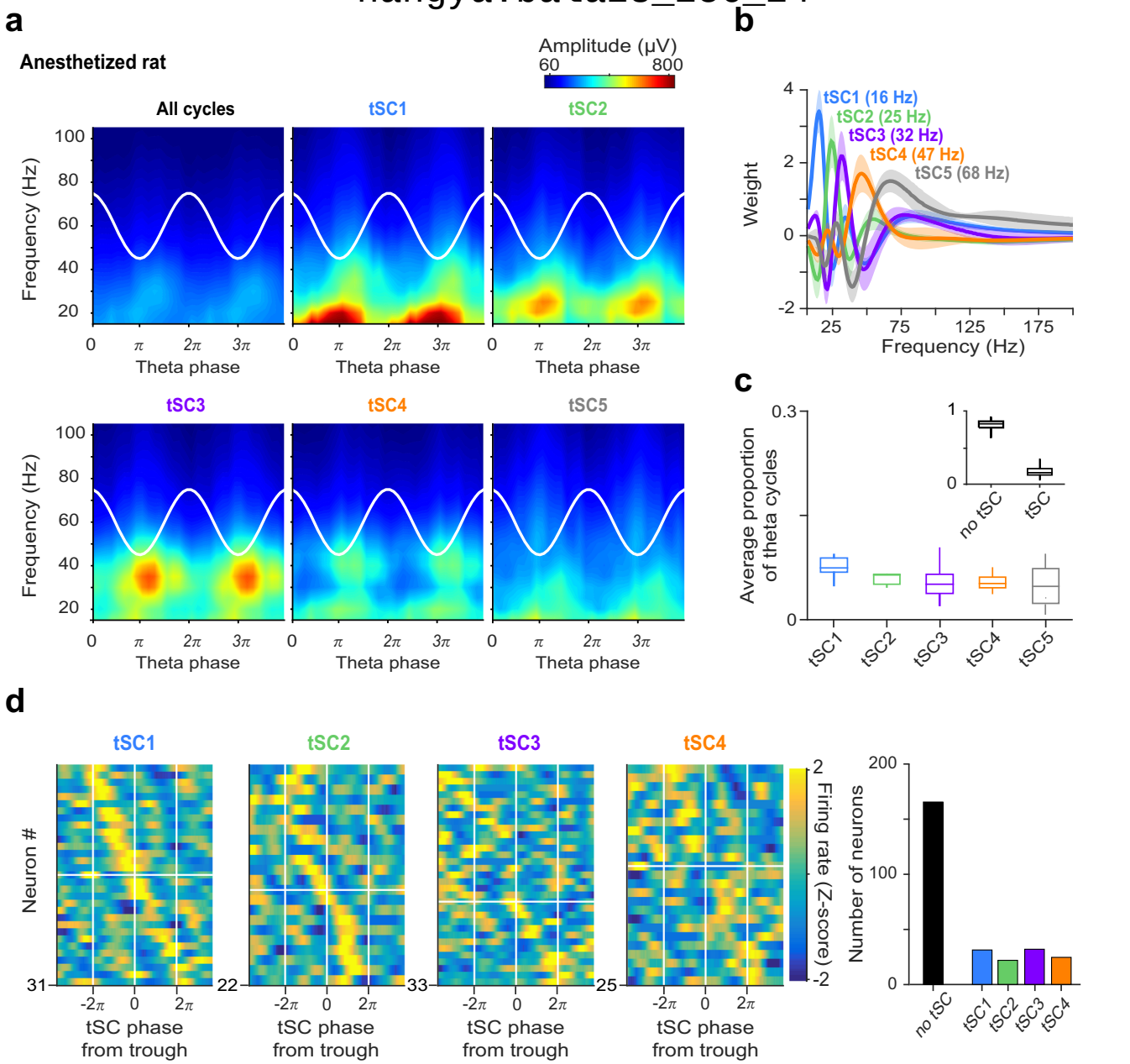

Fig. 7 | MS neurons show phase coupling to hippocampal tSCs in anesthetized rats. a Mean amplitude of supra-theta spectral components as a function of theta phase was computed from the raw LFP of an example session of an anesthetized rat, for all cycles (top left) and for cycles strongly expressing a given tSC. Two theta cycles are shown, indicated by the white cosine curves. **b** Average tSCs spectra in anesthetized rats ($n = 6$). Error shades show the standard error of the mean. Median peak frequencies for all recordings are shown in the brackets. **c** Proportion of theta cycles expressing each tSC ($n = 13$ sessions). Boxes and whiskers show median, interquartile range and non-outlier range. Insets show the proportion of theta cycle expressing any of the tSCs. **d** Left, *Z*-scored phase histograms of all tSC-coupled MS neurons, sorted into four groups based on the tSC they are coupled to (blue, low firing rate; yellow, high firing rate). Zero phase corresponds to tSC troughs (white vertical lines). Cells within each group are sorted by their preferred phase in two blocks: top, cells with maximum firing rate before the most negative tSC trough; bottom, cells with maximal firing after the most negative tSC trough. Right, number of neurons phase-coupled to a given tSC. Source data are provided as a Source Data file.

phase-locking. This is in accordance with a long history of lesion, pharmacology, stimulation and recording studies that identified the MS as a crucial subcortical structure in declarative memory formation[37,45,115,119–131]. Human patients with MS lesions, sometimes caused by jet bleeding after arteria communicans anterior aneurysm rupture, present the classic Korsakoff triad of anterograde and retrograde amnesia and confabulation[132,133].

tSC5 attributed large weights to frequencies in the fast gamma band, which are thought to be generated by local CA1 networks of pyramidal cells and interneurons[19,55]. Also in line with previous findings[15,22,58,59], current source density analysis confirmed that tSC5 signals were most prominent in the pyramidal layer, while slower oscillations emerged from the deeper layers: tSC3 and tSC4 showed strong currents in the lacunosum moleculare layer, while sources of tSC1 and tSC2 signals were more localized to the stratum radiatum than mid-gamma tSCs.

Although the strong phase-coupling of MS neurons to hippocampal theta is well established[49,50,63,67,106], correlations between MS firing and hippocampal gamma oscillations are much less explored[47,64]. We found that a large proportion of MS neurons were phase-coupled

to beta/gamma band tSCs. More neurons coupled to slower tSCs compared to fast ones, although this might partially be the consequence of our analysis being more exposed to noise in case of shorter tSC cycles. MS neurons coupled to tSC1 and tSC2 showed a bias towards the ascending slope of the tSCs. A more in-depth analysis of MS intra-burst spike timing revealed a theta-phase-independent, cycle-by-cycle correlation between MS spike timing and concurrent tSCs, arguing for a close integration of the MS into CA1 gamma generation mechanisms (Supplementary Figs. 6, 7, 11, 12).

In the case of two correlated time series, small changes in either of the variables may predict time-locked changes in the other, reflecting cause-effect relations. For instance, sharp low-latency peaks in spike crosscorrelations have been taken as indirect evidence for functional monosynaptic connections[2,134–137]. Analogously, changes in a point process like a series of spike times may lead to corresponding changes in correlated network oscillations, detectable by a time-varying measure of coupling strength, expressed as a function of time lag between the two variables[49,72]. This has been used to demonstrate directional coupling between the hippocampus and prefrontal cortex[72]. By using the same approach, we found that MS spiking predicts and thus temporally leads CA1 tSCs. The MS population showed negative median time lags, and thus temporal antecedence, by either testing average phase coupling strength (−6 ms) or optimal correlations in individual neurons (−6 ms), despite large variability across tSC-coupled neurons in their optimal time lags (interquartile range: 34 ms). This unexpected result points to a role of the MS in controlling hippocampal network activity that goes beyond its known function in pacing theta and suggests that it is also an important node in the coordination of hippocampal supra-theta oscillations.

A subpopulation of MS neurons exhibit theta-rhythmic burst firing regardless of whether theta oscillation is present in the hippocampus. These constitutive theta-bursting neurons are often considered putative pacemakers of hippocampal theta oscillations, although they may be part of a distributed theta-rhythmic oscillatory network[39,40,49–51,63,110]. Another set of MS neurons only exhibits theta-rhythmic firing when the hippocampus is also in theta state, referred to as theta-associated bursting MS neurons[52]. Although we found that constitutive and theta-associated bursting MS neurons showed similar tendencies to the entire MS population in their relation to supra-theta CA1 oscillations, we also uncovered a number of differences. A larger proportion of the constitutive bursting neurons were coupled to tSCs (78% vs 48% of other MS neurons), and often to more than one component (68%). Constitutive bursting neurons provided a significant part of tSC-anticipating MS neurons, as the vast majority (81%) of their tSC-coupled population were characterized with negative optimal time lags (median: −14 ms), suggesting a key importance of these neurons in the control of tSCs. The theta-associated bursting neurons were also overrepresented among tSC-coupled neurons but to a lesser extent (59%). They also anticipated tSCs (median optimal lag: −14 ms) significantly more than the rest of the population when only the slower tSC1 and tSC2 components were considered.

We tested whether the MS GABAergic network is capable of inducing hippocampal tSCs by optogenetic stimulation; thus, whether the MS is sufficient for tSC generation. We targeted PV-expressing GABAergic MS neurons based on their known projections and roles in CA1 oscillatory control[47,48,52,63,64,74] and previous reports on theta evoked by PV stimulation[25,30]. We found that stimulating PV-expressing MS neurons by theta-modulated beta/gamma bursts of laser light that matched spontaneous tSCs in frequency induced tSC-like oscillations in the CA1 that resembled spontaneous tSCs in their average spectral content and laminar distribution. However, stimulus-evoked gamma components (mostly in the mid-gamma range) differed from spontaneous tSCs in their amplitude modulation by the hippocampal theta phase, possibly due the stimulation-induced artificial synchrony of the MS PV network, which could not reproduce their well-known physiological diversity (Supplementary Fig. 9, see also refs. 48,50,52,63).

In line with these results, a previous study found that septal infusion of the $GABA_A$ receptor agonist muscimol decoupled theta and gamma rhythms and disrupted memory retrieval, while electrical stimulation of the fimbria-fornix with theta-modulated high frequency (500 Hz) stimulation increased theta-gamma co-modulation and partially rescued memory performance[138]. Inactivation or lesion of MS GABAergic neurons reduced hippocampal gamma oscillations induced by NMDA antagonists[139]. Functionally intact inhibition onto hippocampal PV interneurons has been shown to be necessary for physiological theta-gamma coupling[140] and 40-Hz stimulation of MS PV neurons could rescue impaired theta-gamma coupling in a mouse model of Alzheimer's Disease[141]. Nevertheless, whether MS PV neurons are capable of producing the physiological spectrum of theta-nested spectral components of the CA1 has not been addressed before.

Urethane-anesthetized rodents have been used extensively as models of septo-hippocampal theta-frequency synchronization. However, much less is known about hippocampal supra-theta oscillations during anesthesia. Similar to a previous study[22] that described theta-coupled gamma oscillations in the CA1 that used urethane-anesthetized rats supplemented with ketamine-xylazine, we observed tSCs during urethane anesthesia in both mice and rats; however, tSC expression was diminished compared to awake mice. These tSCs were characterized by slower frequencies and uniform theta phase preference. Despite these differences, a smaller proportion of MS neurons exhibited similar phase coupling to these tSCs as in freely moving mice, strengthening the argument that the MS has a general role in hippocampal oscillation genesis.

By what mechanism does the MS contribute to CA1 gamma formation? It seems reasonable to assume that part of the influence is direct: gamma-locked MS GABAergic neurons innervate gamma-locked CA1 interneurons, likely contributing to CA1 gamma oscillations (Fig. 8, pathway (i)). Since septo-hippocampal projections likely innervate multiple types of CA1 interneurons including PV-expressing basket and axo-axonic cells[24,48,103,142,143], gamma-rhythmic septal drive should necessarily contribute to their known gamma-locked discharge[19,56]. Indeed, within the hippocampus, bistratified cells were found to express the strongest phase coupling to gamma[19,144], and were shown to receive selective GABAergic MS input[102].

However, part or even most of the septal influence on tSCs may be indirect via the input regions to CA1. For instance, long-range inhibitory MS neurons innervate the EC[64,103,145–151], thus having the potential to entrain the EC sources of CA1 gamma. More specifically, it has been shown recently that MS Orchid cells project to the EC (Fig. 8, pathway (ii)) and phase-lock to EC mid-gamma oscillations, lending strong support to this hypothesis[64]. To directly test this, we analyzed anatomically identified Orchid, Teevra and low rhythmic neurons projecting to distinct parts of the hippocampal formation[47,48,64]. Teevra cells, which are rhythmically bursting PV-expressing GABAergic MS neurons that mostly project to the CA3[48], were coupled to beta/low-gamma tSC1 and tSC2, in accordance with the assumed role of CA3 in controlling low-gamma oscillations of CA1[22,54] (Fig. 8, pathway (iii)). Orchid cells, also PV-expressing and firing long theta-rhythmic bursts[64], were the only tested neurons which locked to mid-gamma tSC3 and tSC4, confirming the above-mentioned hypothesis of their potential role in controlling the mid-gamma band in CA1 via the entorhinal cortex (Fig. 8, pathway (ii)). Since Orchid cells were found to branch into the dorsal presubiculum[64], which also projects to their termination zone in the entorhinal cortex[152], the potential role of a MS-presubiculum-entorhinal cortical route should also be considered. Importantly, Orchid neurons not only coupled to but also predicted CA1 tSCs. In contrast, the non-PV LRNs only showed consistent coupling to the beta band tSC1. Since these cells innervate interneurons in the dentate gyrus, they may contribute to beta/slow-gamma oscillations observed

https://doi.org/10.1038/s41467-023-41746-0

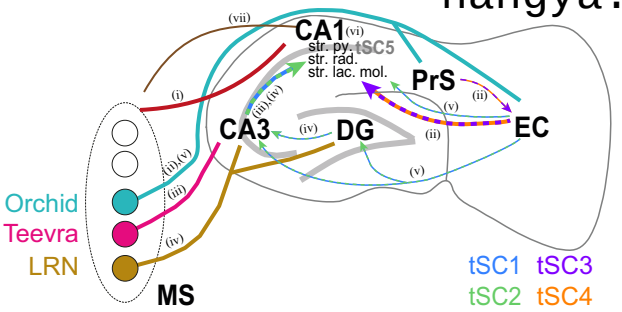

Fig. 8 | Hypothetical schematic of direct and indirect septo-hippocampal pathways mediating tSCs in the CA1. In this schematic, we depict the direct and indirect pathways between the MS and the CA1 implicated in controlling distinct CA1 supra-theta oscillations. Color codes for MS projections, including anatomically identified MS neurons, are shown on the left. Cortico-hippocampal and intrahippocampal pathways are color-coded by their dominant tSCs: tSC1, blue; tSC2, green; tSC3, purple; tSC3, green; tSC4, orange; tSC5, gray. **i** We suggest that direct GABAergic MS-CA1 projections (dark red curve) contribute to tSCs1-4. **ii** Orchid cells (teal) are likely important determinants of tSC3-4 in CA1 via their projections to PrS and EC. **iii** Teevra neurons (magenta) contribute to tSC1-2 through the CA3. **iv** LRNs (mustard) also form part of the tSC1-2 network via their projections to CA3 and DG. **v** Further indirect MS-EC-CA3/DG-CA1 pathways probably also contribute to the control of tSC1-2 components in the CA1. **vi** Local processing in the CA1 strongly contributes to fast gamma (tSC5) oscillations. **vii** Hippocampo-septal feedback by somatostatin-expressing GABAergic neurons (brown) could control tSC generation by negative feedback. MS, medial septum; EC, entorhinal cortex; PrS, dorsal presubiculum; DG, dentate gyrus; LRN, Low-rhythmic neurons; str. py., stratum pyramidale; str. rad., stratum radiatum; str. lac. mol., stratum lacunosum moleculare.

in the DG[59] that might in turn influence CA3 slow-gamma rhythms[153] (Fig. 8, pathway (iv)). However, CA1 has been shown to retain slow gamma activities in the absence of CA3 inputs, arguing for alternative sources of these rhythms in the CA1[154], which may include direct MS inputs to CA1 or the MS-EC pathway[25] (Fig. 8, pathway (v)). Also, as for hippocampal theta, intra-hippocampal gamma oscillators may play a role, especially for tSC5 (Fig. 8, pathway (vi)).

We found that the activity of most MS neurons predicted corresponding CA1 tSCs; however, a subpopulation of MS cells, including non-PV-expressing LRNs rather followed CA1 activity. This raised a potential role of the hippocampo-septal feedback in supra-theta hippocampal oscillations[75–79] (Fig. 8, pathway (vii)). By optogenetic suppression of somatostatin-expressing hippocampo-septal GABAergic fibers, we found that this inhibitory feedback projection suppresses tSC generation in the MS, probably through a biased targeting of tSC-coupled MS neurons. While PV-expressing MS neurons, including Orchid, Teevra, and part of Low Rhythmic Neurons are likely all GABAergic[63,74], Calbindin-expressing PV-negative LRNs may be, at least in part, excitatory glutamatergic neurons. Two of the 3 Calbindin-positive LRNs were not coupled to any of the tSCs, which may further emphasize the role of the GABAergic MS projection in contrast to glutamatergic MS projection neurons[26]. In summary, we propose that the septo-hippocampal GABAergic projection participates in CA1 beta/gamma genesis and the well-established cross-frequency coordination of theta and supra-theta oscillations, known to be crucial for spatial and working memory[20,92,138,155].

Our results also suggest updating the potential role of MS in hippocampal oscillopathies. Specifically, the MS was proposed to play important roles in Alzheimer's disease, schizophrenia, anxiety and pain, and that appropriate MS stimulation strategies may alleviate the negative consequences of these conditions[156,157]. Treatment approaches of memory impairments related to the MS, such as MS cholinergic stimulation and vagus nerve stimulation were also discussed[158]. Griguoli and Pimpinella stressed the importance of the MS in social learning, suggesting that psychopathologies accompanied by the disruption of social life may be another condition in which MS-mediated oscillogenesis is impaired[159]. We expect that exploring mouse models of these pathological conditions and test possible alterations of the MS orchestrating CA1 neurons, focusing on a broad range of frequencies from theta to mid-gamma, will be exciting new directions in the future.

Methods

Experimental model and subject details

We used adult SOM-IRES-Cre mice ($n = 10$; all males; weight: 28–30 g) for the chronic freely moving experiments, adult wild type mice ($n = 11$; 7 males; 6 mice excluded due to <360 detected theta cycles; 22–30 g) for acute mouse recordings, adult wild type Wistar rats ($n = 7$; all males; one rat excluded due to <360 theta cycles; 200–400 g) for acute rat recordings and adult PV-IRES-Cre mice ($n = 19$; 6 males; 22–30 g) for slice electrophysiology, acute awake optogenetic stimulation experiments and verification of the ChR2 expression in PV-expressing neurons. All experiments were approved by the Animal Care and Use Committee of the Institute of Experimental Medicine or the Animal Care Committee of the Research Centre for Natural Sciences and the Committee for Scientific Ethics of Animal Research of the National Food Chain Safety Office and were performed according to the 2010/63/EU Directive of the EC Council.

Animals were kept in temperature- and humidity-controlled (21 ± 1 °C and 50–60%, respectively) housing facilities with a standard 12-h light–dark cycle, with food and water available ad libitum. Mice were housed in 36 × 20 × 15-cm cages. Implanted animals were housed individually. Additionally, we analyzed the firing of previously published juxtacellularly labeled neurons[47,48,64] recorded from head-fixed C57Bl7/J mice ($n = 30$; all males; 24–37.5 g) spontaneously running and resting on a circular treadmill or disc and ventral hippocampal LFP recordings from mice in an elevated plus maze downloaded from a public repository (https://doi.org/10.7272/Q6ZP44B9)[84].

Hippocampal oscillations were examined in both sexes under awake conditions and we did not observe sex-related differences in the theta-gamma phase-amplitude coupling. Chronic electrophysiology recordings were carried out in male mice, because males tolerate chronic implants better due to weight considerations. Nevertheless, optogenetic stimulation of parvalbumin-expressing MS neurons evoked hippocampal theta-nested oscillations in female mice in line with our findings from chronic recordings performed in male mice, thus suggesting that the MS has a similar role in hippocampal oscillation genesis in both sexes. Due to these study design complexities and sample size considerations, we refrained from post-hoc sex-based analyses.

Surgical procedures

Surgeries were performed under general anesthesia. For virus injection surgeries, mice were anesthetized with an intraperitoneal injection of ketamine-xylazine mixture (dose by body weight, 167 and 7 mg/kg, respectively). Mouse chronic electrode implantation surgeries were performed under isoflurane anesthesia induced by ketamine-xylazine mixture (4:1) diluted 6x in Ringer's lactate solution (intraperitoneal injection; dose by body weight, 0.01 mg/g). In acute anesthetized experiments, rats and mice were anesthetized with an intraperitoneal injection of urethane (dose by body weight, 1.48 mg/g and 1.3 mg/g for rats and mice, respectively). The body temperature of the animals was maintained during the experiments with a heating pad. Animals were placed in a stereotaxic frame (David Kopf Instruments, Tujunga, US), the scalp was shaved, disinfected (povidone-iodine) and the skin and connective tissue of the scalp was infused by local anesthetic (Lidocaine s.c.). The eyes of the animals were protected with eye ointment (Laboratories Thea, Clermont-Ferrand, France). The skin was opened, the skull was cleaned, and the head of the animal was levelled using Bregma, Lambda and a pair of lateral points equidistant from the

Table 1 | Implant types and target coordinates in the five experiments

Experiment	CA1 implant	CA1 coordinates	MS implant	MS coordinates	Ground location
Urethane anesthetized rat	linear silicon probe (A1x32-6mm-50-177; NeuroNexus Technologies, Ann Arbor, US)	AP: −4.5 mm ML: 3 mm angle: 0°	Buzsáki-type silicon probe (Buzsaki32; NeuroNexus Technologies, Ann Arbor, US)	AP: 0.4 mm ML: 1.6 mm angle: 15°	nuchal muscles
Urethane anesthetized mice	linear silicon probe (A1x32-6mm-50-177)	AP: −2.2 mm ML: 1.5 mm angle: 0°	single shank custom silicon probe with 32 × 4 square-shaped recording sites[184]	AP: 0.6 mm ML: 0.5 mm angle: 8°	neck muscle
Freely moving mice	linear silicon probe (A1x32-6mm-50-177) or Buzsáki-type silicon probe (Buzsaki32)	AP: −2.5 mm ML: 2 mm angle: 0°	Buzsáki-type silicon probe (Buzsaki32)	AP: 0.9 mm ML: 0.9 mm angle: 12°	cerebellum
Awake head restrained mice for optogenetic stimulation	128 channels UCLA silicon microprobes (128 J or 128 A, Masmanidis lab) in both hippocampi	AP: −2.5 mm ML: 2.5 mm angle: 0°	optic fiber (200 µm core diameter, Thorlabs GmbH)	AP: 0.9 mm ML: 0 mm angle: 0°	cerebellum
Awake head restrained mice for juxtacellular recording	glass electrode filled with 0–3.0% neurobiotin (wt/vol) in 0.5 M NaCl	AP: −2.5 mm ML: 1.7 angle: 10°	glass electrode filled with 2.5–3.0% neurobiotin (wt/vol) or BDA in 0.5 M NaCl	AP: 0.85 mm ML: 0 mm angle: 0°	cerebellum

Target coordinates were defined based on[160, 168]. Coordinates in the table refer to the coordinates of the craniotomy. AP, antero-posterior; ML, medio-lateral.

sagittal suture. Before implantation, red DiI (Thermo Fisher Scientific, Waltham, US) was applied on the probes to aid later histological reconstruction. Stereotaxic coordinates[160] were used to determine the proper antero-posterior (AP) and medio-lateral (ML) positions, craniotomies were opened above the medial septum and the hippocampus, and silicon probe or optic fiber implants were lowered above the dorsal boundary of the MS and into the dorsal CA1. The MS was implanted at an angle with respect to the dorso-ventral direction in the coronal plane to avoid the sinus sagittalis superior. Finally, the ground/reference electrodes were inserted (see Table 1 for implant types, coordinates and the location of the ground/reference electrodes for the different experiments).

In case of the chronic implants, adhesive agents (OptiBond, Kerr, Brea, US) were applied on the cleaned surface of the cranium. The craniotomies were sealed with artificial dura (Cambridge NeuroTech Ltd, Cambridge, UK). Septal and hippocampal probes (Table 1) were mounted on custom-made, adjustable microdrives, and the probe-microdrive assemblies were shielded by copper mesh, preventing the recordings from contamination by environmental electric noise. The mesh was covered by dental acrylic. Before finishing the surgery, Buprenorphine (dose, 0.045 µg/g body weight) was injected subcutaneously. Recordings were started after a one-week-long post-surgery recovery and habituation to connectorization.

Mice involved in the freely moving experiments underwent bilateral injection of AAV2/5-Ef1a-DIO-ChR2-YFP-WPRE or AAV5-Ef1a-DIO-SwiChRca-TS-EYFP or AAV5-Ef1a-DIO-EYFP into the dorsal hippocampi. In case of SwiChR-transduced animals, each four shank of the septal probe was equipped with an optical fiber (50 µm core diameter, 0.22 NA) with tip positioned 75-100 micrometers above the uppermost recording site and glued by optical adhesive. In case of ChR2-transduced animals, one optical fiber (105 µm core diameter, 0.22 NA) was implanted to illuminate the fimbria, independently from the septal silicon probe. Control periods (without stimulation) were analyzed in Figs. 1–4. Stimulation periods were analyzed in Fig. 6f-g and Supplementary Fig. 18. In case of EYFP control transduced animals, two optical fibers (105 µm core diameter, 0.22 NA) were implanted bilaterally into the septum (AP, +0.90 mm; ML, 0.90 mm, at a 10° angle). The SOM-IRES-Cre mouse line and the above AAV constructs were used in a large number of studies without reporting adverse phenotypic changes, and results of these studies were interpreted as general for mice and not specific for the particular strain[64,113,135,161,162]. Therefore, we do not consider using this particular mouse line a significant limitation of our study.

Virus injection surgeries were performed for the optogenetic stimulation experiment in PV-IRES-Cre mice. MS was targeted via a trephine hole (AP, +0.90 mm; ML, 0.90 mm) at a 10° angle. An adeno-associated virus vector allowing Cre-dependent expression of channelrhodopsin2 [AAV 2/5. EF1a.Dio.hChR2(H134R)-eYFP.WPRE.hGH] or eYFP (AAV2/5.DIO.eYFP) was injected into the MS at 3.95, 4.45 and 5.25 mm depth from skull surface (200 nl at each depth). After the viral injections, the skin was sutured and local antibiotics (Neomycin) and analgesics (Buprenorphine 0.1 µg/g, s.c.) were applied.

To perform in vivo, awake, head restrained recordings during optogenetic stimulation, a small lightweight head plate was attached to the skull under isoflurane anesthesia using OptiBond (Kerr, Brea, US) adhesive and Paladur dental acrylic (Kulzer, Hanau, Germany). Two cranial windows (1.5 × 1.5 mm) were drilled above the left and right hippocampi (AP, −2.5 mm; ML, 2.5 mm) under stereotaxic guidance. An optic fiber (200 µm core diameter, Thorlabs GmbH, Newton, US) was implanted above the MS (AP, +0.9 mm; ML, 0 mm; 3.6 mm depth from the brain surface) and fixed with dental acrylic. A hole was drilled above the cerebellum for the insertion of the ground electrode. The craniotomies and drill hole were sealed with fast sealant (Body Double, Smooth-On, Macungie, US). After surgery, the mice were continuously monitored until recovered, then they were returned to their home cages for at least 48 h before starting habituation to head restraint.

Chronic recording procedures

After recovery from the surgery, the Buzsaki-type septal probes were advanced in steps of 75-150 µm per day to reach the zone of cells with theta rhythm-modulated firing pattern. Within this zone, the probe was advanced in steps of 45 µm per day, as long as the theta-modulated firing pattern was still present, through a total of 8-35 days of recording. In four animals, the hippocampus was implanted with a linear silicon probe covering the CA1 layers, which was kept in a fixed position. In two animals, a Buzsaki-type silicon probe was implanted instead of the linear probe, which was advanced stepwise to reach the pyramidal layer of the dorsal hippocampus after the post-surgery recovery period.

The electrophysiological activity was registered by a multiplexing data acquisition system (KJE-1001, Amplipex Ltd, Szeged, Hungary) at 20 kHz sampling rate while the animals were moving freely either in a linear track or in their home cages. The position of the animal was tracked by a marker-based, high speed (120 frame/s) motion capture system and reconstructed in 3D (Motive, OptiTrack, NaturalPoint Inc, Corvallis, US).

Optogenetic manipulations in the chronically implanted mice

Distinct groups of mice were used for activation (transduction with ChR2) and suppression (transduction with SwiChR) of the

hippocampo-septal fibers, as detailed above in the surgical procedures section. In the ChR2-transduced mice, the fibers passing the fimbria were illuminated by 5-ms-long pulses of blue light (447 nm, 5–8 mW, Roithner Lasertechnik, Vienna, Austria) at 20 Hz frequency for 10 s. The illumination epochs were repeated 14-22 times with manual timing during the home cage and linear track recordings. In the SwiChR-transduced mice, a consecutive pair of 10-s-long blue (447 nm, 5–8 mW, Roithner Lasertechnik, Vienna, Austria) and 1-s-long yellow (593 nm, 8-10 mW, IkeCool Corporation, Los Angeles, USA) light pulses (separated by a 2-s-long gap) was delivered by optical fibers glued 75-100 μm above the recording sites of the silicon probe. In mice injected with the EYFP control virus the same illumination protocol was used as in the SwiChR-transduced mice. The illumination was controlled by manual timing, repeated 8–26 times per home cage and linear track recording sessions. After each recording session, the probe implanted into the medial septum was lowered by 75 micrometers and after 12–24 h waiting, a new recording session was started. In both the ChR2- and SwiChR-experiments, the response upon the optogenetic manipulation was evaluated by the average firing rate change calculated in the combination of the home cage and linear track recordings. Neurons were classified as activated or suppressed based on a 10% or greater increase or decrease, respectively, in average firing rate during illumination compared to the 10-s pre-illumination period.

Acute anesthetized recordings

Neural signals were acquired and amplified by multifunction input/output cards (PCI-6259, National Instruments, Austin, US) in rats or an electrophysiological recording system (RHD2000, Intan Technologies, Los Angeles, USA) in mice and digitized at 20 kHz. To increase the single unit yield, in case of the rat recordings, we waited 30 min for the tissue to stabilize after implantation, while implants in mice were inserted slowly (2 μm/s for MS, ~10 μm/s for CA1) with a motorized micromanipulator (Robot Stereotaxic, Neurostar, Tübingen, Germany) to minimize tissue damage[163]. We carried out 30-min-long recordings in rats with 100 μm dorso-ventral separation, and 15-min-long recordings in mice at three distinct dorso-ventral positions within in the MS. Theta oscillations were induced by tail pinch (3 times 1 min in rats; once for 5 mins in mice).

Acute optogenetic stimulation experiments

Prior to the day of the recording, mice were head-fixed and let to spontaneously run or sit on an air supported free-floating Styrofoam ball to adapt to the behavioral conditions. On the day of the recording, 128-channels silicon microprobes (UCLA 128 J, masmanidislab.neurobio.ucla.edu) were lowered into the left and right dorsal hippocampi under isoflurane anesthesia. In four animals, the right hippocampus was implanted with silicon probes equipped with long vertical recording area (1.050 mm; UCLA 128 A, masmanidislab.neurobio.ucla.edu) to enable CSD analysis through CA1 layers. Ground electrode was placed above cerebellum. Mice were allowed to recover from anesthesia for 1 h before recording.

The probes were advanced by using a micromanipulator (Kopf Instruments, Tujunga, US) until the pyramidal layer was detected by increased unit activity and the occurrence of ripple events. Electrophysiological recordings were performed by a signal multiplexing head-stage (RHD 128, Intan Technologies, LA, USA). Signals were acquired at 20k sample/s (Open Ephys 0.4.4.1[164]). Mouse locomotor activity was monitored with an optical computer mouse positioned close to the spherical ball at the equator. Following a 15–30-min-long control period, theta-modulated bursts of laser light (2 ms pulse length, 447 nm, 6-10 mW, Roithner Lasertechnik GmbH, Austria) were transmitted to the MS to stimulate PV neurons (tmS, theta-modulated stimulation). Four different intra-burst frequencies (22 Hz, 35 Hz, 54 Hz, 80 Hz, mimicking the frequency of physiological tSCs1-4) were applied at 8 Hz burst occurrence (Spike2 acquisition software and the CED 1401 laboratory interface family, Cambridge Electronic Design Limited, Cambridge, UK) in separate epochs. Laser stimulations were 2–3 min long during quiet wakefulness, controlled manually. Stimulations were repeated 2–3 times.

Histological verification of the implant positions

After the recording sessions, animals were transcardially perfused with saline for 2 min and 4% para-formaldehyde (PFA) for 20 min and the brain was carefully removed and post-fixed in PFA for 24 h at 4 °C. Standard histological track reconstruction techniques[165] were used to verify the position of the silicon probe and optic fiber implants. Briefly, 60 μm thick coronal sections were cut (Vibratome VT1200S, Leica, Wetzlar, Germany), mounted on microscopic slides and covered with mounting medium (Vectashield, Vector Labs, Burlingame, CA, USA). Silicon probe implant tracks were localized by imaging red fluorescent DiI that had been applied on the electrodes before implantation, using a fluorescence microscope (Nikon Eclipse Ni microscope, Nikon Instruments, Melville, NY, USA). Fluorescent imaging of PV-expressing MS neurons confirmed the septal location of the fiber optic implant in the stimulation experiments (Supplementary Fig. 14). Finally, images were aligned with the corresponding sections of the stereotaxic mouse brain atlas[160] to enable precise reconstruction of the implant trajectory.

Acute slice electrophysiology

Mice were decapitated under deep isoflurane anesthesia. The brain was removed and placed into an ice-cold cutting solution, which had been bubbled with 95% O_2–5% CO_2 (carbogen gas) for at least 30 min before use. The cutting solution contained the following (in mM): 205 sucrose, 2.5 KCl, 26 $NaHCO_3$, 0.5 $CaCl_2$, 5 $MgCl_2$, 1.25 NaH_2PO_4, 10 glucose. Coronal slices of 300-μm thickness were cut using a Vibratome (Leica VT1200S). After acute slice preparation, slices were placed into an interface-type holding chamber for recovery. This chamber contained standard ACSF solution at 35 °C which gradually cooled down to room temperature. The ACSF solution contained the following (in mM): 126 NaCl, 2.5 KCl, 26 $NaHCO_3$, 2 $CaCl_2$, 2 $MgCl_2$, 1.25 NaH_2PO_4, 10 glucose, saturated with 95% O_2–5% CO_2. Recordings were performed under visual guidance using Nikon Eclipse FN1 microscope with infrared differential interference contrast (DIC) optics. Patch pipettes were pulled from borosilicate capillaries (with inner filament, thin-walled, outer diameter (OD) 1.5) with a PC-10 puller (Narishige). The composition of the intracellular pipette solution was as follows (in mM): 110 potassium gluconate, 4 NaCl, 20 4-(2-hydroxyethyl)−1-piperazine-ethanesulfonic acid, 0.1 (ethylenebis(oxonitrilo))tetra-acetate, 10 phosphocreatine, 2 ATP, 0.3 GTP, 3 mg ml^{-1} of biocytin adjusted to pH 7.3–7.35 using KOH (285–295 mosmol l^{-1}). Recordings were performed with a Multiclamp 700B amplifier (Molecular Devices), digitized at 20 kHz with Digidata analog-digital interface (Molecular Devices), and recorded with pClamp11 Software suite (Molecular Devices). For in vitro light illumination, we used a blue LED light source (Prizmatix Ltd.) integrated into the optical light path of the microscope. Two ms long light pulses were delivered at different theta-modulated gamma (tmS1-4, 2 pulses @22 and 3 pulses @ 35/50/80 Hz) frequencies. To record optogenetically evoked IPSCs, cells were clamped to −10 mV. Current clamp recordings of spiking modulation by PV+ MS input stimulation were performed with constant somatic current injection via the recording pipette to evoke spiking.

Immunohistochemistry

To verify the specificity of the ChR2 expression in PV expressing neurons, a separate cohort of PV-Cre mice were sacrificed following 2–3 weeks of the virus injection into the MS ($n = 3$). After re-sectioning of the brain into 50 μm thick slices, sections containing the MS were washed in 0.1 M phosphate buffer and tris-buffered saline, and incubated in blocking medium (1% human serum albumin + 0.1% Triton-X

detergent) for 1 h. Then, sections were incubated in primary antibody against PV (PV 27, Swant, Switzerland, 1:2000) mixed with primary antibody against GFP (Thermofisher Scientific, USA, cat#A10262, 1:1000) in TBS at 4 °C for two days. After an extensive wash in TBS, the tissue was incubated in a secondary antibody solution containing Alexa 488 conjugated goat anti-chicken (Thermofisher Scientific, USA, Cat#A11039, 1:1000), Alexa 594 conjugated donkey anti-rabbit (Jackson ImmunoResearch Europe Ltd., UK, cat#711585152, 1:500) or Alexa 647 conjugated donkey anti-rabbit (Jackson ImmunoResearch Europe Ltd., UK, cat#711605152, 1:500) antibodies at 4 °C overnight. Finally, the sections were mounted on slides in aqua-Poly/Mount mounting medium (cat#18606, Polysciences, Inc., USA) and images were taken with a Nikon A1R confocal microscope.

After acute slice electrophysiology experiments, brain sections were fixed overnight in 4% PFA. After extensive wash in TBS, a similar staining protocol was used to detect parvalbumin or somatostatin immunoreactivity of the recorded cells. In these experiments, we applied SOM primary antibody (Origene, #AP3364SU-N, 1:200) and included 0.1% Triton-X detergent in every incubation step due to the thickness of the brain sections.

Hippocampal theta state detection

The hippocampal pyramidal layer was detected in linear silicon probe recordings by analyzing the phase reversal of the theta oscillation, and was verified by histological reconstruction[6,166,167] similar to ref. 52. We used the signal recorded from the stratum radiatum for detecting theta oscillation, since theta rhythm had the highest amplitude and thus enable the most reliable detection in this layer (~400 μm and 250 μm below pyramidal layer in rats and mice, respectively, based on[160,168]). In case of the 2 mice with Buzsaki-type probes implanted in the hippocampus, we used the deepest channels for theta detection.

Hippocampal LFP was resampled at 1 kHz and filtered in the theta and delta bands (Supplementary Fig. 3a, e and i). Frequency band boundaries were defined based on the Fourier spectra of the raw LFP (delta, 0.5–4 Hz, theta, 4–12 Hz), similarly to ref. 52. The filtered theta and delta signals were Hilbert transformed, and their instantaneous amplitude was calculated as the magnitude of the complex Hilbert-transform. Hippocampal theta and non-theta states were determined based on the amplitude ratio of theta and delta band filtered signals. Theta oscillation was detected whenever this theta-delta amplitude ratio exceeded 2 for at least 3 s. Short interruptions in longer segments were not considered as state transitions (<3 s). Long theta epochs were defined as theta episodes >20 s. Theta transition periods were defined at the margins of long theta epochs, as the time windows in which the amplitude ratio was between 1.5 and 2.

tSC extraction from hippocampal LFP

tSCs were extracted as described by Lopes dos Santos et al.[15] using their open source tSC extraction package (https://data.mrc.ox.ac.uk/data-set/tsc). First, LFPs were downsampled at 1 kHz and Ensemble Empirical Mode Decomposition (EEMD[65]) was applied to decompose the signal into its elementary spectral components called Intrinsic Mode Functions (IMFs). Low frequency, theta and supra-theta signals were defined as the sum of the IMFs with mean instantaneous frequencies below, within and above the theta frequency band, respectively. Second, we searched for local maxima and minima in the theta signal with absolute values above the low-frequency signal to detect potential theta peaks and troughs. We defined individual theta cycles by consecutive troughs occurring at theta band frequency (4–12 Hz in awake mice, 3–7 Hz in anesthetized rats, 2–6 Hz in anesthetized mice), separated by a peak. Third, spectrograms of the supra-theta signal were computed for each detected theta cycle with a set of complex Morlet wavelets with main frequencies ranging from the upper limit of the theta band to 200 Hz, in 1 Hz steps (Figs. 1f, 7a and Supplementary Fig. 14a). Fourth, spectral signatures were defined for each detected theta cycle by taking the mean amplitude of these frequency components. Fifth, dimensionality reduction was performed by principal component analysis on the spectral signatures and tSCs were extracted from the spectral signatures based on the first five principal components using independent component analysis (ICA). Finally, tSC strength across individual theta cycles was defined as the projection of the given tSC onto the single cycle spectral signature. To examine septal firing during strong tSC presence, we defined strong tSCs by the following threshold applied on the tSC strengths, as introduced by[15]:

$$\text{Threshold} = \frac{\sigma \times \text{median}(|p - \text{median}(p)|)}{0.6745} + \text{median}(p) \quad (1)$$

where p is strength distribution for the given tSC and $\text{median}(p)/0.6745$ is an estimate of the standard deviation of p if outlying values are not considered. σ (i.e. the number of standard deviations from the median) was set to 2 in line with[15]. For the short duration juxtacellular recordings we applied the same threshold with $\sigma = 1$ and tSCs expressed in <35 theta cycles recorded simultaneously with the MS neuron were not further analyzed. This lead to the exclusion of 6 juxtacellularly labeled neurons (MS33, MS77b, AJ48j, AJ42m, AJ43n, AJ45h). In an additional 7 juxtacellularly labeled neurons, coupling to tSC3 and/or tSC4 could not be analyzed (marked gray in Fig. 5c).

Spike sorting of septal units

Mouse MS and CA1 recordings were fed to the template-based spike sorting software Kilosort[169]. Kilosort was run on an Nvidia Geforce GTX 1080 graphic card using the Matlab Parallel Computing Toolbox to reduce execution time. Automatically assigned clusters were manually curated by examining violations of the refractory periods, spatial distributions of action potential (AP) energies among neighboring channels, AP shapes and amplitudes, the principal components (PC) of the AP shapes, and crosscorrelograms between pairs of clusters using the Phy template-gui graphical user interface module (https://github.com/cortex-lab/phy). Quality of the retained clusters were assessed by objective measures derived from the interspike interval histograms and cluster isolation distances.

Spike sorting of the anesthetized rat MS recordings were performed using KlustaKwik[170] (http://github.com/klusta-team). Results were curated manually to exclude multi-unit activities and noise clusters by the examination of autocorrelograms (ACG, to exclude refractory period violations) and crosscorrelograms[134]. Similar to above, cluster quality was assessed by the Mahalanobis distance-based cluster isolation distances.

Firing pattern analysis of MS neurons

Inter-spike interval histograms normalized by the number of spikes were calculated for each neuron separately and the average of these histograms was taken for all neurons to demonstrate bursting activity (Fig. 1b). To examine the spectral content of MS spiking activity, single unit spike trains were convolved with an 8-ms Gaussian kernel to generate pseudo-continuous signals[171] and a fast Fourier transform algorithm was applied to compute the frequency spectra of the signals. Spectra were smoothed with a 1 Hz wide moving average window, normalized with the area under the curve in the 4-200 Hz range and averaged across neurons (Fig. 1c).

MS neurons' spiking activity as a function of tSC presence

We defined a number of spiking properties, to compare MS neurons' firing during theta cycles with different tSC presence. First, average firing rates were computed across theta cycles (Fig. 2a) for each neuron. Then, to determine spike phases, hippocampal theta phase was computed by linearly interpolating values between peaks (0 or 2π), zero-crosses (descending, π/2; ascending, 3π/2) and troughs (π), and

the phase values corresponding to the time of the spikes were taken. Significance of theta coupling was judged by Rayleigh's test for circular uniformity at $p < 0.01$ significance level. Theta phase–spiking probability histograms were calculated with π/8 bin width (Fig. 2a). Phase coupling strength and preferred phase were defined by the magnitude and the angle of the first trigonometric moment of the spike phases for each theta-coupled MS neuron.

Next, bursts were detected as series of two or more action potentials with inter-spike intervals <40 ms (typical threshold employed in medial septum studies[52,172]), which allowed us to calculate the burst-skip ratio of each neuron as the ratio of theta cycles without a burst. We calculated the mean intra-burst spike number as the number of spikes in the burst per theta cycle and the mean intra-burst frequency as the ratio of the length of the bursts and the intra-burst spike number.

Differences in these properties (i.e. firing rate, phase coupling strength, intra-burst frequency, intra-burst spike number, burst-skip ratio) as a function of tSC presence were tested with repeated measures ANOVA followed by Tukey's test for post hoc comparisons. In this analysis neurons with stable, sufficient activity were used, to avoid potential bias due to the non-uniform time distribution of tSCs ($n = 198$, MS neurons with >3 Hz firing rate and stable spike amplitude). The entire set of well isolated MS units ($n = 365$) were used for all other analyses, since those were not sensitive to this sampling issue. The properties (P) were normalized with their grand averages across all theta cycles (P_{all}) to better visualize relative differences across theta cycles with different tSCs (Fig. 2b, c, e and Supplementary Fig. 4) with the following formula:

$$P_{tSC\ cycles,\ norm} = \frac{P_{tSC\ cycles} - P_{all\ cycles}}{P_{all\ cycles}} \quad (2)$$

Average phase histograms were calculated from phase values relative to the preferred phase of each neuron (Fig. 2c and Supplementary Fig. 2f–h) or from the preferred phase of the tSCs (Supplementary Fig. 2b).

We calculated the inter-spike interval (ISI) histograms of the action potentials of single neurons during different theta cycles with 5 ms bins (Supplementary Fig. 7). To visualize ISI surplus related the concurrent tSCs, we first calculated the ISI histogram during theta cycles strongly expressing a given tSC. Then we took the same number of theta cycles expressing the given tSC the least (control histogram) and compared these two histograms, focusing on the bins corresponding to the frequency of the concurrent tSC. We repeated this analysis for identified PV-expressing MS neurons, normalized the difference histogram with the baseline firing rate of the neurons and averaged them across neurons. ISI histograms were plotted with both linear and logarithmic scaling to properly visualize ISI differences at lower and higher tSC frequencies (Supplementary Fig. 12).

MS Rhythmicity groups

Rhythmic firing of MS neurons was quantified using autocorrelograms (ACG), similar to ref. 52. ACGs were calculated in a ± 3 s window with 1 ms resolution and smoothed with a 20 ms moving average. MS neurons with >2 spikes per ACG bins on average were further analyzed. ACG peaks were detected between time lags corresponding to the delta (0.5–4 Hz) and theta (4–12 Hz) frequency bands. ACG values were averaged in ±20 ms windows around the peaks. Similarly, ACG values were averaged in ±20 ms windows around assumed troughs at the half and one and a half peak locations. The difference of these mean ACG values around peaks and troughs was normalized to the larger of the two, yielding a Delta and a Theta Rhythmicity Index between −1 and 1. Both indices were calculated during theta and non-theta segments for each MS neuron. To determine the significance of rhythmic modulation, we simulated spike trains using a Poisson-process, with frequencies matched to the firing rate of the recorded neurons. Rhythmicity indices were calculated for the simulated spike trains as above, resulting in distributions corresponding to the null hypothesis of no rhythmic modulation. Critical values corresponding to the $p = 0.05$ significance levels were determined based on these distributions and applied as thresholds for judging significance of rhythmic modulation of MS neurons, for non-theta and theta segments separately. Rhythmicity was categorized by the larger of the two rhythmicity indices for those neurons that were both theta- and delta-rhythmic.

MS neurons that were significantly theta-rhythmic during both non-theta and theta segments were further categorized based on the presence of rhythmic burst firing. A Theta Burst Index (TBI) was calculated by comparing the average ACG in a burst lag window (10-30 ms) to the overall mean (see also ref. 52). MS neurons with TBI > 0 displayed constitutive rhythmic bursting activity, thought to be important for generating hippocampal theta oscillations[11,50,63,106]; they are referred to as constitutive bursting neurons. Theta-rhythmic MS neurons with TBI < 0 showed a regular rhythmic firing pattern, resembling the firing patterns of tonically active neurons of the striatum[173–175]; therefore, we refer to them as tonically active MS neurons. MS neurons that were theta-rhythmic when theta oscillations were present in the CA1 but non-rhythmic otherwise were referred to as theta-associated bursting MS neurons.

Spike/stimulus triggered averages and spectrograms

The CA1 LFP signal or the pseudo-continuous MS signal (see above) was triggered on spikes of MS neurons and the average signal was calculated in ±100 ms time windows around MS spikes (spike triggered average, STA). Individual LFP averages were Z-scored. Similarly, stimulus triggered LFP averages were calculated aligned to optogenetic stimulation in ±200 ms time windows. Photovoltaic artefacts were observed in both the channelrhodopsin2-expressing and the control mice within 7 ms following stimuli, as reported before[176]. These were removed, and corresponding data points were spline interpolated. Stimulation-evoked theta oscillations and tSCs were clearly distinct from photovoltaic artefacts, characterized by longer latencies and phase changes as a function of recording depth.

Spectrograms were calculated by wavelet transformation using Morlet wavelets[177]. Spike and stimulus triggered spectrograms (STS) were calculated similarly to the LFP averages, separately for wavelet amplitudes and wavelet phases. Individual frequencies were normalized with their averages to give equal weight to each spectral component (Figs. 1d, 3a, and Supplementary Figs. 15).

To measure the coherence between CA1 LFP and (pseudo-continuous) MS spiking, we calculated the magnitude squared wavelet coherence. Similar to STS, individual frequencies were normalized with their averages (Fig. 1d).

Phase coupling of MS neurons to tSCs

The IMF with the closest median frequency to the peak frequency of the tSC was considered as a reference signal for theta cycles strongly expressing the given tSC. MS spikes in each theta cycle were aligned to the largest trough of this reference signal and visualized as raster plots and peri-event time histograms (PETHs), smoothed by a Gaussian kernel (standard deviations: tSC1, 10 ms; tSC2, 8 ms; tSC3, 6 ms; tSC4, 4 ms; Fig. 3b and Supplementary Fig. 6).

To quantify phase coupling to tSCs, instantaneous tSC phase was computed as the phase of the complex Hilbert-transform of the reference signal. We considered two full cycles around the largest trough, reflecting the typical number of tSC cycles with sufficient signal-to-noise ratio within one theta cycle. Phase values were assigned to the spikes within this window by taking the instantaneous phase values at the spike times. This resulted in systematically longer time windows for slower tSCs, which could potentially lead to a systematic

bias in statistical power. To correct for this, we determined the tSC with the lowest number of action potentials, and spikes were randomly subsampled to yield an equal number of spikes for the other tSCs for unbiased statistical comparison (except for juxtacellular recordings, because of their short duration). Since we did not observe clear tSC5-coupled firing patterns on the raster plots, we did not include the fastest tSC5 components in this analysis. We tested significant phase locking to the different tSCs after applying different temporal shifts on the MS spike train in the −100 ms – 100 ms range, recognizing that different temporal offsets were possible between the two time series[49,72]. Phase-coupling was tested by Rayleigh's test at each shift separately at $p < 0.05$. To control type I errors caused by testing phase coupling multiple times, we used Storey's false discovery rate method to adjust p-values[73]. Neurons with insufficient number of action potentials (<10 in theta cycles during any of the tSCs) were automatically considered as non-coupled to avoid false positives. Preferred tSC phase of each tSC-coupled MS neuron was defined as the angle of the first trigonometric moment of the spike phases. To control for correlations driven by associations with theta phase, MS spikes were randomly shuffled between theta cycles while conserving their time lag from the theta peaks and phase coupling to tSC was tested as for the non-shuffled spikes.

To visualize tSC-coupling on the population level, peri-event phase histograms (PEPHs) were calculated (Figs. 3c, 5d, 7d and Supplementary Fig. 19d). We calculated the firing rate in bins of π/20 radians around the largest tSC trough. PEPHs were smoothed with a Gaussian kernel (0.3π standard deviation) and Z-score normalized.

We examined the temporal structure of correlation between MS spiking and CA1 tSCs. Similar to crosscorrelation approaches, the temporal lag that maximizes the correlation, here expressed as phase coupling strength, reveals the temporal offset between corresponding changes in the underlying variables. Negative temporal lags indicate shifting the CA1 tSC signal back or, equivalently, shifting the MS spike train forward in time. We calculated Rayleigh's Z-value, the test statistic of Rayleigh's test for circular uniformity, as a function of a temporal shift added to the MS spikes in the range of −100 ms to +100 ms, with a resolution of 1 ms (similar to refs. 49,72). These Z-value functions were normalized by their maxima and averaged across all coupled MS neurons for each tSC. Average Z-value functions were smoothed with a Gaussian kernel (1.5 ms standard deviation) for visualization purposes (Fig. 4c, Supplementary Figs. 9c and 10c).

To examine the frequency accommodation of tSCs, we measured the time difference between the largest trough and the two troughs preceding and following the largest trough in each theta cycle strongly expressing the given tSC (Supplementary Fig. 11a). The average of these time differences was computed for each session and each tSC. To compare these dynamics with their septal counterparts, we first calculated PETHs triggered by the largest tSC trough for each single unit coupled to the given tSC, then bandpass-filtered them around the frequency of the concurrent tSC (passband frequency ranges: tSC1, 18-35 Hz; tSC2, 20-50 Hz; tSC3, 30-70 Hz; tSC4, 60-100 Hz). We searched for local maxima and minima in the filtered signal to detect peaks and troughs. To identify troughs and peaks most likely related to the largest amplitude tSC cycle, we located the trough and peak closest to the optimal lag that maximized the phase coupling and calculated the time difference between preceding and following troughs and peaks (Supplementary Fig. 11b–d).

Analysis of stimulus-evoked CA1 tSCs and spiking activity

Stimulus evoked tSCs were analyzed using the same algorithms as the spontaneous tSCs (see the "tSC extraction from hippocampal LFP" section). Theta cycles and theta phase were automatically detected using EEMD as described in the "tSC extraction from hippocampal LFP" section. Spikes of CA1 single units were aligned to the onset of the first pulse of each tmS burst and visualized as raster plots and peri-stimulus time histograms (PSTHs) smoothed by a Gaussian kernel of 2 ms standard deviation (Fig. 6c). Putative interneurons were identified based on their high firing rate, narrow spike shape and characteristic autocorrelogram (Supplementary Fig. 16b[2,178,179]).

Current source density analysis

Current source density (CSD) analysis was performed on the laminar LFP recorded along the somato-dendritic axis of CA1 pyramidal neurons by linear equidistant ($\Delta z = 50\mu m$) silicon probe contact sites to localize currents sources of CA1 tSCs. It has been shown that if the extracellular conductivity tensor is assumed to be isotropic and homogenous, then the CSD signal can be expressed analogously with the Poisson equation of electrostatics (for the derivation see e.g. ref. 180). Consequently, in laminar structures, where the intra-layer changes in the extracellular potential (ϕ) are negligable, the CSD can be approximated by the second spatial derivative of the LFP along the z-direction perpendicular to the layer[181,182]:

$$\mathrm{CSD} = -\sigma \frac{\partial^2 \phi}{\partial^2 z} \tag{3}$$

where σ is the isotropic and homogeneous extracellular conductivity. Therefore, we estimated the space and time dependent component of the CSD signal ($\widetilde{CSD}$) on the n-th contact site at time t according to the following formula[15,22]:

$$\widetilde{\mathrm{CSD}}(t)_n \sim \mathrm{LFP}(t)_{n-1} + \mathrm{LFP}(t)_{n+1} - 2 \times \mathrm{LFP}(t)_n \tag{4}$$

where $LFP(t)_n$ is the potential measured on the n-th contact site at time t. The theta phase – frequency plots of the supra-theta CSD signal amplitude (Fig. 6d, e and Supplementary Fig. 17) were computed by the same wavelet approach as that applied on the LFPs (e.g. Fig. 1c, see the "tSC extraction from hippocampal LFP" section), similarly to refs. 15,22. Theta phase was defined based on the radiatum layer LFP for all plots, and tSCs were extracted from the radiatum layer LFP for Supplementary Fig. 17.

Reporting summary

Further information on research design is available in the Nature Portfolio Reporting Summary linked to this article.

Data availability

The awake and anesthetized rodent electrophysiology recording data used in this study have been deposited at https://doi.org/10.6084/m9.figshare.23798184. The optogenetic stimulation and electrophysiology recording data generated in this study have been deposited at https://doi.org/10.5281/zenodo.8191988. The juxtacellular recording data from anatomically identified neurons used in this study have been deposited at https://doi.org/10.5281/zenodo.8187903. Ventral hippocampal LFP recordings from mice in an elevated plus maze used in this study are available at https://doi.org/10.7272/Q6ZP44B9[84]. All data points underlying means, line graphs, box plots and scatter plots presented in the figures are provided in a Source Data Excel file with further labeled .mat files for panels presenting multidimensional data. Further data is available from the lead contact upon request. Source data are provided with this paper.

Code availability

MATLAB code developed to analyze the data is available at https://github.com/kiralyb/MS_mod_tSC[183] (https://doi.org/10.5281/zenodo.8197408). Test data of a demo session of a chronically implanted mouse is available at https://doi.org/10.6084/m9.figshare.22060964.

References

1. Vanderwolf, C. Hippocampal electrical activity and voluntary movement in the rat. *Electroencephalogr. Clin. Neurophysiol.* **26**, 407–418 (1969).
2. Csicsvari, J., Hirase, H., Czurkó, A., Mamiya, A. & Buzsáki, G. Oscillatory coupling of hippocampal pyramidal cells and interneurons in the behaving rat. *J. Neurosci.* **19**, 274–287 (1999).
3. O'Keefe, J. & Recce, M. L. Phase relationship between hippocampal place units and the EEG theta rhythm. *Hippocampus* **3**, 317–330 (1993).
4. Colgin, L. L. Mechanisms and functions of theta rhythms. *Annu. Rev. Neurosci.* **36**, 295–312 (2013).
5. O'Keefe, J. Hippocampus, theta, and spatial memory. *Curr. Opin. Neurobiol.* **3**, 917–924 (1993).
6. Buzsáki, G. *Rhythms of the Brain Rhythms of the Brain* (Oxford Univ. Press, 2006).
7. Buzsáki, G. & Moser, E. I. Memory, navigation and theta rhythm in the hippocampal-entorhinal system. *Nat. Neurosci.* **16**, 130–138 (2013).
8. Losonczy, A., Zemelman, B. V., Vaziri, A. & Magee, J. C. Network mechanisms of theta related neuronal activity in hippocampal CA1 pyramidal neurons. *Nat. Neurosci.* **13**, 967–972 (2010).
9. Buzsáki, G. Theta oscillations in the hippocampus. *Neuron* **33**, 325–340 (2002).
10. Kramis, R., Vanderwolf, C. H. & Bland, B. H. Two types of hippocampal rhythmical slow activity in both the rabbit and the rat: Relations to behavior and effects of atropine, diethyl ether, urethane, and pentobarbital. *Exp. Neurol.* **49**, 58–85 (1975).
11. Bland, B. H. The physiology and pharmacology of hippocampal formation theta rhythms. *Prog. Neurobiol.* **26**, 1–54 (1986).
12. Sainsbury, R. S., Heynen, A. & Montoya, C. P. Behavioral correlates of hippocampal type 2 theta in the rat. *Physiol. Behav.* **39**, 513–519 (1987).
13. Mikulovic, S. et al. Ventral hippocampal OLM cells control type 2 theta oscillations and response to predator odor. *Nat. Commun.* **9**, 3638 (2018).
14. Quinn, A. J. et al. Within-cycle instantaneous frequency profiles report oscillatory waveform dynamics. *J. Neurophysiol.* **126**, 1190–1208 (2021).
15. Lopes-dos-Santos, V. et al. Parsing hippocampal theta oscillations by nested spectral components during spatial exploration and memory-guided behavior. *Neuron* **100**, 940–952.e7 (2018).
16. Bragin, A. et al. Gamma (40-100 Hz) oscillation in the hippocampus of the behaving rat. *J. Neurosci.* **15**, 47–60 (1995).
17. Colgin, L. L. & Moser, E. I. Gamma oscillations in the hippocampus. *Physiology* **25**, 319–329 (2010).
18. Fernández-Ruiz, A. et al. Entorhinal-CA3 dual-input control of spike timing in the hippocampus by theta-gamma coupling. *Neuron* **93**, 1213–1226.e5 (2017).
19. Klausberger, T. & Somogyi, P. Neuronal diversity and temporal dynamics: the unity of hippocampal circuit operations. *Science* **321**, 53–57 (2008).
20. Lisman, J. E. & Jensen, O. The theta-gamma neural code. *Neuron* **77**, 1002–1016 (2013).
21. Csicsvari, J., Jamieson, B., Wise, K. D. & Buzsáki, G. Mechanisms of gamma oscillations in the hippocampus of the behaving rat. *Neuron* **37**, 311–322 (2003).
22. Lasztóczi, B. & Klausberger, T. Layer-specific GABAergic control of distinct gamma oscillations in the CA1 hippocampus. *Neuron* **81**, 1126–1139 (2014).
23. Navas-Olive, A. et al. Multimodal determinants of phase-locked dynamics across deep-superficial hippocampal sublayers during theta oscillations. *Nat. Commun.* **11**, 2217 (2020).
24. Freund, T. F. & Antal, M. GABA-containing neurons in the septum control inhibitory interneurons in the hippocampus. *Nature* **336**, 403–405 (1988).
25. Zutshi, I. et al. Hippocampal neural circuits respond to optogenetic pacing of theta frequencies by generating accelerated oscillation frequencies. *Curr. Biol.* **28**, 1179–1188.e3 (2018).
26. Huh, C. Y. L., Goutagny, R. & Williams, S. Glutamatergic neurons of the mouse medial septum and diagonal band of broca synaptically drive hippocampal pyramidal cells: Relevance for hippocampal theta rhythm. *J. Neurosci.* **30**, 15951–15961 (2010).
27. Zaborszky, L., van den Pol, A. & Gyengesi, E. In *The Mouse Nervous System*. Ch. 28 (Elsevier Inc, 2012).
28. Fuhrmann, F. et al. Locomotion, theta oscillations, and the speed-correlated firing of hippocampal neurons are controlled by a medial septal glutamatergic circuit. *Neuron* **86**, 1253–1264 (2015).
29. Norimoto, H., Mizunuma, M., Ishikawa, D., Matsuki, N. & Ikegaya, Y. Muscarinic receptor activation disrupts hippocampal sharp wave-ripples. *Brain Res.* **1461**, 1–9 (2012).
30. Dannenberg, H. et al. Synergy of direct and indirect cholinergic septo-hippocampal pathways coordinates firing in hippocampal networks. *J. Neurosci.* **35**, 8394–8410 (2015).
31. Lee, M. G., Chrobak, J. J., Sik, A., Wiley, R. G. & Buzsáki, G. Hippocampal theta activity following selective lesion of the septal cholinergic system. *Neurosci.* **62**, 1033–1047 (1994)
32. Vandecasteele, M. et al. Optogenetic activation of septal cholinergic neurons suppresses sharp wave ripples and enhances theta oscillations in the hippocampus. *Proc. Natl Acad. Sci. USA* **111**, 13535–13540 (2014).
33. Newman, E. L., Gillet, S. N., Climer, J. R. & Hasselmo, M. E. Cholinergic blockade reduces theta-gamma phase amplitude coupling and speed modulation of theta frequency consistent with behavioral effects on encoding. *J. Neurosci.* **33**, 19635–19646 (2013).
34. Lawson, V. H. & Bland, B. H. The role of the septohippocampal pathway in the regulation of hippocampal field activity and behavior: analysis by the intraseptal microinfusion of carbachol, atropine, and procaine. *Exp. Neurol.* **120**, 132–144 (1993).
35. Vertes, R. P. & Kocsis, B. Brainstem-diencephalo-septohippocampal systems controlling the theta rhythm of the hippocampus. *Neurosci.* **81**, 893–926 (1997).
36. Petsche, H. & Stumpf, C. The origin of theta-rhytm in the rabbit hippocampus. *Wien. Klin. Wochenschr.* **74**, 696–700 (1962).
37. Boyce, R., Glasgow, S. D., Williams, S. & Adamantidis, A. Causal evidence for the role of REM sleep theta rhythm in contextual memory consolidation. *Science* **352**, 812–816 (2016).
38. Yoder, R. M. & Pang, K. C. H. Involvement of GABAergic and cholinergic medial septal neurons in hippocampal theta rhythm. *Hippocampus* **15**, 381–392 (2005).
39. Kocsis, B. & Kaminski, M. Dynamic changes in the direction of the theta rhythmic drive between supramammillary nucleus and the septohippocampal system. *Hippocampus* **16**, 531–540 (2006).
40. Pan, W.-X. & McNaughton, N. The role of the medial supramammillary nucleus in the control of hippocampal theta activity and behaviour in rats. *Eur. J. Neurosci.* **16**, 1797–1809 (2002).
41. Kocsis, B. & Vertes, R. P. Phase relations of rhythmic neuronal firing in the supramammillary nucleus and mammillary body to the hippocampal theta activity in urethane anesthetized rats. *Hippocampus* **7**, 204–214 (1997).
42. Martínez-Bellver, S. et al. Regular theta-firing neurons in the nucleus incertus during sustained hippocampal activation. *Eur. J. Neurosci.* **41**, 1049–1067 (2015).
43. Cervera-Ferri, A. et al. Theta synchronization between the hippocampus and the nucleus incertus in urethane-anesthetized rats. *Exp. Brain Res.* **211**, 177–192 (2011).

44. Szőnyi, A. et al. Brainstem nucleus incertus controls contextual memory formation. *Science* **364**, eaaw0445 (2019).
45. Ma, S. et al. Modulation of hippocampal theta oscillations and spatial memory by relaxin-3 neurons of the nucleus incertus. *Learn. Mem.* **16**, 730–742 (2009).
46. Lu, L. et al. Control of locomotor speed, arousal, and hippocampal theta rhythms by the nucleus incertus. *Nat. Commun.* **11**, 1–16 (2020).
47. Salib, M. et al. GABAergic medial septal neurons with low-rhythmic firing innervating the dentate gyrus and hippocampal area CA3. *J. Neurosci.* **39**, 4527–4549 (2019).
48. Joshi, A., Salib, M., Viney, T. J., Dupret, D. & Somogyi, P. Behavior-dependent activity and synaptic organization of septo-hippocampal GABAergic neurons selectively targeting the hippocampal CA3 area. *Neuron* **96**, 1342–1357.e5 (2017).
49. Hangya, B., Borhegyi, Z., Szilagyi, N., Freund, T. F. & Varga, V. GABAergic neurons of the medial septum lead the hippocampal network during theta activity. *J. Neurosci.* **29**, 8094–8102 (2009).
50. Varga, V. et al. The presence of pacemaker HCN channels identifies theta rhythmic GABAergic neurons in the medial septum. *J. Physiol.* **586**, 3893–3915 (2008).
51. Wang, X.-J. Pacemaker neurons for the theta rhythm and their synchronization in the septohippocampal reciprocal loop. *J. Neurophysiol.* **87**, 889–900 (2002).
52. Kocsis, B. et al. Huygens synchronization of medial septal pacemaker neurons generates hippocampal theta oscillation. *Cell Rep.* **40**, 111149 (2021).
53. Colgin, L. L. Rhythms of the hippocampal network. *Nat. Rev. Neurosci.* **17**, 239–249 (2016).
54. Colgin, L. L. et al. Frequency of gamma oscillations routes flow of information in the hippocampus. *Nature* **462**, 353–357 (2009).
55. Schomburg, E. W. et al. Theta phase segregation of input-specific gamma patterns in entorhinal-hippocampal networks. *Neuron* **84**, 470–485 (2014).
56. Hájos, N. et al. Spike timing of distinct types of GABAergic interneuron during hippocampal gamma oscillations in vitro. *J. Neurosci.* **24**, 9127–9137 (2004).
57. Belluscio, M. A., Mizuseki, K., Schmidt, R., Kempter, R. & Buzsáki, G. Cross-frequency phase-phase coupling between θ and γ oscillations in the hippocampus. *J. Neurosci.* **32**, 423–435 (2012).
58. Lasztóczi, B. & Klausberger, T. Hippocampal place cells couple to three different gamma oscillations during place field traversal. *Neuron* **91**, 34–40 (2016).
59. Lasztóczi, B. & Klausberger, T. Distinct gamma oscillations in the distal dendritic fields of the dentate gyrus and the CA1 area of mouse hippocampus. *Brain Struct. Funct.* **222**, 3355–3365 (2017).
60. Buzsáki, G., Gage, F. H., Czopf, J. & Björklund, A. Restoration of rhythmic slow activity (θ) in the subcortically denervated hippocampus by fetal CNS transplants. *Brain Res.* **400**, 334–347 (1987).
61. Ford, R. D., Colom, L. V. & Bland, B. H. The classification of medial septum-diagonal band cells as σ-on or σ-off in relation to hippocampal EEG states. *Brain Res.* **493**, 269–282 (1989).
62. Manns, I. D., Alonso, A. & Jones, B. E. Rhythmically discharging basal forebrain units comprise cholinergic, GABAergic, and putative glutamatergic cells. *J. Neurophysiol.* **89**, 1057–1066 (2003).
63. Borhegyi, Z. et al. Phase segregation of medial septal GABAergic neurons during hippocampal theta activity. *J. Neurosci.* **24**, 8470–8479 (2004).
64. Viney, T. J. et al. Shared rhythmic subcortical GABAergic input to the entorhinal cortex and presubiculum. *Elife* **7**, 1–35 (2018).
65. Wu, Z. & Huang, N. E. Ensemble empirical mode decomposition: A noise-assisted data analysis method. *Adv. Adapt. Data Anal.* **01**, 1–41 (2009).
66. Chen, Z., Resnik, E., McFarland, J. M., Sakmann, B. & Mehta, M. R. Speed controls the amplitude and timing of the hippocampal gamma rhythm. *PLoS One* **6**, e21408 (2011).
67. Bland, B. H., Oddie, S. D. & Colom, L. V. Mechanisms of neural synchrony in the septohippocampal pathways underlying hippocampal theta generation. *J. Neurosci.* **19**, 3223–3237 (1999).
68. Hassani, O. K., Lee, M. G., Henny, P. & Jones, B. E. Discharge profiles of identified GABAergic in comparison to cholinergic and putative glutamatergic basal forebrain neurons across the sleep-wake cycle. *J. Neurosci.* **29**, 11828–11840 (2009).
69. King, C. et al. The rhythmicity of cells of the medial septum/diagonal band of Broca in the awake freely moving rat: Relationships with behaviour and hippocampal theta. *Eur. J. Neurosci.* **10**, 464–477 (1998).
70. Hasselmo, M. E. Neuronal rebound spiking, resonance frequency and theta cycle skipping may contribute to grid cell firing in medial entorhinal cortex. *Philos. Trans. R. Soc. B Biol. Sci.* **369**, 20120523 (2014).
71. Brandon, M. P., Bogaard, A. R., Schultheiss, N. W. & Hasselmo, M. E. Segregation of cortical head direction cell assemblies on alternating theta cycles. *Nat. Neurosci.* **16**, 739–748 (2013).
72. Siapas, A. G., Lubenov, E. V. & Wilson, M. A. Prefrontal phase locking to hippocampal theta oscillations. *Neuron* **46**, 141–151 (2005).
73. Storey, J. D. A direct approach to false discovery rates. *J. R. Statist. Soc. B* **64**, 479–498 (2002).
74. Freund, T. F. GABAergic septohippocampal neurons contain parvalbumin. *Brain Res.* **478**, 375–381 (1989).
75. Damborsky, J. C. & Yakel, J. L. Regulation of hippocamposeptal input within the medial septum/diagonal band of Broca. *Neuropharmacology* **191**, 108589 (2021).
76. Manseau, F., Goutagny, R., Danik, M. & Williams, S. The hippocamposeptal pathway generates rhythmic firing of GABAergic neurons in the medial septum and diagonal bands: an investigation using a complete septohippocampal preparation in vitro. *J. Neurosci.* **28**, 4096–4107 (2008).
77. Toth, K., Borhegyi, Z. & Freund, T. F. Postsynaptic targets of GABAergic hippocampal neurons in the medial septum-diagonal band of Broca complex. *J. Neurosci.* **13**, 3712–3724 (1993).
78. Melonakos, E. D., White, J. A. & Fernandez, F. R. Gain modulation of cholinergic neurons in the medial septum-diagonal band of broca through hyperpolarization. *Hippocampus* **26**, 1525–1541 (2016).
79. Mattis, J. et al. Frequency-dependent, cell type-divergent signaling in the hippocamposeptal projection. *J. Neurosci.* **34**, 11769–11780 (2014).
80. Hight, D., Voss, L. J., Garcia, P. S. & Sleigh, J. Changes in alpha frequency and power of the electroencephalogram during volatile-based general anesthesia. *Front. Syst. Neurosci.* **11**, 36 (2017).
81. Perouansky, M. et al. Slowing of the hippocampal θ rhythm correlates with anesthetic-induced Amnesia. *Anesthesiology* **113**, 1299–1309 (2010).
82. Hutt, A., Lefebvre, J., Hight, D. & Sleigh, J. Suppression of underlying neuronal fluctuations mediates EEG slowing during general anaesthesia. *Neuroimage* **179**, 414–428 (2018).
83. Purdon, P. L. et al. Electroencephalogram signatures of loss and recovery of consciousness from propofol. *Proc. Natl Acad. Sci. USA* **110**, E1142–E1151 (2013).
84. Cunniff, M. M., Markenscoff-Papadimitriou, E., Ostrowski, J., Rubenstein, J. L. R. & Sohal, V. S. Altered hippocampal-prefrontal communication during anxiety-related avoidance in mice deficient for the autism-associated gene pogz. *Elife* **9**, e54835 (2020).
85. Canolty, R. T. et al. High gamma power Is phase-locked to theta oscillations in human neocortex. *Science* **313**, 1626–1628 (2006).

86. Lisman, J. The theta/gamma discrete phase code occuring during the hippocampal phase precession may be a more general brain coding scheme. *Hippocampus* **15**, 913–922 (2005).
87. Senior, T. J., Huxter, J. R., Allen, K., O'Neill, J. & Csicsvari, J. Gamma oscillatory firing reveals distinct populations of pyramidal cells in the CA1 region of the hippocampus. *J. Neurosci.* **28**, 2274–2286 (2008).
88. Sirota, A. et al. Entrainment of neocortical neurons and gamma oscillations by the hippocampal theta rhythm. *Neuron* **60**, 683–697 (2008).
89. Tort, A. B. L. et al. Dynamic cross-frequency couplings of local field potential oscillations in rat striatum and hippocampus during performance of a T-maze task. *Proc. Natl Acad. Sci. USA* **105**, 20517–20522 (2008).
90. Jones, M. W. & Wilson, M. A. Theta rhythms coordinate hippocampal–prefrontal interactions in a spatial memory task. *PLoS Biol.* **3**, e402 (2005).
91. Buzsáki, G. & Chrobak, J. J. Temporal structure in spatially organized neuronal ensembles: a role for interneuronal networks. *Curr. Opin. Neurobiol.* **5**, 504–510 (1995).
92. Fell, J. & Axmacher, N. The role of phase synchronization in memory processes. *Nat. Rev. Neurosci.* **12**, 105–118 (2011).
93. Soltesz, I. & Deschenes, M. Low- and high-frequency membrane potential oscillations during theta activity in CA1 and CA3 pyramidal neurons of the rat hippocampus under ketamine-xylazine anesthesia. *J. Neurophysiol.* **70**, 97–115 (1993).
94. Lisman, J. E. & Idiart, M. A. P. Storage of 7 ± 2 short-term memories in oscillatory subcycles. *Science* **267**, 1512–1515 (1995).
95. Fukai, T. Sequence generation in arbitrary temporal patterns from theta-nested gamma oscillations: a model of the basal ganglia–thalamo-cortical loops. *Neural Netw.* **12**, 975–987 (1999).
96. Jensen, O. & Colgin, L. L. Cross-frequency coupling between neuronal oscillations. *Trends Cogn. Sci.* **11**, 267–269 (2007).
97. Zhang, L., Lee, J., Rozell, C. & Singer, A. C. Sub-second dynamics of theta-gamma coupling in hippocampal CA1. *Elife* **8**, e44320 (2019).
98. Mark, S., Romani, S., Jezek, K. & Tsodyks, M. Theta-paced flickering between place-cell maps in the hippocampus: A model based on short-term synaptic plasticity. *Hippocampus* **27**, 959–970 (2017).
99. Jezek, K., Henriksen, E. J., Treves, A., Moser, E. I. & Moser, M.-B. Theta-paced flickering between place-cell maps in the hippocampus. *Nature* **478**, 246–249 (2011).
100. Leutgeb, S., Leutgeb, J. K., Moser, M.-B. & Moser, E. I. Place cells, spatial maps and the population code for memory. *Curr. Opin. Neurobiol.* **15**, 738–746 (2005).
101. Siegle, J. H. & Wilson, M. A. Enhancement of encoding and retrieval functions through theta phase-specific manipulation of hippocampus. *Elife* **3**, e03061 (2014).
102. Unal, G. et al. Spatio-temporal specialization of GABAergic septohippocampal neurons for rhythmic network activity. *Brain Struct. Funct.* **223**, 2409–2432 (2018).
103. Unal, G., Joshi, A., Viney, T. J., Kis, V. & Somogyi, P. Synaptic targets of medial septal projections in the hippocampus and extrahippocampal cortices of the mouse. *J. Neurosci.* **35**, 15812–15826 (2015).
104. Sun, Y. et al. Cell-type-specific circuit connectivity of hippocampal CA1 revealed through cre-dependent rabies tracing. *Cell Rep.* **7**, 269–280 (2014).
105. McKenna, J. T. et al. Distribution and intrinsic membrane properties of basal forebrain GABAergic and parvalbumin neurons in the mouse. *J. Comp. Neurol.* **521**, 1225–1250 (2013).
106. Petsche, H., Stumpf, C. & Gogolak, G. The significance of the rabbit's septum as a relay station between the midbrain and the hippocampus I. The control of hippocampus arousal activity by the septum cells. *Electroencephalogr. Clin. Neurophysiol.* **14**, 202–211 (1962).
107. Cobb, S. R., Buhl, E. H., Halasy, K., Paulsen, O. & Somogyi, P. Synchronization of neuronal activity in hippocampus by individual GABAergic interneurons. *Nature* **378**, 75–78 (1995).
108. Robinson, J. et al. Optogenetic activation of septal glutamatergic neurons drive hippocampal theta rhythms. *J. Neurosci.* **36**, 3016–3023 (2016).
109. Mocellin, P. & Mikulovic, S. The role of the medial septum—associated networks in controlling locomotion and motivation to move. *Front. Neural Circuits* **15**, 1–14 (2021).
110. Martínez-Bellver, S. et al. Causal relationships between neurons of the nucleus incertus and the hippocampal theta activity in the rat. *J. Physiol.* **595**, 1775–1792 (2017).
111. Kocsis, B., Varga, V., Dahan, L. & Sik, A. Serotonergic neuron diversity: Identification of raphe neurons with discharge time-locked to the hippocampal theta rhythm. *Proc. Natl Acad. Sci. USA* **103**, 1059–1064 (2006).
112. Varga, V. et al. Fast synaptic subcortical control of hippocampal circuits. *Science* **326**, 449–453 (2009).
113. Kim, T. et al. Cortically projecting basal forebrain parvalbumin neurons regulate cortical gamma band oscillations. *Proc. Natl Acad. Sci. USA* **112**, 3535–3540 (2015).
114. Lozano-Montes, L. et al. Optogenetic stimulation of basal forebrain parvalbumin neurons activates the default mode network and associated behaviors. *Cell Rep.* **33**, 108359 (2020).
115. Hasselmo, M. E., Wyble, B. P. & Wallenstein, G. V. Encoding and retrieval of episodic memories: role of cholinergic and GABAergic modulation in the hippocampus. *Hippocampus* **6**, 693–708 (1996).
116. Iwasaki, S., Sasaki, T. & Ikegaya, Y. Hippocampal beta oscillations predict mouse object-location associative memory performance. *Hippocampus* **31**, 503–511 (2021).
117. Rangel, L. M. et al. Rhythmic coordination of hippocampal neurons during associative memory processing. *Elife* **5**, e09849 (2016).
118. Lockmann, A. L. V., Laplagne, D. A. & Tort, A. B. L. Olfactory bulb drives respiration-coupled beta oscillations in the rat hippocampus. *Eur. J. Neurosci.* **48**, 2663–2673 (2018).
119. Brandon, M. P. et al. Reduction of theta rhythm dissociates grid cell spatial periodicity from directional tuning. *Science* **332**, 595–599 (2011).
120. Hagan, J. J., Salamone, J. D., Simpson, J., Iversen, S. D. & Morris, R. G. M. Place navigation in rats is impaired by lesions of medial septum and diagonal band but not nucleus basalis magnocellularis. *Behav. Brain Res.* **27**, 9–20 (1988).
121. Mizumori, S. J. Y., Perez, G. M., Alvarado, M. C., Barnes, C. A. & McNaughton, B. L. Reversible inactivation of the medial septum differentially affects two forms of learning in rats. *Brain Res.* **528**, 12–20 (1990).
122. Chrobak, J. J., Stackman, R. W. & Walsh, T. J. Intraseptal administration of muscimol produces dose-dependent memory impairments in the rat. *Behav. Neural Biol.* **52**, 357–369 (1989).
123. Pang, K. C. H. & Nocera, R. Interactions between 192-IgG saporin and intraseptal cholinergic and GABAergic drugs: role of cholinergic medial septal neurons in spatial working memory. *Behav. Neurosci.* **113**, 265–275 (1999).
124. Mamad, O., McNamara, H. M., Reilly, R. B. & Tsanov, M. Medial septum regulates the hippocampal spatial representation. *Front. Behav. Neurosci.* **9**, 166 (2015).
125. Walsh, T. J., Herzog, C. D., Gandhi, C., Stackman, R. W. & Wiley, R. G. Injection of IgG 192-saporin into the medial septum produces cholinergic hypofunction and dose-dependent working memory deficits. *Brain Res.* **726**, 69–79 (1996).

126. Ragozzino, M. E. & Gold, P. E. Glucose injections into the medial septum reverse the effects of intraseptal morphine infusions on hippocampal acetylcholine output and memory. *Neuroscience* **68**, 981–988 (1995).
127. Smith, H. R. & Pang, K. C. H. Orexin-saporin lesions of the medial septum impair spatial memory. *Neuroscience* **132**, 261–271 (2005).
128. Winson, J. Loss of hippocampal theta rhythm results in spatial memory deficit in the rat. *Science* **201**, 160–163 (1978).
129. Kloc, M. L., Velasquez, F., Niedecker, R. W., Barry, J. M. & Holmes, G. L. Disruption of hippocampal rhythms via optogenetic stimulation during the critical period for memory development impairs spatial cognition. *Brain Stimul.* **13**, 1535–1547 (2020).
130. Jeong, D. U. et al. Improvements in memory after medial septum stimulation are associated with changes in hippocampal cholinergic activity and neurogenesis. *Biomed. Res. Int.* **2014**, 1–10 (2014).
131. Khakpai, F., Nasehi, M., Haeri-Rohani, A., Eidi, A. & Zarrindast, M. R. Septo-hippocampo-septal loop and memory formation. *Basic Clin. Neurosci.* **4**, 5–23 (2013).
132. Damasio, A. R., Graff-Radford, N. R., Eslinger, P. J., Damasio, H. & Kassell, N. Amnesia following basal forebrain lesions. *Arch. Neurol.* **42**, 263–271 (1985).
133. Irle, E., Wowra, B., Kunert, H. J., Hampl, J. & Kunze, S. Memory disturbances following anterior communicating artery rupture. *Ann. Neurol.* **31**, 473–480 (1992).
134. Barthó, P. et al. Characterization of neocortical principal cells and interneurons by network interactions and extracellular features. *J. Neurophysiol.* **92**, 600–608 (2004).
135. Kvitsiani, D. et al. Distinct behavioural and network correlates of two interneuron types in prefrontal cortex. *Nature* **498**, 363–366 (2013).
136. Fujisawa, S., Amarasingham, A., Harrison, M. T. & Buzsáki, G. Behavior-dependent short-term assembly dynamics in the medial prefrontal cortex. *Nat. Neurosci.* **11**, 823–833 (2008).
137. Czurko, A., Huxter, J., Li, Y., Hangya, B. & Muller, R. U. Theta phase classification of interneurons in the hippocampal formation of freely moving rats. *J. Neurosci.* **31**, 2938–2947 (2011).
138. Shirvalkar, P. R., Rapp, P. R. & Shapiro, M. L. Bidirectional changes to hippocampal theta-gamma comodulation predict memory for recent spatial episodes. *Proc. Natl Acad. Sci. USA* **107**, 7054–7059 (2010).
139. Leung, L. S. & Ma, J. Medial septum modulates hippocampal gamma activity and prepulse inhibition in an N-methyl-D-aspartate receptor antagonist model of schizophrenia. *Schizophr. Res.* **198**, 36–44 (2018).
140. Wulff, P. et al. Hippocampal theta rhythm and its coupling with gamma oscillations require fast inhibition onto parvalbumin-positive interneurons. *Proc. Natl Acad. Sci. USA* **106**, 3561–3566 (2009).
141. Etter, G. et al. Optogenetic gamma stimulation rescues memory impairments in an Alzheimer's disease mouse model. *Nat. Commun.* **10**, 1–11 (2019).
142. Somogyi, P. & Klausberger, T. Defined types of cortical interneurone structure space and spike timing in the hippocampus. *J. Physiol.* **562**, 9–26 (2005).
143. Kaifosh, P., Lovett-Barron, M., Turi, G. F., Reardon, T. R. & Losonczy, A. Septo-hippocampal GABAergic signaling across multiple modalities in awake mice. *Nat. Neurosci.* **16**, 1182–1184 (2013).
144. Tukker, J. J., Fuentealba, P., Hartwich, K., Somogyi, P. & Klausberger, T. Cell type-specific tuning of hippocampal interneuron firing during gamma oscillations in vivo. *J. Neurosci.* **27**, 8184–8189 (2007).
145. Gaykema, R. P. A., Luiten, P. G. M., Nyakas, C. & Traber, J. Cortical projection patterns of the medial septum-diagonal band complex. *J. Comp. Neurol.* **293**, 103–124 (1990).
146. Manns, I. D., Mainville, L. & Jones, B. E. Evidence for glutamate, in addition to acetylcholine and GABA, neurotransmitter synthesis in basal forebrain neurons projecting to the entorhinal cortex. *Neuroscience* **107**, 249–263 (2001).
147. Jeffery, K. J., Donnett, J. G. & O'Keefe, J. Medial septal control of theta-correlated unit firing in the entorhinal cortex of awake rats. *Neuroreport* **6**, 2166–2170 (1995).
148. Gonzalez-Sulser, A. et al. GABAergic projections from the medial septum selectively inhibit interneurons in the medial entorhinal cortex. *J. Neurosci.* **34**, 16739–16743 (2014).
149. Fuchs, E. C. et al. Local and distant input controlling excitation in layer II of the medial entorhinal cortex. *Neuron* **89**, 194–208 (2016).
150. Melzer, S. & Monyer, H. Diversity and function of corticopetal and corticofugal GABAergic projection neurons. *Nat. Rev. Neurosci.* **21**, 499–515 (2020).
151. Chapman, C. A. & Racine, R. J. Converging inputs to the entorhinal cortex from the piriform cortex and medial septum: facilitation and current source density analysis. *J. Neurophysiol.* **78**, 2602–2615 (1997).
152. van Groen, T. & Wyss, J. M. The postsubicular cortex in the rat: characterization of the fourth region of the subicular cortex and its connections. *Brain Res.* **529**, 165–177 (1990).
153. Hsiao, Y. T., Zheng, C. & Colgin, L. L. Slow gamma rhythms in CA3 are entrained by slow gamma activity in the dentate gyrus. *J. Neurophysiol.* **116**, 2594–2603 (2016).
154. Middleton, S. J. & McHugh, T. J. Silencing CA3 disrupts temporal coding in the CA1 ensemble. *Nat. Neurosci.* **19**, 945–951 (2016).
155. Axmacher, N. et al. Cross-frequency coupling supports multi-item working memory in the human hippocampus. *Proc. Natl Acad. Sci. USA* **107**, 3228–3233 (2010).
156. Ariffin, M. Z. et al. Forebrain medial septum sustains experimental neuropathic pain. *Sci. Rep.* **8**, 11892 (2018).
157. Takeuchi, Y. et al. The Medial septum as a potential target for treating brain disorders associated with oscillopathies. *Front. Neural Circuits.* **15**, 701080 (2021).
158. Broncel, A., Bocian, R., Kłos-Wojtczak, P. & Konopacki, J. Medial septal cholinergic mediation of hippocampal theta rhythm induced by vagal nerve stimulation. *PLoS One* **13**, e0206532 (2018).
159. Griguoli, M. et al. Medial septum: relevance for social memory. *Front. Neural Circuits* **16**, 965172 (2022).
160. Paxinos, G. & Franklin, K. B. J. *The Mouse Brain in Stereotaxic Coordinates*, 2nd edn (*Academic,* 2001).
161. Adler, A., Zhao, R., Shin, M. E., Yasuda, R. & Gan, W.-B. Somatostatin-expressing interneurons enable and maintain learning-dependent sequential activation of pyramidal neurons. *Neuron* **102**, 202–216.e7 (2019).
162. Cummings, K. A. & Clem, R. L. Prefrontal somatostatin interneurons encode fear memory. *Nat. Neurosci.* **23**, 61–74 (2020).
163. Fiáth, R. et al. Slow insertion of silicon probes improves the quality of acute neuronal recordings. *Sci. Rep.* **9**, 111 (2019).
164. Siegle, J. H. et al. Open Ephys: an open-source, plugin-based platform for multichannel electrophysiology. *J. Neural Eng.* **14**, 045003 (2017).
165. Király, B. et al. In vivo localization of chronically implanted electrodes and optic fibers in mice. *Nat. Commun.* **11**, 4686 (2020).
166. Buzsáki, G., Czopf, J., Kondákor, I. & Kellényi, L. Laminar distribution of hippocampal rhythmic slow activity (RSA) in the behaving rat: current-source density analysis, effects of urethane and atropine. *Brain Res.* **365**, 125–137 (1986).
167. Green, J. D., Maxwell, D. S., Schindler, W. J., Stumpf, C. & Rabbit, E. E. G. 'theta' rhythm: its anatomical source and relation to activity in single neurons. *J. Neurophysiol.* **23**, 403–420 (1960).
168. Paxinos, G. & Watson, C. *The Rat Brain in Stereotaxic Coordinates 6th edn*. (*Academic*, 2007).

169. Pachitariu, M., Steinmetz, N., Kadir, S., Carandini, M. & Harris, K. Fast and accurate spike sorting of high-channel count probes with KiloSort. *Adv. Neural Inf. Process. Syst.* **4455**, 4463 (2016).
170. Rossant, C. et al. Spike sorting for large, dense electrode arrays. *Nat. Neurosci.* **19**, 634–641 (2016).
171. Leung, L.-W. S. & Buzsáki, G. Spectral analysis of hippocampal unit train in relation to hippocampal EEG. *Electroencephalogr. Clin. Neurophysiol.* **56**, 668–671 (1983).
172. Apartis, E., Poindessous-Jazat, F. R., Lamour, Y. A. & Bassant, M. H. Loss of rhythmically bursting neurons in Rat medial septum following selective lesson of septohippocampal cholinergic system. *J. Neurophysiol.* **79**, 1633–1642 (1998).
173. Apicella, P. Leading tonically active neurons of the striatum from reward detection to context recognition. *Trends Neurosci.* **30**, 299–306 (2007).
174. Apicella, P., Scarnati, E. & Schultz, W. Tonically discharging neurons of monkey striatum respond to preparatory and rewarding stimuli. *Exp. Brain Res.* **84**, 672–675 (1991).
175. Kimura, M. Behaviorally contingent property of movement-related activity of the primate putamen. *J. Neurophysiol.* **63**, 1277–1296 (1990).
176. Mikulovic, S. et al. On the photovoltaic effect in local field potential recordings. *Neurophotonics* **3**, 015002 (2016).
177. Gabor, D. Theory of communication. Part 1: the analysis of information. *J. Inst. Electr. Eng.* **93**, 429–441 (1946).
178. Zhang, L., Ma, X., Chen, G., Barkai, E. & Lin, L. Theta rhythmic clock-like activity of single units in the mouse hippocampus. *J. Neurosci.* **36**, 4415–4420 (2016).
179. Csicsvari, J., Hirase, H., Czurko, A. & Buzsáki, G. Reliability and state dependence of pyramidal cell–interneuron synapses in the hippocampus. *Neuron* **21**, 179–189 (1998).
180. Pettersen, K. H., Lindén, H., Dale, A. M. & Einevoll, G. T. *Extracellular Spikes and Current-source Density* (*Cambridge Univ. Press*, 2010).
181. Mitzdorf, U. Current source-density method and application in cat cerebral cortex: investigation of evoked potentials and EEG phenomena. *Physiol. Rev.* **65**, 37–100 (1985).
182. Nicholson, C. & Freeman, J. A. Theory of current source-density analysis and determination of conductivity tensor for anuran cerebellum. *J. Neurophysiol.* **38**, 356–368 (1975).
183. Király, B. & Hangya, B. *MATLAB code for 'The Medial Septum Controls Hippocampal Supra-theta Oscillations'*. https://doi.org/10.5281/zenodo.8197408 (2023).
184. Fiáth, R. et al. A silicon-based neural probe with densely-packed low-impedance titanium nitride microelectrodes for ultrahigh-resolution in vivo recordings. *Biosens. Bioelectron.* **106**, 86–92 (2018).

Acknowledgements

We thank Drs. György Buzsáki, Péter Somogyi, and László Záborszky for thoughtful comments and discussions on the manuscript. We thank István Katona for kindly providing access to an in vitro electrophysiology setup and Albert M. Barth for additional electrophysiology equipment. We thank Luigi Petrucco and Stoyo Karamihalev for open access science arts at SciDraw (https://doi.org/10.5281/zenodo.3925903 and https://doi.org/10.5281/zenodo.4312494). This work was supported by the "Lendület" Program (LP2015-2/2015) and NAP3.0 (NAP2022-I-1/2022) of the Hungarian Academy of Sciences, NKFIH KH125294, NKFIH K135561, the European Research Council Starting Grant no. 715043, the European Union project RRF-2.3.1-21-2022-00004 within the framework of the Artificial Intelligence National Laboratory and SPIRITS 2020 of Kyoto University to B.H.; NKFIH FK 129019 to M.J. and V.V.; National Brain Research Program 1.2.1-NKP-2017-00002 to R.F. and I.U.; NKFIH PD124175 and PD134196 to R.F.; NKFIH TUDFO/51757-1/2019-ITM to I.U.; ÚNKP-19-3, ÚNKP-20-3 and ÚNKP 21-3 New National Excellence Program of the Ministry for Innovation and Technology from the source of the National Research, Development and Innovation Fund to B.Ki.; the Requalification of the Spanish university system 2021–2023 Maria Zambrano modality (ZA21-009) program to S.M.B.; the Medical Research Council UK (Award MC_UU_00003/4) to D.D. and V.L.d.S. and (Award MRI/R011567/1) to A.J., M.S. and T.V. We thank the FENS-Kavli Network of Excellence for fruitful discussions.

Author contributions

A.D., M.J., S.M.B., D.S., A.J., M.S., T.V., R.F., P.B. and B.H. performed experiments; V.V., T.F.F., T.J.V., I.U. and B.H. supervised experiments; B.Ki. and B.Ko. performed analysis and figures; B.H., V.L.S. and D.D. supervised analysis; B.Ki. and B.H. wrote the manuscript with input from all authors.

Competing interests

The authors declare no competing interests.

Additional information

Supplementary information The online version contains supplementary material available at https://doi.org/10.1038/s41467-023-41746-0.

Correspondence and requests for materials should be addressed to Balázs Hangya.

Peer review information *Nature Communications* thanks Sanja Mikulovic and the other, anonymous, reviewer(s) for their contribution to the peer review of this work. A peer review file is available.

The medial septum controls hippocampal supra-theta oscillations

Király et al.

Supplementary Information

Supplementary Figures

Supplementary Figure 1

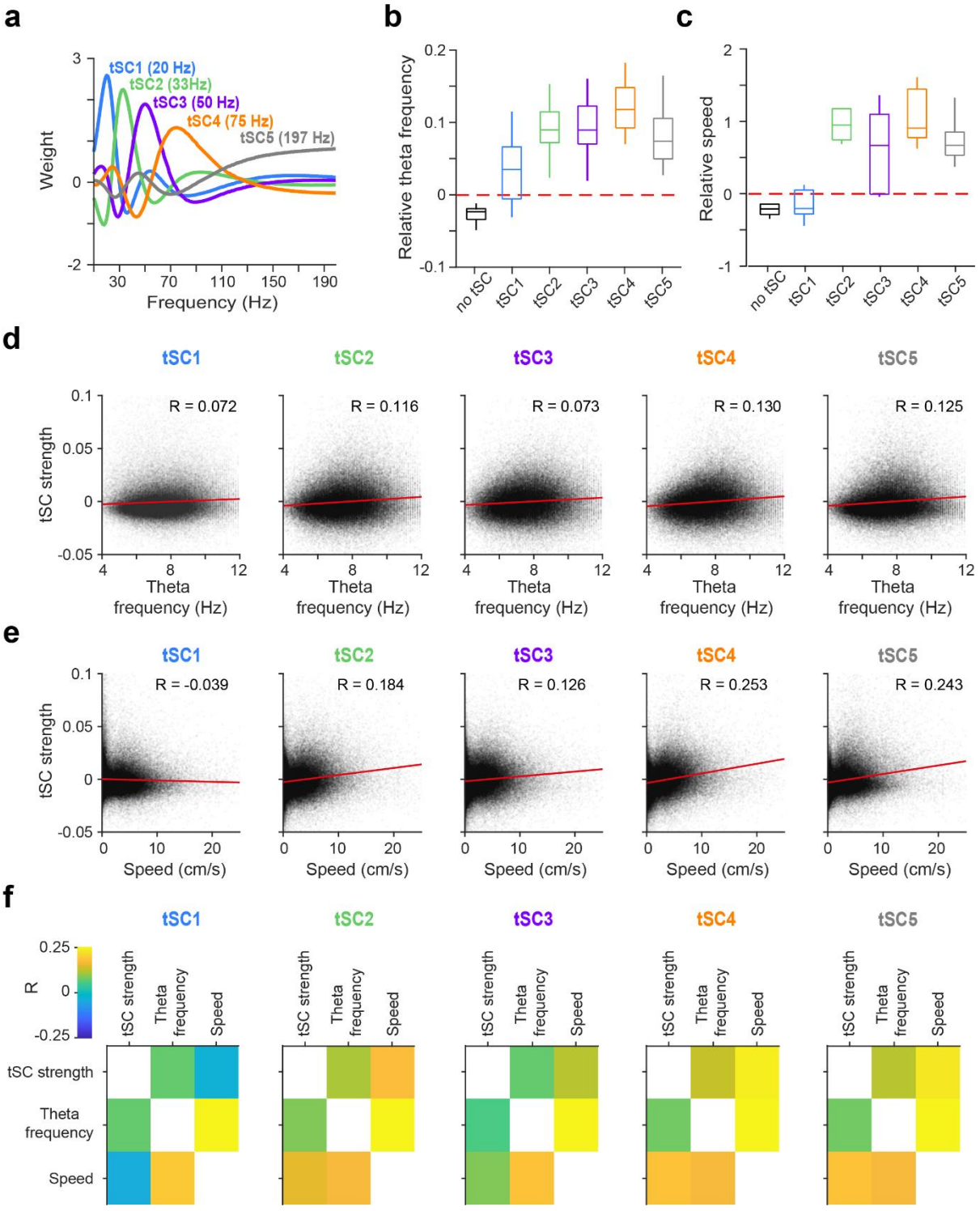

Supplementary Figure 1. Expression of tSCs depends on theta frequency and locomotion speed in freely moving mice.

a The frequency content of each tSC in the example session in Figure 1f. Peak frequencies are shown in brackets. **b,c** Box-whisker plots showing the frequency of theta cycles (**b**, n = 31 sessions**)** and the speed of the animals (**c**, n = 29 sessions) during theta cycles expressing different tSCs, relative to the average over all cycles (red dashed lines). Boxes and whiskers show median, interquartile range and non-outlier range. **d,e** tSC strength as a function of theta frequency (**d**) and the speed of the animal (**e**) during theta cycles expressing different tSCs. Red lines show linear regression model fits; R values represent Spearman correlation coefficient. **f** Partial correlations between tSC strength, theta frequency and animal speed for theta cycles strongly expressing a given tSC. Upper right triangles of the correlation matrices show correlation between the corresponding two variables without controlling for the third variable (see panels **d** and **e**), while the lower left triangles represent partial correlations with controlling for the effect of the third variable. All correlations are significant (Spearman's correlation, two-sided tests with Bonferroni's correction for multiple comparisons, $p < 0.001$). Source data are provided as a Source Data file.

Supplementary Figure 2

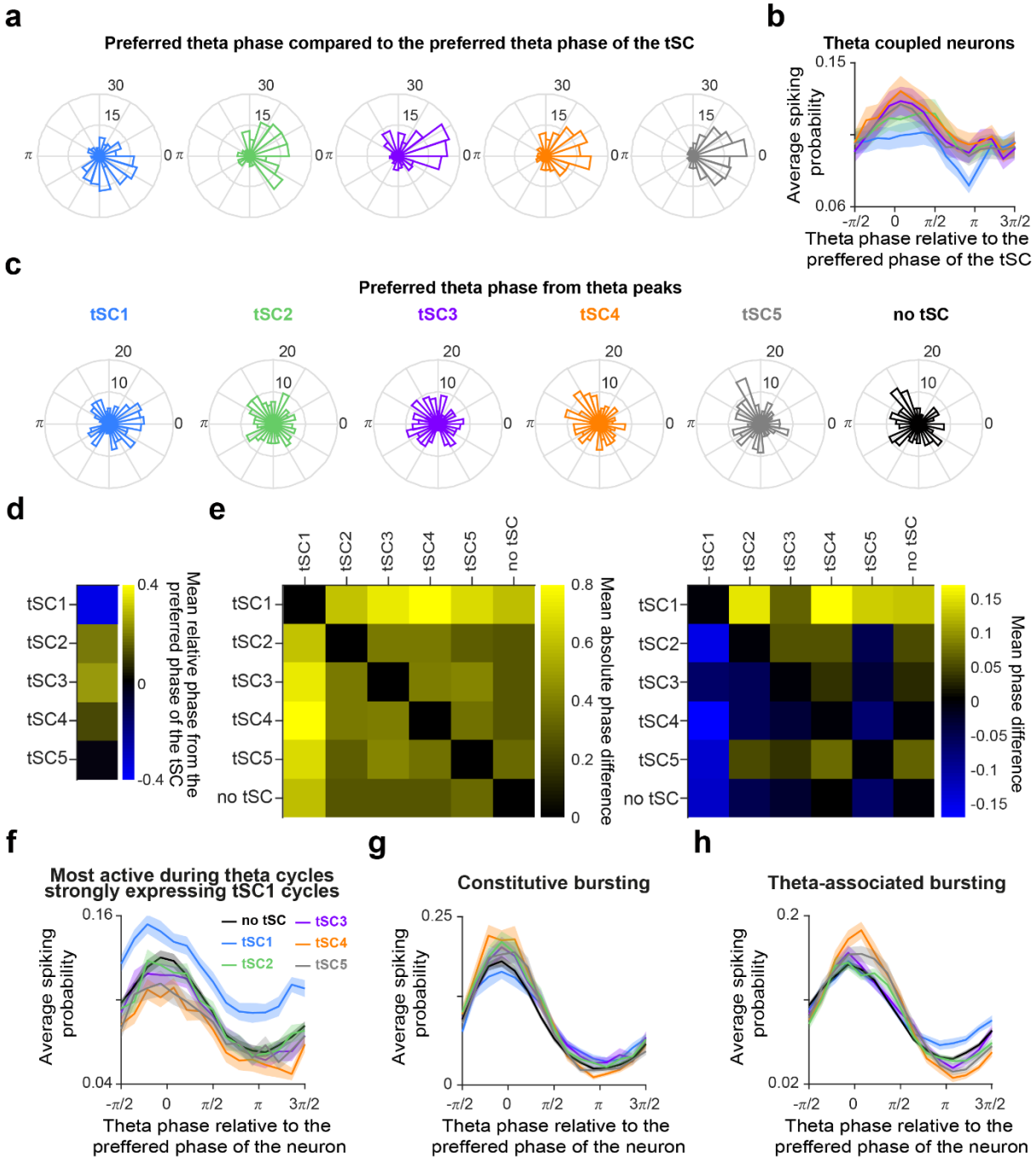

Supplementary Figure 2. MS neurons' phase coupling to hippocampal theta depends on tSCs

a Histograms of preferred phase of the theta-coupled neurons relative to the preferred phase of the concurrent tSCs. **b** Average theta phase histogram (relative to the preferred phase of the different tSCs) of theta-coupled MS neurons during cycles expressing the given tSC. **c** Histogram of the preferred theta phase of the theta-coupled neurons during theta cycles expressing different tSCs. **d** Mean relative preferred theta phase of theta-coupled MS neurons in theta cycles expressing different tSCs. **e** Mean absolute (left) and signed (right) preferred theta phase difference between theta cycles expressing different tSCs. **f-h** Average theta phase histogram (relative to the preferred phase) of MS neurons most active during tSC1 cycles (**f)**, constitutive bursting (**g)** and theta-associated bursting MS neurons (**h**) during theta cycles expressing different tSCs. Error shades show the standard error of the mean. Source data are provided as a Source Data file.

Supplementary Figure 3

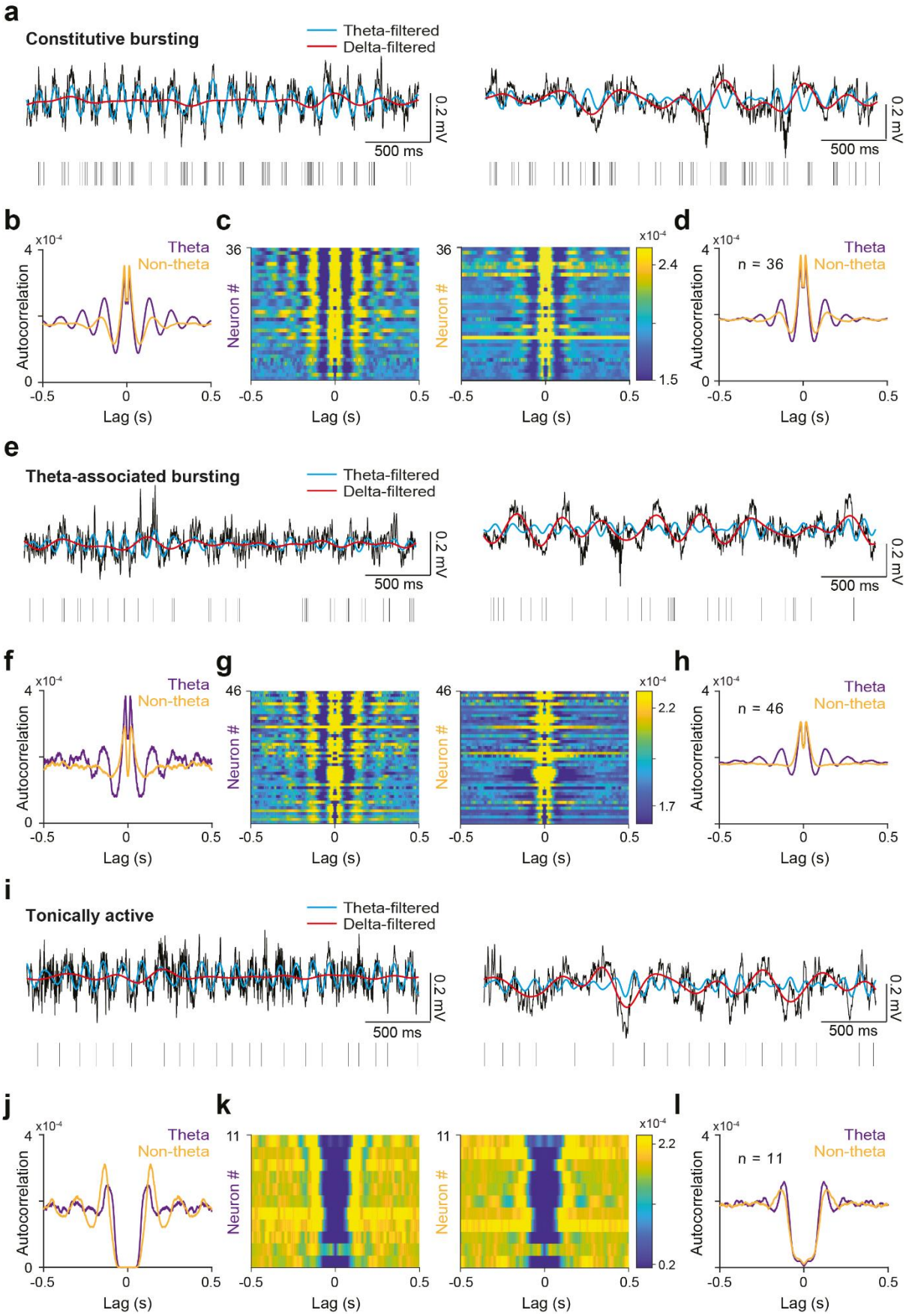

Supplementary Figure 3. Categorizing MS neurons based on their rhythmic firing properties.

a Hippocampal CA1 LFP (top; black, raw; blue, theta band filtered; red, delta band filtered) with spike raster of a constitutive bursting cell during theta (left) and non-theta segments (right). **b** Autocorrelogram of the example neuron in panel **a** during theta (purple) and non-theta (orange) segments. **c** Autocorrelograms of all constitutive bursting MS neurons during theta (left) and non-theta segments (right). **d** Average autocorrelogram of constitutive bursting MS neurons during theta (purple) and non-theta (orange) segments. Constitutive bursting neurons showed theta-rhythmic bursting activity during both theta and non-theta segments and a strong phase locking to CA1 theta. **e** Hippocampal CA1 LFP (top; black, raw; blue, theta band filtered; red, delta band filtered) with spike raster of a theta-associated bursting MS neuron during theta (left) and non-theta segments (right). **f** Autocorrelogram of the example neuron in panel **e** during theta (purple) and non-theta (orange) segments. **g** Autocorrelograms of all theta-associated bursting MS neurons during theta (left) and non-theta segments (right). **h** Average autocorrelogram of theta-associated bursting MS neurons during theta (purple) and non-theta (orange) segments. Theta-associated bursting neurons fired theta-rhythmic bursts of action potentials during CA1 theta but were not rhythmic during non-theta segments. They exhibited significant phase coupling to CA1 theta. **i** Hippocampal CA1 LFP (top; black, raw; blue, theta band filtered; red, delta band filtered) with spike raster of a tonically active MS neurons during theta (left) and non-theta segments (right). **j** Autocorrelogram of the example neuron in panel **i** during theta (purple) and non-theta (orange) segments. **k** Autocorrelograms of all tonically active MS neurons during theta (left) and non-theta segments (right). **l** Average autocorrelogram of tonically active MS neurons. Tonically active cells fired regularly at theta-band frequencies irrespective of CA1 theta oscillations (rhythmicity frequency based on autocorrelation peak, median ± standard error of the median, 8.40 ± 0.37 Hz during theta, 7.15 ± 0.4 Hz during non-theta segments), but showed little to no phase locking to hippocampal theta[52]. Source data are provided as a Source Data file.

Supplementary Figure 4

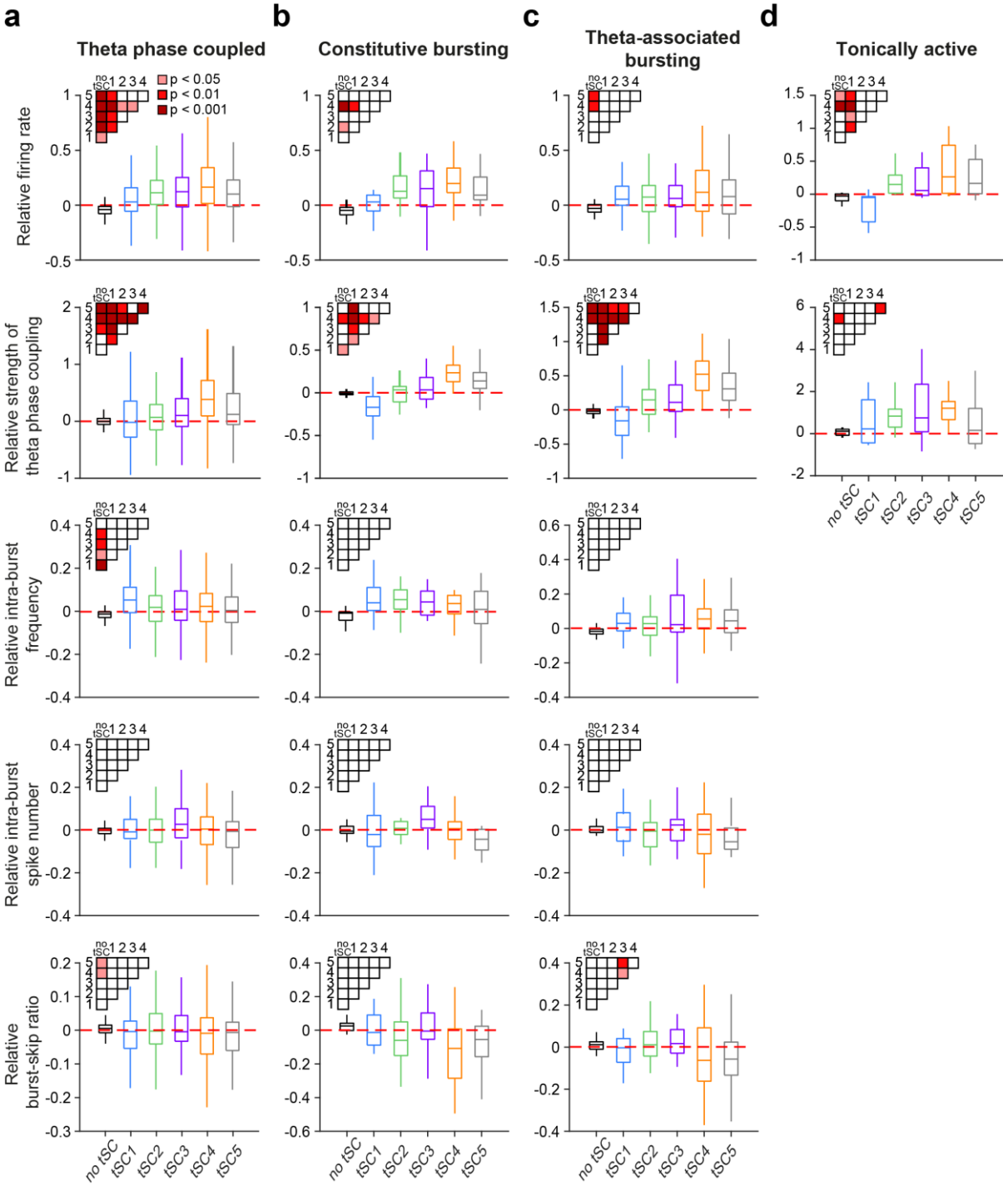

Supplementary Figure 4. Firing parameters of MS neuron populations in theta cycles expressing different tSCs

a Firing rate, phase coupling strength, intra-burst frequency, mean intra-burst spike number and burst-skip ratio distributions of the theta-coupled MS neurons (n = 181**)**, in the function of tSC presence. **b** The same for constitutive bursting MS neurons (n = 19). **c** The same for theta-associated bursting MS neurons (n = 34). **d** The same for tonically active MS neurons (n = 10). All parameters are expressed relative to the average over all cycles (red dashed line). Boxes and whiskers show median, interquartile range and non-outlier range. Differences were statistically tested with two-sided repeated measures ANOVA, followed by Tukey's test for post hoc comparisons. Significant differences are indicated by the color-coded matrices in the insets. Source data are provided as a Source Data file.

Supplementary Figure 5

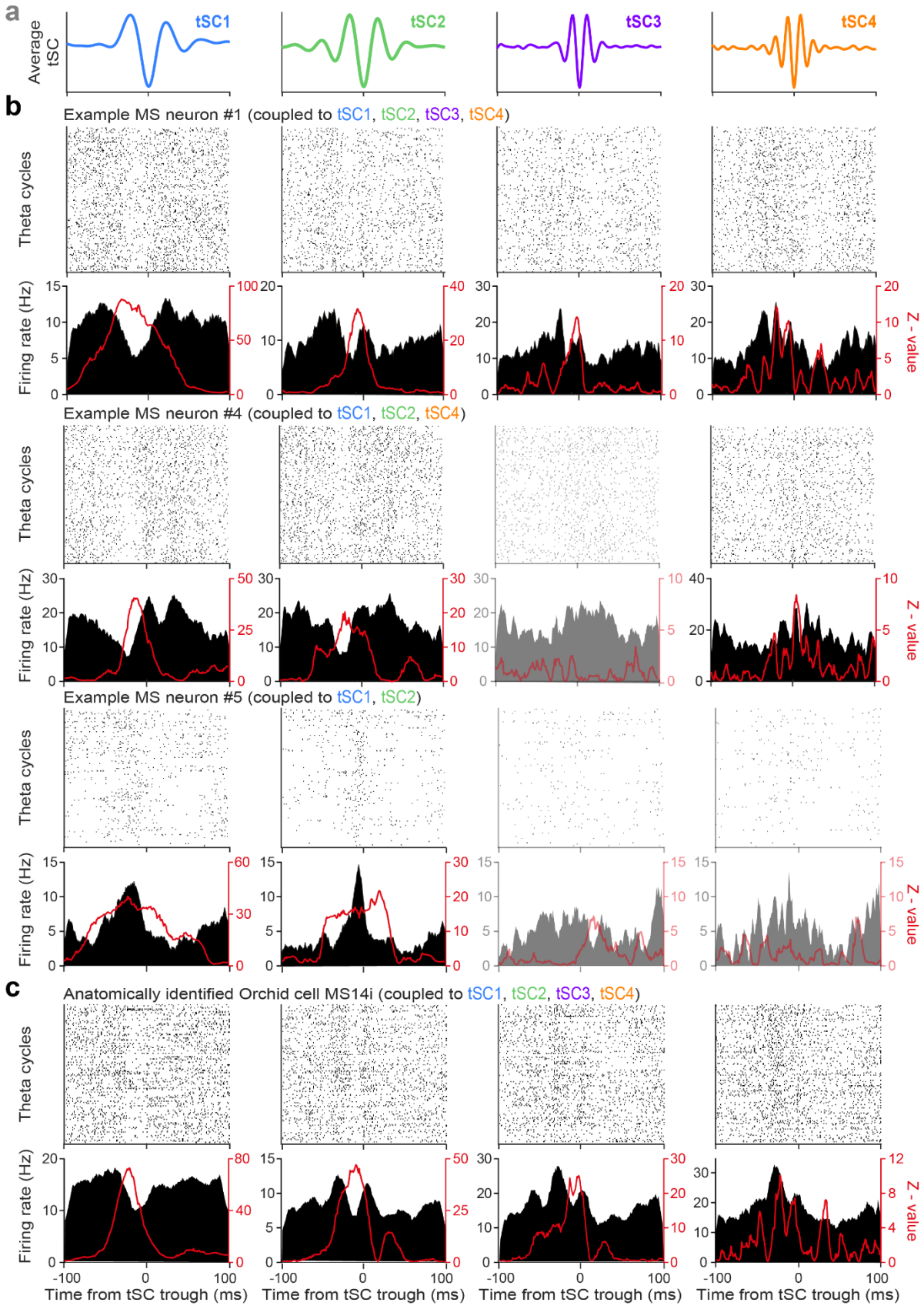

Supplementary Figure 5. Examples of tSC-coupled MS neurons

a Average tSC signals from an example session. **b** Firing pattern of three extracellularly recorded example MS neurons (example neuron #1 is the same as in Figure 3a). Top, spike raster aligned to the most negative tSC troughs within each theta cycle. Bottom, peri-event time histograms (PETHs) corresponding to each spike raster (black; y-axis on the left) and Rayleigh's Z-value as a function of temporal offset between hippocampal tSCs and MS spike trains (red; y-axis on the right). **c** Same as panel **b** for a juxtacellularly labeled example Orchid neuron (MS14i).

Supplementary Figure 6

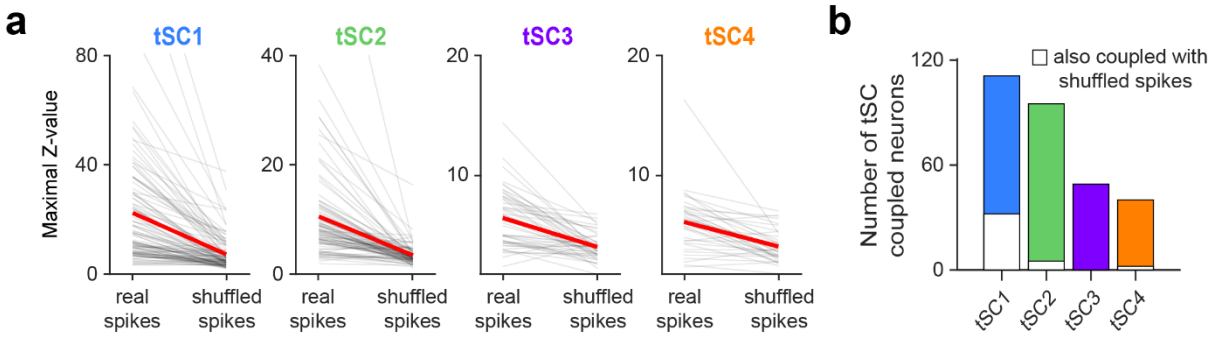

Supplementary Figure 6. Shuffling control for tSC coupling

a The maximal value of Rayleigh's Z statistic for neurons coupled to each tSC compared to the maximal Z-value computed with the spikes shuffled across theta cycles. **b** Number of neurons phase-coupled to each tSC. White bars indicate the number of neurons still significantly coupled after spikes were shuffled across theta cycles. Source data are provided as a Source Data file.

Supplementary Figure 7

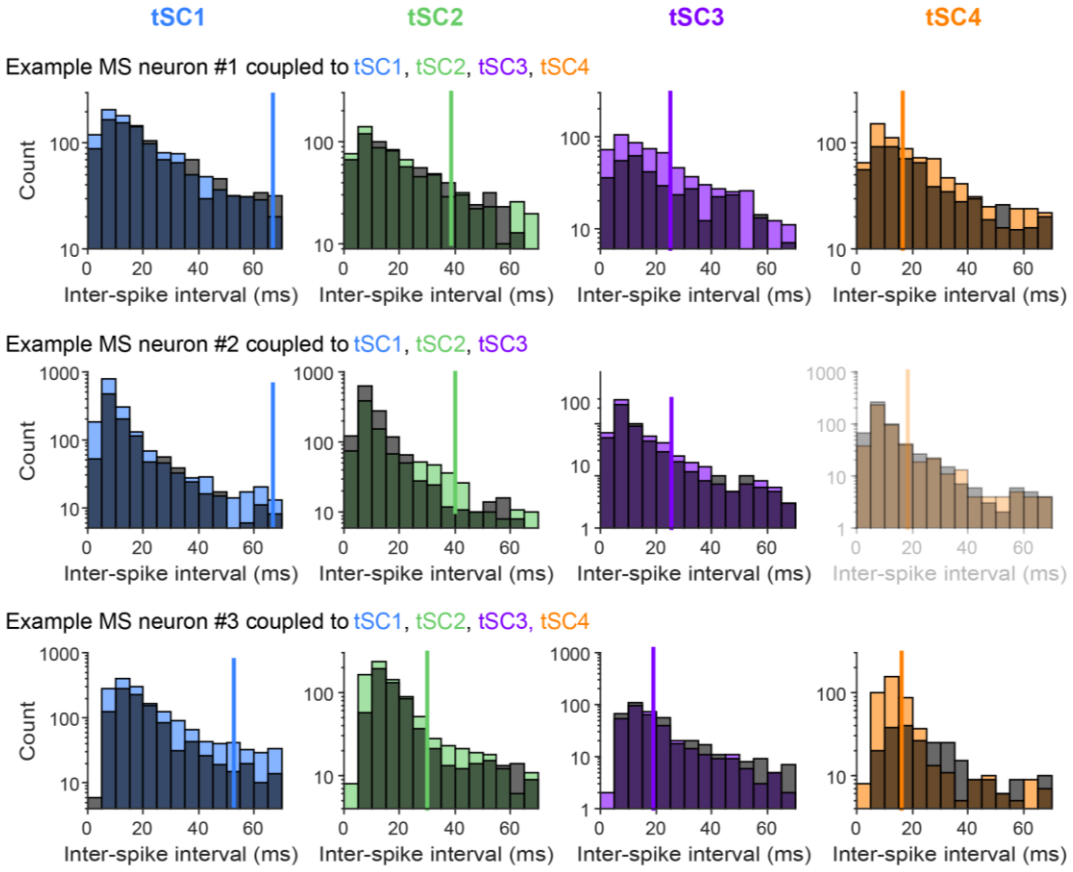

Supplementary Figure 7. Intra-burst frequency of MS neurons is correlated with CA1 tSC presence.

Inter-spike interval histograms of three extracellularly recorded example MS neurons coupled to multiple tSCs (same examples as in Figure 3) during theta cycles strongly expressing a given tSC (colored bars) compared to theta cycles expressing the given tSC the least (gray bars). The tSC4 panel of the example neuron #2 is faded to indicate that this neuron was not coupled to tSC4. The colored vertical lines indicate the frequency of the corresponding tSC. Note the ISI surplus around the corresponding frequency of the concurrent tSC if the neuron was coupled to that tSC in example MS neuron #2 and #3; see also example MS neuron #2 during tSC4 cycles, where no significant coupling was detected and no ISI surplus around the frequency of tSC4 was found, accordingly.

Supplementary Figure 8

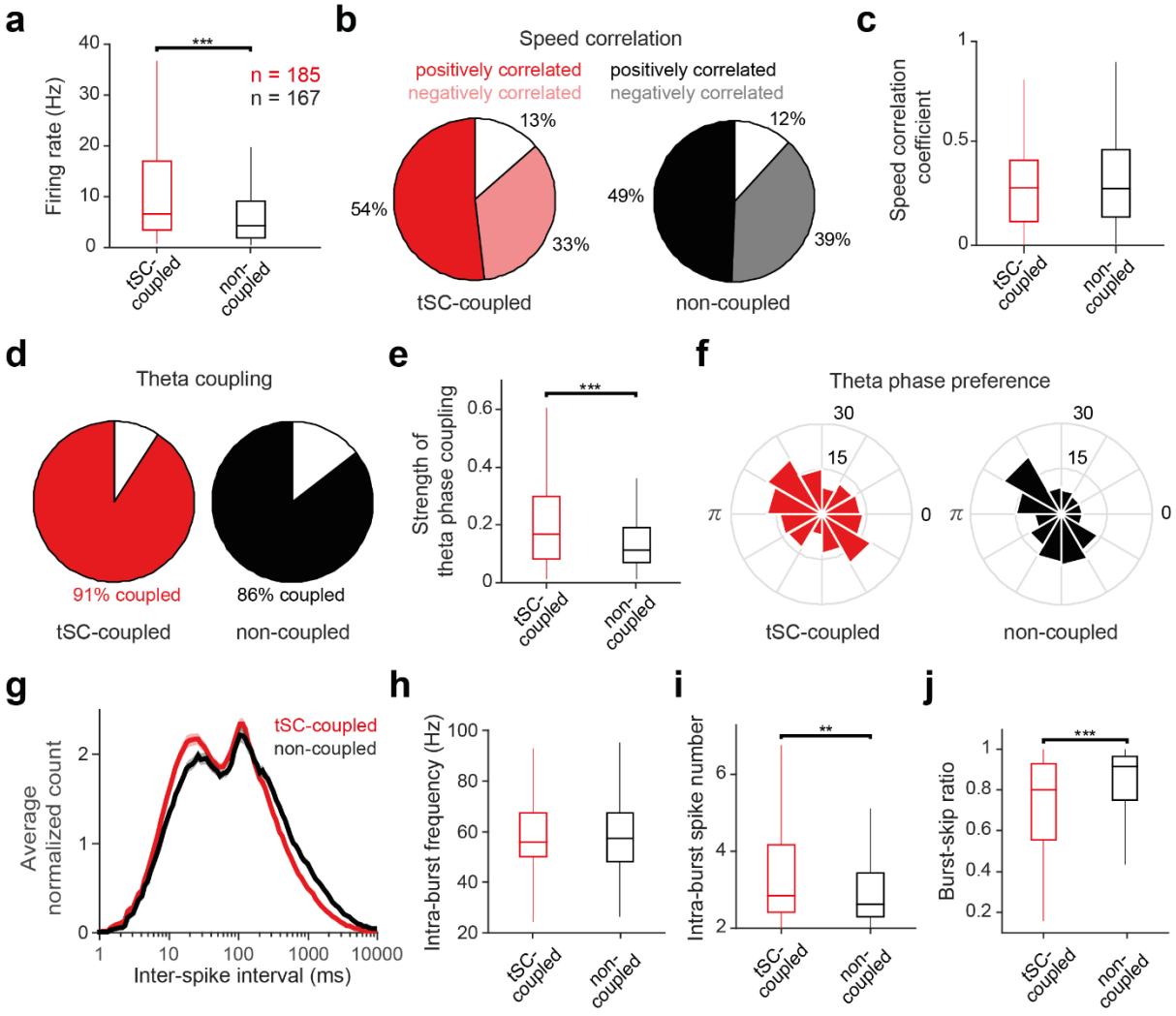

Supplementary Figure 8. Firing parameters of tSC-coupled and not coupled MS neurons

a Mean firing rate distribution of tSC-coupled (n = 185) and non-coupled (n = 167) neurons ($p = 1 \times 10^{-5}$, two-sided Mann-Whitney U-test). **b** Proportion of MS neurons with significant speed correlation (Spearman correlation, two-sided test, $p < 0.01$) in the two MS neuron groups (chi-squared test, $p = 0.555$). **c** Spearman correlation coefficient between the firing rate and the speed of the animal (n = 171 coupled and n = 156 non-coupled neurons, $p = 0.699$, two-sided Mann-Whitney U-test). **d** Proportion of theta-coupled (two-sided Rayleigh test, $p < 0.01$) neurons (chi-squared test, $p = 0.130$). **e** Theta-coupling strength distribution measured by the mean resultant length. (n = 185 coupled and n = 167 non-coupled neurons, $p = 3 \times 10^{-4}$, two-sided Mann-Whitney U-test). **f** Phase histogram of the preferred theta phase of the two neuron groups. **g** Average inter-spike interval histogram of the two neuron populations. The error shades show the standard error of the mean. **h-j** Distribution of burst parameters in the two MS neuron groups (n = 185 coupled and n = 167 non-coupled neurons). **h**, Intra-burst

frequency (p = 0.581, two-sided Mann-Whitney U-test). **i**, Intra-burst spike number (p = 0.0099, two-sided Mann-Whitney U-test). **j**, proportion of skipped theta cycles, termed 'burst-skip ratio' ($p = 5 \times 10^{-6}$, two-sided Mann-Whitney U-test). Boxes and whiskers show median, interquartile range and non-outlier range. *, $p < 0.05$; **, $p < 0.01$; ***, $p < 0.001$; Mann-Whitney U-test. Source data are provided as a Source Data file.

Supplementary Figure 9

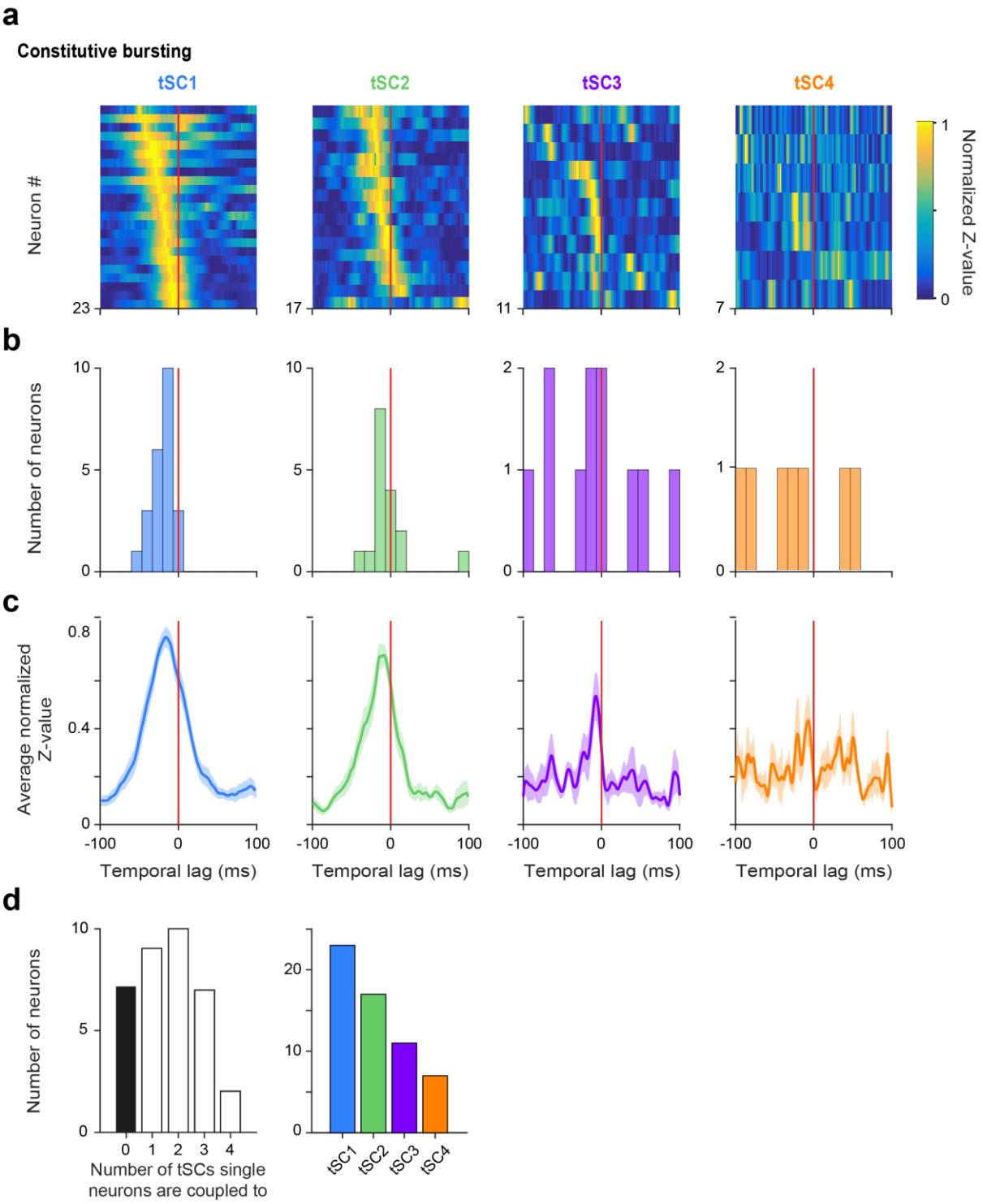

Supplementary Figure 9. Constitutive bursting MS neurons' firing predicts tSCs signals.

a Normalized Rayleigh's Z-value as a function of temporal lag between hippocampal tSCs and MS spike trains. Constitutive bursting MS neurons coupled to the given tSC are shown. Peak Z-values at negative lags indicate that MS signals predict future tSC values. **b** Histograms showing the distribution of time lags across constitutive bursting MS neurons that realize the maximal phase locking as quantified by the Z-values, separately for each tSC. **c** Average normalized Z-value of tSC-coupled constitutive bursting MS neurons as a function of time lag. Error shade represents SEM. **d** Left, histogram of the number of tSCs single constitutive bursting MS neurons are coupled to. Right, number of constitutive bursting MS neurons phase-coupled to each tSC. Source data are provided as a Source Data file.

Supplementary Figure 10

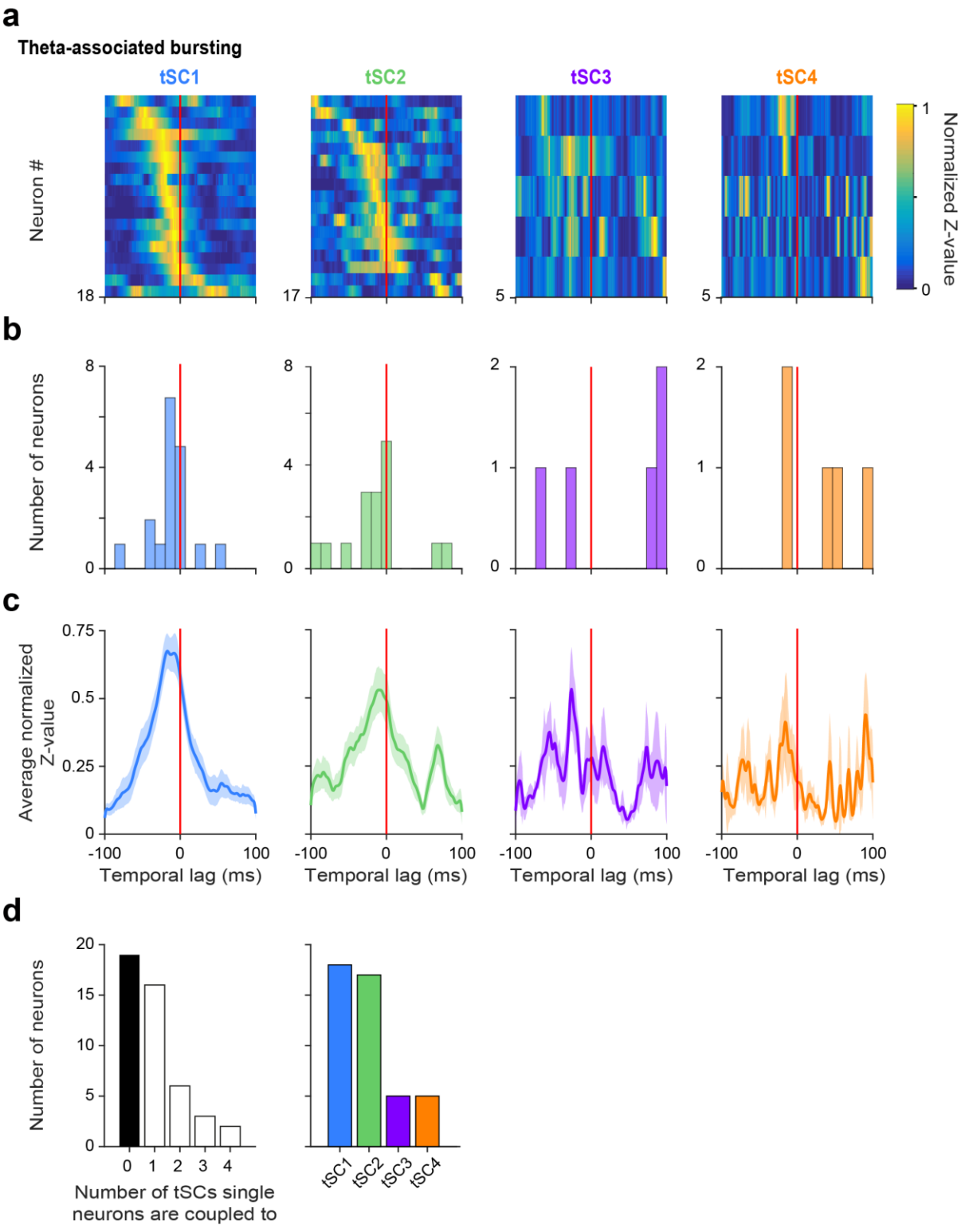

Supplementary Figure 10. Theta-associated bursting MS neurons' firing predicts tSCs signals.

a Normalized Rayleigh's Z-value as a function of temporal lag between hippocampal tSCs and MS spike trains. Theta-associated bursting MS neurons coupled to the given tSC are shown. Peak Z-values at negative lags indicate that MS signals predict future tSC values. **b** Histograms showing the distribution of time lags across theta-associated bursting MS neurons that realize the maximal phase locking as quantified by the Z-values, separately for each tSC. **c** Average normalized Z-value of tSC-coupled theta-associated bursting MS neurons as a function of time lag. Error shade represents SEM. **d** Left, histogram of the number of tSCs single theta-associated bursting MS neurons are coupled to. Right, number of theta-associated bursting MS neurons phase-coupled to each tSC. Source data are provided as a Source Data file.

Supplementary Figure 11

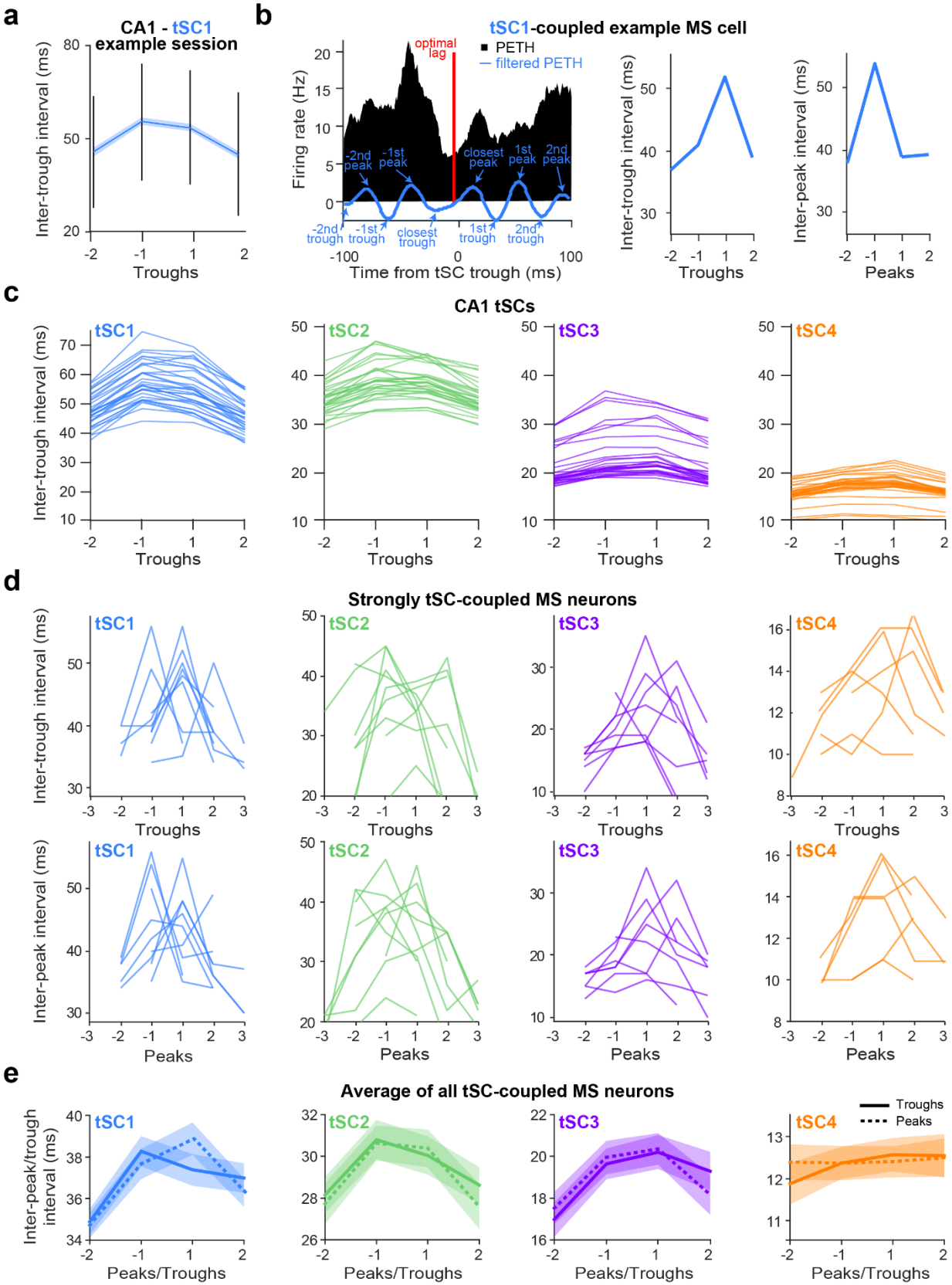

Supplementary Figure 11. Frequency accommodation of CA1 tSCs is reflected in the firing of MS neurons.

a Average tSC1 inter-trough intervals preceding (-2, -1) and following (+1, +2) the largest amplitude trough in an example session. Error bars show the standard deviation to highlight the large variability, while the shaded areas represent the standard error of the mean to demonstrate that the trends revealed are statistically reliable due to the large number of cycles (n = 423) analyzed. **b** Left, peri-event time histogram (PETH) of an example neuron triggered on the largest troughs of CA1 tSC1 cycles from the same session as in panel **a**. The blue line shows the bandpass filtered PETH (18 Hz-35 Hz), which was used to find tSC1-related peaks and troughs before and after the optimal time lag (red line) that realizes the strongest phase locking. Right, inter-trough and inter-peak intervals of the filtered firing rate signal of the example neuron. **c** Average tSC inter-trough intervals for each session (n = 32). **d** Inter-trough and inter-peak intervals of the peaks and troughs of the 10 most tSC-coupled neurons for each tSCs. **e** Average inter-peak/trough intervals of all MS neurons coupled to a given tSC. The shaded areas represent the standard error of the mean. Source data are provided as a Source Data file.

Supplementary Figure 12

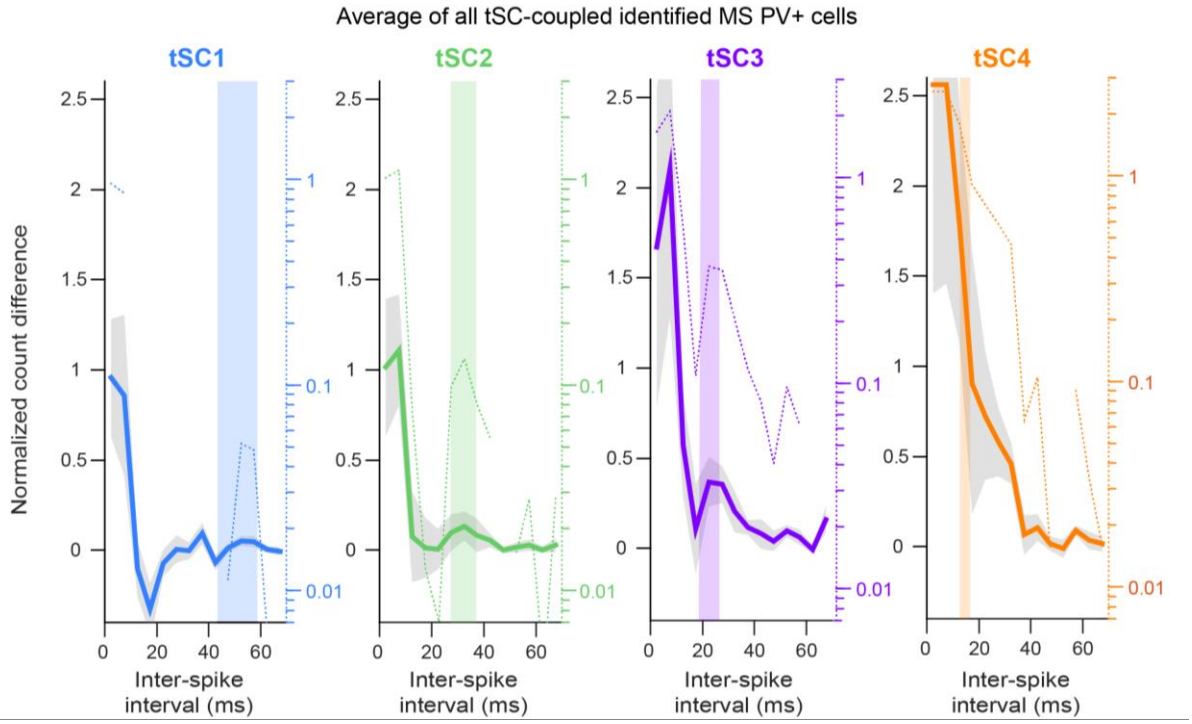

Supplementary Figure 12. Intra-burst frequency of the PV+ MS neuron population is correlated with CA1 tSC presence

Difference between the inter-spike interval histograms during theta cycles with the most and least tSC content (see colored and grey histograms in the examples in Supplementary Figure 7), normalized by firing rate and averaged across identified PV+ tSC-coupled MS neurons. The solid line shows the difference on a linear scale (y-axis on the left), while the dashed line on a logarithmic scale to highlight the difference at slower frequencies (y-axis on the right; note that negative differences cannot be displayed on the logarithmic scale). The error shades show the standard error of the mean. The colored rectangles show the frequency ranges of the tSCs. Source data are provided as a Source Data file.

Supplementary Figure 13

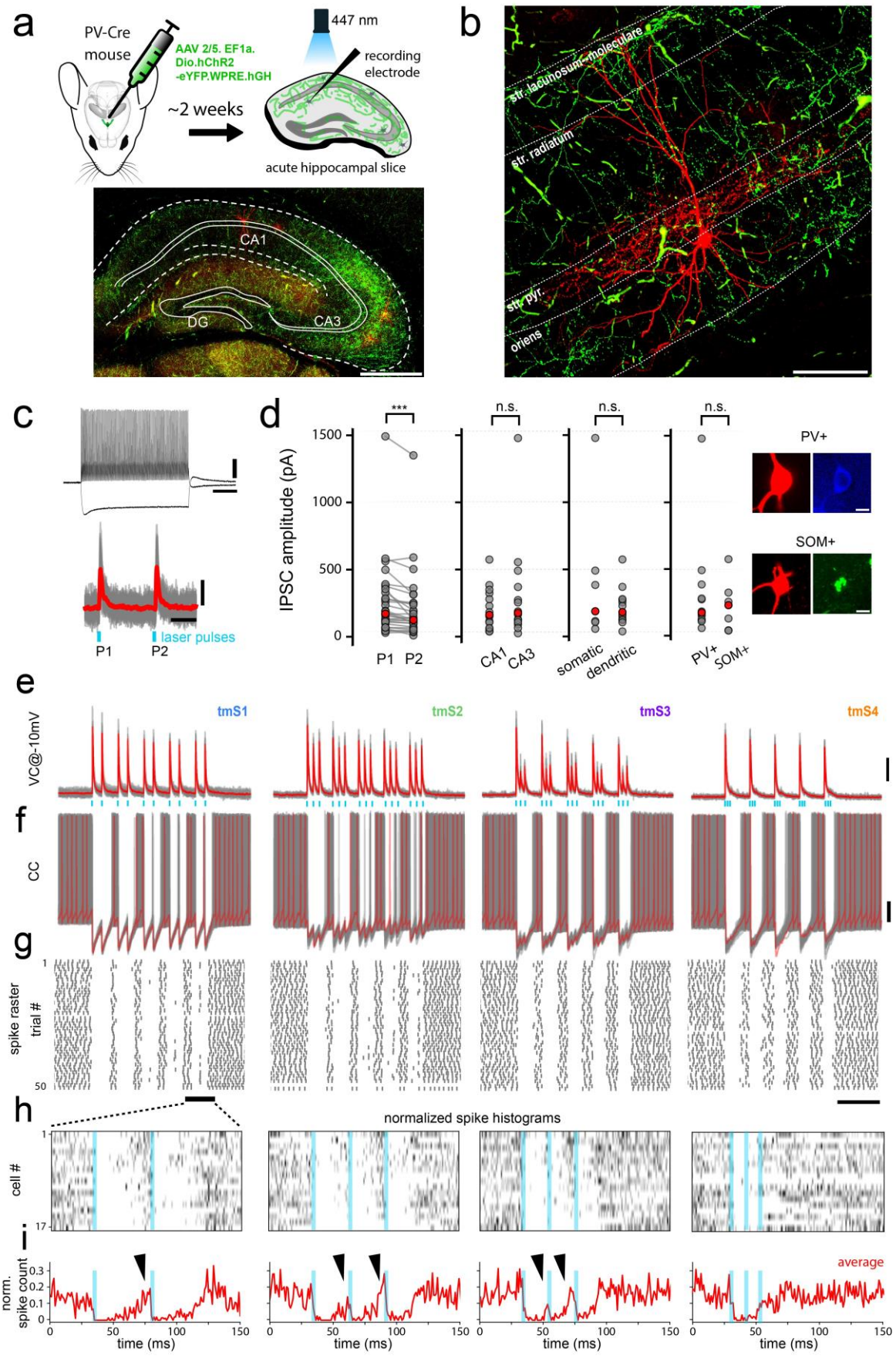

Supplementary Figure 13. CA1 and CA3 PV+ and SOM+ interneurons are targeted by PV+ MS fibers.

a Top, schematic of the acute slice electrophysiology experimental design (Petrucco, Luigi. (2020). Mouse head schema. Zenodo. https://doi.org/10.5281/zenodo.3925903). Cre-dependent AAV vector containing ChR2-eYFP was injected into the MS of PV-Cre animals (n = 6). Coronal acute hippocampal slices were prepared to characterize the PV+ MS inputs to hippocampal interneurons using a series of tmS patterns. Bottom, example of a hippocampal coronal slice with interneurons recorded in the CA3 and CA1 regions (red, biocytin) and PV+ axons arising from the MS expressing ChR2-eYFP (green). Scale bar, 500 µm. **b** Example image of a perisomatic PV+ fast-spiking interneuron recorded in the CA1 region, receiving PV+ MS inhibitory inputs. Scale bar, 100 µm. **c** Somatic current injection evoked spiking pattern (top) and evoked inhibitory currents in response to optogenetic stimulation (2 ms pulse width, 2 pulses @22Hz) of MS fibers (bottom) of the example neuron presented in panel **b** (n = 10 trials overlayed in grey, average in red). Scale bars: top, 200 ms, 20 mV; bottom, 20 ms, 100 pA. **d** Comparison of IPSC amplitudes evoked optogenetically by pulse pairs show moderate but significant short-term depression (n = 29 recorded cells; 2 pulses delivered @22 Hz; P1 and P2 medians, 165.41 and 119.94 pA, respectively, $p = 1.240 \times 10^{-4}$, two-sided Wilcoxon signed-rank test). No significant differences were found between IPSC amplitudes evoked in CA1 versus CA3 (n = 15 and n = 14, respectively; p = 0.621, two-sided Mann-Whitney U-test), soma-targeting versus dendrite-targeting (n = 7 and n = 13; p = 0.817, two-sided Mann-Whitney U-test) or PV+ versus SOM+ (n = 12 and n = 7; p = 0.773, two-sided Mann-Whitney U-test) interneurons. Example image of a PV+ and a SOM+ neuron receiving PV+ MS input are shown on the right (scale bar, 10 µm). **e** Evoked inhibitory currents in response to optogenetic stimulation at different tmS patterns (n = 10 trials overlayed in grey, average in red; scale bar, 100 pA). **f** Effect of tmS stimulation on the spiking of the recorded neuron in panel **e** (n = 50 trials in grey, a single trial is shown in red; scale bar, 20 mV). **g** Raster plot of action potentials of the example neuron for the same tmS patterns (scale bar, 200 ms). **h** Normalized spike histograms of n = 17 cells upon tmS stimulation corresponding to the marked time window in panel **g**. Each line represents normalized spike histogram of a recorded cell, with darker colors indicating higher values. **i** Average normalized spike histograms for the n = 17 cells. Arrowheads highlight peaks in histograms indicating spike modulation by tmS1-3, absent for tmS4. Source data are provided as a Source Data file.

Supplementary Figure 14

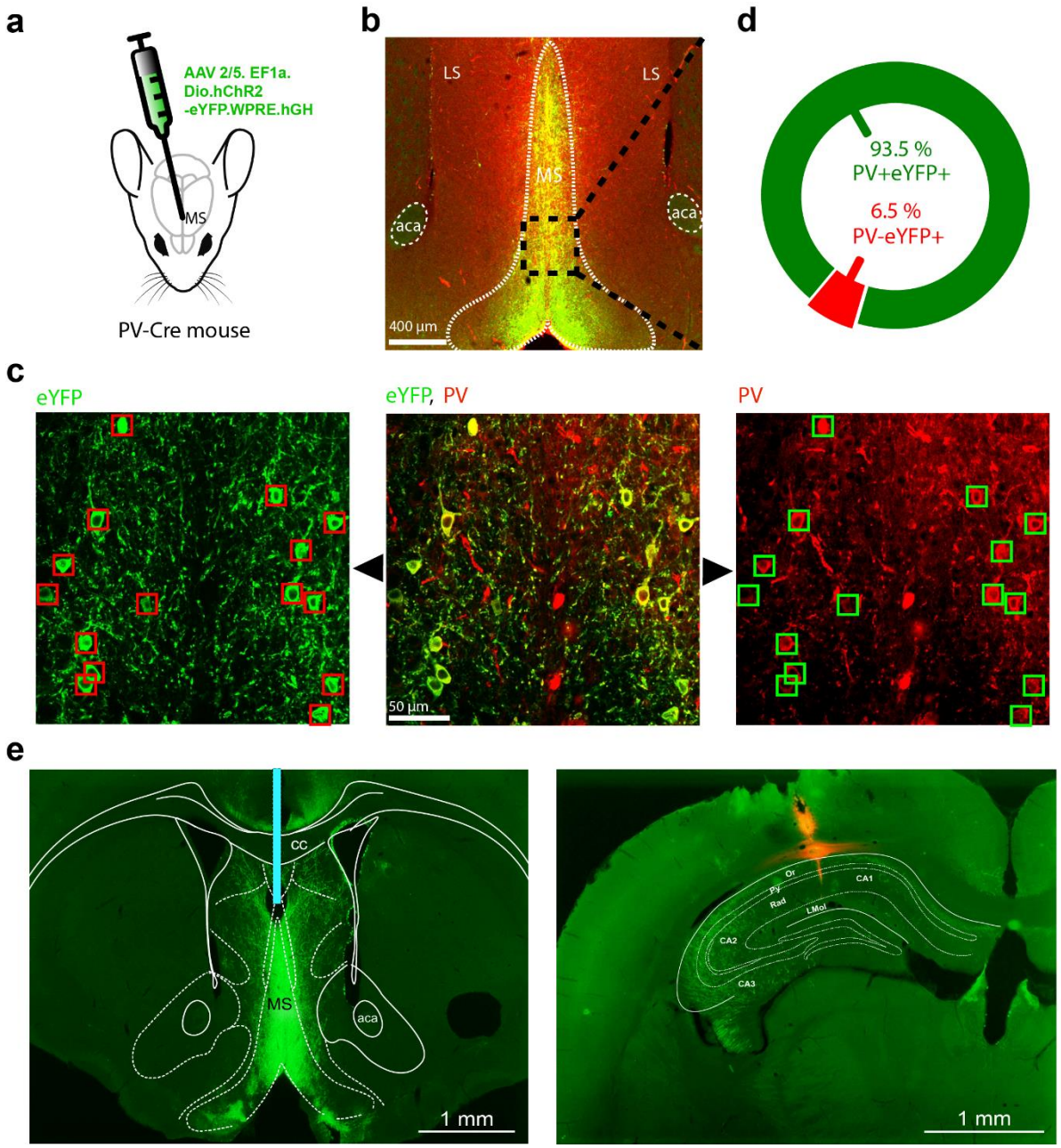

Supplementary Figure 14. Immunohistochemical verification of the cellular identity of the optogenetically stimulated MS neurons targeted in PV-Cre mice and the implant positions

a Schematic of the virus injection experiments (Petrucco, Luigi. (2020). Mouse head schema. Zenodo. https://doi.org/10.5281/zenodo.3925903). **b,c** eYFP and PV expression in the medial septum. The framed area in panel **b** is enlarged in panel **c**. **d** Proportion of PV-expressing neurons among those expressing eYFP (n = 308 cells from n = 3 mice). **e** Fluorescent micrographs of coronal sections showing the position of the optic fiber in the MS (left) and the silicon probe in the CA1 (right) in the same mouse (representative example out of 7 mice;

green, eYFP expressed in septal PV neurons; red, DiI applied on the silicon probes). The blue line indicates the track of the optic fiber above the MS. The corresponding section of the mouse brain atlas[165] was fitted based on anatomical landmarks. aca, anterior commissure anterior part; cc, corpus callosum; Or, oriens layer; Py, stratum pyramidale; Rad, stratum radiatum; LMol, stratum lacunosum moleculare.

Supplementary Figure 15

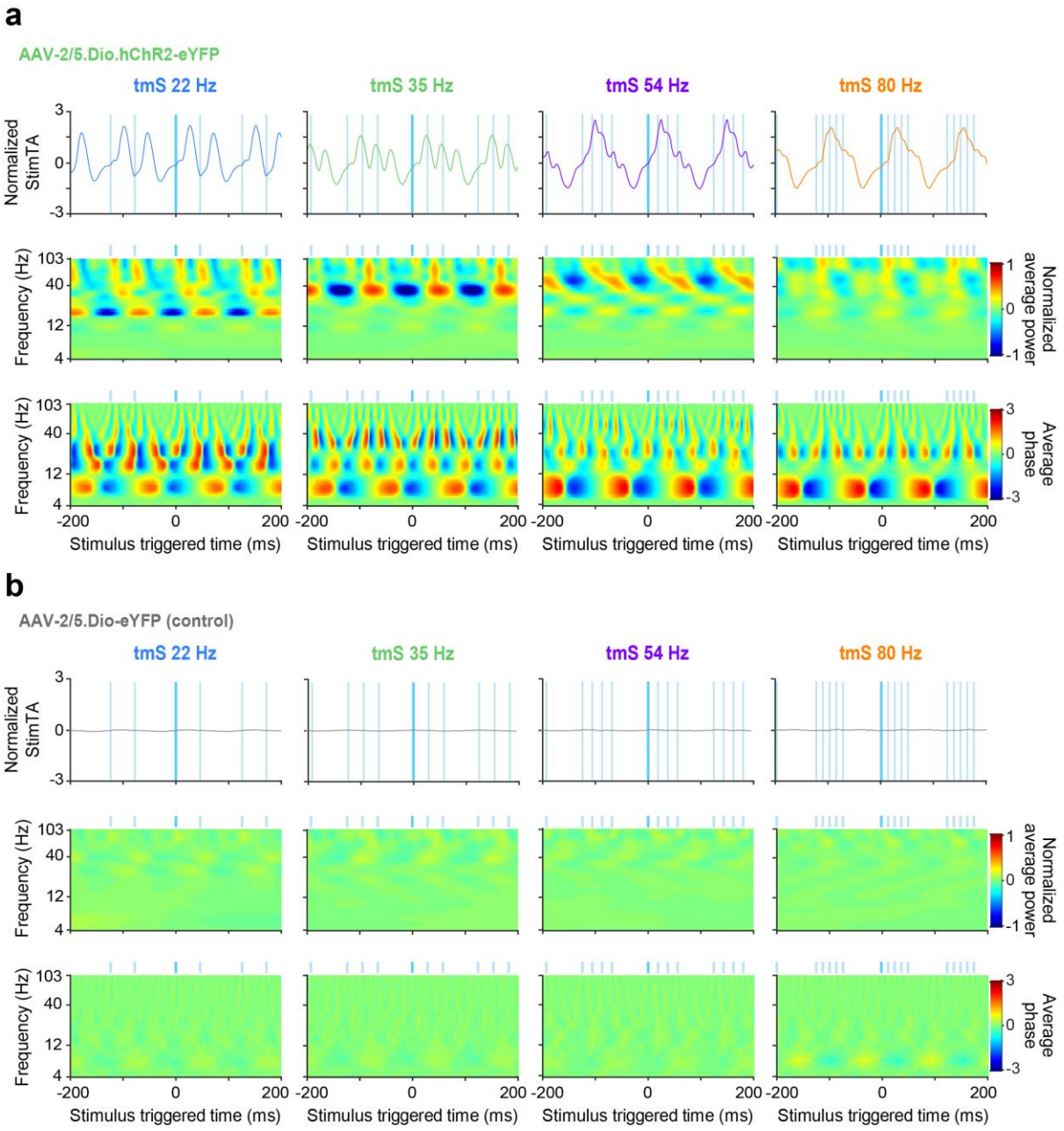

Supplementary Figure 15. Stimulation-evoked tSC-like activity patterns in the CA1

a,b Stimulus triggered averages (StimTA, top) of the raw CA1 LFPs and stimulus triggered spectrograms (middle, power; bottom, phase) for the different tmS protocols applied on PV-expressing MS neurons (**a**) and in the animals injected with the control virus (**b**). Blue lines indicate times of blue laser light pulses.

Supplementary Figure 16

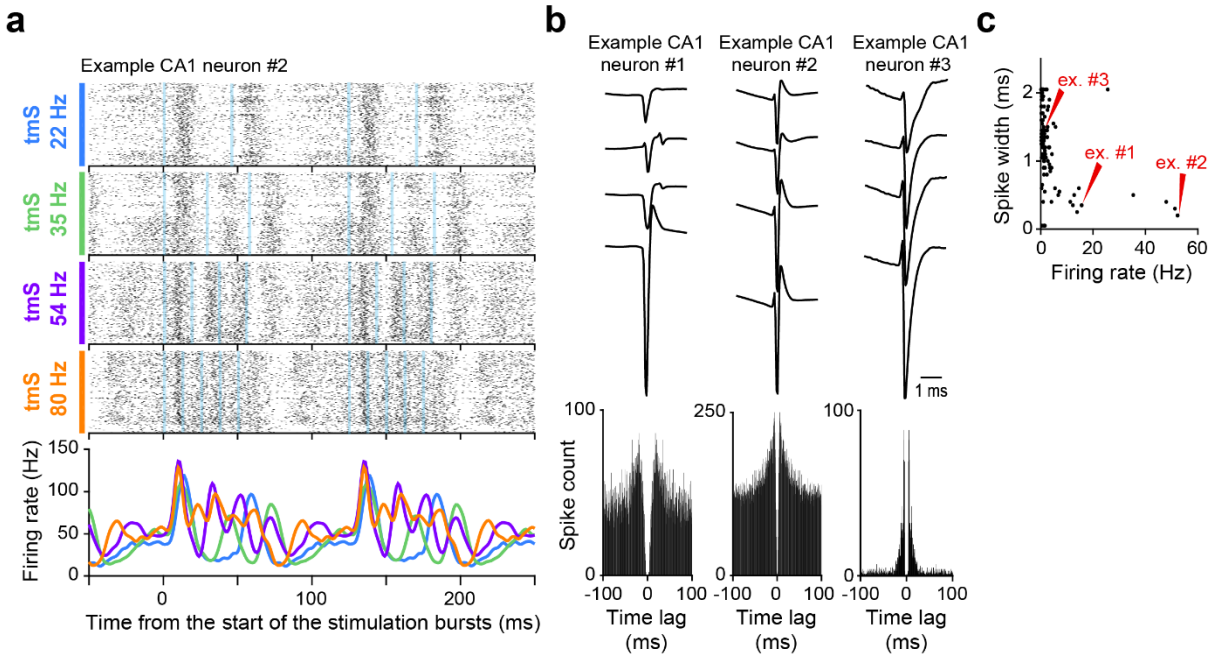

Supplementary Figure 16. Identification of CA1 putative interneurons

a Spike rasters and peri-stimulus time histograms of a putative CA1 interneuron aligned to tmS onset, partitioned by tmS frequency (blue lines, photostimulation). **b** Top, average extracellular action potential shapes for the putative interneuron examples in Fig. 5c (Example CA1 neuron #1) and in Supplementary Figure 11a (Example CA1 neuron #2), compared to a typical putative pyramidal cell (Example CA1 neuron #3). Four channels with the largest spike amplitudes are presented. Bottom, autocorrelograms of the same example neurons. Note the characteristic differences in spike duration and autocorrelograms. **c** Firing rate and spike width (peak-to-valley time) distribution of the recorded CA1 single units from the sessions of the example neurons. Example neurons are marked by red arrowheads. Source data are provided as a Source Data file.

Supplementary Figure 17

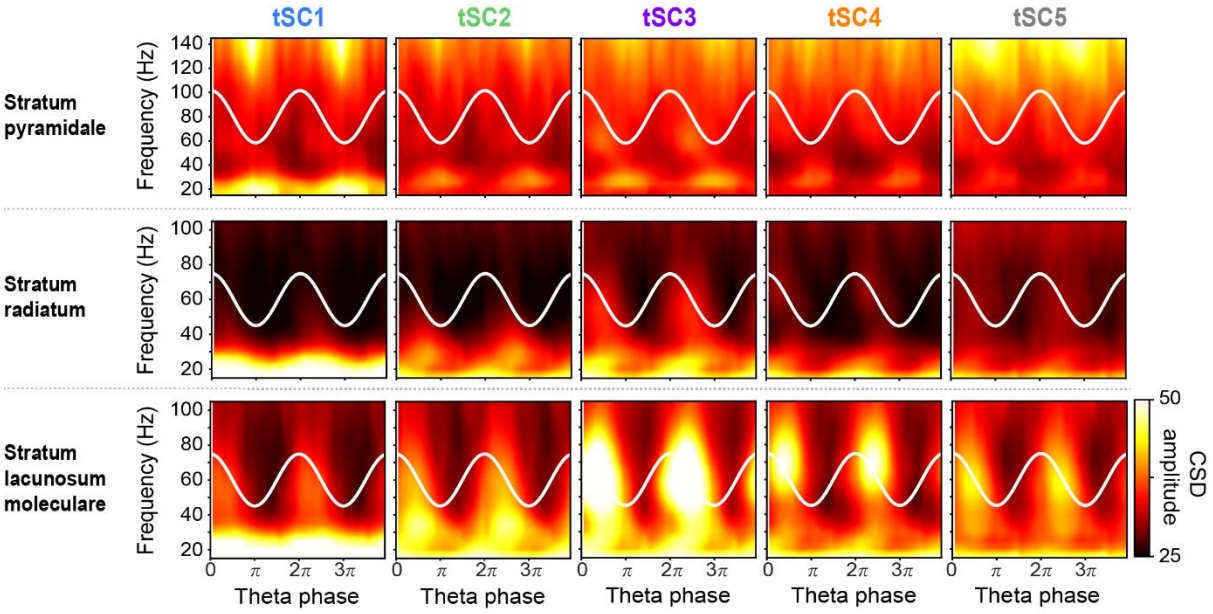

Supplementary Figure 17. Laminar profile of tSC-related currents

Mean amplitude of supra-theta CSD signals as a function of theta phase in different layers of the CA1 from an example session. Theta cycles expressing different tSCs were analyzed separately. Note that the upper limit of the y-axis is extended in the stratum pyramidale panel to visualize fast gamma related currents. Two theta cycles are shown, indicated by the white cosine curves.

Supplementary Figure 18

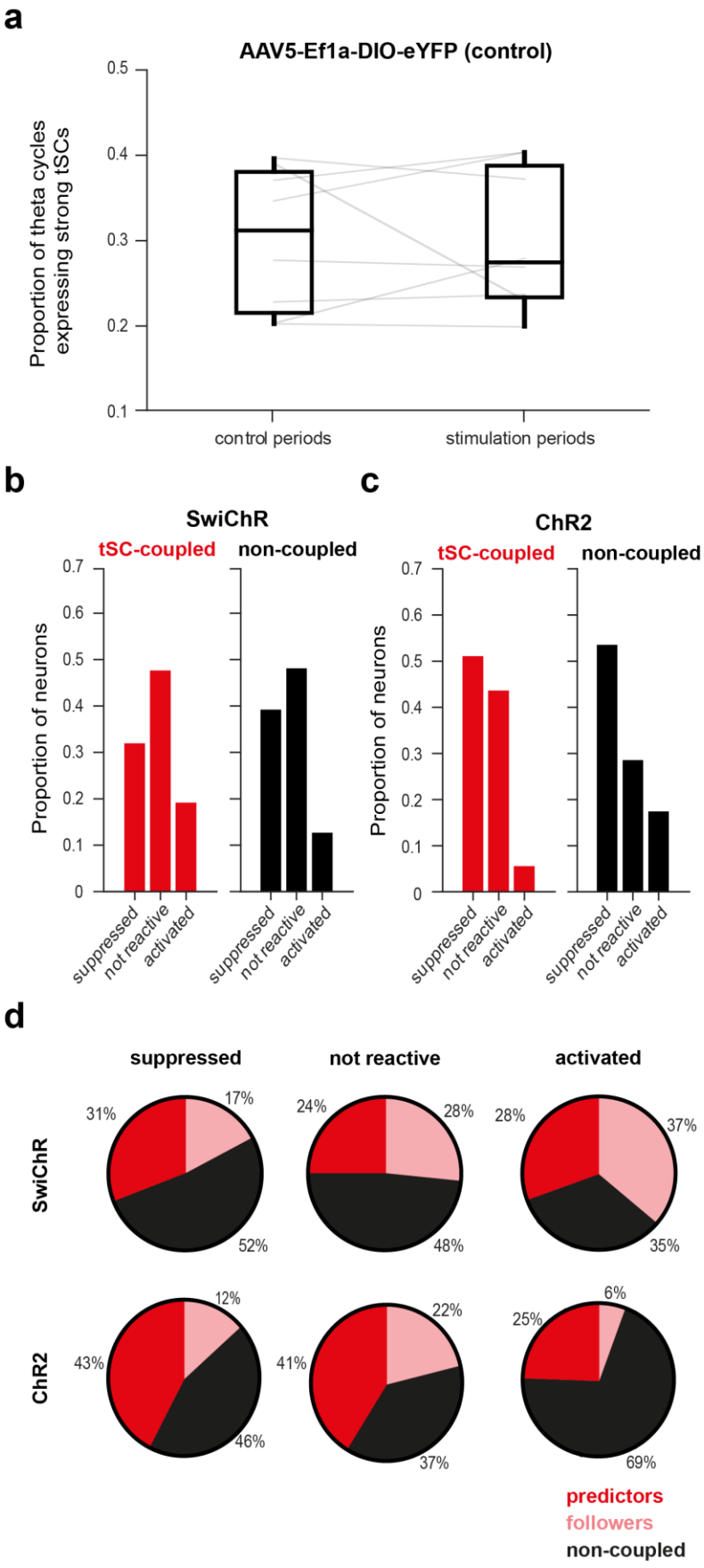

Supplementary Figure 18. The impact of optogenetic manipulations of the hippocampo-septal pathway on MS neurons with different tSC-coupling.

a Proportion of theta cycles expressing tSCs during stimulation and control periods in mice injected with the eYFP control virus. Gray lines connect data points belonging to the same recording sessions (n = 8). Boxes and whiskers show median, interquartile range and non-outlier range. Two-sided Wilcoxon signed-rank test, p = 0.7422. **b** Proportion of MS neurons that showed more than 10% firing rate increase or decrease upon SwiChR-mediated inhibition of the hippocampo-septal projections, shown separately for tSC-coupled and non-coupled MS neuron populations. **c** Same as in panel **a** during optogenetic activation of the hippocampo-septal projections. **d** Proportion of tSC-coupled 'predictor' neurons (maximal tSC phase-locking strength realized by negative time lags), tSC-coupled 'follower' neurons (maximal tSC phase-locking strength realized by positive time lags) and not tSC-coupled neurons among the activated, not reactive and suppressed groups of MS neurons. Source data are provided as a Source Data file.

Supplementary Figure 19

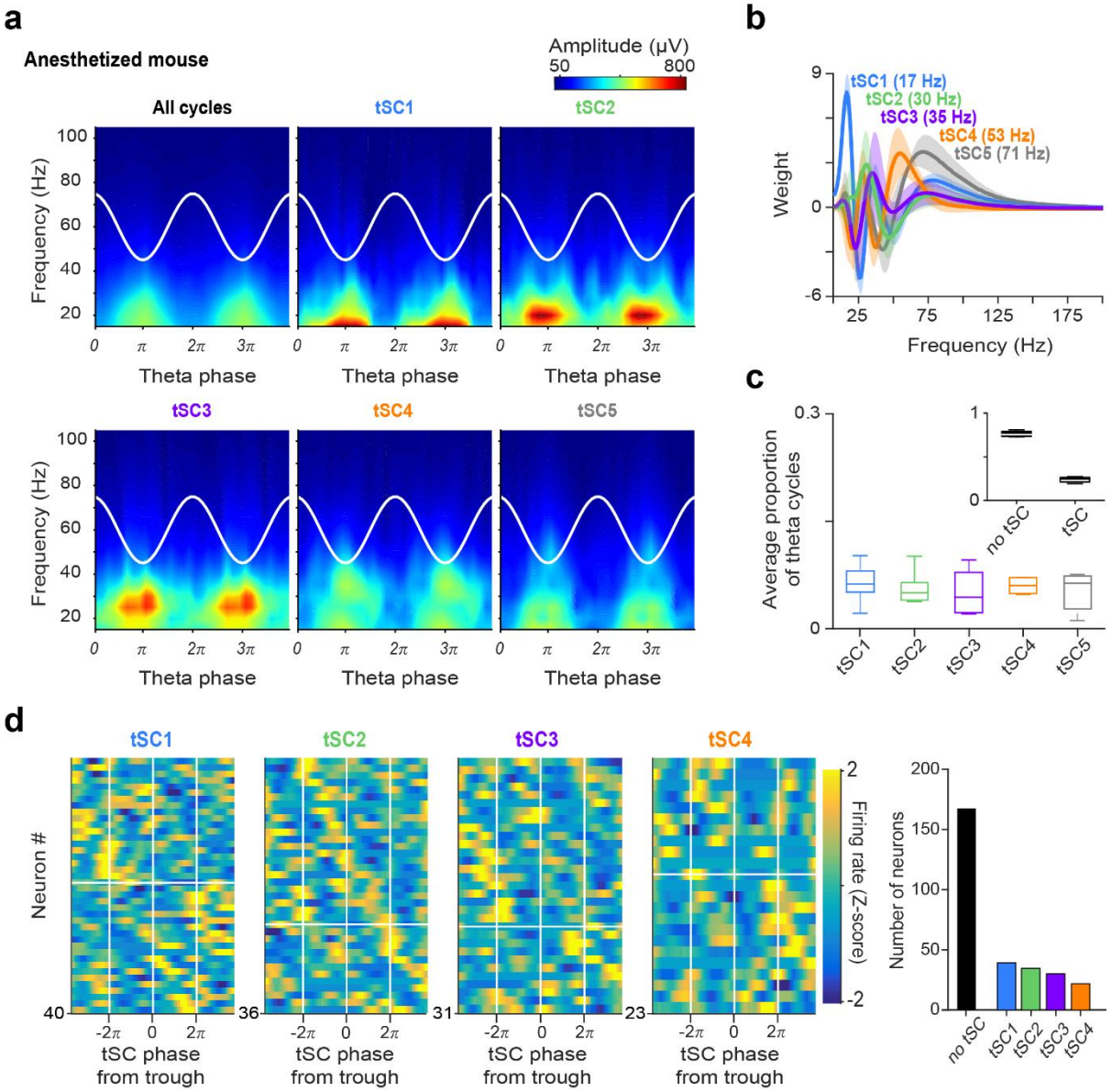

Supplementary Figure 19. MS neurons show phase coupling to hippocampal tSCs in anesthetized mice

a Mean amplitude of supra-theta spectral components as a function of theta phase was computed from the raw LFP of an example session of an anesthetized mouse, for all cycles (top left) and for cycles strongly expressing a given tSC. Two theta cycles are shown, indicated by the white cosine curves. **b** Average tSCs spectra in anesthetized mice (n = 5). Error shades show the standard error of the mean. Peak frequencies are shown in the brackets. **c** Proportion of theta cycles expressing each tSC (n = 5 sessions). Insets show the proportion of theta cycle expressing any of the tSCs. Boxes and whiskers show median, interquartile range and non-outlier range. **d** Left, Z-scored phase histograms of all tSC-coupled MS neurons, sorted into

four groups based on the tSC they are coupled to (blue, low firing rate; yellow, high firing rate). Zero phase corresponds to tSC troughs (white vertical lines). Cells within each group were sorted by their preferred phase in two blocks: top, cells with maximum firing rate before the most negative tSC trough; bottom, cells with maximal firing after the most negative tSC trough. Right, number of neurons phase-coupled to a given tSC. Source data are provided as a Source Data file.

Supplementary Figure 20

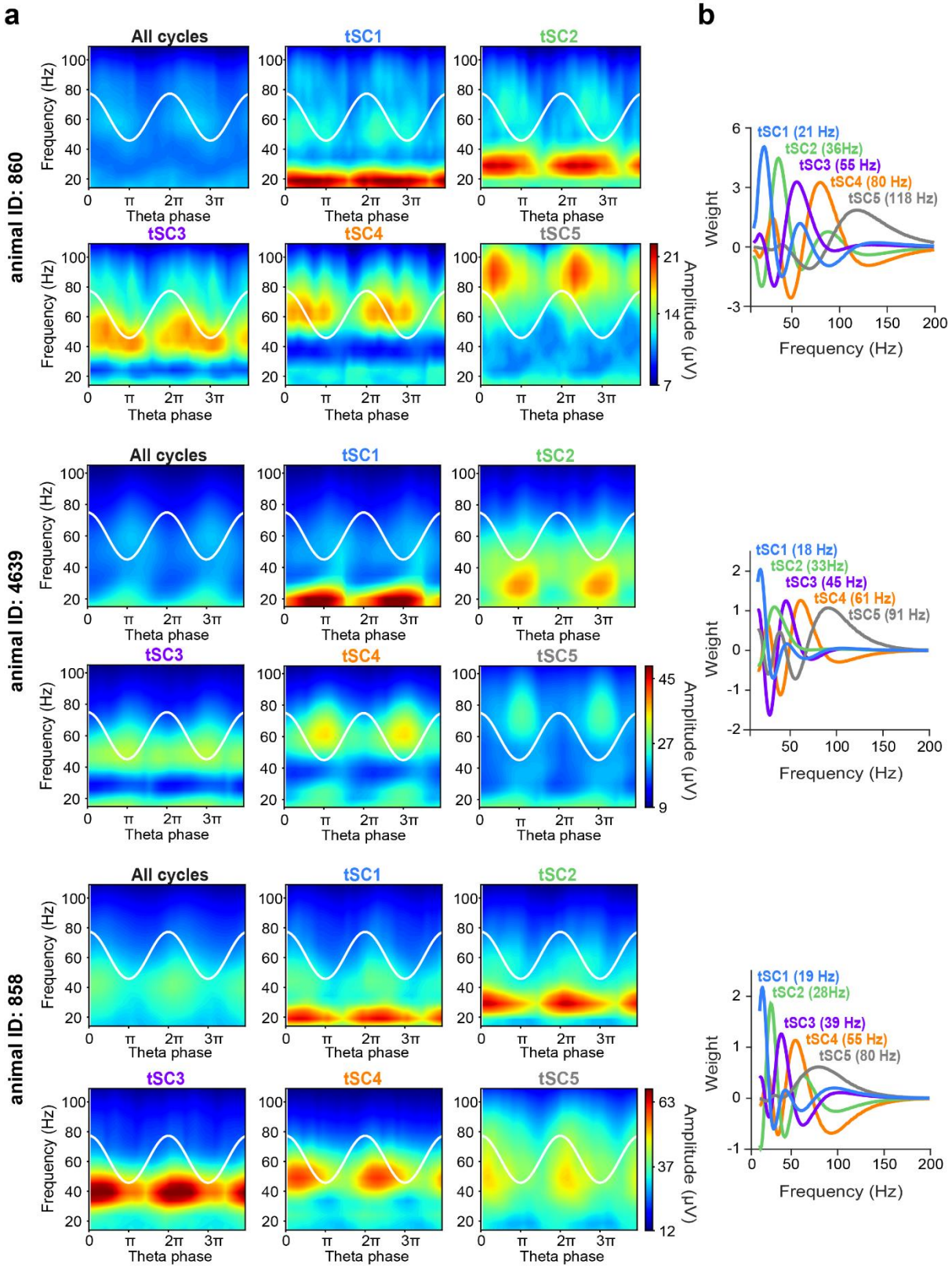

Supplementary Figure 20. Theta nested spectral components in the ventral hippocampal LFP of mice in an elevated plus maze.

a Mean amplitude of supra-theta spectral components as a function of theta phase in three example mice, for all cycles (top left) and for cycles strongly expressing a given tSC. Two theta cycles are shown, indicated by white cosine curves. **b** The frequency content of each tSC in the same example sessions as in panel **a**. Peak frequencies are shown in brackets. Data downloaded from https://datadryad.org/stash/dataset/doi:10.7272/Q6ZP44B9[84].